Synthesis, characterization, and performance of g-C3N4 based materials decorated with Au nanoparticles for (photo) catalytic applications

Pablo Isaí Jiménez-Calvo

UNIVERSITÉ DE STRASBOURG

ÉCOLE DOCTORALE DES SCIENCES CHIMIQUES

Institut de Chimie et Procédés pour l'Energie, l'Environnement et la Santé

ICPEES / CNRS UMR-7515

THÈSE

présentée par:

Pablo Isaí JIMENEZ-CALVO

soutenue le : **17 juin** 2019

pour obtenir le grade de : **Docteur de l'Université de Strasbourg**

Discipline/ Spécialité : Chimie / Chimie - Physique des Matériaux - Photocatalyse

Synthèses, caractérisations et performances de matériaux à base de g-C_3N_4 décorés avec des nanoparticules d´Au pour des applications (photo) catalytiques

Synthesis, characterization, and performance of g-C_3N_4 based materials decorated with Au nanoparticles for (photo) catalytic applications

THÈSE dirigée par:

Mme Valérie KELLER-SPITZER Directrice de Recherche, CNRS/Université de Strasbourg UMR-7515

RAPPORTEURS:

M. Adélio MENDES Professeur, University of Porto, Portugal

M. Giuseppe MARCI Professeur, University of Palermo, Italy

EXAMINATEURS:

M. Paolo FORNASIERO Professeur, University of Trieste, Italy

M. Dan REN Chercheur Post-Doctoral, EPFL, Switzerland

INVITÉ:

Mme Valérie CAPS Chargée de Recherche, CNRS/Université de Strasbourg UMR-7515

"Every great and deep difficulty bears in itself its own solution.
It forces us to change our thinking in order to find it."

Niels Bohr

To my wife, parents and siblings

Acknowledgments

I sincerely acknowledge my thesis supervisor, Dr. **Valérie Keller-Spitzer**, for trusting me with this exploratory research project and for always encouraging me to think independently. She was and is an excellent project manager supporting me daily by handling, with care, all kinds of obstacles (administrative, working-related, and scientific ones). Her efforts during this journey have allowed me to complete this thesis and to expand and refine my critical reasoning. I also extend my thanks to Dr. Cuong Pham-Huu (previous ICPEES director) for his hospitality at the institute and for the private discussions we had throughout my stay.

I thank the jury members Prof. Adélio Mendés, Prof. Giuseppe Marci, Prof. Paolo Fornasiero, and researcher Dr. Dan Ren for taking their time to read, evaluate, and discuss this work. I am also grateful for their availability to travel to Strasbourg to attend my thesis defense.

I am grateful to God for providing me with the opportunity to work in such a fantastic professional environment surrounded by remarkable people. To my parents, whom I consider the most influential mentors of my life, I am and will continue to be a reflection of their endless love for me, their courage, grace and sacrifice have defined the man I am today.

I am also thankful to Dr. Valérie Caps and Dr. Thomas Cottineau for their significant scientific contribution within this project, without their critical advice and high standards, this thesis would not have been possible. A sincere thanks to Dr. Corinne Petit and Dr. Sylvie Begin for the opportunity to pursue a teaching assistantship (TA) within École Européenne de Chimie, Polymères et Matériaux (ECPM) during three academic years. I also thank Caroline Schmitt and Patrick Filizian for trusting me a significant amount of Micro Projects and Industrial missions. Your trust has allowed me to continue developing my pedagogical, leadership and management skills. I will also be forever grateful to Dr. Clément Marchal for introducing me and training me in the field of Materials Chemistry. Dr. Nicolas Keller, I thank for his support and for his continuous interest in my project (I appreciate our informal and thought-provoking chats). Thanks to my office colleagues with whom I shared most of the ups and downs of our everyday life: Marisa Rico, Irene Gonzales, Geoffrey Gerer, Loïc Michel, Florian Gelb, Thomas "*Faveto*", and Steven Bardey ("*les cabrones*"). To the graduate colleagues in photocatalysis field: Joanna Wojciechowska, Claire Holtzinger, Yige Yan, Armelle Pérard, Pauline Barrois, Marvin Motay, Urelle Biapo, Alessio Ghisolfi, Ana Amoros, Hamza El-Marouazi, JP, and to all interns (specifically Cerise Robert), and all others that have been there for me in times of need.

To the University of Strasbourg (Unistra), the International Doctoral Program (PDI), and the Initiative of Excellence Program (IdEx) French program I am thankful for their financial support and for granting me the Ph.D. fellowship that allowed me to pursue my studies in such a vibrant and excellent working environment. To Mme. **Joëlle Hube**, my sincere thanks for her administrative and personal (practical and smart) pieces of advice during the many stages on my project and life. I am also profoundly thankful to Mme. **Virginie Herbasch**, her efficient support and work ethic allowed me and other colleagues to organize

several successful scientific events in Strasbourg, namely: Climate Change Conference and EUCOR Colloquium on Energy Transition in collaboration with Swiss and German universities of the region. For the Spring sessions and meetings with PDI delegates, I had a great time helping for these events. A special and heartfelt thanks to my Ph.D. mate **Raquel López** ("tronca") for everything.

I also thank Prof. Christophe Colbeau-Justin and Dr. Mohamed Nawfal for their welcoming and training on TRMC at Laboratoire de Chimie-Physique (Université Paris-Orsay).

To **Prof. Michael Graetzel** for being enthusiastic about participating in the Climate Change Conference I co-organized in 2016 and for allowing me the opportunity to present a seminar last February (2019) to his Solar Fuels group at École Polytechnique Fédérale de Lausanne (EPFL). To **Dr. Dan Ren** for our new collaboration on Photoluminescence asset and for including us in a European consortium to possibly continue doing research together.

To Institut de Chimie et Procédés pour l'Énergie, l'Environnement et la Santé (ICPEES) staff, especially Mme. **Véronique Verkruysse**, which was always been an incredibly generous person that would never hesitate to extend her help to us in times of need, I have no words to express how grateful I am to her for everything she has done for me. To Mme. Agnes Orb, Mme. Catherine Kientz, Mme. Francine Jacky, Mme. Sylviane Bronner for their constant support and patience in helping me fill out all the necessary administrative paperwork, especially missions and reimbursements. Big thanks to the technicians for their experimental support and mentoring, Vasiliki Papaefthimou (XPS and UPS), Thierry Dintzer (XRD, SEM, and IT), Christophe Melárt (FT-IR, TGA, and Raman), and Dr. Ksenia Parkhomenko (BET). A special thanks to Alain Rach, the "*McGuiver*", he was incredibly helpful during daily technical problems, with my frustration when using NH_3 in the furnace.

Thanks to the external support: Dris Ihiawakrim for TEM, ED, and mapping measurements, Marc Lenertz for XRD measurements, Christophe Lefèvre for XRD discussions (IPCMS), Anne Boos for ICP analyses (IPHC) and Mélanie Legros for zeta potential analyses (ICS).

HIIT training, every Tuesday and Wednesday, over the last 3.5 years has been crucial to keeping me motivated and healthy and have been the fuel to help me stay productive during many afternoons. Thanks to Sergey Pronking the "*sensei*", Mark ("*hombre*"), Houseinnou ("*poto*"), Francois, Viktoria, Marketa, Sophie, , and to all other participants.

Thanks to the institutions that supported me financially throughout the Ph.D. Your funding has allowed me to participate in Summer School (SunMed European Project), International congresses (Royal Society of Chemistry (RSC) and Société Chimique de France (SCF)), and for National congresses (PDI). Also, thanks to PDI and Strasbourg Eurometropole for extending my Ph.D. contract thus allowing to finish pending experiments and publications.

To the international community, for the exciting moments ("*Ticos*, *Français*, *Italiani*, *Españoles*, *Catalanes*, *Portuguese*, *Chilenos*, *Brasileiros*, *Chinese*") *e.g.*, picnics, trips, tandems, cafés and others. Special thanks to Diego Bastos which help me on Sketchup designs and our outdoors rock climb sessions in Alsace spots that made me stronger.

Publications

1- **Influence of gas atmosphere during synthesis of g-C_3N_4 for enhanced photocatalytic H_2 production from water on Au/g-C_3N_4 composites.** P, Jiménez-Calvo*, C, Marchal, T, Cottineau, V, Caps, V, Keller*. ***J. Mater. Chem. A,*** 2019, **7**, 14849-14863. DOI: 10.1039/C9TA01734H

2- **Synergistic effects between titania and carbon nitride in the gold-catalyzed PROX reaction.** P, Jiménez-Calvo, L, Michel, V, Caps, V, Keller. To be submitted

3- **Low content of gC_3N_4 on Au/TiO_2 (P25)-gC_3N_4 composite enhanced sensitization of TiO_2 absorption for remarkably H_2 production from water under visible-light.** P, Jiménez-Calvo, V, Caps, V, Keller. To be submitted

4- **Advances in plasmonic photocatalytic H_2 production via water-splitting on TiO_2 and g-C_3N_4 based materials amongst state-of-the-art H_2 technologies A mini review.** P, Jiménez-Calvo, V, Caps, V, Keller. To be submitted (invited)

Conferences

Oral communications

Graetzel´s group, École Polytechnique Fédérale de Lausanne (EPFL) (Switzerland), 2019

Matériaux – Strasbourg (France), 2018

2nd Advanced Materials/Processes for Environment, Energy & Health (Canada), 2018

C'Nano - The Nanoscience Meeting – Lyon (France), 2017

Doctoral School of Chemical Sciences (EDSC), Unistra, welcome day (France), 2017

International Ph.D. program (PDI), Unistra, welcome day (France), 2016 and 2017

Posters

2nd Advanced Materials/Processes for Environment, Energy & Health (Canada), 2018

10th European Solar Chemistry & Photocatalysis: Environmental Applications (Spain), 2018

Energy Transition: 1st EUCOR Colloquium of young physicists and chemists (France), 2017

Groupement de Recherche (GDR) Solar Fuels (France), 2016

Erice Summer School, Materials for Energy and Sustainability (Italy), 2016

Table of Contents

List of Abbreviations

g-C_3N_4 = graphitic carbon nitride
TiO_2 = titanium dioxide
Au = gold
NPs= nanoparticles
NTs = nanotubes
M = Melamine
DCDA = Dicyandiamide
NC= nanocomposites
SC= semiconductor
H_2 = hydrogen
N_2 = nitrogen
Ar = argon
NH_3 = ammoniac
CO = carbon monoxide
CO_2 = carbon dioxide
CH_4 = methane
H_2O = water
TEOA = Triethanolamine
SPR = surface plasmon resonance
CBM = Minimum conduction band
VBM = Maximum conduction band
AQY = Apparent quantum yield
IQY = Internal quantum yield
HER = hydrogen evolution reaction
OER = oxygen evolution reaction
CSP = concentrated solar power
PVD = physical vapor deposition
CVD = chemical vapor deposition
Syngas = synthesis gas
SR = steam reforming
WGS = water gas shift
PSA = pressure absorption swing
POX = partial oxidation
Pt = platinum
PEC = photoelectrochemical cell
CPOX = catalytic partial oxidation

Roman symbols

A	Absorbance (%)
R	Reflectance (%)
c	Speed of light (m s^{-1})
E_f	Fermi energy level
E_{redox}	Redox potential
l	optical distance in the reactor
q_p	Photon flux
$q_{p(Abs)}$	Photon flux absorbed by the material

Greek symbols

λ	Wavelength
θ	Bragg´s angle
τ	Crystallite mean size
P (λ)	Irradiation power
E (λ)	Photon energy
A (λ)	Absorbance of the nanoparticle suspension
ε_0	Metal permittivity
ω_p	Plasmon pulsation

List of Figures

List of Tables

General Introduction

A) Energy transition

The current economy model has led to a vast consumption of modern commodities. This trend started with industrial revolution when society shifted to a fossil fuel-based economy. The shift led to decades of industrial prosperity fuelled by petroleum which resulted in an acute dependency on this limited resource. The prosperity which society has enjoyed did not slow down despite M. King Hubbert prediction and warnings about the imminent depletion of Earth's oil reserves [1]. The prediction gained veracity with the first oil crisis from 1973 to 1979 [2,3], and since then CO_2 emissions continue to rise unattained. The burn of fossils fuels and subsequent release and accumulation of CO_2 created the well-known greenhouse effect which has caused the rise of Earth's temperature with unforeseeable consequences [4]. In recent decades this has stirred the debate on the necessity of changing society's primary energy supply, a debate which has culminated in the making and promotion of new laws, *e.g.* Kyoto protocol [5] and Paris agreement [6]. With this context, the adopted system of transportation and the different industrial processes that keep using fossil fuels as a raw material have to be replaced by other means, namely renewable sources, to guarantee a livable Earth.

B) Fossil *vs.* solar fuels

Fossil fuels are predominantly rich-energy, a gallon of gasoline has an energy equivalent of 121.8 MJ. This energetic density is a great asset for storing fossil fuels in a proper volumetric space of containers and tanks that consequently facilitates its transportation. Nevertheless, the main drawback relies on the reserves lifetime that depends on a variety of factors, mainly the management of the industrialized countries in how fast they want to transform them and in which volume of production. This scenario, clearly demonstrate the need of substituting part of the fossil fuels by any other means. Renewable energies are considered a potential avenue for substituting the fossil fuels [6–8]. Among the developed and existent renewable energies such as ocean currents, wind, hydroelectric, biomass, geothermal and solar type, solar energy is the most promising alternative due to the use of the most powerful source of energy known: the sun [3,7,9]. Within the solar energy technologies consisting of converting sun-light, one can highlight photocatalysis. Photocatalysis is considered as a promising technology for artificial photosynthesis processes. The "*artificial photosynthesis*" term arises from the idea of mimicking the natural photosynthesis to generate energy-storage molecules from CO_2 and water using sunlight, the so-called solar fuels. Artificial photocatalytic systems to obtain solar fuels processes must accomplish several criteria to be feasible to implement. The desirable (photo) catalytic material features are sustainability, simple synthesis process, moderate cost, easy scalable process, and high quantum yield and efficiency. However, as the best of our knowledge, there is no such existent material that fulfilled all the mentioned requirements. To achieve such process a sustainable visible light-driven photocatalyst, based on multicomponent heterostructures, is desirable.

Thesis objectives

The general objective of this research project is to design, synthesize and engineer novel carbon nitride g-C_3N_4 based 2D nanocomposites with higher activity than the state-of-the-art materials for (photo) catalytic applications by applying three strategies:

(1) Tuning g-C_3N_4 synthesis **atmosphere**

a) Reductive (H_2, NH_3), oxidative (Air), and inert (Ar, N_2)

(2) Coupling g-C_3N_4 with TiO_2 to obtain **TiO_2-gC_3N_4 heterojunction** composites

a) Varying TiO_2-gC_3N_4 relative **proportion** under two **atms** (Air and NH_3)

b) Modifying TiO_2 morphology, 0D (P25 NPs) and 1D (NTs)

The materials synthesize on the two strategies were decorated with Au NPs with constant loading (0.3 wt. %) to form an Au/SC junction to evaluate the chemical differences of the several supports. The purpose of using Au NPs onto the supports relies on two main objectives **(1)** to use a broader part of the solar spectra (visible) by photo activating the Au/SC junction and **(2)** to evaluate the performance of M/(SC1-SC2) heterostructures by using H_2 evolution as model reaction with assistance of a sacrificial agent, to take advantage of the Au NPs functionalities:

a) Co-catalytic properties

b) Electron trapping

c) Surface plasmon induced effect (SPIE)

Globally, the heterojunction coupling between two SCs and the engineer M/(SC1-SC2) junction provides several e^-/h^+ pathways. The advantages of the heterojunction relies on a new energy band diagram, where VB and CB of g-C_3N_4 are above the VB and CB of TiO_2 (staggered type) allowing an upward / downward band bending resulting to the migration of charge carriers on the opposite direction, as analogy of Z-scheme. This allows a better e^-/h^+ spatial separation on several parts of the heterojunction to retard the charges recombination and to prolong the lifetime of free e^- and h^+ and the TiO_2 photosensitization.

A) Strategy

This project envisages the synthesis, characterization, and activity performance of novel Au/g-C_3N_4 and Au/TiO_2-gC_3N_4 based nanocomposites. Two approaches were carried out.
(1) The first study comprises the optimization of g-C_3N_4 synthesis by studying the influence of gas atmosphere during synthesis with the purpose of enhancing photocatalytic H_2 production performance of Au/g-C_3N_4 binary composites. The best synthesis atmospheres were then chosen for the synthesis of the following ternary Au/TiO_2-gC_3N_4 heterostructures.

(2) The second study consisted in the synthesis of TiO_2-gC_3N_4 heterojunction systems to obtain a good quality contact between the two semiconductors in function of their proportion and synthesis atmosphere used. Generally, the quality of the intimate interfacial contact defines the efficiency of hybridization of the orbitals, the creation of new mid-band gaps to enhance the visible absorption, the lifetime and transport of photogenerated species, and the creation of new pores to enhance the diffusion paths of the e^-/h^+. For this purpose, two different morphologies of TiO_2 were chosen, nanoparticles (NPs) and nanotubes (NTs), respectively. For both systems g-C_3N_4-TiO_2 (NPs) and g-C_3N_4-TiO_2 (NTs) two atmospheres of synthesis were used, Air and NH_3.
Those different photocatalytic nanomaterials were evaluated towards H_2 production from water under both solar and visible light irradiation using unusual low amount of sacrificial agent (1% vol. Triethanolamine) and for some of them towards preferential oxidation reaction (PROX). From a fundamental point of view, in-depth structure-activity studies were performed at different steps in order to correlate structural, morphological, optical and electronic properties of the nanocomposites to their (photo) catalytic activities.

B) Thesis outline

This thesis describes investigations concerning the design and synthesis g-C_3N_4 based nanomaterials decorated with Au NPs applied in mainly photocatalytic applications but also catalytic and correlations with their physico-chemical properties.

Chapter 1 comprises the literature review. A bibliographic research study presents an overview and an assessment of the current progress of energy context, recent state-of-the-art of hydrogen production technologies, and semiconductor photocatalysis, specifically for g-C_3N_4, TiO_2, and Au NPs materials on their applications, specifically for two model reactions mainly photocatalytic H_2 production and in lesser extend thermal PROX catalysis.

Chapter 2 presents the g-C_3N_4 and Au/g-C_3N_4 materials are introduced to pointing out the effect of atmosphere during polycondensation synthesis. This study focused on the influence of the gas atmosphere (reductant, inert, and oxidative) during g-C_3N_4 synthesis, which appeals a gap in the research community (this study was recently published in Journal of Materials Chemistry A) and serve as reference to modulate the electronic properties of g-C_3N_4 in function of the desire application. An in-depth analysis on the physico-chemical was carried out with the purpose to correlate the distinctive physico-chemical properties.

Chapter 3 introduces TiO_2(P25 NPs)-gC_3N_4 and Au/TiO_2(P25 NPs)-gC_3N_4 binary and ternary composites, which were in-depth characterized using 12 techniques and evaluating the performance activity by using the same model reaction than **chapter 2**, photocatalytic H_2 production. The experimental strategy for this chapter was based on evaluating the influence of the relative proportion of TiO_2 (P25 NPs) and g-C_3N_4 SCs into the TiO_2 (P25 NPs)-gC_3N_4 composite while changing the atm synthesis (Air and NH_3) (major finding from **chapter 2**).

Chapter 4 shows TiO_2 (NTs)-gC_3N_4 and Au/TiO_2 (NTs)-gC_3N_4 binary and ternary composites, which were in-depth characterized using 8 techniques and evaluating the performance activity by using the main model reaction of the thesis: photocatalytic H_2 production, used on **chapter 2 and 3**, and additional evaluation was performed by using catalytic CO conversion. The experimental strategy for this chapter consisted in assessing the modification of TiO_2 morphology, since **chapter 3** used granular TiO_2 (P25 NPs), by using TiO_2 (NTs). Even though, TiO_2 (NTs) synthesis involves an additional step, besides the wet impregnation followed by the thermal polycondensation step to obtain TiO_2 (NTs)-gC_3N_4, the idea was to increase the specific surface area, that commonly is proportional related with activity, and also to take advantage of 1D TiO_2 (NTs) configuration that provides a direct migration of the photogenerated species to improve spatial separation.

C) References

[1] M.K. Hubbert, Energy from Fossil Fuels., Science. 109 (1949) 103–9. doi:10.1126/science.109.2823.103.

[2] M. Grätzel, Photoelectrochemical cells, Nature. 414 (2001) 338–344. doi:10.1038/35104607.

[3] The Future of Solar Energy | MIT Energy Initiative, MIT Energy Initiat. (2015). http://energy.mit.edu/publication/future-solar-energy/ (accessed May 10, 2018).

[4] C.A. Grimes, O.K. Varghese, S. Ranjan, Light, Water, Hydrogen. The solar generation of hydrogen by water photoelectrolysis, Springer US, Boston, MA, 2008. doi:10.1007/978-0-387-68238-9.

[5] S. Oberthür, H. Ott, The Kyoto Protocol : international climate policy for the 21st century, Springer, 1999. https://books.google.fr/books/about/The_Kyoto_Protocol.html?id=-qp7Wt9GvccC&redir_esc=y (accessed May 10, 2018).

[6] I.E.A. (IEA), Key World Energy Statistics 2016, Stat. Rep. (2016) 24, 80. https://www.iea.org/publications/freepublications/publication/key-world-energy-statistics.html (accessed December 28, 2016).

[7] R. Perez, M. Perez, A Fundamental Look at Supply Side Energy Reserves for the Planet, Int. Energy Agency Sol. Heat. Cool. Program. Sol. Updat. 50 (2009) 4–5. https://www.iea-shc.org/data/sites/1/publications/2015-11-A-Fundamental-Look-at-Supply-Side-Energy-Reserves-for-the-Planet.pdf (accessed May 11, 2018).

[8] P. Kruger, Electric power required in the world by 2050 with hydrogen fuel production—Revised, Int. J. Hydrogen Energy. 30 (2005) 1515–1522. doi:10.1016/J.IJHYDENE.2005.04.003.

[9] D.G. Nocera, The Artificial Leaf, Acc. Chem. Res. 45 (2012) 767–776. doi:10.1021/ar2003013.

Chapter 1

Literature review

A) Energy context

Mankind is facing an energy and environmental crisis simultaneously due to mainly two factors: growth population and the dependency on fossil fuels. The population growth is forecast to increase by 40-50% within the next 50 years, rising to more than 9 billion people by 2050 [1,2]. This intensive growth brings two relevant issues. First, it will increase the energy demand, 28 TW by 2050 as unprecedented energy demand. Second, it will faster the depletion of fossil fuels reserves on earth (coal and natural gas [3]).

To date, the prevalent economic model has a great impact in the life-cycle standards in society. The life-cycle framework involves a vast consumption of modern commodities. This tendency originated back on the flourish industrial revolution when society adopted the fossil fuel-based economy. In this context, the use of petroleum started to diversify in the transport and industrial processes applications and became rapidly the popular fuel. Despite of the great prosperity of petroleum and the implementation of new ways of transports and products, part of the community kept skeptical. It was not until, M. King Hubbert predicted and warned about the imminent depletion of available Earth´s oil reserves [4], due to its formation period that takes too many years in Earth´s crust [5,6]. The prediction gained veracity with the first oil crisis from 1973 to 1979 [7,8], and since then CO_2 emissions continue to rise unattained [9,10] given a significant increase of global surface temperature of 0.9 °C at 2020 [11] according to **Fig. 1.1 (inset)**. The global CO_2 emissions are associated with different sources as **Fig. 1.1** shows, but the use of fossil fuels, whether in solid or liquid state, are leading to the increase over the last decades, and consequently are responsible to climate change [12].

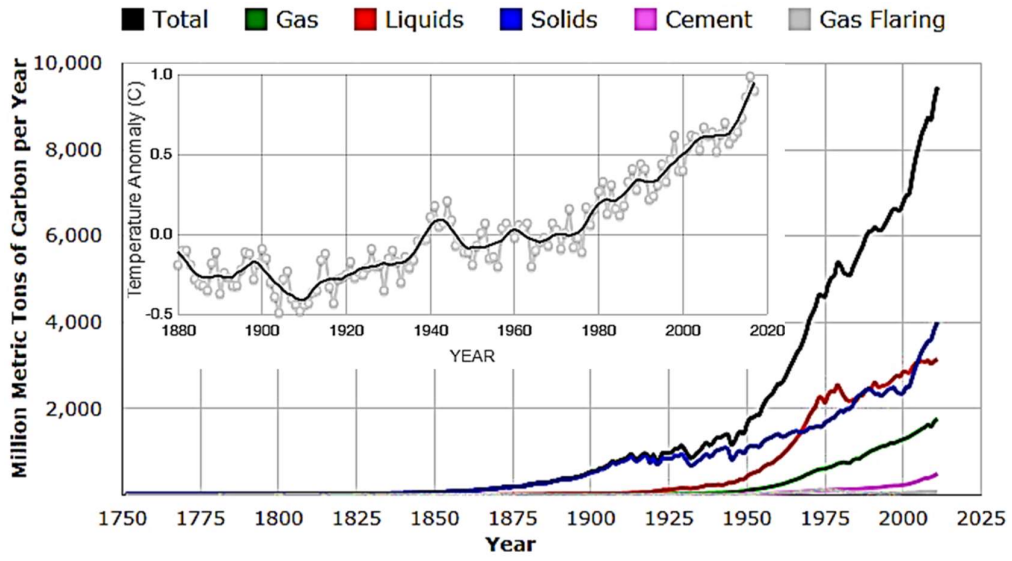

Figure 1.1. Total global carbon emissions per year in function of five sources [9,10]. Zoom) Increase of global temperature (°C) anomaly along the years [11].

Fig. 1.2 a) shows the world energy supply distribution, confirming that the major sources used are fossil fuels, *ca.* coal (40.8%) and natural gas (21.6%). **Fig. 1.2 b)** refers to the world energy reserves amount of the fossil fuels in terawatts. It is forecast, that if

the modern society continuous growing and consuming electricity as of today, in no later than 80 years these fossil fuels reserves will be depleted [1].

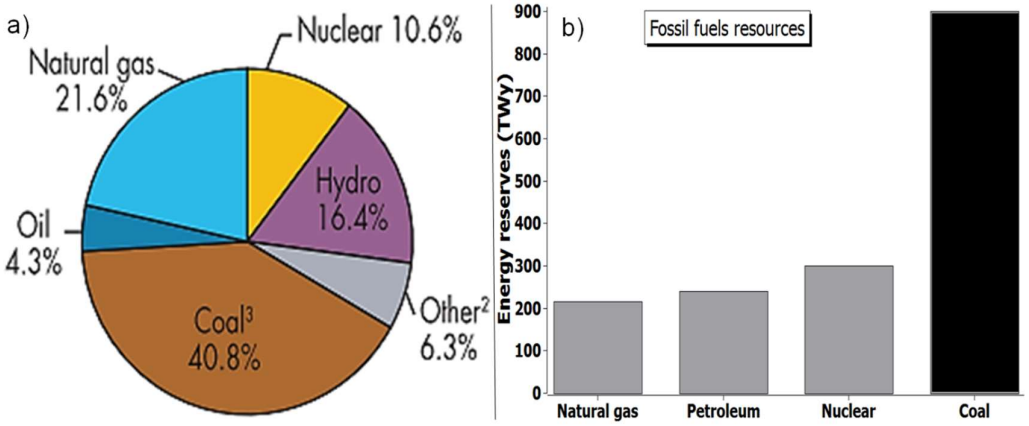

Figure 1.2. a) Distribution of world energy sources for the energy supply. b) World energy reserves amount of the fossil fuels [1,13].

In this context, renewable energies are considered a potential avenue for substituting the fossil fuel [1,7,14–16]. Among the developed renewable energies such as tides/ocean currents, wind, hydroelectric, biomass, geothermal and solar type, solar energy is the most promising alternative due to the use of the most powerful source of energy known: the sun [7,14,17] (**Fig. 1.3**). If we could capture the irradiation arriving to the land surface of the earth efficiently (36000 TW), we would need to transform approximately 0,08 % to supply the current world energy consumption (estimated 16 TW at 2009 and 28 TW at 2050). There has been many efforts and advances within a wide range of solar energy systems. One can say, that photovoltaic and concentrated solar power (CSP) are the most developed until now and consequently most accepted it.

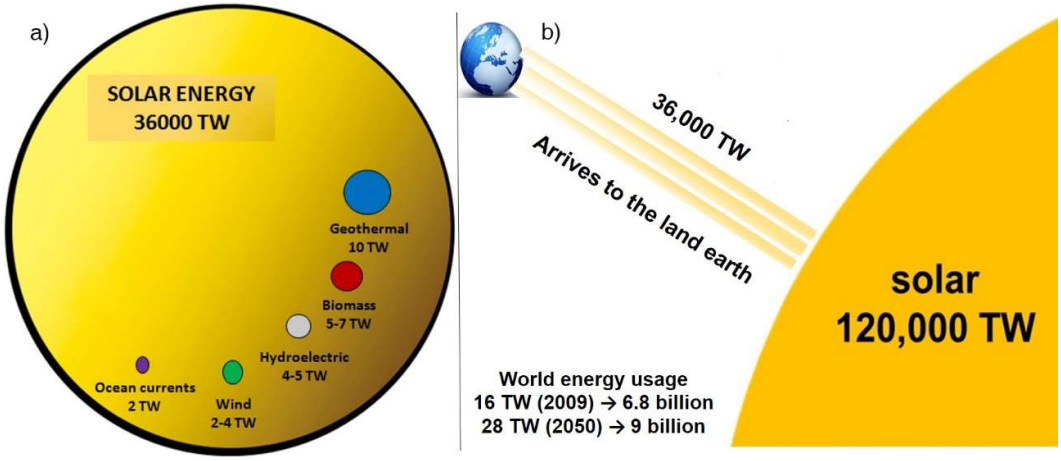

Figure 1.3. a) Renewable energies and solar energy output per year b) The solar energy potential perspective [7,14,17].

Most recently, water splitting for hydrogen generation has been studied ever since the pioneer work of Fujishima and Honda in a photoelectrocatalytic cell (PEC) with Pt deposited n-TiO_2 electrode [18]. Moreover, Bard extended the PEC water splitting to

heterogeneous photocatalysis, specifically to the suspended semiconductor (SC) nanoparticles system [19,20]. Thanks to these breakthroughs, photocatalysis was theoretically presented as the bridge technology to achieve the transformation of solar energy into chemical storage fuels over the last 4 decades. One of the main non fossil-based fuel is hydrogen, which is considered as the future energy carrier. The major problem of using hydrogen gas as fuel relies in its unavailability in nature and the lack of inexpensive of non-fossil and non-nuclear based efficient method to produce it, in addition to storage and transportation issues [21]. Consequently conversion of solar energy into H_2 (solar fuels) is considered as one of the main breakthroughs of the next decades. Photocatalysis has also risen the gold edge of Advanced Oxidation Processes (AOP) mainly in energy and environmental applications [22].

B) Hydrogen

Hydrogen is the lightest of all existing elements and is the most abundant chemical element in the universe [24]. As H_2 is lighter than air, it is not available in earth nature [25]. Whereas it is a very light and a clean burning fuel, it reacts easily with other chemical substances making it a very useful reactant. For that, H_2 can be used as fuel for either direct combustion in an internal combustion engine or in a fuel cell, only producing water as by-product, with no greenhouse gases emissions (no CO_2), making it a storable and clean fuel [26,27].

The conventional sources to produce hydrogen are natural gas, hydrocarbons and water. Nowadays, H_2 production are coming from 48% of natural gas, 30% of heavy oils and naphtha, and 18% of coal [28]. Thanks to its versatile fuel properties, H_2 is used in different industrial processes, *e.g.,* approximately half of its production is employed in the Haber-Bosch process to produce ammoniac (NH_3) as of fertilizer. Another significant area of use is in refinery for several applications, mainly cracking long-chain hydrocarbons into lighter hydrocarbons (hydrocracking process), to remove sulphur from petroleum products (hydrodesulphurization process), and to remove aromatic compounds from a mixture, especially as part of the oil refining process (dearomatisation). In a less proportion, H_2 is used as a rocket propellant [3,13,27].

B.1. Energy vector

H_2 has the highest energy density of all existing fuels and energy carriers. It is considered as the future energy carrier, due to its high massic energy content (142 kJ/mol), which is approximately two to three times higher than the conventional fossil fuels, such as methane (55 kJ/mol), propane (50.3 kJ/mol), gasoline (45.8 kJ/mol) and natural gas (47.2 kJ/mol) (**Fig. 1.4**) [13,29].

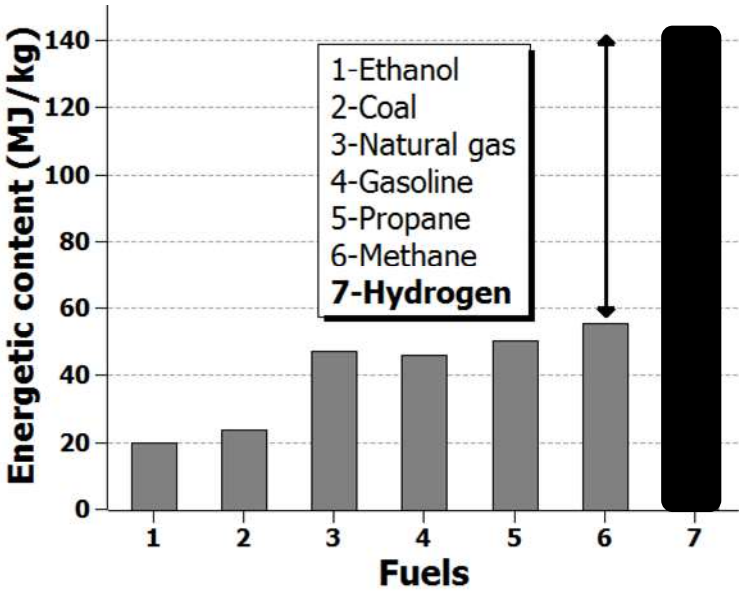

Figure 1.4. Comparison of energy density hydrogen versus conventional fuels [3,13,27,30].

The demand and use of hydrogen is expected to increase thanks to its non-polluting, inexhaustible, efficient, and cost features, associated with the so-called energetic transition from fossil-fuels toward a hydrogen economy that was mentioned after the political instability of Middle East in the eighties [31]. Thanks to this background, society is more motivated to implement hydrogen as an economy model as illustrated in **Fig. 1.5**. The ideal hydrogen production system comprises the water electrolysis method by using a clean electricity source, to guarantee an environmentally cycle.

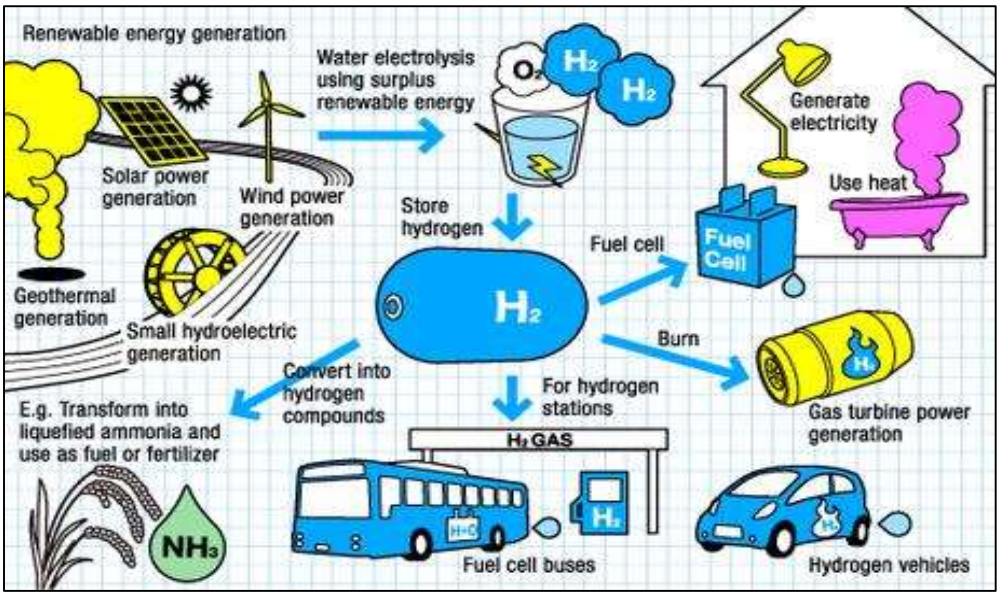

Figure 1.5. Hydrogen economy chart [32].

B.2. Production processes

Hydrogen can be produced from both conventional and alternative energy sources. The production processes can be divided according to H_2 sources, either raw materials, such as fossil fuels or renewable sources. The global hydrogen production methods are based on the use of four main sources as shown in **Fig. 1.6**. Conversion of fossil fuels is responsible for 96% of H_2 production, while electrolysis of water is responsible for the remaining 4%. The typical methods to transform fossil fuels are reforming and pyrolysis. Natural gas steam reforming is the leader and the largest employed technology to transform fossil fuels, covering almost all the hydrogen market demand with approximately 95% [33]. Consequently, steam reforming is the dominant hydrogen production process, it influences directly the production and fuel costs.

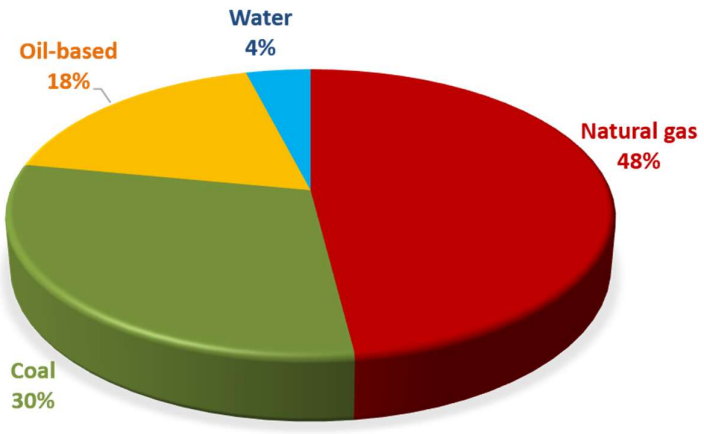

Figure 1.6. Worldwide hydrogen production sources [33].

Commonly, there are three types of conventional **hydrocarbon reforming methods**, in function of the reactant used in the reforming process:

1- Steam reforming

2- Partial oxidation

3- Autothermal reforming

In a smaller scale, renewable sources are contributing to the hydrogen production, mainly from biomass and water. The biomass processes can be divided into two types, *ca.* thermochemical and biological. Whilst, **water splitting** techniques can be classified by their input activation source:

1- Direct electrolysis (electricity)

2- Thermolysis (temperature)

3- Photolysis (light)

4- Photo-(electro) catalysis (light and/or electricity)

The hydrogen production processes that can be divided, depending on the raw sources are summarized in the scheme of **Fig. 1.7** and reviewed in this section **B.2**.

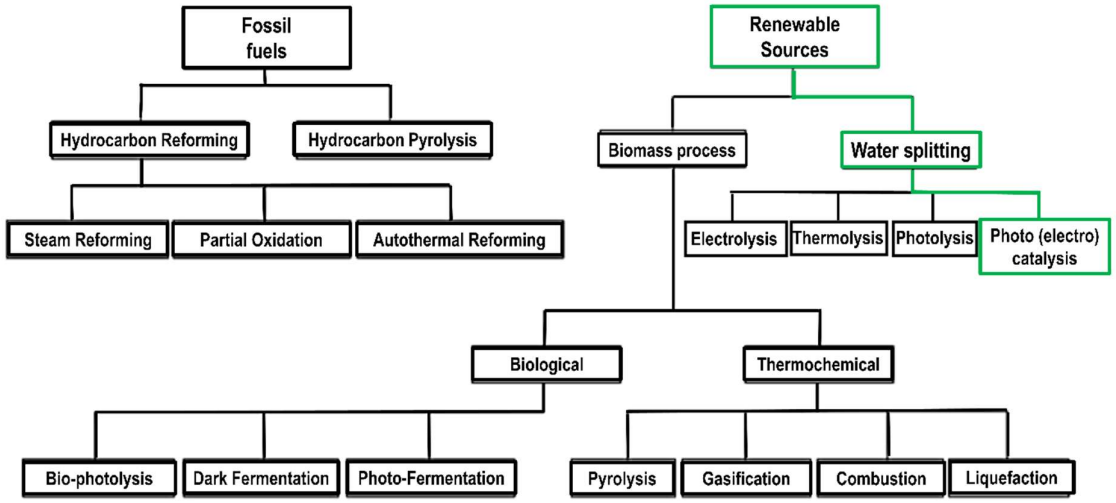

Figure 1.7. Hydrogen production processes [23,29,34].

B.2.1. From fossil fuels

B.2.1.1. Hydrocarbon reforming

The reforming process is also known as synthesis gas (syngas). Generally, the raw hydrocarbon is converted into dihydrogen (H_2), carbon monoxide (CO), carbon dioxide (CO_2), methane (CH_4), water (H_2O), and other hydrocarbons in less proportions, independently of the carbon source. Steam reforming is considered an endothermic process due to the need of an external source to eventually activate the catalyst involved and initiate the reaction. On the contrary, partial oxidation and autothermal reforming are considered exothermically processes because they do not need any external source to initiate the reaction. Moreover, they do not require a catalyst neither.

B.2.1.1.a) Steam reforming

Steam reforming (SR) is the most common and well developed method for H_2 generation, thanks to its controllable large scale reaction conditions. The reaction takes place in presence of water vapor and a catalyst (typically nickel-based) using high temperature (850 - 900°C) and medium pressure (20 – 30 bar). One important drawback of using a nickel-based catalyst is the poisoning coming from the feedstock containing sulphur traces. Therefore, a pre reforming step of desulfurization is commonly used in reforming processes [35]. The steam methane reforming (SMR) conversion efficiency comprehends 75-85%, which is significantly large in comparison with the other reforming methods. The general **equation 1** points out that the reforming can use different types of raw sources, namely, natural gas, light hydrocarbons, and light and heavy naphtha [29].

$$C_mH_n + mH_2O + catalyst \rightarrow mCO + (m + \frac{1}{2}n)H_2 \quad (1)$$

After the reformed gas mixture passes through, a heat recovery step is then conducting the Water Gas Shift (WGS) reaction (**equation 2**). CO reacts with steam to produce additional H_2, followed by CO_2 removal step and finally a purification step (methanation or pressure swing adsorption (PSA)) resulting in a high pure H_2, *ca.* 100% [36,37].

$$CO + H_2O \leftrightarrow CO_2 + H_2 \quad (2)$$

The simplest example is while using methane (simplest hydrocarbon) as feedstock material, represented schematically in **Fig. 5** and in **equation 3**.

$$CH_4 + H_2O \rightarrow CO + H_2 \quad (3)$$

B.2.1.1.b) Partial oxidation

This method can be divided in two categories in function of the use of catalyst or not, catalytic partial oxidation (CPOX) and partial oxidation (POX), respectively.

The non-catalytic POX carries out under oxygen and occurs at 1150-1500 °C (**equation 4**) to guarantee complete conversion and limits carbon by-products. This process is used to transform methane, heavy oil and coal [36].

$$C_mH_n + \frac{1}{2}mO_2 \rightarrow mCO + \frac{1}{2}H_2 \quad (4)$$

The catalytic CPOX undergoes in presence of steam and takes place at 950 °C (**equation 5**), this process is used to transform raw materials from methane to naphtha.

$$C_mH_n + mH_2O \rightarrow mCO + \left(m + \frac{1}{2}n\right)H_2 \quad (5)$$

The reason of using a catalyst in CPOX is basically to lower the operating temperatures. Yet, it has been discussed as not easy task, since the nature of reaction is exothermic. It is difficult to control the temperature with high precision [38,39].

B.2.1.1.c) Autothermal reforming

Autothermal reforming (ATR) is a hybrid method, which combines the exothermic nature of the partial oxidation and the endothermic nature of steam reforming in one process [40]. Typically, the hydrocarbon, the steam and the oxygen or air react simultaneously at resulting in reforming and oxidations reactions (**equation 6**).

$$C_mH_n + \frac{1}{2}mH_2O + \frac{1}{4}mO_2 \rightarrow mCO + (\frac{1}{2}m + \frac{1}{2}n)H_2 \quad (6)$$

The resulting product of this reaction is the syngas. The mixture of gas, already mentioned comprises H_2, H_2O, CO, CO_2, CH_4 and additionally some N_2. After, the gas mixture should follow the same steps (WGS, CO_2 removal, and the purification step) than for reforming syngas products in SR. Particularly, ATR reaction with optimal operation conditions reaches 60-75% of thermal efficiency, meaning that it is still less efficient than both SR and POX.

The following scheme (**Fig. 1.8**) allows us to compare the three main conventional reforming methods and to identify some of their operational parameters.

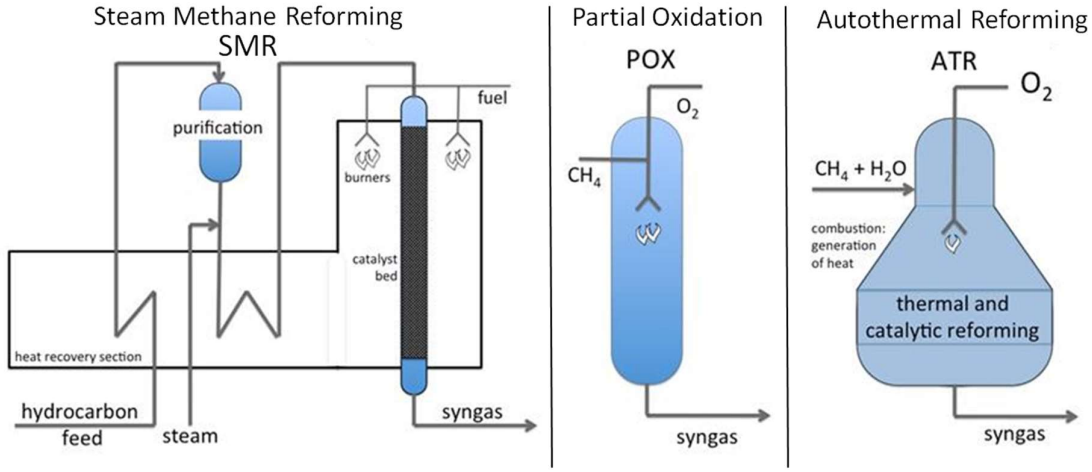

Figure 1.8. Scheme of the main existing reforming processes for syngas production.

B.2.1.2. Pyrolysis

Hydrocarbon pyrolysis consists in using hydrocarbons as raw material and only source of hydrogen. The hydrocarbon undergoes a thermal decomposition at 980 °C forming hydrogen and carbon as the following in the **equation 6**.

$$C_m H_n \rightarrow mC + \frac{1}{2} n\, H_2 \qquad (7)$$

Thermo-catalytic decomposition can take place with two different kinds of hydrocarbons, light and heavy, that present specific boiling point ranges, 50-200 and >350 °C, respectively. In this context, the hydrogen production from CH_4 pyrolysis comprises two steps, namely hydrogasification and cracking [41]. Thermo-catalytic decomposition of hydrocarbons leads to the absence of carbon oxides (CO and CO_2) formation, therefore CO_2 or CO removal secondary reactions (WGS, PrOX, etc.) are no needed [29,39].

B.2.2. From renewable sources

B.2.2.1. From Biomass

The process is based on renewable resources which are considered inexhaustible. Amongst them we can mention the use of waste materials, which can eventually solve two problems at once, waste treatment and energy production.

B.2.2.1.a) Thermochemical process

Thermochemical processes involve the transformation of biomass into hydrogen and hydrogen rich gases [42]. The conventional thermochemical processes are pyrolysis and gasification. Both methods generate products as CH_4 and CO, which can further be

processed for additional hydrogen by using steam reforming and WGS reaction. Nevertheless, biomass also can be transformed by combustion and liquefaction. However, these both techniques lead a low hydrogen production. For combustion the drawback is the pollutant emissions by-products, and for liquefaction it is the difficulty to reach controllable operational conditions in the absence of air [25].

Biomass pyrolysis generates liquid oils, solid charcoal and gases by heating at 375-525 °C and 0.1-0.5 MPa [43]. Usually it takes place in the absence of oxygen, yet, in specific cases partial combustion is necessary to provide the thermal energy needed for the process [24]. Hydrocarbon gases, including methane, are generated. WGS reaction is used as a post-method to produce even more hydrogen in reference to the hydrogen produced in the previous step. The yield of hydrogen formation from pyrolysis depends on the feedstock, catalyst, temperature, and time of residence [44].

Biomass gasification generates syngas in presence of air, oxygen, and/or steam at 500 and 1400 °C under 1-33 bar. The operational conditions depend on the plant scale and final application of the syngas produced. By the time the syngas is produced, it can be treated equally as the product gas of the pyrolysis process. For biomass gasification the parameters that influenced the hydrogen yield were identified, namely, biomass type, particle size, temperature, steam-to-biomass ratio and catalyst. In function of the selected parameters, the overall efficiency can reach 52%, which demonstrates a better conversion rate than pyrolysis [24,45].

B.2.2.1.b) Biological process

The main biological processes for hydrogen generation are direct and indirect bio-photolysis, photo and dark fermentations, and multi-stage or sequential dark and photo fermentation. Bio-photolysis uses the same photosynthesis principles in algae and in plants, with the difference of adaptation for the hydrogen production. It can be divided in two categories, in function of the microorganism capacity of producing hydrogen in one or two steps, direct and indirect bio-photolysis, respectively [46]. Direct bio-photolysis consists in using the green algae to split water molecules to hydrogen proton and oxygen via photosynthesis. The obtained hydrogen protons are transformed to hydrogen gas by hydrogenase enzyme following the **equation 8** [47].

$$2H_2O + light\ energy \rightarrow 2H_2 + O_2 \quad (8)$$

Indirect bio-photolysis consists in using cyanobacteria or blue-green algae to produce hydrogen with a carbohydrate generation intermediate step. Water and carbon dioxide in presence of light can be transformed in carbohydrates, such as glucose, and then, glucose and water in presence of light, with the collaboration of hydrogenase and nitrogenase enzymes, can produce hydrogen [25]. The conversion can be represented by following the **equations 9** and **10**.

$$12H_2O + 6CO_2 + light\ energy \rightarrow C_6H_{12}O_6 + 6O_2 \quad (9)$$

$$C_6H_{12}O_6 + 12H_2O + light\ energy \rightarrow 12H_2 + 6CO_2 \quad (10)$$

Fermentation takes place with or without oxygen (aerobic and anaerobic). Both configurations usually transformed the organic raw material into alcohols, acetone, and hydrogen, and in less proportion CO_2 by using microbial means. Fermentation is considered as an attractive method since it can start with waste materials, generating an inexpensive energy and providing an alternative waste treatment. It can be divided in function if its performance takes place in the absent or presence of light, dark and photo fermentation, respectively. Dark fermentation consists in using an anaerobic bacteria to transform carbohydrates in the absence of oxygen and without light. Taking into account glucose as reference, also acetic acid and butyric acid represent over the 80% of total end-products. The yield of hydrogen, theoretically, are 4 and 2 mol per mole of glucose in acetate and butyrate fermentation, respectively [28].

Photo fermentation consists in using non-photosynthetic or anaerobic and photosynthetic bacteria to transform organic acids, such as acetic, lactic, and butyric into hydrogen and carbon dioxide [48]. The conversion of acetic acid as reactant is presented in **equation 11.**

$$CH_3COOH + 2H_2O + light\ energy \rightarrow 2H_2 + 2CO_2 \quad (11)$$

The hydrogen yield is directly impacted by the light intensity and the time of lighting exposure, but these two parameters might have a negative impact on the light conversion efficiency. Despite of the obtainment of higher yield in illuminated conditions rather than dark, anaerobic photo-bioreactors, demand a large space to obtain a considerable conversion of hydrogen [25]. In this context, the availability of a diverse organic acids range is also another drawback that limits the extend application of this method in comparison with the existing conventional methods of hydrogen production.

Multi-stage configuration is a hybrid system comprising a non-photosynthetic or anaerobic and photosynthetic bacteria in sequence. The versatility of this configuration is based on the use of a variety of carbohydrates that can be transformed by anaerobic bacteria producing hydrogen under dark conditions while the resulting organic acids could then be transformed for photosynthetic bacteria to produce additional hydrogen. Hence, higher hydrogen productions yields are obtained while using less light [49].

B.2.2.2. From Water

Water as natural abundant source is a very attractive raw material largely present on Earth that can be used for hydrogen production through water splitting reaction. Water splitting has been described as the "dream reaction", due to its idealistic facile one simultaneous splitting step into hydrogen (H_2) and oxygen (O_2) by the activation of several means, such as electricity, temperature, light, or any other possible combination between them [21,50,51].

B.2.2.2.a) Direct electrolysis

Electrolysis is a process that uses direct electric current (DC) to drive a non-spontaneous chemical reactions [39,52,53]. It is a method used to produce hydrogen by using an

electrolysis unit or electrolyzer. It is a relative simple process, an electrical current is applied between two separate electrodes immersed in water containing an electrolyte. Whereas, the oxygen evolves (OER) at the anode and the hydrogen evolves (HER) at the cathode via the reactions in **equations 12** and **13**, respectively, which often occurs in acidic conditions. Nevertheless, the electrolytic water splitting can also occur under basic [39] or neutral conditions [54].

$$H_2O \rightarrow \frac{1}{2}\,O_2 + 2H^+ + 2e^- = -1.23\,V \quad (Anode\ /\ E_{oxidation}) \tag{12}$$

$$2H^+ + 2e^- \rightarrow H_2 = 0.0\,V \quad (Cathode\ /\ E_{reduction}) \tag{13}$$

In function of the type of electrolyte, ionic agent, operation temperature and water electrolyzers there are mainly three types of water electrolysis technologies, namely, alkaline [55], proton exchange membrane (PEM) [56], and solid oxide electrolysis cells (SOEC) [57]. In these, two configurations, using alkaline and solid polymeric membranes, the electrolysis could take place at temperatures lower than 100 °C. However, the first is considered to be the most simple and mature technology and the second can undergo in this temperature range under the condition of a sufficient protonic conductivity. The main disadvantage of this technology comes from acidic conditions, where PEM electrolyzers hinders the kinetics of the redox reactions and requires the use of expensive noble metal catalyst. The main limiting step is OER, since HER happens fast. For OER, catalysts such as RuO_2 and IrO_2 exhibit high activity. However, RuO_2 present corrosion in acid conditions and IrO_2 is more stable but less abundant and consequently more expensive. To date, the best electrocatalysts for HER is based on the use of Platinum (Pt) nanoparticles supported on carbon. Yet, Pt is expensive, but low Pt loadings are required. Solid oxide electrolysis (SOE) high temperature water electrolysis provides high efficiencies, with lower total cost compared to low temperature electrolysis due to favorable thermodynamics and kinetics. Typically, it uses solid oxide ceramics as electrolytes. These oxides typically conducts oxygen ions (O^{2-}), but recently proton ions (H^+) too. To date, the best electrocatalysts for HER are Ni-based composites and for OER, perovskite oxides (LSM) due to their high activity, good thermal compatibility with ceramic oxide electrocatalysts and high conductivity.

The overall HER and OER reactions happening are presented in **Fig. 1.9** for each case.

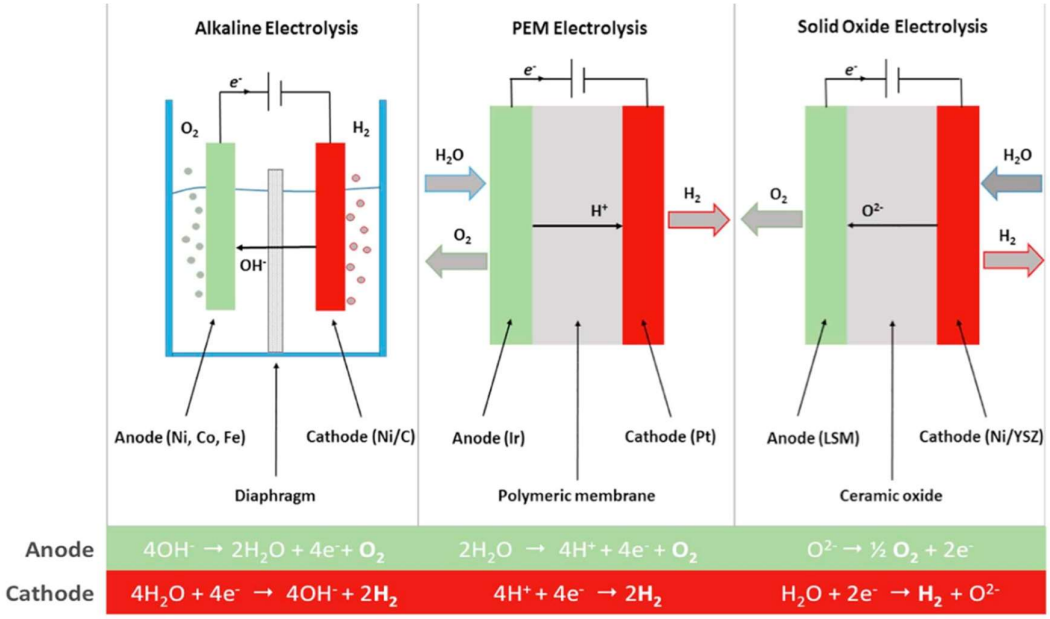

Figure 1.9. Operation principles of alkaline, PEM and SOEC [58].

B.2.2.2.b) Thermolysis

Thermolysis also known as thermochemical water splitting process, in which water is heated to a high temperature until decomposed to H_2 and O_2. Generally, the needed temperature is around 2500 °C [21,59]. Since sustainable heat sources do not provide such amount of energy, several thermochemical cycles have been proposed to lower the operational temperature and improve overall efficiency. The cycles consist in a series of chemical reactions at different temperatures to convert heat in chemical energy H_2 [60].

B.2.2.2.c) Photolysis

Photolysis uses the light energy to split water into H_2 and O_2 [61]. This technology is currently in early stages of research but it had demonstrated an interesting long term H_2 production path with low environmental impact. At the moment, it is not viable for large scale production [46].

B.2.2.2.d) Photo-(electro) catalysis

Photo-(electro) catalysis uses light to activate a SC to undergo the water splitting. This method comprises a photoanode, a (photo) cathode, and additional bias. The operational principle is based on the activation of SC´s constituting the photoelectrodes to generate the charges (electrons and holes) that could perform the two half reactions of water splitting. The application of an additional bias (much lower than the necessary energy for direct electrolysis) helps to separate the photogenerated charges. More details are given later in **section B.3.2.1**.

B.3. Photocatalysis

B.3.1. General definitions, principle, and main applications

Catalysis exists in two main types in function of the nature of the catalyst and the medium. **(a) Homogeneous**: the catalyst and reactants are in the same phase, typically liquid. **(b) Heterogeneous**: the catalyst and the reactants are in different phases. Typically, the catalyst is a solid, whereas the reactants are liquids or gases.

Photocatalysis is a specific heterogeneous catalysis type. It needs light activation instead of heat activation (as usually in thermal catalysis) to diminish the activation energy barrier to undergo more easily some chemical reactions. The pioneer work of Doerffler and Hauffe (1964) cited the word photocatalysis for the first time with the oxidation study of CO using ZnO [63]. To date, the most studied photocatalyst is titanium dioxide (TiO_2), mainly in its anatase structural form.

The ideal photocatalytic mechanism comprises five general steps:

(1) Transfer of the reactants from the fluid phase to the photocatalyst surface

(2) Adsorption of the reactants to the surface of the photocatalyst

(3) Catalyst activation by absorption of photons from the SC. This step can be divided in 4 sub-steps:

(3-a) Photons absorption and exciton generation

(3-b) Exciton disruption into e^- (in the CB of the SC) and h^+ (in the VB of the SC)

(3-c) Migration of the charge carriers (e^-/ h^+) to the surface. It must be underlined that at this step, the charge carriers might encounter themselves whether in the bulk or at the surface to undergo recombination, which is an undesirable mechanism. Charge recombination in non-radioactive process hampers the activity of the photocatalysts

(3-d) Surface oxidation and reduction reactions with adsorbed chemical species

(4) Desorption of the products and reactants

(5) Transfer of the products from the photocatalyst surface to the fluid phase

All the mentioned steps are shown schematically in the following scheme of the **Fig. 1.10**:

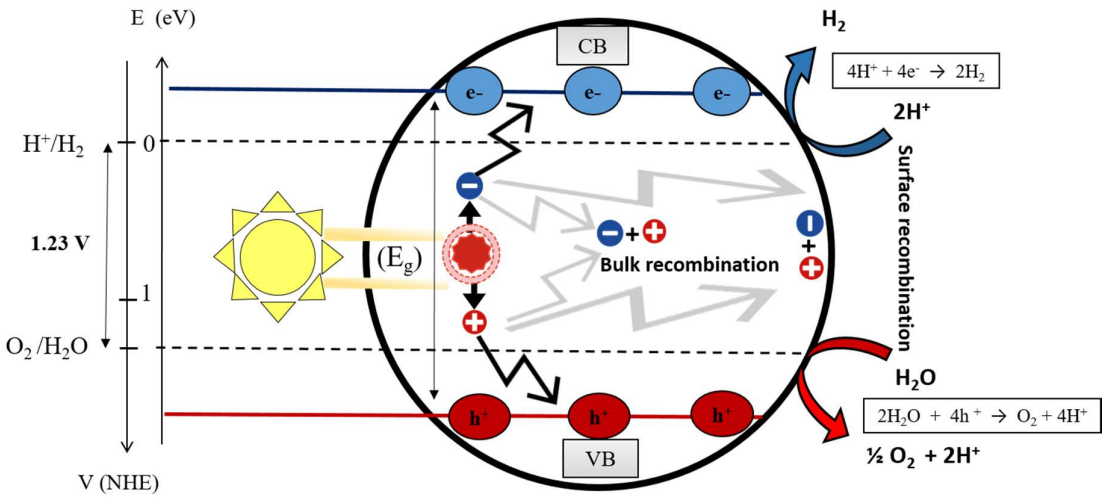

Figure 1.10. Photocatalytic principle scheme.

Steps 1, 2, 4, and 5 are equivalent than in thermal activated catalysis. Yet, the step 3, the photogeneration of charge carriers and redox reactions are specific to photocatalysis.

Over the course of the last decades, photocatalytic systems have been developed for a wide range of applications. The main contributions had been in environmental and energy fields. For environmental applications, one can mainly mention water [64–66] and air [67–69] purification. As a matter of fact, photocatalysis is a versatile technology, since it can oxidize a large variety of organics (alkanes, alcohols, carboxylic acids, sulphur and nitrogen-containing products and others) [70,71] and inorganic (CO, NH_3, H_2S and others) contaminants. The mechanisms involved in these reactions are based on photo-oxidation using highly oxidizing radicals, hydroxyl $OH^{\bullet}$, super oxide $O_2^{\bullet}$, or using directly the photogenerated h^+, ideally ending in a total mineralization when oxidizing organics. At the same time, photocatalysis allows the decomposition of some inorganics (not oxidant conditions) (NO_2, SO_2, and others) [72,73]. SC activation can also lead to alter or inactivate several microorganisms (bacteria, virus, spores), which are considered complex organic molecules [74–76]. Amongst the latest advances, the efforts of photocatalysis on chemical or biological targets are also valued in order to develop coatings or other functionalized surfaces [77,78].

B.3.2. Water splitting

Water splitting refers to the chemical dissociation of water in H_2 and O_2. Photocatalytic water splitting using solar energy can be considered as one of the step of a global process referred as "artificial photosynthesis" that produces solar fuels [79]. In fact, the solar fuel generation occurs mimicking the nature's photosynthesis not only in its redox reaction but also in its thermodynamics (water splitting: 1.23 eV *vs.* glucose formation: 1.24 eV). Water splitting is also considered a very simple process, thanks to its tri-component features: light source (to obtain the photons that activate the SC), the photocatalytic system (a SC which photogenerate the e^-/ h^+ pair), and water (the reactant). Generally, two main approaches are known: **photocatalytic and photo**

(electro) chemical approaches. The general principle for both approaches starts with the absorption of photons possessing an energy greater or equal than to the SC´s bandgap energy (E_g) [80].

Photocatalytic water splitting involves a complex series of photophysical and chemical processes [84]. An efficient conversion depends on several parameters, thus involved at different time scales and spatial resolutions that should be rationally understandable due to the sum of fundamental efficiencies to lead overall efficiency.

The mechanism starts with the transfer of the reactant to the surface of the SC, followed by the **photon absorption (1)** which generates excitons, further dislocated in e^-/ h^+ pairs. The excitation of an e^- occurs from the VB also known as the highest occupied molecular orbital (HOMO) to the CB known as the lowest unoccupied molecular orbital (LUMO) as shown in the **Fig. 1.11** and **equation 14**.

$$SC + hv \rightarrow e^-_{CB} + h^+_{VB} \quad (14)$$

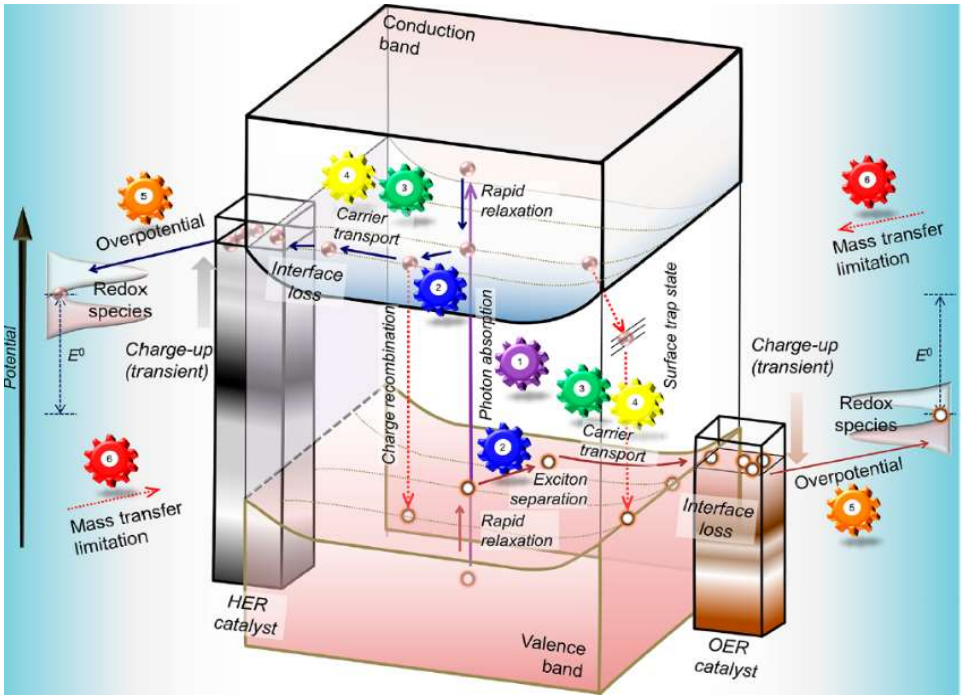

Figure 1.11. Scheme of photo (electro) catalytic water splitting process [79].

This process is followed by **relaxation** of the e^- and the h^+ to the bottom of the CB and the top of the VB, respectively. Then, the exciton is commonly **separated (2)** after overcoming the exciton binding energy determined by the electronic structure, which guide the e^-/ h^+ pairs to move independently. When each specie starts its own pathway and drives the **carriers diffusion and transport (3-4)** take place to the interfaces phase in contact with the catalyst. Due to the nature of SC/catalyst/electrolyte interaction, an **interface loss** is inherent to the system for the different electronic barriers that both e^- and h^+ had to overcome to eventually be available on the surface

catalyst. Successful charge transfer and diffusion typically occurs in the order of microseconds on the direction of the surface catalyst. At this stage, the driving force is the difference in chemical potentials and Fermi levels (**overpotential (5)**) between the e^-_{cat} and h^+_{cat} and OER and HER, respectively, has to be overcome and aligned to enable the electrochemistry reactions to occur. Due to slow kinetics in comparison with prior steps, the active electrochemical species will be charged either negatively or positively to eventually drive **electrocatalytic redox reactions**. Normally, the two half reactions of water splitting happen on the surface of the catalyst. In optimal conditions, the OER carries out by the water oxidation in presence of the h^+ photogenerated, a proton is also produced as a by-product that will be reduced in the following half reaction HER. Both half reactions are represented in **equations 15** and **16**.

$$H_2O + 2h^+_{VB} \rightarrow \frac{1}{2}O_2 + 2H^+ \quad (15)$$

$$2H^+ + 2e^-_{CB} \rightarrow H_2 \quad (16)$$

To obtain high water splitting efficiencies the selection of the components of the photocatalytic system is critical (SC photocatalyst, additional bias, co-catalyst and sacrificial donor/ acceptor). Ideally, the SC should present a VB with a higher electrochemical potential than the redox couple of O_2/H_2O to guarantee the oxidation of water and obtain the O_2 and H^+, and a CB with a lower electrochemical potential than the redox couple of H^+/H_2 to guarantee the reduction of the proton to obtain H_2. Besides the adequate SC band energy alignment requirement (CB and VB positions), another important requirement is the magnitude of its E_g. Ideally the SC should be able to absorb efficiently a large window of wavelengths from the visible and near infra-red range following the standard solar spectrum reported by the NREL that mimics the sun irradiation [85], otherwise a sensitization methodology could be applied. However, finding an unique SC possessing all these features remains a challenge.

B.3.2.1. Photo-(electro) catalytic configuration

Also known as photo electrochemical cell (PEC), as mentioned in the energy context section of this chapter, PEC´s principle consist on using two separate compartments. The most general configuration contains a photoanode (n-type SC) and the other a cathode (Pt, generally) or a photocathode (p-type SC), connected with an external electrical circuit to apply an additional bias (the minimum possible) to avoid charges recombination as shown in **Fig. 1.12**. The two compartments are separated by specific permeable membranes that allows a spatial separation for HER and OER. The applied potential forces photogenerate e^- that migrate through the external circuit, towards the counter electrode [18]. The holes located on the VB of the photoanode undergo the half reaction of water oxidation into O_2 and H^+. H^+ can further migrate to the cathode through a membrane separating the OER and the HER evolution compartments and be reduced by the photogenerated e- that had previously flown to the cathode via the external circuit under the action of the bias. Theoretically, water splitting via PEC is very alike as electrolysis with the difference that the input energy is through light, and thus requires lower additional bias than required for electrolysis. In effect, the use of

additional potential to the system should drive a higher H_2 production yield. Yet, the use of photons as of greater energy source, promotes the decrease of the PEC's electrical energy consumption.

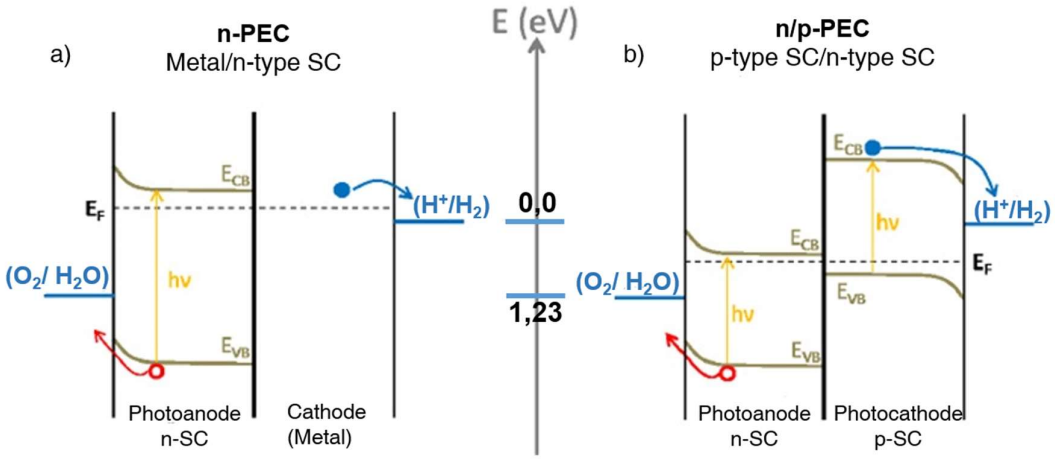

Figure 1.12. PEC principle in two cases a) metal/n-type SC and b) n-type SC/p-type SC [83].

B.3.2.2. Photocatalytic configuration

Typically, SC(s) acts as the light absorber to generate charges required to perform oxidation and reduction half reactions. In the photocatalytic configuration both half reactions occur in the same reactor (single compartment). In the overall water-splitting reaction is very difficult to perform using a single SC (difficulty to perform both half reactions and to absorb visible light radiation), the addition of a co-catalyst is often required. The addition of co-catalyst (usually a metal that could also act as electron trap site) might also be helpful to increase charges separation (e^- / h^+ pairs) [30,81,82]. Likewise, to limit back reaction between O_2 and H_2 produced at the same place, the addition of sacrificial electron donor or electron acceptor molecules is often used. Furthermore, this strategy is useful to study and optimize separately each of the half reaction in order to finally design the best material for overall water-splitting.

B.3.2.2.a) Sacrificial agent, a donor/acceptor specie

The objective of adding a sacrificial agent (SA) within a photocatalytic reactor has for purposes to decrease the rate of one of the two half reactions of water splitting, allowing to study only one evolved gas in detailed (H_2 or O_2) and the corresponding reaction mechanism. As the nature of HER and OER is different, it is mandatory to choose a sacrificial agent according with its capacity of reduction (electron donor or hole scavenger) or oxidation (electron acceptor or electron scavenger) character, respectively. For the study case on HER an electron donor must be used, with two purposes to scavenge the photogenerated holes (enhancement of separation of charges), and in the case that O_2 is present in the reaction medium to consume it (limiting the back reaction). Nevertheless, as the usual reaction medium is aqueous, the water oxidation potential can vary in function of the ionic strength of the medium from 1.229 eV (pH=0) to 0.401 eV (pH=14) *vs.* NHE [86]. Depending on the pH used will lead specific oxidation potentials for both SA and water, which should satisfy the oxidation of water

requirement to guarantee an efficient HER evolution. Parallely, for OER case an electron acceptor must be used, the photogenerated electrons will reduce the oxidant agent (SA) instead of H^+, allowing to block the H_2 production and therefore favoring the O_2 production [87]. It has to be underlined that the correct use of the word "Water-Splitting" or photodissociation of water only applies when the two OER and HER undergoes simultaneously, which is the case of PEC, but not of direct photocatalysis in presence of sacrificial agent. By the fact that a sacrificial agent is commonly used in suspended nanoparticles photocatalytic reactors with only one compartment, referred as H_2 or O_2 production.

Common sacrificial electron donors (reductant agents) include triethanolamine (TEOA), methanol, ethanol, glycerol Na_2S-Na_2SO_3, lactic acid, etc., and sacrificial electron acceptors (oxidant agent) include silver nitride ($AgNO_3$), $Ce(SO_4)_2$, and $FeCl_3$ [88]. For any sacrificial agent, a chemisorption step is needed to access the photogenerated h^+/e^- on the surface of the catalyst. For illustrative purpose, a generic alcohol will be used as an example. **Equation 17** shows a SC/alcohol interface

$$R - CH_2OH_{(l)} \rightarrow R - CH_2O^-{}_{(ads)} + H^+_{(ads)} \quad (17)$$

Followed by the formation of the alkoxide and protons adsorbed on the SC surface. The SC is irradiated to photogenerated h^+/e^- pairs. The h^+ oxidizes the alkoxide as in **equation 18**.

$$R - CH_2O^-{}_{(ads)} + h^+_{SC} \rightarrow R - CH_2O \quad (18)$$

The resulted specie could form an aldehyde and hydrogen atom as **equation 19**.

$$R - CH_2O \rightarrow R - CHO + H_{(ads)} \quad (19)$$

The adsorbed hydrogen is oxidized at the SC surface, and the resulting proton can be reduced in H_2 by the e^- as in **equations 20 and 21**. Consequently, part of the H_2 formation detected during water-splitting can be issued from the sacrificial agent added, more specifically from its alcohol function.

$$H_{(ads)} \rightarrow H^+_{(SC)} + e^-_{(SC)} \quad (20)$$

$$2H^+_{(SC)} + 2e^-_{(SC)} \rightarrow H_{2(g)} \quad (21)$$

TEOA is a tertiary and basic amine that can undergo an irreversible oxidation of the amine to cause a dealkylation to form a secondary amine and an aldehyde in presence of water. Therefore, protons coming from this degradation can eventually produce H_2 via photo-reforming. In fact, TEOA single molecule has three alcohol functions, meaning that it could also lead to H_2 formation through photo reforming as of alcohol functions. TEOA has an oxidation potential of 0.6-0.7 *vs.* NHE, making it easy to oxidize and work as an efficient trap holes site. Wang *et al*, found that TEOA satisfies an electron donor character sufficiently capable of consuming holes to avoid recombination of the g-C_3N_4 photogenerated carriers [89]. Furthermore, it has been observed that when the TEOA

adsorbed on g-C_3N_4 surface via electrostatic interactions, it may promotes an uplift in its Fermi level, leading an induced band bending [87].

C) Fundamentals of semiconductor materials

SCs are polymers or covalent crystals, in which the molecular orbitals HOMO and LUMO (already defined in photocatalysis section) comprise a continuous energy states, rather than discrete energy states. The VB corresponds to the filled band of higher energy and the CB to the empty band of lower energy. Both bands are separated by its E_g (none energy level is accessible), where E_g is the minimal necessary energy to provide the promotion of electrons from the VB to the CB, leaving a h^+ in the VB [90].

C.1. n and p type semiconductors

SCs are mainly divided in two categories: intrinsic and extrinsic [91]. Intrinsic or pure SC's are those that are ideal, with no defects and no impurities. Generally, they present poor conductivity and have an equivalent amount of negative and positive carriers, e^-/ h^+, respectively. Moreover, an extrinsic SC is an "improved" intrinsic SC with impurities (low amount) in order to modify its electrical properties, thus improving its conductivity.

The conventional method of modifying the electronic structure of a SC is doping. Doping consist in an addition of a foreign atom into the structure of the SC. The introduction of foreign atoms (impurities) into the SC modifier its conductivity properties, resulting in two cases: “negative” charged conductor (n-type) and the “positive” charged conductor (p-type). For example, silicon and germanium are the most common intrinsic SC's. When a small percentage of foreign atom containing 5 valence electrons is added in the crystal lattice of an intrinsic SC it leads to n-type SC's by leading to an increase of electron density. In the same manner, the addition of a foreign atom containing 3 valence electrons results in the formation of p-type SC's by creating an increase of hole density or electron deficiency, respectively.

C.2. Direct & indirect transition band gap of semiconductors

SCs are also distinguished by the nature of their band gap. One can mention two types of SCs with a direct or indirect band gap. In a direct band gap SC, the top of the VB and the bottom of the CB occur at the same value of momentum (k space). In this case direct electron jump from the VB to the CB may happen. In an indirect band gap SC, the minimum energy in the CB occurs at a different value of momentum that the maximum energy of the valence band. That means that the recombination of an electron in the conduction band with a hole in the valence band requires the participation of phonons as illustrated in **Fig. 1.13** [90,92].

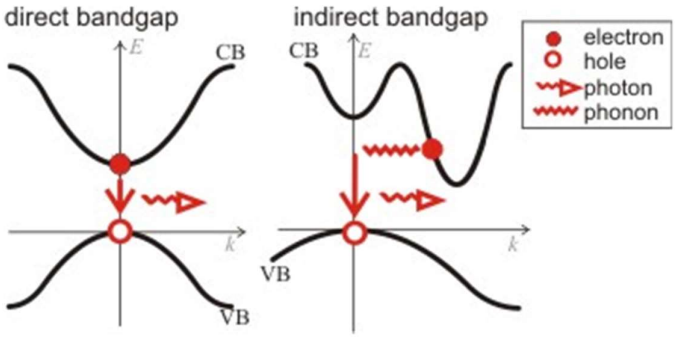

Figure 1.13. Direct and indirect band gap SC [92].

C.3. Semiconductor/electrolyte junction

When a semiconductor is placed in contact with an electrolyte in solution, an electric current initially flows across the junction until reaching an electronic equilibrium, where the Fermi level of the electrons in the solid (E_f) is equal to the redox chemical potential of the electrolyte (E_{redox}), namely flat band potential (a). The application and consequently the transfer of an electric charge produces a region on each side of the junction where the distribution differs from the bulk material, also known as space-charge layer or accumulation (b). This electric charge produces changes on both sides of the system. On the electrolyte side, this corresponds to the familiar electrolytic double layer, known as Helmholtz compact layer followed by a diffuse layer. On the semiconductor side, the nature of the band bending depends on the position of the Fermi level in the solid. If the Fermi level of the electrode is equal to the flat band potential, there is no excess of charge on either side of the junction and the bands are flat. If electrons accumulate at the semiconductor side one obtains an accumulation layer. If yet, they deplete from the solid into the solution, a depletion layer is formed, leaving behind a positive excess charge formed by immobile ionized donor states. Finally, the electron depletion can go so far that their concentration at the interface falls below the intrinsic level. As consequence the semiconductor is p-type at the surface and n-type in the bulk, corresponding to an inversion layer [8,93]. The **Fig. 1.14** is referring to a n-type semiconductor where electrons are the mobile charge carriers. On the contrary, for p-type semiconductor the positive holes are the mobile charge carriers.

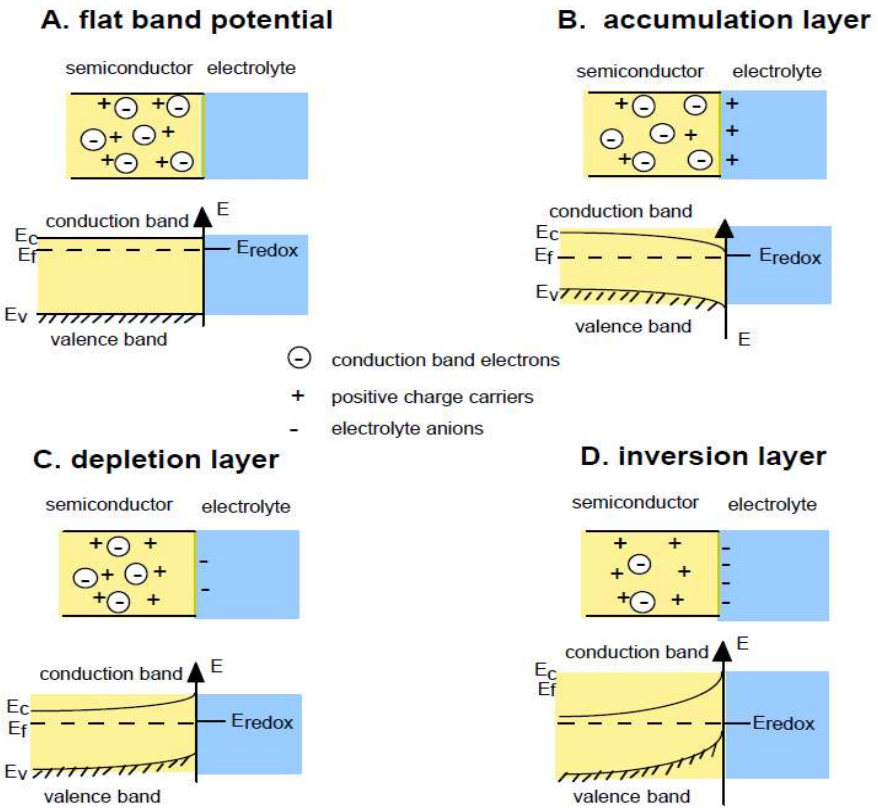

Figure 1.14. Scheme of an n-type semiconductor in contact with an electrolyte. a) flat band potential b) accumulation layer c) depletion layer and d) inversion layer [8,93].

C.4. Heterojunction systems between two semiconductors

An heterojunction systems formation consists in the contact at nanoscale of two SC's (ideally with different E_g, CB and VB energies), forming an interface between the two materials. The resulting new hybrid junction will modified their theoretical Fermi level, band edges positions and therefore e^- / h^+ generation and transfer processes might be modified.

In the case of heterojunction formation between two SCs, one can generally mention three types of heterojunctions (**Fig. 1.15**):

(I) Straddling gap

(II) Staggered gap

(III) Broken gap

Type I, the case of junction between a larger (SC1) and a smaller (SC2) band gap SCs. Within the band alignment structure, both VB and CB potentials of SC2 are confined within the larger band gap of SC1, creating the **straddling band alignment**. After light irradiation with sufficient energy equivalent to or greater than the E_g of the SC's, photogeneration of e^- / h^+ occurred, resulting in one direction transfer and thus accumulation of all charge carriers in a single component within the hybrid structure

owing to the band edge positions. Since the charge carriers are accumulated in one SC, there is no enhancement of charge separation, impairing the photoredox efficiency.

Type II, the band edge potentials are **staggered** between SC1 and SC2. As a result of difference in chemical potential between both SC's, upward or downward band bending is formed, leading to the migration of charge carriers in the opposite direction. This enhances the e^- / h^+ spatial separation on several parts of the heterojunction to retard the charges recombination and thus to prolong the lifetime of free e^- and h^+. To date, most studied heterojunction junction between two SC's are type II. As such, the oxidation / reduction reactions take place in different spaces in the two different SC's.

Type III, both VB and CB edges of SC2 are located above the CB potential of SC1 without crossing each other. The two SC's work alone, therefore there is no enhancement on the charge transfer terms [94,95].

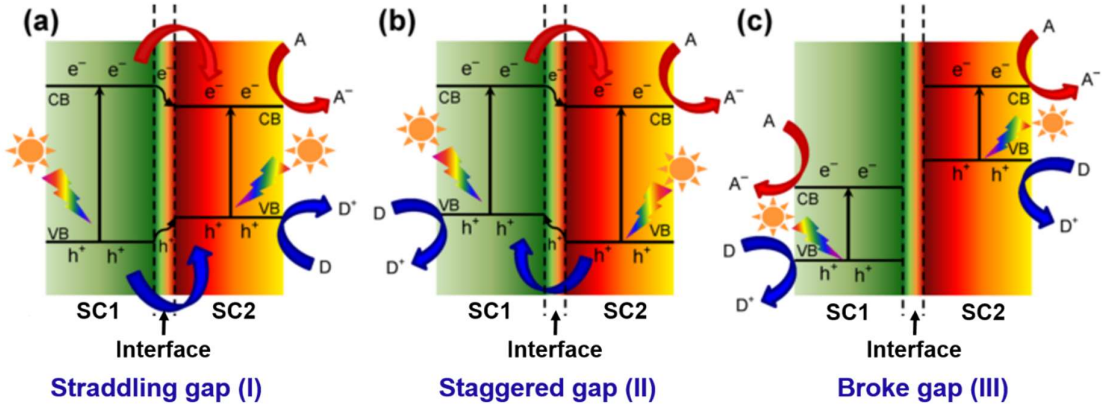

Figure 1.15. General three types of heterojunctions between two semiconductors with different band gaps and band edges positions [94,95].

There are several reasons why the community working on photocatalytic materials is studying the design and synthesis of heterojunction hybrid systems. The first advantage is the capacity of absorbing more photons from the visible range in the case the junction allows to do so. Another expected advantage relies in the increase of charge separation of the photogenerated species in case of the type II heterojunction. In this ideal configuration it is possible to combine visible photons absorption to enhanced spatial charge separation. Another expected advantage relies on the beneficial performance on two half reactions of water-oxidation and proton reduction, requiring adequate VB and CB positions in reference to the electrochemical potentials of the half reactions.

D) Photocatalytic nanomaterials

The framework of this thesis comprises the design and synthesis of binary and ternary nanocomposites combining two semiconductors and metallic nanoparticles, namely, TiO_2, g-C_3N_4 and Au NPs, respectively. In this context, this section will present the state-of-the-art of each of the mentioned materials including the advantages and disadvantages that each one presents on the hierarchical hybrid nanocomposite.

D.1. Titanium dioxide (TiO_2)

D.1.1. History

Titanium dioxide (TiO_2) compound presents interesting features such as strong oxidizing abilities [82] under irradiation, chemical stability, long term durability, biocompatibility, reasonable cost, light and strong mechanical resistance. Due to its characteristics, TiO_2 is present in a wide range of daily products such as toothpaste, sun-blockers, white pigment, paints, papers, plastics, excipient within medicaments, among others. Moreover, TiO_2 has been profoundly studied in different research areas, namely environmental and energy-related fields [22]. The main research had been undergoing in photoactivity, more specifically, photocatalytic water dissociation (Water-Splitting) [52], dye-sensitized solar cells (DSSCs) or photovoltaic cells (Gratzel cell) [96,97], lithium-ion batteries [98], photocatalytic oxidation, especially for water [64–66] and air [67,68] decontamination processes, superhydrophilicity [99], electrochromic [100], biomedical coatings, and sensors.

D.1.2. Synthesis

Nanoscience and nanotechnology has risen the interest of designing nanostructured materials, namely TiO_2. The TiO_2 high performance at nanoscale is possible by controlling several synthesis parameters that tune particle size and distribution, shape, crystalline phase(s), and specific surface. This section will overview some approaches of two types of TiO_2 synthesis methods: physical and chemical.

D.1.2.1. Physical methods: sputtering

Sputtering synthesis, also known as cathodic pulverization, is a thin layer deposition method. It is a method that allows the synthesis of several materials from the condensation of a metal vapor from a solid source (target) onto a substrate [101]. The principle consists on the application of potential between the solid source and the walls of the reactor (in Ar atmosphere) that allows the creation of cold plasma. This plasma comprises electrons, ions, photons, and neutrons; the positive charge species collide with the solid source and start the atom spray that will deposit onto the substrate. In the case, that the solid source is metallic Ti, controlling the temperature, the reaction chamber pressure, and the quantity of O_2 (gas reactant) is thus possible to obtain TiO_2 homogeneous films [102].

D.1.2.2. Chemical methods

D.1.2.2.a) Chemical Vapor Deposition (CVD)

CVD allows the synthesis of crystalline films of TiO_2 with particles size of approximately 10 nm [103]. Typically, a Ti precursor is used, most commonly titanium (IV) isopropoxide (TIP), is immersed in a gas mixture (He/O_2) in a reactor. There are two main particularities with this method, that relies on obtainment of films with a significant specific surface and at the same time allows to control the particle size, and the crystallinity, without mentioning the need of a high temperature treatment [104].

D.1.2.2.b) Microemulsion / Micelles

These two methods allow the synthesis of ultrafine powders, with the advantage of controlling precisely the final particle size [105]. Microemulsion consists on the mixture of two microemulsions containing reactants or precursors in constant magnetic agitation. Then, the droplets in suspension interact and coalescence, the reactants will react together and form TiO_2. Concerning, the micelles synthesis, they consists on the same mentioned principle of microemulsion, with the difference of the use of surfactants during synthesis. The surfactant molecules can self-assembly thanks to their hydrophilic and lipophilic properties to finally form ordered structures [106]. The surfactant´s nature allows to obtain different morphology type (spherical, hexagonal, nanowires, nanospheres, etc.) [107]. Even though the resulting particle size and morphology are well-defined, the crystallographic structure is often amorphous, meaning that a post-calcination step is necessary to crystallize the synthesized powders.

D.1.2.2.c) Electrochemical anodization

The anodization consists on using a electrochemical cell comprising an electrolyte and two electrodes of Pt (cathode) and of Ti (anode) [108]. The principle consists on the application of a voltage between the electrodes that generates the reduction of the proton (cathode) and the oxidation of metallic Ti (anode) as in the **equations 22 - 23**:

$$4H^+ + 4e^- \rightarrow 2H_2 \quad (22)$$

$$Ti + 4H_2O \rightarrow TiO_2 + 4H^+ + 4e^- \quad (23)$$

By modifying some synthesis parameters such as the nature of the electrolyte, different TiO_2 morphologies can be obtained. The organized addition of fluoride ions within the electrolyte allows the formation of both an oxide layer and pores according with the **equation 24**:

$$TiO_2 + 6F^- + 4H^+ \rightarrow [TiF_6]^{-2} + 2H_2O \quad (24)$$

The creation of a polarized electric field weakens the Ti-O bond that allows the release and the complexation of the Ti^{4+} ions by the fluorides. These reactions take place in the oxide/electrolyte interface. The formed pores also self-organized in such a way to promote a homogeneous distribution of the electric field on the surface of the electrode. Then, the fluorides attack preferentially the pores because the electric field is more intense due to the lower oxide thickness. The pores increase and a tubular structure is gradually forming. After the nanotubes growth, the barrier layer of TiO_2 keep constant at the bottom of the tube because the oxidation reaction and the dissolution are in equilibrium. This layer digs the Ti metallic substrate. The nanotubes growth finishes when the dissolution speed of the oxide at the top of the tube is equal to the speed of penetration of the barrier layer. This synthesis method allows to obtain uni dimensional oriented and aligned TiO_2 nanotubes [109].

D.1.2.2.d) Sol-gel synthesis

Sol-gel is considered a simple (no need of sophisticated equipment), cost-effective, mild conditions (atmospheric pressure and ambient temperature) method that has been used for various catalyst materials [110] due to its high purity, homogeneity, scale and controllable morphology [111].

Sol-gel metal oxide solid synthesis comprises two steps, the **hydrolysis** and **condensation** of metal precursors followed by aging and drying under ambient atmosphere [110]. The word "**sol**" refers to the dispersion of colloidal particles in a liquid, while "**gel**" is an interconnected rigid network with pores in the polymeric chains of the micrometer average length. Colloids refer to solid particles in suspension and with diameters of 1-100 nm [112]. A gel interconnected, rigid network of polymeric chains (average length ≥ 1 μm) with micrometer pores is obtained.

For TiO_2 synthesis, the main sol-gel route precursors are titanium alkoxides (*ca.* titanium isopropoxide (TIP) and titanium n-butoxide), organic solvent, acid/base catalysts and water. The resulted TiO_2 gel corresponds to a dense cross-linked 3D structure, which is obtained during hydrolysis and condensation steps. By applying this route it is possible to obtain four different kinds of structures: (1) ordered lamellar structures (2) disordered covalent polymeric networks (3) disordered polymer networks formed through physical aggregation and (4) particular disordered structures.

Typically, TiO_2 sol-gel synthesis carries out in two main steps:

Hydrolysis, a Ti precursor is hydrolyzed to initiate the synthesis mechanism. Typically, TIP is used with or without structural agents or pore genes (carboxylic acids for example). Thanks to the quelates formation by the agents, the formation speed of the gel polycondensation in self assemblies can be controlled. The $Ti(OH)_4$ formation is favored for a great hydrolysis rate within the solution as shown in **equation 25**.

$$Ti(OR)_n + H_2O \rightarrow Ti(OH)(OR)_{n-1} + ROH \quad (25)$$

Condensation, the Ti-O-Ti chains are formed by oxygen bridges new bonds via oxolation reactions and are favored for a low hydrolysis rate in a titanium alkoxide excess in the solution. The presence of Ti-OH conducts the particles agglomeration in the gel, meanwhile the Ti-O-Ti chains form the tridimensional structure via alcoxolation and the release of water molecules as shown in **equation 26**. The obtained gel presents an amorphous structure, a calcination step is therefore needed to crystallize the TiO_2.

$$-Ti-OH + HO-Ti- \rightarrow -Ti-O-Ti- + H_2O \quad (26)$$

Influential experimental parameters tailor the TiO_2 nanostructure with a defined structure, texture and morphology. For instance, Ti precursor and the hydrolysis agent define a large diversity of materials structures via sol-gel process. By changing the hydrolysis agent a crystalline TiO_2 with different anatase/rutile ratio can be obtained, also allowing a control on the specific surface, which may result in a direct influence on the photocatalytic activity [113]. Li *et al* had reported the impact of precursor concentration, pH, time, and temperature of calcination on the final nano-TiO_2 [114].

Also Addamo *et al* showed a study with the conditions to obtain TiO_2 thin films showing a photocatalytic activity on the degradation of an organic molecule [115].

D.1.2.2.e) Hydrothermal (solvothermal) synthesis

i. History

Hashimoto *et al*, were the pioneers in synthesizing TiO_2 nanotubes for photovoltaics applications [116]. It was not until 1998, that the pioneer work of Kasuga and co-workers founded the formation of TiO_2 titanates or nanotubes or via highly basic hydrothermal synthesis (typically 10 M of NaOH, sodium hydroxide), starting from TiO_2 powder or Ti metal foil [117] without using sacrificial templates. Since then, there has been an interest of using this synthesis due to the formation of TiO_2 nanotubes using a conventional technique able to obtain unique physico-chemical properties such as morphological, structural, optical, electronical, and chemical. By just changing the water for any other solvent, this synthesis is also called solvothermal.

ii. Texture and morphology

The hydrothermal synthesis process leads to the formation of inorganic nanocrystalline materials with several sizes and shapes like presented in **Fig. 1.16**. For example nanoparticles, nanotubes, nanosheets, nanorods, nanowires, nanofibers, nanoribbons, and nanobelts structures, with controlled monodisperse distribution in sizes and with specific surfaces varying from 150-400 $m^2\ g^{-1}$, with good reproducibility. Some conventional precursors used are $TiCL_4$, $TiSO_4$, $TiO\ (NO_3)_2$ and also TiO_2 already crystallized like commercial TiO_2 P25. In function of which precursor and synthesis parameters are used, *e.g.,* temperature, pressure, reaction time, will impact the resulting crystalline phase, whether anatase, rutile, anatase/rutile or TiO_2 (B) [118]. The TiO_2 nanotubes formation yields almost a 100 % efficiency, with a diameter of 70 – 100 nm and aspect ratios of 40-100 times [119].

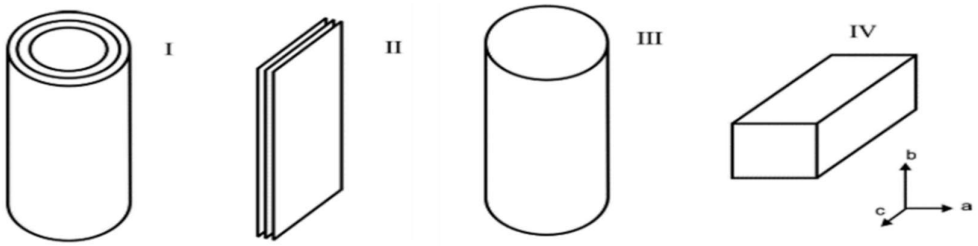

Figure 1.16. TiO_2 morphologies: (I) nanotubes, (II) nanosheets, (III) nanorods or nanowires, and (IV) nanofibers, nanoribbons, or nanobelts [120].

iii. General and specific steps

The hydrothermal synthesis comprises several steps: (I) Adding the raw TiO_2 in a closed stainless steel batch reactor with a 10 M NaOH solution to solubilize then dissolve the oxide. The reactor inside of a stove is heated between 100-180 °C leading to autogene a pressure lower than 100 bars to start the growth of layered nanosheets of sodium tritinatates [121,122]. Then, the saturated vapor pressure increases within the reactor and consequently increases the rate of particles nucleation [118]. (II) Exfoliation of

nanosheets starts (III) Crystallization of dissolved titanate nanosheets (IV) formation of tubular structure by washing using HCl 0.1-1 M and exchanging Na^+ by H^+, which induces the curving and wrapping from nanosheets to nanotubes, (V) Growth of nanotubes along their length, and (VI) Final calcination can be applied to increase crystallinity.

iv. Influential synthesis parameters

Literature mentioned that several parameters influence the TiO_2 or titanate nanotubes formation. However, there are some more predominant, such as: textural and morphological properties of the precursor, temperature and hydrothermal time, nature of the basic media, washing the post-thermal treatment. (I) Depending on the starting TiO_2 precursor will determined the crystalline structure (anatase, rutile, brookite, TiO_2 (B), or any possible mixture) and therefore the shape and size of the crystallites and global specific surface area of the resulted material. (II) Temperature and hydrothermal time are key parameters to define the NTs morphology. In fact, temperature influences the nucleation and crystalline growth of the titanates NTs [123]. For lower temperatures than 100 °C the NTs formation does not be achieved [124]. For temperatures between 170-180 °C the NTs formation yield diminishes significantly and instead preferentially form nanoribbons or nanofibers [123,125]. (III) The selection of NaOH or KOH bases and their concentration also impact the synthesis selectivity in 1D morphology structures, whether nanotubes [126], nanofibers, or nanoribbons [127]. Also, there is a direct impact on the crystallinity and specific surface [128,129]. (IV) The acidity of the washing solution influences the elemental composition and specific surface [130]. Generally, the acid washing solution is HCl, the optimal concentration ranges from 0.5 to 1.5 M. For lower concentrations than 0.5 M, the washing is not efficient enough to remove the Na^+ ions properly. For higher concentrations than 2 M, a destruction on the tubular structure takes place [131]. (V) Calcination post-thermal treatment impacts the crystallinity, morphology, specific surface and the pore structure of the NTs. Literature reported studies on the calcination temperature to point out the transition of the amorphous phase to the crystalline structures and their respective transformations. Generally, by using a higher calcination temperature the TiO_2 NTs crystallinity also increases [132]. Besides, the appearance of phases and crystalline structures starts approximately between 300-400 °C [127]. However, appearance of TiO_2 (B) have also been reported at similar temperatures and is difficult to differentiate from anatase. Rutile simultaneously appears at 700 °C which is also the temperature at which the transformation from nanoparticles to the tubular structure occurs totally. Even if from 300 °C tubular assembly destruction can start to take place. This destruction was attributed to the elimination of hydroxyl groups located in between the layers with the increase of temperature.

After many studies on finding the best optimal parameters and understanding in the comprehension of the growth mechanism of TiO_2 nanotubes [133–135], the formation intermediate steps are still not fully uncovered yet.

v. Formation mechanism

As already mentioned, the complete list of intermediate species formed during the hydrothermal synthesis are not elucidated yet. However, among the different chemical compositions, those of the type $Na_2Ti_3O_7$, $Na_xH_{2x}Ti_3O_7$ and $H_2Ti_3O_7$ had been more accepted and even characterized [136,137]. Even a proposed mechanism of TiO_2 NTs formation is schematically represented in the following **equations 27-30**:

(I) TiO_2 partial dissolution

$$TiO_2 + 2NaOH \rightarrow TiO_3^{-2} + H_2O \quad (27)$$

(II) TiO_2 disolution and crystallization of dissolved titanates in nanosheets (NS)

$$2Na^+ + TiO_3^{-2} \leftrightarrow [Na_2TiO_3]_{NS} \quad (28)$$

(III) Curving the NS by mechanical tensions to wrap the NS into NTs

$$[Na_2TiO_3]_{nNS} + TiO_3^{-2} + 2Na^+ \leftrightarrow [Na_2TiO_3]_{nNTs} \quad (29)$$

(IV) Washing to exchange sodium ions for H^+ and stabilize the NTs formed

$$[Na_2TiO_3]_{nNTs} + 2H_2O \leftrightarrow [H_2TiO_3]_{nNTs} + 2NaOH \quad (30)$$

For simplicity the dissolved TiO_2 was considered as of monotitanate form TiO_3^{2-} or $TiO_2(OH)_2^{2-}$, rather than polytitanates $Ti_nO_{2n+m}^{2m-}$.

The exchange ions rate from Na^+ to H^+ within the interstitials spaces in between the NS. The crystallographic structure comprises TiO_6 octahedrons interconnected in sheets and stabilized by Na^+ or H^+ ions. The growth / formation mechanism was proposed by Peng and co-workers [137], two paths for $H_2Ti_3O_7$ are described. **(I)** The crystalline TiO_2 reacts, after being dissolved in concentrated NaOH, to form in the surface the nanolayers of $Na_2Ti_3O_7$. Then, the $Na_2Ti_3O_7$ layers will separate from the starting TiO_2 nanocrystals to form independent nanolayers. At this stage, the nanolayers detach progressively from the TiO_2 particles in solution and are therefore stabilized by the intercalated ions around of the layers. The washing and neutralization, by using the diluted HCl (H^+/H_2O), is a key step because it promotes the progressive replacement of Na^+ ions by the H^+ ions, creating an asymmetrical environment on the layer that will provide the necessary tension forces to curve the nanolayers and therefore start the wrapping of them into a tubular structure like shown in a **Fig. 1.17** [133]. This explanation gives raise to the so called "titanates nanotubes" and it seems the most logical approach and the less controversial one. Nevertheless, the growth mechanism should be further studied and some conclusions regarding the rolling and washing steps should be further investigated.

(II) The second path starts exactly in the same way from the previous one with the crystalline TiO_2 being dissolved in NaOH, but forming a highly distorted phase that recrystallizes in a similar phase than $H_2Ti_3O_7$ in long plates or nanoribbons. It forms a hydrogen deficiency structure in the surface that causes an asymmetrical environment which is the main force to split the $H_2Ti_3O_7$ layers and causing the wrapping of

multilayer spiral nanotubes. The asymmetrical environment increases with a higher degree on hydrogen deficiency that stimulates the surface tension possibly overcoming the forces binding the sub-surface layers. This would involve a detachment of layers from the sheets, which would roll into a tubular structure.

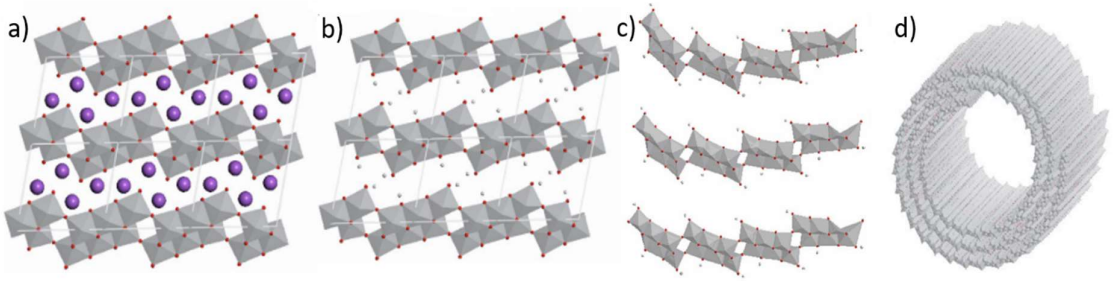

Figure 1.17. a) $Na_2Ti_3O_7$ relaxed layer b) $H_2Ti_3O_7$ relaxed layer c) $H_2Ti_3O_7$ curved layer d) Rolled trititanate nanotube [136,137]. The nomenclature of colors are attributed to purple, grey, and red that stands for sodium, hydrogen, and oxygen atoms, respectively.

Globally, the chemical approaches for synthesizing TiO_2 are the most popular (template assisted, anodic oxidation, sol-gel, and alkaline hydrothermal). Amongst the TiO_2 syntheses presented, hydrothermal and sol-gel are the most used thanks to their simplicity, good reproducibility, high synthesis yield, reasonable cost, and especially due to its possibility of controlling accurately certain structure parameters, such as size and shape of particles, crystallinity and specific surface area. Regarding, the other TiO_2 synthesis approaches, they are often used aiming at specific crystallography and crystallite size or even significant specific surface areas. The post-thermal treatment is therefore necessary to obtain a crystalline TiO_2 structure.

In the framework of this thesis, **two TiO_2 morphologies** were used: **nanoparticles** (commercial TiO_2 P25) and **nanotubes** (via hydrothermal method). TiO_2 (Evonik) has also been used as precursor for the hydrothermal synthesis to obtain tubular nanotubes.

D.1.3. Physical and chemical properties

TiO_2 as the most studied SC, is a n-type (ϕ = 4.9-5.2 eV) with a wide band gap of 3.1-3.2 eV and with band edges positions of -0.5 and 2.7 V vs. NHE for CB and VB, respectively, which confers a strong oxidizing character to undergo the water oxidation half reaction, but much limited reductant character to undergo the reduction half reaction. In general, the ideal SC to carry out the photo-dissociation of water efficiently should have a CB with a higher energy (absolute) than the standard reduction potential of the proton to dihydrogen, and a VB with a lower energy than the standard oxidation potential of the water to dioxygen. Having a sufficient gap between the VB and the standard oxidation potential may allow the positive holes with sufficient difference in energy levels to oxidize the water efficiently. **Fig. 1.18** shows different SC materials that respond to the criteria of the band gap position, such as ZnO (Zinc oxide), n-TiO_2, $SrTiO_3$ (Strontium titanate), $NaTaO_3$ (perovskite) and WO_3 (Tungsten trioxide). Most of the mentioned SCs have a particularly wide band gap to fulfil both oxidation and reduction half reactions of water splitting, thus absorbing only a small portion of the photons of the global solar

spectra, mostly photons from the UV range, representing only 4-6% of the solar spectra. This limitation of absorption influences the possible photocatalytic applications at large scale. In the following section dealing with different experimental strategies will be shown on how to improve the TiO_2 photons absorption response towards the visible range. On the contrary, the SCs with a medium or smaller band gap, such as Ag_3PO_4 (silver phosphate), Fe_2O_3 (Iron (III) oxide or hematite or ferric oxide), g-C_3N_4, CdS (cadmium sulphide)., MoS_2 (Molybdenum disulfide), CdSe (Cadmium selenide), and CdTe (Cadmium telluride), can absorb a significant amount of photons from the visible but can only undergo efficiently (theoretically) one of the two water-splitting half reaction [138].

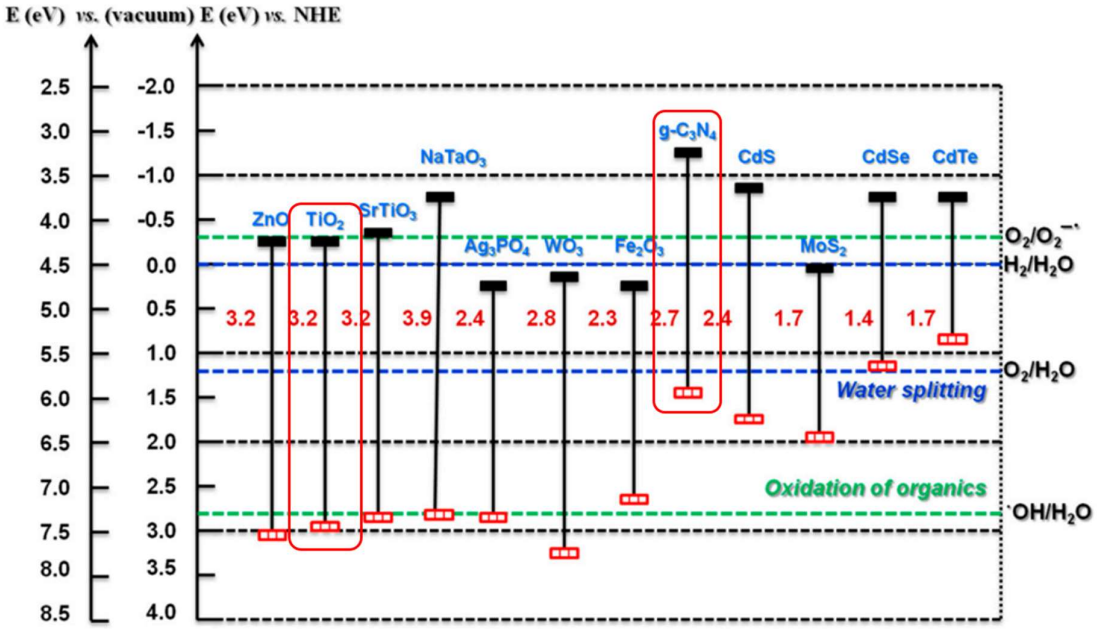

Figure 1.18. Energy band alignment diagram of several wide and narrow gap SCs, marking TiO_2 and g-C_3N_4, with their standard potential of the two water splitting half reactions and organic oxidation [138,139].

For the case of g-C_3N_4 SC possesses a narrow band gap for absorbing some visible-light, besides being able to perform water oxidation and proton reduction, making it interesting.

TiO_2 presents mainly four polymorphs, anatase (tetragonal, space group I 41 / amd), rutile (tetragonal, space group P 42 / mnm), brookite (orthorhombic, space group Pbca), and TiO_2 (B) (monoclinic, space group C2m) [140]. The respective crystallographic structures are presented in **Fig. 1.19** [141].

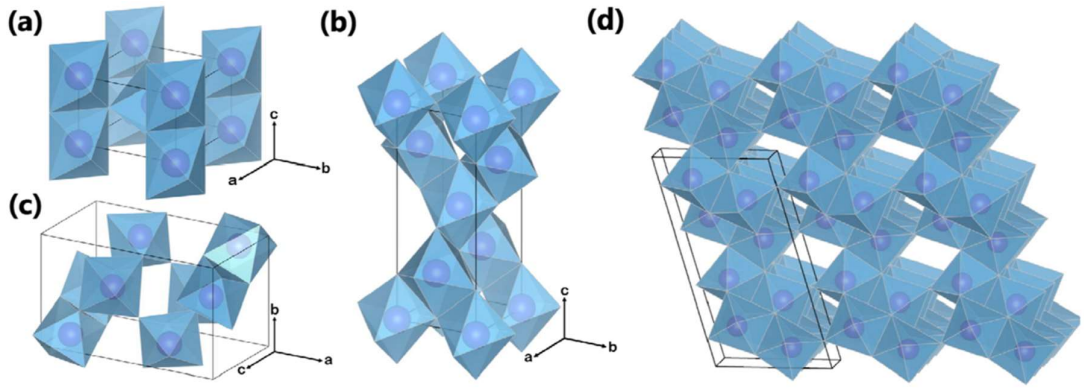

Figure 1.19. Crystal structures of TiO_2 main polymorphs: a) Rutile b) Anatase c) Brookite d) TiO_2 (B). Purple spheres represent Ti atom, and the blue octahedrons represent TiO_6 blocks. Oxygen atoms at the corner of the octahedron are omitted for clarity [141].

The basic unit of the crystalline structure of TiO_2 is constituted by an octahedron formed by oxygen atoms at the lattices points and for titanium atom at the center. The main difference between anatase and rutile relies on the octahedrons distortion. For the anatase case, the O^{2-} ions form a compact and deformed cubic stack. Contrarily for the rutile case the ions form a compact and deformed hexagonal stack. The average length of the Ti-O bond is 1.97 Å within the rutile and 1.93 Å within the anatase [52]. These differences are translated at the level of electronic structure of these two allotropic forms. The magnitude of the band gap of rutile is 3.0 eV while that for anatase is 3.2 eV. Thermodynamically, the stable phase of TiO_2 is rutile, but anatase is metastable at low temperature. The respective stability of the two phases rutile and anatase can be inversed when the crystals are of nanometric size. The anatase is more stable than rutile when the sizes of the grains are inferior of 14 nm [142]. Brookite and anatase transform in rutile over a wide range of temperature (T > 650 °C) [143]. Brookite is an orthorhombic network with a more complex structure than anatase and rutile. Comparing the occupied space volume for one unit of TiO_2 of the three structures shows that the compactness decreases following the sequence rutile > brookite > anatase.

TiO_2 (B) is a metastable polymorph of TiO_2 monoclinic structure and its density is weaker than the anatase one. It can be synthesized for example by using the hydrothermal method, by the decomposition of a titanium alkoxide (isopropoxide of titanium (IV) $Ti(OCH(CH_3)_2)_4$) in an acid solution followed by a thermal treatment (240 ° C) for a few hours.

D.1.4. Modifications

Despite of the TiO_2 advantages, its wide band gap nature requires a high energy for activation. It is commonly not used for visible-light applications yet without being modified. Several TiO_2 photosensitization strategies had been proposed to increase its absorption of photons from the visible range, such as coupling with lower band gap SCs, deposition of metallic NPs, (with plasmonic effects), doping, and dye grafting. For this section only the coupling, deposition of metallic NPs, and doping strategies will be

covered. Meanwhile, the plasmonic fundamentals will be discussed separately in an independent section **E.2**.

D.1.4.1. Coupling

TiO_2 can be coupled through heterojunction formation with other semiconductors with different band gap and energy levels to extend its absorption wavelength range towards the visible-light region and to hamper the recombination of generated carriers [144]. It has been reported that an adequate matching of the CB and VB positions of the semiconductors could guarantee an efficient vectorial transfer of the charge carriers from one to another. TiO_2 as wide band gap semiconductor preferably is coupled with small band gap semiconductor (CdS, CdSe, WO_3, SnO_2, or g-C_3N_4), which absorb photons from the visible-light range (E_g TiO_2 > E_g SC2). Preferably with a more negative CB level, the excited electrons generated in the SC2 can be injected to the TiO_2 CB. By respecting this condition of a more negative CB on the SC2, its VB position will be in a lower energetic level in reference to the TiO_2 VB, which means that TiO_2 can transfer h^+ from its VB to the SC2 VB. These two paths are shown in **Fig. 1.20** when TiO_2 is coupled specifically with g-C_3N_4 in a staggered heterojunction type. In this optimal configuration, in addition to visible-light activation of the composite materials the promotion of the overall separation between the photogenerated e^-/h^+ pair is enhanced.

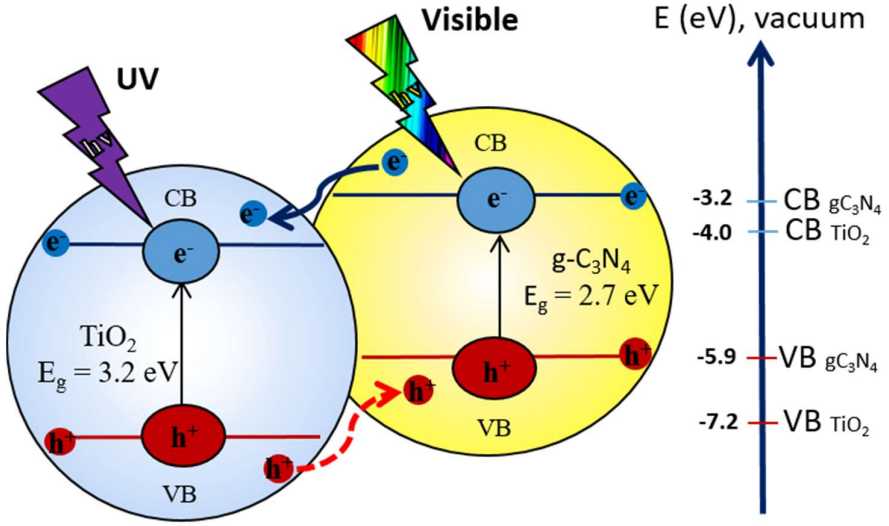

Figure 1.20. TiO_2 coupled with g-C_3N_4 in a heterojunction type II (staggered type). The photo-sensitization mechanism, under visible-light irradiation is shown. Also, the possibility of transferring h^+ from TiO_2 (VB) to g-C_3N_4 (VB).

D.1.4.2. Deposition of metallic NPs

The aim of depositing metallic nanoparticles onto the surface of a semiconductor is to create a M/SC interface [145,146], which brings several beneficial functionalities in photocatalytic reactions [147]. Amongst the M NPs functionalities, one can mention that electron trapping and co-catalytic properties are the predominant, without forgetting the Surface Plasmon Induced Effect (SPIE). More details are described in section **E.3**.

D.1.4.3. Morphology

TiO_2 morphology modification is an interesting method by the possibility of synthesizing different one-dimensional morphologies such as nanofibers, nanotubes, nanoribbons, etc. [120]. Studies have shown that in TiO_2 nanotubes, besides of a significant gaining on the specific surface aspects, the charge recombinations of photogenerated carriers is significantly diminished, in reference to others TiO_2 morphologies. The main difference relies on the decoupling of photon absorption direction and electron collection and a more straightforward electron transfer path [148].

D.1.4.4. Doping

Chemical doping or band gap engineering of TiO_2 consists on introducing an additional atoms, and thus intermediate levels into its band gap. These new species can substitute the titanium atoms by cations and the oxygen atoms by anions elements in the TiO_2 unit cell. The objective of inserting their atomic orbitals within the TiO_2 band gap is to enables TiO_2 to absorb at longer wavelengths.

The presence of metal ions (impurities) inside the unit cell of semiconductor, promotes the creation of new energy levels within its band gap, called "band tails". The process to form the new band tails comprises several steps.

The typical methods to doped TiO_2 are: **(I)** treating the final or growing TiO_2 nanomaterials in presence of doping species, **(II)** production of nanomaterials by co-sputtering or sputtering in an atmosphere of doping species **(III)** high-energy ion implantation [149].

The different doping cases are introduced: anionic, cationic, co-doped, co-alloyed, and the resulting modified TiO_2 energy band gap for each case are shown in **Fig 1.21**. The first two cases correspond to ion co-doping, and the second two cases correspond to double ion doping (one anionic and the other cationic). All the mentioned cases are compared with the TiO_2 anatase reference with a band gap of 3.1 eV.

The **anionic doping** consists on introducing p orbitals of non-metals anions such as C, N, F, P, and S [150–152]. The aim is to mix the new p orbitals of any of the mentioned non-metals with the existing 2p orbitals of oxygen. Asahi and co-workers introduced in 2001 the first successful nitrogen doping [153]. They demonstrated by density of states calculus that nitrogen is the best candidate to enhance the efficiency of visible-light absorption. Thanks to the hybridization between the p orbitals of nitrogen and oxygen, it reduces effectively the TiO_2 band gap and consequently enhances the generation of e^-/h^+ at longer wavelengths. The C and P doping introduce energy levels inside the band gap, which are very localized for the photogenerated carriers that can be efficiently transferred to the surface to react with the adsorbed species.

The **cationic doping** consists on inserting a metallic atom cation by replacing the titanium cation of the unit cell. The compatible metals should be selected according of their d orbitals energy. In fact, the success of an efficient cationic doping depends on the hybridization between the 3d titanium orbitals and the d orbitals of the dopant. This

doping type has explored several transition metals on the first-row elements such as V, Cr, Mn, Fe, Co, Ni, Cu, but also belonging to the second-row elements such as Nb, Mo, Ru, and finally third-row Ta, Hf [154]. Among the mentioned metals, Cr and V were described as successful in activating a TiO_2 response in the visible-light range. Another particular case is Fe^{+3} due to its ability to serve as a shallow trap for both electrons and holes [145]. Zhang *et al*. found that Fe^{+3} loading in the photocatalyst and the size of the support particle has a relationship, which impacts the photoactivity. They concluded that there is an optimal Fe^{+3} loading for each particle size, hence the optimal doping levels are typically < 1atom % [155].

The **co-doping** consists on inserting in two different steps anions and cations within the TiO_2 structure. The aim is to form new hybrid orbitals as the resulting fusion of p orbitals of the anion and of the d orbitals of the cation. The new hybrid orbitals comprised discrete energy levels. One can say that a great advantage of TiO_2 co-doped material is to be more stable in reference to a mono doped. The stability comes from the effective compensation of charges on the formation of the hybrid orbital comprising both anion and cation. Density of Functional Theory (DFT) calculations have explored the formation of hybrid orbitals on TiO_2 of couples such as (C, Ta), (C, Hf), (C, Fe), (N, Hf), (N, Fe), and (N, Ta). However, experimental measurements have confirmed the predictions of the calculations only for non-stoichiometric incorporation of impurity pairs, rather than desirable stoichiometric co-doped samples, which makes a limitation of the strategy. As an example of both cases, $Ti_{1-(5x/4)}Nb_xN_yO_{2-y-\delta}$ [156] and (Nb, N) TiO_2 [157] are samples prepared from two different groups to obtain the same co-doped target (Nb, N) but eventually with different stoichiometry, loading, and proportions. Nevertheless, the global aim was achieved, both samples led to reduced TiO_2 band gap and to enhancement of the visible-light absorption and consequently increased the activity in comparison to the mono-doped material.

The **co-alloyed** strategy consists on the exactly same principle than co-doped on introducing in two steps the cation and anion, respectively. The main difference is the dopant concentration which is higher in comparison to the co-doped method. The increased dopant concentration generates a creation of more close energy levels that confers a continuous character and leads to junction with the maximum level of the VB and the minimum level of the CB forming a cloud energetic type.

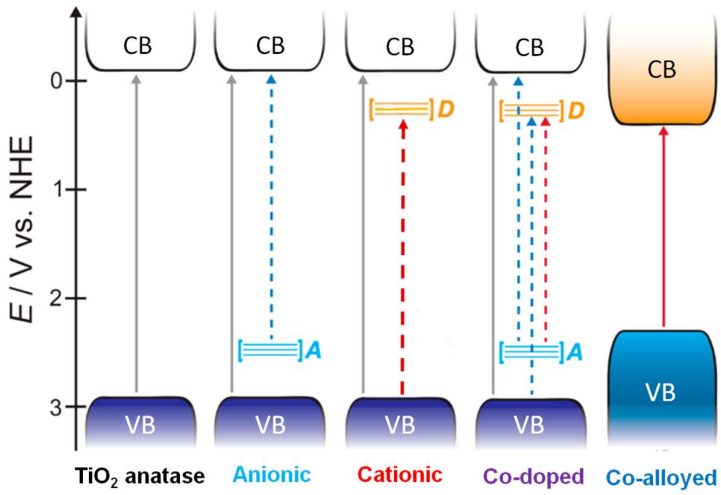

Figure 1.21. Density of states scheme of TiO_2 energy bands for the different doping types. Orange represents several energy states on the CB, blue represents several energy states on the VB, A stands for orbital p of the anion, and D stands for the metal [158].

D.1.4.5. Dye grafting / sensitization

TiO_2 can be grafted with organic dyes onto its surface to enhance its visible-light response [159]. The dyes are generally chromophores. When they are grafted onto TiO_2 they serve as photosensitizers. The principle, proposed from 1960s, operates by visible-light activation on the dye molecules that passed to an photo-excited state leading to inject electrons into the CB of the n-type SC substrates [160]. A disadvantage of this method is the chromophore stability in oxidizing environment, the dyes can be photo-oxidized in contact with TiO_2 along the time.

D.2. Graphitic Carbon Nitride (g-C_3N_4)

D.2.1. History

Carbon nitride (C_3N_4) is a wide family of carbon and nitrogen containing material, with hydrogen impurities. It is considered as the oldest synthetic polymer, firstly synthesized by solid state in 19th century. More precisely in 1834, the first attempt was carried out by Berzelius. He prepared C_3N_4 using mercury (II) thiocyanate ($Hg(SCN)_2$), and a yellow pale solid, amorphous, insoluble product was obtained, more commonly known as Pharaoh´s snakes, by its analogue pyrotechnic growth. It was named as "melon" by Liebig due to its color. The second attempt took place one year after (1835), when Gmelin, synthesized potassium hydromelonate ($K_3C_6N_7NCN$) when heating potassium ferricyanide and sulphur [161]. Nevertheless, the elucidation of both g-C_3N_4 and $K_3C_6N_7NCN$ structures was, thus, not possible due to the lack of advanced analytical and characterization tools to do so. In 1922, Franklin introduced the concept of carbon nitride $(C_3N_4)_x$. By the thermolysis of Hg $(SCN)_2$, he had synthesized an amorphous C/N compound as the final polymerization product while deamination of the amino-carboxylic acid [162]. He proposed the 2, 5, 8 triamino-tri-s-triazine ($C_{126}H_{21}N_{175}$) structure, amongst several structures too, but the experimental results lack of strong characterization evidences. A XRD study was needed, to demonstrate the different phases inside the polymeric structure of g-C_3N_4. In this context, Pauling and Sturdivant,

suggested for the first time the coplanar tricyclic tri-s-triazine (s-heptazine) unit as the elementary structural motif with XRD evidence. Three years after, Lucas and Redemann found an inconsistency of melon's composition proposed by Liebig and Franklin. Thus, they proposed the structures of melam, melem and melon. Still, their major contribution was to report that "melon" has a graphite structure [163]. From 1950-1980, Finkel'shtein and co-workers carried out a series of experiments to confirm the different derivates of g-C_3N_4 mentioned so far [164]. A theoretical study conducted by Teter and Hemley in 1996, also suggested a triazine-based structure for g-C_3N_4 [165]. In 1989, a theoretical prediction drawn by Liu and Cohen, of an ultra-hard carbon nitride material (ß-C_3N_4, sp^3), even harder than diamond, which has risen the C_3N_4 materials research [166]. Nevertheless, it was until 2008 that Wang, Antonietti *et al*, revealed in a milestone analysis its C_3N_4 photocatalytic H_2 and O_2 evolution capacity under visible irradiation by using a co-catalyst, in assistance of an electron donor and/or acceptor, respectively [89]. Since then, the research on g-C_3N_4 had tremendously increased in that area.

D.2.2. Synthesis

Several synthesis methods had been reported to obtain g-C_3N_4, namely physical vapor deposition (PVD), chemical vapor deposition (CVD), solvothermal, thermal condensation, microwave irradiation, and solid state reaction [167]. From all the synthesis methods, thermal condensation is the most accepted, due to its simplicity. Typically, the organic precursors used for the thermal polycondensation are cheap nitrogen-rich species. **Fig. 1.22**, shows the molecular structure of urea, thiourea, melamine, cyanamide, dicyandiamide (DCDA), and others like ammonium thiocyanate, etc., used as precursors.

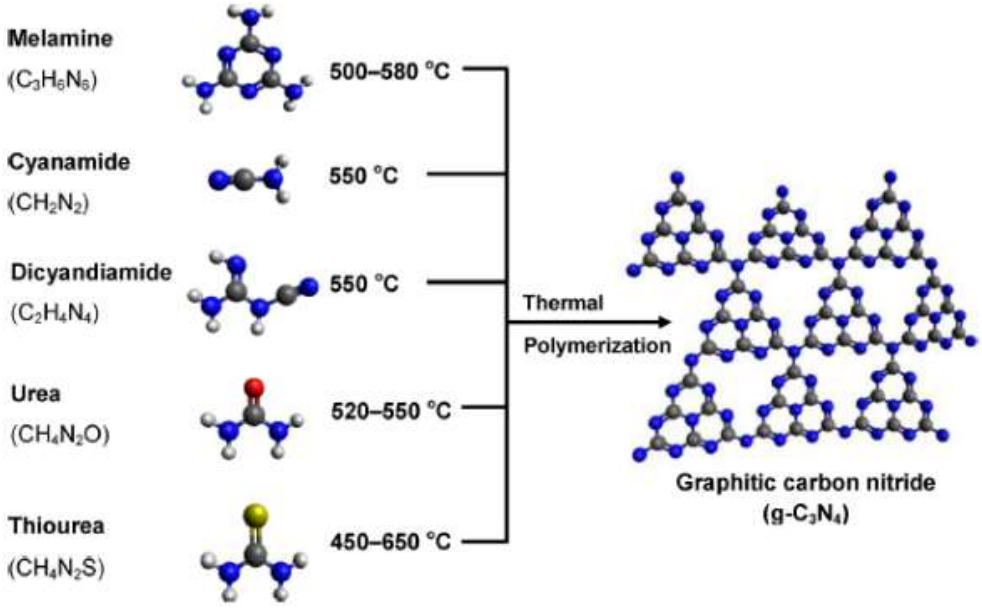

Figure 1.22. Scheme of different g-C_3N_4 precursors undergoing under thermal polymerization, *e.g.*, melamine, cyanamide, dicyandiamide, urea, and thiourea [168]. The black, blue, white, red, and yellow circles stand for C, N, H, O, and S atoms, respectively.

For each precursor the thermal decomposition transformation might occur with a different polyaddition and polycondensation mechanistic paths but with equivalent melamine formation step. For instance, between 200 – 235 °C, Wang *et al* had reported that cyanamide molecules are condensed to dicyandiamide and then to melamine (aromatic block) [89]. After 300 °C, the intermediate species are the same to form the final g-C_3N_4 structure, independently of the initial precursor. **Fig. 1.23** shows a postulated thermal polycondensation mechanism for the specific case of melamine. One can notice, that the pyrolysis of melamine leads to the self-condensation resulting in the formation of the so-called melam and melem at 320 °C. While the condensation continues undergoing to form the corresponding intermediates, a deamination process is taken place via thermal reaction simultaneously. Once melam and melem are well-formed and the temperature rises above 390 °C, the melon structure appears. All in all, when the temperature reaches 520 °C, the crystalline phases of g-C_3N_4 appears leading to the formation of tri-s-triazine and s-triazine based g-C_3N_4. Theoretically, around 600 °C, the tri-s-triazine becomes unstable, and the polymeric g-C_3N_4 decomposed from 700 °C [169]. Bear in mind, that there is a debate in the research community of whether the existence of these intermediates can be experimentally proved by crystallography due to the lack of in-situ measurement coupled with an XRD equipment and considering the difficulty of doing it while ammonia (corrosive gas) that is released in different steps. Nevertheless, until now this model is the most accepted postulated thermal polycondensation mechanism.

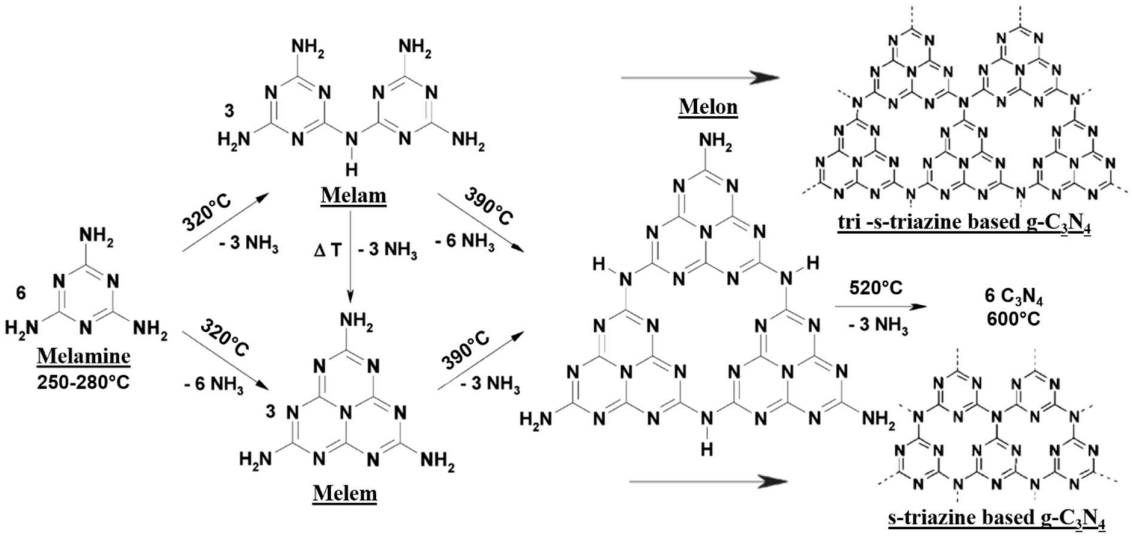

Figure 1.23. Modified thermal polycondensation mechanism of melamine inspired from [169].

Thomas *et al* [167], have calculated by ab initio method the polyaddition and condensation reactions to clarify the reaction path with further details. Using a density-functional theory (DFT) with a cut-off at 550 eV, they have demonstrated that the cohesive energy of the thermal polycondensation of melamine increases while forming melem. Melamine and melem are considered as molecular crystals due to their strong covalent bonds inside the molecular building blocks, while the crystal interacts by weak interactions. They have confirmed a very similar reaction pathway, including the

presence of the same intermediates than in **Fig. 1.23**. Hence, the calculations indicated that the shape of the melon chain is defined by a competition between both an energy gain by extending the π-electron system into a linear chain and the repulsion between the lone pair of electrons located on the nitrogen atom located on the edges. Once the g-C_3N_4 linear chain is formed, it remains strongly distorted due to the interaction of several N atoms on the tri-s-triazine edges to maximize their distance and position [167]. Parallely, Kroke *et al*, contributed with another DFT study, confirming that tri-s-triazine based structure is 30 kJ mol^{-1} more thermodynamically stable than s-triazine, thus the most accepted unit for g-C_3N_4 [170].

With the Wang *et al* work, the g-C_3N_4 formation evidences and mechanism explanation on the thermal polycondensation was an important advance in heterogeneous photocatalysis field. Moreover, this work has included g-C_3N_4 as a new potential, organic "metal free" SC into the list of active materials for H_2 production under visible-light irradiation [89]. Nevertheless, due to a **small specific surface**, lower than 20 m^2 g^{-1}, was limiting its applications. Especially in fields where the surface, pore characteristics, and active sites plays a key role. Several theoretical calculations opened strategies to overcome the small surface area issue. One can mention new synthesis methods or g-C_3N_4 modifications that have been developed, *e.g.*, "hard", "soft", "self", and "free" templates [171–174], liquid impregnation [175], copolymerization with different agents [176], cave and interlayer doping [177], and layers exfoliation [178]. All mentioned methods aim at improving the g-C_3N_4 physico-chemical properties to ultimately enhance its global activity. These modifications will be further explained in section **D.2.4**.

Vast R & D efforts for improving g-C_3N_4 materials performance have been carried out by identifying and understanding which the key parameters are. For example, precursors, atmosphere synthesis, temperature ramp rate, polycondensation temperature, and reaction time. These parameters defines the polymerization degree of g-C_3N_4, which determines its resulted physico-chemical properties.

D.2.2.1. Influence of the precursors

Typical precursors, derived-precursors, water [179] / sulfur [180,181] / sucrose [182] / others-mediated reactants can be used before (pre-treatment) or during the polycondensation synthesis for rational design of g-C_3N_4.

Martin *et al*, synthesized g-C_3N_4 by using urea, thiourea, and dicyandiamide. They showed that the urea-derived g-C_3N_4 produced higher H_2 production than thiourea and dicyandiamide-derived g-C_3N_4 counterparts, presumably due to larger surface area, a higher degree of polymerization, improved charge migration, and movement of delocalized electrons from the oxygen-containing precursor despite absorbing less light [183]. Yuan *et al*, reported the synthesis of g-C_3N_4 with two different precursors oxygen-free melamine and oxygen containing urea under the same operational conditions, *ca.* 580 °C for 3h. They found that the urea-derived g-C_3N_4 exhibited a higher surface area than the melamine-derived g-C_3N_4, 39.5 and 3.7 m^2 g^{-1}, respectively. It was also found that urea-derived precursor leaded to effective photoinduced charge separation and better photocatalytic CO_2 reduction. This enhancement might be explained by the

generation of pores on the urea-derived g-C_3N_4 that brought two simultaneous benefits, increasing the number of active sites, and decreasing the diffusion length of photoinduced charge transportation to minimize recombination rate [184]. Zhang *et al*, obtained urea-derived g-C_3N_4 at 550 °C for 3h with larger porosity. The porosity might come from the generated NH_3 at a low temperature and CO_2 at high temperature. Thanks to the porous structure and small flake sheets exhibited, its surface area and pore volume were increased as well, therefore enhancing the activity [185].

The pre-treatment of the precursors by different means, namely acid solution (HCl, H_2SO_4, HNO_3) is considered an attractive and simple strategy to improve properties. One step pretreatment with HCl to melamine resulted in different morphologies, such as belt- or ribbon-like porous g-C_3N_4 with aggregated bundles or cables and higher surface-to-volume ratio than bare g-C_3N_4 [186,187]. For the case of H_2SO_4-treated melamine, a g-C_3N_4 with higher specific surface than the bare counterpart was obtained, presumably due to the different condensation process [188]. By heating HNO_3-protonated melamine via rolling-up mechanism, 1D tubular g-C_3N_4 with highly porous structure was obtained, possibly due to the decomposition of self-assembled rod-like protonated melamine hampering the recombination rate [189].

In the same context, other precursors containing different atoms than C, N, and H, can be also used. In this case positive modifications on g-C_3N_4 morphology and texture was observed [190].

D.2.2.2. Influence of the atmosphere nature

Structure of g-C_3N_4 is greatly influenced by the nature of reaction atmosphere used during the thermal polycondensation synthesis. The influence of the reaction on g-C_3N_4 continuous gas flow synthesis is controlled by the gas flow rate. The gas flow rate will define the concentration (saturation) of the atmosphere inside the furnace environment. It is believed that depending on which atmosphere is used, it might induce disordered structures defects, and carbon and nitrogen vacancies in a greater or lower degree. Defects on g-C_3N_4 structure are interesting in photocatalysis because the controlled mesoporosity increases the active sites number within the material without destroying its structure. Parallely, C and N vacancies introduces intermediate energy levels within the g-C_3N_4 electronic structure, *e.g.* additional energy bands between the VB and the CB, thus increasing the optical response of the photocatalyst [191].

D.2.2.2.a) Oxidative atmosphere

The most common atmosphere for synthesizing g-C_3N_4 is air. A huge amount of literature has been working with this atmosphere, due to its facility to use and low price, especially in static condition but also under continuous gas flow. Even Antonietti pioneer work uses air to synthesize g-C_3N_4 [89]. Nevertheless, within the studies that have used air as atmosphere there is a repeating pattern, small surface area. Therefore, studies on using different type of atmospheres have getting a lot of attention.

D.2.2.2.b) Reductive atmosphere

The use of H_2 atmosphere as post-calcination step and source of vacancies and distortion on the g-C_3N_4 structure was reported by Niu *et al*. They evidenced an additional optical absorption above 460 nm, presumably due to the small size of H_2 that can easily access the channels among the layers to interact and therefore react with the skeleton atoms in g-C_3N_4 forming vacancies as illustrated in **Fig. 1.24 a)**. On top of that, by deduction of the higher hydrogen bonding interactions, the distortion is promoted on the planar g-C_3N_4 configuration, forming lone pairs on the edge of N atoms in the tri-s-triazine based g-C_3N_4 units within the π-conjugated system. This new position leads to new electronical transition n → π*, which allows a greater e^- density in the π-conjugated system, facilitating the e^- mobility to the CB and initiating the photocatalytic process [192].

Yang *et al* published a study on g-C_3N_4 synthesis under partial NH_3 pressure. The NH_3 treatment displayed a significant specific surface area increase in the new mesoporous material, thus the photocatalytic hydrogen evolution from water was enhanced too. One can say that the decomposition of NH_3 in high temperatures forms two active radical species, *i.e.* NH_2*, NH* as illustrated in **Fig. 1.24 b)**. These radicals can etch different N-$(C)_3$, C-N=C, and C=C lattice sites, resulting in the creation of new pores. These pores may enhanced e^-/h^+ pairs separation efficiency and longer charge lifetimes occur [193].

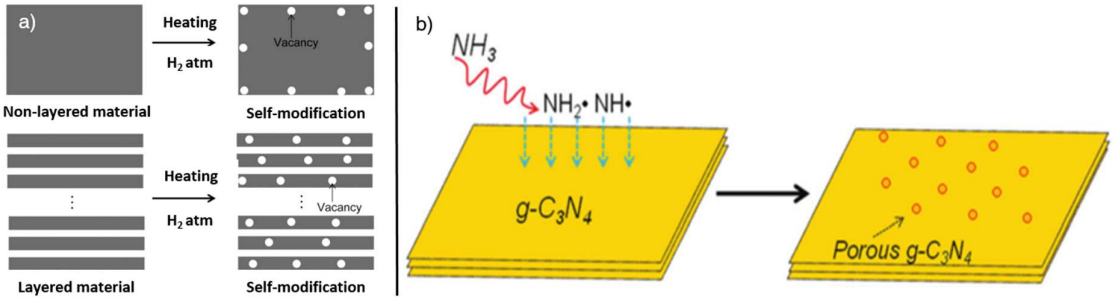

Figure 1.24. a) Scheme of self-modification to promote oriented vacancies in two type of materials [192]. b) Use of NH_3 atm on the g-C_3N_4 synthesis and the creation of two radical species that lead to increase the surface porosity [193].

D.2.2.2.c) Inert atmosphere

The use of N_2 during the g-C_3N_4 synthesis has been reported by Dong *et al* [194]. The introduction of nitrogen vacancies has led to a better photocatalytic N_2 fixation ability, presumably, due to the improved separation efficiency of photogenerated carriers and the e- transfer from g-C_3N_4 to adsorbed N_2. In another study, Maschmeyer *et al* [195] reported that the g-C_3N_4 photocatalytic performance was enhanced due to new hydrogenated defects within the g-C_3N_4 nanosheets. As already mentioned defects can act trap sites for charge carriers, reduce the charge carrier lifetime, and additional band tail (vacancies) that impact its electronic / optical properties.

D.2.2.2.d) Vacuum condition

Another strategy by using vacuum during polycondensation synthesis was reported by Yuan *et al*, accomplishing 61 % yield, using melamine as precursor. The band structure,

electronic properties, and surface areas of g-C_3N_4 could be modified by controlling specific reaction parameters, which leads to improved photocatalytic materials [196].

Independently of the atmosphere used, the presence of lattice disorders and defects within the g-C_3N_4 structure leads to the formation of midgap states, also known as "band tail" states. These g-C_3N_4 modifications serve to enhance the excitation of e^-/h^+ pairs and the optical response of the photocatalyst [197]. Also, disordered defects can function as trapping sites, and retard the recombination rate of charge carriers [198].

D.2.2.3. Influence of the time and temperature of reaction

The heating ramp rate, time, and temperature of the thermal polycondensation is another strategy to modulate the g-C_3N_4 structure. A study consisting in heating urea at 550 °C for different **duration of reaction** ranging from 0 to 240 min (**Fig. 1.25 a**), resulted in specific surfaces ranging from 31 - 288 $m^2\ g^{-1}$ [199]. Another particularity of the obtained materials was the increased porosity and decreased layer thickness ranging from 36 - 16 nm. This indication of exfoliation-type might be associated with the previously reported hydrogen bonding between the NH/NH_2 groups of the melon polymeric strands that drives the stacking layer force of g-C_3N_4. The hydrogen bonds under thermal oxidation conditions are not resilient enough and therefore the g-C_3N_4 layers will progressively disrupt during the thermal annealing through a layer-by-layer exfoliation path [200]. Yan *et al*, reported a g-C_3N_4 synthesis using melamine at different reaction temperatures ranging from 500 - 580 °C [201]. The study demonstrated that the C/N ratio can be modified in function of the increase of the reaction temperature and different ratios were obtained *ca.* 0.721 - 0.742 with decreasing band gap values, *ca.* 2.8 - 2.75 eV. Presumably for the amine existing groups containing 2% of hydrogen, the C/N ratio was smaller than the ideal "perfect" g-C_3N_4 (0.75). In another study was reported that nano-sized g-C_3N_4 samples synthesized at temperatures of 550, 600, 625, 650, 675, and 700 °C showed a blue-shift which was related to the $\pi \rightarrow \pi^*$ transitions and quantum size confinement. The samples shown in **Fig. 1.25 b**, present a transition from yellow to light and dark orange with the increase of temperature, which confirms the different absorptions.

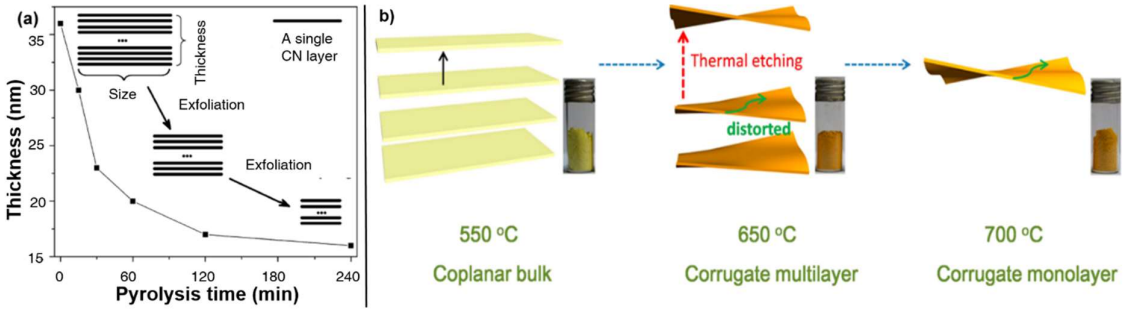

Figure 1.25. a) Layer thickness in function of the pyrolysis duration of g-C_3N_4, pointing out the Layer-by-Layer exfoliation and splitting mechanisms [199] b) Scheme of the synthesis pathway of structurally distorted g-C_3N_4 nanosheets [202].

D.2.3. Physical and chemical properties

Seven different crystalline polymorphs (allotropes) are well described in experimental and theoretical literature, six of them are 3D: α-C_3N_4, ß-C_3N_4, cubic-C_3N_4, pseudocubic-C_3N_4, g-h-triazine, and g-h-heptazine and the last allotrope is 2D: graphitic g-C_3N_4 which is the most stable [166,168,203]. The graphitic phase presents a chemical structure analogue to graphene, several in-plane π conjugated systems, which are based on perpendicular weak interactions (Van der Waals) with both top and bottom sheets, are stacked in a 2D network of hexagons based on aromatic rings, such bulk configuration.

For the case of g-C_3N_4 (ϕ = 4.65 eV), theoretical predictions have been made and identified a crystalline and an amorphous phases as shown in **Fig. 1.26**. Typically, g-C_3N_4 layer structure comprises a planar bonding which is partially due to hydrogen bonding between the polymeric melon units with NH/NH_2 groups. The **crystalline structure** presents a great planar cohesion together with the weak interplanar interaction allowing a long-range atomic order in both directions perpendicular and parallel for homogeneous amorphization. One can say that the strong covalent C-N bonds in the melem units are more stable than van der Waals and hydrogen bonds. The C-N stability avoids internal bonding rupture and consequently retains the short-range atomic order, even if a high temperature treatment is applied. For the case of the **amorphous structure**, the monolayer tends to disorganize itself after applying a high thermal treatment, leading to a crystalline C_3N_4 polymer. Two significant structure changes are expected: (i) the rupture of in-plane hydrogen bonds between strands of polymeric melon units (ii) the outward twisting of melon units due to large outward movement of the NH_2 groups from the original crystalline C_3N_4 plane [204].

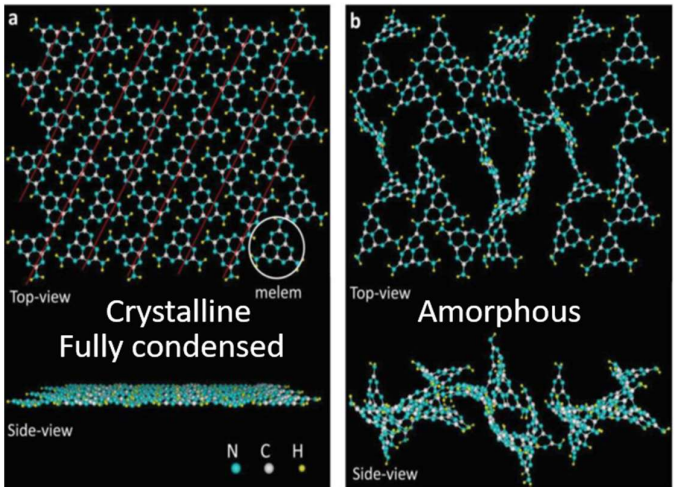

Figure 1.26. Scheme of monolayer a) crystalline and b) amorphous structure of graphitic carbon nitride. N, C, and H atoms are light blue, white, small yellow circles [204].

D.2.4. Modifications

Nanoarchitecture design of g-C_3N_4 can be obtained by tailoring structural properties and interlayer interactions in orienting a specific morphology with controlled order porosity and higher specific surface area by using templating, copolymerization, and exfoliation.

D.2.4.1. Templates

D.2.4.1.a) Hard-template

This approach or nanocasting is a simple, flexible, and effective methodology for designing various structures and geometries of g-C_3N_4, such as spheres, rods, tubes, and sheets with the assistance of sacrificial templates [205]. Macro/mesoporous g-C_3N_4 with significant surface area (up to 517-623 m^2 g^{-1}) [171] could be obtained with length of scales of nanometers and micrometers [206]. The agent by excellence in hard template strategy is **silica**, because it can construct several controllable hierarchical architectural nanostructures [207,208]. However, other hard templates have been reported, such as porous anodic Al_2O_3 [209], $CaCO_3$ [210], graphene oxide nanosheets [189], CMK-3 mesoporous carbon [171] and applied to g-C_3N_4. Mesoporous silica templates, namely, SBA-15, SBA-16, KCC-1, and KIT-6 have been used to synthesize ordered g-C_3N_4. The ordered g-C_3N_4 properties are important because they determine the photocatalytic activity. By the time, the guest molecules at the surface of the catalyst are oriented in the nanopores, thus a gathering of catalytic cofactors inside the porous are taken place. Generally, the principle starts when g-C_3N_4 precursors are impregnated with a mesoporous silica template, it will result in a dried powder to be calcined and condensed into a g-C_3N_4 network confined within the silica template. Then, the silica template is removed with NH_4HF_2 of HF solutions to obtain only the ordered mesoporous g-C_3N_4. Kailasam *et al* reported a pioneer work by mixing and condensing cyanamide (NH_2CN) and tetraethylorthosilicate (TEOS) forming interpenetrating mesophases forming the mesoporous g-C_3N_4 or silica after selective removal of one of the phases. For the case of obtaining g-C_3N_4, NH_4HF_2 removal step is needed, and for the case of SiO_2, a thermal treatment under air is needed as shown in **Fig. 1.27 a**. The obtained g-C_3N_4 films or monoliths enhanced the photocatalytic H_2 production in comparison to the bulk [206].

D.2.4.1.b) Soft-template

The "greener" approach targeting the synthesis of porous g-C_3N_4 micro and nanostructures, besides designing various geometries can also simplify the synthesis route [172]. This methodology uses **soft structure directing agents**, *ca.* ionic liquids, block polymers, and surfactants which are considered amphiphilic organic molecules that are capable of forming micelles and induce the growth of precursors around them and consequently direct the final structure [213] as shown in **Fig. 1.27 b**. Typical soft structure agents used as ionic liquids [214,215] are Pluronic P123 [172], Triton X-100 [216,217], bubble [181,182,218], and biomolecules [182,218]. Zhang *et al* reported that the mixture of 1-butyl-3-methylimidazolium tetrafluoroborate (BmimBF4) as soft-template and dicyandiamide resulted in B/F-co-doped mesoporous g-C_3N_4 with a large specific surface area of 444 m^2 g^{-1} with a 0.32 cm^3 g^{-1} [214]. A very similar study used Pluronic P123 as soft template and exhibited 299 m^2 g^{-1} [172].

D.2.4.1.c) Supramolecular

Self-assembly template occurs when the formation of supramolecular assemblies (aggregates or complex) based on hydrogen-bonding conditions adopt molecules orientation of the medium in the absence of an optimized external template [173]. The

hydrogen bonding plays a key role to form the ordered molecular building blocks, resulting in an aggregate with usual reversibility, specificity, and directionality of the noncovalent interactions that will determine the morphology of g-C_3N_4 [219,220]. One limitation of this method is the low amount of precursors which form stable and ordered aggregates in a solvent. Interestingly, by a simple organic cooperative approach of triazine building block units it was possible to synthesize 3D macroscopic low-dimensional g-C_3N_4, namely nanoparticles, nanotubes, and nanosheets. The strategy to select which morphology predominates was basically for modifying rationally the ratio of monomers, crystallization solvent, precipitation solvent, precipitation temperature, and pairs of hydrogen bonding donor-acceptor [220]. For photocatalytic materials, crystallinity plays a key role in directional flow of electrons. It is well known that incomplete polymerization generates a g-C_3N_4 with low crystallinity and highly amorphous. Photocatalytic activity was found to increase when polymerization temperature increased, presumably for n → π* transition, propose as an important electronic parameter leading to enlargement of the band gap, *ca.* 3.01 eV [222].

D.2.4.1.d) Template-free

Template free synthesis consists on using typically the (hydro) solvothermal and freezing assistant assembly [174] to build porous g-C_3N_4. Also called as nontemplating approach, it is a versatile methodology to obtain different morphologies, such as nanorods, quantum dots, "seaweed" architecture, microspheres, nanofibers, and others [223–225]. In comparison with other methods, like hard templates that uses silica as sacrificial templates, this approach does not need post-removing templates steps, therefore it does not use hazardous fluorine-containing agents (HF, NH_4HF_2). Besides, there is no need of post-treatments like when using conventional surfactants for complete removal of carbon or any heteroatom coming from the soft-template molecules. Template free approach responds to a simpler and eco-friendly urgently need for expanding the g-C_3N_4 application field effectively. Gu *et al* reported template free synthesis to obtain g-C_3N_4 microspheres with enhanced hydrogen generation. For example, simple solvothermal methodology was used with post-heating step to obtain hierarchical microspheres with nanoporous surfaces [225]. In another study, nano g-C_3N_4 were synthesized by a simple dissolve-regrowth step with HNO_3 followed by a calcination step. These materials show an enhanced photoactivity on degradating methylene blue (MB) [224].

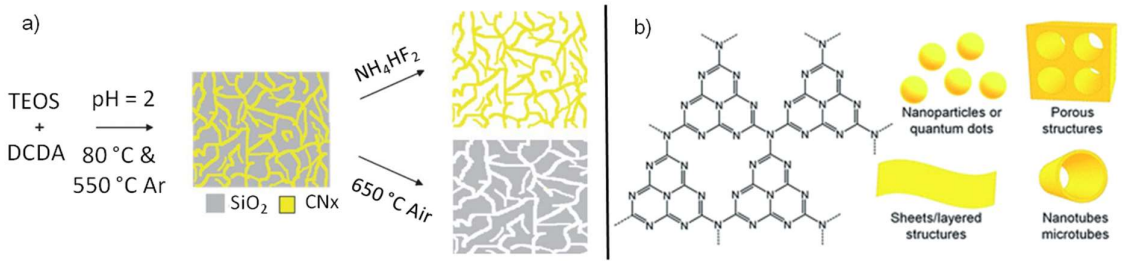

Figure 1.27. a) "Hard" template approach combining sol-gel/thermal condensation methods [206] b) Different morphologies that can be obtained by "Soft" and "Hard" templates approach based on g-C_3N_4 [213].

D.2.4.2. Copolymerization

Copolymerization modification is considered as a molecular doping to modify the intrinsic π-conjugated systems of g-C_3N_4, yielding a modification of the electronic and optical properties, band structure, and therefore enhancement of the photocatalytic performances. However, a few challenges are present, such as rapid recombination of charge carriers, inadequate absorption, low use of sunlight and low surface areas as a consequence of the defective polymerization of organic frameworks, inhibiting possible photo (electro) catalytic functionalities with high quantum yields [176,226]. Therefore, it is envisaged to tune the polymeric π-conjugated system (intrinsic property) to enable a more efficient **delocalization** of the **π electrons.** This delocalization can be extended by anchoring additional g-C_3N_4 structure-matching aromatic groups or organic additives to g-C_3N_4 structure during copolymerization synthesis [227–230]. A bottom-up strategy was introduced while adding pyromellitic dianhydride (PMDA, an e^- deficient specie) into g-C_3N_4 and to form a polyimide (PI). Basically, the PMDA specie was introduced as an intramolecular connector between heptazine units. One can say, that this band engineer strategy demonstrated the modulation of the g-C_3N_4 BG and photo-oxidation strength that improved the photocatalytic activity [230].

D.2.4.3. Exfoliation

Exfoliation process consists on using a mechanical, physical, or chemical force to separate the individual g-C_3N_4 layers that constitute the same stacked bulk unit. It means that the bulk thickness will diminish, and the specific surface will tend to increase thanks to the higher amount of smaller bulk units available. This phenomena is possible due to the presence of weak van der Waals forces between the g-C_3N_4 layers.

Analog to graphite materials, for graphene based materials, efforts have been taken to apply the same exfoliation principle for bulk g-C_3N_4. The idea is to reduce the macroscopic 3D g-C_3N_4 structure into a microscopic 2D one. Two-dimensional (2D) NS are interesting due to their exceptional electronic, optical, and biocompatible properties in reference to the bulk material [231]. The 2D anisotropy of g-C_3N_4 NS possesses great advantages, *i.e.* high electron mobility, favorable band potentials, large surface area and exposed active sites, reduced surface defects, increased lifetime of charge carriers, and stronger reduction potential of the photoexcited electrons [178]. Typically, there are three conventional methods for g-C_3N_4 exfoliation: post-thermal oxidation, chemical, and liquid exfoliation assisted with ultrasounds.

D.2.4.3.a) Post-thermal oxidation exfoliation

It can undergo under air or any other oxidant atmospheres. The pioneer work for this approach was reported by Niu *et al* in 2012. Since, this method is consider a cost-effective, scalable, and friendly environmental, and has attracted a great attention. **Fig. 1.28 a)** shows that the thermal exfoliation undergoes progressively with the thermal treatment duration. That means that the duration of etching influences directly the resulted g-C_3N_4 thickness. This behaviour has been attributed to the breaking of

hydrogen-bonds that link the closest layers in oxidation conditions, these bondings becoming unstable and the layers starting to disjoin one from the other [200].

D.2.4.3.b) Chemical exfoliation

Chemical exfoliation of g-C_3N_4 in alkaline or acid media is possible thanks to its high chemical stability. An alkaline hydrothermal method was reported by Sano *et al*, by using a 0.1 M NaOH solution at different hydrothermal times and they noticed that the C/N ratio did not change, but H and O quantities increased. This findings lead to the removal of unstable domains and to the formation of a mesoporous structure with an enlarged surface area of 8 times than compared to bare g-C_3N_4 [232]. For acid exfoliation, a recent performed study by Papailias *et al*, was published by using concentrated H_2SO_4 for different stirring times (**Fig. 1.28 b**). The study led to high pore volume and specific surface area, wider band gap with more positive VB edge in comparison to bare g-C_3N_4.

D.2.4.3.c) Liquid exfoliation

Liquid exfoliation assisted with ultrasounds was first reported by Zhang *et al* in 2013. It is considered as a "green" route from bulk g-C_3N_4 in water to obtain ultrathin g-C_3N_4 nanosheets as illustrated in **Fig. 1.28 c)**. The exfoliation efficiency of the liquid-exfoliation process can be measured using the enthalpy mixing as shown **equation 31**:

$$\frac{\Delta H_{mix}}{\Delta V_{mix}} = \frac{2}{T_{bulk}} \ (\delta_G - \delta_{sol})^2 \ \varphi \qquad (31)$$

Where ΔH_{mix} is enthalpy of mixing, ΔV_{mix} is volume of mixing, T_{bulk} is thickness of bulk g-C_3N_4, δ_G is square root of surface energy, δ_{sol} is square root of surface energy of the solution, ϕ is volume fraction of g-C_3N_4 [235]. When the bulk and solvent, match on their surface energy, the enthalpy of mixing is reduced and therefore the exfoliation efficiency increases. Knowing the surface energy of g-C_3N_4 (115 mJ m^2) and of H_2O (~ 102 mJ m^2), it has being concluded that water can remarkably disperse the g-C_3N_4 nanosheets. Generally, polar solvents could effectively swell and intercalate in between the NS of the bulk g-C_3N_4 until obtain exfoliated transparent ultrathin NS with ultrasound.

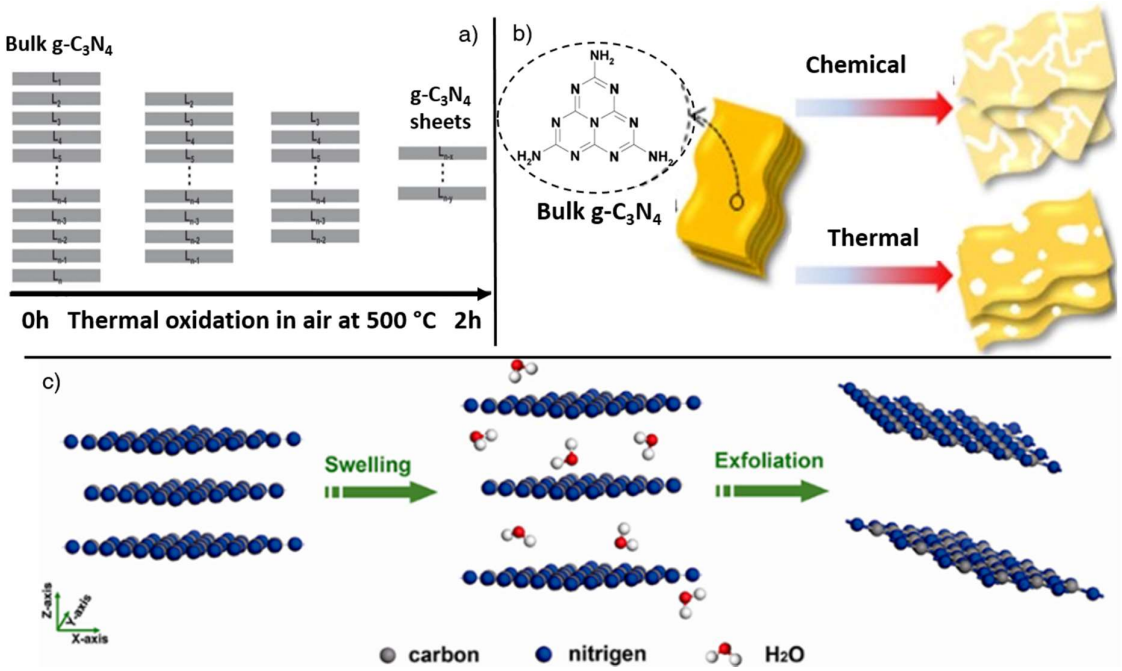

Figure 1.28. a) Scheme of surface self-modification with vacancies in a layer and non-layered material after a H_2 thermal treatment [192] b) Scheme of exfoliating a bulk g-C_3N_4 via chemical and thermal methods [233] c) Scheme of liquid exfoliation initiating from the bulk g-C_3N_4 to ultrathin nanosheets [236].

D.2.5. g-C_3N_4-based nanocomposites

Due to the g-C_3N_4 intrinsic drawbacks, *e.g.*, high recombination rates, low electrical conductivity, limited absorption at 460 nm and small surface area, a strategy evolves on synthesizing more efficient g-C_3N_4-based composites [237]. To overcome some drawbacks, for example: (i) enhancement of charge separation and transfer through Schottky junctions (metal/SC or p-type SC1/n-type SC2) (ii) broader use of the light spectra towards visible (iii) improvement of surface stability by protecting active sites and functional groups onto the SC's surface (iv) lowering the redox overpotential at the active sites with the use of co-catalyst. For this purpose g-C_3N_4 as a 2D flat morphology nanosheets acts as an ideal platform for the synthesis of enormous based composites to overcome their limitations and obtain higher efficiencies of the hybrid composite.

D.2.5.1. Carbon-based g-C_3N_4 – Metal-free heterojunction

Different types of heterojunctions comprising g-C_3N_4 have been reported, thanks to the versatility of other carbon-based materials that can also be attached to g-C_3N_4 via surface functional groups by chemical and/or physical interactions. By selecting carbon-based materials with different physicochemical properties from g-C_3N_4, it is envisaged to obtain functional advanced materials for photocatalytic applications, *e.g.*, isotype g-C_3N_4/g-C_3N_4 (varying the precursors), graphene/g-C_3N_4, carbon nanotubes (CNT)/g-C_3N_4, fullerenes-C60/g-C_3N_4, and carbon-based g-C_3N_4 materials.

D.2.5.1.a) Isotype

The isotype g-C_3N_4/g-C_3N_4 system is made out of two dissimilar crystal phases of the same material. This is also referred as crystal-phase junctions and it can develop an efficient charge migration and separation based on the principle of SC1-SC2 heterojunction formation [238–240]. A g-C_3N_4 (ACNS)/g-C_3N_4 binary composite was reported as an efficient visible-light-driven acidified photocatalyst. It was obtained via ultrasonic assisted electrostatic self-assembly method. The rational design of an alternative approach may allow to overcome intrinsic limitations of g-C_3N_4 without depending on additional SCs to obtain high efficient photocatalysis.

D.2.5.1.b) Graphene

Graphene-based structures have a good reputation in photoredox catalysis, mainly due to the 2D graphene unique electrical, mechanical, and thermal properties that endow an excellent mobility of charge carriers, large surface area, high thermal conductivity, optical transparency, and good chemical stability [241–243]. On top of this positive features, when graphene and g-C_3N_4 nanosheets are in a junction, it can be geometrically advantageous in a 2D/2D face-to-face interaction that takes advantage of most of the specific surface of both components. As an example, Xiang *et al* prepared a graphene/g-C_3N_4 composite by a combined impregnation-chemical reduction method, involving melamine polymerization in presence of graphene oxide as precursors and hydrazine hydrate as reducing agent, finally calcined at 550 °C. The resulting 1 wt. % graphene/g-C_3N_4 composite showed that graphene sheets act as electronic conductive channels to enhance the photogenerate charge carriers separation coming from the g-C_3N_4, increasing 3 times photocatalytic H_2 production in comparison with g-C_3N_4 [244].

D.2.5.1.c) Carbon nanotubes (CNT)

The 1D CNT in junction with 2D g-C_3N_4 [245] has been found to be a promising material for catalytic applications [246,247] due to the synergy of two materials with different intrinsic properties. For instance, Pawar *et al*, elaborated a gold nanoparticle modified graphitic carbon nitride/multi-walled carbon nanotube (g-C_3N_4/CNTs/Au) hybrid photocatalyst via sonication photo(electro)chemical water splitting. The hybrid composites increased its photoactivity in reference to the single components, this enhancement was partially attributed to better photogenerated charge carriers separation, and the large specific surface area of CNTs which provided a significant number of active sites to undergo the photoredox reactions [246]. In the same context, a hybridized g-C_3N_4 with multiwalled CNTs (MWCNTs) composite was compared with the pure two components samples, and it displayed a red-shift and consequently strong absorption in the visible-light region. The superior performance was attributed to excellent electron storage capability by MWCNTs, hampering the recombination of charge carriers [248].

D.2.5.1.d) Fullerenes-C60

Chai *et al* published a C_{60}/g-C_3N_4 composites via simple adsorption method with superior photocatalytic activity under visible-light (degradation of rhodamine B). The optimal

amount of C_{60} found was 1 wt.% and the higher activity was related to an efficient separation of photogenerated e^-/h^+ pairs [251].

D.2.5.1.e) Other carbon-based materials

Materials literature has mentioned other carbonaceous materials, namely, carbon nanodots, graphene quantum dots, carbon fibers, ordered mesoporous materials that can be associated with g-C_3N_4 for overcoming its intrinsic limitations without using other inorganic SCs [252–254]. Especially, carbon quantum nanodots have gained attention for their excellent optical, electronic, and quantum effect (broad optical absorption, light absorbers, and electron reservoirs) properties [254]. Xia *et al* elaborated a g-C_3N_4/carbon quantum nanodots (5-10 nm of diameter) composite in a one-pot hydrothermal synthesis with considerable H_2 production at 808 nm due to the synergy effect on coupling g-C_3N_4 nanosheets and carbon quantum nanodots that enables a large spectral absorption towards NIR [255].

D.2.5.2. g-C_3N_4 / Metal oxide

Different g-C_3N_4-based heterojunctions with metal oxides SC have been developed for different applications, but TiO_2 is regarded as the most active and powerful candidate to couple with g-C_3N_4. Several TiO_2/g-C_3N_4 heterojunctions have been reported. For example, g-C_3N_4/P25 photocatalysts were synthesized with different mass ratios, however the 84/16 proportion presented the highest apparent constant for MB degradation due to the synergic effect between the two SCs that resulted in an efficient separation and transfer of photo-induced charge carriers [257]. Similarly, Yan *et al* reported a TiO_2/g-C_3N_4 binary system via one-step hydrothermal process [258]. Also, Miranda *et al* prepared 2 wt. % g-C_3N_4/ 98 wt. % TiO_2 by a simple impregnation method with a 70% photoactivity yield for the degradation of phenol, possibly due to modifications of specific surface and pore size distribution. In another study, Muñoz-Batista *et al* synthesized g-C_3N_4 with TiO_2 in different weight content ranging from 0.25 - 4 wt. %. It was found that samples 0.5-1 wt. % g-C_3N_4 enhanced the photoactivity and selectivity, presumably as a result of the intimate contact between both SCs, thus leading a better charge carriers separation [259].

Amongst various metal oxides, ZnO [260,261], WO_3 [262–264], Cu_2O [265], Fe_2O_3 [266,267], Fe_3O_4 [268], Co_3O_4 [269], CeO [270] have also been coupled with g-C_3N_4. The idea was to use SCs with different band gaps, thus light absorption properties, and band energy potentials, to enabling an efficient and optimal coupling through type II heterojunctions. In this context, ZnO hybridized g-C_3N_4 via a monolayer method led to 5 times enhanced photocurrent under visible-light and 3.5 times higher photocatalytic activity under UV-light for H_2 production. Both behaviours were induced by a better separation efficiency of photoinduced holes from ZnO to the g-C_3N_4 [260]. In different g-C_3N_4/WO_3 composites, where WO_3 particles size ranged from 100–300 nm, and were in direct contact with the g-C_3N_4 sheets, enhanced acetaldehyde degradation due to increase of separation of charge carriers [263] was reported. Lastly, Christoforidis *et al*, synthesized a visible-light active β-Fe_2O_3/g-C_3N_4 photocatalyst via *in-situ* method. It was noticed a growth approach in a solid state reaction with higher efficiency (degradation of

MO) than the single components. They stated that the behaviour was due to narrower band gap and to more efficient separation of the photoinduced charge carriers driven by matched band edges in the heterostructure [267].

D.2.5.3. g-C_3N_4 / Metal organic Frameworks (MOFs)

MOFs are a class of porous crystalline hybrid organic-inorganic materials with infinite and homogeneous framework linked covalently by using inorganic (3D metal-comprising clusters) and organic linkers [271]. Following the metal oxide and metal-free heterojunction systems, MOFs can serve as photocatalysts and consequently photogenerate charge carriers under visible-light irradiation including adequate oxidative and reductive potentials that allows them to initiate light-driven photoredox reactions [272]. One outstanding property of MOFs is their significant specific surface area as well as the tunable cavities, controllable pore size and tunable light harvesting capacity [273,274].

Amongst different MOFs structure a few of them have been coupled with g-C_3N_4. For instance Fu *et al* published a work on MIL-125(Ti)/g-C_3N_4 hybrid nanocomposite synthesized via solvothermal method at 150 °C presenting interesting characteristics, such as, high surface area, high thermal stability, mesoporous structure, and improved visible-light absorption. Besides, the presence of opened mesoporous channels (enhanced mass transfer), the formation of heterostructure Ti-N bonds resulted to an improved charge transfer during the photoactivity as a consequence of the synergy effect between the two SCs: MIL-125(Ti) and g-C_3N_4 [286].

D.2.5.4. Intercalation of non-metal or metallic NPs on g-C_3N_4

The deposition of metal, non-metal elements or a combination of both onto g-C_3N_4 have received noticeable attention in some cases due to their excellent electronic and optical characteristics [287]. The modification of g-C_3N_4 with monometallic or bimetallic nanoparticles responds to a band gap engineering approach. Ideally the optimal SC should present a band gap of *ca.* 2.0 eV to be able to harvest the highest amount of photons from the visible range (44% from the solar spectra) and therefore enhance the generation and lifetime of the photogenerate charge carriers with suitable driving forces to undergo the photocatalytic redox reactions [81]. Nevertheless, the theoretical 2.7 eV band gap of g-C_3N_4 makes it a medium band gap SC, which is attractive but limited to absorb solar light wavelengths only until 460 nm. Therefore, g-C_3N_4 doping is a pertinent and direct approach to further extend its capacity of absorption within the visible range.

D.2.5.4.a) Monometallic systems

i. Non-metal

Non-metal g-C_3N_4 doping has commonly taken place via chemical replacement of the N atoms in the aromatic triazine rings with elements like: S [288,289], P [290,291], B [292], O [293], and I [294] and finally the replacement of the bridge N atoms by using C doping [295]. Despite of the element used for doping, all delocalizes on the π-conjugated

system, which leads to conductivity, mobility, and photogenerated charge carriers separation is envisaged. In case of β-g-C_3N_4 elaborated by Lu *et al*, they found that the g-C_3N_4 band gap diminished and its absorption on the visible-light was enhanced promoting increase of photocatalytic efficiency in comparison with g-C_3N_4 alone [292].

ii. Metal

For the case of cation doping, it can take place under two different modalities, cave and/or interlayer [177,296] as shown in **Fig. 1.29 a, b**. The metal ions can be placed in the interior of the triangular pores of the triazine in-plane connections of g-C_3N_4 by using the strong coordination interactions between them and the lone electron pair of the nitrogen atoms, (**cave doping**) [297]. The **transition metal ions** reported for g-C_3N_4 are Fe^{3+}, Zn^{2+}, Mn^{3+}, Co^{3+}, Ni^{3+}, and Cu^{2+} [298]. Moreover, deposition of **plasmonic noble metals** such as Au [300], Ag [301], Pt [302], and Pd [303] has also been deposited onto g-C_3N_4. One Au/g-C_3N_4 nanohybrid composite was reported by Chen *et al*, exhibiting strong trapping properties and storing the e^- from the CB of g-C_3N_4 [300]. In the same context, cave doping was reported by using **alkali-metal ions**, *e.g.,* Li^+, Na^+, and K^+, which induces a non-homogeneous spatial charge distribution in some intercalate spaces (**interlayer doping**) increasing the free charged carriers concentration, improving charge transport and separation rate [304].

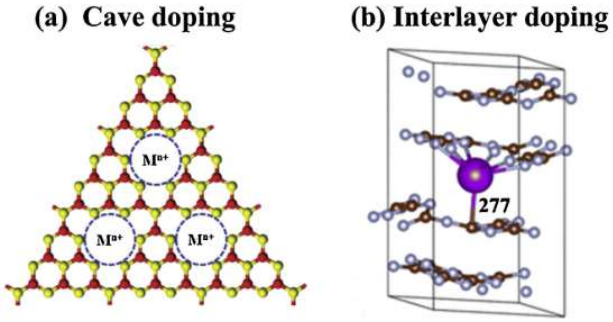

Figure 1.29. Two metal doping modalities on the g-C_3N_4 structure a) cave doping b) interlayer doping [177,296].

D.2.5.4.b) Bimetallic system

Bimetallic systems have noticeably gained attention in the materials community due to the multiple functionalities that can be obtained, namely activity, selectivity, and stability. One can underline that the chemical transformations achieved by a monometallic catalytic system can be surpassed by a bimetallic system easily [305]. This behaviour of bimetallic systems is attributed to the synergic effect of the two metals that influences on the overall activity by their intimate contact and unique physico chemical properties [306]. Recently, Majeed *et al* reported a 1 wt. % $Pd_{0.7}Ag_{0.3}$/g-C_3N_4 photocatalyst showing noticeable superior activity of 1.5 and 5.7 times compared to the monometallic references Pd and Ag, respectively, in terms of hydrogen production, *ca.* 1250 μmol g^{-1} h^{-1} [307]. Similarly, Han *et al* presented an 0.5 wt. % AuPd/g-C_3N_4 composite synthesized via in situ chemical method with higher H_2 production of 3.5 and 1.6 times in comparison to the references Au and Pd, respectively [308]. This higher H_2

production activity was attributed to the AuPd co-catalytic effect and to the promotion of an effective separation of photogenerated charge carriers in g-C_3N_4. Both mentioned strategies are illustrated in **Fig. 1.30**.

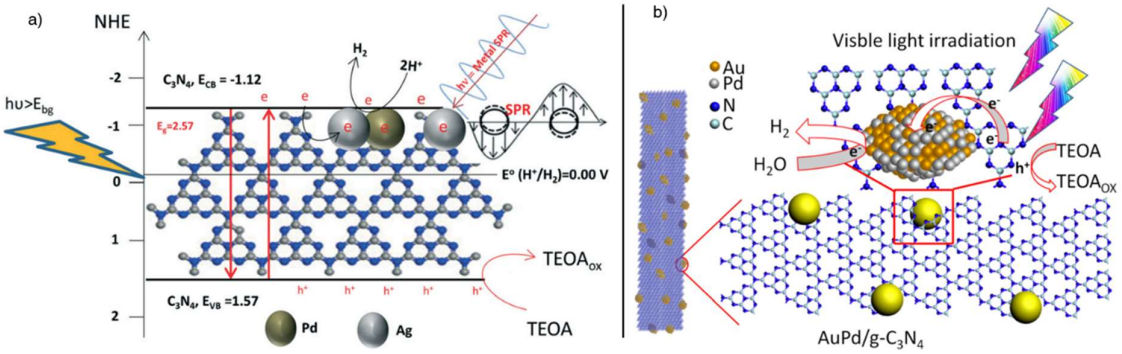

Figure 1.30. Bimetallic systems a) PdAg/g-C_3N_4 b) AuPd/g-C_3N_4 [307,308].

D.2.5.5. g-C_3N_4 / Multi-component systems

Since the discovery of the g-C_3N_4 photocatalytic activity in 2008, enormous studies have been conducted on different forms of complex compound/g-C_3N_4 ternary and quaternary composites with the objective to overcome the three major limitations: visible-light absorption until 460 nm, high recombination rate, and small surface area. With the term of complex compound is referring to a compound containing at least 3 components, and the modification of g-C_3N_4 with some of the selected components. Amongst several multicomponent systems, one can mention a few of the many reported, Bi_2MoO_6/g-C_3N_4 [309], $BiPO_4$/g-C_3N_4 [310], $Bi_2O_2CO_3$/g-C_3N_4 [311], $Bi_5Nb_3O_{15}$/g-C_3N_4 [312], Bi_5O_7I/g-C_3N_4 [313], $Bi_4O_5I_2$/g-C_3N_4 [314], BiOI/g-C_3N_4 [315], $Bi_{20}TiO_{32}$/g-C_3N_4 [316], $InVO_4$/g-C_3N_4 [317], $SmVO_4$/g-C_3N_4 [318], YVO_4/g-C_3N_4 [319], $CdWO_4$/g-C_3N_4 [320], $CdLa_2S_4$/g-C_3N_4 [321], $Zn_xCd_{1-x}S$/g-C_3N_4 [322], $ZnFe_2O_4$/g-C_3N_4 [323], $MgFe_2O_4$/g-C_3N_4 [324], $ZnIn_2S_4$/g-C_3N_4 [325], Zn_2SnO_4/g-C_3N_4 [326], $CuGaSe_2$/g-C_3N_4 [327], $ZnWO_4$/g-C_3N_4 [328], Ag_2CrO_4/g-C_3N_4 [329], Ag_2CO_3/g-C_3N_4 [330], $AgIO_3$/g-C_3N_4 [331], Ag_2WO_4/g-C_3N_4 [332], Ag_3VO_4/g-C_3N_4 [333], and many others.

For example, Cheng *et al* reported a C,N co-doped TiO_2 nanoparticles/g-C_3N_4 ultrathin layers heterostructures by one-pot solvothermal in presence of HNO_3 with enhanced photocatalytic H_2 generation compared to single C,N-TiO_2 NPs and pure g-C_3N_4 NSs, presumably due to the improvement of photon absorption and lengthening lifetime of charge carriers [334]. In a similar study, Yang *et al* published a low carbon-doped TiO_2/g-C_3N_4 with enhanced photocatalytic H_2 generation with excellent photostability. This ternary nanocomposite presented a narrow band gap and longer lifetime of charge carriers thanks to the heterojunction effect [335].

All in all, the vast amount of works center on g-C_3N_4 are a "hot spot" in the materials research, mainly due to the fact that g-C_3N_4 is a polymeric-like, cheap, stable, scalable, and tunable nanomaterial with chemical features that allows to combine with ease many different types of other materials to extend its activity for photocatalytic and

catalytic applications. To date, there has been a great contribution in the field of g-C_3N_4 material modification and is expected to continuously be studied.

E) Plasmonic photocatalysis

Plasmonic photocatalysis is an attractive and simple strategy because it typically uses metallic (M) nanoparticles (NPs) (*e.g.,* Au, Ag, Pt) dispersed onto semiconductor photocatalysts (*e.g.,* TiO_2, g-C_3N_4, ZnO) surface. Several parameters influence the photoreactions and their efficiencies, such as NP material type, NP size and morphology, inter-particle spacing, metal loading, surrounding medium, pH, temperature, etc. [336]

For instance, the contribution of the pioneers' plasmon scientists, the beneficial aspects in photocatalysis, the influential surface plasmon parameters, the M/SC junction, and the metals presenting plasmonic properties will be overviewed in this section.

E.1. Fundamentals

Plasmon is defined as a collective oscillation of free electrons inside the M NPs. The term plasmon refers to the plasma-like behaviour of the created free electrons in a M produced after the influence of an external electromagnetic radiation [337]. As plasmonic photocatalysis has brought an enhanced photocatalytic efficiency shift in the visible light materials applications, many efforts have been conducted. The photocatalytic plasmon applications are possible thanks to the establishments of different models applied in different systems that have brought a better understanding.

In the XX century, Paul Drude proposed an electrical conduction model applied for metals (nanometric scale) using the same principle of kinetic theory of gases but for electrons behaviour in a solid to deduce the M dielectric permittivity [338,339]. The plasmon is characterized by the plasma frequency or pulsation (ω_p) that depends on the electronic density (n), elementary charge (e), the M permittivity (ε_0), and the electron mass (m) as shown in **equation 32**

$$\omega_p = \sqrt{\frac{n\, e^2}{\varepsilon_0\, m}} \tag{32}$$

Drude's model principle describes how the oscillation cloud coming from the free electrons from a M particle resonates after an external electrical field is applied. The oscillation number of a plasmon calculation comprises the plasma wave (f_p), also known as the electrical charges present in conductive media. The plasma wave in plasmons could be quantified as shown in **equation 33**.

$$f_p = \frac{1}{2\,\pi} * \omega_p \tag{33}$$

In 1920, the plasmon was classified as a wave. The quantification of the plasmon (plasma oscillation) can be calculated by applying the Maxwell's equations using a strict boundaries conditions [340]. For a single M spherical particle, Mie theory describes properly the properties when there is an electrodynamic response [341].

The electronic cloud of the M displace in one direction along the external field, it creates a charge deficit in one side and an excess in the other. Yet, the total mechanic energy is preserved and there is no energy dispersion. The charge gradient induced by the external field establishes a repelling force that will promote the oscillation of the electronic cloud in resonance with the applied electrical field as illustrated in **Fig. 1.31**.

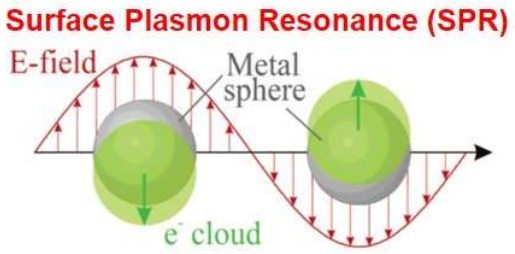

Figure 1.31. Scheme of a sphere with plasmon oscillation after an electrical field is applied, showing the formation of an electronic cloud due to the conduction electron charge relative to the nuclei [342].

E.1.1. Localized resonance and propagated surface plasmon wave

Surface plasmons (SP) are waves that propagate along the interface surface of a conductor and dielectric materials [343]. When a beam of light travels in a non-conductor media, also known as dielectric (air, water, glass), and reaches the surface of a conductor material (Au, Ag, M) at the interface of the M and the dielectric, a surface wave is generated. Under specific resonance conditions a travelling surface wave is generated in an impinging point of light. The wave travels along the interface and it generates an intensity contour of the associated electromagnetic field, this wave is called a **Surface Plasmon (SP) Polaritron**. By the time the SP polaritron is created, it generates a propagating wave that extends away from its initial surface point. In the case of SP, it is possible to identify three characteristic distances: the evanescent field in the dielectric (δ_{diel}), the evanescent field in the metal (δ_{metal}), and the surface plasmon propagation (SPP) (δ_{SPP}), as illustrated in **Fig. 1.32**. Each distance corresponds to different physical meaning, δ_{diel} represents how far in the dielectric the SP wave extends, δ_{metal} represents how far into the metal the SP wave reaches, δ_{SPP} represents how far from the exaltation point the SP can travel along the M/dielectric interface [344].

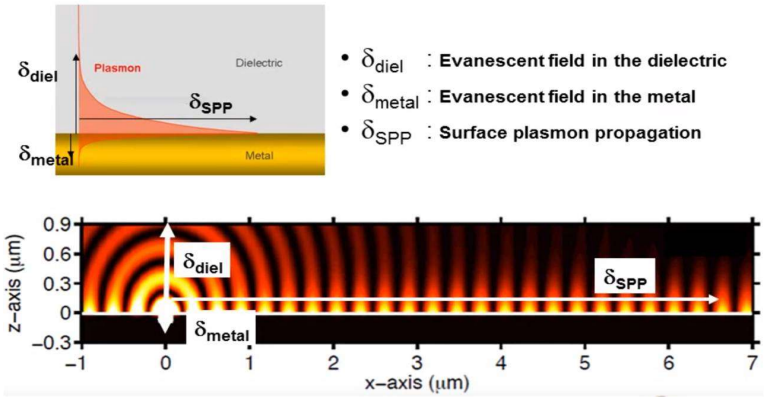

Figure 1.32. Characteristic lengths of M NP Surface Plasmon in contact with a dielectric material [344].

The localized surface plasmon resonance (LSPR) can be described with the extinction (absorption + scattering) cross section C_{ext} (**eq. 34**) that depends on particle radius (R), excitation wavelength (λ), relative dielectric constant of the medium surrounding the M nanosphere (ε_m), imaginary part dielectric function (ε_i), and real part dielectric function (ε_r). The following equation is obtained thanks to combination of Mie theory and Maxwell equations that enables a solution for a M nanosphere [345].

$$C_{ext} = \frac{24\,\pi^2\,R^3\,\varepsilon_m^{\frac{3}{2}}}{\lambda}\left[\frac{\varepsilon_i}{(\varepsilon_r + 2\varepsilon_m)^2 + \varepsilon_i^2}\right] \quad (34)$$

An additional interesting plasmon parameter is the **quality factor** (**Q**), which defines the **force of the surface plasmon** [346]. This factor indicates the **oscillations number** taking place before the dissipation of the light energy into heat. A study on the Q of different M was made in function of their wavelength. It was highlighted that the plasmonic properties were different in function of the M but also in function of the wavelength. Not many M have an interesting Q (Q ≥1) in the work region wavelength, mainly Au, Ag, Al, and Li are interesting, knowing that for plasmonic applications the ideal is Q ≥ 10.

E.2. Surface plasmon benefits for photocatalysis

The surface plasmon driven enhancement in photocatalytic reactions is possible mainly for two beneficial mechanisms: SC light absorption exaltation and the hot electron injection. These two effects occur after the M NP surface is irradiated with an incident electromagnetic wave and the M NP starts resonating.

Despite of the multiple light absorption and energy transfer mechanisms on a resonating M NP (with SP effect) in contact with a SC, it is mandatory to know the energy level positions of each individual system: M NP and SC. The energy band positions of TiO_2, as of SC, are well described and known, yet, the phenomenon of the band bending at the interface with a M has to be taken into account especially if there is an overpotential possibility (undesirable mechanism). The energy bands of the M NPs are less known and depend highly on their light-interactions.

In order, to distinguish the **SC light absorption excitation** and **hot electrons injection** mechanisms, one can say that the both phenomena comprehend **two sequential photophysical steps**, one internal and another external with the SC. The main difference relies on the charge carriers generation and transfer kinetics from the NP to the SC. On SC light absorption exaltation, the charge carriers are formed after a resonating M is relaxed and on hot e^- injection, the hot charge carriers are photogenerated inside the resonating M NP structure, both mechanisms will be explained separately.

E.2.1. Semiconductor light absorption exaltation mechanism

The SC light absorption exaltation mechanism (**Fig. 1.33**) comprises two effects. The first effect comprehends the **electromagnetic field intensification** in the surroundings of the metal nanoparticle. The second effect consists in the **photonic diffusion** over the SC surface in intimate contact with the metallic nanoparticle coming from the relaxation of the plasmons of the resonating metallic nanoparticle. Once the incident electromagnetic energy irradiates the metallic nanoparticle surface, its vicinity intensifies is resonance distance, including several nanometers. Therefore, the electronic cloud of the resonating nanoparticle lead and/or enhance the **formation of e^-/h^+ pairs** within the SC by exaltation. Taking into account that theoretically the number of e^-/h^+ pairs is proportional to the **squared of the incident field** (**E-field² = e^-/h^+ pairs**). It has also to be mentioned that the photogenerated h^+ (minority) remain on the surface with an exposed location that enable them to react with species in solution before recombining with e^-.

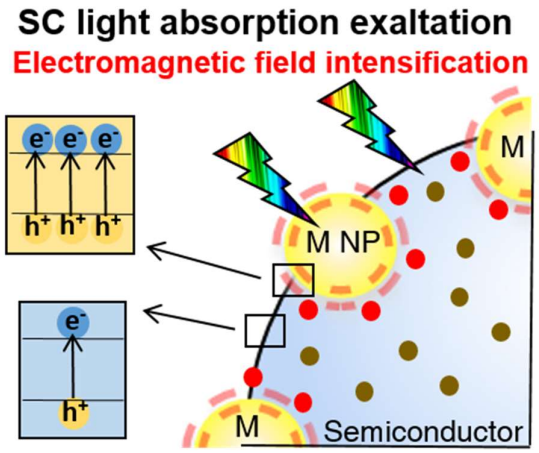

Figure 1.33. Scheme of the electromagnetic field intensification on M NPs.

E.2.2. Hot electron injection mechanism

The hot electron injection mechanism (**Fig. 1.34**) has been extensively described. The mechanism starts with an associated energy level link to the oscillation energy of the electronic cloud of the M NP. This oscillation of the M NP can be related to the electron transfer mechanism from the NP to the SC [97]. For the case of metallic nanoparticles, the electronic cloud oscillation is influenced by the electromagnetic incident field,

creating zones around the nanoparticle with a richer electron environment than others, consequently creating hot electrons and holes [350]. When the specie absorb light, lowest occupied level pass to an excited state to the highest hot electrons can be injected to the CB of the SC by two possible paths: direct transfer [347] and tunnel effect transfer [348,349]. Those hot electrons and holes are not equivalent to the photogenerated e^-/h^+ pairs of a SC, but as any other excited electron, the hot electron are vulnerable to relax if a lower energy state is available, and therefore to be transferred to the CB of the SC if there is a lower energy in reference to the energy level of the plasmonic resonance. Noble metal nanoparticles are characterized by an excellent electronic mobility, as well as efficient capacity of absorption, even presenting 10^5 times more than organic dyes, conferring them a potential candidates for this type of energy transfer [97]. Regarding the generated hot h^+ in the metallic nanoparticle it has been more poorly describe. However, the transfer of the hot e^- follows the same principle of the metallic band diagram applied for the hot h^+ that migrates from the VB of the SC to the interior of the metallic nanoparticle. This charge transfer happens when M NP oscillates and is in intimate contact with the SC with a positive charge deficit, then the probability of transferring one hot h^+ might be possible as analog as of the Z-scheme for the SC heterojunction type II. It has to be underlined that this possible transfer is merely a hypothesis that could explain a path on how to compensate the global generation of hot charges within the metallic nanoparticle.

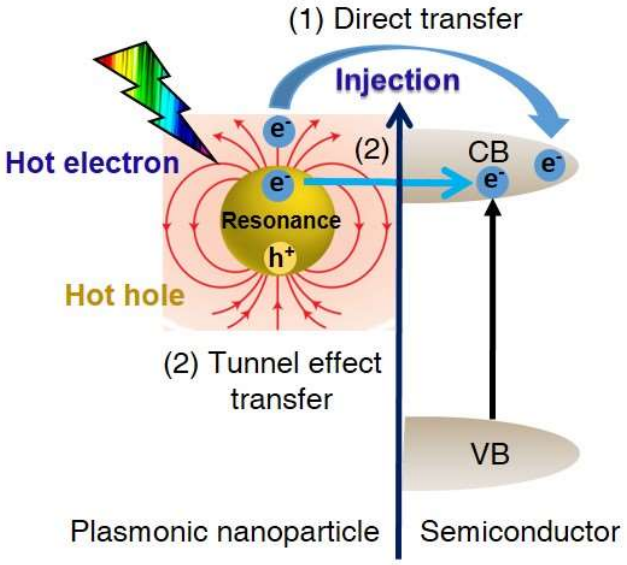

Figure 1.34. The hot electron injection mechanism from the metallic / plasmonic nanoparticle into the semiconductor conduction band.

SC light absorption exaltation and hot electron injection mechanisms may occur simultaneously if the band structure of the SC and the absorption plasmon resonance, are suitable but they are complicated to distinguish. Nevertheless, for the SC light absorption exaltation takes place when one condition is fulfilled. The SC absorption window has to overlap the resonance wavelength range of the M NPs, in order to obtain the antenna functionality on behalf of the M NP. This condition does not apply for the case of the hot electron injection, as long as one M NP is in a good quality contact with the support (SC with suitable band structure) the hot electron transfer may take place.

E.3. Surface plasmon parameters influencing

E.3.1. Optical response of M NPs

In function of the shape of the used M NP, it produces a strict analytical solution in response to an electromagnetic field that be solved by using the Maxwell equations [351] with the Mie theory interpretation that defines electrodynamic response [352]. The nanoparticles that can be described by using the Maxwell/Mie model, should have a diameter size smaller than the incident electromagnetic wave. We have to bear in mind, that this approximation is valid only for M NPs up to 100 nm. Therefore, meeting this condition, one can say that the phase change over the volume of the NP can happen through spatial distribution of the electric field (via electrostatic field) [353].

E.3.2. Band edge positions of M NPs, and SC, and redox species

The band positions of typical plasmonic photocatalytic materials defines the charge transfer performance of the three component system. The interactions between the SC photocatalyst, the noble metal, and the redox species in solution is schematically shown in **Fig. 1.35**. For this specific case using n-type SC, its Fermi level is close to the CB energy and its VB energy is far below. Before contact, M NPs have a work function and the redox pair D/D^+ has an electrochemical potential (E_{redox}). Those E_f, W, and E_{redox} could be different in function of which material are used, for that reason **Fig. 1.35 a)** shows the general example. For instance, when the materials contact, the electrons and holes flow and build up a new equilibrium state, in which E_f, W, and E_{redox} are in the same energetic level. In the usual plasmonic photocatalytic system, the available energy states in the SC photocatalyst and in the M NPs are much lower than those in the solution, consequently E_{redox} does not change whereas the other two line-up with E_{redox}. To happen the mentioned behaviour the next condition has to fill out $E_f > E_{redox} > W$ [336].

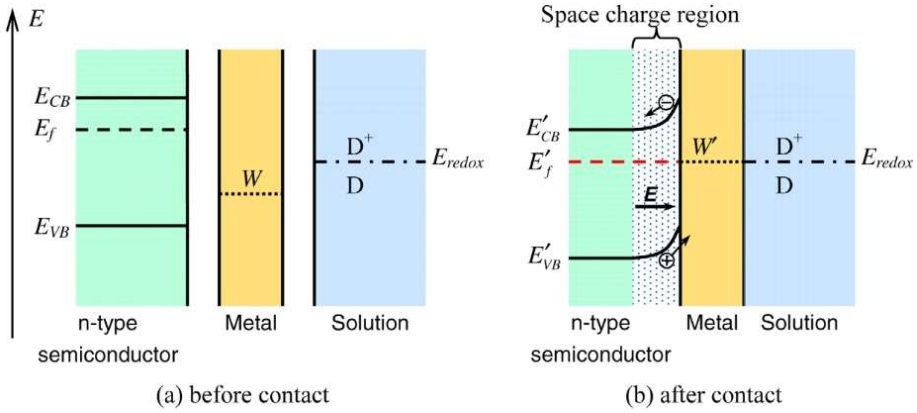

Figure 1.35. Energy diagrams of the plasmonic SCs materials a) before b) after contact [336].

E.3.3. Morphology of M NPs

Morphology and shape of the plasmon M NPs in function of its resonating magnitude defines the absorption response. For example, in the case of an elongated nanoparticle shape or nanotube, two different plasmonic responses can be distinguished: transversal and longitudinal modes (**Fig. 1.36**) according with modified Mie´s theory.

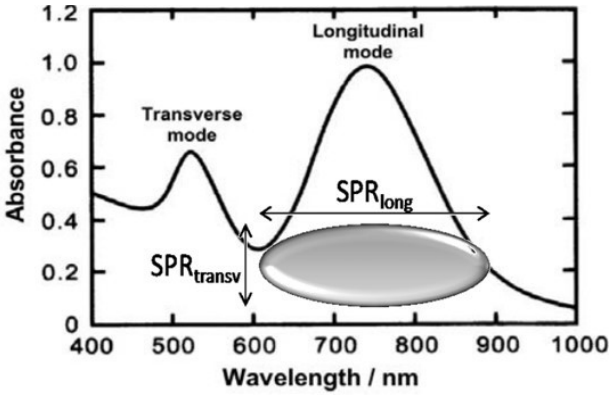

Figure 1.36. Typical spectrum of non-spherical nanoparticles, describing the two plasmon resonances for the transverse and longitudinal modes [354].

Each signal response result in a different plasmonic resonance along the x and y axes. The longitudinal response results in a broader signal at higher wavelengths region (*ca.* 700 nm). On the contrary the transversal response results in a narrower signal at a shorter wavelength (*ca.* 520 nm) [354].

E.4. Metal nanoparticle/semiconductor junction

One can say that once the M/SC are in intimate contact, a junction is formed. The quality junction is defined by the type of interaction between the M NP and the SC, which simultaneously depends on the work function of both components. **Work function (ϕ)** is defined as the energy difference between the Fermi level and the vacuum level. It also represents the minimum energy to transfer an e^- from the solid to a position in the vacuum outside its surface that allows to escape on a single M [355].

When using a M NP/n-type SC junction three cases can happen:

(1) $|\phi_M| = |\phi_{SC}|$, the Fermi energy level of the metal ($E_{F,M}$) and the SC ($E_{F,SC}$) are aligned before contact. But, after contact, there is no exchange of charge carriers.

(2) Ohmic junction, $|\phi_M| < |\phi_{SC}|$, after contact, M (e^-) with interface has higher energy than the SC (e^-), therefore M (e^-) will transfer to the SC up to $E_{F,M}$ / $E_{F,SC}$ alignment.

(3) Schottky junction, $|\phi_M| > |\phi_{SC}|$, after contact, SC (e^-) on the interface have higher energy than the ones in the M NP, then the SC (e^-) will transfer up to Fermi alignment.

One can notice that M NP/n-type SC Schottky junction (3rd case) is the one that comprises Au NP/ TiO_2 or Au NP/g-C_3N_4 examples. In that case theoretically the M NP can act as as e^- pump. Thanks to this electronic advantage that a better charge carrier's separation is induced within the irradiated SC assisted with the deposited M NP on its surface. This condition allows to decrease direct recombination of e^-/h^+ pairs and guarantees that the photogenerated e^- migrate from the CB_{TiO_2} towards the M NP, assuming that the Schottky barrier height allows the e^- migration from one component to other [356,357].

For any of the two M NPs functionalities (**co-catalyst** and **electron trap site**) take place, the photogenerate e^- in the bulk must migrate to the surface to be transferred to the metallic nanoparticle. On the contrary, the photogenerated e^- in the surface have the ease to be recombined with an h^+, which is undesirable due to its hampering effect on the overall activity. By the time the e^- are trapped within the M NP, they can undergo reduction reactions, *e.g.,* proton reduction to hydrogen as shown in **Fig. 1.37**.

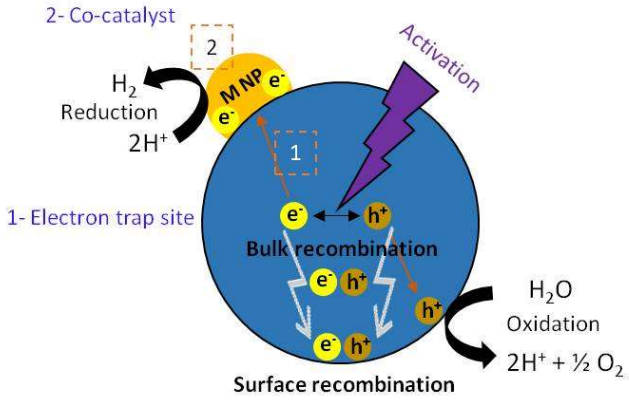

Figure 1.37. Metal nanoparticle deposited onto a semiconductor nanoparticle surface, showing the different mechanisms and photogenerated charge carriers transfer paths.

The M/SC junction is broadly used to build up the **space-charge region** or **depletion layer** (**Schottky barrier**) inside M/SC interface after being illuminated. At the M/SC interface of the two components, electrons transfer from one component to the other to align the Fermi energy levels, occurs thus avoiding the charge recombination and enhancing the photocatalytic performance [358]. Hence, the electrons and holes are force to move in different directions once they are created inside or near the Schottky junction [359]. On top of the Schottky junction, the M NP also provides a fast lane for charge transfer [360], and its surface acts as a charge-trap center to host more active sites for reaction steps. It is only at this point that both the Schottky junction and the fast-lane charge transfer work together to hamper the electron-hole recombination.

Before contact, both components, M (our case Au) and SC, (our case TiO_2 or g-C_3N_4, both n-type) have different Fermi levels or electropotentials. A condition has to be filled in order to get the Schottky layer formation at the interface, the $\phi_M > \phi_S$. If it's the opposite situation $\phi_S > \phi_M$, there is no Schottky layer but an Ohmic contact takes place.

The equilibrium condition is reached (without illumination) a Helmhotz double layer is formed (further details can be found on section **C.3**), there is a balancing between the Fermi level of the SC ($E_{f,S}$) and the work function of the metal (ϕ_M) compared to the level of the vacuum and there is no transfer of charges possible through the barrier of Schottky due to insufficient concentration of free charge carriers in the SC. The electric field between the M and SC interfaces cannot effectively function as bridge to transfer the carriers from one side to the other. Nevertheless, this free charge carriers concentration near the SC surface to be depleted compared to the bulk, is also known as **space charge region**. For example, in the case of an n-type SC (e^- as majority of charge

carriers), the e^- are depleted in the space charge region (also **depletion layer**) characterized by excess positive charges.

Illuminated system, alters the equilibrium condition. It is thus possible to generate a higher charge carrier´s concentration which will consequently be transferred. In the case the Schottky layer is present, it can be identified for an upwards band bending presence due to the repulsion from the negatively charged layer located on the metal surface and the positively charged layer on the SC. The three mentioned cases are illustrated in a detailed scheme on **Fig. 1.38**.

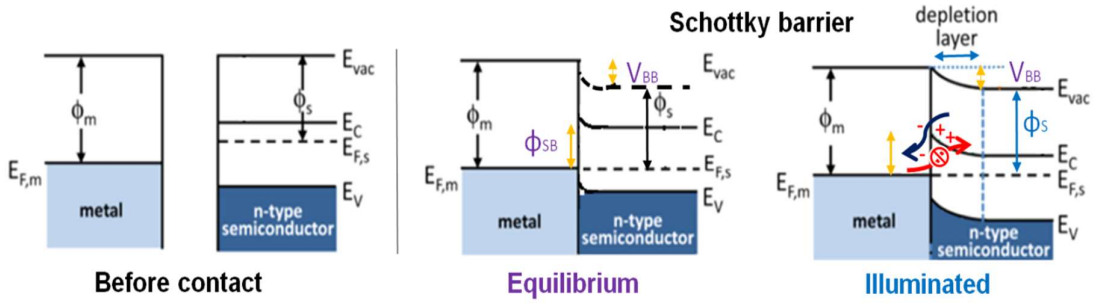

Figure 1.38. Scheme of ideal energy band diagram of metal and n-type semiconductor contact, evidencing the Schottky barrier in the metal nanoparticle/semiconductor interface, before contact, in equilibrium and when it is illuminated [361]. For the nomenclature: ϕ_m, ϕ_S, and ϕ_{SB}, stands for the work function of metal, semiconductor, and Schottky barrier, respectively; $E_{F,m}$, $E_{F,s}$, stands for Fermi energy level of the metal and semiconductor, respectively; E_{vac}, E_C, E_V stands for vacuum, conduction, and valence, respectively; V_{BB} stands for degree of bending of the energy band of the SC at the interface ($V_{BB} = |\phi_m - \phi_S|$).

E.5. Metals with plasmon properties

Plasmonic photocatalysis has been used gold (Au) and silver (Ag) NPs mainly due to their capacity to absorb visible-light efficiently [362]. One can mention that gold (ϕ_{Au} = -5.1 eV absolute potential) and silver (ϕ_{Ag} = -4.7 eV) are very interesting for photo (catalytic) applications. The reason relies on their different morphologies, specific optical response of their bulk, and their unique electronic structure. Other metals more and less noble, *e.g.,* Pt, Pd, Rh, Cu, Li, and Co present certain properties when they are in nanoparticle shape. The metals nanostructures can serve as antennas to convert light into localized electric fields or as waveguides to route light to desired locations with nanometer precision [363].

E.5.1. Gold nanoparticles

The crystal structure for gold is cubo-octahedron with a face-centered cubic (fcc), containing a unit cell of cubic geometry where the atoms are located at each of the corners and the centers of all the cube faces. For the fcc crystal structure, each corner atom is shared among eight unit cells, whereas a face-centered atom belongs to only two. The characteristic atomic radius of gold is 0.1442 nm [364].

E.5.2. Gold nanoparticles synthesis

Different "bottom up" and "top down" methods are known to synthesize Au NPs, *e.g.*, physical, chemical, and colloidal. The most popular physical method is pulse laser deposition (PLD), which consists in bombarding a block of metal, immersed in a liquid or in a control atmosphere, with laser pulses of about tens of ns. This technique allows to synthesize directly the pure metallic NPs with an important size dispersion. This method can be also be used to deposit bimetallic NPs by bombarding an alloy of two metals with the laser [366]. The chemical methods are softer than physical and allows some of them to obtain colloidal NPs less polydispersed. The formation mechanism is generally the following metal precursor, dissolved within a solvent in which it can be reduced in presence of a stabilizing agent (typically a polymer) that will surround the NPs avoiding aggregation phenomena. The synthesis can be divided in two steps: during growing and the stabilizing polymer. The seed formation growth take place when the metal is reduced by a reductant agent and the resulting seed structure is random. Then, the stabilizing polymer, and the other species in solution settle in the seeds surface and the reduction will continuously take place and will growth the size of the metal clusters until the formation of the final NPs. By selecting the type and quantity of the protecting polymer it is possible to synthesize NPs with different shapes, such as spheres, cubes, tubes, tetrahedron, pyramids, discs, etc. To determine the shape, it is only needed that a specie settle in one of the crystallographic face of the metal clusters in growth to block the growth along that crystalline face and therefore promote the growth in the other directions [367]. It must be mentioned that this formation mechanism can also take place with the precursors already adsorbed onto a substrate.

F) References

[1] I.E.A. (IEA), Key World Energy Statistics 2016, Stat. Rep. (2016) 24, 80. https://www.iea.org/publications/freepublications/publication/key-world-energy-statistics.html (accessed December 28, 2016).

[2] R. Taagepera, A world population growth model: Interaction with Earth's carrying capacity and technology in limited space, Technol. Forecast. Soc. Change. 82 (2013) 34–41. doi:10.1016/J.TECHFORE.2013.07.009.

[3] A. Züttel, A. Remhof, A. Borgschulte, O. Friedrichs, Hydrogen: the future energy carrier., Philos. Trans. A. Math. Phys. Eng. Sci. 368 (2010) 3329–42. doi:10.1098/rsta.2010.0113.

[4] M.K. Hubbert, Energy from Fossil Fuels., Science. 109 (1949) 103–9. doi:10.1126/science.109.2823.103.

[5] P.J. McCabe, D.L. Gautier, M.D. Lewan, C. Turner, The future of energy gases, 1993. doi:10.3133/CIR1115.

[6] The Origin of Petroleum, Nature. 112 (1923) 627–628. doi:10.1038/112627a0.

[7] The Future of Solar Energy | MIT Energy Initiative, MIT Energy Initiat. (2015). http://energy.mit.edu/publication/future-solar-energy/ (accessed May 10, 2018).

[8] M. Grätzel, Photoelectrochemical cells, Nature. 414 (2001) 338–344.

doi:10.1038/35104607.

[9] U.S. Department of Energy, Global Fossil Fuel Carbon Emissions - Graphics, (n.d.). http://cdiac.ess-dive.lbl.gov/trends/emis/glo_2014.html (accessed August 30, 2018).

[10] T.A. Boden, R.J. Andres, G. Marland, Global, Regional, and National Fossil-Fuel CO2 Emissions (1751 - 2014) (V. 2017), (2017). doi:10.3334/CDIAC/00001_V2017.

[11] J. Hansen, R. Ruedy, M. Sato, K. Lo, Global Surface Temperature Change, Rev. Geophys. 48 (2010) RG4004. doi:10.1029/2010RG000345.

[12] S. Oberthür, H. Ott, The Kyoto Protocol : international climate policy for the 21st century, Springer, 1999. https://books.google.fr/books/about/The_Kyoto_Protocol.html?id=-qp7Wt9GvccC&redir_esc=y (accessed May 10, 2018).

[13] C. Ronneau, Énergie, pollution de l'air et développement durable, (2004). http://books.openedition.org/pucl/607?lang=fr (accessed December 11, 2015).

[14] R. Perez, M. Perez, A Fundamental Look at Supply Side Energy Reserves for the Planet, Int. Energy Agency Sol. Heat. Cool. Program. Sol. Updat. 50 (2009) 4–5. https://www.iea-shc.org/data/sites/1/publications/2015-11-A-Fundamental-Look-at-Supply-Side-Energy-Reserves-for-the-Planet.pdf (accessed May 11, 2018).

[15] P. Kruger, Electric power required in the world by 2050 with hydrogen fuel production—Revised, Int. J. Hydrogen Energy. 30 (2005) 1515–1522. doi:10.1016/J.IJHYDENE.2005.04.003.

[16] Lord Turner, A. Mathur, Who We Are | Energy Transitions Commission, (n.d.). http://www.energy-transitions.org/who-we-are (accessed May 11, 2018).

[17] D.G. Nocera, The Artificial Leaf, Acc. Chem. Res. 45 (2012) 767–776. doi:10.1021/ar2003013.

[18] A. Fujishima, K. Honda, Electrochemical photolysis of water at a semiconductor electrode., Nature. 238 (1972) 37–38. doi:10.1038/238037a0.

[19] A.J. Bard, Photoelectrochemistry and heterogeneous photocatalysis at semiconductors, J. Photochem. 10 (1979) 59–75. doi:10.1016/0047-2670(79)80037-4.

[20] A.J. Bard, Photoelectrochemistry, Science (80-.). 207 (1980) 139–144. doi:10.1126/science.207.4427.139.

[21] A. Steinfeld, Solar thermochemical production of hydrogen—a review, Sol. Energy. 78 (2005) 603–615. doi:10.1016/J.SOLENER.2003.12.012.

[22] K. Nakata, A. Fujishima, TiO2 photocatalysis: Design and applications, J. Photochem. Photobiol. C Photochem. Rev. 13 (2012) 169–189. doi:10.1016/J.JPHOTOCHEMREV.2012.06.001.

[23] G.E. Rodgers, G.E. Rodgers, Descriptive inorganic, coordination, and solid state chemistry, Brooks/Cole, Cengage Learning, 2012. https://books.google.fr/books/about/Descriptive_Inorganic_Coordination_and_S.html?id=g_ybia0hGw8C&redir_esc=y (accessed May 12, 2018).

[24] P. Parthasarathy, K.S. Narayanan, Hydrogen production from steam gasification of biomass: Influence of process parameters on hydrogen yield – A review, Renew. Energy. 66 (2014) 570–579. doi:10.1016/J.RENENE.2013.12.025.

[25] M. Ni, D.Y.C. Leung, M.K.H. Leung, K. Sumathy, An overview of hydrogen production from biomass, Fuel Process. Technol. 87 (2006) 461–472.

doi:10.1016/J.FUPROC.2005.11.003.

[26] G. Marbán, T. Valdés-Solís, Towards the hydrogen economy?, Int. J. Hydrogen Energy. 32 (2007) 1625–1637. doi:10.1016/J.IJHYDENE.2006.12.017.

[27] Air Liquide Group, Gas Encyclopedia, Hydrogen. (2018). https://encyclopedia.airliquide.com/hydrogen.

[28] H. Balat, E. Kırtay, Hydrogen from biomass – Present scenario and future prospects, Int. J. Hydrogen Energy. 35 (2010) 7416–7426. doi:10.1016/J.IJHYDENE.2010.04.137.

[29] P. Nikolaidis, A. Poullikkas, A comparative overview of hydrogen production processes, Renew. Sustain. Energy Rev. 67 (2017) 597–611. doi:10.1016/J.RSER.2016.09.044.

[30] C.A. Grimes, O.K. Varghese, S. Ranjan, Light, Water, Hydrogen. The solar generation of hydrogen by water photoelectrolysis, Springer US, Boston, MA, 2008. doi:10.1007/978-0-387-68238-9.

[31] A. Heeger, Solar Fuels and Artificial Photosynthesis. Science and innovation to change our future energy options, 2012. www.rsc.org/sustainable-energy (accessed August 23, 2018).

[32] J. Hislop, Study explores BC's renewable hydrogen energy potential - Energi News, (n.d.). https://energi.news/british-columbia/study-explores-renewable-hydrogen-energy/ (accessed August 28, 2018).

[33] I.E.A. (IEA), Technology Roadmap Hydrogen and Fuel Cells, 2015. www.iea.org/t&c/ (accessed December 16, 2018).

[34] L.W. Jones, Toward a liquid hydrogen fuel economy, (1970). https://deepblue.lib.umich.edu/handle/2027.42/5800 (accessed May 12, 2018).

[35] W. Balthasar, Hydrogen production and technology: today, tomorrow and beyond, Int. J. Hydrogen Energy. 9 (1984) 649–668. doi:10.1016/0360-3199(84)90263-5.

[36] M. Steinberg, H.C. Cheng, Modern and prospective technologies for hydrogen production from fossil fuels, Int. J. Hydrogen Energy. 14 (1989) 797–820. doi:10.1016/0360-3199(89)90018-9.

[37] S.S. Bharadwaj, L.D. Schmidt, Catalytic partial oxidation of natural gas to syngas, Fuel Process. Technol. 42 (1995) 109–127. doi:10.1016/0378-3820(94)00098-E.

[38] L.J.M.J. Blomen, M.N. Mugerwa, Fuel cell systems, Plenum Press, New York, 1993. http://www.worldcat.org/title/fuel-cell-systems/oclc/804784623 (accessed August 26, 2018).

[39] J.D. Holladay, J. Hu, D.L. King, Y. Wang, An overview of hydrogen production technologies, Catal. Today. 139 (2009) 244–260. doi:10.1016/J.CATTOD.2008.08.039.

[40] J. Rostrup-Nielsen, L.J. Christiansen, Concepts in Syngas Manufacture, 2011. http://cds.cern.ch/record/1619924/files/9781848165670_TOC.pdf (accessed August 23, 2018).

[41] N.Z. Muradov, How to produce hydrogen from fossil fuels without CO2 emission, Int. J. Hydrogen Energy. 18 (1993) 211–215. doi:10.1016/0360-3199(93)90021-2.

[42] S. Liu, J. Zhu, M. Chen, W. Xin, Z. Yang, L. Kong, Hydrogen production via catalytic pyrolysis of biomass in a two-stage fixed bed reactor system, Int. J. Hydrogen Energy. 39 (2014) 13128–13135. doi:10.1016/J.IJHYDENE.2014.06.158.

[43] A. Demirbaş, Biomass resource facilities and biomass conversion processing for fuels and chemicals, Energy Convers. Manag. 42 (2001) 1357–1378. doi:10.1016/S0196-

8904(00)00137-0.

[44] A. Demirbaş, Yields of hydrogen-rich gaseous products via pyrolysis from selected biomass samples, Fuel. 80 (2001) 1885–1891. doi:10.1016/S0016-2361(01)00070-9.

[45] M. Balat, Hydrogen-Rich Gas Production from Biomass via Pyrolysis and Gasification Processes and Effects of Catalyst on Hydrogen Yield, Energy Sources, Part A Recover. Util. Environ. Eff. 30 (2008) 552–564. doi:10.1080/15567030600817191.

[46] Energy Sources | Department of Energy, (n.d.). https://www.energy.gov/science-innovation/energy-sources (accessed August 27, 2018).

[47] I.K. Kapdan, F. Kargi, Bio-hydrogen production from waste materials, Enzyme Microb. Technol. 38 (2006) 569–582. doi:10.1016/J.ENZMICTEC.2005.09.015.

[48] D. Das, T.N. Veziroglu, Advances in biological hydrogen production processes, Int. J. Hydrogen Energy. 33 (2008) 6046–6057. doi:10.1016/J.IJHYDENE.2008.07.098.

[49] D. Das, T.N. Veziroğlu, Hydrogen production by biological processes: a survey of literature, Int. J. Hydrogen Energy. 26 (2001) 13–28. doi:10.1016/S0360-3199(00)00058-6.

[50] Y. Zhang, Z. Ying, J. Zhou, J. Liu, Z. Wang, K. Cen, Electrolysis of the Bunsen Reaction and Properties of the Membrane in the Sulfur–Iodine Thermochemical Cycle, Ind. Eng. Chem. Res. 53 (2014) 13581–13588. doi:10.1021/ie502275s.

[51] B. Coelho, A.C. Oliveira, A. Mendes, Concentrated solar power for renewable electricity and hydrogen production from water—a review, Energy Environ. Sci. 3 (2010) 1398. doi:10.1039/b922607a.

[52] X. Chen, S. Shen, L. Guo, S.S. Mao, Semiconductor-based Photocatalytic Hydrogen Generation, Chem. Rev. 110 (2010) 6503–6570. doi:10.1021/cr1001645.

[53] M.G. Walter, E.L. Warren, J.R. McKone, S.W. Boettcher, Q. Mi, E.A. Santori, N.S. Lewis, Solar Water Splitting Cells, Chem. Rev. 110 (2010) 6446–6473. doi:10.1021/cr1002326.

[54] M.W. Kanan, D.G. Nocera, In situ formation of an oxygen-evolving catalyst in neutral water containing phosphate and Co2+., Science. 321 (2008) 1072–5. doi:10.1126/science.1162018.

[55] X. Dong, F. Cheng, Recent development in exfoliated two-dimensional g-C3N4 nanosheets for photocatalytic applications, J. Mater. Chem. A. 3 (2015) 23642–23652. doi:10.1039/C5TA07374J.

[56] M. Carmo, D.L. Fritz, J. Mergel, D. Stolten, A comprehensive review on PEM water electrolysis, Int. J. Hydrogen Energy. 38 (2013) 4901–4934. doi:10.1016/J.IJHYDENE.2013.01.151.

[57] M.A. Laguna-Bercero, Recent advances in high temperature electrolysis using solid oxide fuel cells: A review, J. Power Sources. 203 (2012) 4–16. doi:10.1016/J.JPOWSOUR.2011.12.019.

[58] F.M. Sapountzi, J.M. Gracia, C.J. (Kees-J. Weststrate, H.O.A. Fredriksson, J.W. (Hans) Niemantsverdriet, Electrocatalysts for the generation of hydrogen, oxygen and synthesis gas, Prog. Energy Combust. Sci. 58 (2017) 1–35. doi:10.1016/J.PECS.2016.09.001.

[59] J. E. Funk, Thermochemical hydrogen production: past and present, Int. J. Hydrogen Energy. 26 (2001) 185–190. doi:10.1016/S0360-3199(00)00062-8.

[60] P. McKendry, Energy production from biomass (part 1): overview of biomass, Bioresour. Technol. 83 (2002) 37–46. doi:10.1016/S0960-8524(01)00118-3.

[61] R. Kothari, D. Buddhi, R.L. Sawhney, Comparison of environmental and economic aspects of various hydrogen production methods, Renew. Sustain. Energy Rev. 12 (2008) 553–563. doi:10.1016/J.RSER.2006.07.012.

[62] J.J. Berzelius, Quelques Idées sur une Nouvelle Force Agissant Dans les Combinaisons des Corps Organiques, in: Ann. Der Chemie, 1836: pp. 146–151.

[63] W. Doerffler, K. Hauffe, Heterogeneous photocatalysis I. The influence of oxidizing and reducing gases on the electrical conductivity of dark and illuminated zinc oxide surfaces, J. Catal. 3 (1964) 156–170. doi:10.1016/0021-9517(64)90123-X.

[64] D. Cazoir, L. Fine, C. Ferronato, J.-M. Chovelon, Hydrocarbon removal from bilgewater by a combination of air-stripping and photocatalysis, J. Hazard. Mater. 235–236 (2012) 159–168. doi:10.1016/j.jhazmat.2012.07.037.

[65] S. Helali, E. Puzenat, N. Perol, M.-J. Safi, C. Guillard, Methylamine and dimethylamine photocatalytic degradation—Adsorption isotherms and kinetics, Appl. Catal. A Gen. 402 (2011) 201–207. doi:10.1016/J.APCATA.2011.06.004.

[66] M. Karkmaz, E. Puzenat, C. Guillard, J.M. Herrmann, Photocatalytic degradation of the alimentary azo dye amaranth: Mineralization of the azo group to nitrogen, Appl. Catal. B Environ. 51 (2004) 183–194. doi:10.1016/J.APCATB.2004.02.009.

[67] P.-A. Bourgeois, E. Puzenat, L. Peruchon, F. Simonet, D. Chevalier, E. Deflin, C. Brochier, C. Guillard, Characterization of a new photocatalytic textile for formaldehyde removal from indoor air, Appl. Catal. B Environ. 128 (2012) 171–178. doi:10.1016/J.APCATB.2012.03.033.

[68] D. Vildozo, R. Portela, C. Ferronato, J.-M. Chovelon, Photocatalytic oxidation of 2-propanol/toluene binary mixtures at indoor air concentration levels, Appl. Catal. B Environ. 107 (2011) 347–354. doi:10.1016/J.APCATB.2011.07.035.

[69] A.H. Aïssa, E. Puzenat, A. Plassais, J.-M. Herrmann, C. Haehnel, C. Guillard, Characterization and photocatalytic performance in air of cementitious materials containing TiO2. Case study of formaldehyde removal, Appl. Catal. B Environ. 107 (2011) 1–8. doi:10.1016/J.APCATB.2011.06.012.

[70] T. Sano, E. Puzenat, C. Guillard, C. Geantet, S. Matsuzawa, Degradation of C2H2 with modified-TiO2 photocatalysts under visible light irradiation, J. Mol. Catal. A Chem. 284 (2008) 127–133. doi:10.1016/J.MOLCATA.2008.01.014.

[71] P.-A. Deveau, F. Arsac, P.-X. Thivel, C. Ferronato, F. Delpech, J.-M. Chovelon, P. Kaluzny, C. Monnet, Different methods in TiO2 photodegradation mechanism studies: Gaseous and TiO2-adsorbed phases, J. Hazard. Mater. 144 (2007) 692–697. doi:10.1016/j.jhazmat.2007.01.097.

[72] A. Zafra, J. Garcia, A. Milis, X. Dom&nech, Kinetics of the catalytic oxidation of nitrite over illuminated aqueous suspensions of TiO2, 1991. https://ac.els-cdn.com/030451029180129Q/1-s2.0-030451029180129Q-main.pdf?_tid=1456cc4f-5548-467c-adb2-54e755befd9e&acdnat=1538332420_14ca4ec91e433738fe3421a510fce1ea (accessed September 30, 2018).

[73] S.N. Frank, A.J. Bard, Heterogeneous photocatalytic oxidation of cyanide and sulfite in aqueous solutions at semiconductor powders, J. Phys. Chem. 81 (1977) 1484–1488. doi:10.1021/j100530a011.

[74] J.H.O.S. Pereira, A.C. Reis, V. Homem, J.A. Silva, A. Alves, M.T. Borges, R.A.R. Boaventura, V.J.P. Vilar, O.C. Nunes, Solar photocatalytic oxidation of recalcitrant natural metabolic by-products of amoxicillin biodegradation, Water Res. 65 (2014) 307–320. doi:10.1016/J.WATRES.2014.07.037.

[75] O. Rosseler, M. Sleiman, V.N. Montesinos, A. Shavorskiy, V. Keller, N. Keller, M.I. Litter, H. Bluhm, M. Salmeron, H. Destaillats, Chemistry of NO x on TiO 2 Surfaces Studied by Ambient Pressure XPS: Products, Effect of UV Irradiation, Water, and Coadsorbed K +, J. Phys. Chem. Lett. 4 (2013) 536–541. doi:10.1021/jz302119g.

[76] S. Josset, J. Taranto, N. Keller, V. Keller, M.-C. Lett, M.J. Ledoux, V. Bonnet, S. Rougeau, UV-A photocatalytic treatment of high flow rate air contaminated with Legionella pneumophila, Catal. Today. 129 (2007) 215–222. doi:10.1016/j.cattod.2007.08.010.

[77] A. Kar, Y.R. Smith, V. Subramanian, Improved photocatalytic degradation of textile dye using titanium dioxide nanotubes formed over titanium wires., Environ. Sci. Technol. 43 (2009) 3260–5. http://www.ncbi.nlm.nih.gov/pubmed/19534144 (accessed September 30, 2018).

[78] N.M. Bedford, A.J. Steckl, Photocatalytic Self Cleaning Textile Fibers by Coaxial Electrospinning, ACS Appl. Mater. Interfaces. 2 (2010) 2448–2455. doi:10.1021/am1005089.

[79] K. Takanabe, Photocatalytic Water Splitting: Quantitative Approaches toward Photocatalyst by Design, ACS Catal. 7 (2017) 8006–8022. doi:10.1021/acscatal.7b02662.

[80] T. Bak, J. Nowotny, M. Rekas, C.. Sorrell, Photo-electrochemical properties of the TiO2-Pt system in aqueous solutions, Int. J. Hydrogen Energy. 27 (2002) 19–26. doi:10.1016/S0360-3199(01)00090-8.

[81] A. Kudo, Y. Miseki, Heterogeneous photocatalyst materials for water splitting., Chem. Soc. Rev. 38 (2009) 253–78. doi:10.1039/b800489g.

[82] M.R. Hoffmann, S.T. Martin, W. Choi, D.W. Bahnemann, Environmental Applications of Semiconductor Photocatalysis, Chem. Rev. 95 (1995) 69–96. doi:10.1021/cr00033a004.

[83] P.-A. Gross, Modification de nanotubes de TiO2 pour la production d'hydrogène par photodissociation de l'eau sous lumière solaire, Http://Www.Theses.Fr. (2014). https://www.theses.fr/2014STRAF053 (accessed December 21, 2018).

[84] K. Takanabe, Solar Water Splitting Using Semiconductor Photocatalyst Powders, in: Top. Curr. Chem., 2015: pp. 73–103. doi:10.1007/128_2015_646.

[85] National Renewable Energy Laboratory (NREL), Reference Air Mass 1.5 Spectra | Grid Modernization | NREL, (n.d.). https://www.nrel.gov/grid/solar-resource/spectra-am1.5.html (accessed October 12, 2018).

[86] M. Pourbaix, Atlas of electrochemical equilibria in aqueous solutions, [1st English ed.]., Pergamon Press, Oxford ;New York, 1966. http://www.worldcat.org/title/atlas-of-electrochemical-equilibria-in-aqueous-solutions/oclc/2168509 (accessed July 12, 2018).

[87] Y. Pellegrin, F. Odobel, Sacrificial electron donor reagents for solar fuel production, Comptes Rendus Chim. (2016). doi:10.1016/j.crci.2015.11.026.

[88] M. Wang, S. Shen, L. Li, Z. Tang, J. Yang, Effects of sacrificial reagents on photocatalytic hydrogen evolution over different photocatalysts, J. Mater. Sci. 52 (2017) 5155–5164. doi:10.1007/s10853-017-0752-z.

[89] X. Wang, K. Maeda, A. Thomas, K. Takanabe, G. Xin, J.M. Carlsson, K. Domen, M. Antonietti, A metal-free polymeric photocatalyst for hydrogen production from water under visible light, Nat. Mater. 8 (2009) 76–80. doi:10.1038/nmat2317.

[90] J.I. Pankove, Optical processes in semiconductors, Dover, 1975.

[91] M.L. Cohen, J.R. Chelikowsky, Electronic Structure and Optical Properties of

Semiconductors, Springer Berlin Heidelberg, Berlin, Heidelberg, 1988. doi:10.1007/978-3-642-97080-1.

[92] T. Wang, B. Daiber, J.M. Frost, S.A. Mann, E.C. Garnett, A. Walsh, B. Ehrler, Indirect to direct bandgap transition in methylammonium lead halide perovskite, Energy Environ. Sci. 10 (2017) 509–515. doi:10.1039/c6ee03474h.

[93] W. Schmickler, E. Santos, The semiconductor-electrolyte interface, in: Interfacial Electrochem., Springer Berlin Heidelberg, Berlin, Heidelberg, 2010: pp. 117–131. doi:10.1007/978-3-642-04937-8_11.

[94] R. Marschall, Semiconductor Composites: Strategies for Enhancing Charge Carrier Separation to Improve Photocatalytic Activity, Adv. Funct. Mater. 24 (2014) 2421–2440. doi:10.1002/adfm.201303214.

[95] Y.-P. Yuan, L.-W. Ruan, J. Barber, S.C. Joachim Loo, C. Xue, Hetero-nanostructured suspended photocatalysts for solar-to-fuel conversion, Energy Environ. Sci. 7 (2014) 3934–3951. doi:10.1039/C4EE02914C.

[96] K. Hou, B. Tian, F. Li, Z. Bian, D. Zhao, C. Huang, Highly crystallized mesoporous TiO2 films and their applications in dye sensitized solar cells, J. Mater. Chem. 15 (2005) 2414. doi:10.1039/b417465h.

[97] B. O'Regan, M. Grätzel, A low-cost, high-efficiency solar cell based on dye-sensitized colloidal TiO2 films, Nature. 353 (1991) 737–740. doi:10.1038/353737a0.

[98] J.M. Szeifert, J.M. Feckl, D. Fattakhova-Rohlfing, Y. Liu, V. Kalousek, J. Rathousky, T. Bein, Ultrasmall Titania Nanocrystals and Their Direct Assembly into Mesoporous Structures Showing Fast Lithium Insertion, J. Am. Chem. Soc. 132 (2010) 12605–12611. doi:10.1021/ja101810e.

[99] R. Wang, K. Hashimoto, A. Fujishima, M. Chikuni, E. Kojima, A. Kitamura, M. Shimohigoshi, T. Watanabe, Light-induced amphiphilic surfaces, Nature. 388 (1997) 431–432. doi:10.1038/41233.

[100] S. Hashimoto, H. Matsuoka, Lifetime of Electrochromism of Amorphous WO3-TiO2 Thin Films, J. Electrochem. Soc. 138 (1991) 2403. doi:10.1149/1.2085985.

[101] Lidia Armelao, * and Davide Barreca, G. Bottaro, A.G. And, E. Tondello, M. Ferroni, S. Polizzi, Au/TiO2 Nanosystems: A Combined RF-Sputtering/Sol−Gel Approach, Chem. Mater. 16 (2004) 3331–3338. doi:10.1021/CM0353308.

[102] ‡ Masahide Takahashi, *,†, † Kaori Tsukigi, † Enkhtuvshin Dorjpalam, ‡ and Yomei Tokuda, T. Yoko†, Effective Photogeneration in TiO2/VO2/TiO2 Multilayer Film Electrodes Prepared by a Sputtering Method, Phys. Chem. B. 107 (2003) 13455–13458. doi:10.1021/JP036493M.

[103] X. Zhang, M. Zhou, L. Lei, Preparation of anatase TiO2 supported on alumina by different metal organic chemical vapor deposition methods, Appl. Catal. A Gen. 282 (2005) 285–293. doi:10.1016/J.APCATA.2004.12.022.

[104] D. Byun, Y. Jin, B. Kim, J. Kee Lee, D. Park, Photocatalytic TiO2 deposition by chemical vapor deposition, J. Hazard. Mater. 73 (2000) 199–206. doi:10.1016/S0304-3894(99)00179-X.

[105] T. Mishra, Anion supported TiO2–ZrO2 nanomaterial synthesized by reverse microemulsion technique as an efficient catalyst for solvent free nitration of halobenzene, Catal. Commun. 9 (2008) 21–26. doi:10.1016/J.CATCOM.2007.05.013.

[106] S. Priyanto, G.A. Mansoori, A. Suwono, Measurement of property relationships of nano-

structure micelles and coacervates of asphaltene in a pure solvent, Chem. Eng. Sci. 56 (2001) 6933–6939. doi:10.1016/S0009-2509(01)00337-2.

[107] X. Sui, Y. Chu, S. Xing, M. Yu, C. Liu, Self-organization of spherical PANI/TiO2 nanocomposites in reverse micelles, Colloids Surfaces A Physicochem. Eng. Asp. 251 (2004) 103–107. doi:10.1016/J.COLSURFA.2004.08.015.

[108] S. Li, G. Zhang, D. Guo, L. Yu, W. Zhang, Anodization Fabrication of Highly Ordered TiO2 Nanotubes, J. Phys. Chem. C. 113 (2009) 12759–12765. doi:10.1021/jp903037f.

[109] V. Zwilling, M. Aucouturier, E. Darque-Ceretti, Anodic oxidation of titanium and TA6V alloy in chromic media. An electrochemical approach, Electrochim. Acta. 45 (1999) 921–929. doi:10.1016/S0013-4686(99)00283-2.

[110] L.L. Hench, J.K. West, The sol-gel process, Chem. Rev. 90 (1990) 33–72. doi:10.1021/cr00099a003.

[111] L.L. Hench, S.H. Wang, The sol-gel glass transformation of silica, Phase Transitions. 24–26 (1990) 785–834. doi:10.1080/01411599008210251.

[112] A. Saupe, Interfacial Phenomena. VonJ. T. Davies undE. K. Rideal. Academic Press, New York-London 1963. 2. Aufl., VIII, 480 S., zahlr. Abb. u. Tab., geb. $ 15.—., Angew. Chemie. 77 (1965) 276–276. doi:10.1002/ange.19650770625.

[113] N. Venkatachalam, M. Palanichamy, V. Murugesan, Sol–gel preparation and characterization of nanosize TiO2: Its photocatalytic performance, Mater. Chem. Phys. 104 (2007) 454–459. doi:10.1016/J.MATCHEMPHYS.2007.04.003.

[114] B. Li, X. Wang, M. Yan, L. Li, Preparation and characterization of nano-TiO2 powder, Mater. Chem. Phys. 78 (2003) 184–188. doi:10.1016/S0254-0584(02)00226-2.

[115] M. Addamo, V. Augugliaro, A. Di Paola, E. García-López, V. Loddo, G. Marcì, L. Palmisano, Photocatalytic thin films of TiO2 formed by a sol–gel process using titanium tetraisopropoxide as the precursor, Thin Solid Films. 516 (2008) 3802–3807. doi:10.1016/J.TSF.2007.06.139.

[116] † Qingshuo Wei, † Kouske Hirota, † and Keisuke Tajima, † Kazuhito Hashimoto*, Design and Synthesis of TiO2 Nanorod Assemblies and Their Application for Photovoltaic Devices, (2006). doi:10.1021/CM061697B.

[117] † Tomoko Kasuga, *, † Masayoshi Hiramatsu, † Akihiko Hoson, ‡ and Toru Sekino, K. Niihara‡, Formation of Titanium Oxide Nanotube, Langmuir. (1998) 3160–3163. doi:10.1021/LA9713816.

[118] D.S. Kim, S.-Y. Kwak, The hydrothermal synthesis of mesoporous TiO2 with high crystallinity, thermal stability, large surface area, and enhanced photocatalytic activity, Appl. Catal. A Gen. 323 (2007) 110–118. doi:10.1016/J.APCATA.2007.02.010.

[119] H. Nakamura, Y. Matsui, Silica Gel Nanotubes Obtained by the Sol-Gel Method, J. Am. Chem. Soc. 117 (1995) 2651–2652. doi:10.1021/ja00114a031.

[120] D. V. Bavykin, J.M. Friedrich, F.C. Walsh, Protonated Titanates and TiO2 Nanostructured Materials: Synthesis, Properties, and Applications, Adv. Mater. 18 (2006) 2807–2824. doi:10.1002/adma.200502696.

[121] Y.V. Kolen'ko, B.R. Churagulov, M. Kunst, L. Mazerolles, C. Colbeau-Justin, Photocatalytic properties of titania powders prepared by hydrothermal method, Appl. Catal. B Environ. 54 (2004) 51–58. doi:10.1016/J.APCATB.2004.06.006.

[122] Z.-Y. Yuan, B.-L. Su, Titanium oxide nanotubes, nanofibers and nanowires, Colloids

Surfaces A Physicochem. Eng. Asp. 241 (2004) 173–183. doi:10.1016/J.COLSURFA.2004.04.030.

[123] Y. Lan, X.P. Gao, H.Y. Zhu, Z.F. Zheng, T.Y. Yan, F. Wu, S.P. Ringer, D.Y. Song, Titanate Nanotubes and Nanorods Prepared from Rutile Powder, Adv. Funct. Mater. 15 (2005) 1310–1318. doi:10.1002/adfm.200400353.

[124] H.-K. Seo, G.-S. Kim, S.G. Ansari, Y.-S. Kim, H.-S. Shin, K.-H. Shim, E.-K. Suh, A study on the structure/phase transformation of titanate nanotubes synthesized at various hydrothermal temperatures, Sol. Energy Mater. Sol. Cells. 92 (2008) 1533–1539. doi:10.1016/J.SOLMAT.2008.06.019.

[125] C.-K. Lee, M.-D. Lyu, S.-S. Liu, H.-C. Chen, The synthetic parameters for the preparation of nanotubular titanate with highly photocatalytic activity, J. Taiwan Inst. Chem. Eng. 40 (2009) 463–470. doi:10.1016/J.JTICE.2008.12.007.

[126] J. Rossmeisl, Z.-W. Qu, H. Zhu, G.-J. Kroes, J.K. Nørskov, Electrolysis of water on oxide surfaces, J. Electroanal. Chem. 607 (2007) 83–89. doi:10.1016/J.JELECHEM.2006.11.008.

[127] M. Graetzel, Artificial photosynthesis: water cleavage into hydrogen and oxygen by visible light, Acc. Chem. Res. 14 (1981) 376–384. doi:10.1021/ar00072a003.

[128] X. Meng, D. Wang, J. Liu, S. Zhang, Preparation and characterization of sodium titanate nanowires from brookite nanocrystallites, Mater. Res. Bull. 39 (2004) 2163–2170. doi:10.1016/J.MATERRESBULL.2004.08.011.

[129] D. V Bavykin, B.A. Cressey, M.E. Light, F.C. Walsh, An aqueous, alkaline route to titanate nanotubes under atmospheric pressure conditions, Nanotechnology. 19 (2008) 275604. doi:10.1088/0957-4484/19/27/275604.

[130] C.L. Wong, Y.N. Tan, A.R. Mohamed, A review on the formation of titania nanotube photocatalysts by hydrothermal treatment, J. Environ. Manage. 92 (2011) 1669–1680. doi:10.1016/J.JENVMAN.2011.03.006.

[131] C.-K. Lee, C.-C. Wang, M.-D. Lyu, L.-C. Juang, S.-S. Liu, S.-H. Hung, Effects of sodium content and calcination temperature on the morphology, structure and photocatalytic activity of nanotubular titanates, J. Colloid Interface Sci. 316 (2007) 562–569. doi:10.1016/J.JCIS.2007.08.008.

[132] L.-Q. Weng, S.-H. Song, S. Hodgson, A. Baker, J. Yu, Synthesis and characterisation of nanotubular titanates and titania, J. Eur. Ceram. Soc. 26 (2006) 1405–1409. doi:10.1016/J.JEURCERAMSOC.2005.01.058.

[133] G.H. Du, Q. Chen, R.C. Che, Z.Y. Yuan, L.-M. Peng, Preparation and structure analysis of titanium oxide nanotubes, Appl. Phys. Lett. 79 (2001) 3702–3704. doi:10.1063/1.1423403.

[134] Q. Chen, W. Zhou, G.H. Du, L.-M. Peng, Trititanate Nanotubes Made via a Single Alkali Treatment, Adv. Mater. 14 (2002) 1208–1211. doi:10.1002/1521-4095(20020903)14:17<1208::AID-ADMA1208>3.0.CO;2-0.

[135] W. Wang, O.K. Varghese, M. Paulose, C.A. Grimes, Q. Wang, E.C. Dickey, A study on the growth and structure of titania nanotubes, J. Mater. Res. 19 (2004) 417–422. doi:10.1557/jmr.2004.19.2.417.

[136] S. Zhang, L.-M. Peng, Q. Chen, G.H. Du, G. Dawson, W.Z. Zhou, Formation Mechanism of H2Ti3O7 Nanotubes, Phys. Rev. Lett. 91 (2003) 256103. doi:10.1103/PhysRevLett.91.256103.

[137] S. Zhang, Q. Chen, L.-M. Peng, Structure and formation of H2Ti3O7 nanotubes in an alkali environment, Phys. Rev. B. 71 (2005) 014104. doi:10.1103/PhysRevB.71.014104.

[138] S. Kumar, S. Karthikeyan, A. Lee, S. Kumar, S. Karthikeyan, A.F. Lee, g-C3N4-Based Nanomaterials for Visible Light-Driven Photocatalysis, Catalysts. 8 (2018) 74. doi:10.3390/catal8020074.

[139] Y. Cui, Z. Ding, P. Liu, M. Antonietti, X. Fu, X. Wang, Metal-free activation of H2O2 by g-C3N4 under visible light irradiation for the degradation of organic pollutants, Phys. Chem. Chem. Phys. 14 (2012) 1455–1462. doi:10.1039/C1CP22820J.

[140] D. Spitzer, T. Cottineau, N. Piazzon, S. Josset, F. Schnell, S.N. Pronkin, E.R. Savinova, V. Keller, Bio-Inspired Nanostructured Sensor for the Detection of Ultralow Concentrations of Explosives, Angew. Chemie Int. Ed. 51 (2012) 5334–5338. doi:10.1002/anie.201108251.

[141] Y. Zhang, Z. Jiang, J. Huang, L.Y. Lim, W. Li, J. Deng, D. Gong, Y. Tang, Y. Lai, Z. Chen, Titanate and titania nanostructured materials for environmental and energy applications: a review, RSC Adv. 5 (2015) 79479–79510. doi:10.1039/C5RA11298B.

[142] Z. Zheng, H. Liu, J. Ye, J. Zhao, E.R. Waclawik, H. Zhu, Structure and contribution to photocatalytic activity of the interfaces in nanofibers with mixed anatase and TiO2(B) phases, J. Mol. Catal. A Chem. 316 (2010) 75–82. doi:10.1016/J.MOLCATA.2009.10.002.

[143] S. ANDERSSON, A.D. WADSLEY, Crystallographic Shear and Diffusion Paths in Certain Higher Oxides of Niobium, Tungsten, Molybdenum and Titanium, Nature. 211 (1966) 581–583. doi:10.1038/211581a0.

[144] R. Daghrir, P. Drogui, D. Robert, Modified TiO2 For Environmental Photocatalytic Applications: A Review, Ind. Eng. Chem. Res. 52 (2013) 3581–3599. doi:10.1021/ie303468t.

[145] W. Choi, A. Termin, M.R. Hoffmann, The Role of Metal Ion Dopants in Quantum-Sized TiO2: Correlation between Photoreactivity and Charge Carrier Recombination Dynamics, J. Phys. Chem. 98 (1994) 13669–13679. doi:10.1021/j100102a038.

[146] B. Hvolbæk, T.V.W. Janssens, B.S. Clausen, H. Falsig, C.H. Christensen, J.K. Nørskov, Catalytic activity of Au nanoparticles, Nano Today. 2 (2007) 14–18. doi:10.1016/S1748-0132(07)70113-5.

[147] U. Banin, Y. Ben-Shahar, K. Vinokurov, Hybrid Semiconductor–Metal Nanoparticles: From Architecture to Function, Chem. Mater. 26 (2014) 97–110. doi:10.1021/cm402131n.

[148] Takashi Tachikawa, and Mamoru Fujitsuka, T. Majima*, Mechanistic Insight into the TiO2 Photocatalytic Reactions: Design of New Photocatalysts, (2007). doi:10.1021/JP069005U.

[149] P. Roy, S. Berger, P. Schmuki, TiO2 Nanotubes: Synthesis and Applications, Angew. Chemie Int. Ed. 50 (2011) 2904–2939. doi:10.1002/anie.201001374.

[150] B. Yuan, Y. Wang, H. Bian, T. Shen, Y. Wu, Z. Chen, Nitrogen doped TiO2 nanotube arrays with high photoelectrochemical activity for photocatalytic applications, Appl. Surf. Sci. 280 (2013) 523–529. doi:10.1016/J.APSUSC.2013.05.021.

[151] C.-C. Hu, T.-C. Hsu, S.-Y. Lu, Effect of nitrogen doping on the microstructure and visible light photocatalysis of titanate nanotubes by a facile cohydrothermal synthesis via urea treatment, Appl. Surf. Sci. 280 (2013) 171–178. doi:10.1016/J.APSUSC.2013.04.120.

[152] P. Wang, P.-S. Yap, T.-T. Lim, C–N–S tridoped TiO2 for photocatalytic degradation of tetracycline under visible-light irradiation, Appl. Catal. A Gen. 399 (2011) 252–261. doi:10.1016/j.apcata.2011.04.008.

[153] T. Morikawa, R. Asahi, T. Ohwaki, K. Aoki, Y. Taga, Band-Gap Narrowing of Titanium Dioxide by Nitrogen Doping, Jpn. J. Appl. Phys. 40 (2001) L561–L563. doi:10.1143/JJAP.40.L561.

[154] G.C. Vásquez, M.A. Peche-Herrero, D. Maestre, A. Cremades, J. Ramírez-Castellanos, J.M. González-Calbet, J. Piqueras, Effects of Transition Metal Doping on the Growth and Properties of Rutile TiO 2 Nanoparticles, J. Phys. Chem. C. 117 (2013) 1941–1947. doi:10.1021/jp3101656.

[155] † Zhibo Zhang, ‡ Chen-Chi Wang, ‡ and Rama Zakaria, ‡ Jackie Y. Ying*, Role of Particle Size in Nanocrystalline TiO2-Based Photocatalysts, (1998). doi:10.1021/JP982948+.

[156] T.M. Breault, B.M. Bartlett, Lowering the Band Gap of Anatase-Structured TiO 2 by Coalloying with Nb and N: Electronic Structure and Photocatalytic Degradation of Methylene Blue Dye, J. Phys. Chem. C. 116 (2012) 5986–5994. doi:10.1021/jp2078456.

[157] T. Cottineau, N. Béalu, P.-A. Gross, S.N. Pronkin, N. Keller, E.R. Savinova, V. Keller, One step synthesis of niobium doped titania nanotube arrays to form (N,Nb) co-doped TiO 2 with high visible light photoelectrochemical activity, J. Mater. Chem. A. 1 (2013) 2151–2160. doi:10.1039/C2TA00922F.

[158] J.J. Brancho, B.M. Bartlett, Challenges in Co-Alloyed Titanium Oxynitrides, a Promising Class of Photochemically Active Materials, Chem. Mater. 27 (2015) 7207–7217. doi:10.1021/acs.chemmater.5b02357.

[159] H. Park, Y. Park, W. Kim, W. Choi, Surface modification of TiO2 photocatalyst for environmental applications, J. Photochem. Photobiol. C Photochem. Rev. 15 (2013) 1–20. doi:10.1016/J.JPHOTOCHEMREV.2012.10.001.

[160] H. Gerischer, M.E. Michel-Beyerle, F. Rebentrost, H. Tributsch, Sensitization of charge injection into semiconductors with large band gap, Electrochim. Acta. 13 (1968) 1509–1515. doi:10.1016/0013-4686(68)80076-3.

[161] L. Gmelin, Ueber einige Verbindungen des Melon's, Ann. Der Pharm. 15 (1835) 252–258. doi:10.1002/jlac.18350150306.

[162] E.C. Franklin, THE AMMONO CARBONIC ACIDS, J. Am. Chem. Soc. 44 (1922) 486–509. doi:10.1021/ja01424a007.

[163] C.E. Redemann, H.J. Lucas, Some Derivatives of Cyameluric Acid and Probable Structures of Melam, Melem and Melon, J. Am. Chem. Soc. 62 (1940) 842–846. doi:10.1021/ja01861a038.

[164] A.I. Finkel'shtein, N. V Spiridonova, CHEMICAL PROPERTIES AND MOLECULAR STRUCTURE OF DERIVATIVES OF sym -HEPTAZINE [1,3,4,6,7,9,9b-HEPTAAZAPHENALENE, TRI-1,3,5-TRIAZINE], Russ. Chem. Rev. 33 (1964) 400–405. doi:10.1070/RC1964v033n07ABEH001443.

[165] D.M. Teter, R.J. Hemley, Low-Compressibility Carbon Nitrides, Science (80-.). 271 (1996) 53–55. doi:10.1126/science.271.5245.53.

[166] A.Y. Liu, M.L. Cohen, Prediction of new low compressibility solids., Science. 245 (1989) 841–2. doi:10.1126/science.245.4920.841.

[167] A. Thomas, A. Fischer, F. Goettmann, M. Antonietti, J.-O. Müller, R. Schlögl, J.M. Carlsson, Graphitic carbon nitride materials: variation of structure and morphology and their use as metal-free catalysts, J. Mater. Chem. 18 (2008) 4893. doi:10.1039/b800274f.

[168] W.-J. Ong, L.-L. Tan, Y.H. Ng, S.-T. Yong, S.-P. Chai, Graphitic Carbon Nitride (g-C3N4)-Based Photocatalysts for Artificial Photosynthesis and Environmental Remediation: Are We a Step Closer To Achieving Sustainability?, Chem. Rev. (2016). doi:10.1021/acs.chemrev.6b00075.

[169] B. Jürgens, E. Irran, J. Senker, P. Kroll, H. Müller, W. Schnick, Melem (2,5,8-Triamino-

tri- s -triazine), an Important Intermediate during Condensation of Melamine Rings to Graphitic Carbon Nitride: Synthesis, Structure Determination by X-ray Powder Diffractometry, Solid-State NMR, and Theoretical Studies, J. Am. Chem. Soc. 125 (2003) 10288–10300. doi:10.1021/ja0357689.

[170] E. Kroke, M. Schwarz, E. Horath-Bordon, P. Kroll, B. Noll, A.D. Norman, Tri-s-triazine derivatives. Part I. From trichloro-tri-s-triazine to graphitic C3N4 structuresPart II: Alkalicyamelurates M3[C6N7O3], M = Li, Na, K, Rb, Cs, manuscript in preparation., New J. Chem. 26 (2002) 508–512. doi:10.1039/b111062b.

[171] Y. Zheng, Y. Jiao, J. Chen, J. Liu, J. Liang, A. Du, W. Zhang, Z. Zhu, S.C. Smith, M. Jaroniec, G.Q. (Max) Lu, S.Z. Qiao, Nanoporous Graphitic-C3N4 @Carbon Metal-Free Electrocatalysts for Highly Efficient Oxygen Reduction, J. Am. Chem. Soc. 133 (2011) 20116–20119. doi:10.1021/ja209206c.

[172] Y. Wang, X. Wang, M. Antonietti, Y. Zhang, Facile One-Pot Synthesis of Nanoporous Carbon Nitride Solids by Using Soft Templates, ChemSusChem. 3 (2010) 435–439. doi:10.1002/cssc.200900284.

[173] M. Shalom, S. Inal, C. Fettkenhauer, D. Neher, M. Antonietti, Improving Carbon Nitride Photocatalysis by Supramolecular Preorganization of Monomers, J. Am. Chem. Soc. 135 (2013) 7118–7121. doi:10.1021/ja402521s.

[174] Y. Cui, Z. Ding, X. Fu, X. Wang, Construction of Conjugated Carbon Nitride Nanoarchitectures in Solution at Low Temperatures for Photoredox Catalysis, Angew. Chemie Int. Ed. 51 (2012) 11814–11818. doi:10.1002/anie.201206534.

[175] C. Miranda, H. Mansilla, J. Yáñez, S. Obregón, G. Colón, Improved photocatalytic activity of g-C3N4/TiO2 composites prepared by a simple impregnation method, J. Photochem. Photobiol. A Chem. 253 (2013) 16–21. doi:10.1016/j.jphotochem.2012.12.014.

[176] J. Zhang, F. Guo, X. Wang, An Optimized and General Synthetic Strategy for Fabrication of Polymeric Carbon Nitride Nanoarchitectures, Adv. Funct. Mater. 23 (2013) 3008–3014. doi:10.1002/ADFM.201203287.

[177] T. Xiong, W. Cen, Y. Zhang, F. Dong, Bridging the g-C3N4 Interlayers for Enhanced Photocatalysis, ACS Catal. 6 (2016) 2462–2472. doi:10.1021/acscatal.5b02922.

[178] Q. Lin, L. Li, S. Liang, M. Liu, J. Bi, L. Wu, Efficient synthesis of monolayer carbon nitride 2D nanosheet with tunable concentration and enhanced visible-light photocatalytic activities, Appl. Catal. B Environ. 163 (2015) 135–142. doi:10.1016/J.APCATB.2014.07.053.

[179] Z. Wang, W. Guan, Y. Sun, F. Dong, Y. Zhou, W.-K. Ho, Water-assisted production of honeycomb-like g-C_3N_4 with ultralong carrier lifetime and outstanding photocatalytic activity, Nanoscale. 7 (2015) 2471–2479. doi:10.1039/C4NR05732E.

[180] J. Zhang, J. Sun, K. Maeda, K. Domen, P. Liu, M. Antonietti, X. Fu, X. Wang, Sulfur-mediated synthesis of carbon nitride: Band-gap engineering and improved functions for photocatalysis, Energy Environ. Sci. 4 (2011) 675–678. doi:10.1039/C0EE00418A.

[181] F. He, G. Chen, Y. Yu, Y. Zhou, Y. Zheng, S. Hao, The sulfur-bubble template-mediated synthesis of uniform porous g-C_3N_4 with superior photocatalytic performance, Chem. Commun. 51 (2015) 425–427. doi:10.1039/C4CC07106A.

[182] F. He, G. Chen, Y. Zhou, Y. Yu, Y. Zheng, S. Hao, The facile synthesis of mesoporous g-C3N4 with highly enhanced photocatalytic H2 evolution performance, Chem. Commun. 51 (2015) 16244–16246. doi:10.1039/C5CC06713H.

[183] D.J. Martin, K. Qiu, S.A. Shevlin, A.D. Handoko, X. Chen, Z. Guo, J. Tang, Highly

efficient photocatalytic H_2 evolution from water using visible light and structure-controlled graphitic carbon nitride., Angew. Chem. Int. Ed. Engl. 53 (2014) 9240–5. doi:10.1002/anie.201403375.

[184] J. Mao, T. Peng, X. Zhang, K. Li, L. Ye, L. Zan, Effect of graphitic carbon nitride microstructures on the activity and selectivity of photocatalytic CO2 reduction under visible light, Catal. Sci. Technol. 3 (2013) 1253. doi:10.1039/c3cy20822b.

[185] Y. Zhang, J. Liu, G. Wu, W. Chen, Porous graphitic carbon nitride synthesized via direct polymerization of urea for efficient sunlight-driven photocatalytic hydrogen production, Nanoscale. 4 (2012) 5300. doi:10.1039/c2nr30948c.

[186] G. Dong, L. Zhang, Porous structure dependent photoreactivity of graphitic carbon nitride under visible light, J. Mater. Chem. 22 (2012) 1160–1166. doi:10.1039/C1JM14312C.

[187] X.-S. Zhang, J.-Y. Hu, H. Jiang, Facile modification of a graphitic carbon nitride catalyst to improve its photoreactivity under visible light irradiation, Chem. Eng. J. 256 (2014) 230–237. doi:10.1016/J.CEJ.2014.07.012.

[188] H. Yan, Y. Chen, S. Xu, Synthesis of graphitic carbon nitride by directly heating sulfuric acid treated melamine for enhanced photocatalytic H2 production from water under visible light, Int. J. Hydrogen Energy. 37 (2012) 125–133. doi:10.1016/J.IJHYDENE.2011.09.072.

[189] Y. Zhong, Z. Wang, J. Feng, S. Yan, H. Zhang, Z. Li, Z. Zou, Improvement in photocatalytic H2 evolution over g-C3N4 prepared from protonated melamine, Appl. Surf. Sci. 295 (2014) 253–259. doi:10.1016/J.APSUSC.2014.01.008.

[190] A. Naseri, M. Samadi, A. Pourjavadi, A.Z. Moshfegh, S. Ramakrishna, Graphitic carbon nitride ($g\text{-}C_3N_4$)-based photocatalysts for solar hydrogen generation: recent advances and future development directions, J. Mater. Chem. A. 5 (2017) 23406–23433. doi:10.1039/C7TA05131J.

[191] V.W. Lau, M.B. Mesch, V. Duppel, V. Blum, J. Senker, B. V. Lotsch, Low-Molecular-Weight Carbon Nitrides for Solar Hydrogen Evolution, J. Am. Chem. Soc. 137 (2015) 1064–1072. doi:10.1021/ja511802c.

[192] P. Niu, L.-C. Yin, Y.-Q. Yang, G. Liu, H.-M. Cheng, Increasing the Visible Light Absorption of Graphitic Carbon Nitride (Melon) Photocatalysts by Homogeneous Self-Modification with Nitrogen Vacancies, Adv. Mater. 26 (2014) 8046–8052. doi:10.1002/adma.201404057.

[193] L.L. and Z.Z. Pengju Yang, Jianghong Zhao, Wei Qiao, Ammonia-induced robust photocatalytic hydrogen evolution of graphitic carbon nitride, Nanoscale. 7 (2015) 18887–18890. doi:10.1039/C5NR05570A.

[194] G. Dong, W. Ho, C. Wang, Selective photocatalytic N2 fixation dependent on g-C3N4 induced by nitrogen vacancies, J. Mater. Chem. A. 3 (2015) 23435–23441. doi:10.1039/C5TA06540B.

[195] X. Li, G. Hartley, A.J. Ward, P.A. Young, A.F. Masters, T. Maschmeyer, Hydrogenated Defects in Graphitic Carbon Nitride Nanosheets for Improved Photocatalytic Hydrogen Evolution, J. Phys. Chem. C. 119 (2015) 14938–14946. doi:10.1021/acs.jpcc.5b03538.

[196] Y. Yuan, L. Zhang, J. Xing, M.I.B. Utama, X. Lu, K. Du, Y. Li, X. Hu, S. Wang, A. Genç, R. Dunin-Borkowski, J. Arbiol, Q. Xiong, High-yield synthesis and optical properties of $g\text{-}C_3N_4$, Nanoscale. 7 (2015) 12343–12350. doi:10.1039/C5NR02905H.

[197] T.L.T. and, J.. John T. Yates, Surface Science Studies of the Photoactivation of TiO2New Photochemical Processes, (2006). doi:10.1021/CR050172K.

[198] X. Chen, L. Liu, P.Y. Yu, S.S. Mao, Increasing solar absorption for photocatalysis with black hydrogenated titanium dioxide nanocrystals., Science. 331 (2011) 746–50. doi:10.1126/science.1200448.

[199] F. Dong, Z. Wang, Y. Sun, W.-K. Ho, H. Zhang, Engineering the nanoarchitecture and texture of polymeric carbon nitride semiconductor for enhanced visible light photocatalytic activity, J. Colloid Interface Sci. 401 (2013) 70–79. doi:10.1016/j.jcis.2013.03.034.

[200] P. Niu, L. Zhang, G. Liu, H.-M. Cheng, Graphene-Like Carbon Nitride Nanosheets for Improved Photocatalytic Activities, Adv. Funct. Mater. 22 (2012) 4763–4770. doi:10.1002/adfm.201200922.

[201] S.C. Yan, Z.S. Li, Z.G. Zou, Photodegradation Performance of g-C3N4 Fabricated by Directly Heating Melamine, Langmuir. 25 (2009) 10397–10401. doi:10.1021/la900923z.

[202] Y. Chen, B. Wang, S. Lin, Y. Zhang, X. Wang, Activation of n → π* Transitions in Two-Dimensional Conjugated Polymers for Visible Light Photocatalysis, J. Phys. Chem. C. 118 (2014) 29981–29989. doi:10.1021/jp510187c.

[203] G.-M. Rignanese, J.-C. Charlier, X. Gonze, First-principles study of vibrational and dielectric properties of C3N4 polymorphs, Phys. Rev. B. 66 (2002) 205416. doi:10.1103/PhysRevB.66.205416.

[204] Y. Kang, Y. Yang, L.-C. Yin, X. Kang, G. Liu, H.-M. Cheng, An Amorphous Carbon Nitride Photocatalyst with Greatly Extended Visible-Light-Responsive Range for Photocatalytic Hydrogen Generation, Adv. Mater. 27 (2015) 4572–4577. doi:10.1002/adma.201501939.

[205] Z. Zhao, Y. Dai, J. Lin, G. Wang, Highly-Ordered Mesoporous Carbon Nitride with Ultrahigh Surface Area and Pore Volume as a Superior Dehydrogenation Catalyst, Chem. Mater. 26 (2014) 3151–3161. doi:10.1021/cm5005664.

[206] K. Kailasam, J.D. Epping, A. Thomas, S. Losse, H. Junge, Mesoporous carbon nitride–silica composites by a combined sol–gel/thermal condensation approach and their application as photocatalysts, Energy Environ. Sci. 4 (2011) 4668. doi:10.1039/c1ee02165f.

[207] X. Li, A.F. Masters, T. Maschmeyer, Photocatalytic Hydrogen Evolution from Silica-Templated Polymeric Graphitic Carbon Nitride-Is the Surface Area Important?, ChemCatChem. 7 (2015) 121–126. doi:10.1002/cctc.201402567.

[208] J. Huang, W. Ho, X. Wang, Metal-free disinfection effects induced by graphitic carbon nitride polymers under visible light illumination, Chem. Commun. 50 (2014) 4338. doi:10.1039/c3cc48374f.

[209] X.-H. Li, J. Zhang, X. Chen, A. Fischer, A. Thomas, M. Antonietti, X. Wang, Condensed Graphitic Carbon Nitride Nanorods by Nanoconfinement: Promotion of Crystallinity on Photocatalytic Conversion, Chem. Mater. 23 (2011) 4344–4348. doi:10.1021/cm201688v.

[210] J. Wang, C. Zhang, Y. Shen, Z. Zhou, J. Yu, Y. Li, W. Wei, S. Liu, Y. Zhang, Environment-friendly preparation of porous graphite-phase polymeric carbon nitride using calcium carbonate as templates, and enhanced photoelectrochemical activity, J. Mater. Chem. A. 3 (2015) 5126–5131. doi:10.1039/C4TA06778A.

[211] Y. Fukasawa, K. Takanabe, A. Shimojima, M. Antonietti, K. Domen, T. Okubo, Synthesis of Ordered Porous Graphitic-C3N4 and Regularly Arranged Ta3N5 Nanoparticles by Using Self-Assembled Silica Nanospheres as a Primary Template, Chem. - An Asian J. 6 (2011) 103–109. doi:10.1002/asia.201000523.

[212] X. Wang, K. Maeda, X. Chen, K. Takanabe, K. Domen, Y. Hou, X. Fu, M. Antonietti, Polymer Semiconductors for Artificial Photosynthesis: Hydrogen Evolution by Mesoporous Graphitic Carbon Nitride with Visible Light, J. Am. Chem. Soc. 131 (2009) 1680–1681.

doi:10.1021/ja809307s.

[213] Z. Yang, Y. Zhang, Z. Schnepp, Soft and hard templating of graphitic carbon nitride, J. Mater. Chem. A. 3 (2015) 14081–14092. doi:10.1039/C5TA02156A.

[214] Y. Wang, J. Zhang, X. Wang, M. Antonietti, H. Li, Boron- and Fluorine-Containing Mesoporous Carbon Nitride Polymers: Metal-Free Catalysts for Cyclohexane Oxidation, Angew. Chemie Int. Ed. 49 (2010) 3356–3359. doi:10.1002/anie.201000120.

[215] J. Zhang, X. Chen , K. Takanabe, K. Maeda, K. Domen, J.D. Epping, X. Fu, M. Antonietti, X. Wang , Synthesis of a Carbon Nitride Structure for Visible-Light Catalysis by Copolymerization, Angew. Chemie Int. Ed. 49 (2010) 441–444. doi:10.1002/anie.200903886.

[216] Q. Fan, J. Liu, Y. Yu, S. Zuo, A template induced method to synthesize nanoporous graphitic carbon nitride with enhanced photocatalytic activity under visible light, RSC Adv. 4 (2014) 61877–61883. doi:10.1039/C4RA12033G.

[217] W. Shen, L. Ren, H. Zhou, S. Zhang, W. Fan, Facile one-pot synthesis of bimodal mesoporous carbon nitride and its function as a lipase immobilization support, J. Mater. Chem. 21 (2011) 3890. doi:10.1039/c0jm03666h.

[218] J. Liu, M. Antonietti, Bio-inspired NADH regeneration by carbon nitride photocatalysis using diatom templates, Energy Environ. Sci. 6 (2013) 1486. doi:10.1039/c3ee40696b.

[219] T. Jordan, N. Fechler, J. Xu, T.J.K. Brenner, M. Antonietti, M. Shalom, “Caffeine Doping” of Carbon/Nitrogen-Based Organic Catalysts: Caffeine as a Supramolecular Edge Modifier for the Synthesis of Photoactive Carbon Nitride Tubes, ChemCatChem. 7 (2015) 2826–2830. doi:10.1002/cctc.201500343.

[220] Y.-S. Jun, J. Park, S.U. Lee, A. Thomas, W.H. Hong, G.D. Stucky, Three-Dimensional Macroscopic Assemblies of Low-Dimensional Carbon Nitrides for Enhanced Hydrogen Evolution, Angew. Chemie Int. Ed. 52 (2013) 11083–11087. doi:10.1002/anie.201304034.

[221] M.K. Bhunia, K. Yamauchi, K. Takanabe, Harvesting Solar Light with Crystalline Carbon Nitrides for Efficient Photocatalytic Hydrogen Evolution, Angew. Chemie Int. Ed. 53 (2014) 11001–11005. doi:10.1002/anie.201405161.

[222] X. Fan, Z. Xing, Z. Shu, L. Zhang, L. Wang, J. Shi, Improved photocatalytic activity of g-C_3N_4 derived from cyanamide–urea solution, RSC Adv. 5 (2015) 8323–8328. doi:10.1039/C4RA16362A.

[223] Z. Huang, F. Li, B. Chen, G. Yuan, Hydrogen from Water over Openly-Structured Graphitic Carbon Nitride Polymer through Photocatalysis, ChemSusChem. 9 (2016) 478–484. doi:10.1002/cssc.201501520.

[224] Y. Xu, M. Xie, S. Huang, H. Xu, H. Ji, J. Xia, Y. Li, H. Li, High yield synthesis of nano-size g-C_3N_4 derivatives by a dissolve-regrowth method with enhanced photocatalytic ability, RSC Adv. 5 (2015) 26281–26290. doi:10.1039/C5RA01206F.

[225] Q. Gu, Y. Liao, L. Yin, J. Long, X. Wang, C. Xue, Template-free synthesis of porous graphitic carbon nitride microspheres for enhanced photocatalytic hydrogen generation with high stability, Appl. Catal. B Environ. 165 (2015) 503–510. doi:10.1016/J.APCATB.2014.10.045.

[226] J. Zhang, M. Zhang, R.-Q. Sun, X. Wang, A Facile Band Alignment of Polymeric Carbon Nitride Semiconductors to Construct Isotype Heterojunctions, Angew. Chemie Int. Ed. 51 (2012) 10145–10149. doi:10.1002/anie.201205333.

[227] J. Zhang, X. An, N. Lin, W. Wu, L. Wang, Z. Li, R. Wang, Y. Wang, J. Liu, M. Wu,

Engineering monomer structure of carbon nitride for the effective and mild photooxidation reaction, Carbon N. Y. 100 (2016) 450–455. doi:10.1016/J.CARBON.2016.01.027.

[228] X. Ye, Y. Cui, X. Wang, Ferrocene-Modified Carbon Nitride for Direct Oxidation of Benzene to Phenol with Visible Light, ChemSusChem. 7 (2014) 738–742. doi:10.1002/cssc.201301128.

[229] X. Fan, L. Zhang, R. Cheng, M. Wang, M. Li, Y. Zhou, J. Shi, Construction of Graphitic C3N4 -Based Intramolecular Donor–Acceptor Conjugated Copolymers for Photocatalytic Hydrogen Evolution, ACS Catal. 5 (2015) 5008–5015. doi:10.1021/acscatal.5b01155.

[230] S. Chu, Y. Wang, Y. Guo, J. Feng, C. Wang, W. Luo, X. Fan, Z. Zou, Band Structure Engineering of Carbon Nitride: In Search of a Polymer Photocatalyst with High Photooxidation Property, ACS Catal. 3 (2013) 912–919. doi:10.1021/cs4000624.

[231] A.K. Geim, K.S. Novoselov, The rise of graphene, Nat. Mater. 6 (2007) 183–191. doi:10.1038/nmat1849.

[232] T. Sano, S. Tsutsui, K. Koike, T. Hirakawa, Y. Teramoto, N. Negishi, K. Takeuchi, Activation of graphitic carbon nitride (g-C3N4) by alkaline hydrothermal treatment for photocatalytic NO oxidation in gas phase, J. Mater. Chem. A. 1 (2013) 6489. doi:10.1039/c3ta10472a.

[233] I. Papailias, N. Todorova, T. Giannakopoulou, N. Ioannidis, N. Boukos, C.P. Athanasekou, D. Dimotikali, C. Trapalis, Chemical vs thermal exfoliation of g-C3N4 for NOx removal under visible light irradiation, Appl. Catal. B Environ. 239 (2018) 16–26. doi:10.1016/J.APCATB.2018.07.078.

[234] J. Tong, L. Zhang, F. Li, M. Li, S. Cao, An efficient top-down approach for the fabrication of large-aspect-ratio g-C 3 N 4 nanosheets with enhanced photocatalytic activities, Phys. Chem. Chem. Phys. 17 (2015) 23532–23537. doi:10.1039/C5CP04057D.

[235] Y. Hernandez, V. Nicolosi, M. Lotya, F.M. Blighe, Z. Sun, S. De, I.T. McGovern, B. Holland, M. Byrne, Y.K. Gun'Ko, J.J. Boland, P. Niraj, G. Duesberg, S. Krishnamurthy, R. Goodhue, J. Hutchison, V. Scardaci, A.C. Ferrari, J.N. Coleman, High-yield production of graphene by liquid-phase exfoliation of graphite, Nat. Nanotechnol. 3 (2008) 563–568. doi:10.1038/nnano.2008.215.

[236] X. Zhang, X. Xie, H. Wang, J. Zhang, B. Pan, Y. Xie, Enhanced Photoresponsive Ultrathin Graphitic-Phase C3N4 Nanosheets for Bioimaging, J. Am. Chem. Soc. 135 (2012) 18–21. doi:10.1021/ja308249k.

[237] S. Zhang, J. Li, X. Wang, Y. Huang, M. Zeng, J. Xu, Rationally designed 1D Ag@AgVO3 nanowire/graphene/protonated g-C3N4 nanosheet heterojunctions for enhanced photocatalysis via electrostatic self-assembly and photochemical reduction methods, J. Mater. Chem. A. 3 (2015) 10119–10126. doi:10.1039/C5TA00635J.

[238] X. Yang, F. Qian, G. Zou, M. Li, J. Lu, Y. Li, M. Bao, Facile fabrication of acidified g-C3N4/g-C3N4 hybrids with enhanced photocatalysis performance under visible light irradiation, Appl. Catal. B Environ. 193 (2016) 22–35. doi:10.1016/J.APCATB.2016.03.060.

[239] B. Choudhury, P.K. Giri, Isotype heterostructure of bulk and nanosheets of graphitic carbon nitride for efficient visible light photodegradation of methylene blue, RSC Adv. 6 (2016) 24976–24984. doi:10.1039/C6RA00933F.

[240] L. Shi, L. Liang, F. Wang, M. Liu, J. Sun, Facile synthesis of a g-C $_3$ N $_4$ isotype composite with enhanced visible-light photocatalytic activity, RSC Adv. 5 (2015) 101843–101849. doi:10.1039/C5RA19833J.

[241] L.K. Putri, W.-J. Ong, W.S. Chang, S.-P. Chai, Heteroatom doped graphene in

photocatalysis: A review, Appl. Surf. Sci. 358 (2015) 2–14. doi:10.1016/J.APSUSC.2015.08.177.

[242] F. Li, X. Jiang, J. Zhao, S. Zhang, Graphene oxide: A promising nanomaterial for energy and environmental applications, Nano Energy. 16 (2015) 488–515. doi:10.1016/J.NANOEN.2015.07.014.

[243] N. Gao, X. Fang, Synthesis and Development of Graphene–Inorganic Semiconductor Nanocomposites, Chem. Rev. 115 (2015) 8294–8343. doi:10.1021/cr400607y.

[244] Q. Xiang, J. Yu, M. Jaroniec, Preparation and Enhanced Visible-Light Photocatalytic H2-Production Activity of Graphene/C3N4 Composites, J. Phys. Chem. C. 115 (2011) 7355–7363. doi:10.1021/jp200953k.

[245] L.-L. Tan, W.-J. Ong, S.-P. Chai, A.R. Mohamed, Growth of carbon nanotubes over non-metallic based catalysts: A review on the recent developments, Catal. Today. 217 (2013) 1–12. doi:10.1016/J.CATTOD.2012.10.023.

[246] R.C. Pawar, S. Kang, S.H. Ahn, C.S. Lee, Gold nanoparticle modified graphitic carbon nitride/multi-walled carbon nanotube (g-C $_3$ N $_4$ /CNTs/Au) hybrid photocatalysts for effective water splitting and degradation, RSC Adv. 5 (2015) 24281–24292. doi:10.1039/C4RA15560B.

[247] G. Wu, Y. Hu, Y. Liu, J. Zhao, X. Chen, V. Whoehling, C. Plesse, G.T.M. Nguyen, F. Vidal, W. Chen, Graphitic carbon nitride nanosheet electrode-based high-performance ionic actuator, Nat. Commun. 6 (2015) 7258. doi:10.1038/ncomms8258.

[248] L. Ge, C. Han, Synthesis of MWNTs/g-C3N4 composite photocatalysts with efficient visible light photocatalytic hydrogen evolution activity, Appl. Catal. B Environ. 117–118 (2012) 268–274. doi:10.1016/J.APCATB.2012.01.021.

[249] Y. Zhang, A. Thomas, M. Antonietti, X. Wang, Activation of Carbon Nitride Solids by Protonation: Morphology Changes, Enhanced Ionic Conductivity, and Photoconduction Experiments, J. Am. Chem. Soc. 131 (2009) 50–51. doi:10.1021/ja808329f.

[250] S. Patnaik, S. Martha, S. Acharya, K.M. Parida, An overview of the modification of g-C $_3$ N $_4$ with high carbon containing materials for photocatalytic applications, Inorg. Chem. Front. 3 (2016) 336–347. doi:10.1039/C5QI00255A.

[251] B. Chai, X. Liao, F. Song, H. Zhou, Fullerene modified C 3 N 4 composites with enhanced photocatalytic activity under visible light irradiation, Dalt. Trans. 43 (2014) 982–989. doi:10.1039/C3DT52454J.

[252] D. Jiang, Y. Zhang, H. Chu, J. Liu, J. Wan, M. Chen, N-doped graphene quantum dots as an effective photocatalyst for the photochemical synthesis of silver deposited porous graphitic C $_3$ N $_4$ nanocomposites for nonenzymatic electrochemical H $_2$ O $_2$ sensing, RSC Adv. 4 (2014) 16163–16171. doi:10.1039/C4RA00601A.

[253] J.-P. Zou, L.-C. Wang, J. Luo, Y.-C. Nie, Q.-J. Xing, X.-B. Luo, H.-M. Du, S.-L. Luo, S.L. Suib, Synthesis and efficient visible light photocatalytic H2 evolution of a metal-free g-C3N4/graphene quantum dots hybrid photocatalyst, Appl. Catal. B Environ. 193 (2016) 103–109. doi:10.1016/j.apcatb.2016.04.017.

[254] Y. Guo, P. Yao, D. Zhu, C. Gu, A novel method for the development of a carbon quantum dot/carbon nitride hybrid photocatalyst that responds to infrared light irradiation, J. Mater. Chem. A. 3 (2015) 13189–13192. doi:10.1039/C5TA02262B.

[255] X. Xia, N. Deng, G. Cui, J. Xie, X. Shi, Y. Zhao, Q. Wang, W. Wang, B. Tang, NIR light induced H 2 evolution by a metal-free photocatalyst, Chem. Commun. 51 (2015) 10899–10902. doi:10.1039/C5CC02589C.

[256] H. Zhang, L. Zhao, F. Geng, L.-H. Guo, B. Wan, Y. Yang, Carbon dots decorated graphitic carbon nitride as an efficient metal-free photocatalyst for phenol degradation, Appl. Catal. B Environ. 180 (2016) 656–662. doi:10.1016/J.APCATB.2015.06.056.

[257] H. Zhu, D. Chen, D. Yue, Z. Wang, H. Ding, In-situ synthesis of g-C3N4-P25 TiO2 composite with enhanced visible light photoactivity, J. Nanoparticle Res. 16 (2014) 2632. doi:10.1007/s11051-014-2632-7.

[258] J. Yan, H. Wu, H. Chen, Y. Zhang, F. Zhang, S.F. Liu, Fabrication of TiO2/C3N4 heterostructure for enhanced photocatalytic Z-scheme overall water splitting, Appl. Catal. B Environ. 191 (2016) 130–137. doi:10.1016/j.apcatb.2016.03.026.

[259] M.J. Muñoz-Batista, A. Kubacka, M. Fernández-García, Effect of g-C3N4 loading on TiO2-based photocatalysts: UV and visible degradation of toluene, Catal. Sci. Technol. 4 (2014) 2006. doi:10.1039/c4cy00226a.

[260] Y. Wang, R. Shi, J. Lin, Y. Zhu, Enhancement of photocurrent and photocatalytic activity of ZnO hybridized with graphite-like C3N4, Energy Environ. Sci. 4 (2011) 2922. doi:10.1039/c0ee00825g.

[261] D. Chen, K. Wang, D. Xiang, R. Zong, W. Yao, Y. Zhu, Significantly enhancement of photocatalytic performances via core–shell structure of ZnO@mpg-C3N4, Appl. Catal. B Environ. 147 (2014) 554–561. doi:10.1016/J.APCATB.2013.09.039.

[262] W. Yu, J. Chen, T. Shang, L. Chen, L. Gu, T. Peng, Direct Z-scheme g-C3N4/WO3 photocatalyst with atomically defined junction for H2 production, Appl. Catal. B Environ. (2017). doi:10.1016/j.apcatb.2017.08.018.

[263] K. Katsumata, R. Motoyoshi, N. Matsushita, K. Okada, Preparation of graphitic carbon nitride (g-C3N4)/WO3 composites and enhanced visible-light-driven photodegradation of acetaldehyde gas, J. Hazard. Mater. 260 (2013) 475–482. doi:10.1016/J.JHAZMAT.2013.05.058.

[264] I. Aslam, C. Cao, M. Tanveer, W.S. Khan, M. Tahir, M. Abid, F. Idrees, F.K. Butt, Z. Ali, N. Mahmood, The synergistic effect between WO3 and g-C3N4 towards efficient visible-light-driven photocatalytic performance, New J. Chem. 38 (2014) 5462–5469. doi:10.1039/C4NJ01370K.

[265] J. Chen, S. Shen, P. Guo, M. Wang, P. Wu, X. Wang, L. Guo, In-situ reduction synthesis of nano-sized Cu2O particles modifying g-C3N4 for enhanced photocatalytic hydrogen production, Appl. Catal. B Environ. 152–153 (2014) 335–341. doi:10.1016/J.APCATB.2014.01.047.

[266] S. Ye, L.-G. Qiu, Y.-P. Yuan, Y.-J. Zhu, J. Xia, J.-F. Zhu, Facile fabrication of magnetically separable graphitic carbon nitride photocatalysts with enhanced photocatalytic activity under visible light, J. Mater. Chem. A. 1 (2013) 3008. doi:10.1039/c2ta01069k.

[267] K.C. Christoforidis, T. Montini, E. Bontempi, S. Zafeiratos, J.J.D. Jaén, P. Fornasiero, Synthesis and photocatalytic application of visible-light active ß-Fe2O3/g-C3N4 hybrid nanocomposites, Appl. Catal. B Environ. 187 (2016) 171–180. doi:10.1016/j.apcatb.2016.01.013.

[268] S. Kumar, S. T, B. Kumar, A. Baruah, V. Shanker, Synthesis of Magnetically Separable and Recyclable g-C $_3$ N $_4$ –Fe $_3$ O $_4$ Hybrid Nanocomposites with Enhanced Photocatalytic Performance under Visible-Light Irradiation, J. Phys. Chem. C. 117 (2013) 26135–26143. doi:10.1021/jp409651g.

[269] J. Zhang, M. Grzelczak, Y. Hou, K. Maeda, K. Domen, X. Fu, M. Antonietti, X. Wang, Photocatalytic oxidation of water by polymeric carbon nitride nanohybrids made of sustainable elements, Chem. Sci. 3 (2012) 443–446. doi:10.1039/C1SC00644D.

[270] J. Chen, S. Shen, P. Wu, L. Guo, Nitrogen-doped CeO_x nanoparticles modified graphitic carbon nitride for enhanced photocatalytic hydrogen production, Green Chem. 17 (2015) 509–517. doi:10.1039/C4GC01683A.

[271] J.-R. Li, J. Sculley, H.-C. Zhou, Metal–Organic Frameworks for Separations, Chem. Rev. 112 (2012) 869–932. doi:10.1021/cr200190s.

[272] A. Dhakshinamoorthy, A.M. Asiri, H. García, Metal-Organic Framework (MOF) Compounds: Photocatalysts for Redox Reactions and Solar Fuel Production, Angew. Chemie Int. Ed. 55 (2016) 5414–5445. doi:10.1002/anie.201505581.

[273] S. Wang, J. Lin, X. Wang, Semiconductor–redox catalysis promoted by metal–organic frameworks for CO2 reduction, Phys. Chem. Chem. Phys. 16 (2014) 14656. doi:10.1039/c4cp02173h.

[274] J. Hong, C. Chen, F.E. Bedoya, G.H. Kelsall, D. O'Hare, C. Petit, Carbon nitride nanosheet/metal–organic framework nanocomposites with synergistic photocatalytic activities, Catal. Sci. Technol. 6 (2016) 5042–5051. doi:10.1039/C5CY01857A.

[275] Francesc X. Llabrés i Xamena, * and Avelino Corma, H. Garcia*, Applications for Metal−Organic Frameworks (MOFs) as Quantum Dot Semiconductors, (2006). doi:10.1021/JP063600E.

[276] T. Zhou, Y. Du, A. Borgna, J. Hong, Y. Wang, J. Han, W. Zhang, R. Xu, Post-synthesis modification of a metal–organic framework to construct a bifunctional photocatalyst for hydrogen production, Energy Environ. Sci. 6 (2013) 3229. doi:10.1039/c3ee41548a.

[277] R. Wang, L. Gu, J. Zhou, X. Liu, F. Teng, C. Li, Y. Shen, Y. Yuan, Quasi-Polymeric Metal-Organic Framework UiO-66/g-C_3N_4 Heterojunctions for Enhanced Photocatalytic Hydrogen Evolution under Visible Light Irradiation, Adv. Mater. Interfaces. 2 (2015) 1500037. doi:10.1002/admi.201500037.

[278] C. Wang, Z. Xie, K.E. deKrafft, W. Lin, Doping Metal–Organic Frameworks for Water Oxidation, Carbon Dioxide Reduction, and Organic Photocatalysis, J. Am. Chem. Soc. 133 (2011) 13445–13454. doi:10.1021/ja203564w.

[279] J. Gao, J. Miao, P.-Z. Li, W.Y. Teng, L. Yang, Y. Zhao, B. Liu, Q. Zhang, A p-type Ti(iv)-based metal–organic framework with visible-light photo-response, Chem. Commun. 50 (2014) 3786–3788. doi:10.1039/C3CC49440C.

[280] D. Wang, R. Huang, W. Liu, D. Sun, Z. Li, Fe-Based MOFs for Photocatalytic CO_2 Reduction: Role of Coordination Unsaturated Sites and Dual Excitation Pathways, ACS Catal. 4 (2014) 4254–4260. doi:10.1021/cs501169t.

[281] W.-T. Xu, L. Ma, F. Ke, F.-M. Peng, G.-S. Xu, Y.-H. Shen, J.-F. Zhu, L.-G. Qiu, Y.-P. Yuan, Metal-organic frameworks MIL-88A hexagonal microrods as a new photocatalyst for efficient decolorization of methylene blue dye., Dalton Trans. 43 (2014) 3792–8. doi:10.1039/c3dt52574k.

[282] K.G.M. Laurier, F. Vermoortele, R. Ameloot, D.E. De Vos, J. Hofkens, M.B.J. Roeffaers, Iron(III)-Based Metal–Organic Frameworks As Visible Light Photocatalysts, J. Am. Chem. Soc. 135 (2013) 14488–14491. doi:10.1021/ja405086e.

[283] R. Liang, F. Jing, L. Shen, N. Qin, L. Wu, M@MIL-100(Fe) (M = Au, Pd, Pt) nanocomposites fabricated by a facile photodeposition process: Efficient visible-light photocatalysts for redox reactions in water, Nano Res. 8 (2015) 3237–3249. doi:10.1007/s12274-015-0824-9.

[284] Y. Xu, M. Lv, H. Yang, Q. Chen, X. Liu, F.W. Fengyu Wei, $BiVO_4$ /MIL-101 composite having the synergistically enhanced visible light photocatalytic activity, RSC Adv. 5

(2015) 43473–43479. doi:10.1039/C4RA11383G.

[285] Y. Fu, D. Sun, Y. Chen, R. Huang, Z. Ding, X. Fu, Z. Li, An Amine-Functionalized Titanium Metal-Organic Framework Photocatalyst with Visible-Light-Induced Activity for CO2 Reduction, Angew. Chemie Int. Ed. 51 (2012) 3364–3367. doi:10.1002/anie.201108357.

[286] X.. b c W.Y.. Z.G.. b C.X.. L.L.. b L.H.. Wang H.a b Yuan, Synthesis and applications of novel graphitic carbon nitride/metal-organic frameworks mesoporous photocatalyst for dyes removal, Appl. Catal. B Environ. 174–175 (2015) 445–454. doi:10.1016/j.apcatb.2015.03.037.

[287] C. Tan, X. Huang, H. Zhang, Synthesis and applications of graphene-based noble metal nanostructures, Mater. Today. 16 (2013) 29–36. doi:10.1016/J.MATTOD.2013.01.021.

[288] K. Wang, Q. Li, B. Liu, B. Cheng, W. Ho, J. Yu, Sulfur-doped g-C3N4 with enhanced photocatalytic CO2-reduction performance, Appl. Catal. B Environ. 176–177 (2015) 44–52. doi:10.1016/j.apcatb.2015.03.045.

[289] J. Hong, X. Xia, Y. Wang, R. Xu, Mesoporous carbon nitride with in situ sulfur doping for enhanced photocatalytic hydrogen evolution from water under visible light, J. Mater. Chem. 22 (2012) 15006. doi:10.1039/c2jm32053c.

[290] S. Guo, Y. Tang, Y. Xie, C. Tian, Q. Feng, W. Zhou, B. Jiang, P-doped tubular g-C 3 N 4 with surface carbon defects: Universal synthesis and enhanced visible-light photocatalytic hydrogen production, Appl. Catal. B Environ. 218 (2017) 664–671. doi:10.1016/j.apcatb.2017.07.022.

[291] J. Ran, T.Y. Ma, G. Gao, X.-W. Du, S.Z. Qiao, Porous P-doped graphitic carbon nitride nanosheets for synergistically enhanced visible-light photocatalytic H 2 production, Energy Environ. Sci. (2015). doi:10.1039/C5EE02650D.

[292] C. Lu, R. Chen, X. Wu, M. Fan, Y. Liu, Z. Le, S. Jiang, S. Song, Boron doped g-C3N4 with enhanced photocatalytic UO22+ reduction performance, Appl. Surf. Sci. 360 (2016) 1016–1022. doi:10.1016/j.apsusc.2015.11.112.

[293] J. Li, B. Shen, Z. Hong, B. Lin, B. Gao, Y. Chen, A facile approach to synthesize novel oxygen-doped g-C3N4 with superior visible-light photoreactivity, Chem. Commun. 48 (2012) 12017. doi:10.1039/c2cc35862j.

[294] G. Zhang, M. Zhang, X. Ye, X. Qiu, S. Lin, X. Wang, Iodine Modified Carbon Nitride Semiconductors as Visible Light Photocatalysts for Hydrogen Evolution, Adv. Mater. 26 (2014) 805–809. doi:10.1002/adma.201303611.

[295] G. Dong, K. Zhao, L. Zhang, Carbon self-doping induced high electronic conductivity and photoreactivity of g-C3N4, Chem. Commun. 48 (2012) 6178. doi:10.1039/c2cc32181e.

[296] S. Cao, J. Low, J. Yu, M. Jaroniec, Polymeric photocatalysts based on graphitic carbon nitride, Adv. Mater. 27 (2015) 2150–2176. doi:10.1002/adma.201500033.

[297] H. Gao, S. Yan, J. Wang, Z. Zou, Ion coordination significantly enhances the photocatalytic activity of graphitic-phase carbon nitride, Dalt. Trans. 43 (2014) 8178–8183. doi:10.1039/C3DT53224K.

[298] Z. Li, C. Kong, G. Lu, Visible Photocatalytic Water Splitting and Photocatalytic Two-Electron Oxygen Formation over Cu- and Fe-Doped g-C 3 N 4, J. Phys. Chem. C. 120 (2016) 56–63. doi:10.1021/acs.jpcc.5b09469.

[299] L. Bi, D. Xu, L. Zhang, Y. Lin, D. Wang, T. Xie, Metal Ni-loaded g-C3N4 for enhanced photocatalytic H 2 evolution activity: the change in surface band bending, Phys. Chem.

Chem. Phys. 17 (2015) 29899–29905. doi:10.1039/C5CP05158D.

[300] L. Chen, X. Zeng, P. Si, Y. Chen, Y. Chi, D.-H. Kim, G. Chen, Gold Nanoparticle-Graphite-Like C3N4 Nanosheet Nanohybrids Used for Electrochemiluminescent Immunosensor, Anal. Chem. 86 (2014) 4188–4195. doi:10.1021/ac403635f.

[301] X. Bai, R. Zong, C. Li, D. Liu, Y. Liu, Y. Zhu, Enhancement of visible photocatalytic activity via Ag@C3N4 core–shell plasmonic composite, Appl. Catal. B Environ. 147 (2014) 82–91. doi:10.1016/J.APCATB.2013.08.007.

[302] H. Pan, Y.-W. Zhang, V.B. Shenoy, H. Gao, Ab Initio Study on a Novel Photocatalyst: Functionalized Graphitic Carbon Nitride Nanotube, ACS Catal. 1 (2011) 99–104. doi:10.1021/cs100045u.

[303] C. Chang, Y. Fu, M. Hu, C. Wang, G. Shan, L. Zhu, Photodegradation of bisphenol A by highly stable palladium-doped mesoporous graphite carbon nitride (Pd/mpg-C3N4) under simulated solar light irradiation, Appl. Catal. B Environ. 142–143 (2013) 553–560. doi:10.1016/J.APCATB.2013.05.044.

[304] H. Gao, S. Yan, J. Wang, Y.A. Huang, P. Wang, Z. Li, Z. Zou, Towards efficient solar hydrogen production by intercalated carbon nitride photocatalyst, Phys. Chem. Chem. Phys. 15 (2013) 18077. doi:10.1039/c3cp53774a.

[305] R. Mu, Q. Fu, H. Xu, H. Zhang, Y. Huang, Z. Jiang, S. Zhang, D. Tan, X. Bao, Synergetic Effect of Surface and Subsurface Ni Species at Pt−Ni Bimetallic Catalysts for CO Oxidation, J. Am. Chem. Soc. 133 (2011) 1978–1986. doi:10.1021/ja109483a.

[306] X. Liu, D. Wang, Y. Li, Synthesis and catalytic properties of bimetallic nanomaterials with various architectures, Nano Today. 7 (2012) 448–466. doi:10.1016/J.NANTOD.2012.08.003.

[307] I. Majeed, U. Manzoor, F.K. Kanodarwala, M.A. Nadeem, E. Hussain, H. Ali, A. Badshah, J.A. Stride, M.A. Nadeem, Pd–Ag decorated g-C 3 N 4 as an efficient photocatalyst for hydrogen production from water under direct solar light irradiation, Catal. Sci. Technol. 8 (2018) 1183–1193. doi:10.1039/C7CY02219K.

[308] C. Han, L. Wu, L. Ge, Y. Li, Z. Zhao, AuPd bimetallic nanoparticles decorated graphitic carbon nitride for highly efficient reduction of water to H2 under visible light irradiation, Carbon N. Y. 92 (2015) 31–40. doi:10.1016/j.carbon.2015.02.070.

[309] H. Li, J. Liu, W. Hou, N. Du, R. Zhang, X. Tao, Synthesis and characterization of g-C3N4/Bi2MoO6 heterojunctions with enhanced visible light photocatalytic activity, Appl. Catal. B Environ. 160–161 (2014) 89–97. doi:10.1016/J.APCATB.2014.05.019.

[310] Z. Li, S. Yang, J. Zhou, D. Li, X. Zhou, C. Ge, Y. Fang, Novel mesoporous g-C3N4 and BiPO4 nanorods hybrid architectures and their enhanced visible-light-driven photocatalytic performances, Chem. Eng. J. 241 (2014) 344–351. doi:10.1016/J.CEJ.2013.10.076.

[311] W. Shan, Y. Hu, Z. Bai, M. Zheng, C. Wei, In situ preparation of g-C3N4/bismuth-based oxide nanocomposites with enhanced photocatalytic activity, Appl. Catal. B Environ. 188 (2016) 1–12. doi:10.1016/J.APCATB.2016.01.058.

[312] S. Zhang, Y. Yang, Y. Guo, W. Guo, M. Wang, Y. Guo, M. Huo, Preparation and enhanced visible-light photocatalytic activity of graphitic carbon nitride/bismuth niobate heterojunctions, J. Hazard. Mater. 261 (2013) 235–245. doi:10.1016/j.jhazmat.2013.07.025.

[313] C. Liu, H. Huang, X. Du, T. Zhang, N. Tian, Y. Guo, Y. Zhang, In Situ Co-Crystallization for Fabrication of g-C 3 N 4 /Bi 5 O 7 I Heterojunction for Enhanced Visible-Light Photocatalysis, J. Phys. Chem. C. 119 (2015) 17156–17165. doi:10.1021/acs.jpcc.5b03707.

[314] J. Xia, M. Ji, J. Di, B. Wang, S. Yin, Q. Zhang, M. He, H. Li, Construction of ultrathin C3N4/Bi4O5I2 layered nanojunctions via ionic liquid with enhanced photocatalytic performance and mechanism insight, Appl. Catal. B Environ. 191 (2016) 235–245. doi:10.1016/J.APCATB.2016.02.058.

[315] J. Di, J. Xia, S. Yin, H. Xu, L. Xu, Y. Xu, M. He, H. Li, Preparation of sphere-like g-C3N4/BiOI photocatalysts via a reactable ionic liquid for visible-light-driven photocatalytic degradation of pollutants, J. Mater. Chem. A. 2 (2014) 5340. doi:10.1039/c3ta14617k.

[316] H. Cheng, J. Hou, O. Takeda, X.-M. Guo, H. Zhu, A unique Z-scheme 2D/2D nanosheet heterojunction design to harness charge transfer for photocatalysis, J. Mater. Chem. A. 3 (2015) 11006–11013. doi:10.1039/C5TA01864A.

[317] B. Hu, F. Cai, T. Chen, M. Fan, C. Song, X. Yan, W. Shi, Hydrothermal Synthesis g-C_3N_4/Nano-$InVO_4$ Nanocomposites and Enhanced Photocatalytic Activity for Hydrogen Production under Visible Light Irradiation, ACS Appl. Mater. Interfaces. 7 (2015) 18247–18256. doi:10.1021/acsami.5b05715.

[318] T. Li, L. Zhao, Y. He, J. Cai, M. Luo, J. Lin, Synthesis of g-C3N4/SmVO4 composite photocatalyst with improved visible light photocatalytic activities in RhB degradation, Appl. Catal. B Environ. 129 (2013) 255–263. doi:10.1016/J.APCATB.2012.09.031.

[319] J. Cai, Y. He, X. Wang, L. Zhang, L. Dong, H. Lin, L. Zhao, X. Yi, W. Weng, H. Wan, Photodegradation of RhB over YVO4/g-C3N4 composites under visible light irradiation, RSC Adv. 3 (2013) 20862. doi:10.1039/c3ra43592j.

[320] N. Tian, H. Huang, Y. Zhang, Mixed-calcination synthesis of CdWO4/g-C3N4 heterojunction with enhanced visible-light-driven photocatalytic activity, Appl. Surf. Sci. 358 (2015) 343–349. doi:10.1016/J.APSUSC.2015.07.154.

[321] H. Liu, Z. Xu, Z. Zhang, D. Ao, Highly efficient photocatalytic H2 evolution from water over CdLa2S4/mesoporous g-C3N4 hybrids under visible light irradiation, Appl. Catal. B Environ. 192 (2016) 234–241. doi:10.1016/J.APCATB.2016.03.074.

[322] H. Liu, Z. Jin, Z. Xu, Hybridization of $Cd_{0.2}Zn_{0.8}S$ with g-C_3N_4 nanosheets: a visible-light-driven photocatalyst for H_2 evolution from water and degradation of organic pollutants, Dalt. Trans. 44 (2015) 14368–14375. doi:10.1039/C5DT01364J.

[323] J. Chen, S. Shen, P. Guo, P. Wu, L. Guo, Spatial engineering of photo-active sites on g-C3N4 for efficient solar hydrogen generation, J. Mater. Chem. A. 2 (2014) 4605. doi:10.1039/c3ta14811d.

[324] J. Chen, D. Zhao, Z. Diao, M. Wang, L. Guo, S. Shen, Bifunctional Modification of Graphitic Carbon Nitride with $MgFe_2O_4$ for Enhanced Photocatalytic Hydrogen Generation, ACS Appl. Mater. Interfaces. 7 (2015) 18843–18848. doi:10.1021/acsami.5b05714.

[325] B. Lin, H. Li, H. An, W. Hao, J. Wei, Y. Dai, C. Ma, G. Yang, Preparation of 2D/2D g-C3N4 nanosheet@ZnIn2S4 nanoleaf heterojunctions with well-designed high-speed charge transfer nanochannels towards high-efficiency photocatalytic hydrogen evolution, Appl. Catal. B Environ. (2017). doi:10.1016/j.apcatb.2017.08.071.

[326] L. Zhang, X. Wang, Q. Nong, H. Lin, B. Teng, Y. Zhang, L. Zhao, T. Wu, Y. He, Enhanced visible-light photoactivity of g-C3N4 via Zn2SnO4 modification, Appl. Surf. Sci. 329 (2015) 143–149. doi:10.1016/J.APSUSC.2014.12.154.

[327] T. Tyborski, C. Merschjann, S. Orthmann, F. Yang, M.-C. Lux-Steiner, T. Schedel-Niedrig, Crystal structure of polymeric carbon nitride and determination of its process-temperature-induced modifications, J. Phys. Condens. Matter. 25 (2013).

http://www.diss.fu-berlin.de/docs/servlets/MCRFileNodeServlet/FUDOCS_derivate_000000004048/Manuskript_Tyborski_PCN.pdf (accessed May 26, 2017).

[328] L. Sun, X. Zhao, C.-J. Jia, Y. Zhou, X. Cheng, P. Li, L. Liu, W. Fan, Enhanced visible-light photocatalytic activity of g-C3N4–ZnWO4 by fabricating a heterojunction: investigation based on experimental and theoretical studies, J. Mater. Chem. 22 (2012) 23428. doi:10.1039/c2jm34965e.

[329] L. Shi, L. Liang, F. Wang, M. Liu, J. Sun, Ag2CrO4 nanoparticles loaded on two-dimensional large surface area graphite-like carbon nitride sheets: simple synthesis and excellent photocatalytic performance., Dalton Trans. 45 (2016) 5815–24. doi:10.1039/c5dt04644k.

[330] Y. Li, L. Fang, R. Jin, Y. Yang, X. Fang, Y. Xing, S. Song, Preparation and enhanced visible light photocatalytic activity of novel g-C_3N_4 nanosheets loaded with Ag_2CO_3 nanoparticles, Nanoscale. 7 (2015) 758–764. doi:10.1039/C4NR06565D.

[331] Y. Li, K. Li, Y. Yang, L. Li, Y. Xing, S. Song, R. Jin, M. Li, Ultrathin g-C_3N_4 Nanosheets Coupled with $AgIO_3$ as Highly Efficient Heterostructured Photocatalysts for Enhanced Visible-Light Photocatalytic Activity, Chem. - A Eur. J. 21 (2015) 17739–17747. doi:10.1002/chem.201502945.

[332] Y. Li, R. Jin, X. Fang, Y. Yang, M. Yang, X. Liu, Y. Xing, S. Song, In situ loading of Ag2WO4 on ultrathin g-C3N4 nanosheets with highly enhanced photocatalytic performance, J. Hazard. Mater. 313 (2016) 219–228. doi:10.1016/J.JHAZMAT.2016.04.011.

[333] W. Zhao, Z. Wei, H. He, J. Xu, J. Li, S. Yang, C. Sun, Supporting 1-D AgVO3 nanoribbons on single layer 2-D graphitic carbon nitride ultrathin nanosheets and their excellent photocatalytic activities, Appl. Catal. A Gen. 501 (2015) 74–82. doi:10.1016/J.APCATA.2015.05.020.

[334] W. Chen, T.-Y. Liu, T. Huang, X.-H. Liu, G.-R. Duan, X.-J. Yang, S.-M. Chen, A novel yet simple strategy to fabricate visible light responsive C,N-TiO_2/g-C_3N_4 heterostructures with significantly enhanced photocatalytic hydrogen generation, RSC Adv. 5 (2015) 101214–101220. doi:10.1039/C5RA18302B.

[335] C. Yang, J. Qin, Z. Xue, M. Ma, X. Zhang, R. Liu, Rational design of carbon-doped TiO2 modified g-C3N4 via in-situ heat treatment for drastically improved photocatalytic hydrogen with excellent photostability, Nano Energy. 41 (2017) 1–9. doi:10.1016/J.NANOEN.2017.09.012.

[336] X. Zhang, Y.L. Chen, R.-S. Liu, D.P. Tsai, Plasmonic photocatalysis, Reports Prog. Phys. 76 (2013) 046401. doi:10.1088/0034-4885/76/4/046401.

[337] X.D. Li, T.P. Chen, Y. Liu, K.C. Leong, Influence of localized surface plasmon resonance and free electrons on the optical properties of ultrathin Au films: a study of the aggregation effect, Opt. Express. 22 (2014) 5124. doi:10.1364/OE.22.005124.

[338] P. Drude, Zur Elektronentheorie der Metalle, Ann. Phys. 306 (1900) 566–613. doi:10.1002/andp.19003060312.

[339] P. Drude, Zur Elektronentheorie der Metalle; II. Teil. Galvanomagnetische und thermomagnetische Effecte, Ann. Phys. 308 (1900) 369–402. doi:10.1002/andp.19003081102.

[340] M. Rahm, S.A. Cummer, D. Schurig, J.B. Pendry, D.R. Smith, Optical design of reflectionless complex media by finite embedded coordinate transformations, (2007). doi:10.1103/PhysRevLett.100.063903.

[341] C.F. Bohren, D.R. Huffman, eds., Absorption and Scattering of Light by Small Particles, Wiley-VCH Verlag GmbH, Weinheim, Germany, 1998. doi:10.1002/9783527618156.

[342] K.L. Kelly, E. Coronado, L.L. Zhao, G.C. Schatz, The Optical Properties of Metal Nanoparticles: The Influence of Size, Shape, and Dielectric Environment, (2003). doi:10.1021/jp026731y.

[343] W.L. Barnes, A. Dereux, T.W. Ebbesen, Surface plasmon subwavelength optics, Nature. 424 (2003) 824–830. doi:10.1038/nature01937.

[344] N.C. Lindquist, P. Nagpal, K.M. McPeak, D.J. Norris, S.-H. Oh, Engineering metallic nanostructures for plasmonics and nanophotonics, Reports Prog. Phys. 75 (2012) 036501. doi:10.1088/0034-4885/75/3/036501.

[345] P. Mulvaney, Surface Plasmon Spectroscopy of Nanosized Metal Particles, Langmuir. 12 (1996) 788–800. doi:10.1021/la9502711.

[346] X. Fan, W. Zheng, D.J. Singh, Light scattering and surface plasmons on small spherical particles, Light Sci. Appl. 3 (2014) e179–e179. doi:10.1038/lsa.2014.60.

[347] E.C. Le Ru, E. Blackie, M. Meyer, P.G. Etchegoin, Surface Enhanced Raman Scattering Enhancement Factors: A Comprehensive Study, (2007). doi:10.1021/jp0687908.

[348] B.N.J. Persson, A. Baratoff, Theory of photon emission in electron tunneling to metallic particles, Phys. Rev. Lett. 68 (1992) 3224–3227. doi:10.1103/PhysRevLett.68.3224.

[349] Y. Shiraishi, N. Yasumoto, J. Imai, H. Sakamoto, S. Tanaka, S. Ichikawa, B. Ohtani, T. Hirai, Quantum tunneling injection of hot electrons in Au/TiO2 plasmonic photocatalysts, Nanoscale. 9 (2017) 8349–8361. doi:10.1039/C7NR02310C.

[350] S. Linic, P. Christopher, D.B. Ingram, Plasmonic-metal nanostructures for efficient conversion of solar to chemical energy, Nat. Mater. 10 (2011) 911–921. doi:10.1038/nmat3151.

[351] C.F. Bohren, D.R. Huffman, Absorption and scattering of light by small particles, New York Wiley, 1983. (1983). http://adsabs.harvard.edu/abs/1983asls.book.....B (accessed March 8, 2019).

[352] U. Kreibig, M. Vollmer, Introduction, in: 1995: pp. 1–12. doi:10.1007/978-3-662-09109-8_1.

[353] S.A. Maier, Plasmonics : fundamentals and applications, Springer, 2007.

[354] H.E. Toma, V.M. Zamarion, S.H. Toma, K. Araki, The coordination chemistry at gold nanoparticles, J. Braz. Chem. Soc. 21 (2010) 1158–1176. doi:10.1590/S0103-50532010000700003.

[355] A. Kahn, Fermi level, work function and vacuum level, Mater. Horizons. 3 (2016) 7–10. doi:10.1039/C5MH00160A.

[356] S.S. Kocha, J.A. Turner, A.J. Nozik, Study of the Schottky barrier and positions of band edges at the n-electrode 1 electrolyte interface determination of the energetic and p-type gallium indium phosphide, 1994. https://ac.els-cdn.com/002207289303020P/1-s2.0-002207289303020P-main.pdf?_tid=40c72951-29df-464f-b4be-7a90b7a16995&acdnat=1542994833_2581b6fe65f7256ea33e9c8085aa448d (accessed November 23, 2018).

[357] ‡ Vaidyanathan Subramanian, †, A. Eduardo Wolf, *, † Prashant V. Kamat*, Semiconductor−Metal Composite Nanostructures. To What Extent Do Metal Nanoparticles Improve the Photocatalytic Activity of TiO2 Films?, (2001). doi:10.1021/JP011118K.

[358] Z. Zhao, Y. Sun, F. Dong, Graphitic carbon nitride based nanocomposites: a review, Nanoscale. 7 (2015) 15–37. doi:10.1039/C4NR03008G.

[359] Z. Wang, J. Liu, W. Chen, Plasmonic Ag/AgBr nanohybrid: synergistic effect of SPR with photographic sensitivity for enhanced photocatalytic activity and stability, Dalt. Trans. 41 (2012) 4866. doi:10.1039/c2dt12089e.

[360] J.R. Lombardi*, R.L. Birke, A Unified Approach to Surface-Enhanced Raman Spectroscopy, (2008). doi:10.1021/JP800167V.

[361] Z. Zhang, J.T. Yates, Band Bending in Semiconductors: Chemical and Physical Consequences at Surfaces and Interfaces, Chem. Rev. 112 (2012) 5520–5551. doi:10.1021/cr3000626.

[362] J.-J. Chen, J.C.S. Wu, P.C. Wu, D.P. Tsai, Plasmonic Photocatalyst for H2 Evolution in Photocatalytic Water Splitting, J. Phys. Chem. C. 115 (2011) 210–216. doi:10.1021/jp1074048.

[363] M. Rycenga, C.M. Cobley, J. Zeng, W. Li, C.H. Moran, Q. Zhang, D. Qin, Y. Xia, Controlling the synthesis and assembly of silver nanostructures for plasmonic applications., Chem. Rev. 111 (2011) 3669–712. doi:10.1021/cr100275d.

[364] W.D. Callister, Materials science and engineering : an introduction, John Wiley & Sons, 2007. http://adsabs.harvard.edu/abs/2006msea.book.....C (accessed March 9, 2019).

[365] C. Genet, T.W. Ebbesen, Light in tiny holes, Nature. 445 (2007) 39–46. doi:10.1038/nature05350.

[366] A.W. Sanders, B.J.W. David A. Routenberg, Y. Xia, A. Eric R. Dufresne, M.A. Reed, Observation of Plasmon Propagation, Redirection, and Fan-Out in Silver Nanowires, (2006). doi:10.1021/NL052471V.

[367] K. Obata, H. Irie, K. Hashimoto, Enhanced photocatalytic activities of Ta, N co-doped TiO2 thin films under visible light, Chem. Phys. 339 (2007) 124–132. doi:10.1016/J.CHEMPHYS.2007.07.044.

Chapter 2

Synthesis, characterization, and photocatalytic evaluation of g-C_3N_4 and Au/g-C_3N_4 materials

A) Introduction

Graphitic carbon nitride, g-C_3N_4 (band gap 2.7 eV) [1,2], has revealed in milestone studies its photocatalytic H_2 and O_2 evolution capacity under visible irradiation by using a co-catalyst, in presence of an electron donor and/or an acceptor, respectively [3–5]. Since the pioneering work of Antonietti *et al* [2], g-C_3N_4 has attracted a lot of attention in the scientific community. However, despite of the g-C_3N_4 advantages, *e.g.*, facile and rapid synthesis, cheap precursors, and scalable methodology, efficiency towards visible light-mediated H_2 production has to be enhanced. Many studies are dealing with several experimental approaches aiming at overcoming this challenge. Modifications on the g-C_3N_4 structure can be induced by three general strategies: **(1) changing its experimental synthesis conditions**, namely: precursors, polycondensation temperature, temperature ramp, reaction duration and atmosphere, **(2) diverse modifications** by different methods such as exfoliation, copolymerization, and use of templates, and **(3)** elaboration of **g-C_3N_4-based composite nanomaterials**, leading to the formation of heterojunctions between g-C_3N_4 and a second component SC [6].

Amongst, various experimental synthesis parameters to play with, the **synthesis atmosphere** has been identified as an important condition that influences g-C_3N_4 physico chemical properties in both 1D planar monolayer and 2D bulk configurations. In a planar orientation, the crystalline structure (crystallite size and interlayer distance), the contributions of tri-s-triazine based g-C_3N_4 and s-triazine based g-C_3N_4 phases, the flat *vs*. deformed orientation layer are parameters can be described. In a 2D configuration (bulk), the number of layers, thickness of the stacks, and the amorphous character can be known as well. Together, all these physico chemical features can be correlated with the polymerization degree of g-C_3N_4 that can be tuned by only changing the atmosphere used during its synthesis. Therefore, the influence of g-C_3N_4 synthesis atmosphere has been the first investigation approach of this thesis, aiming at contributing with an innovative study by using different kinds of atmospheres, *e.g.,* oxidative, reductive, and inert.

Here, the photocatalytic efficiency of g-C_3N_4 towards H_2 production from water under solar and visible light irradiations has been studied and correlated by changing the synthesis gas atmosphere during the g-C_3N_4 polycondensation. Different oxidative, reductive and inert atmospheres were selected, namely Air, H_2, NH_3, N_2 and Ar. The H_2 production was evaluated by coupling these modified g-C_3N_4 in a binary composite (Au/g-C_3N_4) with low loading of Au NPs (*ca.* 0.3 wt. %). The goal was not to study the influence of Au loading but it was focused on the modification of the g-C_3N_4 structure by varying the synthesis atmosphere. The different materials were then evaluated toward H_2 production from water using unusual low quantity of sacrificial agent (1 vol. % triethanolamine, TEOA).

B) Synthesis and characterization of g-C_3N_4 synthesized under different atmospheres

B.1. Synthesis of g-C_3N_4

Bare g-C_3N_4 samples are synthesized via thermal polycondensation of an equimolar ratio of melamine (Mel; 1.92 g) and dicyandiamide (DCDA; 1.28 g) as described elsewhere [6] and shown in **Fig. 2.1**. Precursors Mel and DCDA are put into an alumina crucible with a top cuvette. Thermal polycondensation is carried out in a tubular furnace at 550 °C during 3 h applying a heating ramp of 5 °C min^{-1} in a continuous flow of 100 mL min^{-1} of the designated atmosphere, *i.e.* Air, H_2, NH_3, N_2 and Ar. These samples will be compared to g-C_3N_4 synthesized under static air in a muffle furnace, as commonly prepared by the scientific community in this domain and to a commercial reference (Fairlandtech), g-C_3N_4-commercial, synthesized under vacuum [7]. The as-prepared samples are denoted as g-C_3N_4-atm, where atm stands for the nature of the atmosphere used during its synthesis or the commercial or the static air sample. During this thermal treatment period, the precursors undergo a transformation in tri-s-triazine based g-C_3N_4 (TSTCN), s-triazine based g-C_3N_4 (STCN), and in amorphous phase. For the case of the crystalline phases, TSTCN and STCN, the formation mechanism was already mentioned in **chapter 1**, **section D.2**. Yet, the exact proportion of the different phases is unknown and difficult to calculate.

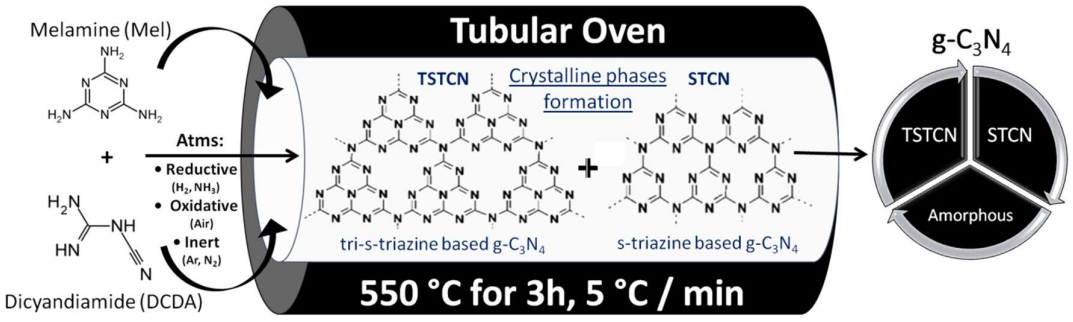

Figure 2.1. Thermal continuous polycondensation synthesis of g-C_3N_4 under different atmospheres.

B.1.1. Kinetics decomposition of g-C_3N_4 precursors

Thermal gravimetric analysis (TGA) allows to follow the kinetics decomposition of g-C_3N_4 precursors. A brief study shows the difference between the decomposition of melamine (Mel) and dicyandiamide (DCDA) separate and mix in an equimolar relationship under air atmosphere and 5 °C / min as illustrated in **Fig. 2.2 a, b, c**. The decomposition of Mel occurs in one-pot step, all mass weight is loss at 277 °C. Nevertheless, its theoretical melting point is 350-354 °C [8]. The DCDA decomposition occurs in three decomposition steps at 251, 358, and 595 °C, respectively. The DCDA decomposition is in a good agreement with the DCDA condensation reaction pathway proposed by Zhang *et al* [9], presenting the formation of Mel, melem, and g-C_3N_4 polymeric network. For the Mel and DCDA mix decomposition in an equimolar ratio, as for mimicking the reaction condition used for g-C_3N_4 materials, occur in five steps at

241, 286, 310, 359, and 586 °C, respectively. Two weights are well identified with 50 and 28 % losses at 241 and 586 °C that stands for Mel and g-C_3N_4 decompositions, respectively. For the other three weight losses representing 7 % loss each one, probably constitute by melem units disrupted or in formation process, resulting in weight losses with close decomposition temperatures. The **Fig. 2.2c inset** shows two intermediates before the melem unit is formed, these two molecules might be the two weight losses mentioned before [10].

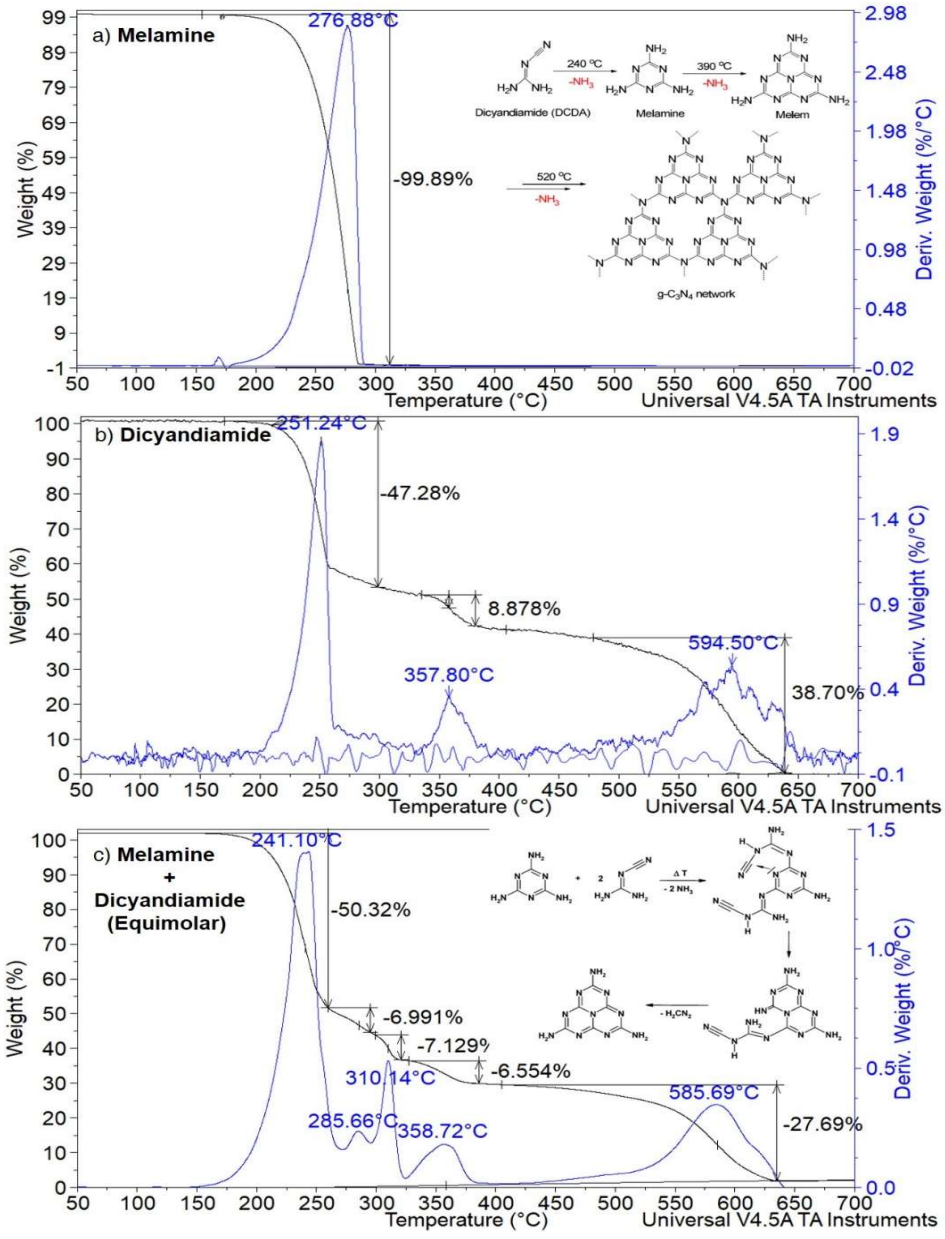

Figure 2.2. Thermal gravimetric kinetic decomposition of a) Melamine inset) associated proposed reaction pathway formation of dicyandiamide [9], b) Dicyandiamide, c) Mel and DCDA in equimolar relationship inset) proposed formation of melem by polycondensation of Mel and DCDA [10].

B.2. Characterization of g-C_3N_4 photocatalysts

For this section, the results of each technique will be introduced with their corresponding discussion aspects.

B.2.1. FT-IR characterization

FT-IR spectra **(Fig. 2.3)** for all samples exhibit the characteristic peaks of the g-C_3N_4 [11]. The broad absorption band extending from 3000 to 3500 cm^{-1} and observed on all the samples were assigned primarily to the N-H stretching vibration of amine groups (secondary and primary). Secondary amines are found in the bridges of the repeating motif phases as C-NH-C, and primary amines are found in the terminating edges of each g-C_3N_4 layer as C-NH_2 [12]. In the same region, a large part of the absorption is also attributed to O-H originated from physically adsorbed water species on g-C_3N_4 surface resulting in a broad peak, making difficult to distinguish the specific contribution of each amine type. The region with the majority of peaks ranging from 1240 to 1640 cm^{-1} is attributed to the fingerprint of tri-s-triazine units. The bands positioned at 1631, and 1538 cm^{-1}, are assigned to the side-chain asymmetric C-N stretch vibrations. Signals at 1455, 1396, 1312 and 1230 cm^{-1} correspond to the characteristic C-N bonding of secondary and tertiary aromatic amines. These group of signals are an indication of the formation of dimelem units [12,13]. The absorption band at approximatively 890 cm^{-1} is due to the characteristic deformation mode of N-H in amino groups. The sharp absorption band at 806 cm^{-1} matches with the typical tri-s-triazine ring breathing mode [12]. All the as-prepared samples present the overall peaks described, **showing clear qualitative evidence for the polymeric g-C_3N_4 structure**.

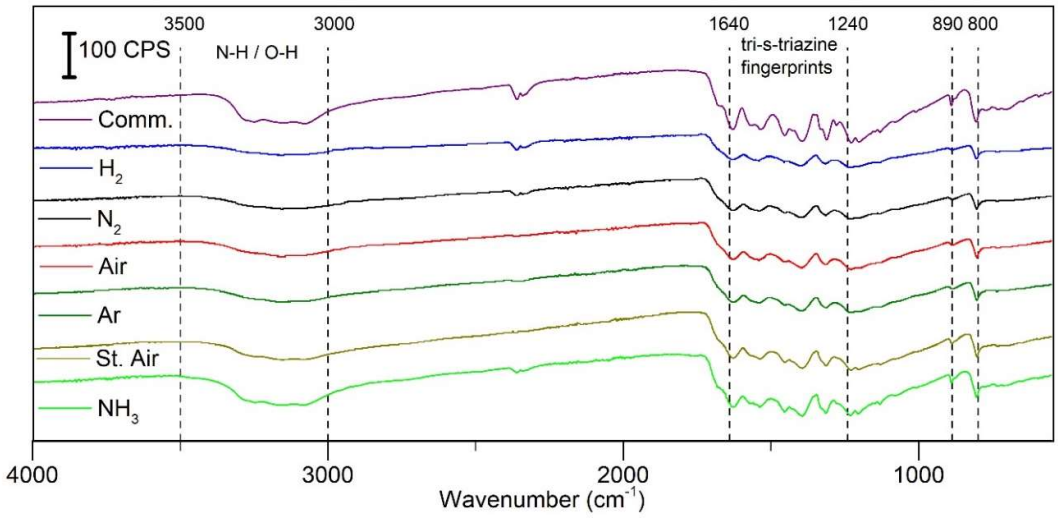

Figure 2.3. FT-IR spectra of the as-prepared g-C_3N_4-atm samples.

B.2.2. Raman characterization

Raman spectra (**Fig. 2.4**) exhibit the characteristic peak pattern of g-C_3N_4 for all the as-prepared samples, even for g-C_3N_4-H_2, for which the Raman spectrum barely emerge from a strong fluorescence background. The most intense peak in the spectra appears at 707 cm^{-1} and is attributed to breathing 2 mode of the s-triazine ring [12,14]. Next to 707

cm^{-1}, a weak signal at 718 cm^{-1} could be observed. The two signals, *ca.* at 707 and 718 cm^{-1}, were predicted by theoretical simulations, ascribing them to the vibrational frequencies of g-C_3N_4 with an active Raman E" vibration [15]. Breathing 1 mode of the s-triazine unit was also present at 977 cm^{-1} [12,14]. Other major peaks are present at 472, 752, 1150, and 1232 cm^{-1}, which are ascribed to in-plane twisting vibrations of the heptazine heterocycle, out-of-plane deformation vibrations of CN heterocycles (also referred to as layer-layer vibrations), A_1' vibrations of the tri-s-triazine ring, and =C (sp^2) bending vibrations, respectively [12,16]. The weaker signal at 1310 cm^{-1} has previously been ascribed to a C-N vibration of aromatic secondary amines, which could indicate the presence of the dimelem unit [12]. It could also be attributed to the C-N stretching vibration of terminal amide groups [17].

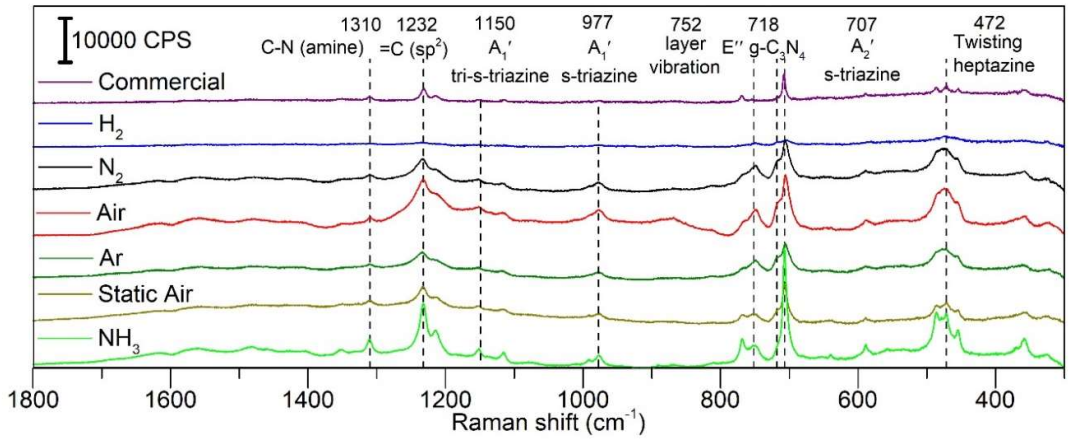

Figure 2.4. Background corrected Raman spectra of the as-prepared g-C_3N_4-atm samples.

Significant differences may be found between the samples regarding the normalized intensities of the peaks at 470, 750 and 977 cm^{-1} (**Fig. 2. 5 a-c, Table 2.1).** In general, g-C_3N_4-commercial and g-C_3N_4-H_2 exhibit much weaker signals than the other samples, whereas g-C_3N_4-NH_3 and g-C_3N_4-Air show the most intense signals.

The I_{750}/I_{707} ratio in particular has been discussed previously in relation with the number of layers in the sample [16]. It was shown that bulk g-C_3N_4 exhibited much lower I_{750}/I_{707} and I_{472}/I_{707} ratios than a 1-layer sample. Besides, all the I_{472}/I_{707}, I_{750}/I_{707} and I_{977}/I_{707} ratios have been shown to decrease when the degree of polycondensation is increased by increasing the temperature of the process [12].

Table 2.1. Raman intensity ratios in the as-prepared g-C_3N_4-atm samples.

g-C_3N_4	I_{977}/I_{707}	I_{750}/I_{707}	I_{472}/I_{707}
Commercial	0.07	0.08	0.25
H_2	0.44	0.46	1.79
N_2	0.24	0.56	0.29
Air	0.21	2.04	0.32
Argon	0.23	0.36	0.32
Static Air	0.10	0.89	0.25
NH_3	0.08	0.16	0.18

I = Raman peak intensity

Hence it may be argued that the polycondensation was more complete in g-C_3N_4-commercial and in g-C_3N_4-NH_3 materials. It is noted that the signals exhibited by g-C_3N_4-H_2, g-C_3N_4-N_2, g-C_3N_4-Air and g-C_3N_4-Ar are very similar in intensities. Nevertheless, g-C_3N_4-H_2 stands out in the case of the signal at 472 cm^{-1}, by exhibiting a much larger intensity than its counter-parts. This may be interpreted as a lower degree of polymerization and crystallization. Namely, the strong fluorescence observed for g-C_3N_4-H_2 sample is also reminiscent of the one observed on g-C_3N_4 monolayer [16] and is thus consistent with a lower stacking order.

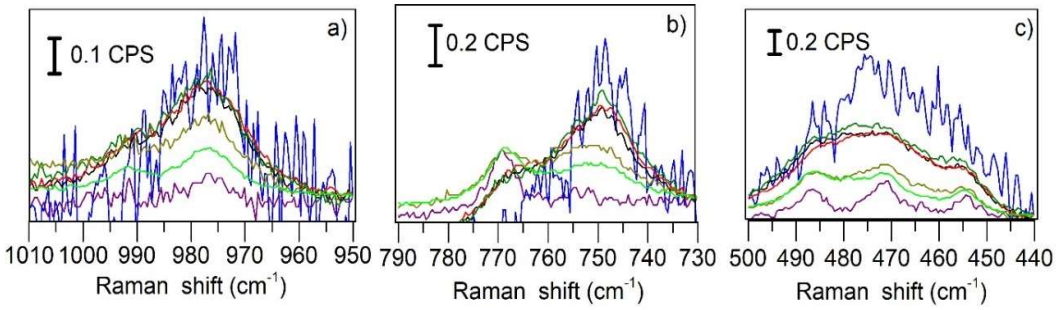

Figure 2.5. Normalized signals of the 950-1010 cm^{-1}, 730-790 cm^{-1}, and 440/500 cm^{-1} ranges, corresponding to the breathing mode of s-triazine ring, to the layer-layer deformation vibration (out of plane deformation vibration of CN heterocycles), and to the in plane twisting vibration of the heptazine heterocycle, respectively

B.2.3. Structural characterization (XRD)

The XRD patterns of the as-prepared samples exhibit the basic diffraction peaks at around 2□ = 13.1° and 2□ = 27.6°, corresponding respectively to the repeating motifs of the tri-s-triazine (also referred as heptazine) unit of the aromatic system, and to the interlayer stacking of π-conjugated aromatic systems, indexed as (002) diffraction plane, characteristic for graphitic materials [2,13,18] (**Fig. 2.6 a**). The diffraction peak at 17.4°

(Fig. 2.6 b) is attributed to the diffraction plane of the repeating motifs of the s-triazine (aromatic system) [19–21].

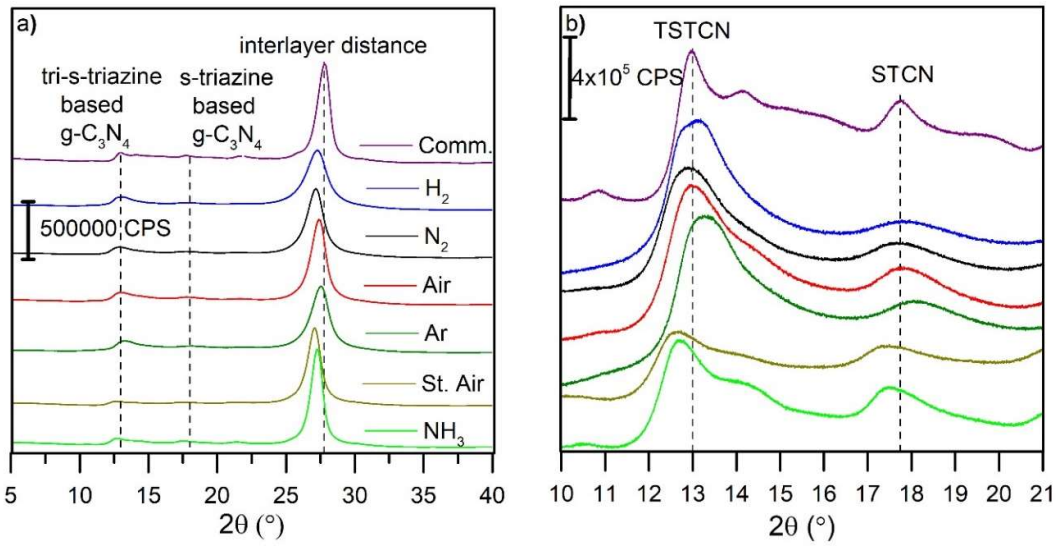

Figure 2.6. a) General XRD patterns and b) zoom of the (10-21°) region of the references and of the as-prepared g-C_3N_4-atm samples.

The relative proportion between TSTCN and STCN phases are determined by fitting the two corresponding peaks (**Fig. 2.7**). First, it was observed that the main diffraction peak at 27.6° was more or less shifted to lower angles compared to the commercial g-C_3N_4 sample. Consequently, the $d_{interlayer}$ distances of the samples varied between 3.22 to 3.29 Å (**Table 2.2**). The less important shift was observed for g-C_3N_4-Ar, *i.e.* the sample using an inert synthesis atmosphere. It has also been reported that decrease of $d_{interlayer}$ may be the result of the removal of nitrogen-containing species from g-C_3N_4 skeleton, which is thus hindered when using Ar as synthesizing atm [22].

The calculated d_{TSTCN} distance of the synthesized samples increased in the following order of synthesis atm: Ar (6.67 Å) < H_2 < Air < Comm. < N_2 < St. Air = NH_3 (6.94 Å). Furthermore, it must be noticed that both g-C_3N_4-Static Air and g-C_3N_4-NH_3 materials also exhibit the largest d_{STCN} among all samples. Yet, those distances remain respectively smaller and higher than the theoretical size of TSTCN (*ca.* 7.13 Å) and of STCN (*ca.* 4.7 Å), probably due to small tilt angularity in the assembly [23].

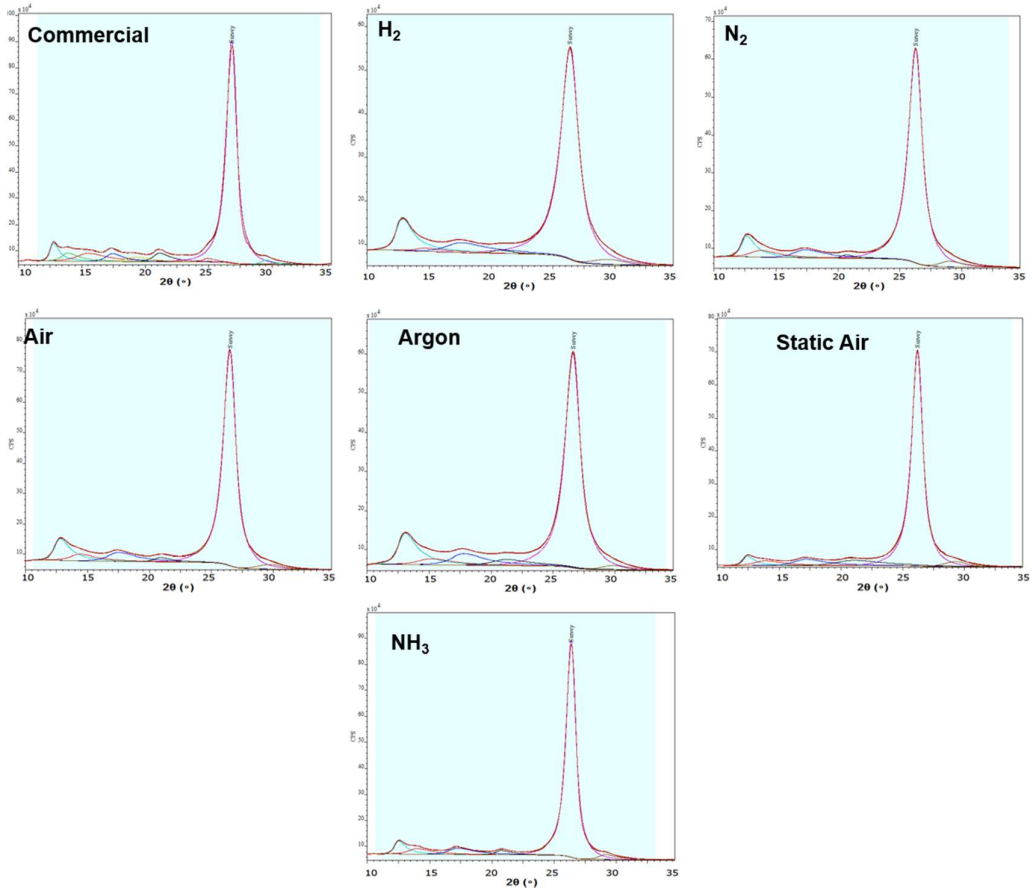

Figure 2.7. XRD deconvoluted peaks for the calculus of the distances of STCN, TSTC and interlayer.

From **Table 2.2**, one can also observe, that the smallest A_{TSTCN} /A_{Total} proportion amongst the synthesized samples is obtained for the g-C_3N_4-Static Air and g-C_3N_4-NH_3 materials (0.35 and 0.47), respectively. It is noteworthy to mention that these calculations are based on the assumption that the graphitic carbon nitride is constituted by only two crystalline phases, tri-s-triazine based g-C_3N_4 and s-triazine based g-C_3N_4.

Looking further at the mean crystallite size, the largest crystallites are obtained for g-C_3N_4-NH_3 with 8.4 nm, which is much more important than the one observed for g-C_3N_4-H_2 (4.6 nm) and g-C_3N_4 synthesized in other atmospheres, and also slightly larger to that of the commercial reference. According to some studies, this may be related to higher polymerization degree [24]. The number of g-C_3N_4 layers followed the same tendency, the highest packing being observed for g-C_3N_4-NH_3 (average of 26 layers) and the lowest for g-C_3N_4-H_2 (average of 14 layers).

Table 2.2. Size of TSTCN and STCN, d-interlayer distances and phase proportions of TSTCN, mean thickness of graphitic stacks [25], and number of layers of g-C_3N_4.

g-C_3N_4	d_{TSTCN} (Å)	d_{STCN} (Å)	$d_{interlayer}$(Å)	A_{TSTCN} /A_{Total}	τ* (nm)	N° layers**
Commercial	6.81±0.02	4.99±0.02	3.22±0.01	0.54	7.9±0.4	25±1
H_2	6.76±0.02	4.97±0.02	3.28±0.01	0.59	4.6±0.4	14±1
N_2	6.85±0.02	4.99±0.02	3.29±0.01	0.54	5.9±0.4	18±1
Air	6.79±0.02	4.96±0.02	3.26±0.01	0.56	6.6±0.4	20±1
Argon	6.67±0.02	4.89±0.02	3.25±0.01	0.59	5.5±0.4	17±1
Static Air	6.94±0.02	5.06±0.02	3.29±0.01	0.35	6.4±0.4	19±1
NH_3	6.94±0.02	5.04±0.02	3.27±0.01	0.47	8.4±0.4	26±1
NH_3[ł]	6.49±0.15	4.59±0.15	3.19±0.15	-	-	-
Theoretical	7.13	4.70	3.26	-	-	-

ł = obtained by ED measurements; * = mean thickness of stacks; ** = calculated as in Saner *et al* [18]

B.2.4. Thermal stability (TGA) analysis

TGA profiles (**Fig. 2.8 a**) reveal a one-pot decomposition with a maximum located between 585 and 640 °C, suggesting a construction of heptazine-base units in all samples, in accordance with reported literature [3,26]. However, depending on the synthesis atmosphere, g-C_3N_4 decomposition temperature increased from g-C_3N_4-Static Air (585 °C), g-C_3N_4-H_2 (590 °C), g-C_3N_4-N_2 (595 °C), g-C_3N_4-NH_3 (600 °C), g-C_3N_4-Air (615 °C), g-C_3N_4-Ar (615 °C), and g-C_3N_4-commercial (640 °C). Thus, the highest and lowest decomposition temperatures are obtained for the g-C_3N_4-commercial and g-C_3N_4-Static Air, respectively.

This highest decomposition temperature may be correlated with the largest graphitic stack thickness increasing along with the number of sheets, which confers stronger Van der Waals interactions between the single layers. Moreover, thermal stability is also related with ideal condensation of g-C_3N_4 as graphitic structure materials [13]. Thus, the g-C_3N_4-Static Air sample present the lowest decomposition temperature, *ca.* 585 °C, presumably for presenting the lowest A_{TSTCN} proportion, *ca.* 0.35, confirming the energetic stability of tri-s-triazine unit over s-triazine unit with a 30 kJ mol^{-1} difference [27]. It must be underlined that the wider range of decomposition temperature (difference between the starting and the finishing decomposition temperature) among the samples (**Fig. 2.8 b**) was presented for g-C_3N_4-NH_3 (ΔT = 145°), presumably for the combination of the largest graphitic stack thickness and flatter in-plane organization (less tilt angularity).

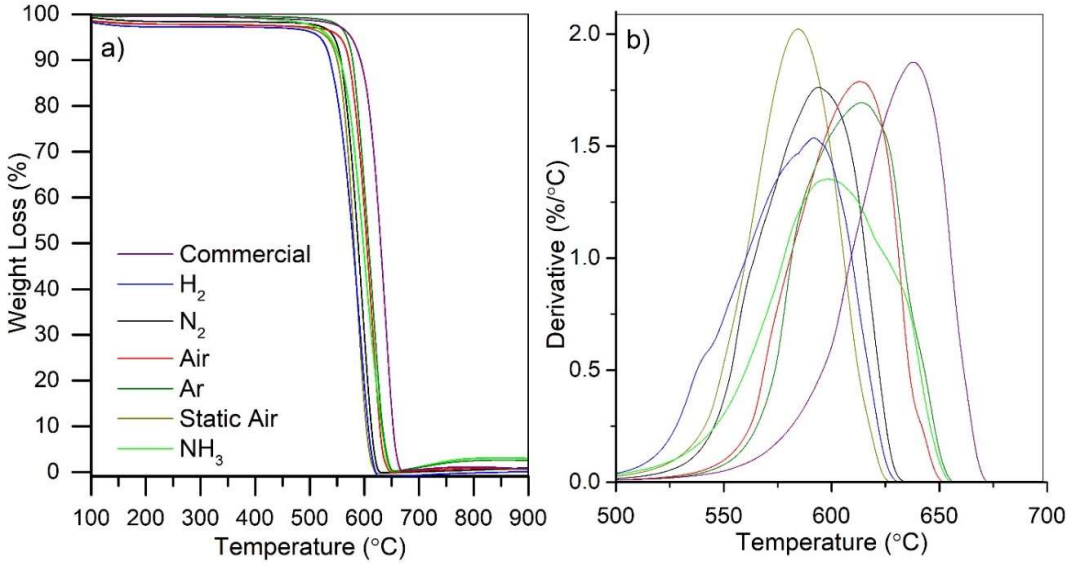

Figure 2.8. a) TGA profiles b) Derivatives of weight loss of the as-prepared g-C_3N_4-atm samples.

B.2.5. XPS model analysis

From the survey spectra in **Fig. 2.9 a**, it can be observed that the major contributions correspond to N 1s and C 1s at binding energy of *ca.* 400 and 280 eV, respectively. For all samples, a small peak attributed to O 1s appear approximately at 530 eV.

The **C 1s signal** (**Fig. 2.9 b)** displays two contributions, a minor one at 284.6 eV and a major one at binding energies varying between 287.9 and 288.2 eV. The first contribution can be assigned to C=C (sp^2) from adventitious carbon and to sp^3 defects on the edge of graphitic domains. The second contribution was attributed to sp^2-bonded C of $(N)_2$-C=N from the heterocyclic ring [12]. One may observe that the binding energy of the second contribution is significantly shifted to lower binding energy for g-C_3N_4-H_2 sample, meaning that the sp^2-carbon may also be bonded to more reduced N species. It can also be mentioned that amongst the synthesized materials, the percentage of the second contribution is higher for g-C_3N_4-Ar and g-C_3N_4-NH_3 samples.

The **N 1s signal** (**Fig. 2.9 c)** exhibits two contributions, a major one at 398.5 eV and a minor one at 400.4 eV, assigned to sp^2-hybridized pyridine nitrogen of C=N-C from the heterocyclic ring and to the N-$(C)_3$ tertiary nitrogen, respectively [28–30]. One can also notice that there is no evidence for the presence of a third contribution due to the presence of terminal amino groups at higher binding energies. However, knowing the complexity of XPS deconvolution for small contributions, one cannot exclude the presence of small amounts of terminal amino-groups.

As **O 1s signal** (**Fig. 2.9 d**) presents lower intensity, it was not deconvoluted, but it displays the main contribution assigned to –OH surface groups at 532.1 eV. For better clarity, only the narrow region going from 528 to 536 eV was analysed in details.

Almost all the as-prepared g-C_3N_4 samples exhibit C/N ratio (*ca.* 0.76 for g-C_3N_4-Comm, Air, Static Air and 0.75 for g-C_3N_4-N_2, Ar, NH_3) very close to the theoretical value of

C/N= 0.75, thus, indicating a high quality g-C_3N_4, except for g-C_3N_4-H_2 presenting a 0.70 ratio suggesting that there is less nitrogen content in this material. This lower nitrogen content might be associated with less amino groups, which is consistent with the lower degree of polymerization indicated from XRD and Raman results for this material.

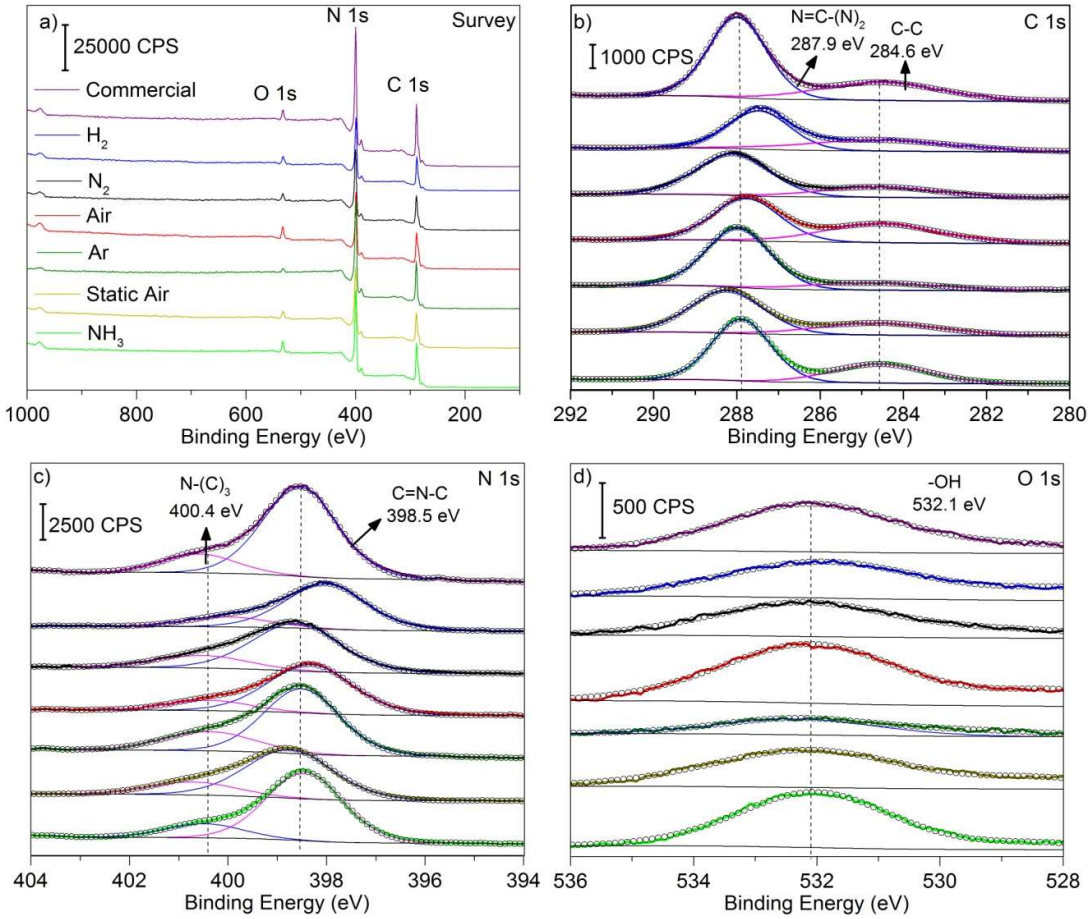

Figure 2.9. XPS spectra analysis of the as-prepared g-C_3N_4-atm samples a) XPS survey spectra showing the three contributions for the g-C_3N_4 components. b) N 1s spectra c) C 1s spectra d) O 1s spectra.

B.2.6. BET surface area measurements

From Brunauer, Emmett, and Teller (BET) measurements (**Fig. 2.10 a, Table 2.3**), it can be observed that all the references and the as-prepared samples exhibit a type-IV adsorption-desorption isotherm profile characteristic of mesoporous materials. Moreover, for all synthesized g-C_3N_4 samples, the hysteresis loop shows a type-H4 profile characteristic of slit-like pores [31] which is in a good agreement with the (002) facet ascribed from XRD for graphitic materials, constituted by stacked layers.

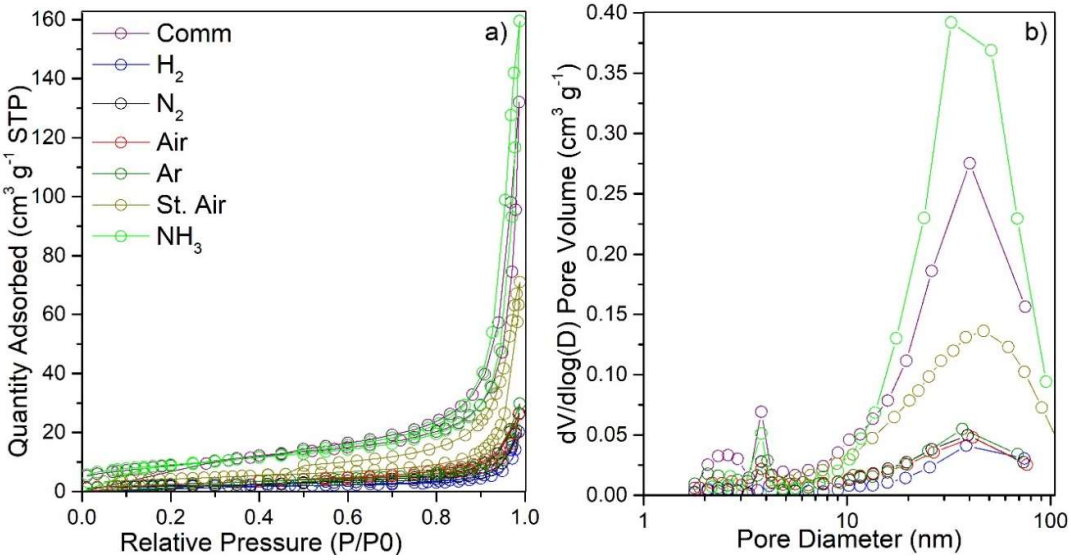

Figure 2.10. a) Nitrogen adsorption-desorption isotherms. b) BJH pore-size distribution of the as-prepared g-C_3N_4-atm samples.

The BJH pore-size distribution exhibit a bimodal type, *ca.* 4 nm and 33-47 nm, with small narrow and broad distribution, respectively **(Fig. 2.10 b)**. The large mesopore size distribution of the synthesized samples increases following the synthesis atmosphere from Ar (36±3 nm), H_2, N_2, Commercial, Air = NH_3, to Static Air (47±5 nm). One can say that the mesopore size tendency differs from the pore volume, which increases following the respective order Air-Ar-N_2-H_2 (0.05 cm^3 g^{-1}), Static Air, Commercial and NH_3 (0.39 cm^3 g^{-1}). Amongst the synthesized g-C_3N_4 materials, g-C_3N_4-NH_3 exhibits the largest pore volume, which is in correlation with the largest surface area obtained. Pore volume and size values suggested that g-C_3N_4-NH_3 is showing a different spatial arrangement with the largest average mesopore size and pore volume. This phenomena can be attributed to a profound deep channel and/or high amount of mesopores, which make us speculate that NH_3 atmosphere participate in the polycondensation, with a positive impact on mesoporosity.

Table 2.3. Specific surface area (S_{BET}), pore volume (V_{pore}), pore size, and IEP of the as-prepared g-C_3N_4-atm samples.

g-C_3N_4	S_{BET}* ($m^2\ g^{-1}$)	V_{pore} ($cm^3\ g^{-1}$)	Pore size** (nm)	IEP (pH)
Commercial	33±3	0.27±0.02	40±4	5.35
H_2	6±1	0.04±0.02	39±4	6.00
N_2	7±1	0.05±0.02	39±4	5.30
Air	10±1	0.05±0.02	42±4	5.20
Argon	10±1	0.05±0.02	36±4	5.50
Static Air	15±2	0.14±0.02	47±5	5.00
NH_3	32±3	0.39±0.02	42±3	5.90

* = Specific surface area calculated with BET; ** = calculated with BJH

B.2.7. Zeta potential measurements

From the auto-titration measurements (**Fig. 2.11, Table 2.3**), it can be observed that all the references and the as-prepared samples exhibit the same tendency at various pH's. g-C_3N_4 particles present positive and negative charged values at pH values below and above the IEP, respectively. The references and as-prepared samples obtain an IEP in the range of pH 5-6, which is in a good agreement with previous works [32]. These values confirm the amphoteric functionality of g-C_3N_4 [3] associated with g-C_3N_4 capacity of protonation and deprotonation of specific groups on the g-C_3N_4 surface, namely, surface O-H hydroxyl group, and primary (C-NH_2) and secondary (C_2-NH) amines (already described by FT-IR, Raman, and XPS for some of them). Amino groups preferentially act as proton acceptors in basic conditions, due to the available lone pair of electrons of the nitrogen atom, to obtain positive surface charges [33]. But in acidic conditions, hydroxyl groups can be transformed into hydroxyl ions, to obtain negative surface charges. The IEP's of most of the samples vary slightly, ranging from 6.00 to 5.00 for g-C_3N_4-H_2 and g-C_3N_4-Static Air, respectively. Furthermore, the lowest IEP might be associated with the lowest tri-s-triazine phase proportion, *ca.* 0.35. Due to the presence of amino groups on the edge of each C_3N_4 sheet and considering the size difference between s-triazine and tri-s-triazine building blocks, a higher number of local charges is expected for STCN phase. However, for the other samples (for example g-C_3N_4- NH_3) the tendency in IEP might also be correlated to other parameters.

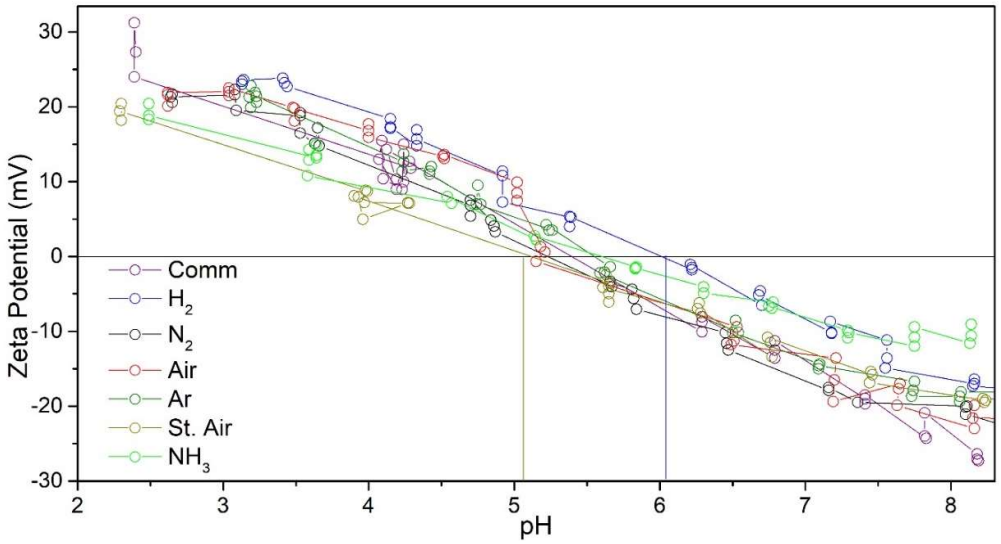

Figure 2.11. Auto-titration of the references and of the as-prepared g-C_3N_4-atm samples to obtain the IEP.

B.2.8. TRMC measurements

From TRMC measurements performed at 360, 450 and 550 nm (**Fig. 2.12**), no signal has been observed. These results might suggest that either no significant free electrons are photogenerated or that they recombine too fast to be detected.

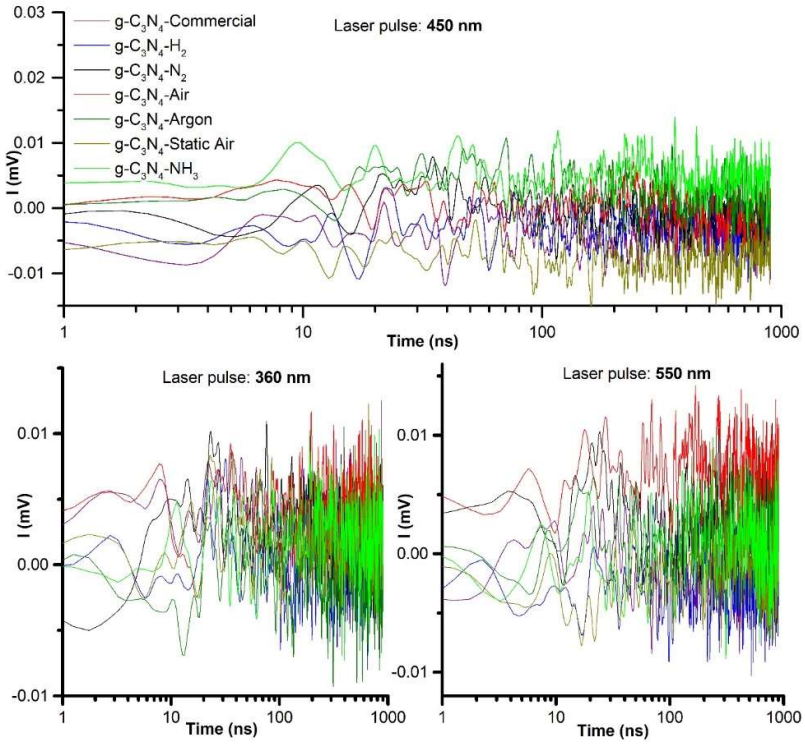

Figure 2.12. TRMC measurements of the references and of the as-prepared g-C_3N_4-atm samples at 360, 450, and 550 nm.

C) Synthesis and characterization of Au/g-C_3N_4 binary composites

C.1. Synthesis of Au/g-C_3N_4 composites

Au/g-C_3N_4 samples were prepared via chemical reduction of chloroauric acid ($HAuCl_4$) [34] precursors in presence of the as-prepared g-C_3N_4 samples and schematically illustrated in **Fig. 2.13**. The support (300 mg) is dispersed into a methanol/ethanol mixture (91/9 v/v, 55 mL) with a tip sonicator (700 W, 20 kHz) during 30 min (**T_0**), using 30% of maximum sonication power. The mixture is then transferred to a bath sonicator (280 W, 50/60Hz) and cooled down to room temperature (22 °C) before the sonication is turned on. A given volume of a methanol/ethanol solution of $HAuCl_4$ ($2.5(\pm0.2) \times 10^{-3}$ mol L^{-1}) is then added in order to target a gold loading of 0.3 wt. %, selected according to a parametric study performed (**Fig. A.1, Appendix 1**). Sonication was carried out for 1 h (**T_1**) before 5 mL of a fresh methanol/ethanol solution of $NaBH_4$ solution (2.5×10^{-2} mol L^{-1}) was added. Sonication is then continued for 10 min (**T_2**).

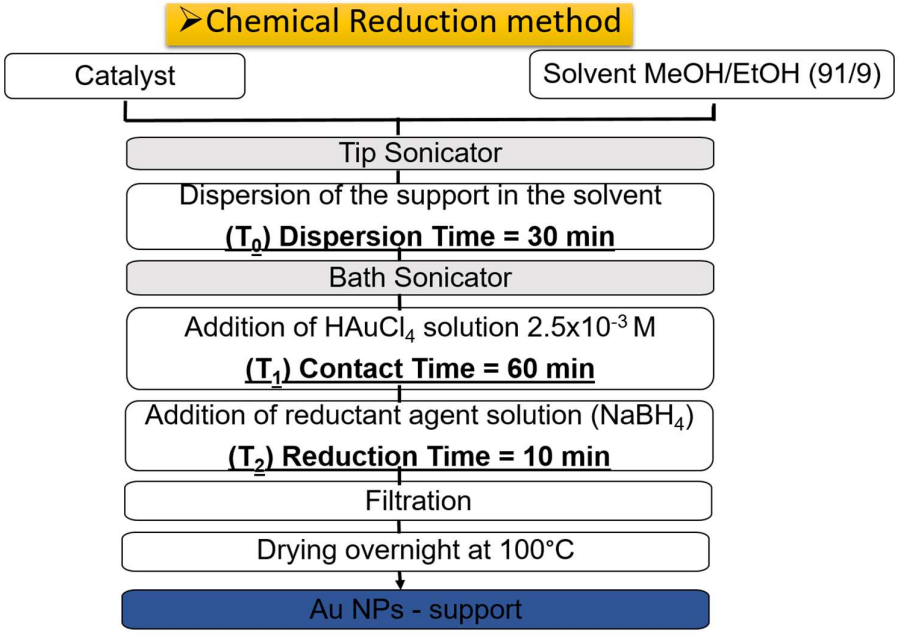

Figure 2.13. Au NPs deposition via chemical reduction method [34].

C.1.1. Calculation to control the Au loading

The Au metallic NPs deposition comprises a sequence of different steps. To begin, a Au mother solution ($C_{HAuCl4\ 0}$) has to be prepared by using chloroauric acid as Au precursor (**equation 1**). The mass, volume, and molecular weight have to be known values, m_{HAuCl4}, V_{HAuCl4}, and MM_{HAuCl4}, respectively.

$$C_{HAuCl4\ o} = \frac{m_{HAuCl4}}{V_{HAuCl4} * MM_{HAuCl4}} \quad (1)$$

Once the mother solution was prepared in a volumetric flask, an aliquot, with the calculated amount of Au in moles, can be transferred to the beaker containing the support material dispersed in the methanol/ethanol mixture in function of the selected Au loading percentage that depends on the initial mass of the support material ($m_{support}$) (**equations 2 and 3**).

$$Mol_{Au} = \frac{\%Au_{loading} * m_{support}}{MM_{Au}} \quad (2)$$

$$V_{HAuCl4} = \frac{Mol_{Au}}{C_{HAuCl4_O}} * 1000 \quad (3)$$

At this point, a final concentration of chloroauric acid ($C_{HAuCl_4 f}$) can be calculated taking into account the volumes of gold precursor added, initial solvent mixture (typically 55 mL), and the reductant agent solution in **equation 4**.

$$C_{HAuCl4\ F} = \frac{C_{HAuCl4_O} * V_{Au}}{V_{Au} + V_{Solvent} + V_{NaBH_4}} \quad (4)$$

However, to guarantee the total reduction of Au^{+3} in solution to Au^0 in metallic NPs grafted to the support material, an excess of $NaBH_4$ is used. It means that for each Au mol 10 moles of $NaBH_4$ are added. V_{NaBH4} is constant (10 mL) and the C_{NaBH4} is calculated in **equation 5**.

$$C_{NaBH4} = \frac{Mol_{NaBH4}}{V_{NaBH_4}} \quad (5)$$

For accuracy the molecular weight of the different chemicals include four digits after comma:$M_{\mathrm{HAuCl4}} = 339.7865 g/mol$; $M_{\mathrm{NaBH4}} = 37.8323 g/mol$

C.1.2. Mechanism of Au NPs deposition onto g-C_3N_4 support

The Au NPs deposition mechanism principle for the specific case of using $HAuCl_4$ as gold precursor being reduced chemically by the reductant agent $NaBH_4$ in excess comprises two steps (**Fig. 2.14**): the **adsorption** of the gold (III) chloride ions onto the exposed surface groups of the support material. Two examples of surface groups are presented: mainly primary amines and secondary amines which are the most common for g-C_3N_4. Then, the **surface chemistry reduction** could take place with the participation of the boron hydrate ion reacting with the grafted gold (III) chloride ion leading to the formation of the Au NPs and consequently leading to the Au NPs deposition onto the support catalyst. The size, shape, growth, dispersion, and coverage of Au NPs depend directly on the nature of the support catalyst, *e.g.,* surface groups, roughness, among others.

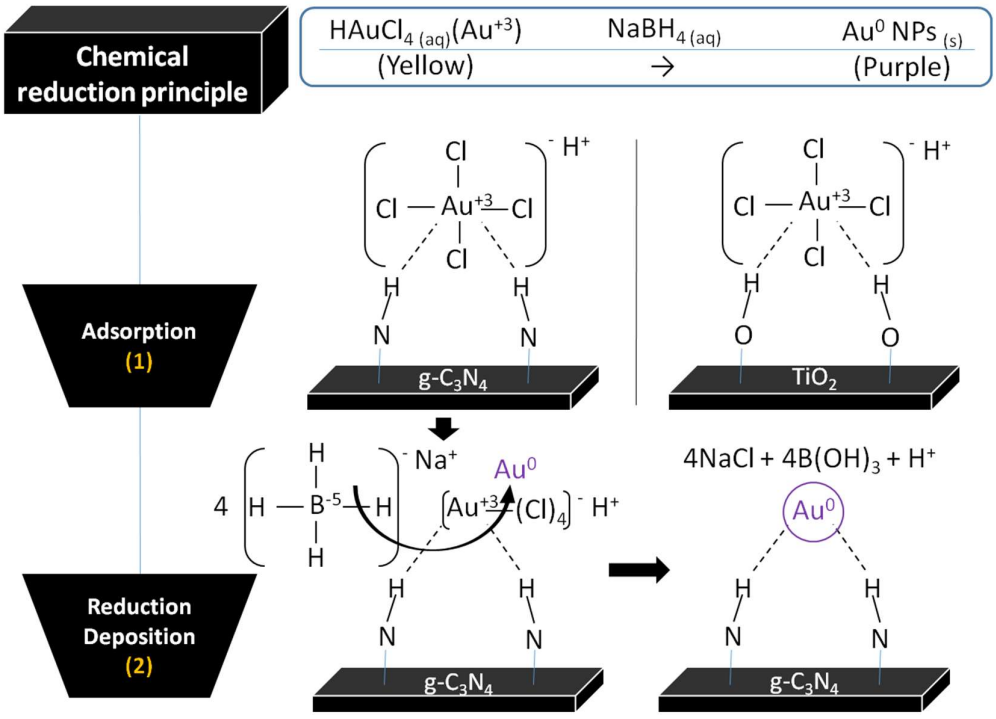

Figure 2.14. Illustrative scheme of Au NPs deposition mechanism principle.

C.2. Characterization of Au/g-C_3N_4 composites

C.2.1. Elemental analysis

The deposition yield achieved was of *ca.* 75% for all Au/g-C_3N_4-*atm* samples. This result confirms the accuracy and suitability of the Au NPs deposition chemical reduction method for the g-C_3N_4 surface type. One can say that one objective is to obtain the most intimate metal/SC contact. Nevertheless, another objective is to obtain the best interaction with the functional groups of the support surface and the driven forces involved in given the NPs with specific characteristics, namely, shape, size, coverage, and distribution.

For this reason, the deposition yield parameter alone provides a minimum idea of only the first objective. For the second objective TEM analysis is mandatory, and the correlation of both provides a solid analysis.

C.2.2. TEM characterization and electron diffraction (ED)

The distances related to the main diffraction planes corresponding to tri-s-triazine units, to s-triazine units and to the interlayer stacking of π-conjugated aromatic system distance (002) were measured by electron diffraction for only the most crystalline g-C_3N_4-NH_3 sample **(Fig. 2.15)**. One can see that the values obtained from XRD and ED for the size of d_{TSTCN} (6.94; 6.49 Å), and d_{STCN} (5.04; 4.59 Å) phases, and $d_{Interlayer}$ (3.27; 3.19 Å) are consistent, confirming the use of the two characterization techniques as complementary analysis. Yet, when comparing with the theoretical values of 7.13 Å, 4.70 Å, and 3.26 Å [2,19], one can see lower and higher experimental values for the

d_{TSTCN} and d_{STCN} (Å), respectively, which presumably indicates a tilt angularity in the assembly, also discussed previously in the XRD section.

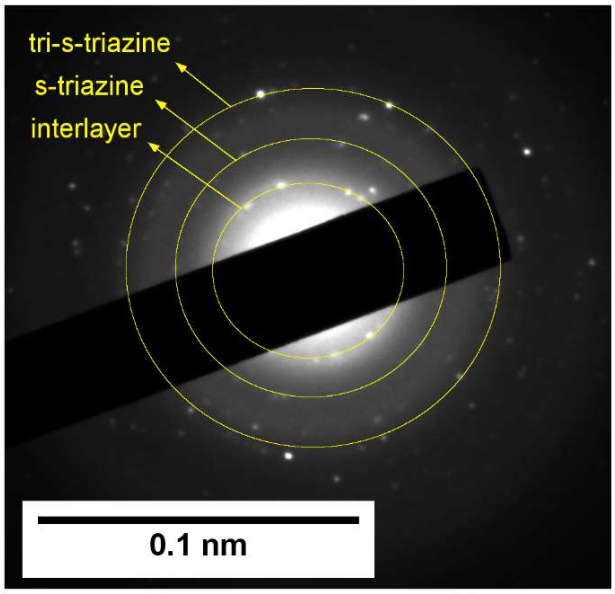

Figure 2.15. Electron diffraction image of the g-C_3N_4-NH_3 grain lattice planes.

TEM images **(Fig. 2.16)** reveal the typical lamellar-type structure with entangled nanosheets [35], for all the Au/g-C_3N_4-atm samples. TEM micrographs further show that Au NPs were round shaped in all samples. However, Au NPs coverage, dispersion and size differ from sample to sample (**Fig. 2.17**). The most homogeneous coverage is observed onto g-C_3N_4-NH_3 surface (**Fig. 2.16 h**). The Au/g-C_3N_4-NH_3 composite also exhibits the smallest Au NP mean size (3.2 nm), associated with the smallest standard deviation (1.1 nm). All other composites show larger mean particle sizes (3.7-5.1 nm), but maybe more importantly, larger standard deviations on the average size and significantly less homogeneous dispersions. Au/g-C_3N_4-Air and Au/g-C_3N_4-Ar in particular show the largest standard deviation of all (2.4 nm), resulting from a significant contribution of larger Au NPs, *ca.* 6 - 10 nm. In the case of Au/g-C_3N_4-Air sample, it displays a quasi-bimodal distribution with local maxima at 3.5 nm and 6.5 nm. All catalysts, except Au/g-C_3N_4-NH_3, also present aggregates of Au NPs. Au/g-C_3N_4-Ar exhibits a particularly inhomogeneous distribution of Au NPs over the support. In this catalyst, like in most catalysts, extensive areas with no particles may be found, associated with areas containing a high density of particles, which can also explain the presence of aggregates in these samples. On the contrary, no aggregate or Au NP-free areas are observed in Au/g-C_3N_4-NH_3. This sample displays a particularly homogeneous density of Au NPs throughout the sample, of about 2000 particles/μm^2 (average distance of 23 nm between two Au NPs). Therefore, one can conclude that there is a direct impact of the support nature on the growth, final size and distribution of Au NPs over the support. More specifically, these results suggest that the specific surface chemistry of the NH_3-derived C_3N_4 provides stronger interactions with the gold precursor used in the synthesis, as well as with the resulting seeds and particles, leading to better size control of the final Au NPs size and coverage.

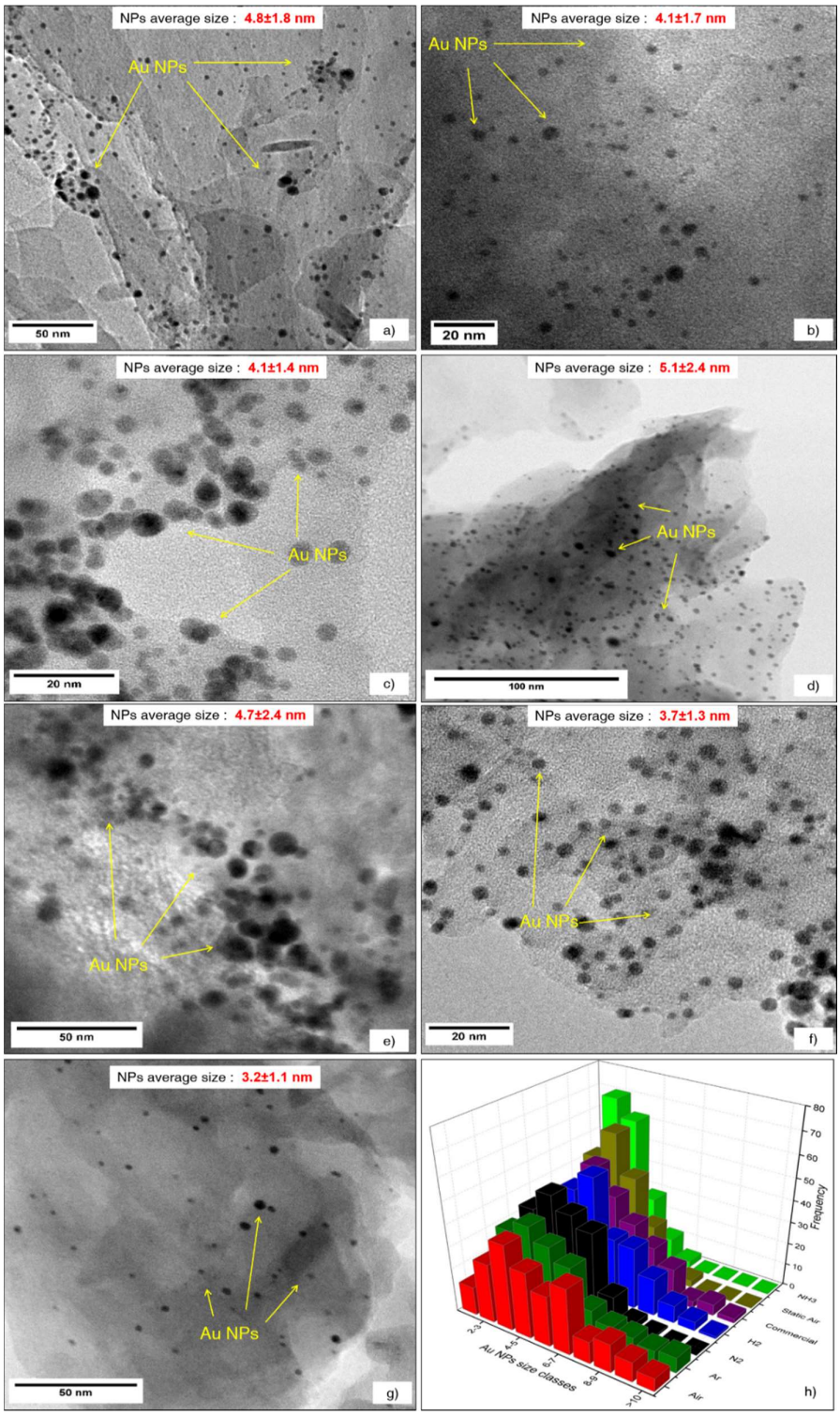

Figure 2.16. TEM images for the Au/g-C_3N_4-atm composites, including the mean particles size with their standard deviation, a) Au/g-C_3N_4-Commercial b) Au/g-C_3N_4-H_2 c) Au/g-C_3N_4-N_2 d) Au/g-C_3N_4-Air e) Au/g-C_3N_4-Ar f) Au/g-C_3N_4-Static Air g) Au/g-C_3N_4-NH_3 h) Au NPs size distribution determined from TEM characterization of Au/g-C_3N_4-atm samples (obtained from a selection of 200 Au NPs for each sample).

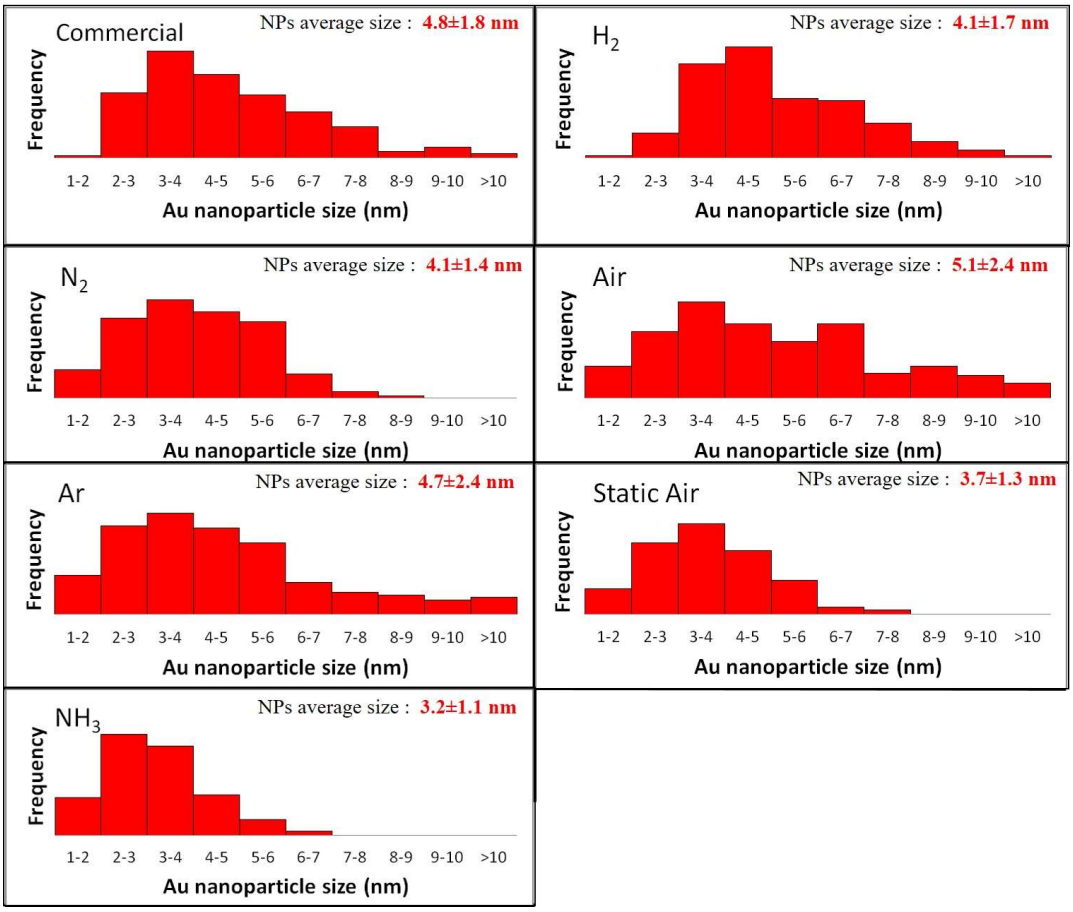

Figure 2.17. Particle size distribution obtained by TEM (200 NPs for sample) for references and from the g-C_3N_4-atm as-prepared samples.

C.2.3. UV-Vis absorption properties

Figure 2.18 a presents the color of each g-C_3N_4 samples after synthesis. One can notice the diverse range of colors obtained as a function of the atmosphere used for g-C_3N_4 synthesis, from light to dark yellow for NH_3-N_2, Ar, Air-Static Air, to reddish and brownish for the H_2 atmosphere and the Commercial sample, respectively. This color change shows that the g-C_3N_4 synthesis atmosphere, (oxidative, inert or reductive), directly impacts the g-C_3N_4 optical and electronic properties of the semiconductor [36].

From the UV-Vis spectra **(Fig. 2.18 b)**, one can observe that all the 0.3 wt.% Au/g-C_3N_4 composites exhibit a maximum absorption in the UV/blue range of the spectra, with an absorption band edge at 450-460 nm, characteristic for g-C_3N_4 semiconductors [36–39]. It is attributed to π →π* electronic transitions [36] found in π-conjugated systems of tri-s-triazine and s-triazine units. It must also be pointed out that Au/g-C_3N_4-H_2 and Au/g-C_3N_4-commercial samples present an absorption tail at higher wavelengths. This behaviour might be explained by the occurrence of additional n →π* electronic transitions [36], which is attributed to a more pronounced layer deformation, as already experimentally and theoretically described elsewhere [26]. The n →π* transition is indeed characteristic for the presence of lone electron pairs of the N atoms in the g-C_3N_4 skeleton. A second contribution with a maximum located at *ca.* 550 nm is ascribed to the

presence of Surface Plasmon Induced Effect (SPIE) of Au NPs. Nevertheless, **Fig. 2.18 b (inset)**, shows that the absorption of the SPIE is quite weak for all the binary composites due to the low loading of Au NPs (0.3 wt.%) and the small particle size (≤5.1 nm). For the Au/g-C_3N_4-H_2 and Au/g-C_3N_4-commercial material, the SPIE overlaps with the n →π* electronic transitions of g-C_3N_4 and thus cannot be distinguished.

From the band-gap determination **(Fig. 2.18 c)** calculated using the Tauc equation, one can observe that the Au/g-C_3N_4-H_2 and Au/g-C_3N_4-NH_3 photocatalyst present respectively the lowest (2.49 eV) and the highest (2.75 eV) band-gap. The main difference relies on the potential of deformation of the in-plane motifs. The lower absorption of Au/g-C_3N_4-NH_3 sample in the visible range might be explained by a less pronounced layer deformation of the nanosheets. This phenomenon might be the result of the larger abundance of A_{STCN} with respect to A_{TSTCN} (as already mentioned in the XRD Section), the former one presenting a higher stability toward tilt angularity effect. Furthermore, using NH_3 as synthesis atmosphere can lead to the occurrence of another phenomenon. As NH_3 is one of the by-products of the polycondensation, the saturated NH_3 environment inside the crucible may provide suitable conditions for growing well-planar nanosheets, thereby favouring stacking of the layers (and thus π →π*transitions) and minimizing n →π* transitions (due to layer deformation or distortion). On the contrary, H_2 as synthesis atmosphere of g-C_3N_4 may promote the insertion of H atoms in between layers leading to strong interaction by H bonding with other skeleton atoms [40], preferentially edged or bridged N atoms. Thanks to this new interaction forces an interplanar induced layer distortion appears, allowing an additional n →π* transition. On the other hand, the g-C_3N_4-Commercial-N_2-Air-Ar-Static Air samples, present similar band gap values in reference to the theoretical polymeric semiconductor value, *ca.* 2.70 eV [2,13].

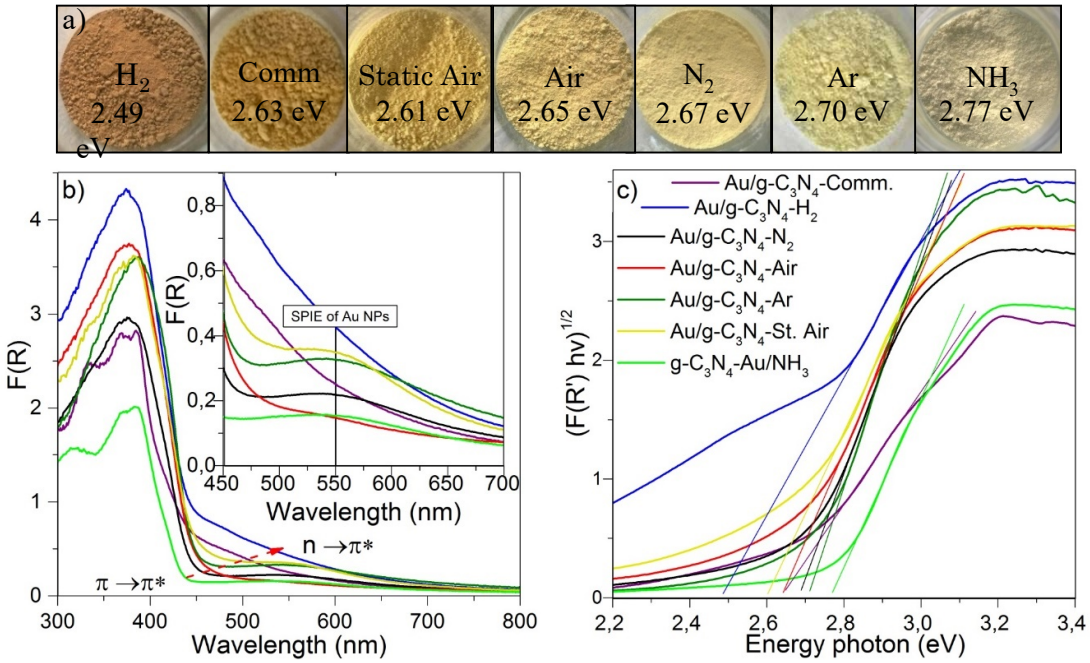

Figure 2.18. a) Color of the powders of the bare g-C_3N_4 samples b) UV-Vis spectra of the Au/g-C_3N_4-atm composites. Inset) zoom of the spectral domain corresponding to SPIE signal of Au NPS at *ca.* 550 nm. c) Tauc plot to determine the apparent band gap of Au g-C_3N_4-*atm* composites.

D) Photocatalytic performances toward H_2 production

The photocatalytic activities of the as-prepared samples are evaluated toward several criteria, namely, H_2 production, cumulated H_2 evolution, stability (cycling tests), and internal quantum yield (IQY). All mentioned tests are performed by using the semiconductor material suspended in water under artificial solar-light irradiation and adding a very low amount of triethanolamine (TEOA) as sacrificial agent (1 vol. %) in a photocatalytic set-up **(Fig. 2.20 and 2.21)**. This photocatalytic system is also known as **suspended particle photoreactor** as illustrated in **Fig. 2.19**. The advantages of a suspended particles reactor relies on the simplicity of the four-component system: H_2O (reactant), lamp as an artificial light (photon source for activation), and suspended photocatalyst (to split the water molecule) and sacrificial agent. Likewise, water splitting via direct conversion of solar into chemical energy, without using an additional bias to enhance the photogenerated charge carriers separation is a quite recent H_2 production process. Another advantage is the reasonable cost of building up this set-up type. Thus, for all the mentioned advantages makes it an attractive approach to evaluate activity´s materials.

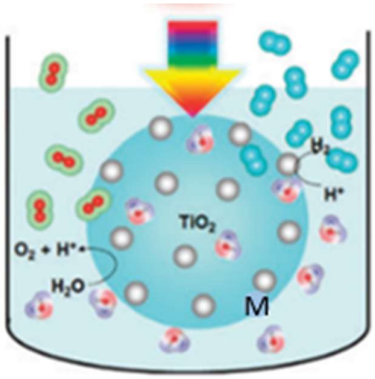

Figure 2.19. Schematic illustration of a suspended particles photoreactor, TiO_2 decorated with M NPs is used as an example to undergo water splitting reaction under solar-light irradiation. H_2 is in blue and O_2 is in red.

D.1. Experimental set-up

D.1.1. Photocatalytic reactor

In details, H_2 production was carried out in a quartz vessel containing 1L of Milli-Q deionized water and TEOA (1 vol. %) (pH = 11), equipped with an inner central jacket quartz tube containing a 150 W Ceramic-Metal-Halide Hg Lamp (BLV-Licht), simulating artificial solar-light. The jacket quartz is suitable for containing the lamp as it has low impurity content allowing both UV and visible photons to pass through without any absorption. On top of that, the quartz vessel is wrapped with aluminium foil to avoid photons losses. A visible light simulated irradiation was achieved by adding a Nigrosing solution of 0.1 g L^{-1} into the cooling solution flowing into the plunging quartz tube with the purpose of cutting-off the UV photons. The jacket is linked to a water cooling bath to continuously cool it off (at 20°C) during all the experiment with the purpose of avoiding any increase in water temperature due to the possible heating from the light source. Indeed, according with Arrhenius law, a small increase of water temperature (≥2.5 °C) in this type of system leads to an increase on the rate reaction constant and therefore to an increase in the H_2 production by means of thermal-activation heat and not light-activation. The photocatalytic tests are performed by suspending 250 mg of catalyst in ultra-pure water under continuous nitrogen flow (100 mL min^{-1}) and with a mechanical stirring at 700 rpm. For the continuous stirring condition, a PTFE magnetic stirring bar is used to produce a radial flow, consequently the photocatalyst particles are induced by rotation in the liquid as a suspension. Tests are performed at atmospheric pressure. The reactor also comprehends a hermetic sealing by using a silicon ring which fits between the top of the quartz vessel and the stainless steel lid. This sealing provides an airtight seal throughout the continuous gas phase acquisition guarantying to quantify only the evolved gases inside the quartz vessel. Before switching on the lamp, a prior nitrogen (Alphagaz 2, SMARTOP) purge at 500 mL min^{-1} for 1h takes place, aiming at removing residual O_2, remaining O_2 quantities might lead to biased results, because remaining O_2 might react with evolved H_2 and produce H_2O (undesirable back reaction). After the nitrogen purge, the lamp is switched on and the reaction products are analysed online for every 100 s by a micro-gas

chromatography analyser (µGC). Typically, quantitatively photocatalytic test last 2.5 h, considering 10% relative error exists on the H_2 massic yield (**Appendix 2**).

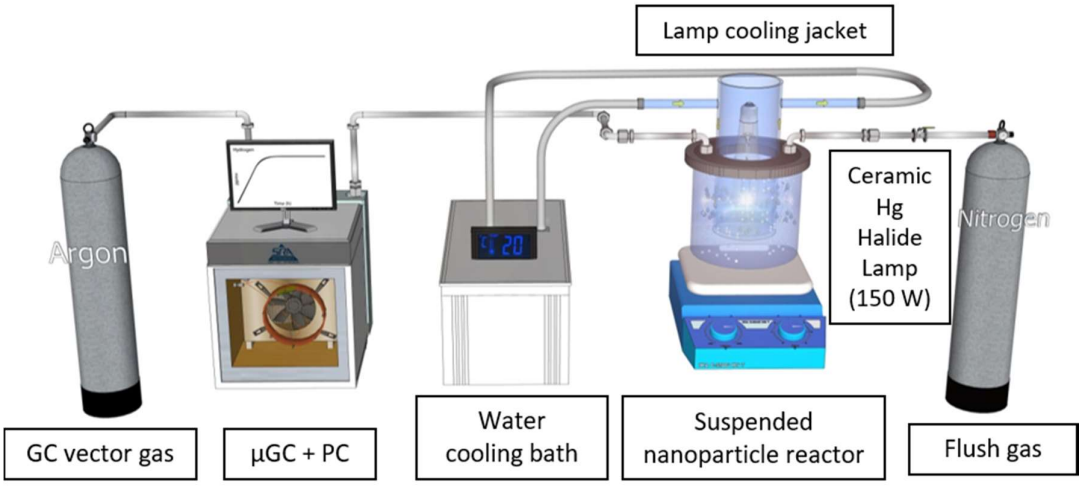

Figure 2.20. Scheme of the photocatalytic set-up with all its components. Designed with Sketchup ©.

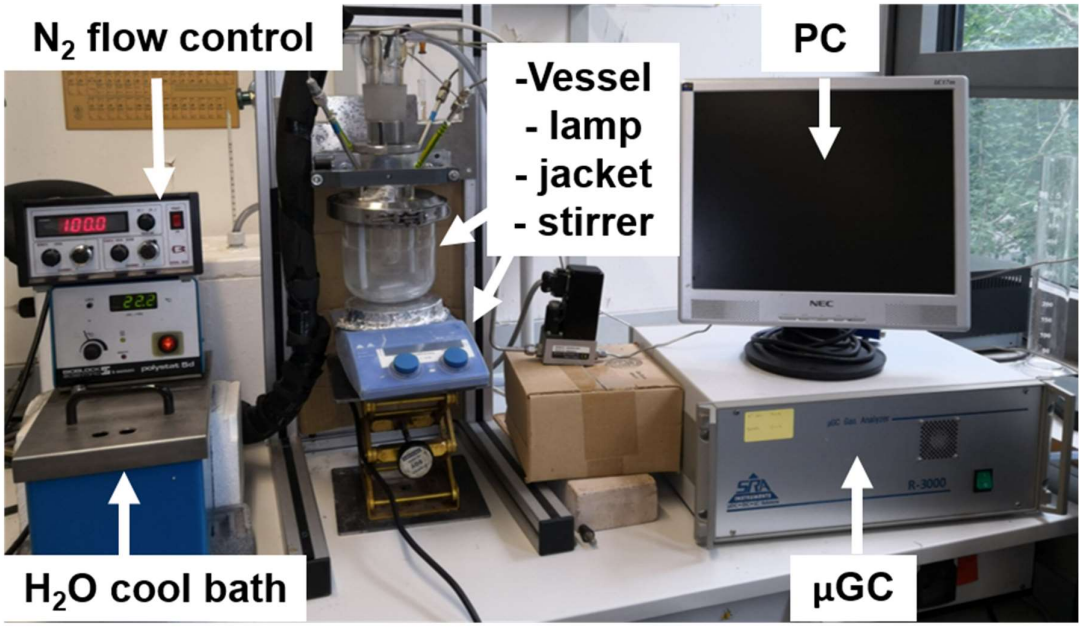

Figure 2.21. Photocatalytic set-up with all its components at ICPEES laboratory.

D.1.2. Irradiation conditions

The light emission lamp spectra and irradiated surface area measurements and calculation are introduced schematically in **Fig. 2.22** and **Fig 2.23.** The light emission lamp spectra is measured "in situ", in experimental working conditions through the reactor under both solar (23.6 mW cm^{-2}, **Fig. 2.22**) and visible (3.6 mW cm^{-2}, **Fig. 2.22**) light irradiations by using an ILT-900-R spectroradiometer (International Light

Technologies) and placed 18 cm away from the lamp position to start acquiring the irradiance spectra by using spectra light software.

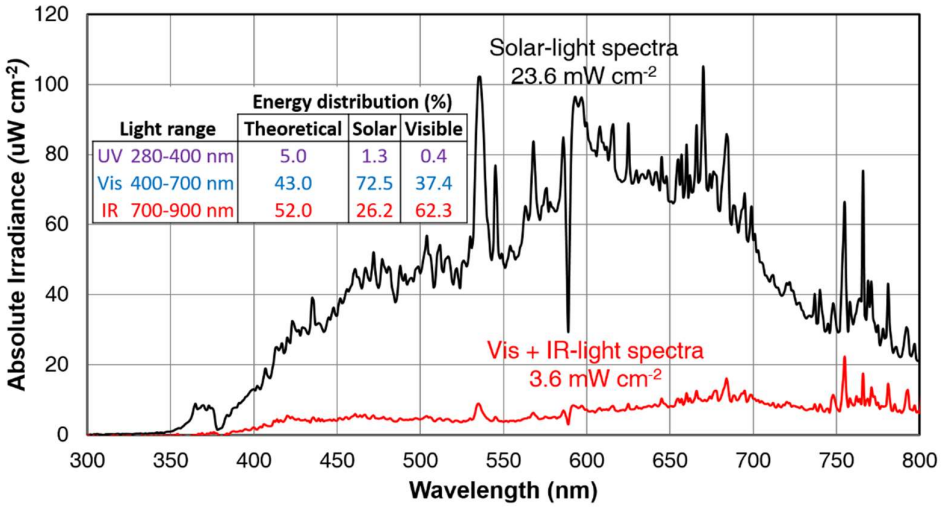

Figure 2.22. Light emission spectra of the Ceramic metal halide Hg lamp (150 W) determined in working configuration and used with the two artificial solar and visible illumination configurations. For the visible configuration, a Nigrosing solution of 0.1 g L-1 was added within the plunging quartz tube. The light emission was measured by using an ILT-900-R spectroradiometer from International Light Technologies.

The calculated irradiated surface area measurement takes into account the cylinder reactor with circular base as an important experimental parameter since it is involved on the IQY calculation. Therefore, the global irradiated surface area comprises a vertical cylinder and a circular base, the involved equations and measurements were taken to obtain an irradiated surface area of 1288 cm^{-2}.

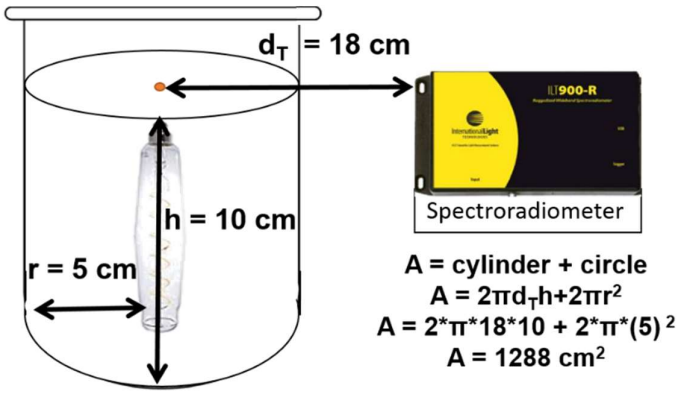

Figure 2.23. Reactor vessel geometry and illustration on how the lamp irradiance spectra was measured.

D.2. Analytical system for evolved gas quantification

D.2.1. Gas chromatography set-up

The µGC analyser is a SRA Instruments model R-3000 driven by Soprane software V.2.7.6. The µGC is equipped with three independent channels. Each channel, 1 and 2,

disposes of a Molsieve column (length: 10 m / PPU 3m) and a thermal conductivity detector (TCD). The difference relies on the gas vector. Channel 1 is flushed with Argon (Ar) allowing to follow the hydrogen production evolution, and channel 2 is flushed with He to follow the oxygen production evolution. The third channel equipped with a PlotQ column (length: 8 m / VAR PPQ / Lq Loop), is flushed with He to enable to quantify the production of CO_2 or other volatile organic compounds. Relative to the carrier gases (**Table 2.4**), Ar presents low thermal conductivity, consequently all produced peaks will be positive, making the integration thus possible for quantification. Samples were taken by using an injector with 10 µL sample loop that is filled with the gaseous sample.

Table 2.4. Gases and their associated thermal conductivity at STP

Gas	Thermal conductivity (W m^{-1} K^{-1})
Hydrogen	0.1805
Nitrogen	0.0259
Oxygen	0.0266
Argon	0.0177
Helium	0.1513

The signal recorded and processed from the TCD provides a chromatogram on Soprane software. The chromatogram (**Fig. 2.24**) is a plot of signal (µV) in function of time (s). It presents two peaks, hydrogen and nitrogen gases, with residential times of T_{RH2} = 43.5 s and T_{RN2} = 56.9 s, respectively. As for a Gaussian peak, the area under the peak (µV s) is proportional to the concentration of the corresponding gas-product. By applying a baseline followed by an automatic integration with the software, an accurate signal area can be processed, therefore online quantification every 100 s takes place and allows to follow the kinetics of evolution of the desired gas.

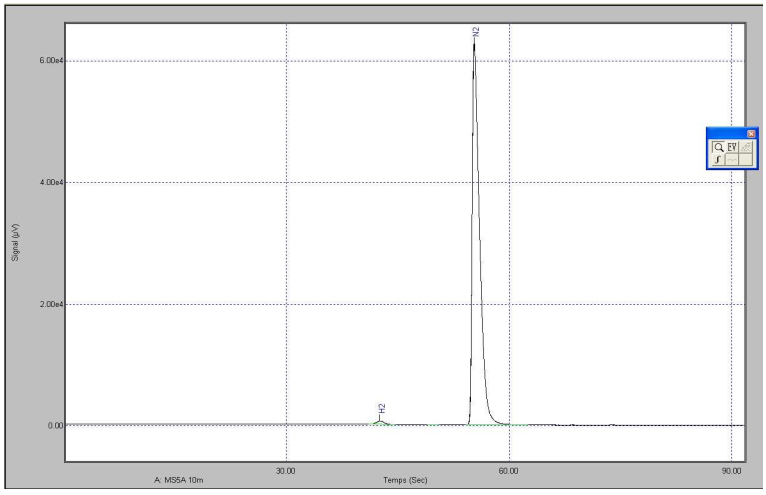

Figure 2.24. Chromatogram example showing H_2 and N_2 peaks.

D.2.2. Quantification of evolved H_2

For the quantification of H_2 production a previous calibration step is necessary. We have chosen to express the resulting concentration in part per million by volume (ppm_v) as by definition in **equation 7**.

$$1\ ppm_v = \frac{1\ volume\ of\ H_2}{10^6\ volume\ of\ air} \quad (6)$$

However, one of the indicator for photocatalytic activity should be expressed in hydrogen formation rate (r_{H2}) as follows in **equation 8**. Where r_{H2} is defined as the evolution of H_2 along time ($dn\ dt^{-1}$). Q_{N2} stands for nitrogen flux and $V_{m\ H2,\ 20\ °C}$ stands for molar volume of H_2 at 20 °C. The units are presented.

$$r_{H_2} = \frac{dn}{dt} = \frac{ppm_v * Q_{N_2}}{V_{m_{H_{2,20°C}}}}\ ;\ \left[\frac{L}{h} * \frac{mol}{L}\right] = \left[\frac{mol}{h}\right] \quad (7)$$

The accurate expression for H_2 evolution is often expressed in terms of the massic hydrogen rate production ($r_{(m)H2}$), which is the r_{H2} divided by the mass of catalyst (m_{cat}) as showed in **equation 9**. The units are also presented.

$$r_{(m)_{H2}} = \frac{r_{H_2}}{m_{cat}} = \frac{ppm_v * Q_{N_2}}{m_{cat} * V_{m_{H_{2,20°C}}}}\ ;\ \left[\frac{mol}{h * g_{cat}}\right] \quad (8)$$

It has to be underlined that the test conditions were 20 °C and atmospheric pressure (1 atm), therefore the hydrogen molar volume value used was **24.06 L mol^{-1}**.

D.2.3. General H_2 production curves

Concerning the obtained plot that follows the H_2 evolution over time, it follows the same general tendency with two phases. The transition and stationary phases as shown in **Fig 2.25**. In more details, the transition phase where the H_2 concentration starts to increase (induction period, diffusion from dissolved H_2 to gas phase, until filling the upper empty part of the reactor and then transfer of the gases from the reaction media to the analytical system). After that, the stationary phase starts and the H_2 evolution reaches a **plateau**, stable for at least 2.5 hours. At that point, where H_2 production is stable (µmol h^{-1} g_{cat}^{-1}) the mean reaction rate was determined by taking into account the average of all the points. Generally, the duration of photocatalytic test is fixed to 3 h.

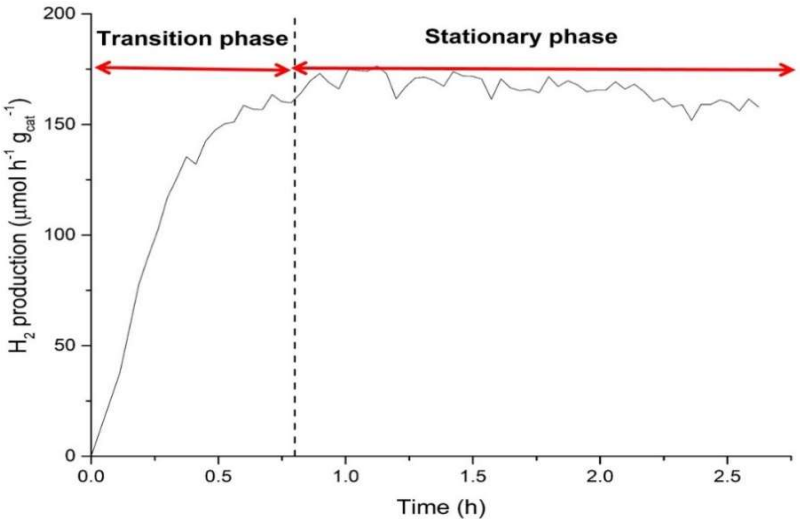

Figure 2.25. H_2 production evolution over time.

D.2.4. Standard gas and calibration measurements

With the purpose of acquiring an accurate calibration of H_2, a suitable standard H_2 bottle (Alphagaz 2, SMARTOP) with a known concentration of 300 ± 15 ppm / He was used. The calibration consists on the acquisition measurement of H_2 coming directly for the main channel with a constant volume doses to the GC every 100 s. For statistical purposes, each acquisition test takes place in three consecutive days (considering 14 measurements per day) to assess different environmental conditions and increase the population number (**Table 2.5**).

The average H_2 concentration value obtained was **289 ± 20 ppm_v** (6.70 relative error) with its associated standard deviation (STD), which is similar to the standard gas value deviation (**300 ± 15**) **mol ppm** .

Table 2.5. Obtained H_2 values in parts per million in volume with the standard gas bottle for calibration.

Acquisition test (number)					
1		2		3	
Measurements	H_2 (ppmv)	Measurements	H_2 (ppmv)	Measurements	H_2 (ppmv)
1	302.19	15	264.90	29	300.17
2	306.98	16	261.05	30	263.03
3	263.66	17	264.96	31	263.30
4	302.58	18	302.11	32	262.76
5	262.07	19	303.37	33	257.07
6	303.07	20	304.98	34	303.26
7	303.59	21	304.84	35	306.75
8	264.17	22	306.25	36	262.03
9	306.17	23	302.53	37	305.15
10	263.92	24	302.82	38	306.61
11	255.7	25	302.07	39	301.75
12	303.52	26	263.48	40	301.41
13	304.59	27	304.65	41	303.05
14	299.17	28	256.58	42	304.49
			Average	288.73 ppm	
			STD	20.37 ppm	
			Measured	289 ± 20 ppm	

E) Evaluation of photocatalytic activity toward H_2 evolution under solar and visible light irradiation

Comparison of photocatalytic performances of the as-synthesized and references Au/g-C_3N_4 materials has been tested after reaching the activity plateau in term of (massic) reaction rate (µmol h^{-1} g_{cat}^{-1}), of cumulated H_2 evolution (µmol), stability test over 2.5 h and internal quantum yield determination (by combining UV-Vis results).

E.1. H_2 production (massic) reaction rate

E.1.1. Under solar-light activation

From the H_2 production results obtained under **artificial solar-light irradiation (Fig. 2.26)** the samples can be divided into three main categories as a function of their activity magnitude: the most active one, Au/g-C_3N_4-NH_3 (leading to 324 H_2 µmol h^{-1} g_{cat}^{-1}), the ones exhibiting moderate activity, Au/g-C_3N_4-Comm-N_2-Static Air-Ar (yielding 125, 101, 99, and 75 H_2 µmol h^{-1} g_{cat}^{-1}, respectively), and the less performing materials, Au/g-C_3N_4-Air-H_2 (producing 41 and 36 H_2 µmol h^{-1} g_{cat}^{-1}, respectively). One can notice the superiority of Au/g-C_3N_4-NH_3, exhibiting activity between 3 and 9 times higher than the second more active composite (Au/g-C_3N_4-Comm) and the least active photocatalyst (Au/g-C_3N_4-H_2), respectively.

E.1.2. Under visible-light activation

In case of **artificial visible-light irradiation**, the Au/g-C_3N_4-NH_3 nanocomposite was the only one to exhibit a measurable activity with 26 µmol h^{-1} g_{cat}^{-1} H_2 produced. However, it must be pointed out that the utilization of Nigrosing as cut-off filter yield a decrease of the overall photon flux emission, besides cutting-off the UV-photons.

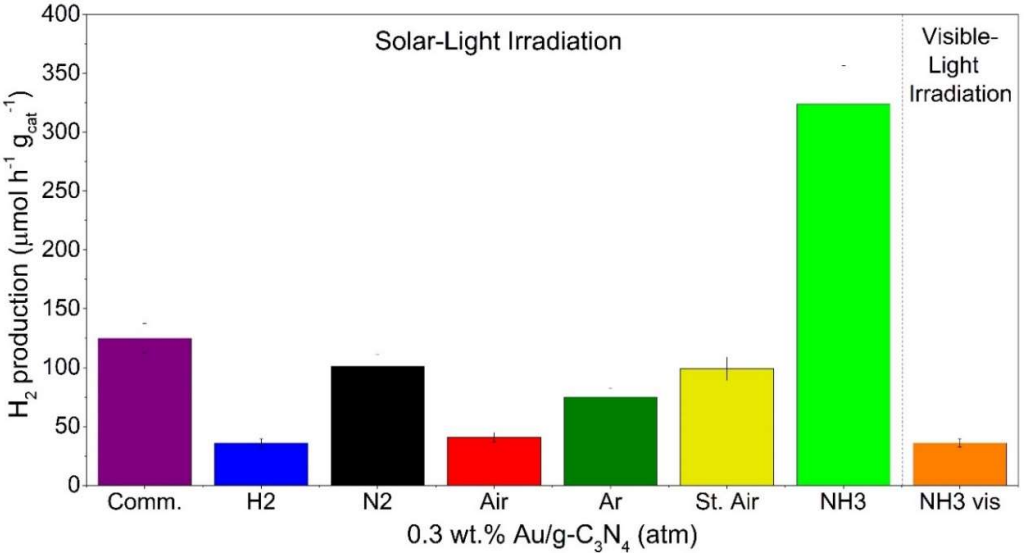

Figure 2.26. Mean hydrogen formation rate per hour and per mass of 0.3wt% Au/g-C_3N_4-atm photocatalyst using 10 mL TEOA (1 vol %) as sacrificial agent under solar and visible-light irradiation.

Blank experiments: A first series of blank tests was performed without light activation (the other experimental conditions being unchanged) and no H2 evolution was detected. The second kind of blank test consisted on carrying out the experiments under solar activation without any suspended photocatalyst (only presence of water + TEOA (1 vol. %)), exhibiting no activity and demonstrating the absence of photolysis. Last blank experiment was performed on g-C_3N_4 samples without Au NPs deposition, they did not produce any H_2 either.

E.2. Cumulated evolution of hydrogen (µmol)

From **Fig. 2.27** showing the cumulated H_2 during the complete photocatalytic test (over 2.5 h of simulated solar-light irradiation after reaching the plateau of H_2 formation), the best photocatalyst, *i.e.* Au/g-C_3N_4-NH_3.produced up to 175 µmol H_2.

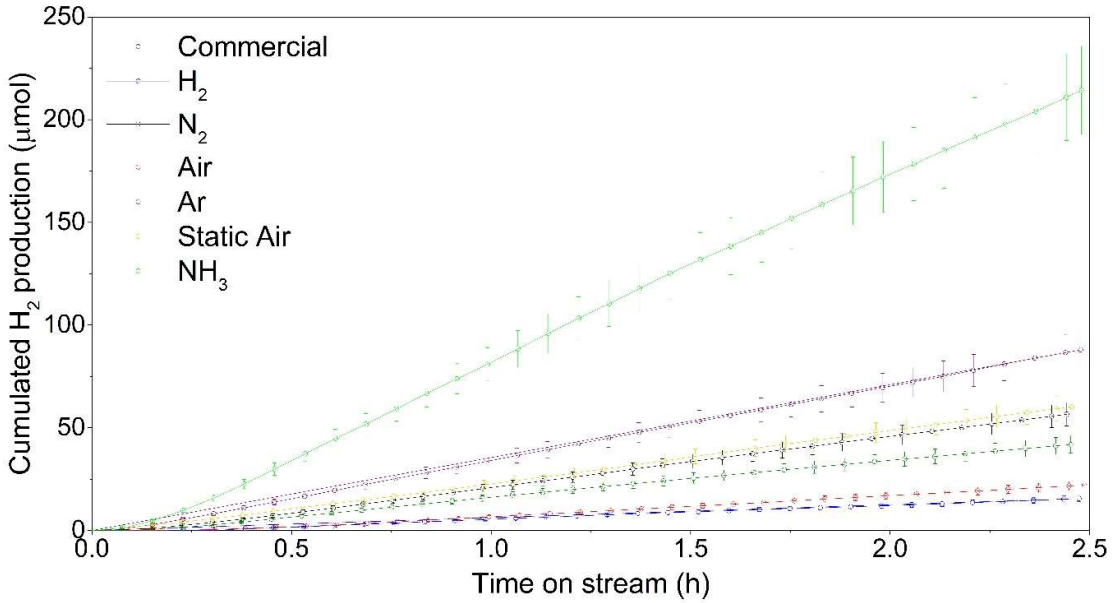

Figure 2.27. Cumulated evolution of hydrogen with 1 vol% TEOA under solar-light irradiation.

E.3. Cycling tests

Stability and recycling tests were performed under solar-light activation using the same initial photocatalyst for the most active samples only, *i.e.* Au/g-C_3N_4-NH_3. After each photocatalytic test (2.5 h after reaching the plateau of H_2 concentration), the photocatalyst was filtered, washed and dried. The photocatalyst was then re-used as previously described in the photocatalytic reactor, it should be noticed that after each washing cycle there was a 5% mass loss, taken into account for the calculation of the massic reaction rates. From the cycling tests carried out on the most performant Au/g-C_3N_4-NH_3 material **(Fig. 2.28)**, one can observe a relative decrease of H_2 production of 20 and 26% after the second and third cycle, respectively, compared to the first test. This behaviour could be explained by means of TEOA degradation and by-products formation that may poison the catalyst [41].

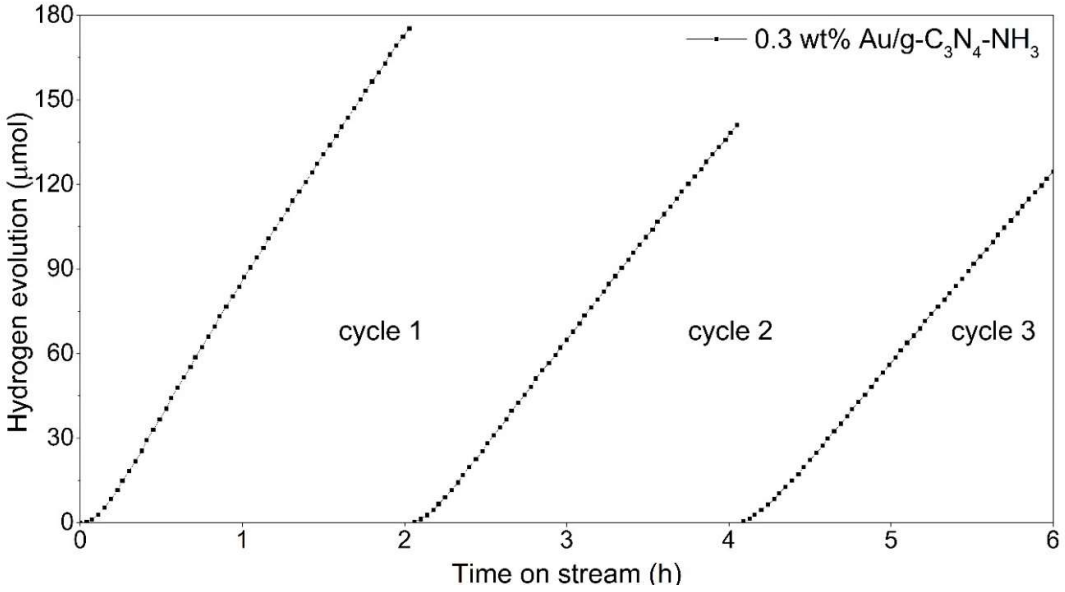

Figure 2.28. Cycling tests on 0.3wt% Au/g-C_3N_4-NH_3 with 1 vol% TEOA under solar-light irradiation.

E.4. Internal Quantum yield

Internal Quantum Yield (IQY) values were determined by measuring the absorbance of the photocatalyst suspension at the same concentration (0.25 g L^{-1}) than in the photocatalytic test. These absorbances were measured at the entrance and exit port of the integrating sphere, in order to measure mainly the absorbance of the sample while minimizing the contribution of diffusion from catalyst particles. For the determination of the photon flux, the absolute irradiance of the lamp (**Fig. 2.22**) was measured by using a spectroradiometer ILT900-R (International light technologies) exactly in the same experimental conditions than during photocatalytic measurements.

Internal quantum yield (IQY) was calculated using the following **equation 9**:

$$IQY = 2 \times \frac{r_{H_2}}{q_{p\,(Abs)}} \qquad (9)$$

Defining r_{H_2} as the hydrogen formation rate (mol h^{-1}) and $q_{p\,(Abs)}$ as the photon flux absorbed by the photocatalytic material calculated according to the following **equation 10**:

$$q_{p(Abs)} = \int_{\lambda_{min}}^{\lambda_{max}} \frac{P(\lambda) \times (1 - 10^{A(\lambda)l})}{E(\lambda)}\, d(\lambda) \qquad (10)$$

Defining P (λ), E(λ), and A(λ) respectively as the irradiation power, the photon energy and the absorbance of the nanoparticles suspension at a given wavelength (λ) of each sample used in the photochemical reactor which as an optical path l = 5 cm.

Fig. 2.29 summarizes the internal quantum yields (IQY) determined under both solar-light and visible-light irradiation. Under simulated solar-light activation, Au/g-C_3N_4-NH_3 reveals the highest IQY of 1.85, compared to 0.55 for the Au/g-C_3N_4-commercial material and to 0.20 for the least performing one (Au/g-C_3N_4-H_2). This value is higher than the ones calculated for all the other samples under solar-light irradiation (also including UVA contribution). It must also be highlighted that the Au/g-C_3N_4-NH_3 photocatalyst shows an IQY of ca. 0.60% under visible-light irradiation.

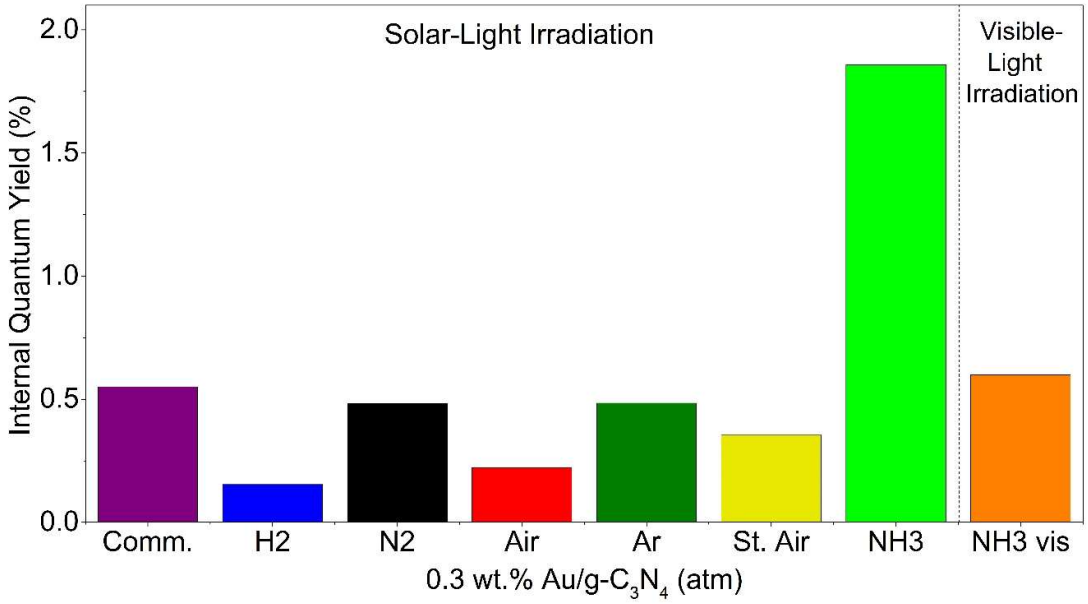

Figure 2.29. Internal quantum yield (IQY, %) of the as-prepared composites under solar and visible-light irradiation.

F) Overall discussion and correlations

To compare and discuss the photocatalytic activities of the different 0.3 wt. % Au/g-C_3N_4-atm samples, different contributions and effects have to be considered.

F.1. Role and influence of the sacrificial agent

The addition of a sacrificial agent (TEOA) as hole scavenger or for O_2 consumption should avoid O_2 evolution. Consequently, the resulted pH solution reaches 11. At this value the potentials for water oxidation and proton reduction are 0.58 V and -0.65 *vs* NHE, respectively [3,42–44]. It must also be considered that TEOA is an aliphatic tertiary amine with an oxidation potential of 0.6-0.7 *vs* NHE. As TEOA presents a low oxidation potential, it may be easily oxidized and act as efficient trap hole sites [45]. TEOA can undergo an irreversible oxidation of the amine to cause a dealkylation to form a secondary amine and an aldehyde in presence of water [41,46]. However one can mention that protons issued from TEOA degradation may also be implied in H_2 production mechanism in addition to water-splitting. These protons can have the origin from the two decomposition pathways proposed by Pellegrin *et al,* as shown in the **Fig. 2.30**. Furthermore the three alcohol functions can also be a source of H_2 production through photo-reforming processes, thus overestimating pure water-splitting

contribution. However, in our case the use of very small amounts of TEOA may strongly limit the contribution of these other pathways of H_2 production making water-splitting the predominant one.

Due to the lone electron pair of the N atom, in the TEOA molecule, it may interact with the electron pair of the N atoms of the g-C_3N_4 skeleton, possibly modifying the overall surface charge. Moreover, one cannot exclude a theoretical uplift band bending of the suspended semiconductor in contact with TEOA diluted solution [46,47].

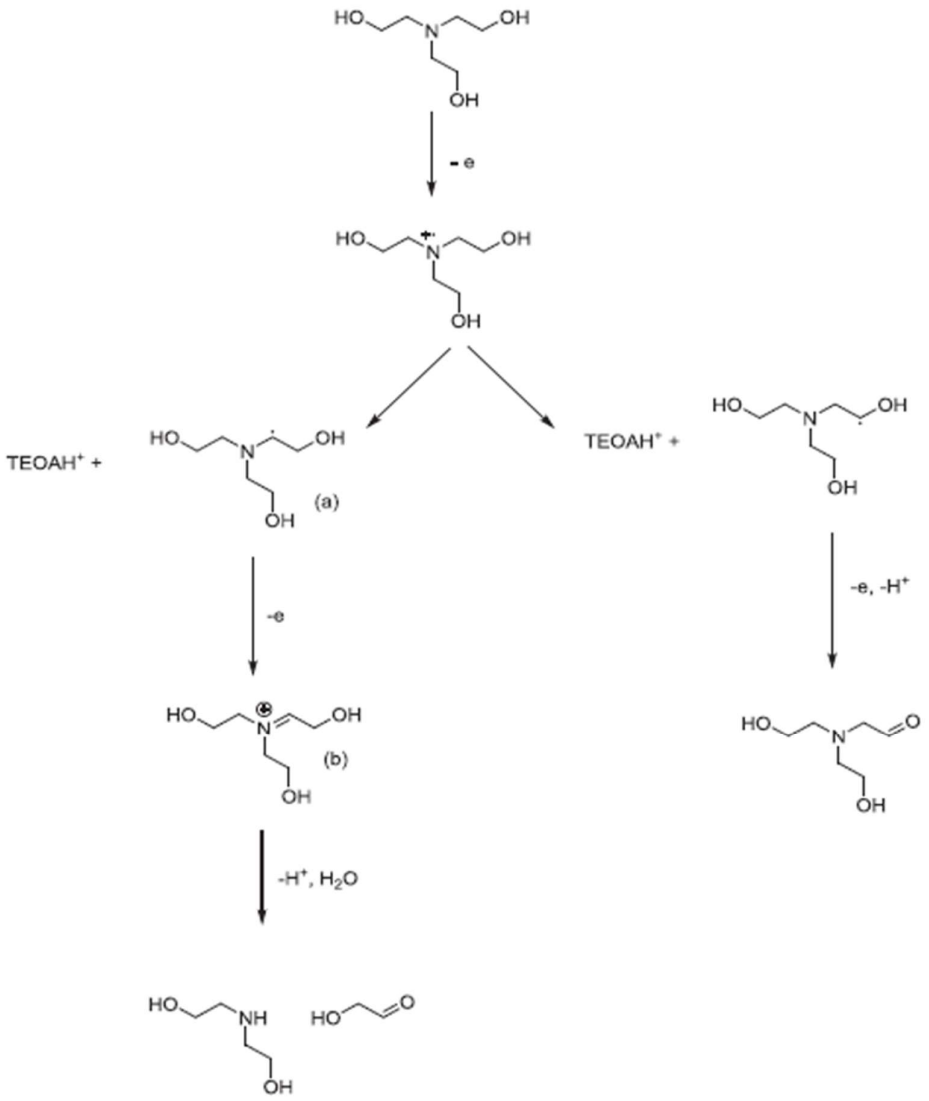

Figure 2.30. TEOA decomposition mechanism in a double pathway upon monoelectronic oxidation [41].

F.2. Role of Au NPs

Most of the studies have shown that even if the position of the conduction band of g-C_3N_4 materials is suitably disposed in regard to HER evolution, they poorly undergo direct reduction of H^+ into H_2 alone, for that reason a co-catalyst is mandatory. Au NPs can generally act as (1) electron traps leading to better charges separation, (2) co-

catalyst for the reduction of H^+ into H_2 [48] or/and (3) plasmonic promoter via surface plasmon-induced effects (SPIE). When Au NPs are deposited onto a semi-conductor (SC) support, SPIE are essentially explained according to literature by means of hot electron injection from conduction band of Au NPs to conduction band of the SC or enhancement of the intensity of the electric field around Au NPs thus leading to increased photons absorption by the SC at the vicinity of Au NPs [49,50]. However, recently some studies were also looking with the direct injection of hot electrons for Au NPs to the molecule [51]. Therefore, Au NPs size and dispersion [52,53], Au NPs loading [54] and quality of interface with the SC [55] are crucial for those properties. In turn, the coverage of the SC by Au NPs may play a key role in the photocatalyst global activity, due to the potential role of Au in all the above mentioned phenomena.

The main reaction steps that might be involved in the global photocatalytic process in presence of a sacrificial agent implying Au/g-C_3N_4-atm can be summarized within the following equations:

$$Au/g\text{-}C_3N_4 + hv \rightarrow e_{CB}^- + h_{VB}^+ \qquad \text{(Charge carriers generation)}$$

$$2e_{CB}^- + 2H^+ \rightarrow H_2 \qquad \text{(HER on g-}C_3N_4\text{)}$$

$$e_{CB}^- \rightarrow e_{Au\ NP}^- \quad \text{(electron shuttling and trapping)}$$

$$2e_{Au\ NP}^- + 2H^+ \rightarrow H_2 \qquad \text{(co-catalysis)}$$

$$e_{Au\ NP}^- \rightarrow e_{CB}^- \text{ (SPIE hot electron injection in g-}C_3N_4\text{ CB)}$$

$$TEOA + h_{VB}^+ \rightarrow TEOA^+ \qquad \text{(TEOA photo-oxidation/ Hole scavenger) [46]}$$

F.3. Correlation of structure / optical properties / photocatalytic activity

From all materials, 0.3wt% Au/g-C_3N_4-NH_3 photocatalyst allowed enhanced photocatalytic activity toward H_2 production under both solar (324 µmol h^{-1} g_{cat}^{-1}, IQY: 1.85) and visible-light (26 µmol h^{-1} g_{cat}^{-1}, IQY: 0.60) irradiation. This enhanced photocatalytic performance is between 3 and 9 times higher in comparison to the two references and to the synthesis performed under the other gas atmospheres, using unusual low vol% of sacrificial agent (1 vol.%). These enhanced performances might be correlated with its specific properties.

F.3.1. On g-C_3N_4 materials

Structural analyses performed by XRD showed that **g-C_3N_4-NH_3** sample exhibited the largest crystallite size, and the thicker stack of layers. On the contrary, g-C_3N_4-H_2 exhibited the lowest crystallite size, and the narrower stacks of layers. The set of XRD measurements revealed the strong influence of the synthesis atmosphere on the g-C_3N_4 formation. It appears that inert (Ar, N_2) and also the reductive H_2 gas resulted in g-C_3N_4 sheets with fewer layers than under oxidative atmosphere. On the opposite, even if NH_3 is a reductive gas, it resulted in thicker g-C_3N_4 particles, suggesting that NH_3 is involved in a reaction with the precursors or the reaction intermediates. From the

overall comparisons from ED, XRD and theoretical values obtained by simulations, one can notice that the d_{TSTCN} is even smaller than theoretical reference value, indicating the presence of tilt angularity. Nevertheless, for the d_{STCN} the behaviour is the opposite, the XRD values are higher than the theoretical one, presumably for the presence of tilt angularity too. Furthermore, the size values determination of the TSTCN and STCN phases revealed the clear presence of tilt angularity in the assembly, which might be explained with layer distortion. However in the case of g-C_3N_4-NH_3 sample, the size of tri-s-triazine phase exhibited the smallest deviation compared to the theoretical value of the perfect g-C_3N_4 structure. For the g-C_3N_4-H_2 material, it has been described in literature [40] that the insertion of H_2 molecules in-between the layers affects the Van der Waals forces and promotes an in-plane distortion.

From the surface characterization, one can underline that the BET area of both g-C_3N_4-NH_3 and g-C_3N_4-commercial materials showed the same highest value (32 m^2 g^{-1}). However, both samples presented a difference in activity of factor three, suggesting that the surface area is not the only parameter influencing the activity. g-C_3N_4-NH_3 exhibited the largest pore volume, mainly constituted of mesoporous contribution, contrarily to the other g-C_3N_4-atm samples. It has already been suggested elsewhere [56] that during NH_3 post-synthesis annealing, NH_2* and NH* species were formed after the degradation of NH_3 at high temperatures, those active radicals might be responsible for the increase of the porosity in terms of mesoporosity.

From UV-Vis results, one can notice that the samples presenting the more pronounced red shift were not precisely the more active. On the contrary, the g-C_3N_4-NH_3 sample exhibiting the lowest absorption in the visible range was the one with the highest activity under solar-light irradiation (also under visible-light activation). It may thus be argued that another parameter, *i.e.* the additional $\pi \rightarrow \pi^*$ electronic transition, only existing when lone electron pairs of N atoms are in a close vicinity to promote it, and resulting from layer deformation, may also inhibit the photocatalytic activity.

F.3.2. On Au/g-C_3N_4 composites

The surface amino functions might certainly drive the interaction of g-C_3N_4 support with the $HAuCl_4$ precursor and consequently the Au NPs size (the lowest one, *ca.* 3.2 nm) and their well distributed dispersion. Some studies already mentioned that this Au NPs may be of the optimal size to present quantum confinement effects [57], exhibit optimal charge transfers to and from the support [50] and good spatial corner position for Au^0 atoms to interact efficiently with the external environment species [58]. It may thus be argued that the presence of Au in the binary nanocomposite is essentially co-catalytic, presenting an enhancement of diffusion/migration of hydrogen atoms, facilitating the half reaction reduction from H^+ to H_2 [6]. At the same manner, Au NPs electron trap properties have been reported, enhancing the separation of the photogenerated charge carriers and simultaneously enable the co-catalytic functionality One may be mention that this study showed evidence that monodisperse and well distributed Au NPs, directly contribute to the photocatalytic activity, since a higher density of available nanoparticles onto the g-C_3N_4 surface increases the number of active sites for co-

catalytic H^+ reduction. Therefore, one can conclude that there is a direct impact of the nature of the support on the growth, geometry shape and size of Au NPs.

Optical measurements, evidenced the two expected absorptions for the two components, *i.e.* g-C_3N_4 ($\lambda \approx 460$ nm) and Au plasmon ($\lambda \approx 550$ nm). From TEM, it can be noticed that all samples followed a more or less monodispersion distribution of Au NPs, with different surface distribution. However, in the case of the most active sample, it was found that the distribution of Au NPs presented the narrower monomodal distribution with the best surface coverage and the lowest average Au NPs size. This result, suggest that well distributed and small NPs (≤5 nm) might determine the global co-catalytic effect, since they determine the availability and amount of Au NPs. Besides, one cannot exclude a possible Z-scheme mechanism when using the Au NPs as electron shuttles [47].

From the different complementary characterizations and analyses carried out, one could not confirm the presence of SPIE on the synthesized and studied Au/g-C_3N_4 composites. **Fig. 2.31** summarizes a detailed scheme of the possible charge transfer pathways.

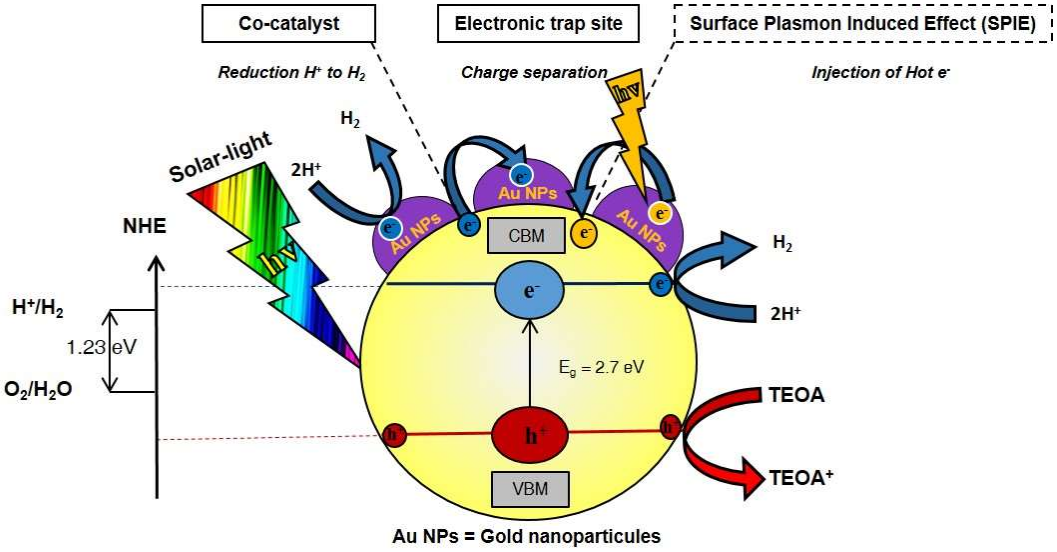

Figure 2.31. Scheme of the proposed H_2 production mechanism for Au/g-C_3N_4-NH_3 composite, pointing out the two half reactions of water splitting and different electron transfers pathways [59].

G) Summary

The present chapter investigation demonstrated and confirmed that the g-C_3N_4 synthesis atmosphere plays a key role on the polycondensation synthesis and final structure of g-C_3N_4. A mathematical relationship along with a fine physico-chemical interpretation allowed to correlate the g-C_3N_4 activity in function of the ratio between tri-s-triazine and s-triazine based g-C_3N_4 phases. For the case of the binary Au/g-C_3N_4 composites, several findings were discussed. It was underlined that the homogeneous coverage with small Au NPs yielded high quality metal/semiconductor intimate contact. Also, the compromise experimental condition on using a very low quantities of both Au NPs loading (0.3 wt. %) and sacrificial agent (1 vol. % TEOA) allowed to conduct the

structure-activity analysis to discover the effect of different contributions that drive unique behaviour on polymeric g-C_3N_4-*atm* materials.

The engineered design of Au/g-C_3N_4 binary nanocomposites allowed to highlight that the gas atmosphere impacted the photocatalytic activity. The 0.3 wt% Au/g-C_3N_4-NH_3 composite exhibited enhanced photocatalytic activity toward H_2 production under both solar and also visible-light irradiations using low amounts of sacrificial agent and co-catalyst. The resulting enhanced H_2 production was related to the structural organization, optical, electronic, surface and porous properties of the support (g-C_3N_4). Specific characterizations revealed very relevant evidences such as the thicker stack of graphitic domain, the largest crystallite size, and the largest mesoporous pore volume. Detailed determination and relative contribution of TSTCN and STCN phases led to underline that this Au/g-C_3N_4-NH_3 catalyst also exhibited amongst the lower s-triazine content, lowering tilt angularity and thus layer deformation in respect to the theoretical values for perfect g-C_3N_4.

The tri-s-triazine/s-triazine based g-C_3N_4 samples ratios was for the first time determined and correlated with synthesis atmospheres and physico-chemical properties.

H) References

[1] S. Ghosh, N.A. Kouamé, L. Ramos, S. Remita, A. Dazzi, A. Deniset-Besseau, P. Beaunier, F. Goubard, P.-H. Aubert, H. Remita, Conducting polymer nanostructures for photocatalysis under visible light, Nat. Mater. 14 (2015) 505–511. doi:10.1038/nmat4220.

[2] X. Wang, K. Maeda, A. Thomas, K. Takanabe, G. Xin, J.M. Carlsson, K. Domen, M. Antonietti, A metal-free polymeric photocatalyst for hydrogen production from water under visible light, Nat. Mater. 8 (2009) 76–80. doi:10.1038/nmat2317.

[3] W.-J. Ong, L.-L. Tan, Y.H. Ng, S.-T. Yong, S.-P. Chai, Graphitic Carbon Nitride (g-C3N4)-Based Photocatalysts for Artificial Photosynthesis and Environmental Remediation: Are We a Step Closer To Achieving Sustainability?, Chem. Rev. (2016). doi:10.1021/acs.chemrev.6b00075.

[4] J. Wen, J. Xie, X. Chen, X. Li, A review on g-C3N4-based photocatalysts, Appl. Surf. Sci. (2016). doi:10.1016/j.apsusc.2016.07.030.

[5] X. Wang, K. Maeda, X. Chen, K. Takanabe, K. Domen, Y. Hou, X. Fu, M. Antonietti, Polymer Semiconductors for Artificial Photosynthesis: Hydrogen Evolution by Mesoporous Graphitic Carbon Nitride with Visible Light, J. Am. Chem. Soc. 131 (2009) 1680–1681. doi:10.1021/ja809307s.

[6] C. Marchal, T. Cottineau, M.G. Méndez-Medrano, C. Colbeau-Justin, V. Caps, V. Keller, Au/TiO2-gC3N4 Nanocomposites for Enhanced Photocatalytic H2 Production from Water under Visible Light Irradiation with Very Low Quantities of Sacrificial Agents, Adv. Energy Mater. (2018) 1702142. doi:10.1002/aenm.201702142.

[7] Nicanite Graphitic Carbon Nitride - Nanodiamonds - additives for thermal management and wear resistant nanocomposites, coatings and plating, Carbodeon. (n.d.). http://www.carbodeon.com/index.php/en/carbodeon-news/nicanite-graphitic-carbon-nitride (accessed May 14, 2018).

[8] A. Cousson, B. Nicolaï, F. Fillaux, Melamine (1,3,5-triazine-2,4,6-triamine): a neutron diffraction study at 14 K, Acta Crystallogr. Sect. E Struct. Reports Online. 61 (2005) o222–o224. doi:10.1107/S160053680403332X.

[9] Y. Zhang, T. Mori, L. Niu, J. Ye, Non-covalent doping of graphitic carbon nitride polymer with graphene: controlled electronic structure and enhanced optoelectronic conversion, Energy Environ. Sci. 4 (2011) 4517. doi:10.1039/c1ee01400e.

[10] B. Jürgens, E. Irran, J. Senker, P. Kroll, H. Müller, W. Schnick, Melem (2,5,8-Triamino-tri- s -triazine), an Important Intermediate during Condensation of Melamine Rings to Graphitic Carbon Nitride: Synthesis, Structure Determination by X-ray Powder Diffractometry, Solid-State NMR, and Theoretical Studies, J. Am. Chem. Soc. 125 (2003) 10288–10300. doi:10.1021/ja0357689.

[11] Q. Liang, Z. Li, Z.-H. Huang, F. Kang, Q.-H. Yang, Holey Graphitic Carbon Nitride Nanosheets with Carbon Vacancies for Highly Improved Photocatalytic Hydrogen Production, Adv. Funct. Mater. 25 (2015) 6885–6892. doi:10.1002/adfm.201503221.

[12] I. Papailias, T. Giannakopoulou, N. Todorova, D. Demotikali, T. Vaimakis, C. Trapalis, Effect of processing temperature on structure and photocatalytic properties of g-C3N4, Appl. Surf. Sci. 358 (2015) 278–286. doi:10.1016/j.apsusc.2015.08.097.

[13] A. Thomas, A. Fischer, F. Goettmann, M. Antonietti, J.-O. Müller, R. Schlögl, J.M. Carlsson, Graphitic carbon nitride materials: variation of structure and morphology and their use as metal-free catalysts, J. Mater. Chem. 18 (2008) 4893. doi:10.1039/b800274f.

[14] P. V. Zinin, L.-C. Ming, S.K. Sharma, V.N. Khabashesku, X. Liu, S. Hong, S. Endo, T. Acosta, Ultraviolet and near-infrared Raman spectroscopy of graphitic C3N4 phase, Chem. Phys. Lett. 472 (2009) 69–73. doi:10.1016/j.cplett.2009.02.068.

[15] G.-M. Rignanese, J.-C. Charlier, X. Gonze, First-principles study of vibrational and dielectric properties of C3N4 polymorphs, Phys. Rev. B. 66 (2002) 205416. doi:10.1103/PhysRevB.66.205416.

[16] J. Jiang, L. Ou-yang, L. Zhu, A. Zheng, J. Zou, X. Yi, H. Tang, Dependence of electronic structure of g-C3N4 on the layer number of its nanosheets: A study by Raman spectroscopy coupled with first-principles calculations, Carbon N. Y. 80 (2014) 213–221. doi:10.1016/j.carbon.2014.08.059.

[17] A. Sumayya, C.Y. Panicker, H.T. Varghese, B. Harikumar, Vibrational spectroscopic studies and AB inition calculations of l-glutamic acid 5-amide, RJC Rasayan J. Chem. 1 (2008) 548–555. http://www.rasayanjournal.co.in/vol-1/issue-3/18.pdf (accessed May 14, 2018).

[18] M.J. Bojdys, J.-O. Müller, M. Antonietti, A. Thomas, Ionothermal synthesis of crystalline, condensed, graphitic carbon nitride., Chemistry. 14 (2008) 8177–82. doi:10.1002/chem.200800190.

[19] J. Gao, Y. Zhou, Z. Li, S. Yan, N. Wang, Z. Zou, High-yield synthesis of millimetre-long, semiconducting carbon nitride nanotubes with intense photoluminescence emission and reproducible photoconductivity, Nanoscale. 4 (2012) 3687. doi:10.1039/c2nr30777d.

[20] T. Tyborski, C. Merschjann, S. Orthmann, F. Yang, M.-C. Lux-Steiner, T. Schedel-Niedrig, Crystal structure of polymeric carbon nitride and the determination of its process-temperature-induced modifications, J. Phys. Condens. Matter. 25 (2013) 395402. doi:10.1088/0953-8984/25/39/395402.

[21] F. Fina, S.K. Callear, G.M. Carins, J.T.S. Irvine, Structural Investigation of Graphitic Carbon Nitride via XRD and Neutron Diffraction, Chem. Mater. 27 (2015) 2612–2618. doi:10.1021/acs.chemmater.5b00411.

[22] J. Xu, L. Zhang, R. Shi, Y. Zhu, Chemical exfoliation of graphitic carbon nitride for efficient heterogeneous photocatalysis, J. Mater. Chem. A. 1 (2013) 14766. doi:10.1039/c3ta13188b.

[23] Z. Tong, D. Yang, T. Xiao, Y. Tian, Z. Jiang, Biomimetic fabrication of g-C3N4/TiO2 nanosheets with enhanced photocatalytic activity toward organic pollutant degradation, Chem. Eng. J. 260 (2015) 117–125. doi:10.1016/J.CEJ.2014.08.072.

[24] J. Xu, Y. Li, S. Peng, G. Lu, S. Li, Eosin Y-sensitized graphitic carbon nitride fabricated by heating urea for visible light photocatalytic hydrogen evolution: the effect of the pyrolysis temperature of urea, Phys. Chem. Chem. Phys. 15 (2013) 7657. doi:10.1039/c3cp44687e.

[25] B. Saner, F. Okyay, Y. Yürüm, Utilization of multiple graphene layers in fuel cells. 1. An improved technique for the exfoliation of graphene-based nanosheets from graphite, Fuel. 89 (2010) 1903–1910. doi:10.1016/J.FUEL.2010.03.036.

[26] Y. Chen, B. Wang, S. Lin, Y. Zhang, X. Wang, Activation of n → π* Transitions in Two-Dimensional Conjugated Polymers for Visible Light Photocatalysis, J. Phys. Chem. C. 118 (2014) 29981–29989. doi:10.1021/jp510187c.

[27] E. Kroke, M. Schwarz, E. Horath-Bordon, P. Kroll, B. Noll, A.D. Norman, Tri-s-triazine derivatives. Part I. From trichloro-tri-s-triazine to graphitic C3N4 structuresPart II: Alkalicyamelurates M3[C6N7O3], M = Li, Na, K, Rb, Cs, manuscript in preparation., New J. Chem. 26 (2002) 508–512. doi:10.1039/b111062b.

[28] Y. Cui, J. Zhang, G. Zhang, J. Huang, P. Liu, M. Antonietti, X. Wang, Synthesis of bulk and nanoporous carbon nitride polymers from ammonium thiocyanate for photocatalytic hydrogen evolution, J. Mater. Chem. 21 (2011) 13032. doi:10.1039/c1jm11961c.

[29] J.S. Kim, J.W. Oh, S.I. Woo, Improvement of the photocatalytic hydrogen production rate of g-C3N4 following the elimination of defects on the surface, Catal. Today. 293–294 (2017) 8–14. doi:10.1016/J.CATTOD.2016.11.018.

[30] A. Vinu, Two-Dimensional Hexagonally-Ordered Mesoporous Carbon Nitrides with Tunable Pore Diameter, Surface Area and Nitrogen Content, Adv. Funct. Mater. 18 (2008) 816–827. doi:10.1002/adfm.200700783.

[31] S. Brunauer, P.H. Emmett, E. Teller, Adsorption of Gases in Multimolecular Layers, J. Am. Chem. Soc. 60 (1938) 309–319. doi:10.1021/ja01269a023.

[32] B. Zhu, P. Xia, W. Ho, J. Yu, Isoelectric point and adsorption activity of porous g-C3N4, Appl. Surf. Sci. 344 (2015) 188–195. doi:10.1016/J.APSUSC.2015.03.086.

[33] B. Singh, S. Gaydardzhiev, P. Ay, Stabilization of Aqueous Silicon Nitride Suspension with Dolapix A88, J. Dispers. Sci. Technol. 27 (2006) 91–97. doi:10.1081/DIS-200066756.

[34] F. Vigneron, A. Piquet, W. Baaziz, P. Ronot, A. Boos, I. Janowska, C. Pham-Huu, C. Petit, V. Caps, Hydrophobic gold catalysts: From synthesis on passivated silica to synthesis on few-layer graphene, Catal. Today. 235 (2014) 90–97. doi:10.1016/J.CATTOD.2014.04.016.

[35] Y. Li, J. Wang, Y. Yang, Y. Zhang, D. He, Q. An, G. Cao, Seed-induced growing various TiO2 nanostructures on g-C3N4 nanosheets with much enhanced photocatalytic activity under visible light, J. Hazard. Mater. 292 (2015) 79–89. doi:10.1016/J.JHAZMAT.2015.03.006.

[36] A.B. Jorge, D.J. Martin, M.T.S. Dhanoa, A.S. Rahman, N. Makwana, J. Tang, A. Sella, F. Corà, S. Firth, J.A. Darr, P.F. McMillan, H2 and O2 Evolution from Water Half-Splitting Reactions by Graphitic Carbon Nitride Materials, J. Phys. Chem. C. 117 (2013) 7178–7185. doi:10.1021/jp4009338.

[37] Y. Wang, X. Wang, M. Antonietti, Polymeric graphitic carbon nitride as a heterogeneous organocatalyst: from photochemistry to multipurpose catalysis to sustainable chemistry., Angew. Chem. Int. Ed. Engl. 51 (2012) 68–89. doi:10.1002/anie.201101182.

[38] Valery N. Khabashesku, A. John L. Zimmerman, J.L. Margrave, Powder Synthesis and Characterization of Amorphous Carbon Nitride, Chem. Mater. 12 (2000) 3264–3270. doi:10.1021/CM000328R.

[39] A. Du, S. Sanvito, Z. Li, D. Wang, Y. Jiao, T. Liao, Q. Sun, Y.H. Ng, Z. Zhu, R. Amal, S.C. Smith, Hybrid Graphene and Graphitic Carbon Nitride Nanocomposite: Gap Opening, Electron–Hole Puddle, Interfacial Charge Transfer, and Enhanced Visible Light Response, J. Am. Chem. Soc. 134 (2012) 4393–4397. doi:10.1021/ja211637p.

[40] W. Ho, Z. Zhang, M. Xu, X. Zhang, X. Wang, Y. Huang, Enhanced visible-light-driven photocatalytic removal of NO: Effect on layer distortion on g-C3N4 by H2 heating, Appl. Catal. B Environ. 179 (2015) 106–112. doi:10.1016/j.apcatb.2015.05.010.

[41] Y. Pellegrin, F. Odobel, Sacrificial electron donor reagents for solar fuel production, Comptes Rendus Chim. (2016). doi:10.1016/j.crci.2015.11.026.

[42] Y. Cui, Z. Ding, P. Liu, M. Antonietti, X. Fu, X. Wang, Metal-free activation of H2O2 by g-C3N4 under visible light irradiation for the degradation of organic pollutants, Phys. Chem. Chem. Phys. 14 (2012) 1455–1462. doi:10.1039/C1CP22820J.

[43] M. Pourbaix, Atlas of electrochemical equilibria in aqueous solutions, [1st English ed.]., Pergamon Press, Oxford ;New York, 1966. http://www.worldcat.org/title/atlas-of-electrochemical-equilibria-in-aqueous-solutions/oclc/2168509 (accessed July 12, 2018).

[44] J. Ran, T.Y. Ma, G. Gao, X.-W. Du, S.Z. Qiao, Porous P-doped graphitic carbon nitride nanosheets for synergistically enhanced visible-light photocatalytic H 2 production, Energy Environ. Sci. (2015). doi:10.1039/C5EE02650D.

[45] X.C. and, S.S. Mao†, Titanium Dioxide Nanomaterials: Synthesis, Properties, Modifications, and Applications, (2007). doi:10.1021/CR0500535.

[46] M. Wang, S. Shen, L. Li, Z. Tang, J. Yang, Effects of sacrificial reagents on photocatalytic hydrogen evolution over different photocatalysts, J. Mater. Sci. 52 (2017) 5155–5164. doi:10.1007/s10853-017-0752-z.

[47] Z.-F. Huang, J. Song, X. Wang, L. Pan, K. Li, X. Zhang, L. Wang, J.-J. Zou, Switching charge transfer of C3N4/W18O49 from type-II to Z-scheme by interfacial band bending for highly efficient photocatalytic hydrogen evolution., Nano Energy. (n.d.).

[48] C. Marchal, A. Piquet, M. Behr, T. Cottineau, V. Papaefthimiou, V. Keller, V. Caps, Activation of solid grinding-derived Au/TiO2 photocatalysts for solar H2 production from water-methanol mixtures with low alcohol content, J. Catal. 352 (2017) 22–34. doi:10.1016/J.JCAT.2017.04.035.

[49] P. Zhang, T. Wang, J. Gong, Mechanistic Understanding of the Plasmonic Enhancement for Solar Water Splitting, Adv. Mater. 27 (2015) 5328–5342. doi:10.1002/adma.201500888.

[50] S.C. Warren, E. Thimsen, Plasmonic solar water splitting, Energy Environ. Sci. 5 (2012) 5133–5146. doi:10.1039/C1EE02875H.

[51] S. Mukherjee, L. Zhou, A.M. Goodman, N. Large, C. Ayala-Orozco, Y. Zhang, P. Nordlander, N.J. Halas, Hot-Electron-Induced Dissociation of H 2 on Gold Nanoparticles Supported on SiO 2, J. Am. Chem. Soc. 136 (2014) 64–67. doi:10.1021/ja411017b.

[52] P. Suchomel, L. Kvitek, R. Prucek, A. Panacek, A. Halder, S. Vajda, R. Zboril, Simple size-controlled synthesis of Au nanoparticles and their size-dependent catalytic activity, Sci.

Rep. 8 (2018) 4589. doi:10.1038/s41598-018-22976-5.

[53] S. Wang, B. Zeng, C. Li, Effects of Au nanoparticle size and metal-support interaction on plasmon-induced photocatalytic water oxidation, Chinese J. Catal. 39 (2018) 1219–1227. doi:10.1016/S1872-2067(18)63094-3.

[54] J. Nie, J. Schneider, F. Sieland, S. Xia, D.W. Bahnemann, The role of Au loading for visible-light photocatalytic activity of Au-TiO2 (anatase), J. Photochem. Photobiol. A Chem. 366 (2018) 111–117. doi:10.1016/j.jphotochem.2018.03.016.

[55] Y. Shiraishi, N. Yasumoto, J. Imai, H. Sakamoto, S. Tanaka, S. Ichikawa, B. Ohtani, T. Hirai, Quantum tunneling injection of hot electrons in Au/TiO2 plasmonic photocatalysts, Nanoscale. 9 (2017) 8349–8361. doi:10.1039/C7NR02310C.

[56] L.L. and Z.Z. Pengju Yang, Jianghong Zhao, Wei Qiao, Ammonia-induced robust photocatalytic hydrogen evolution of graphitic carbon nitride, Nanoscale. 7 (2015) 18887–18890. doi:10.1039/C5NR05570A.

[57] B. Hvolbæk, T.V.W. Janssens, B.S. Clausen, H. Falsig, C.H. Christensen, J.K. Nørskov, Catalytic activity of Au nanoparticles, Nano Today. 2 (2007) 14–18. doi:10.1016/S1748-0132(07)70113-5.

[58] W.D. Williams, M. Shekhar, W.-S. Lee, V. Kispersky, W.N. Delgass, F.H. Ribeiro, S.M. Kim, E.A. Stach, J.T. Miller, L.F. Allard, Metallic Corner Atoms in Gold Clusters Supported on Rutile Are the Dominant Active Site during Water−Gas Shift Catalysis, J. Am. Chem. Soc. 132 (2010) 14018–14020. doi:10.1021/ja1064262.

[59] P. Jiménez, C. Marchal, T. Cottineau, V. Caps, V. Keller, Influence of gas atmosphere during synthesis of g-C3N4 for enhanced photocatalytic H2 production from water on Aug-C3N4 composites, J. Mater. Chem. A. (2019). doi:10.1039/C9TA01734H.

Chapter 3

Synthesis, characterization, and photocatalytic evaluation of TiO_2(P25)-gC_3N_4 and Au/TiO_2(P25)-gC_3N_4 composites

A) Introduction

Titanium dioxide (TiO_2) semiconductor exhibits one of the highest known photocatalytic activity under UV-A irradiation toward many reactions with many interesting characteristics, namely, strong oxidizing abilities, photo-stability, long durability, biocompatibility, reasonable cost, light and strong mechanical resistance [1]. Nevertheless, its large band gap (E_g > 3.1-3.2 eV), hampers the utilization of visible light, thus limiting solar light harvesting [1]. In order to overcome TiO_2 limitations, many strategies were implemented to improve its performance, likely visible light response and quantum yields increase. In the last decades, several modification strategies have been investigated, *e.g.,* coupling with another lower band gap SC, deposition of metallic NPs, use of different morphologies, doping with different atoms, and sensitizing the SC with different dyes. A great deal of attention has been attributed to coupling approaches. A large number of inorganic semiconductors with lower band gaps than TiO_2 such as (oxy) nitrides [2] and sulfides [3], transition metal or post-transition metal oxides [4] have been coupled with TiO_2 presenting more or less performance improvements. In 2008, graphitic carbon nitride (g-C_3N_4), a medium band gap (E_g > 2.7 eV) 2D polymeric and metal free SC, revealed visible absorption capacity, which makes it an attractive material besides its easy to synthesize and modify [5]. Thanks to its band edge positions (-1.3 VB and 1.4 eV CB vs. NHE) it could be satisfactory coupled with TiO_2 expecting a staggered heterojunction type II [6,7]. This heterojunction is also known as the Z-scheme, and it has been described as the best heterojunction type, due to the upward or downward band bending on the CB and VB respectively, leading to the migration of charge carriers in the opposite direction with some facility extend. As such, water splitting oxidation and reduction reactions may take place preferentially in the two different SC's, namely the OER in the SC with the lower valence band edge potential, and the HER in the SC with the higher CB edge potential.

Amongst the mentioned strategies, the deposition of metallic NPs is considered to be a great approach to increase electron trapping and surface catalytic effects with a interface junction formation. Moreover, Au NPs deposited onto SCs may also induce the beneficial Surface Plasmon Induced Effect (SPIE), along with their electron trap capacity and co-catalytic functionalities [8]. Thus, hybrid photocatalyst, Au/TiO_2-gC_3N_4 might promote positive synergic relationships with the contribution of each component to enhance its overall activity either with the heterojunction SC1/SC2 or the metallic NP/SC junction approaches.

Here, the design of Au/TiO_2(P25)-gC_3N_4 ternary nanocomposites are presented to evaluate two effects: the **variation of the proportions between** TiO_2(P25) and g-C_3N_4 SCs and the impact of the g-C_3N_4 polycondensation **synthesis atmosphere** in presence of TiO_2 that determines the binary heterojunction composite properties. Thus, the target of synthesizing step by step TiO_2(P25)-gC_3N_4 and Au/TiO_2(P25)-gC_3N_4 binary and ternary systems, respectively, is to obtain certain advantages: **(1)** TiO_2-gC_3N_4 high quality heterojunction contact leading to increased photogenerated charges separation and to TiO_2 photosensitization thanks to g-C_3N_4 visible light absorption capacity and **(2)**

Fine elaboration of ternary Au/TiO_2-gC_3N_4 composites aiming at forming high quality Au NPs/support contact, resulting to increased photogenerated charges separation, to introduction of co-catalytic properties and eventually induction of additional SPIE effects. Therefore, the overall scientific strategy aims at enhancing the photocatalytic activity performance in terms of H_2 production rate and quantum yields.

B) Synthesis and characterization of binary TiO2(P25)-gC3N4-atm photocatalysts

B.1. Synthesis TiO_2(P25)-gC_3N_4-atm photocatalysts

B.1.1. Experimental protocol

Wet impregnation methods present several advantages in reference to other physical or chemical methods, such as the use of mild conditions (atmospheric pressure and room temperature), the use of the universal and environmental friendly solvent (water), as well as simple and common laboratory wares (beaker, magnetic stirrer, and stirrer). Therefore, wet impregnation method is considered a "green process".

In our case, the wet impregnation method consists in two-pot successive steps:

(i) A prior wet impregnation of g-C_3N_4 precursors onto the (commercial) TiO_2(P25) followed by overnight drying at 100 °C and

(ii) Solid-state g-C_3N_4 polycondensation reaction in presence of pre-impregnated precursors on TiO_2.

Typically, the first wet impregnation step comprises a solid state mixture of g-C_3N_4 precursors (Mel and DCDA in an equimolar relationship) with the commercial TiO_2 P25 (purchased in Evonik Industry). Then, a small volume of water is added into the vessel containing all the solid mixture, leading to dissolution of Mel and DCDA precursors. The mixture is maintained over a gentle stirring until evaporation of the solvent. Thus resulting solid (gel type) is then put into a muffle furnace overnight at 100 °C. The obtained solid is scratched from the beaker and transferred to an alumina crucible to undergo the thermal polycondensation in a tubular furnace at 550 °C during 3 h with a heating ramp of 5 °C min^{-1} in a continuous flow of 100 mL min^{-1} under synthesis atmosphere (as described previously on chapter two for g-C_3N_4-*atm* synthesis). All mentioned synthesis steps are summarized schematically in **Fig. 3.1**.

The chosen atmospheres were selected based on the results obtained after H_2 evolution performances of g-C_3N_4-*atm* samples (chapter 2). It, must be remind that the most photoactive synthesized samples were 0.3 wt. % Au/g-C_3N_4-NH_3 and 0.3wt. % Au/g-C_3N_4-Air. Thus, those two synthesis atmospheres (**NH_3 and Air**) were selected for the elaboration of TiO_2-gC_3N_4 binary composites according to the protocol summarized below.

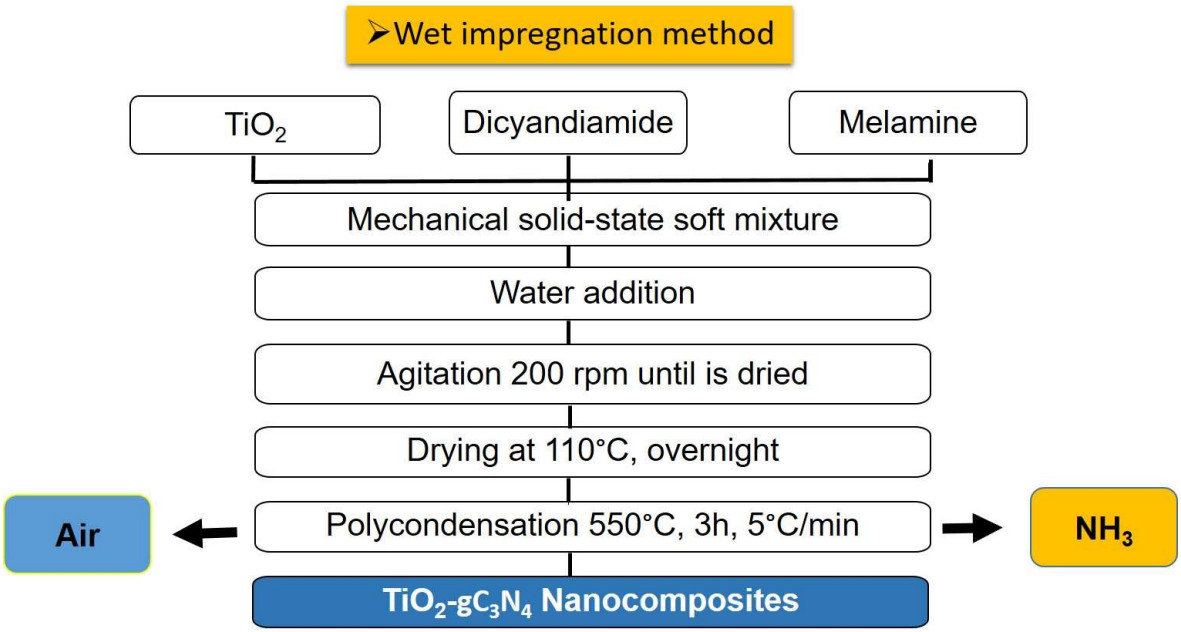

Figure 3.1. Scheme of the heterojunction binary system TiO_2/gC_3N_4–atm obtained via impregnation method.

References TiO_2: for each selected atmosphere, TiO_2 reference was calcined in the same conditions than for g-C_3N_4 synthesis, *i.e.* 550 °C/Air and 550 °C/NH_3. The resulting nomenclatures sample are **TiO_2 550C(Air)** and **TiO_2 550C(NH_3)**.

Physical mixtures samples were prepared for comparison reasons. They were used in photocatalytic tests, TRMC, XPS, and zeta potential characterization analysis to be compared with the wet impregnation composites. They are tested under the exactly same experimental conditions than composites and regular references. The physical mixture comprehends the mass proportion of the contribution of each SC present on the heterojunction system decorated with Au NPs (same total Au loading). As the total mass of catalyst was established 250 mg to be used on the reactor, it was thus possible to distribute this total mass of catalyst in the specific desired proportions for example, 125 mg 0.3wt.% Au/TiO_2 plus 125 mg 0.3wt.% Au/ gC_3N_4, for the 50/50 composite case, for example.

B.1.2. Criteria to select the TiO_2(P25)-gC_3N_4 proportions

The relative proportions of TiO_2 and g-C_3N_4 into the binary heterojunction composites were chosen to conduct the parametric study for chapters 3 and 4. Hence, a set of binary nanocomposites are synthesized under the same principle of g-C_3N_4 thermal polycondensation in presence of the as-prepared TiO_2. The main difference for TiO_2 nanomaterial is its morphology. In chapter 3 and 4, TiO_2 P25 nanoparticles (TiO_2 NPs) and TiO_2 nanotubes (TiO_2 NTs) have been chosen, respectively, to be associated with g-C_3N_4.

In order to cover the broader range of relative heterojunction proportions, a first **screening** methodology was applied to select a first series of TiO_2-gC_3N_4 relative massic proportions of 75-25, 50-50, and 25-75, respectively. The aim was to select opposite and intermediate proportions to view and fairly compare the different composites with their associated physico chemical properties. Therefore, after the obtainment of the photocatalytic results of the screening composites, it has been decided to extend the present investigation into a narrower range of relative heterojunction proportions towards a higher content of TiO_2 (or lower content of g-C_3N_4). This approach is defined as the **zoom** method, with the relative massic proportions of TiO_2-gC_3N_4 of 97.5-2.5, 95-5, and 90-10, respectively. This general methodology is summarized in **Figure 3.2**.

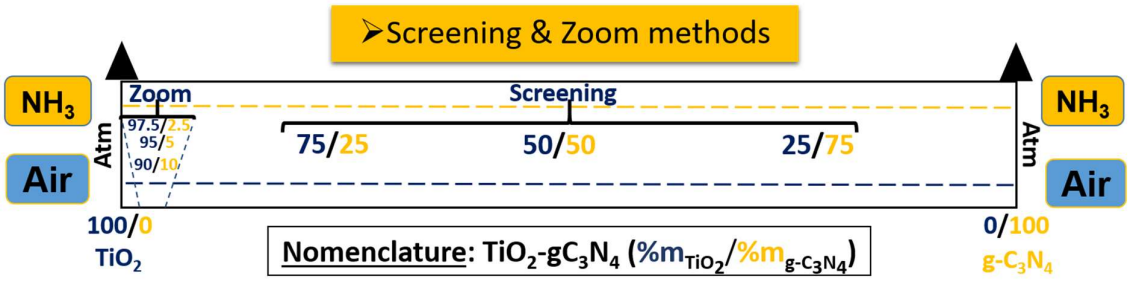

Figure 3.2. Scheme for the screening and zoom methods applied for selecting the TiO_2-gC_3N_4 proportions.

B.1.3. Mathematical model to determine and control TiO_2-gC_3N_4 massic proportions

The objective of this model is to express the mass of one of the g-C_3N_4 precursor, such as melamine ($mC_3N_6H_6$) in function of the polycondensation reaction yield (% R.Y.). This relationship may enable us to predict the final massic proportion of TiO_2 and g-C_3N_4. Assuming that the variation of the polycondensation reaction yield is influenced by the variation of initial mass of g-C_3N_4 precursors and of TiO_2.

To start, **polycondensation reaction yield** (% R.Y.) is mandatory in **equation 1**:

$$\%R.Y. = \frac{m_{C_3N_4(Exp)}}{m_{C_3N_4(Theo)}} * 100 \qquad (1)$$

The **theoretical maximum weight of g-C_3N_4** (mC_3N_4 (Theo)) can be defined as the total conversion of any of the two g-C_3N_4 precursors (since they are in equimolar relationship) by using the adequate stoichiometric factors of the conversion reaction. The following approach has been established taken into account the synthesis performed under air atmosphere. In this context, the stoichiometric relationship (**equation 2**) of the global polycondensation reaction including the molecular weight definition relations **(equations 3** and **4)** must be known, aiming at reducing the variables number **(equation 5)**. For calculus reasons, dicyandiamide ($C_2N_4H_4$) precursor was selected as representing g-C_3N_4 precursor, knowing that it is present in equimolar ratio with melamine ($C_3N_6H_6$).

$$3C_3N_6H_6 + \mathbf{3}C_2N_4H_4 + \frac{15}{2}O_2 \rightarrow \mathbf{5}C_3N_4 + 15H_2O + 5N_2 \quad (2)$$

$$m_{C_3N_4} = n_{C_3N_4} * M_{C_3N_4} \quad (3)$$

$$m_{C_2N_4H_4} = n_{C_2N_4H_4} * M_{C_2N_4H_4} \quad (4)$$

$$m_{C_3N_4(Theo)} = \frac{\frac{5}{3} * m_{C_2N_4H_4} * M_{C_3N_4}}{M_{C_2N_4H_4}} \quad (5)$$

Each parameter is described, $n_{C_3N_4}$ = moles of g-C_3N_4, $m_{C_3N_4}$ = mass of g-C_3N_4, $M_{C_3N_4}$ = molecular weight of g-C_3N_4, $n_{C_2N_4H_4}$= moles of dicyandiamide, $m_{C_2N_4H_4}$= mass of dicyandiamide, $M_{C_2N_4H_4}$= molecular weight of dicyandiamide.

The **experimental mass of g-C_3N_4** ($m_{C_3N_4\ (Exp)}$) is the mass of g-C_3N_4 obtained after the polycondensation thermal treatment is applied. Thus, two parameters should be defined, the e**xperimental mass proportion of g-C_3N_4** (%$m_{C_3N_4\ (Exp)}$) within the nanocomposite and the **final mass of the nanocomposite** ($m_{Nanocomposite}$) collected in the alumina crucible after polycondensation synthesis, corresponding to the TiO_2-gC_3N_4 composite mass, which is the sum of TiO_2 and g-C_3N_4, calculated in **equations 6-7:**

$$\%m_{C_3N_4} = \frac{m_{C_3N_4(Exp)}}{m_{Nanocomposite}} * 100 \quad (6)$$

$$m_{Nanocomposite} = m_{C_3N_4(Exp)} + m_{TiO_2(Exp)} \quad (7)$$

Therefore, associating **equations 6** and **7**, leads to obtain **equation 8**:

$$\%m_{C_3N_4} = \frac{m_{C_3N_4(Exp)}}{m_{C_3N_4(Exp)} + m_{TiO_2(Exp)}} * 100 \quad (8)$$

Generally, three additional parameters are necessary to elucidate the unknown **experimental mass of TiO_2** ($m_{TiO_2(Exp)}$), the total mass contained in the crucible before the polycondensation synthesis that comprises the sum of initial **dicyandiamide mass** ($m_{C_2N_4H_4}$), plus **melamine mass** ($m_{C_3N_6H_6}$) and the **theoretical mass of TiO_2** ($m_{TiO_2(Theo)}$) **(equation 9)**. The equimolar stoichiometric relationship between Mel and DCDA **(equation 10)** allows to express $m_{C_2N_4H_4}$ in $m_{C_3N_6H_6}$ terms. The **TiO_2 weight loss contribution** (%W.L.) **(equation 11)** is obtained after heating TiO_2 at 550 °C in a controlled chosen atm to obtain TiO_2 550 °C (atm) references. According to previous studies performed in the team concerning the optimization of the initial mass of precursors (Mel + DCDA in equimolar proportions), 3.2 g was chosen [9] and put into the crucible.

$$3.2g = m_{C_2N_4H_4} + m_{C_3N_6H_6} + m_{TiO_2(Theo)} \quad (9)$$

$$m_{C_2N_4H_4} = \frac{m_{C_3N_6H_6} * M_{C_2N_4H_4}}{M_{C_3N_6H_6}} \quad (10)$$

$$m_{TiO_2(Exp)} = m_{TiO_2(Theo)} - \%W.L. * m_{TiO_2(Theo)} \quad (11)$$

Therefore, associating **equations 9-11**, leads to a new hybrid **equation 12**:

$$m_{TiO_2(Exp)} = \left\{3.2g - \left[\left(1 + \frac{M_{C_2N_4H_4}}{M_{C_3N_6H_6}}\right) * m_{C_3N_6H_6}\right]\right\} - \%W.L.* \left\{3.2g - \left[\left(1 + \frac{M_{C_2N_4H_4}}{M_{C_3N_6H_6}}\right) * m_{C_3N_6H_6}\right]\right\} \quad (12)$$

Regarding the %W.L. of TiO_2 NPs, it was evaluated after calcination under the two atmospheres (Air and NH_3) and was determined as *ca.* 10% for both atms.

Associating **equations 8** and **12** described previously, **equation 13** is presented containing all the known initial stoichiometric relationships that enables to run the mathematical model controlling accurately the proportion of both SCs on the composite.

$$\%m_{C_3N_4} = \frac{\left(\%R.Y.* \frac{\frac{5}{3} * m_{C_2N_4H_4} * M_{C_3N_4}}{M_{C_2N_4H_4}}\right)}{\left(\%R.Y.* \frac{\frac{5}{3} * m_{C_2N_4H_4} * M_{C_3N_4}}{M_{C_2N_4H_4}}\right) + \left\{3.2g - \left[\left(1 + \frac{M_{C_2N_4H_4}}{M_{C_3N_6H_6}}\right) * m_{C_3N_6H_6}\right]\right\} - \%W.L.* \left\{3.2g - \left[\left(1 + \frac{M_{C_2N_4H_4}}{M_{C_3N_6H_6}}\right) * m_{C_3N_6H_6}\right]\right\}} \quad (13)$$

$M_{C_2N_4H_4} = 84.0798 g/mol;\ M_{C_3N_6H_6} = 126.1197 g/mol;\ M_{TiO_2} = 79.8658 g/mol;\ M_{C_3N_4} = 92.0589 g/mol$

Three variables are missing in **equation 13**, dicyandiamide and melamine masses and the mathematical expression of the reaction yield. For this purpose, the expression of the reaction yield can be obtained with a calibration curve (different for each atmosphere synthesis). Thermal polycondensation must be performed to collect experimental data (error and trial) with different proportions. With that information, the reaction yield in function of the proportion of carbon nitride can be plot selecting the best trend line fit criteria, and select the correlation coefficient (R^2) closer to the unit applying either linear, exponential or power trend. For the TiO_2(P25)-gC_3N_4 synthesized under air and NH_3, the best fit was obtained with exponential and linear trends, respectively. To simplify, the $\%m_{C_3N_4}$ is chosen arbitrarily in function of the interest of the final heterojunction proportion. Therefore, including the reaction yield expression obtained from the calibration curve (accordingly for air and NH_3: exponential or linear) into the **equation 13** leads to have only one unknown variable, $m_{C_3N_6H_6}$.

Finally, calculating and obtaining $m_{C_3N_6H_6}$, is thus possible to calculate $m_{C_2N_4H_4}$ and then $m_{TiO_2(Theo)}$ by equations 10 - 9, respectively. In conclusion, the establishment of equation 13 allowed us to target different theoretical massic content of g-C_3N_4 into the TiO_2-gC_3N_4 composite. In the case of TiO_2-gC_3N_4 (NH_3) composites, as it was not obvious to determine the stoichiometric coefficient (as the g-C_3N_4 synthesis under pure NH_3 was never performed before) and also knowing that NH_3 is also a reaction product, the same mathematical model was therefore applied and further verified.

B.2. Characterizations of TiO_2(P25)-gC_3N_4 composites

For the characterizations of TiO_2(P25)-g-C_3N_4 composites, two classifications were made: by **atmosphere** used (**Air** and **NH_3**) and by method applied, *i.e.* the **screening** or the **zoom** methods as described in **section B.1.2**. The characterization techniques used are typically TGA, FT-IR, XRD, and BET to determine thermal, chemical, structural, and surface properties of materials.

B.2.1. Characterizations of TiO_2(P25)-gC_3N_4-Air

B.2.1.1. Screening method (Air)

B.2.1.1.a) Thermal stability (TGA)

TGA measurements were performed with the purpose of obtaining a more accurate weight loss (%) of g-C_3N_4 component that typically occurs around *ca.* 500 - 600 °C and thus to determine the exact massic proportion of g-C_3N_4, to be compared with the theoretical one (previously calculated in **section B.1.3**). This characterization allowed us to determine the exact amount of g-C_3N_4 into the TiO_2(P25)-g-C_3N_4 composite. Thus, a simple normalization analysis on subtracting the weight losses due to the presence of impurities on both SCs or to TiO_2 dehydroxylation before 400 °C ($\%W.L._{\text{Corrected}}$) was applied to calculate the normalized g-C_3N_4 weight loss (%) ($\%m_{\text{C3N4 Normalized}}$) (**equations 14 and 15)**.

$$\%W.L._{Corrected} = 100 - \%W.L._{Before\ 400°C} \quad (14)$$

$$\%m_{C_3N_4\ Normalized} = \frac{\%W.L._{Corrected}}{\%m_{C_3N_4\ Measured}} * 100 \quad (15)$$

Where $\%m_{\text{C3N4 Corrected}}$ stands for the weight loss (%) related with g-C_3N_4 decomposition.

The resulting normalized weight losses (and thus g-C_3N_4 massic content in TiO_2(P25)-g-C_3N_4–Air composite) were (30-70) (52-48) and (70-30) corresponding respectively to the theoretical values of (25-75) (50-50) and (75-25). It must be underlined that the lowest g-C_3N_4 content led to the more important uncertainty between theoretical and real g-C_3N_4 massic content. In the following section, the **g-C_3N_4 massic content for the screening composites is expressed as the experimental values** determined from TGA analysis.

TGA profiles (**Fig. 3.3**) of TiO_2-g-C_3N_4 (30-70; 52-48) reveal a one-pot decomposition with a maximum located at 613 and 582 °C, respectively. For TiO_2-g-C_3N_4 (70-30) two pronounced decomposition steps with maximums located at 574 and 522 °C were observed. In the case of the weight loss at higher temperature, ranging from 574 to 613 °C, it reveals the presence of heptazine-base units in all samples, in accordance with reported literature [10,11]. For the weight-loss located at lower temperatures, we can thus suggest that TiO_2 helps for catalysing g-C_3N_4 decomposition by thermal oxidation. The only composite with two decomposition steps corresponds to the lowest content of g-C_3N_4 (30 wt. %). In this case one may assign the first contribution to weight loss of g-C_3N_4 in close contact with TiO_2 NPs and the second one (i.e. 522 °C) of bulk-like g-C_3N_4 domains. However, it must be underlined that the second contribution (at higher temperature) is shifted toward lower temperature compared to the bulk g-C_3N_4 (Air) reference.

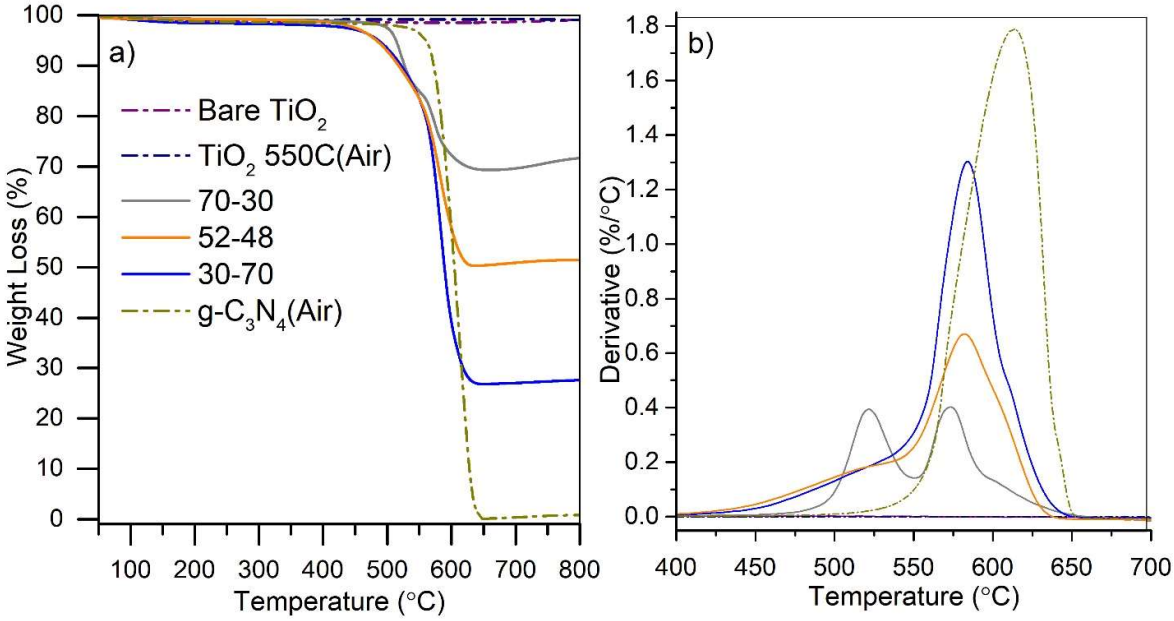

Figure 3.3. a) TGA profiles b) Derivatives of weight loss for TiO_2-gC_3N_4-Air screening composites and references.

B.2.1.1.b) FT-IR characterization

To investigate the chemical changes on the TiO_2 and g-C_3N_4 structural groups within the composites Air, FT-IR spectroscopy was used. FT-IR spectra (**Fig. 3.4**) for the three screening composites exhibit the characteristic peaks of g-C_3N_4 [12]. The broad absorption band from 3000 to 3500 cm^{-1} is attributed to the N-H stretching vibration of amine groups (secondary and primary). However, one cannot exclude the O-H associated to the typical surface hydroxyl groups of TiO_2 [13,14]. The region with the majority of peaks ranging from 1240 to 1640 cm^{-1} is assigned to the fingerprint of tri-s-triazine (TST) units [15]. Detailed assignation of each peak within this region can be found in **chapter 2,** section **B.2.1**. Then, the last two absorption bands at approximately 890 and 806 cm^{-1} are characteristic for the deformation mode N-H (amino groups) and the tri-s-

triazine ring breathing mode [15], respectively. These last two bands are only present for the two composites with ≥ 50 wt. % g-C_3N_4 content, meaning that for TiO_2-gC_3N_4 (70-30) the predominant character is TiO_2.

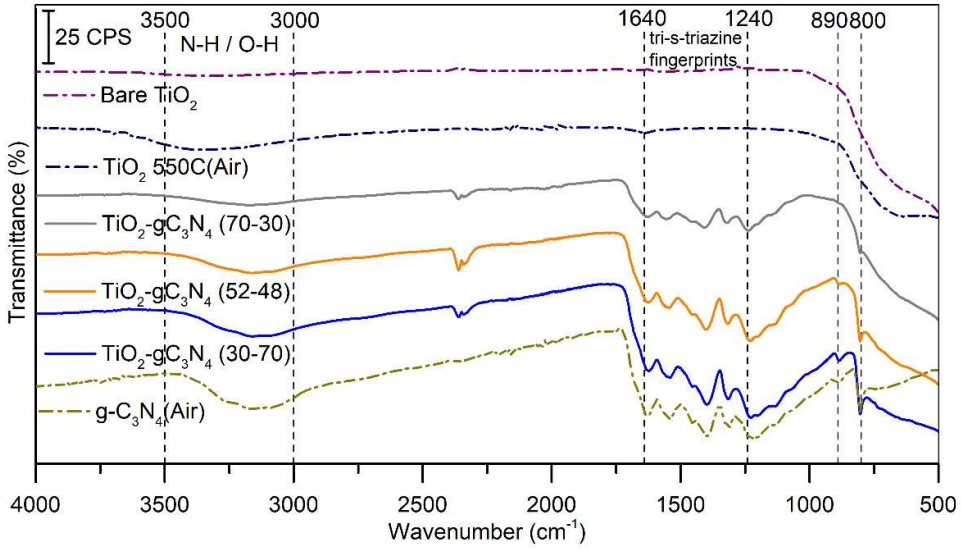

Figure 3.4. FT-IR spectra of TiO_2-gC_3N_4-Air screening composites and references.

B.2.1.1.c) Structural characterization (XRD)

The XRD patterns (**Fig. 3.5 a**) of the screening Air composites exhibit with no doubt the main characteristic diffraction peaks at 2θ = 25.2° and 2θ = 27.4°, corresponding to the anatase phase of TiO_2, indexed as (101) diffraction plane in good agreement with JCPDS file 89-4921 [1,16]. After enlargement of the 2θ region ranging from 26 to 29° (**Fig. 3.5 b**) it is not obvious to clearly distinguish between the positions of the rutile and g-C_3N_4 diffraction peaks, *i.e.* the interlayer stacking of π-conjugated aromatic systems of g-C_3N_4, indexed as (002) diffraction plane, characteristic for graphitic materials [5,17,18], respectively. However, by using Debye-Scherrer relationship and fitting meticulously each involved peak, the crystallite sizes were calculated. The only difference could rely on the peak width, associated to different crystallite size between rutile and g-C_3N_4, the crystallite associated to g-C_3N_4 being generally smaller (broader peak). It is thus assumed that diffraction peaks of the three composites could be assigned to the presence of g-C_3N_4 and no evidence of the presence of rutile was observed.

Even though, the nanocomposites evidence the presence of g-C_3N_4, none of them present the XRD peaks of TSTCN or STCN at 2θ = 13.1° and 17.4°, respectively, presumably because of the dilution effect into the composite.

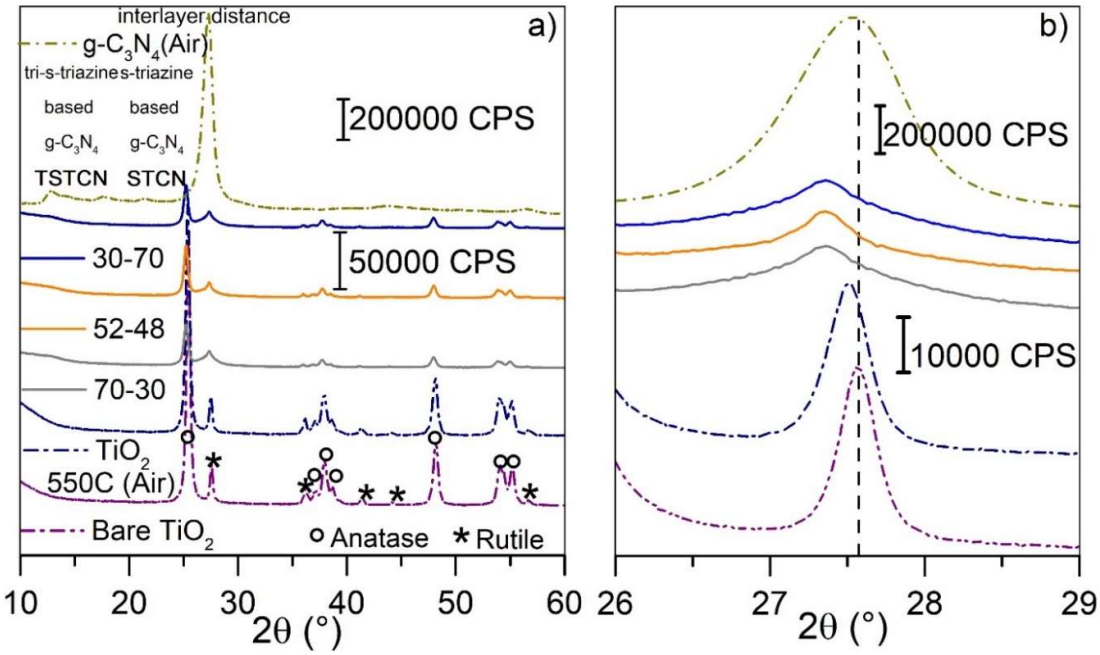

Figure 3.5. a) General XRD patterns b) zoom of the (26-29°) region of the TiO_2-gC_3N_4-Air screening composites and references.

Concerning the mean crystallite sizes (**Table 3.1**) of the different crystalline phases, one can say that anatase is present in all the screening composites air with the same value (*i.e.* 20±1 nm) equally as for the reference TiO_2 550 °C (Air) sample value. For all the TiO_2-gC_3N_4 (70-30) (52-48) (30-70) composites no significant difference on the crystallite size was found in comparison to bare g-C_3N_4. As a result, the N° of layers is equal for all composites (*i.e.* 21±1), which is significantly lower than for g-C_3N_4 reference (*i.e.* 26±1), suggesting that on the binary composites the g-C_3N_4 sheets seems to be thinner than in the bulk structure.

Table 3.6. Mean crystallite size of the crystalline phases of TiO_2-gC_3N_4-Air screening composites and references, anatase, rutile, and graphitic domain of g-C_3N_4, and number of layers of g-C_3N_4.

	Mean crystallite size (nm)			
Sample	Anatase (101)	Rutile (110)	g-C_3N_4 (002)	N° layers
Bare TiO_2	24±1	41±2	-	-
TiO_2 550 °C (Air)	20±1	38±1	-	-
70-30	20±1	-	6.9±0.4	21±1
52-48	20±1		6.8±0.4	21±1
30-70	20±1	-	6.7±0.4	21±1
g-C_3N_4 (Air)	-	-	6.6±0.4	26±1

B.2.1.1.d) BET surface area measurements

From BET measurements (**Table 3.2, Fig. 3.6 a**), it can be observed that all screening composites air, including references, exhibit a type-IV adsorption-desorption isotherm profile, consistent with the mesoporous materials features [19–21]. Moreover, g-C_3N_4 reference and screening composites shows a negligible type-IV hysteresis loop profile characteristic for slit-like pores, which confirms the graphitic domain character seen from (002) diffraction plane in XRD analysis, constituted by stacked layers (bulks). Concerning, the S_{BET} obtained values, only g-C_3N_4 reference presents *ca.* 3-5 times lower value than all the other five samples. For the screening composites, a linear tendency (see discussion section) is found. There is an increase of S_{BET} in function of the content increase of TiO_2, *i.e.,* 31, 39, and 46 m^2 g^{-1} corresponding to TiO_2-gC_3N_4 (30-70; 52-48; and 70-30), respectively. This result demonstrates a linear transition from the gC_3N_4 character to the TiO_2 one in terms of specific surface area.

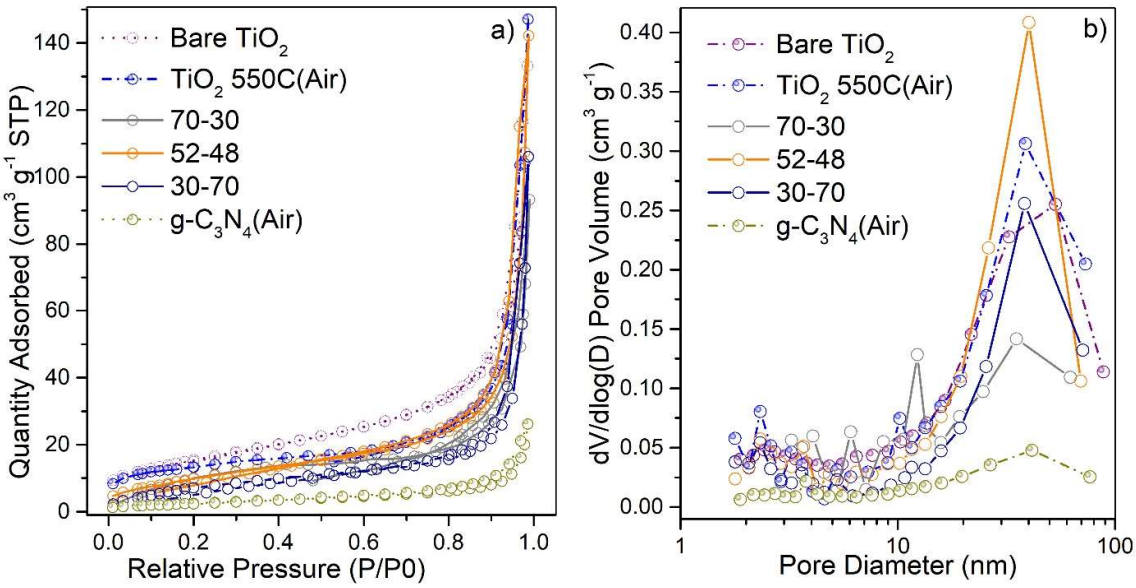

Figure 3.6. a) Nitrogen adsorption-desorption isotherms b) BJH pore-size distribution of the TiO_2-gC_3N_4–Air screening composite and references.

BJH pore-size distribution (**Table 3.2, Fig. 3.6 b**) exhibits mainly a monomodal type for all samples. A significant difference was found for bare TiO_2 pore size centered at *ca.* 53 nm. For the other five samples no difference between them was observed, presenting a pore size centered at lower values ranging from 35 to 42 nm, thanks to the extent of their associated standard deviation. However, comparing the pore volume values, brings a decreasing trend from TiO_2-gC_3N_4 (52-48), TiO_2 550 °C, TiO_2-gC_3N_4 (30-70) to bare TiO_2, TiO_2-gC_3N_4 (70-30), and g-C_3N_4 with 0.41, 0.31, 0.26, 0.26, 0.14, and 0.05 cm^3 g^{-1}, respectively. Therefore, when increasing the amount of g-C_3N_4, a significant difference between the pore volume of the screening composites in comparison to the three references was observed, demonstrating an noticeable volume pore change in presence of g-C_3N_4, building a variety of pore channels.

Table 3.7. Specific surface area (S_{BET}), pore volume (V_{pore}), pore size of the Au/TiO_2-g-C_3N_4–Air screening composites and references.

Sample	S_{BET}* (m^2 g^{-1})	V_{pore} (cm^3 g^{-1})	Pore size** (nm)
Bare TiO_2	56±6	0.26±0.02	53±5
TiO_2 550 °C (Air)	46±5	0.31±0.02	39±4
70-30	46±5	0.14±0.02	35±4
52-48	39±4	0.41±0.03	40±4
30-70	31±3	0.26±0.02	38±4
g-C_3N_4 (Air)	10±1	0.05±0.02	42±4

* = calculated using BET method; ** = calculated using BJH method

B.2.1.2. Zoom method (Air)

B.2.1.2.a) Thermal stability (TGA)

From TGA profiles (**Fig. 3.7 a, b**) of bare and calcined TiO_2 (references) and theoretical content of (97.5-2.5; 95-5) TiO_2-gC_3N_4 composites no significant decomposition was found after normalization (section **B.2.1.1 a**). But for TiO_2-gC_3N_4 (90-10), the mass loss signal reveals three decomposition steps with maximums located at 564, 494, and 321 °C, respectively. The first decomposition (564 °C) is related with the presence of heptazine-base units [10,11], evidencing the presence of g-C_3N_4 in a good agreement with literature. The second decomposition at lower temperature (494 °C) is presumably associated to a second type of g-C_3N_4, one that might be in closer contact with TiO_2 NPs, thus leading to better oxidation. A third decomposition (321°C) is associated to melem structure [22]. Therefore, one can say that 10 wt. % g-C_3N_4 (in the binary composite) is the lowest limit to detect g-C_3N_4 decomposition by using TGA analysis evidencing the effective formation of polymeric g-C_3N_4 structure. Nevertheless, one cannot exclude the formation of g-C_3N_4 in the composites ≤ 10 wt. %. **For that reason, in the following section, the g-C_3N_4 content in the zoom composites will be expressed only in terms of theoretical g-C_3N_4 values** (section **B.1.3**).

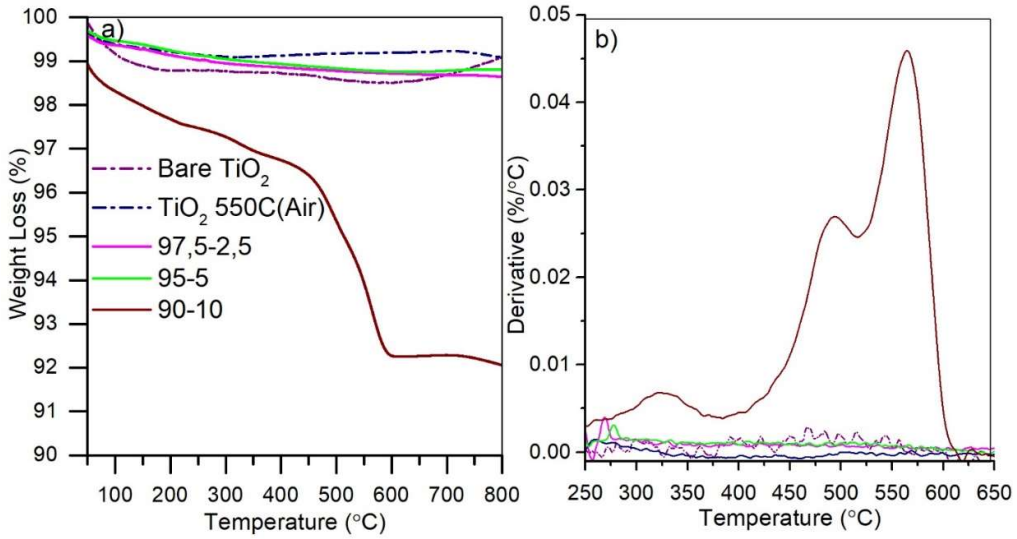

Figure 3.7. a) TGA profiles b) Derivatives of weight loss for TiO_2-g-C_3N_4-Air zoom composites and references.

B.2.1.2.b) FT-IR characterization

FT-IR spectra (**Fig. 3.8**) of the three zoom composites follow the main features of TiO_2 reference, with the only noticeable and clear signal at approximately 3500-3000 cm^{-1}, which is assigned from a combination of major O-H (hydroxyl) contribution and of N-H minor (amine) contribution surface groups. The presence of g-C_3N_4 is difficult to observe, due to its presence is in lower proportion than in case of the screening composites (Air). Nevertheless, one can notice a signal intensity at approximately 1640 cm^{-1} (it can be an evidence of N-H presence from the amino groups of g-C_3N_4) for the TiO_2-gC_3N_4 (95-5) composite, presumably for a slight formation of g-C_3N_4 within the composite structure.

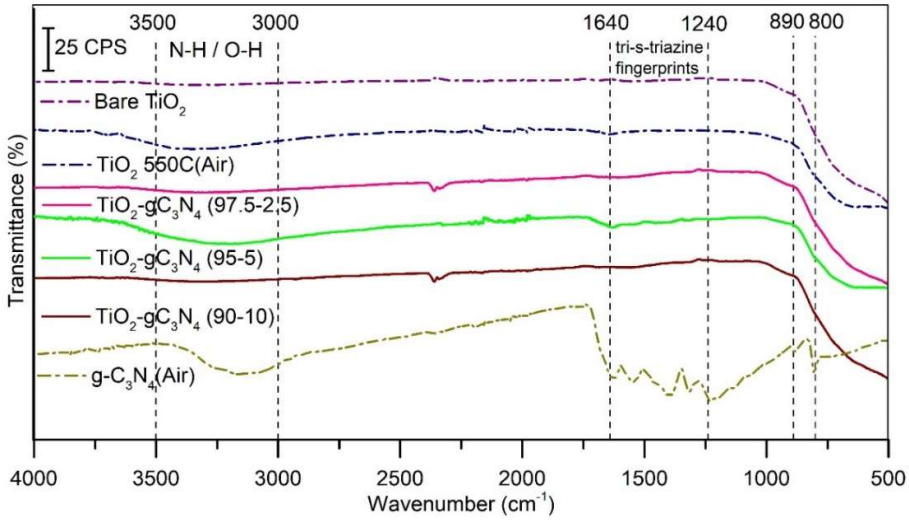

Figure 3.8. FT-IR spectra of TiO_2-gC_3N_4-Air zoom composites and references

B.2.1.2.c) Structural characterization (XRD)

The XRD patterns (**Fig. 3.9 a**) of the zoom Air composites exhibit the main characteristic diffraction peaks at 2θ = 25.2° corresponding to the anatase phase of TiO_2, indexed as (101) diffraction plane. Concerning the diffraction peak observed between 27 ° and 28 ° (**Fig. 3.9 b**) and considering its width it may be assigned to TiO_2 rutile phase indexed as (110) diffraction plane rather than to the interlayer stacking of π-conjugated aromatic systems of g-C_3N_4 (indexed as (002) plane). For g-C_3N_4 content ≤ 10 wt. % composites XRD analysis could not evidence its presence because the predominant crystallographic structure of TiO_2 is observed.

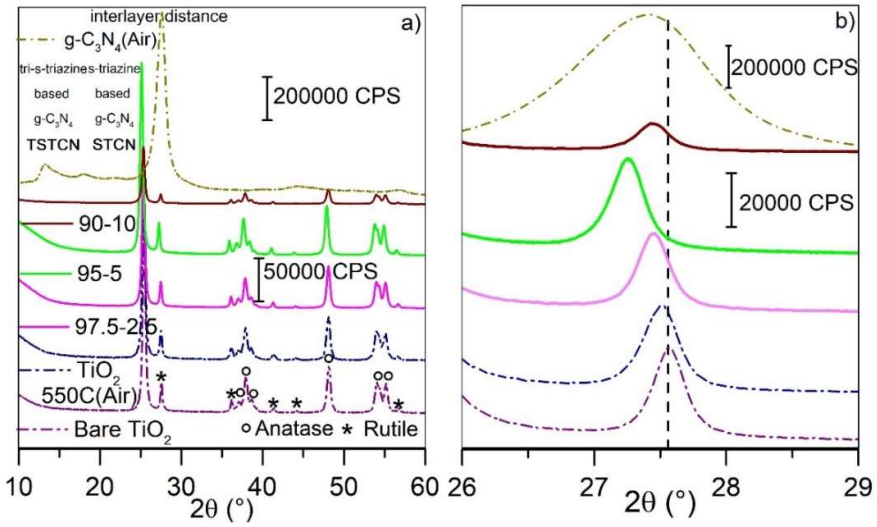

Figure 3.9. a) General XRD patterns b) zoom of the (26-29°) region of the TiO_2-gC_3N_4-Air zoom composites and references.

By using Debye-Scherrer relationship, it is thus possible to determine the mean crystallite sizes (**Table 3.3**). One can notice no significant difference in any of the two crystallites (anatase and rutile) in comparison with TiO_2 reference.

Table 3.8. Mean crystallite size of the crystalline phases of the TiO_2-gC_3N_4-Air zoom composites and references and graphitic domain of g-C_3N_4.

	Mean crystallite size (nm)		
Sample	Anatase (101)	Rutile (110)	g-C_3N_4 (002)
TiO_2 550C(Air)	20±1	27±1	-
97.5-2.5	24±1	26±1	-
95-5	21±1	27±1	-
90-10	21±1	27±1	-
g-C_3N_4(Air)	-	-	6.6±0.4

B.2.1.2.d) BET surface area measurements

From BET measurements (**Table 3.4, Fig. 3.10 a**), it can be observed that all zoom composites Air, in addition to references, exhibit a type-IV adsorption-desorption isotherm profile, consistent with the mesoporous materials features [19–21]. Concerning, the S_{BET} obtained values, only g-C_3N_4 reference presents *ca.* 5 times lower value than all the other four samples. For all the zoom composites, with a very small amount of g-C_3N_4 content (≤ 10 wt. %) the S_{BET} values do not vary significantly between them, certainly due to the low amount of g-C_3N_4.

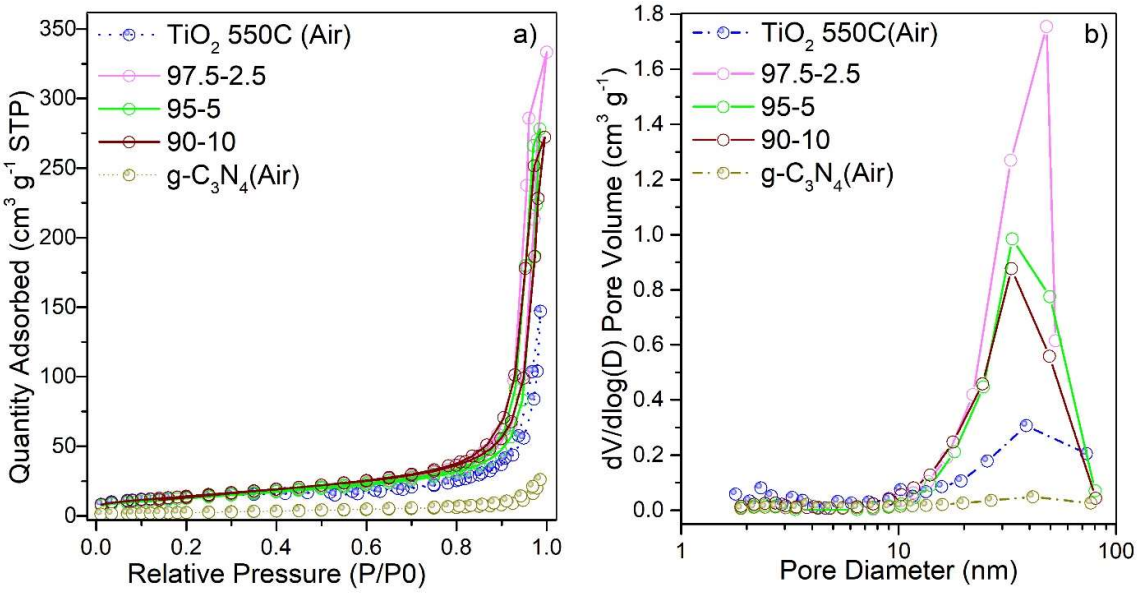

Figure 3.10. a) Nitrogen adsorption-desorption isotherms b) BJH pore-size distribution of the TiO_2-gC_3N_4-Air zoom composites and references.

BJH pore-size distributions (**Table 3.4, Fig. 3.10 b**) exhibits a monomodal type for all samples. Bare TiO_2 (P25) exhibit the largest pores with pore size centered at *ca.* 53 nm. The other five samples show smaller pores from 35 to 42 nm. However, when comparing the pore volume values of the composites samples brings a different tendency. One can observe an increase of the pore volume when decreasing g-C_3N_4 content into the TiO_2-gC_3N_4 (90-10) (95-5) (97.5-2.5) composites, representing 6, 3.3, and 2.9 times higher values than the TiO_2 550°C (Air) reference, and 36, 20, and 17 times higher pore volume than the g-C_3N_4 reference, respectively. One can notice a significant difference between the pore volume of the zoom composites in comparison to the two references, leading to an evidence that the pore volume increases when adding already synthesized TiO_2 into g-C_3N_4 (Air) synthesis to obtain low contents of g-C_3N_4 in the composite. This pore volume increase allowed building deeper pore channels. It must be also underlined that this tendency is different from the one observed at higher g-C_3N_4 loading (screening composites).

Table 3.9. Specific surface area (S_{BET}), pore volume (V_{pore}), pore size of the Au/TiO_2-gC_3N_4-Air zoom composites and references.

g-C_3N_4	S_{BET}* (m^2 g^{-1})	V_{pore} (cm^3 g^{-1})	Pore size** (nm)
TiO_2 550C(Air)	46±5	0.31±0.02	39±4
97.5-2.5	50±5	1.80±0.06	48±5
95-5	47±5	1.00±0.04	33±3
90-10	52±5	0.87±0.04	33±3
g-C_3N_4(Air)	10±1	0.05±0.02	42±4

* = calculated using BET method; ** = calculated using BJH method

B.2.2. Characterizations of TiO_2(P25)-gC_3N_4-$\underline{NH_3}$

B.2.2.1. Screening method (NH_3)

B.2.2.1.a) Thermal stability (TGA)

TGA analysis of the TiO_2-gC_3N_4 composites with theoretical weight ratios of (25-75), (50-50), and (75-25) but applying the calculation described in section **B.1.3** lead to experimental ratios of (23-77), (48-52), and (73-27), respectively, i.e. relative uncertainty ranging from 2 to 8 %. Consequently in this section, the relative weight ratios for the screening NH_3 composites will be expressed as experimental values from TGA analysis.

TGA profiles (**Fig. 3.11**) of g-C_3N_4 (NH_3) (reference) and TiO_2-g-C_3N_4 (23-77) composite reveal a one-pot decomposition with a maximum located at 598 and 590 °C, respectively. For TiO_2-g-C_3N_4 (48-52; 73-27) composites two decomposition steps are identified with maximums located at 592/530 and 522/432 °C, respectively. In the case of the weight loss at higher temperatures, ranging from 522 to 598 °C, it is assumed to be related to the presence of bulk-like heptazine-base units in all samples [10,11]. The decomposition at lower temperature can be assigned to g-C_3N_4 domains in close interaction with TiO_2, while the second weight loss at higher temperature is attributed to g-C_3N_4 bulk-like domains. Contrarily, the composite with 27 wt. % g-C_3N_4 only exhibit one decomposition step (at lower temperature) that could be related to exclusively TiO_2-gC_3N_4 high and homogeneous interaction between both SCs.

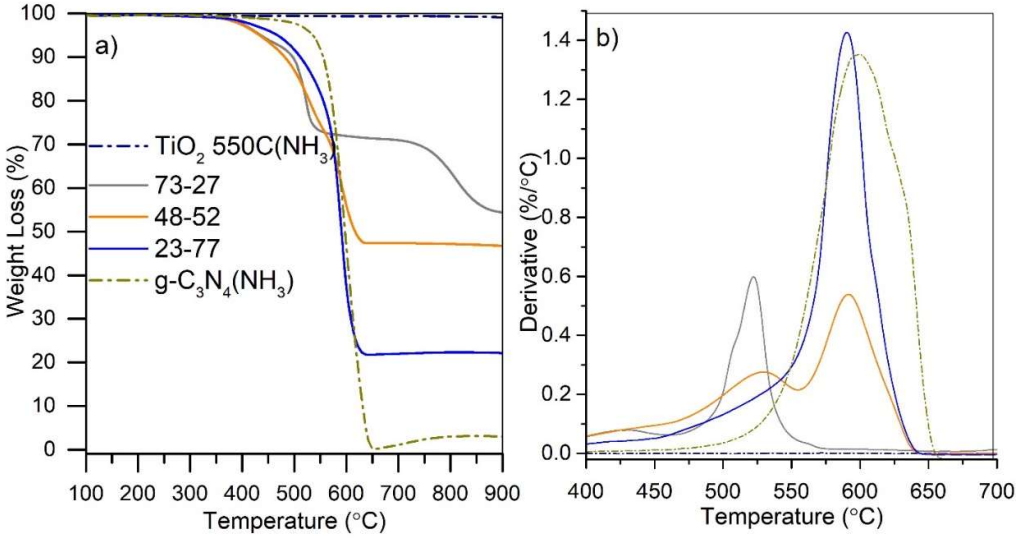

Figure 3.11. TGA profiles b) Derivatives of weight loss for TiO_2-g-C_3N_4-NH_3 screening composites and references.

B.2.2.1.b) FT-IR characterization

Following the investigations on chemical changes on the TiO_2 and g-C_3N_4 functional groups within the composites, this time provoked by reductive atmosphere (NH_3), FT-IR spectroscopy was performed. FT-IR spectra (**Fig. 3.12**) for only two (out of three) screening NH_3 composites exhibit the characteristic peaks of g-C_3N_4 already described at 3000-3500, 1240-1640, 690, and 806 cm^{-1}, attributed to N-H from amino groups (g-C_3N_4) or O-H from hydroxyl groups (TiO_2), fingerprints of TST unit, N-H deformation, and TST ring breathing, respectively [12–14]. One can notice that the g-C_3N_4 absorption bands are only present for the two composites with ≥ 50 wt. % of g-C_3N_4 content. For TiO_2-gC_3N_4 (73-27) sample only TiO_2 fingerprint is predominant, as likewise TiO_2 reference signals.

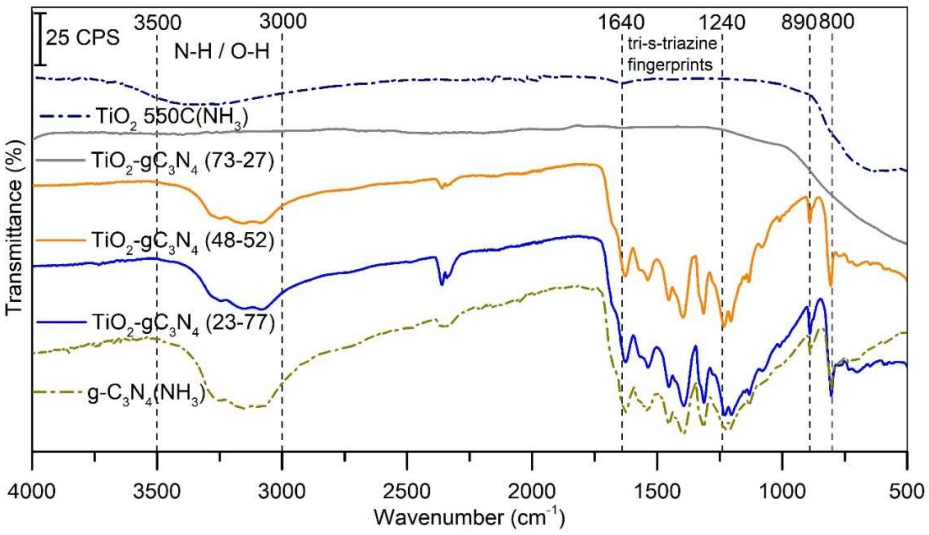

Figure 3.12. FT-IR spectra of TiO_2-gC_3N_4-NH_3 screening composites and references.

B.2.2.1.c) Structural characterization (XRD)

The XRD patterns (**Fig. 3.13 a**) of the screening NH_3 composites exhibit the main characteristic diffraction peaks at 2θ = 25.2° corresponding to the anatase phase of TiO_2. The second diffraction peak located around 27° (**Fig. 3.13 b**) can be attributed to the interlayer stacking of π-conjugated aromatic systems of g-C_3N_4, indexed as (002) diffraction plane, characteristic for graphitic materials [5,17,18] rather than for TiO_2 rutile phase, considering the width of the peaks (and the corresponding crystallite sizes). It must however been mentioned that this second diffraction peak is shifted to higher Bragg angles for the composite samples, contrary to what was observed under Air. One can notice the relative proportion intensity evolution of the graphitic (002) diffraction plane in reference to anatase peak from 27 to 73 % on g-C_3N_4 content. It must also been underlined that the crystallite sizes of g-C_3N_4 is larger for screening NH_3 composites (**Table 3.5**) than for screening Air composites (**Table 3.1**), whereas the number of layers are quite the same between the two series of composites.

Hence, one can say that NH_3 provides optimal conditions (*e.g.* internal pressure on the alumina crucible, gas environment, etc.) for g-C_3N_4 interlayer growth or expansion. Despite the evidence of g-C_3N_4 presence, none composite present the TSTCN or STCN XRD peaks, possibly because of the g-C_3N_4 content, these diffraction peaks being already low on pure g-C_3N_4.

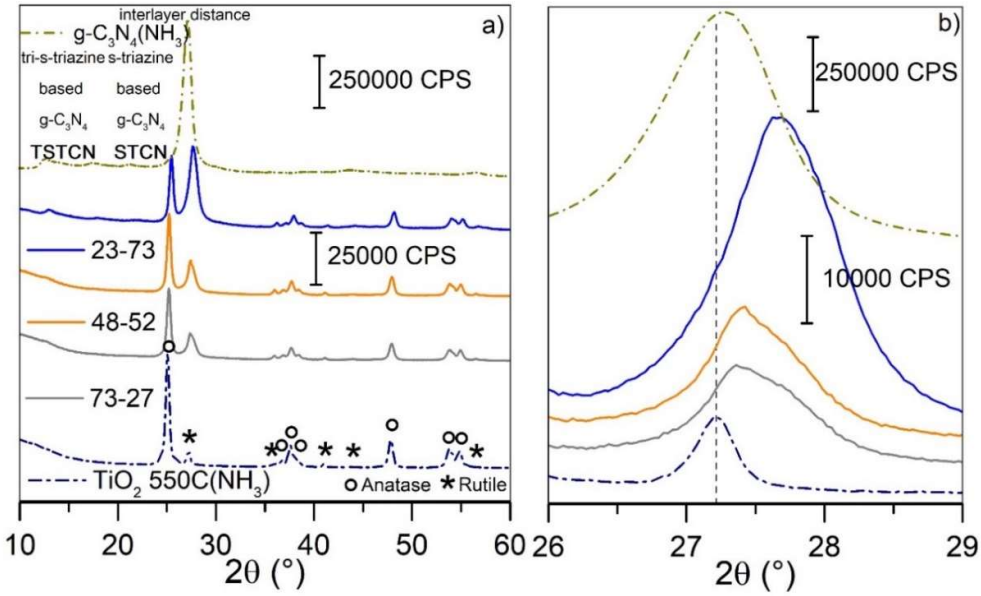

Figure 3.13. a) General XRD patterns b) zoom of the (26-29°) region of the TiO_2-g-C_3N_4-NH_3 screening composites and references.

Concerning the mean crystallite sizes (**Table 3.5**) of anatase into the composites values ranging from 18 to 25 nm are observed. One can notice two groups in anatase size, TiO_2 reference with TiO_2-gC_3N_4 (23-77) (*ca.* 18-20 nm), and TiO_2-gC_3N_4 (73-27 with 48-52) (*ca.* 24-25 nm). This result suggest, that TiO_2-gC_3N_4 (23-77) is out of tendency, probably because its higher proportion of g-C_3N_4, then anatase crystallite growth is hindered. Contrarily, than for the two screening composites Air, generally slightly higher crystallinity is observed for both TiO_2 anatase and g-C_3N_4 phases. No rutile phases were detected on any composites

Table 3.10. Mean crystallite size of the crystalline phases of the TiO_2-gC_3N_4-NH_3 screening composites and references and graphitic domain of g-C_3N_4 and number of layer of g-C_3N_4.

	Mean crystallite size (nm)			
Sample	Anatase (101)	Rutile (110)	g-C_3N_4 (002)	N° layers
TiO_2 550C(NH_3)	18±1	24±1	-	-
73-27	25±1	-	10.4±0.5	26±1
48-52	24±1	-	10.9±0.5	24±1
23-77	20±1	-	8.4±0.4	26±1
g-C_3N_4(NH_3)	-	-	8.4±0.4	26±1

B.2.2.1.d) BET surface area measurements

From BET measurements (**Table 3.7, Fig. 3.14 a**), it can be observed that all screening NH_3 composites, in addition to references, exhibit a type-IV adsorption-desorption isotherm profile, in accordance with mesoporous materials features [19–21]. Likewise, g-C_3N_4 reference and composites shows a negligible type-IV hysteresis loop profile characteristic for slit-like pores, which confirms the graphitic domain character seen from (002) diffraction plane in XRD analysis. Concerning the S_{BET} obtained values, besides g-C_3N_4 reference (32 m^2 g^{-1}) all the other four samples do not present a significant difference ranging from 43 to 53 m^2 g^{-1}.

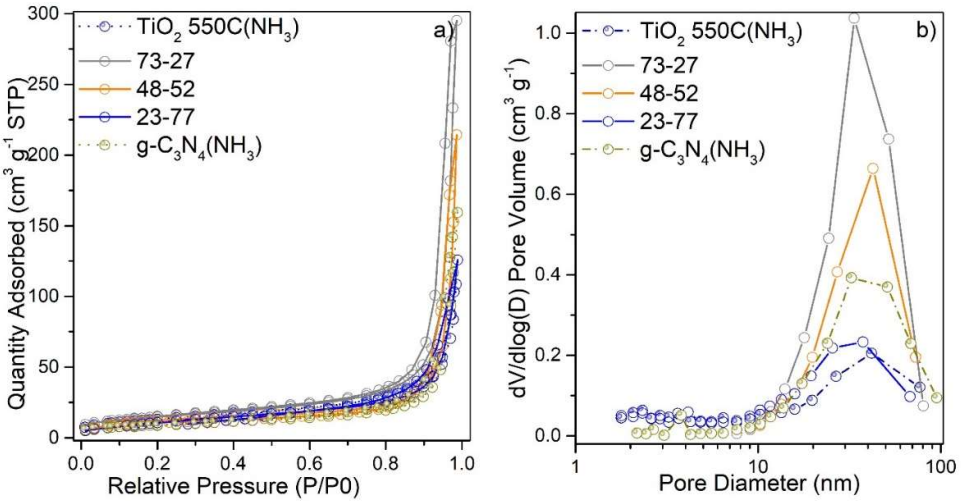

Figure 3.14. a) Nitrogen adsorption-desorption isotherms b) BJH pore-size distribution of TiO_2-gC_3N_4–NH_3 screening composites and references.

BJH pore-size distribution (**Table 3.7, Fig. 3.14 b**) exhibits a monomodal type for all samples. Samples can be classified in two groups, TiO_2-gC_3N_4 (73-27) with pore size centered at *ca.* 34 nm, while all the other samples did not present a significant difference between them with pore sizes ranging from 43 to 38 nm. However, when comparing the pore volume values, TiO_2-gC_3N_4 (73-27) composite present the largest pores. Hence, there is a decreasing trend on the screening composites pore volume in function of the increase of g-C_3N_4 content, TiO_2-gC_3N_4 (73-27, 48-52, and 23-77) exhibiting *ca.* 1.04, 0.66, and 0.23 cm^3 g^{-1}, respectively. It must be remind that the inverse tendency was noticed on the screening composites Air. This result suggest that despite of the dilution into the composites, the one with lowest g-C_3N_4 content (*ca.* 27 wt. %) leads to larger mesoporous pores. One can point out, a significant difference between the pore volume of TiO_2-gC_3N_4 (73-27) composite in respect to the references, five and three times higher than TiO_2 and g-C_3N_4 ones.

Table 3.11. Specific surface area (S_{BET}), pore volume (V_{pore}), pore size of TiO_2-gC_3N_4-NH_3 screening composites and references.

Sample	S_{BET}* (m^2 g^{-1})	V_{pore} (cm^3 g^{-1})	Pore size** (nm)

TiO_2 550C(NH_3)	48±5	0.21±0.02	42±4
73-27	53±5	1.04±0.04	34±3
48-52	46±5	0.66±0.03	43±4
23-77	43±4	0.23±0.02	38±4
g-C_3N_4(NH_3)	32±3	0.39±0.02	42±4

* = calculated using BET method; ** = calculated using BJH method

B.2.2.2. Zoom method (NH_3)

B.2.2.2.a) Thermal stability (TGA)

TGA profiles (**Fig. 3.15**) of TiO_2 and of TiO_2-g-C_3N_4 (theoretical value of 97.5-2.5 and 95-5) do not present a significant weight loss. For that reason and for better clarity, in the following section (zoom method NH_3) the relative weight contents will be expressed as the theoretical values (as it was also the case for the zoom method Air series). Furthermore for g-C_3N_4 ≤ 10 wt. %, it is difficult to quantify and to discriminate between the contributions resulting either from bulk-like stacks or g-C_3N_4 domains in close interaction with TiO_2.

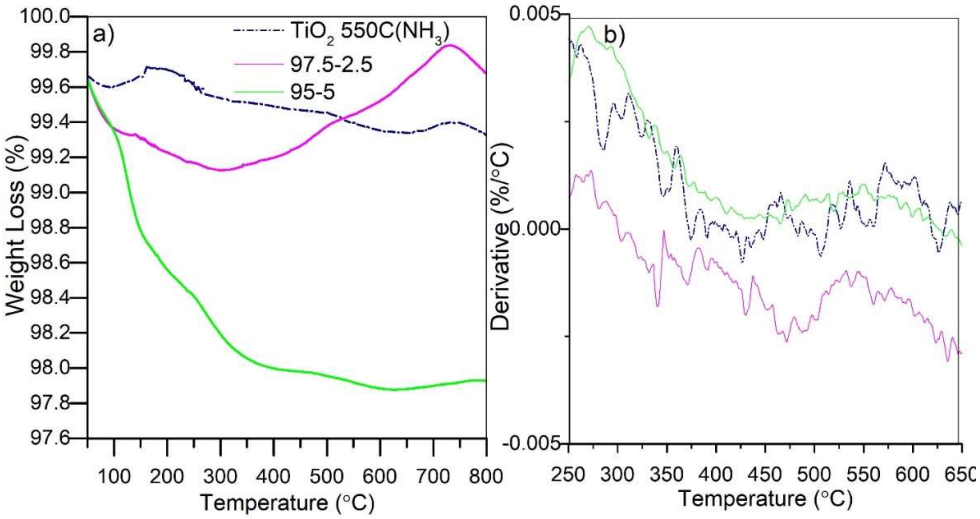

Figure 3.15. TGA profiles b) Derivatives of weight loss for TiO_2-gC_3N_4-NH_3 zoom composites and references.

B.2.2.2.b) FT-IR characterization

Due to the low amount of g-C_3N_4, the FT-IR spectra (**Fig. 3.16**) shows for the two zoom composites the absorption signal of TiO_2 reference at approximately 3500-3000 cm^{-1},

which is associated mainly to O-H from the hydroxyl surface groups.

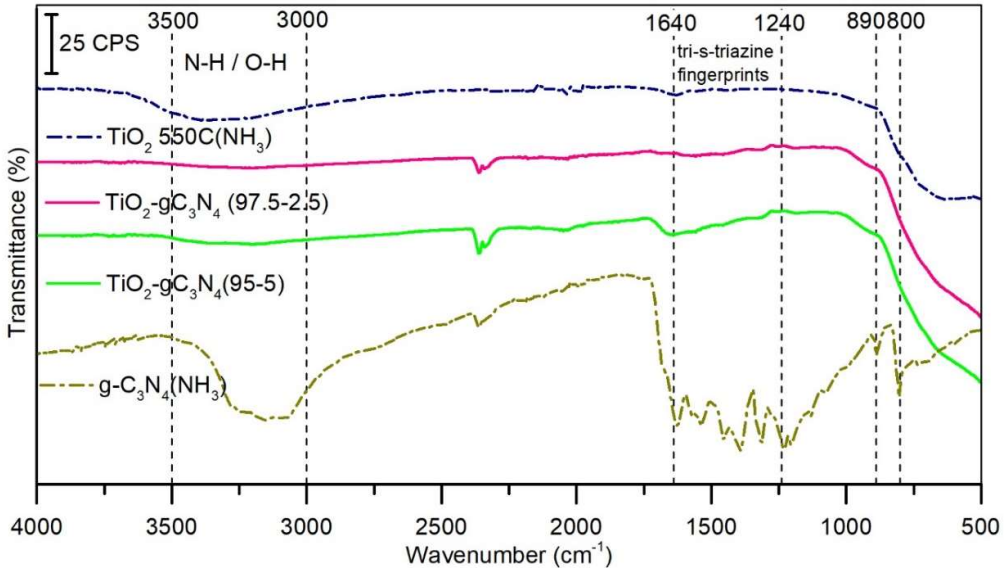

Figure 3.16. FT-IR spectra of TiO_2-gC_3N_4-NH_3 zoom composites and references.

B.2.2.2.c) Structural characterization (XRD)

The XRD patterns (**Fig. 3.17 a**) of the zoom NH_3 composites exhibit the main characteristic diffraction peaks at 2θ = 25.2° corresponding to the anatase phase of TiO_2, indexed as (101) diffraction plane. In the 27 – 28° region (**Fig. 3.17 b**) TiO_2-gC_3N_4 (95-5) does not present any XRD peak neither from TiO_2 rutile nor from g-C_3N_4 interlayer stacking.

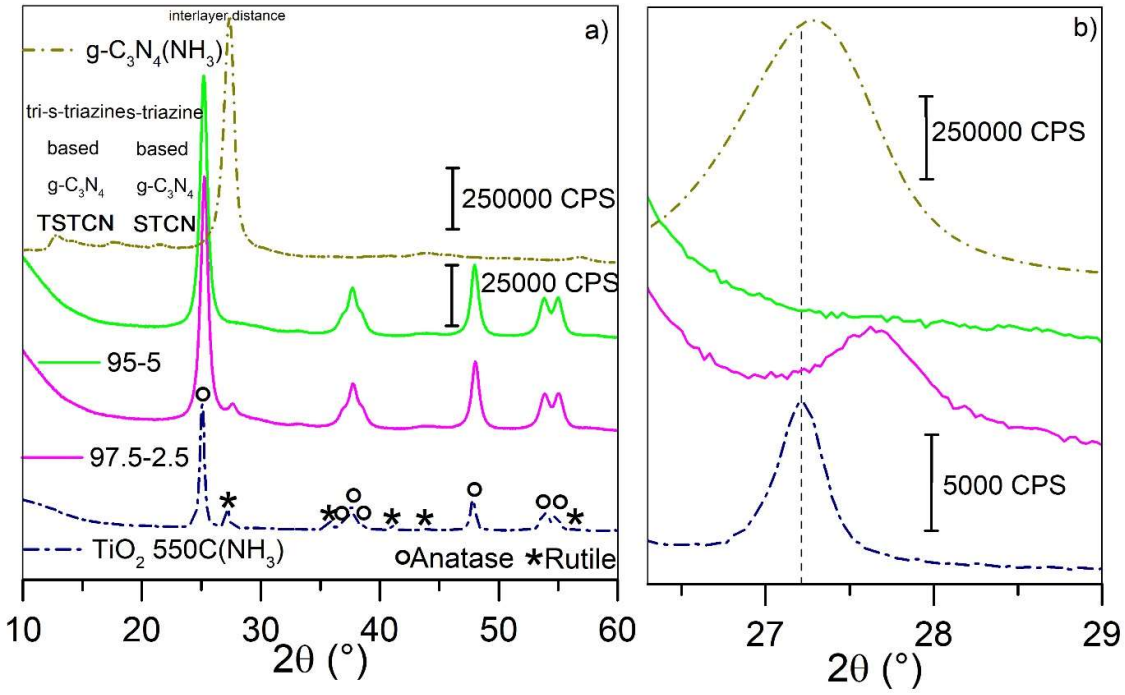

Figure 3.17. a) General XRD patterns b) zoom of the (26-29°) region of the TiO_2-g-C_3N_4-NH_3 zoom composites and references.

In the case of TiO_2-gC_3N_4 (97.5-2.5) material, the diffraction peak located at *ca.* 27.5° is not easy to assign to TiO_2 rutile phase indexed as (110) plane. However, due to the very low content of g-C_3N_4, it is not related to g-C_3N_4 crystallites; it can thus be assumed that it corresponds to TiO_2 rutile (shifted).

By using Debye-Scherrer relationship, it is thus possible to determine the mean crystallite size (**Table 3.7**) by using the respective fitted peaks. One can notice a significant difference in the two zoom composites looking at the anatase crystallite size, with a significant decrease in anatase mean crystallite size of 10 nm (TiO_2-gC_3N_4 (95-5)) compared to the bare TiO2 (P25) (24 ± 1 nm). One can mention that this tendency was not observed with the TiO_2-gC_3N_4 NH_3 screening composites (**Table 3.5**) neither with the TiO_2-gC_3N_4 Air zoom composites, meaning that this effect is particularly present at low g-C_3N_4 content (≤ 5 wt. %) NH_3 composites.

It must also be mentioned that drastic diminution of TiO_2 crystallite size has already been observed in other study dealing with grinding preparation methods as the result of rigorous solid grinding between TiO_2 and g-C_3N_4 for the obtainment of TiO_2-gC_3N_4 composites with low g-C_3N_4 amount ((≤ 5 wt. %) (in high quality interaction with TiO_2) [9], and was attributed to the abrasive effect brought by the presence of small amounts of g-C_3N_4, which has already been compared with a similar hardness than diamond [23]. However, to the best of our knowledge, nothing is known about the hardness of g-C_3N_4 synthesized under pure NH_3 atmosphere, meaning that our assumption is pure speculation.

Table 3.12. Mean crystallite size of the crystalline phases of the TiO_2-gC_3N_4-NH_3 zoom composites, references and graphitic domain of g-C_3N_4.

Sample	Mean crystallite size (nm)		
	Anatase (101)	Rutile (110)	g-C_3N_4 (002)
TiO_2 550C(NH_3)	18±1	24±1	-
97.5-2.5	12±1	14±1	-
95-5	10±1	n.f.	-
g-C_3N_4(NH_3)	-	-	8.4±0.4

n.f. = not found

B.2.2.2.d) BET surface area measurements

From BET measurements (**Table 3.9, Fig. 3.18 a**), it can be observed that all zoom NH_3 composites, in addition of references, exhibit a type-IV adsorption-desorption isotherm profile, which is in a good agreement with mesoporous materials features [19–21]. Concerning, the S_{BET} obtained values, apart from g-C_3N_4 reference (32 m^2 g^{-1}) all the other three samples do not present a significant difference, ranging from 48 to 56 m^2 g^{-1}, confirming that the two zoom composites exhibit surface areas closer than TiO_2, as expected, since g-C_3N_4 content is very low, ca. ≤ 5 wt.%.

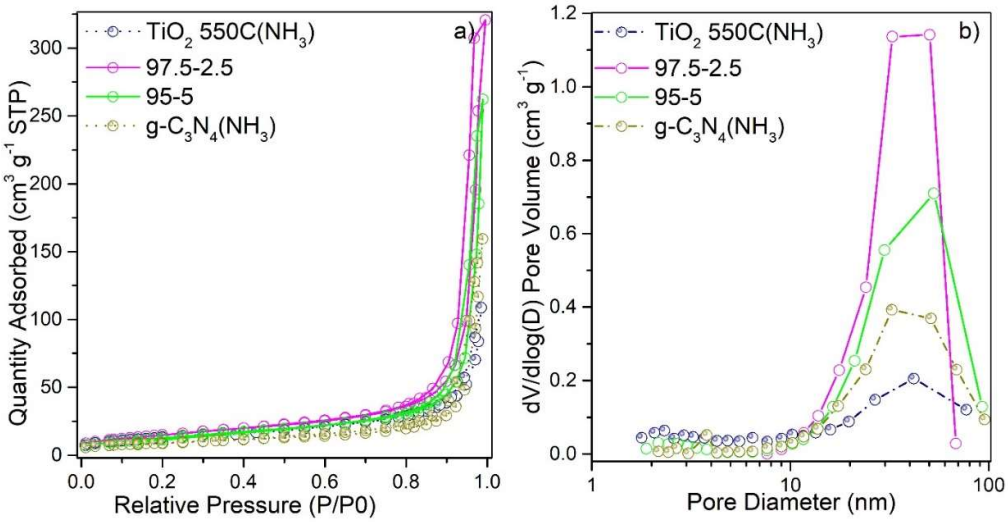

Figure 3.18. a) Nitrogen adsorption-desorption isotherms b) BJH pore-size distribution of the TiO_2-g-C_3N_4–NH_3 zoom composites and references.

From BJH pore-size distribution (**Table 3.9, Fig. 3.18 b**) one can observe a monomodal type for all samples. The main pore size values vary from 42 nm to 53 nm, with higher volume obtained for the composites compared to the two references. Looking at pore volume, one can say that it is larger for the composites compared to the references, with

the highest volume obtained for TiO_2-gC_3N_4 (97.5-2.5) (*ca.* 1.14 cm^3 g^{-1}). Therefore, one can notice a significant difference between the pore volume of the zoom composites, assuming that introduction of already synthesized TiO_2 increase mesoporous pore volume compared to the references, as it was already observed for the TiO_2-gC_3N_4 Air zoom series.

Table 3.13. Specific surface area (S_{BET}), pore volume (V_{pore}), pore size of the TiO_2-g-C_3N_4–NH_3 zoom composites and references.

g-C_3N_4	S_{BET}* (m^2 g^{-1})	V_{pore} (cm^3 g^{-1})	Pore size** (nm)
TiO_2 550 °C	48±5	0.21±0.02	42±4
97.5-2.5	56±6	1.14±0.04	50±5
95-5	48±5	0.71±0.03	53±5
g-C_3N_4	32±3	0.39±0.02	42±4

* = calculated using BET method; ** = calculated using BJH method

C) Synthesis and characterization of the ternary hybrid Au/TiO_2(P25)-gC_3N_4-atm composites

C.1. Synthesis of ternary Au/TiO_2(P25)-gC_3N_4 atm composites

Au/TiO_2(P25)-gC_3N_4-atm ternary nanocomposites were elaborated using two successive steps: (1) Synthesis of TiO_2(P25)-gC_3N_4 heterojunction (described in section **B**, **Fig. 3.1**) followed by (2) Deposition of Au NPs onto the as-synthesized heterojunction systems (described in **chapter two, section C.1**).

Au loading used in this work is expressed in weight percentage as the first term. For comparison reasons, Au loading was constant for all the materials synthesized to conclude accurately that the differences obtained on hydrogen evolution is only a consequence of the physico chemical differences due to the proportion between gC_3N_4 and TiO_2 within the composites and/or to the synthesis atmosphere. Therefore, the **0.3 wt. %** value was chosen according to previous studies [8,24–27] in the team and in literature. The second and third terms are associated with the relative mass content of each SC. All in all, the first parametric study (for a given atmosphere) was dedicated to the influence of the relative mass ratio between both SCs.

C.2. Characterization of Au/TiO_2(P25)-gC_3N_4

For the characterizations of Au/TiO_2(P25)-gC_3N_4-atm composites, the same classification presented for section **B.3** based on atmosphere used (Air and NH_3) and by method applied (screening and zoom, **Fig. 3.2**) are used in this section. The following section will introduce Au/TiO_2(P25)-g-C_3N_4-atm composites characterizations using techniques such as ICP-AES, TEM, and UV-Vis measurements.

C.2.1. Characterizations of Au/TiO_2(P25)-gC_3N_4-Air

C.2.1.1. Screening method (Air)

C.2.1.1.a) Elemental analysis

The deposition yield (**Table 3.10**) achieves *ca.* 75 % for all the Au/TiO_2(P25)-gC_3N_4-Air screening composites, lower than on the g-C_3N_4 reference. This result confirms the well use of Au NPs deposition via chemical reduction method for this type of support materials. Moreover, the small difference in the deposition yield guarantees a close Au NPs content, which enables to compare fairly the photocatalytic H_2 production, independently of the Au loading. However, it must be mentioned that the highest yield deposition was obtained for g-C_3N_4 surface.

Table 3.14. ICP-AES results of the Au/TiO_2(P25)-gC_3N_4-Air screening composites and references.

Sample	Dep. Yield (%)	Au content (wt. %)
Bare TiO_2	76±4	0.23±0.01
TiO_2 550C(Air)	72±4	0.22±0.01
70-30	73±4	0.22±0.01
52-48	71±4	0.21±0.01
30-70	75±4	0.23±0.01
g-C_3N_4(Air)	82±4	0.25±0.01

C.2.1.1.b) TEM characterization

TEM images (**Fig. 3.19**) show three samples, Au/Bare TiO_2 (P25) (**a, b**), Au/TiO_2 550 °C (Air) (**c, d**), and Au/TiO_2-gC_3N_4 (30-70) (**e, f**). TEM micrographs exhibit Au NPs round shaped, slightly agglomerated and well dispersed in all samples. In terms of Au NPs coverage and dispersion, it differs from sample to sample due to the support nature.

Compared to Au/TiO_2 references, the Au/TiO_2-gC_3N_4 (30-70) exhibits the smallest Au NP mean size (2.7 nm) associated with the smallest standard deviation (0.8 nm). It is thus possible to observe dense regions, well covered by Au NPs (**Fig. 3.19 f**) that might be related with the high g-C_3N_4 content and to higher affinity of Au NPs deposition, compared to the Au/TiO_2 550 °C and Au/Bare TiO_2 (P25) (Air) references with only TiO_2 surfaces. One can notice the TiO_2 crystalline planes on the two references TEM images (**a, c**). For the Au/g-C_3N_4 TEM images, please referred **chapter 2 section C 2.2**, where they were already analysed and discussed, with Au NPs mean size of 3.2 nm.

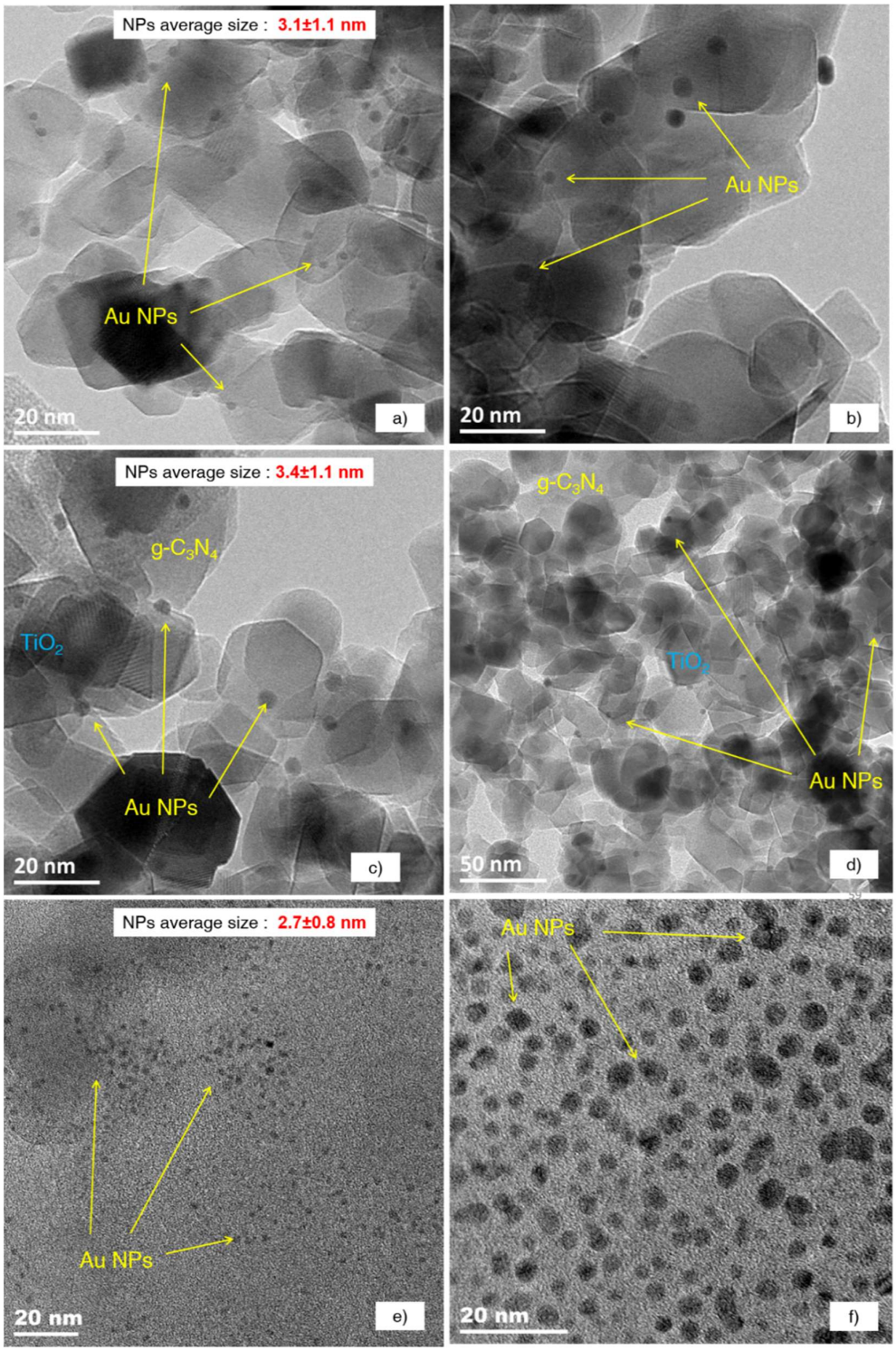

Figure 3.19. TEM images for Au/ TiO_2-gC_3N_4-Air screening composite and references, including the mean particle size with their corresponding standard deviation, a, b) 0.3 wt. % Au/Bare TiO_2 (P25), c, d) 0.3 wt. % Au/TiO_2 550 °C Air, e, f) 0.3 wt. % Au/ TiO_2-gC_3N_4 (30-70).

C.2.1.1.c) UV-Vis absorption properties

Fig. 3.20 (top) presents the color of TiO_2-gC_3N_4-Air screening composites and references after synthesis and treatment at 550 °C. One can notice the diverse range of colors obtained as function of the g-C_3N_4 content. The three screening composites present a yellowish tones, but not as sharp as for g-C_3N_4 reference.

From the UV-vis spectra (**Fig. 3.20 a**), one can observe that all the screening composites exhibit a maximum absorption in the UV/blue range of the spectra, with an absorption band edge at 450-460 nm, characteristic for g-C_3N_4 semiconductors [28–31], and attributed to $\pi \rightarrow \pi^*$ electronic transitions [11] found in π-conjugated systems of TST and ST units. A second contribution with a maximum located at *ca.* 550 nm is ascribed to the presence of Surface Plasmon Induced Effect (SPIE) of Au NPs. Nevertheless, **Fig. 3.20 a (inset)** shows that the SPIE absorption is quite weak for Au/g-C_3N_4, more pronounced for Au/TiO_2-gC_3N_4 (70-30 and 30-70) compared to Au/TiO_2, and overlapped with Au/TiO_2-gC_3N_4 (52-48) absorption signal. For the weak SPIE signal, it might mean that perhaps not all the surface of the Au NP is exposed a part of it may be located inside of the pores of the mesoporous g-C_3N_4. On the other hand, for the pronounced SPIE signal the Au NPs might be more exposed onto the crystalline TiO_2 surface favouring their exposure-excitation, therefore resonating more easily. Lastly, the overlapped SPIE signal might be due to the additional band tail, presumably resulting from the occurrence of additional $n \rightarrow \pi^*$ electronic transition, which may be attributed to the pronounced layer deformation on g-C_3N_4 formed as described elsewhere [11]. One can also observe that in the case of the composites an important part of TiO_2 absorption is by overlapped by gC_3N_4 absorption.

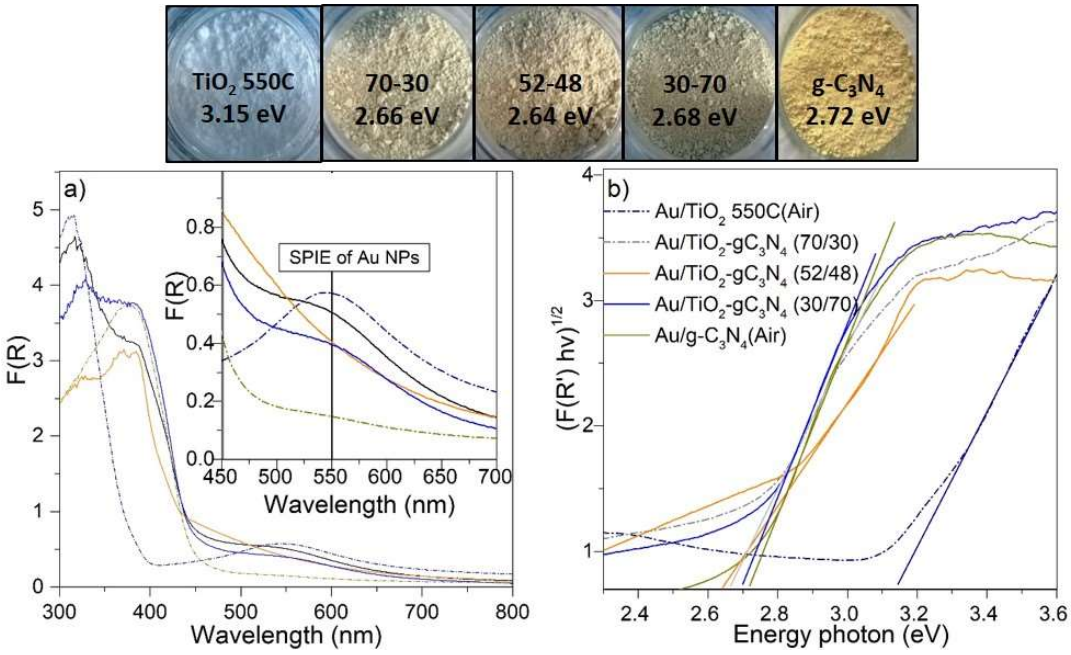

Figure 3.20. a) UV-Vis spectra of Au/TiO_2-gC_3N_4-Air screening composites and references Inset) zoom of the spectral domain corresponding to SPIE signal of Au NPS at approximately 550 nm.

b) Tauc plot to determine the apparent band gap of Au/TiO_2-gC_3N_4-Air screening composites and references.

From the band-gap determination (**Fig. 3.20 b**) calculated using Tauc equation [32], one can observe that the TiO_2-gC_3N_4 (52-48) and TiO_2 550 °C (Air) photocatalysts present the lowest (2.64 eV) and the largest (3.15 eV) band-gap, respectively.

C.2.1.2. Zoom method (Air)

C.2.1.2.a) Elemental analysis

Like previously, in case of the higher loaded gC_3N_4 samples, the deposition yields (**Table 3.11**) reach *ca.* 70-80 % for all the Au/TiO_2(P25)-gC_3N_4 Air zoom composites. It must be mentioned that the Au deposition yield is higher for the gC_3N_4-containing samples compared to the reference TiO_2 550C (Air).The small differences on the deposition yield on the samples leading to small variations on Au content ensure to fairly compare the photocatalytic H_2 production at same Au content.

Table 3.15. ICP-AES results of Au/TiO_2(P25)-gC_3N_4-Air zoom composites and references.

Sample	Dep. Yield (%)	Au content (wt. %)
TiO_2 550C (Air)	72±4	0.22±0.01
97.5-2.5	68±4	0.20±0.01
95-5	84±5	0.25±0.01
90-10	76±4	0.23±0.01
g-C_3N_4(Air)	82±4	0.25±0.01

C.2.1.2.b) TEM, PSD, and mapping characterization

TEM images (**Fig. 3.21**) show two samples, Au/TiO_2 550 °C (Air) (**a, b, c**), and Au/TiO_2-gC_3N_4 (95-5) (**d, e, f**). The two samples exhibit the exactly same Au NP mean size (3.4 nm) and its standard deviation (1.1 nm). This result suggest that the small content on g-C_3N_4 (5 wt. %) do not impact the Au NPs mean particle size distribution compared to Au/TiO_2.

Moreover, the obtained Au NPs deposition coverage onto Au/TiO_2-gC_3N_4 (95-5) composite does not greatly change the final Au NPs size compared to TiO_2 550 ° (Air), even though this reference have been submitted to the same heating treatment.

From **Fig. 3.21 f)** it can be observed a similar value for TiO_2 anatase d-space on both Au/TiO_2 550°C (Air) reference and Au/ TiO_2-gC_3N_4 (95-5) composite compared to theoretical value for anatase TiO_2 *ca.* 0.3562 nm.

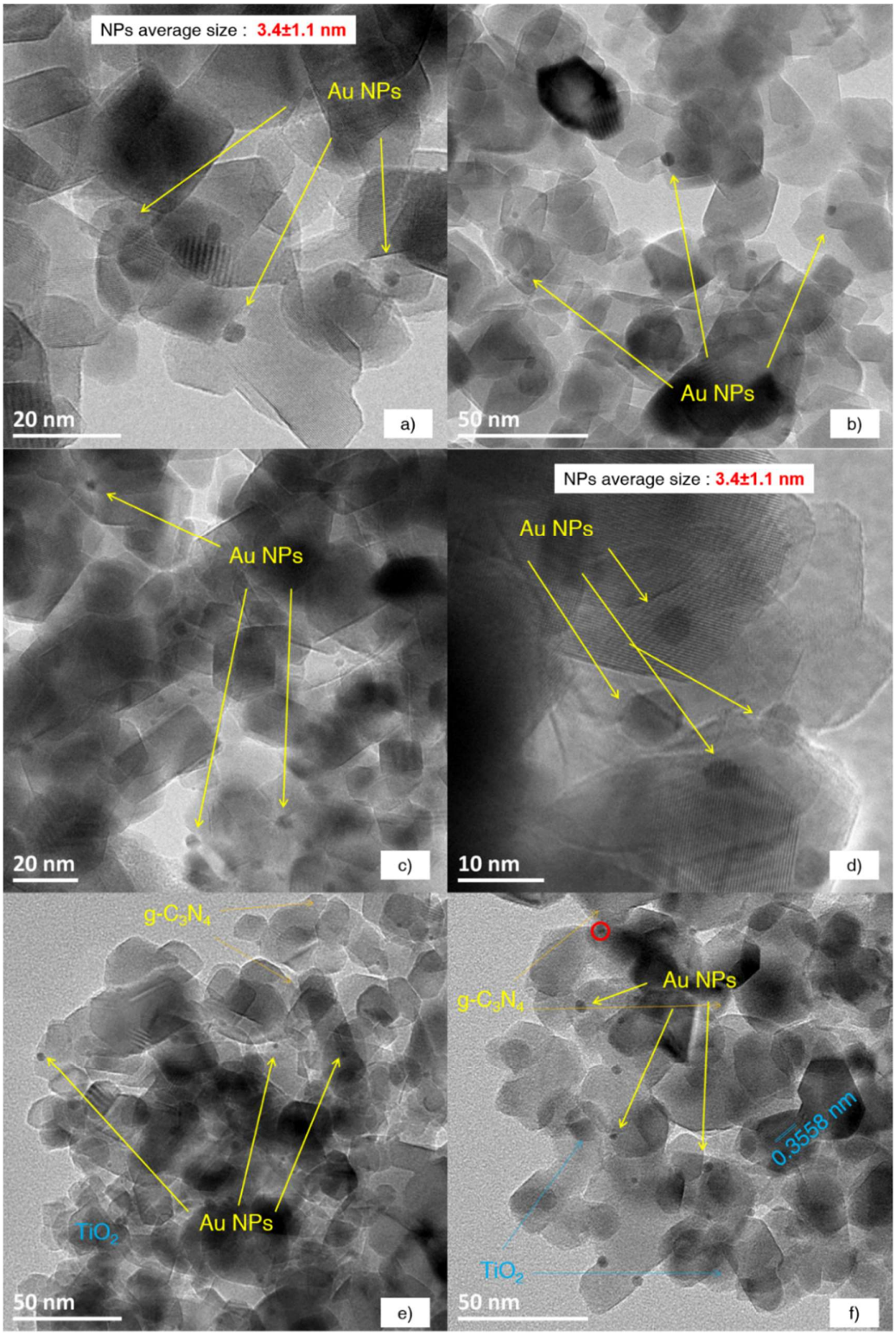

Figure 3.21. TEM images for Au/TiO_2-gC_3N_4 Air zoom composite and reference, including the mean particle size with their corresponding standard deviation, a, b, c) 0.3 wt. % Au/TiO_2 550 °C (Air), d, e, f) 0.3 wt. % Au/ TiO_2-gC_3N_4 (95-5).

From the particle size distribution (**Fig. 3.22**) of the zoom composites Air (compared to the higher g-C_3N_4 loaded Au/ TiO_2-gC_3N_4 (30-70) composite) and to the references, one can notice that all the samples exhibit a monomodal distribution with the exception of Au/g-C_3N_4 reference that displays rather a quasi-bimodal distribution with local maxima at 3.5 and 6.5 nm. For Au/TiO_2-gC_3N_4 (30-70) composite, a maximum at 2.7 nm is obtained, meaning that there is a predominant population of small Au NPs size. This sample also presents the smallest standard deviation (0.8 nm), which at the same time means more homogeneous coverage of NPs over the surface support. This sample is characteristic for having the highest g-C_3N_4 content amongst the Au/TiO_2-gC_3N_4 (Air) composites.

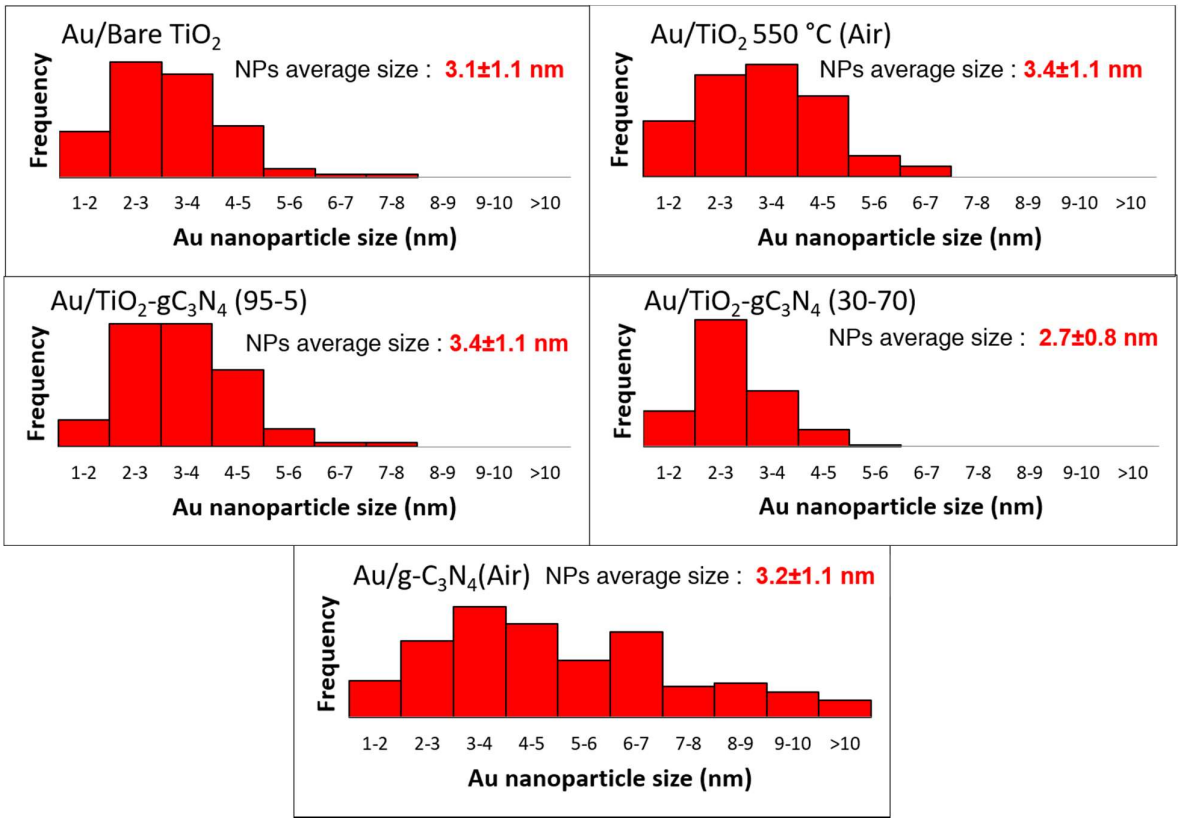

Figure 3.22. Particle size distribution of screening and zoom composites and references synthesized under air atmosphere obtained by TEM (100-200 NPs for sample).

The Selected Area Electron Diffraction (SAED) pattern of Au/ TiO_2-gC_3N_4 (95-5) are shown in **Fig. 3.23**. One can notice that the distribution varies from element to element, the most present atom is C (red), which is the most abundant and well dispersed among all. Then, Ti (purple) and O (yellow) exhibit an intermediate density, but N (green) exhibit a more attenuated presence in comparison with Ti and O. Lastly, the least present atom is Au, as expected. Elemental ratio (**Fig. A.2, appendix 3**) exhibit 0.25 wt. % Au, which is the same result exhibited by ICP-AES (attributed to 84% of deposition yield of Au NPs onto the support), meaning that both techniques are effectively comparable in quantitative terms for the Au element case.

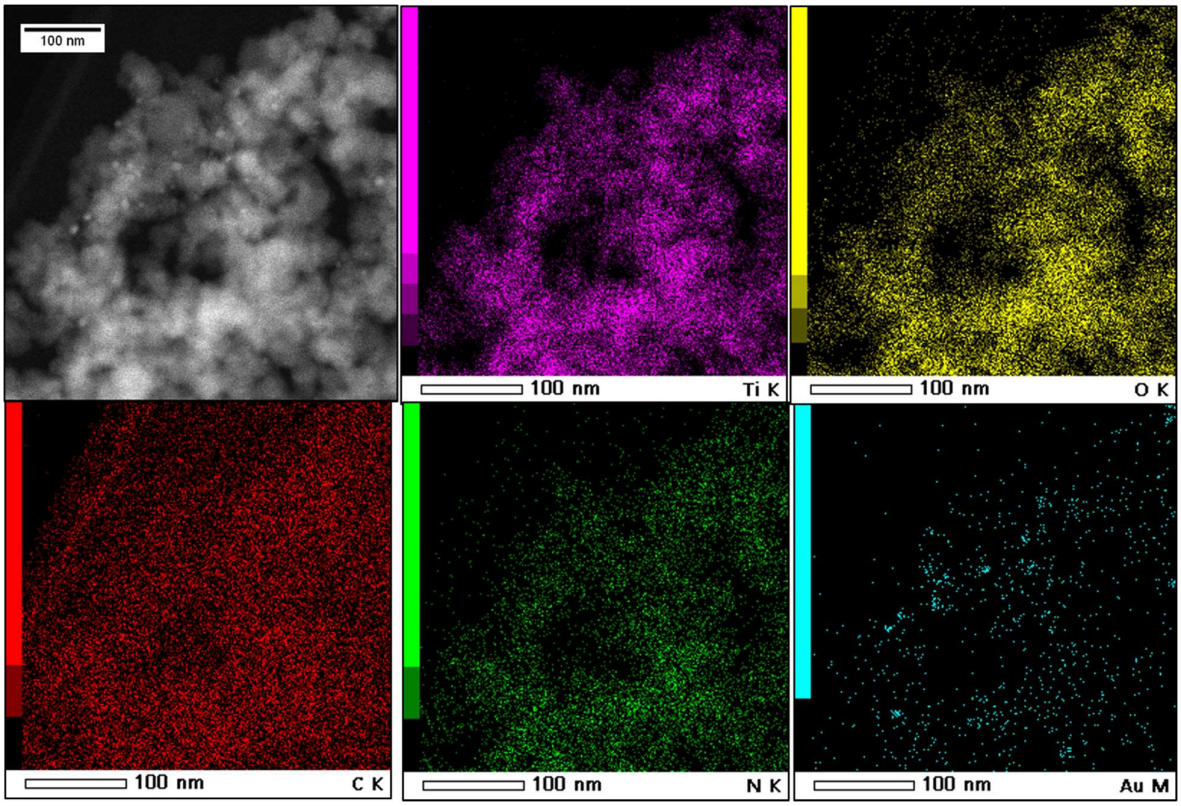

Figure 3.23. SAED mapping of 0.3%. wt Au/TiO_2(P25)-gC_3N_4 (95-5) composite with the localized elements distribution.

C.2.1.2.c) UV-Vis absorption properties

Fig. 3.24 (top) exhibits the color of TiO_2-gC_3N_4-Air zoom composites and references. The three zoom composites are white, likewise TiO_2 550 °C reference.

UV-vis spectra (**Fig. 3.24 a**) show that all zoom composites exhibit a maximum absorption in the UV/blue range of the spectra (band edge at 386 nm) characteristic for TiO_2. It must however been mentioned that the absorption edge is slightly red-shifted for the zoom composites. A second contribution with a maximum located at *ca.* 550 nm is attributed to SPIE of Au NPs. Thus, **Fig. 3.24 a (inset)**, shows that the SPIE absorption is pronounced for all zoom composites as for the TiO_2 550 °C (Air) except for the weak g-C_3N_4 SPIE, already seen in the screening composites series.

From the obtained band-gap values obtained (**Fig. 3.24 b**) by Tauc equation [32], one can notice that g-C_3N_4 (Air) and TiO_2 550 °C (Air) references present the lowest (2.70 eV) and the largest (3.15 eV) band-gap, respectively. For the three zoom composites their band gap are in between the references values but closer to TiO_2, due to the lowest g-C_3N_4 content compared to the screening composites.

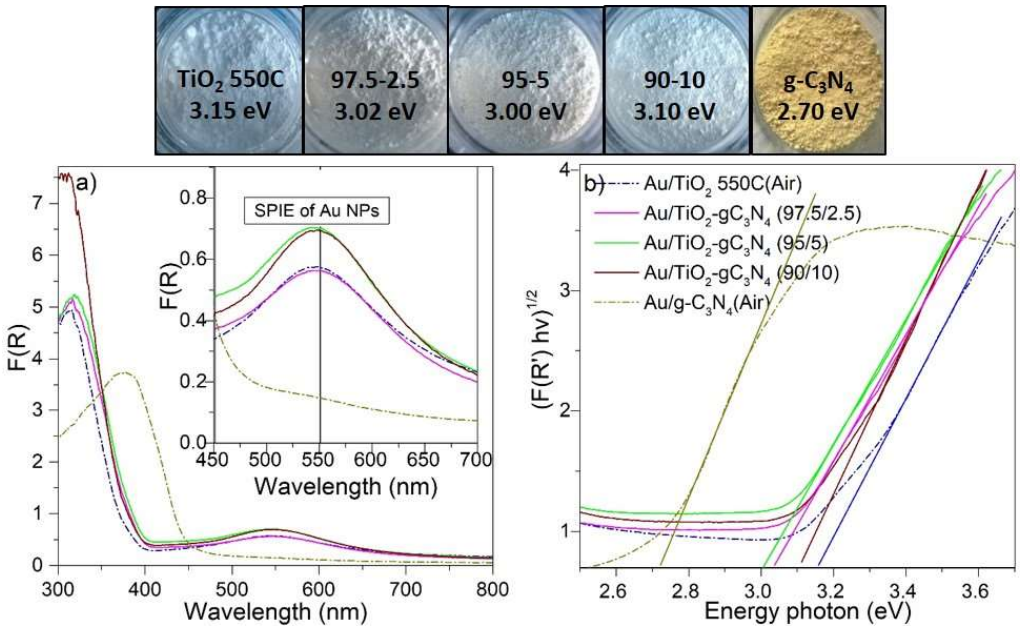

Figure 3.24. a) UV-Vis spectra of Au/TiO_2-gC_3N_4-Air zoom composites and references Inset) zoom of the spectral domain corresponding to SPIE signal of Au NPS at approximately 550 nm b) Tauc plot to determine the apparent band gap of Au/TiO_2-g-C_3N_4-Air zoom composites.

C.2.2. Characterization of Au/TiO_2(P25)-gC_3N_4-NH_3

C.2.2.1. Screening method (NH_3)

C.2.2.1.a) Elemental analysis

The deposition yield (**Table 3.12**) achieve *ca.* 78 % for all the Au/TiO_2(P25)-gC_3N_4 NH_3 screening composites, lower than the g-C_3N_4 reference but higher than the TiO_2 reference. Those observations have already been done on the Air composites, evidencing that Au NPs deposition is favored onto g-C_3N_4 surfaces. Yet, this slight difference on Au NPs deposition on the samples, might not interfere in the comparison of the photocatalytic H_2 production of the materials since it is small variation on Au content, from 0.23 to 0.27 wt. %.

Table 3.16. ICP-AES results of Au/TiO_2(P25)-g-C_3N_4-NH_3 screening composites and references.

Sample	Dep. Yield (%)	Au content (wt. %)
TiO_2 550C(NH_3)	73±4	0.22±0.01
73-27	78±4	0.23±0.01
48-52	76±4	0.23±0.01
23-77	78±4	0.23±0.01
g-C_3N_4(NH_3)	89±5	0.27±0.01

C.2.2.1.b) TEM characterization

TEM images (**Fig. 3.25**) show the example of two samples, the reference Au/TiO_2 550 °C (NH_3) (**a, b, c**) compared to Au/TiO_2-gC_3N_4 (23-77) (**d, e, f**). As referred from all air composites (screening and zoom), TEM micrographs of NH_3 composites also exhibit Au NPs round shaped. Au NPs coverage and dispersion aspects differs from sample to sample in function of the support nature.

The Au/TiO_2-gC_3N_4 (23-77) (NH_3) exhibit the smallest Au NP mean size (2.7 nm) associated with the smallest standard deviation (1.0 nm). The reference (Au/TiO_2 550 °C (NH_3)) show larger mean particles size (5.1 nm), but more importantly with larger standard deviation (1.7 nm), resulting from a contribution of small population of larger Au NPs. Besides, as already mentioned, g-C_3N_4 seems to present a higher affinity toward Au NPs deposition via chemical reduction. One cannot exclude a positive synergy effect between the two SCs since there are Au NPs deposited simultaneously onto both SCs surfaces and maybe also at their interface. For the Au/g-C_3N_4 TEM images, please refer to **chapter 2 section C 2.2**, where they were already analysed and discussed.

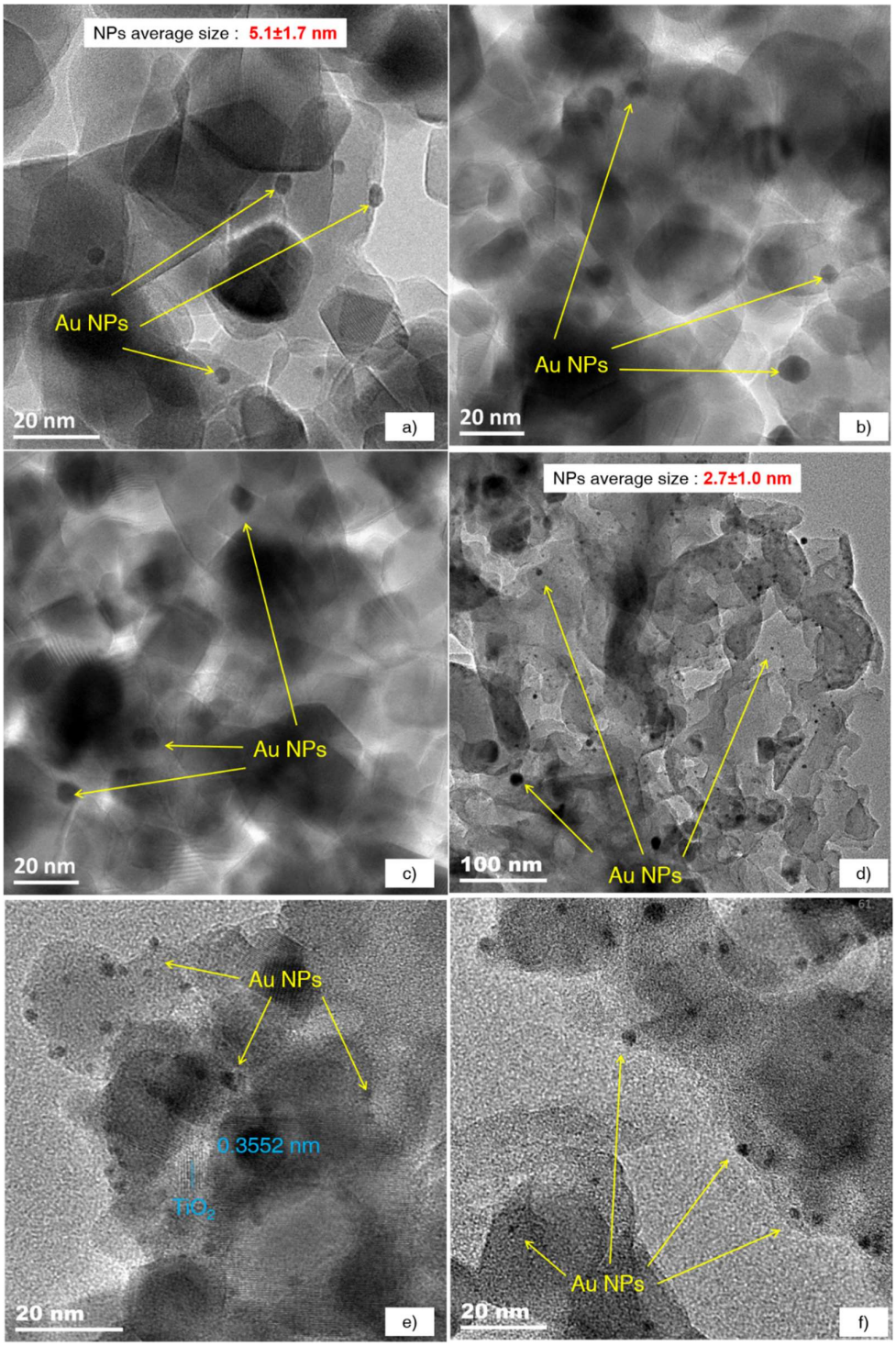

Figure d.3.25. TEM images for Au/TiO_2-gC_3N_4-NH_3 screening composite and reference, including the mean particle size with their correspondent standard deviation, a, b, c) 0.3 wt. % Au/TiO_2 550 °C (NH_3), d, e, f) 0.3 wt. % Au/TiO_2-gC_3N_4 (23-77).

C.2.2.1.c) UV-Vis absorption properties

Fig. 3.26 (top) presents the color of TiO_2-gC_3N_4-Air screening composites and references after synthesis at 550 °C under NH_3. It can be observed a variation of colors as function on the g-C_3N_4 content. The three screening composites present a light brownish color as an evidence that formation of g-C_3N_4 took place but also, resulting from the dilution effect compared to g-C_3N_4 reference (yellow).

From the UV-vis spectra (**Fig. 3.26 a**), the same observations (than the ones obtained on screening composites Air samples) can be made concerning an absorption band edge at 450-460 nm, characteristic for g-C_3N_4 semiconductors [28–31], attributed to $\pi \rightarrow \pi^*$ electronic transitions [11] found in π-conjugated systems of TST and ST units. One can notice an additional contribution at higher wavelengths for all the screening composites but much more pronounced for TiO_2-gC_3N_4 (48-52), which might be possibly associated with N-doped TiO_2 [33,34] or with vacancies-containing TiO_2 (Ti^{4+} reduction to Ti^{3+}) [35], as it will be evidenced further in the XPS section (**E.1**). However, this contribution is not evidenced on the Au/TiO_2 550°C (NH_3) reference. A second contribution with a maximum located at *ca.* 550 nm is ascribed to the presence of SPIE of Au NPs. Nevertheless, **Fig. 3.26 a (inset)**, shows that the SPIE absorption is not as pronounced as for Au/TiO_2 550°C (NH_3). Due to a gentle additional band tail on the screening composites in less or more extend, the SPIE signal may be overlapped. From band-gap values obtained (**Fig. 3.26 b**) by Tauc equation [32], one can observe that amongst the composite samples the TiO_2-gC_3N_4 (23-77) present the lowest one (2.80 eV).

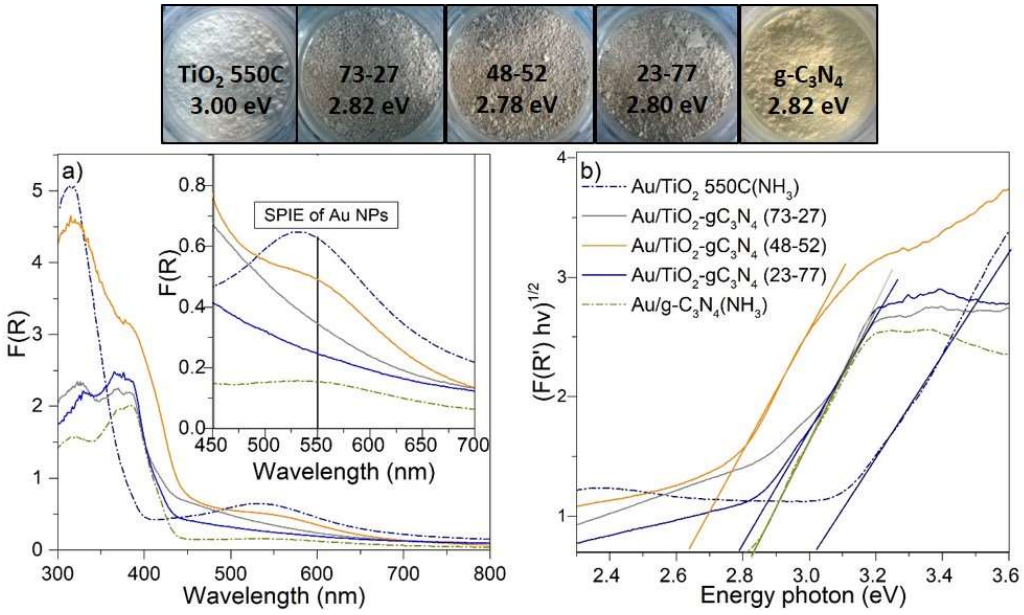

Figure 3.26. a) UV-Vis spectra of Au/TiO_2-g-C_3N_4-NH_3 screening composites and references. Inset) zoom of the spectral domain corresponding to SPIE signal of Au NPS at approximately 550 nm. b) Tauc plot to determine the apparent band gap of the mentioned Au/TiO_2-g-C_3N_4-NH_3 composites and references.

C.2.2.2. Zoom method (NH_3)

C.2.2.2.a) Elemental analysis

The deposition yields (**Table 3.13**) obtained range from 73 to 81 % for the two Au/TiO_2(P25)-gC_3N_4-NH_3 zoom composites and TiO_2 reference and increases along with the g-C_3N_4 content with the highest value obtained, for g-C_3N_4 (NH_3) reference (89 %), confirming the better affinity of Au NPs deposition onto g-C_3N_4 surfaces even more after NH_3 treatment (compared to g-C_3N_4 (Air) reference). Despite of this difference on the Au NPs deposition, it does not influence the fair comparison of the photocatalytic H_2 production of the materials since it represents a small variation on Au content, from 0.23 to 0.27 wt. %.

Table 3.17. ICP-AES results of Au/TiO_2(P25)-gC_3N_4-NH_3 zoom composites and references.

Sample	Dep. Yield (%)	Au content (wt. %)
TiO_2 550C(NH_3)	73±4	0.22±0.01
97.5-2.5	77±4	0.23±0.01
95-5	81±4	0.24±0.01
g-C_3N_4(NH_3)	89±5	0.27±0.01

C.2.2.2.b) TEM and PSD characterization

TEM images (**Fig. 3.27**) show the example of two samples, the reference Au/TiO_2 550 °C (NH_3) (**a, b, c**), and the composite Au/TiO_2-gC_3N_4 (95-5) (**d, e, f**). Regarding Au NPs coverage and dispersion are different due to different supports.

The Au/TiO_2-gC_3N_4 (95-5) exhibit the smallest Au NP mean particle size (4.1 nm) associated with the smallest standard deviation (1.4 nm). The reference sample (Au/TiO_2 550 °C) shows larger mean particles size (5.1 nm), with larger standard deviation (1.7 nm), resulting from a contribution of small population of larger Au NPs, *ca.* ≥ 8 nm. The lower Au NPs size for the composite sample (comprising only 5 wt. % of g-C_3N_4), suggest two possible options, whether a positive synergy effect between the two SCs favoring the smaller size in respect to TiO_2 550 °C (NH_3), or due to the small content on g-C_3N_4 within the composite that greatly impacts the growth of Au NPs of ≤ 5 nm, as it was the case of the main TEM conclusion for chapter 2. For Au/g-C_3N_4 TEM images, please referred **chapter 2 section C 2.2**, where they were already analysed and discussed.

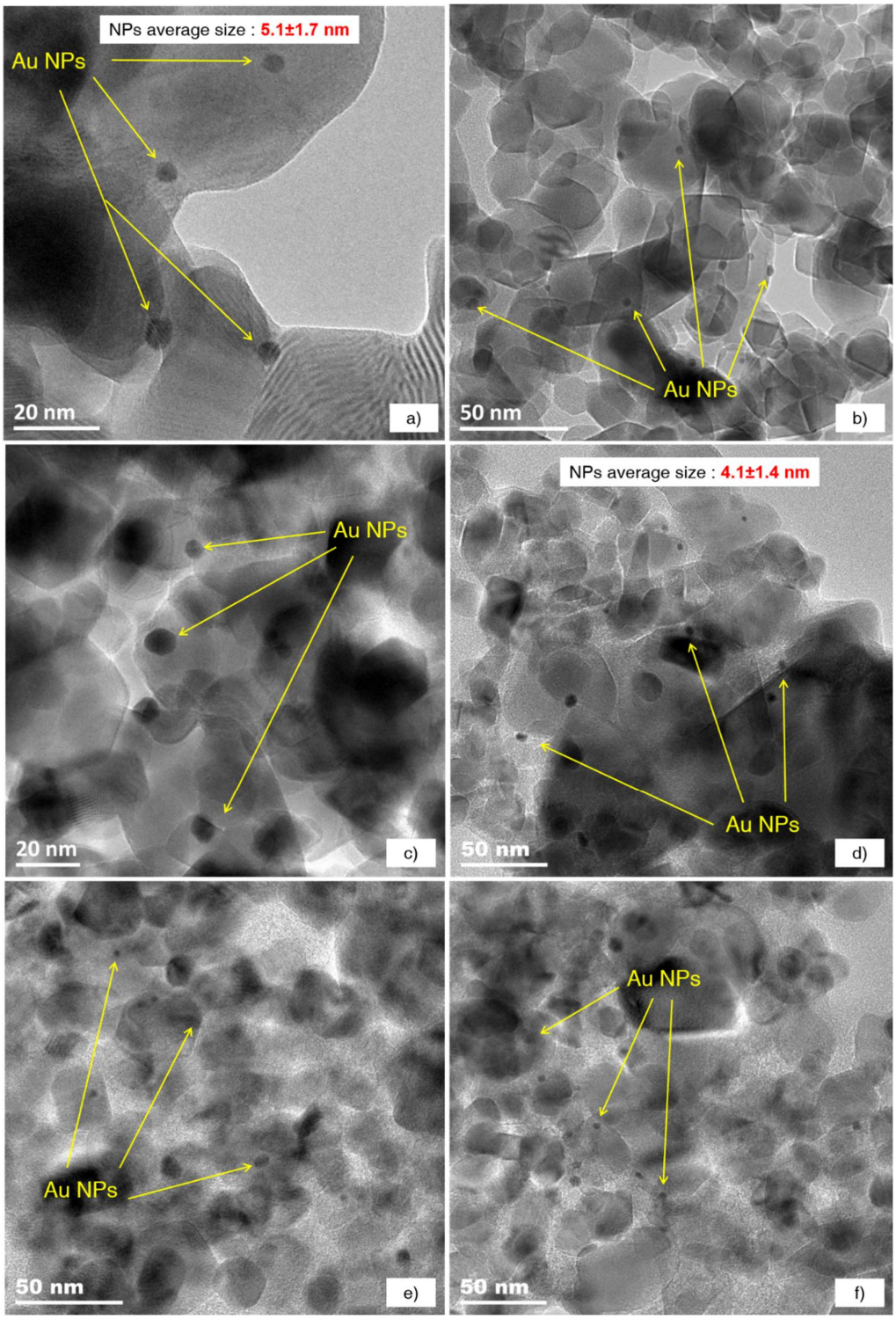

Figure 3.27. TEM images for Au/TiO_2-gC_3N_4-NH_3 zoom composite and reference, including the mean particle size with their correspondent standard deviation, a, b, c) 0.3 wt. % Au/TiO_2 550 °C (NH_3), d, e, f) 0.3 wt. % Au/ TiO_2-gC_3N_4 (95-5).

From the particle size distribution (**Fig. 3.28**), one can notice that all the samples display a monomodal distribution with the exception of Au/TiO_2 550 °C (NH_3) reference that displays a quasi-bimodal distribution with local maxima at 3.5 and 7.5 nm. For Au/TiO_2-gC_3N_4 (23-77) composite belonging to the NH_3 screening composite series, a clear local maximum at 2.7 nm is obtained. Meaning that higher g-C_3N_4 content leads to smaller Au NPs deposition.

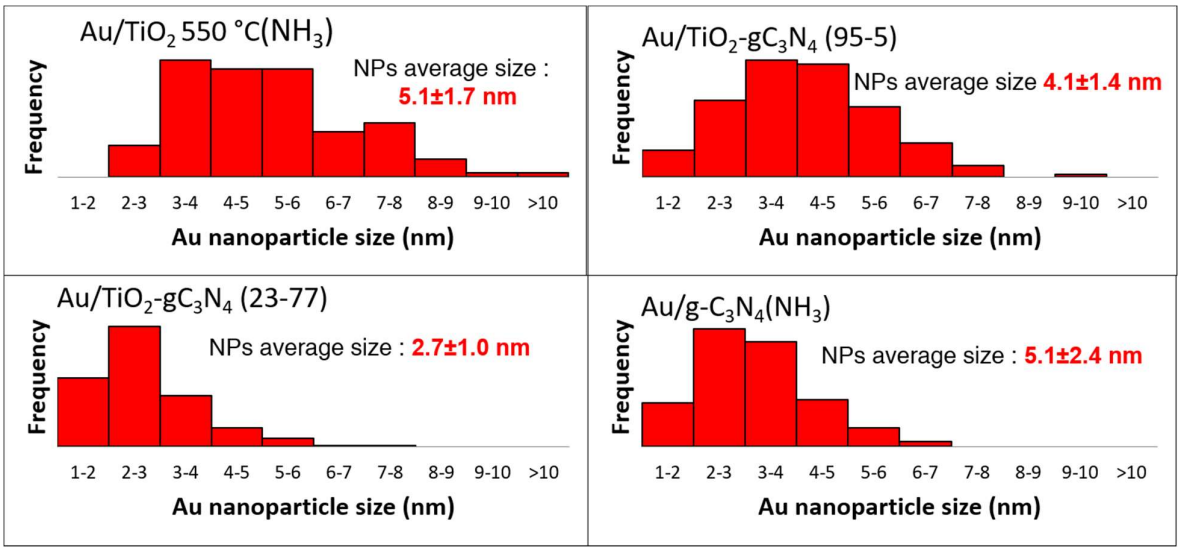

Figure 3.28. Particle size distribution of screening and zoom composites and references synthesized under NH_3 atmosphere obtained by TEM (100-200 NPs for sample).

C.2.2.2.c) UV-Vis absorption properties

Fig. 3.29 (top) presents the color of TiO_2-gC_3N_4 NH_3 screening composites and references. Both zoom composites are yellowish powders, suggesting that the formation of g-C_3N_4 took place during synthesis, despite of the small content of g-C_3N_4 (≤ 5 wt. %).

UV-vis spectra (**Fig. 3.29 a**), for all the screening composites exhibit a maximum absorption precisely at a band edge at 450-460 nm (UV/blue range), characteristic for g-C_3N_4 semiconductors [28–31], ascribed for π→π* transitions [11] typical for π-conjugated systems. Moreover, as it was the case for the NH_3 screening composites series, an additional band tail at higher wavelengths for all the zoom composites is observed, which might be possibly associated with N-doped TiO_2 [33,34] or due to Ti^{4+} reduction to Ti^{3+} [35] under NH_3 atmosphere leading to oxygen vacancies-structure of TiO_2. Another contribution with a maximum located at *ca.* 550 nm is ascribed to the presence of SPIE of Au NPs. Nevertheless, **Fig. 3.29 a (inset)**, shows that the SPIE absorption is quite weak for g-C_3N_4, more pronounced for TiO_2, and slightly overlapped for TiO_2-gC_3N_4 (97.5-2.5 and 95-5). Lastly, the overlap SPIE signal, might be due to the additional band tail, presumably form by the occurrence of additional n→π* electronic transition, which is attributed to the pronounced layer deformation on g-C_3N_4 formed as described elsewhere [11].

From band-gap values obtained (**Fig. 3.29 b**) by Tauc equation [32], one can observe that the presence of low g-C_3N_4 content leads to band gap values close to the one obtained on the reference g-C_3N_4. It must be underlined that this important band gap decrease was not observed for the Au/TiO_2-gC_3N_4 (Air) zoom composite.

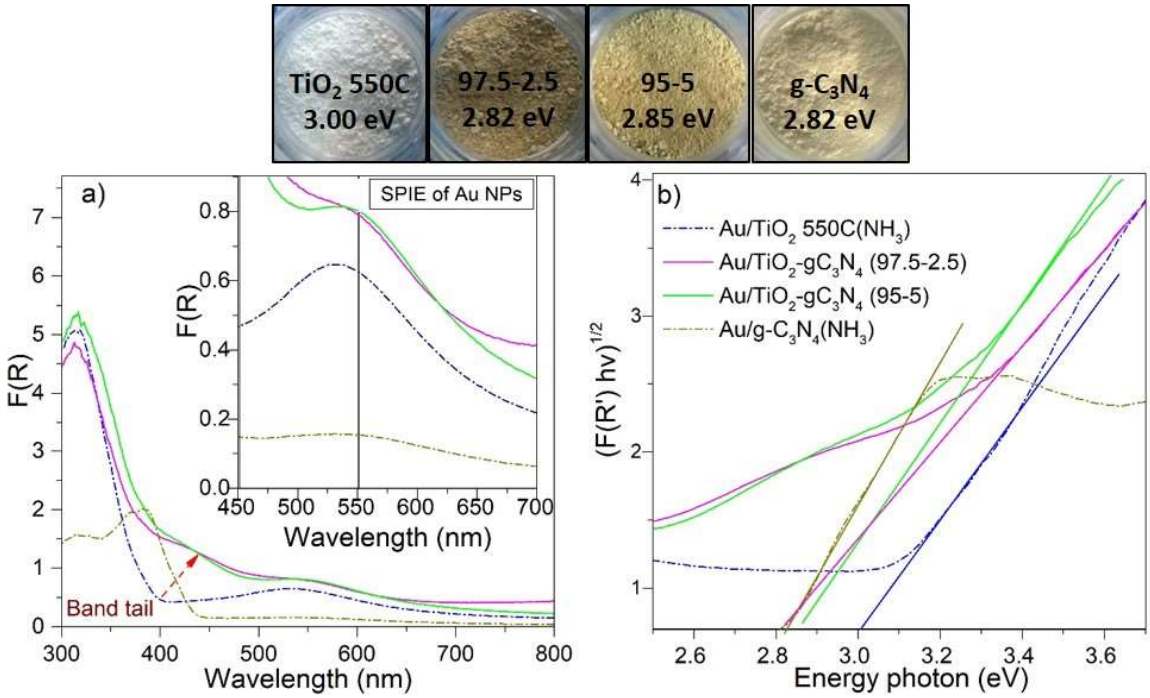

Figure 3.29 a) UV-Vis spectra of Au/TiO_2-g-C_3N_4-NH_3 zoom composites and references. Inset) the spectral domain corresponding to SPIE signal of Au NPS at approximately 550 nm. b) Tauc plot to determine the apparent band gap of Au/TiO_2-g-C_3N_4-NH_3 zoom composites.

D) Photocatalytic performance of Au/TiO_2(P25)-gC_3N_4-atm composites

For the evaluation of the photocatalytic performances of Au/TiO_2(P25)-g-C_3N_4-atm composites, the same classification presented for section **B.3** based on atmosphere used (Air and NH_3) and by method applied (screening and zoom, **Fig. 3.2**) are used in this section. Therefore, the following section will introduce the photocatalytic indicators such as H_2 massic reaction rate (µmol h^{-1} g_{cat}^{-1}), cumulated evolution of hydrogen (µmol), cycling tests for stability studies, and internal quantum yield (%). The photocatalytic H_2 production was acquired by using the photocatalytic set-up already described in **chapter 2** [36]. From the H_2 production rate determined after reaching the plateau of activity under artificial solar-light or visible-light irradiation using TEOA as sacrificial agent, bearing in mind a 10 % relative error on H_2 measurements.

D.1. Photocatalytic performances of Au/TiO_2(P25)-gC_3N_4-Air

D.1.1. Screening method (Air) under solar-light irradiation

From **Fig. 3.30** one can observe that the reference Au/TiO_2 calcined at 550 °C (Air) sample exhibit the highest activity with 1541 H_2 µmol h^{-1} g_{cat}^{-1}. This reaction rate tends to decrease when increasing the g-C_3N_4 content, the Au/g-C_3N_4 (Air) reference sample loading to the lowest activity (producing 41 µmol h^{-1} g_{cat}^{-1}).

Parallely, physical mixtures samples with the same g-C_3N_4 content were tested under the same experimental conditions for comparison. H_2 production rates of the Au/TiO_2-gC_3N_4 physical mixtures, corresponding to the equivalent proportions of 75/25, 50/50, 25/75, exhibited a decay trend yielding 1077, 818, 468 H_2 µmol h^{-1} g_{cat}^{-1}, respectively. One can underline the superiority of the physical mixtures in reference to the screening composites, meaning that the chemical interaction of the two SCs applying the two steps reaction is not beneficial with those tested proportions.

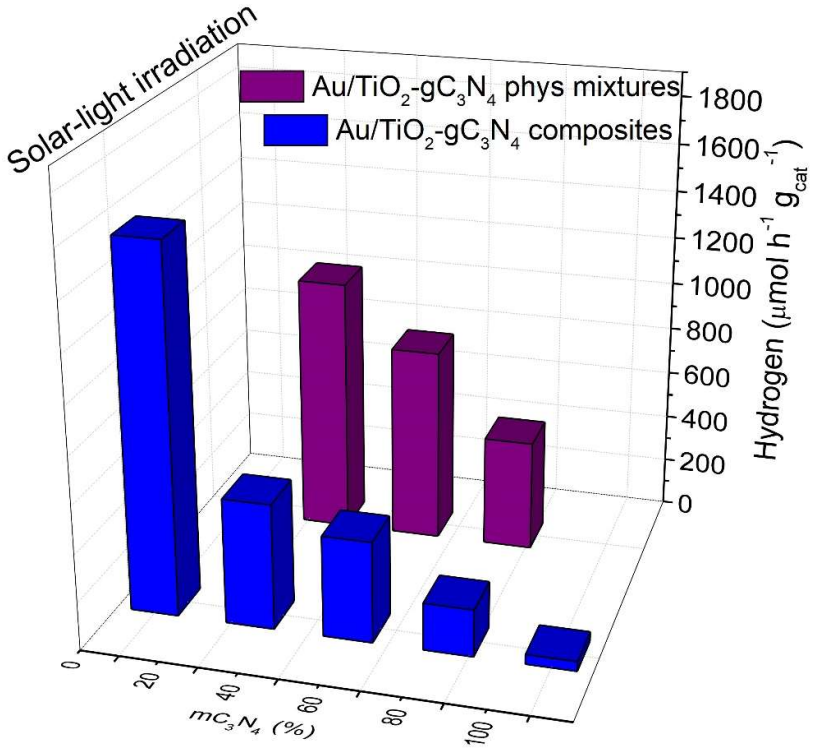

Figure 3.30. Mean hydrogen formation rate per hour and per mass with 1 vol% TEOA of Au/TiO_2-gC_3N_4-Air screening composites and references under solar-light irradiation. Additionally, physical mixtures equivalent to the screening properties composition were added for comparison.

D.1.2. Zoom method (Air) under solar and visible irradiation

From the mean H_2 production (**Fig. 3.31**) obtained for Au/TiO_2-gC_3N_4-Air zoom composite irradiated with artificial solar-light, only one reference was selected (Au/TiO_2 550 °C (Air)), because H_2 formation rate for the reference Au/g-C_3N_4 (Air) was very low in comparison to the magnitudes on H_2 formation obtained for the composites with very

low g-C_3N_4 (high content of TiO_2). One can notice a clear higher H_2 formation rate for Au/TiO_2-gC_3N_4-(95-5) composition in reference to its counterparts with 10 and 2.5 wt. % g-C_3N_4 and to Au/TiO_2 550 °C (Air) reference. Following the same idea applied for the screening method, **the most performant composite (*i.e.* containing 5 wt. % g-C_3N_4)** was compared to a mechanical mixture also containing 5 wt. % g-C_3N_4. In this case one can underline that contrary to the results obtained at higher g-C_3N_4 content (screening method) the synthesized composite with 5 wt. % g-C_3N_4 performs higher than its equivalent physical mixture. Thus, one may assume that lower g-C_3N_4 content leads to higher quality interface between g-C_3N_4 and TiO_2 SCs.

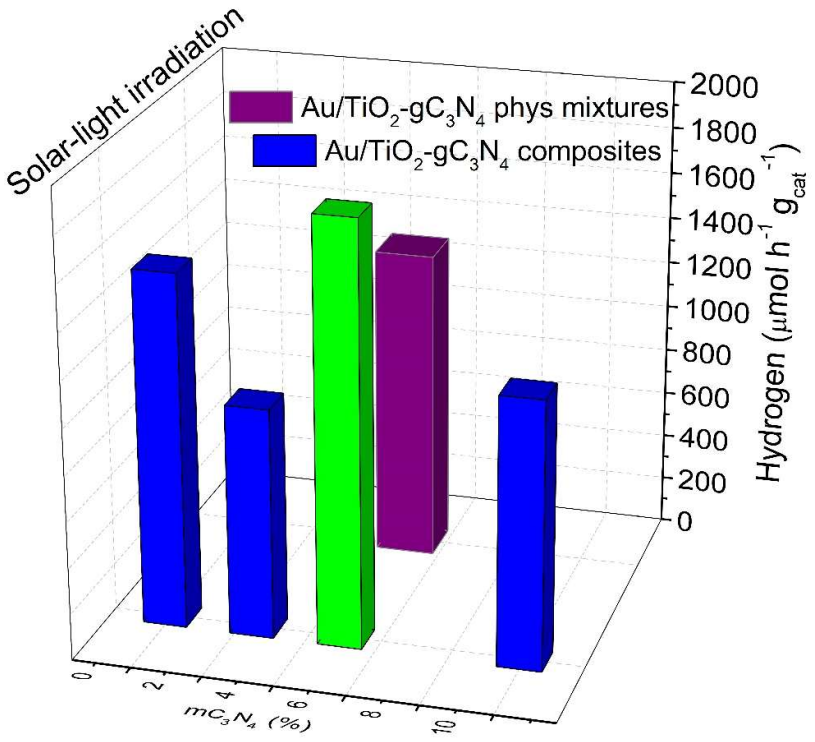

Figure 3.31. Mean hydrogen formation rate per hour and per mass with 1 vol% TEOA of Au/TiO_2-gC_3N_4-Air zoom composites and one reference under solar-light irradiation. Additionally, the physical mixture equivalent to the zoom properties composition of the most performant composite was added for comparison.

Looking further at the interesting photocatalytic performance of Au/TiO_2(P25)-gC_3N_4-(95-5)-Air, several parameters were used to evaluate its photocatalytic activity toward H_2 evolution under solar and visible light irradiation using all the photocatalytic tests mentioned in section **D**, which are shown in this sub-section with the pertinent reference samples treated under the exactly same conditions as referred in **chapter 2, section E**.

D.1.2.1. H_2 massic reaction rate

From the mean H_2 production (**Fig. 3.32**), one can observe the noticeable superiority of **Au/TiO_2-gC_3N_4-(95-5) composite (producing 1839 µmol h^{-1} g_{cat}^{-1})** over Au/Bare TiO_2 (P25), Au/TiO_2 550 °C (Air), Au/TiO_2-gC_3N_4-(95-5) physical mixture, and Au/g-C_3N_4 with differences of 31, 16, 27, 98 %, respectively, irradiated with **artificial solar-light**. This result suggest a synergic effect between the two SCs at this distribution composition (95-5), presumably sufficiently for obtaining either enhanced TiO_2 photosensitization, charge carriers separation and overall photocatalytic activity in comparison with the closest references Au/TiO_2 550 °C (Air) and Au/TiO_2-gC_3N_4-(95-5) physical mixture.

The same trend is found while performing H_2 production test with **artificial visible-light**. One can notice the relative H_2 production increase obtained on **Au/TiO_2-gC_3N_4-(95-5) composite (producing 419 µmol h^{-1} g_{cat}^{-1})** in reference to Au/Bare TiO_2 (P25), Au/TiO_2 550 °C (Air) and Au/TiO_2-gC_3N_4-(95-5) physical mixture (45%, 21%, and 27%, respectively).

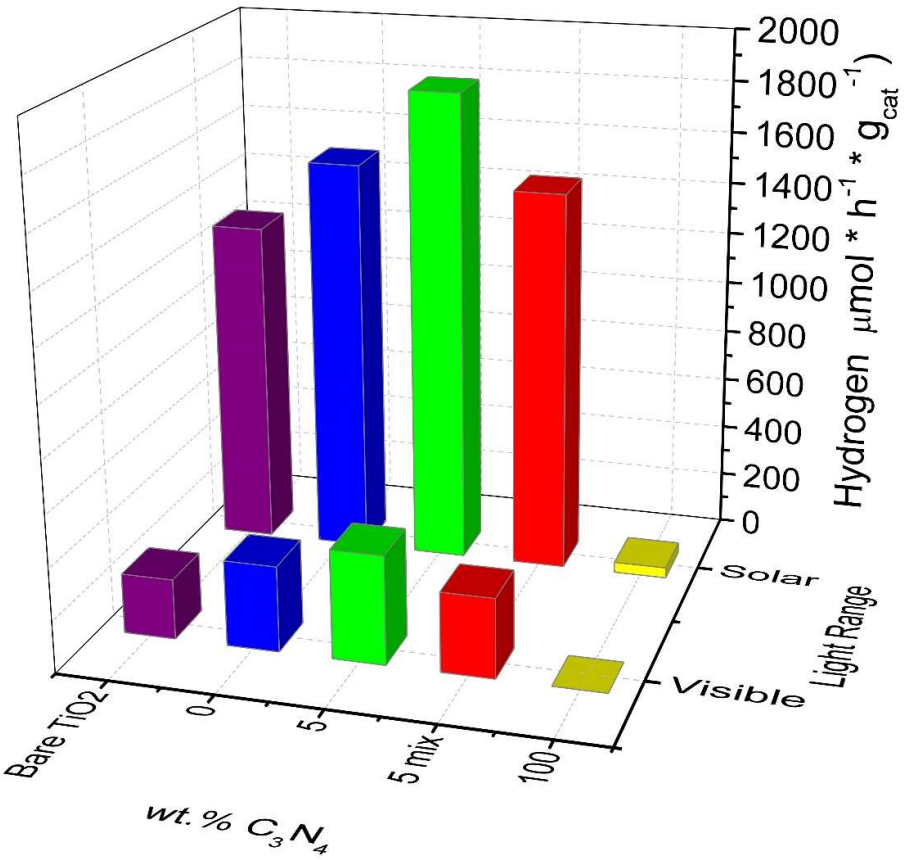

Figure 3.32. Mean hydrogen formation rate per hour and per mass with 1 vol% TEOA of Au/TiO_2-gC_3N_4 (95/5)-Air composite, references, and a physical mixture with the same equivalent massic ratio under solar and visible-light irradiation.

D.1.2.2. Cumulated evolution of hydrogen (µmol)

From the cumulated evolution of hydrogen (**Fig. 3.33**) obtained under solar-light irradiation, one can notice the same trend than for the mean massic hydrogen formation rate. Au/TiO_2(P25)-gC_3N_4-(95-5) composite exhibits the highest cumulated H_2 produced with **978 µmol in only 2.5 h**, corresponding to **21.9 mL of H_2 formed**.

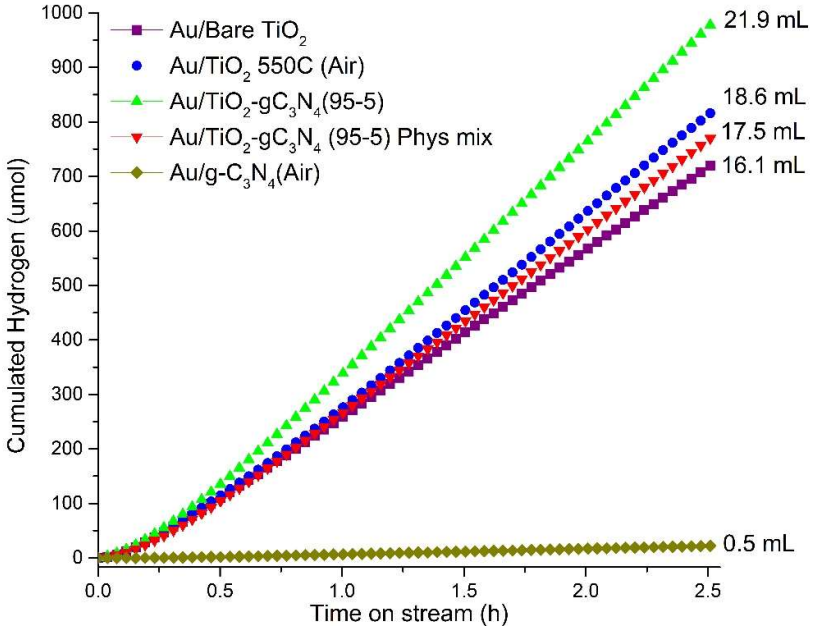

Figure 3.33. Cumulated evolution of hydrogen under solar-light irradiation with 1 vol% TEOA for Au/TiO_2-gC_3N_4 (95/5)-Air composite, three references, and one physical mixture with the same equivalent massic ratio (95-5).

From the cumulated evolution of hydrogen (**Fig. 3.34**) obtained under visible-light irradiation, one can notice the same trend than for the corresponding mean massic hydrogen formation rate. Au/TiO_2-gC_3N_4 (95-5) sample exhibit the highest cumulated H_2 with **224 µmol in only 2.5 h**, corresponding to **5.0 mL of H_2 formed**.

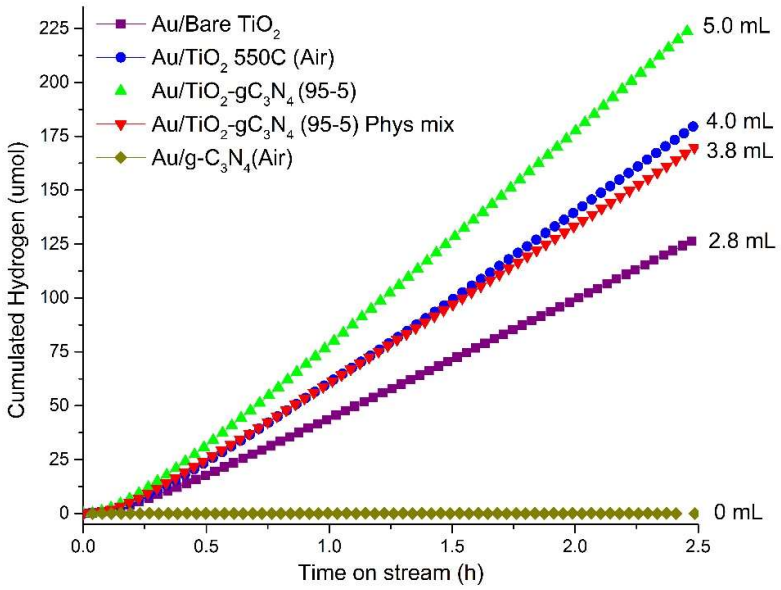

Figure 3.34. Cumulated evolution of hydrogen with 1 vol% TEOA under visible-light irradiation with 1 vol. % TEOA for Au/TiO_2-gC_3N_4 (95/5)-Air composite, three references, and one physical mixture with the same massic ratio (95-5).

D.1.2.3. Cycling tests

From the cycling tests protocol described in **Chapter 2** (**Fig. 3.35**), three cycles have been carried out for the most performant composite (Au/TiO_2-gC_3N_4 (95-5)), and for three references (bare TiO_2(P25) and calcined TiO_2 550C (Air), and g-C_3N_4 (Air)). For each material tested, a more or less important activity decrease was observed. The relative difference for Au/TiO_2-gC_3N_4 (95-5) and Au/TiO_2 550 °C (Air) from the first to the second and third cycles are 2 %, 2 %, 14 % and 12 %, respectively, meaning that both samples present a relative good stability on the second cycle, but least on the third cycle. However for the third cycle, there is a considerable diminishment that might be attributed to a TEOA degradation and by-products formation that may poison the catalyst. The TEOA degradation has an immediate impact in the second cycle for bare Au/TiO_2 550 °C (Air) and Au/g-C_3N_4 (Air) references with 12 and 10 % activity decrease in comparison to cycle 1.

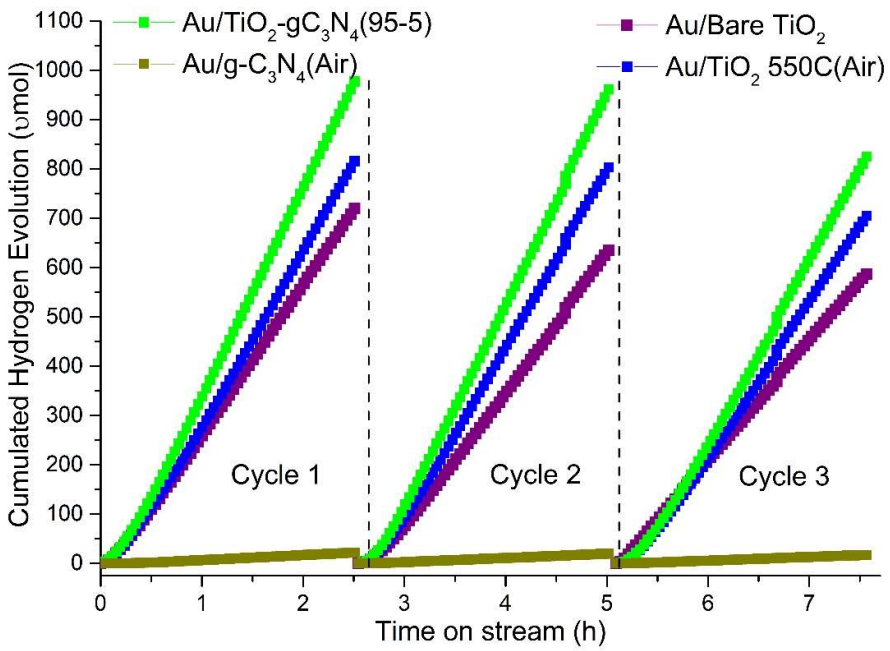

Figure 3.35. Cycling tests on Au/TiO_2-gC_3N_4 (95-5) Air zoom composite with 1 vol. % TEOA under solar light irradiation.

D.1.2.4. Internal Quantum yields

From the internal quantum yield (IQY) (**Fig. 3.36**) determination, one can see the same trend independently of the irradiation used (solar or visible). There is only a slight difference between the TiO_2 references and the Au/TiO_2(P25)-gC_3N_4 (95-5) composite (not significant). Therefore, one can conclude that light absorption (density of absorbed photons) is an important parameter contributing to the material's activity, but not the only one. It must be underlined that for the Au/TiO_2(P25)-gC_3N_4 (95-5) physical mixture the IQY is 3.3 times lower than for the composite with the same g-C_3N_4 content.

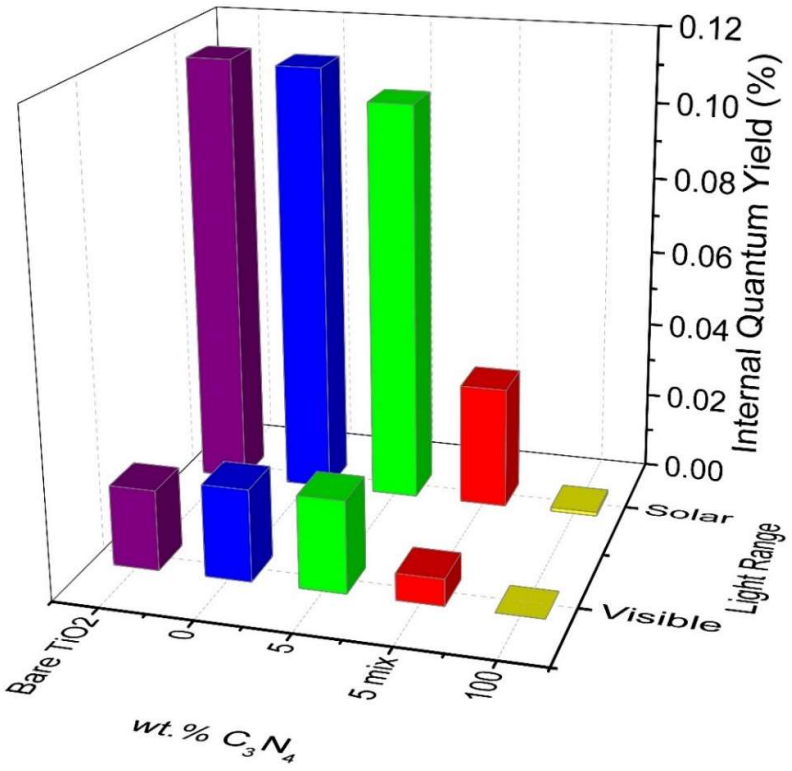

Figure 3.36. Internal quantum yield (IQY, %) of the Au/TiO_2-gC_3N_4 (95/5) composite, three references, and physical mixture with the same massic ratio under solar and visible-light irradiation.

D.2. Photocatalytic performance of Au/TiO_2(P25)-gC_3N_4-$\underline{NH_3}$ under solar-light irradiation

D.2.1. Screening method (NH_3)

The references and composite samples (**Fig. 3.37**) exhibited a lower activity than the two references, Au/TiO_2 550 °C (NH_3) being the most active sample (leading to 737 µmol h^{-1} g_{cat}^{-1} of H_2), followed by Au/gC_3N_4 (NH_3) material with 324 H_2 µmol h^{-1} g_{cat}^{-1}. Hence, the Au/TiO_2-gC_3N_4 composite with compositions 75-25, 50-50, 25-75 yielded 125, 231, and 146 µmol h^{-1} g_{cat}^{-1} of H_2. Even though the results are lower than their own references, one can notice that it seems that the optimal proportion can be found near by the Au/TiO_2-gC_3N_4 (50/50), which present a higher activity in comparison to its counterparts.

Regarding, the Au/TiO_2-gC_3N_4 physical mixtures with compositions of 75-25, 50-50, 25-75, they exhibited a linear decay trend for H_2 production, 577, 446, 320 µmol h^{-1} g_{cat}^{-1}, respectively. One can notice the superiority of the physical mixtures in reference to the composites, meaning that the interaction between the two SCs, resulted by applying the two-pot steps (wet impregnation and polycondensation treatment) reaction is not beneficial in photocatalytic terms with those tested proportions, separately synthesized under NH_3.

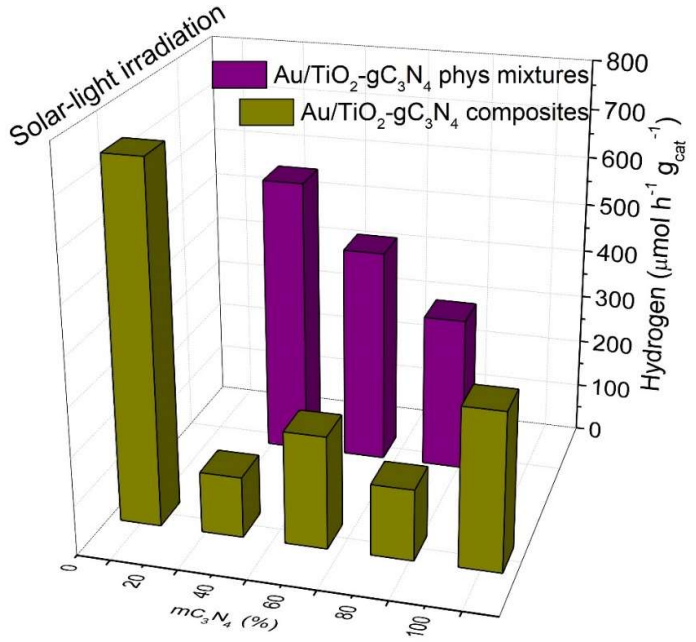

Figure 3.37. Mean hydrogen formation rate per hour and per mass with 1 vol% TEOA of Au/TiO_2-gC_3N_4-NH_3 composites and references under solar-light irradiation. Additionally, the physical mixtures equivalent to the selected massic ratio composition were added for comparison.

D.2.2. Zoom method (NH_3)

From the H_2 production (**Fig. 3.38**) obtained on the zoom method for the Au/TiO_2-gC_3N_4-NH_3 composites irradiated with artificial solar-light, only one reference was selected (Au/TiO_2 550 °C) for comparison. The H_2 production obtained for Au/TiO_2-gC_3N_4-NH_3 composites with composition 97.5/2.5 and 95-5 yielded 75, and 144 µmol h^{-1} g_{cat}^{-1}, respectively, which are lower in comparison to Au/TiO_2 550 °C (*ca.* 737 µmol h^{-1} g_{cat}^{-1}).

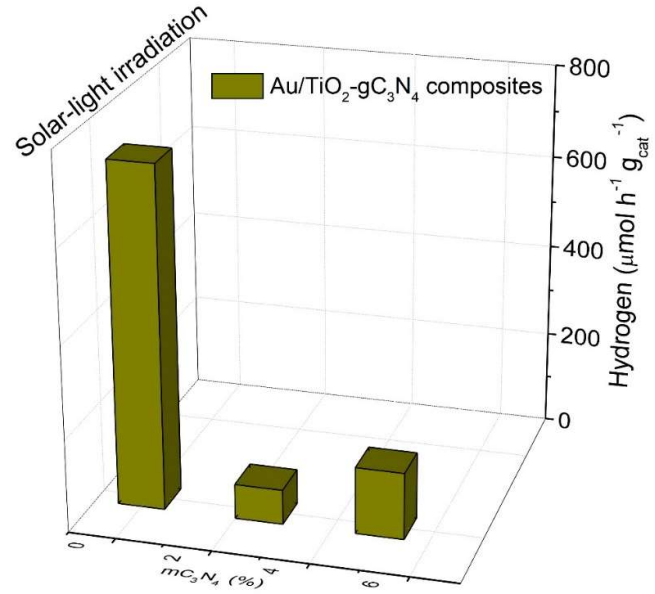

Figure 3.38. Mean hydrogen formation rate per hour and per mass with 1 vol% TEOA of Au/TiO_2-gC_3N_4 NH_3 zoom composites and TiO_2 550C (NH_3) reference under solar-light irradiation.

E) Complementary characterizations for the most active composite Au/TiO_2-gC_3N_4 (95-5) Air

The following section will introduce complementary characterization performed on the most performant Au/TiO_2-gC_3N_4 (95-5) Air composite and pertinent references using techniques such as XPS, UPS, TRMC, and zeta potential (IEP) measurements.

E.1. X-Ray Photoemission Spectroscopy (XPS)

From the survey spectra in **Fig. 3.39**, one can notice the contributions of O 1s, Ti 2p, N 1s, C 1s, and Au 4f at binding energies of *ca.* 530, 460, 400, 285, and 85 eV, respectively for almost all samples. Major contributions are N 1s and C1s for Au/g-C_3N_4 (Air) reference and Ti 2p and O 1s for TiO_2-based samples. Minor contributions are O 1s for Au/g-C_3N_4 and C 1s for TiO_2 based samples. For comparison, the corresponding mechanical mixture (Au/TiO_2-gC_3N_4 (95-5) mix) was also added.

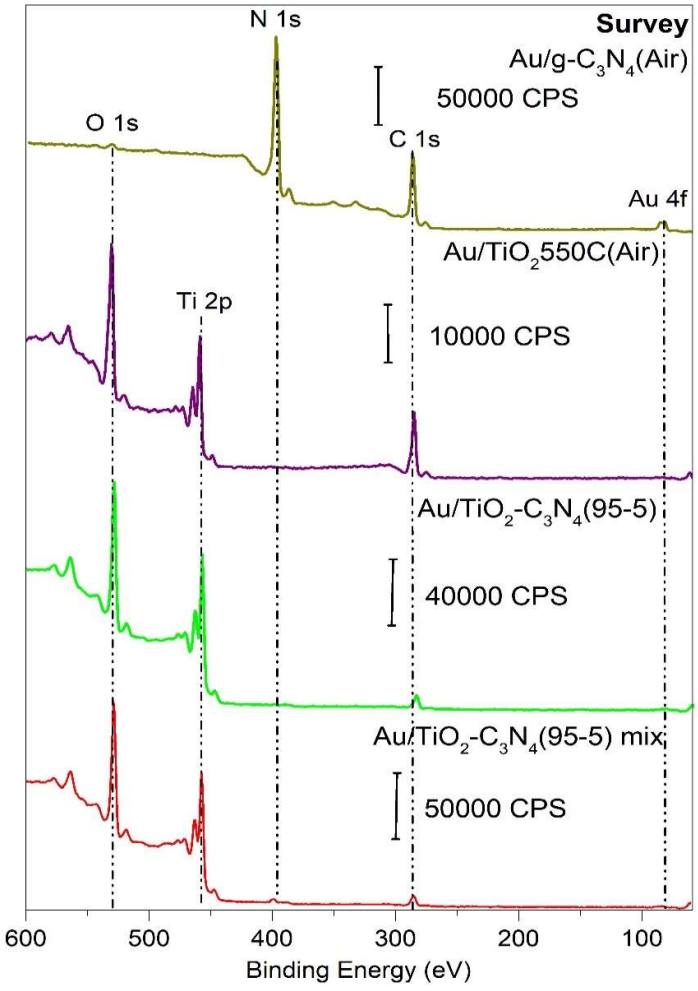

Figure 3.39. XPS survey spectra of Au/TiO_2-gC_3N_4 (95-5) Air zoom composite and references showing the five binding energy region of Au 4f, C 1s, N 1s, Ti 2p, and O 1s.

The Ti 2p signal in the two TiO_2 based samples, Au/TiO_2 550°C (Air) and Au/TiO_2-gC_3N_4 (95-5) Air (**Fig. 3.40**) displays 2 main contributions at 463.9 and 458.1 eV ascribed to Ti $2p_{1/2}$ and Ti $2p_{3/2}$, respectively, characteristic for Ti^{4+} in TiO_2. Nevertheless, the composite did not present any significant shift (lower than 0.5 eV as minimum) compared to the reference Au/TiO_2 550°C (Air). However when comparing the Au/TiO_2 550°C (Air) composite with the physical mixture (Au/TiO_2-gC_3N_4 (95-5) mix), a significant binding energy shift of *ca.* 1.4 eV is observed on the two Ti^{4+} peaks, indicating a possible chemical environment change. Moreover, one cannot exclude the presence of small non detectable contribution of the two satellite peaks at 463.5 and 458.2 eV ascribed for Ti^{3+} $2p_{1/2}$ and Ti^{3+} $2p_{3/2}$, respectively, on TiO_2-based samples (reference, composite, and physical mixture), due to the use of $NaBH_4$ (mild reductant agent) during Au deposition to reduce the Au^{3+} precursor (Au NPs deposition step) into metallic Au^0, as already observed in literature [35,37].

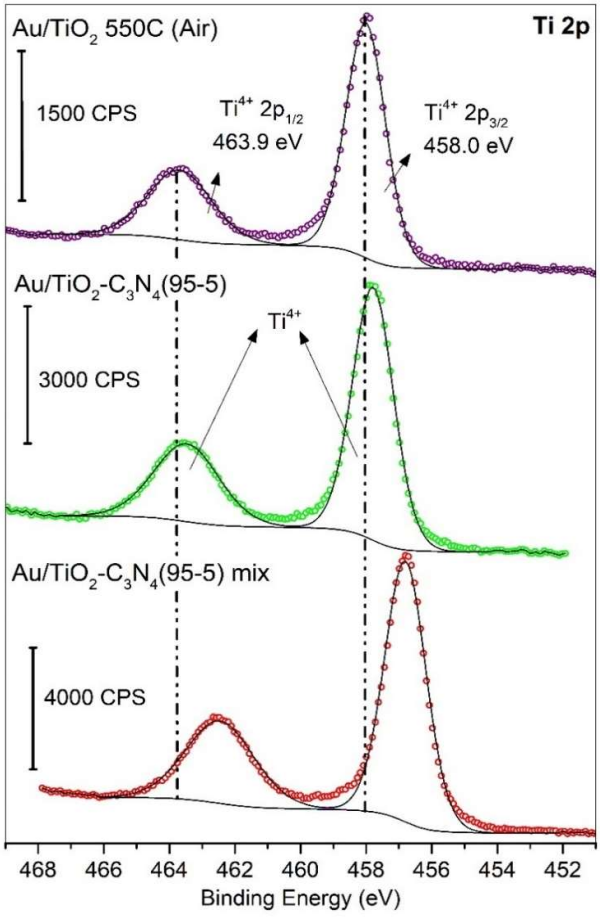

Figure 3.40. XPS Ti 2p spectra of the Au/TiO_2-gC_3N_4-(95-5) composite Au/TiO_2-gC_3N_4-(95-5) physical mixture and Au/TiO_2 550 °C (Air) reference.

The C 1s signal in the Au/TiO_2-gC_3N_4 (95-5) composite (**Fig. 3.41**) displays 3 contributions at 288.4, 286.3, and 284.6 eV ascribed to C=O, C-O or C-N=C, and C-C, respectively. Those species can be attributed to carbonyl groups, to sp^2-bonded C of N=C-$(N)_2$ from the heterocyclic ring [38] (coming only from g-C_3N_4 skeleton structure) or to O-

Ti-O-C-N interactions [39] (evidencing the interaction between TiO_2 and g-C_3N_4, confirming the heterojunction), and to sp^2 adventitious carbon, which could come from defects of graphitic domains. One can notice that Au/TiO_2 550C (Air) and Au/g-C_3N_4 (Air) references displays only two contributions but with different attributions. As described in **chapter 2**, for Au/g-C_3N_4 (Air) the major contribution (287.4 eV) is attributed to sp^2-bonded C of N=C-$(N)_2$ from the heterocyclic ring and the minor contribution (284.6 eV) to the adventitious carbon. For the case of Au/TiO_2 550C (Air), the major contribution (284.6 eV) is attributed to the adventitious carbon and the minor contribution (288.4 eV) is attributed to C=O from carbonyl groups from O_2 adsorbed species. Au/TiO_2-gC_3N_4 (95-5) physical mixture presents two signals equally as for Au/TiO_2 550C (Air) reference samples (same mentioned major and minor contributions) with only different ratio between the two contributions (less contamination C).

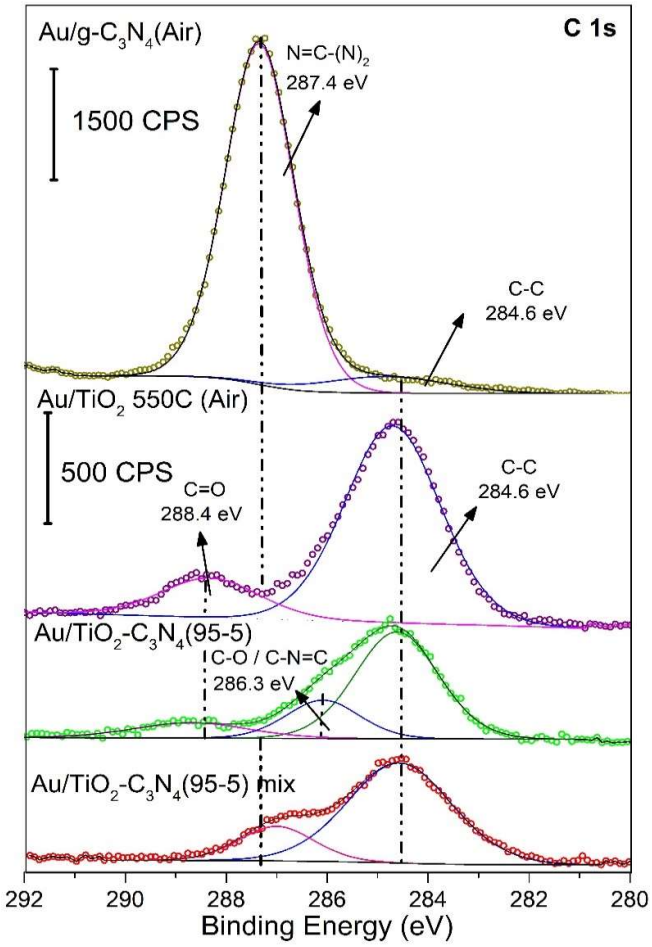

Figure 3.41. XPS C 1s spectra of the Au/TiO_2-gC_3N_4-(95-5) composite, Au/TiO_2-gC_3N_4-(95-5) physical mixture Au/TiO_2 550 °C (Air), and Au/g-C_3N_4 (Air) references.

The N 1s signal in Au/g-C_3N_4 reference (**Fig. 3.42**) displays 2 characteristic contributions, a major one at 399.9 and a minor one at 397.9 eV assigned to sp^2-hybridized pyridine nitrogen of C=N-C from the heterocyclic ring and to the N-$(C)_3$ tertiary nitrogen, respectively [40–42]. However it must be underlined that in the

mechanical mixture samples, N 1s signal is relatively low making deconvolution more difficult. Even though the low intensity, it can be seen the two signals are shifted to lower binding energies, presumably the same two found on Au/g-C_3N_4 (Air) reference but with some slight chemical environment changes. For Au/TiO_2-gC_3N_4 (95-5) composite, N 1s signal is even lower than for the physical mixture, but the two deconvoluted peaks are attributed equally, and no significant shift was found. For the C/N ratio results, it has been obtained 0.75 for reference g-C_3N_4, referring to the same theoretical value, meaning that the polymeric g-C_3N_4 structure is highly polymerized. Nevertheless, for the Au/TiO_2-gC_3N_4 (95-5) composite the C/N obtained value was lower (0.52) compared to the reference Au/g-C_3N_4 (Air), possibly due to the low massic g-C_3N_4 content leads to the formation of different type of g-C_3N_4 structure (linearly polymerized). For Au/TiO_2-gC_3N_4 (95-5) physical mixture exhibited a C/N of 0.66, it can be observed a relative closer theoretical value than the composite, which is in good agreement with the chemical composition of this sample since the Au/g-C_3N_4 proportion remains slightly intact in presence of Au/TiO_2 proportion.

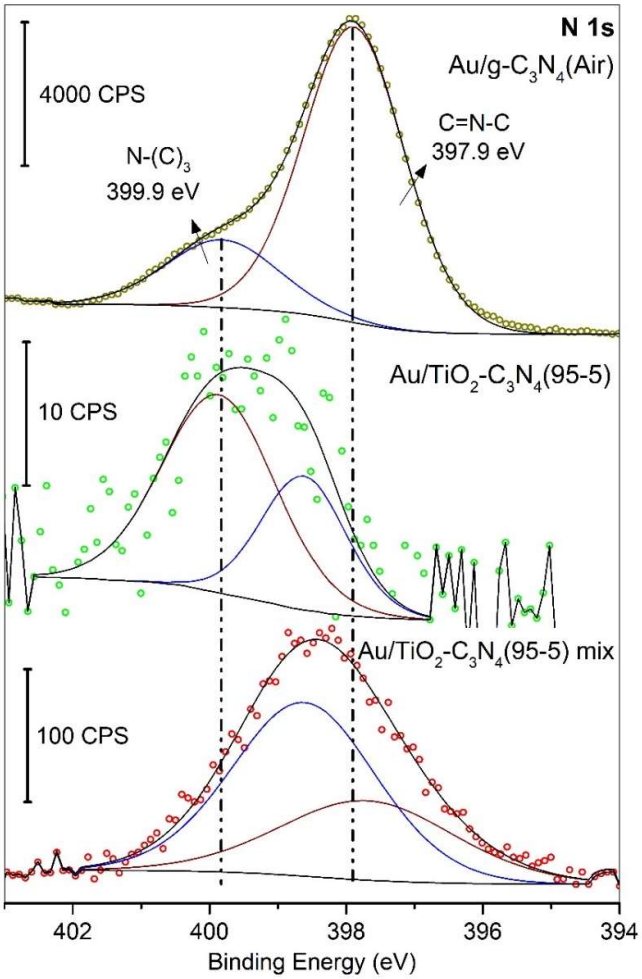

Figure 3.42. XPS N 1s spectra of the Au/TiO_2-gC_3N_4-(95-5)-Air composite, Au/TiO_2-gC_3N_4-(95-5) physical mixture, and Au/g-C_3N_4 (Air) references.

The Au 4f signals (**Fig. 3.43**) display the two typical contributions at 86.3 and 82.7 eV ascribed for bulk Au^0 $4f_{7/2}$ and Au^0 $4f_{5/2}$ [43], respectively, for all samples, with the exception of the Au/TiO_2-gC_3N_4 (95-5) physical mixture that present a significant shift to lower binding energies at 85.3 and 81.5 eV, respectively. This observation may indicate a different chemical interaction of Au NPs with the respective SC support. This Au 4f doublet has been described in literature as the interaction of Au NPs with an electron-donor support specie [44], namely TiO_2 or g-C_3N_4 in our case.

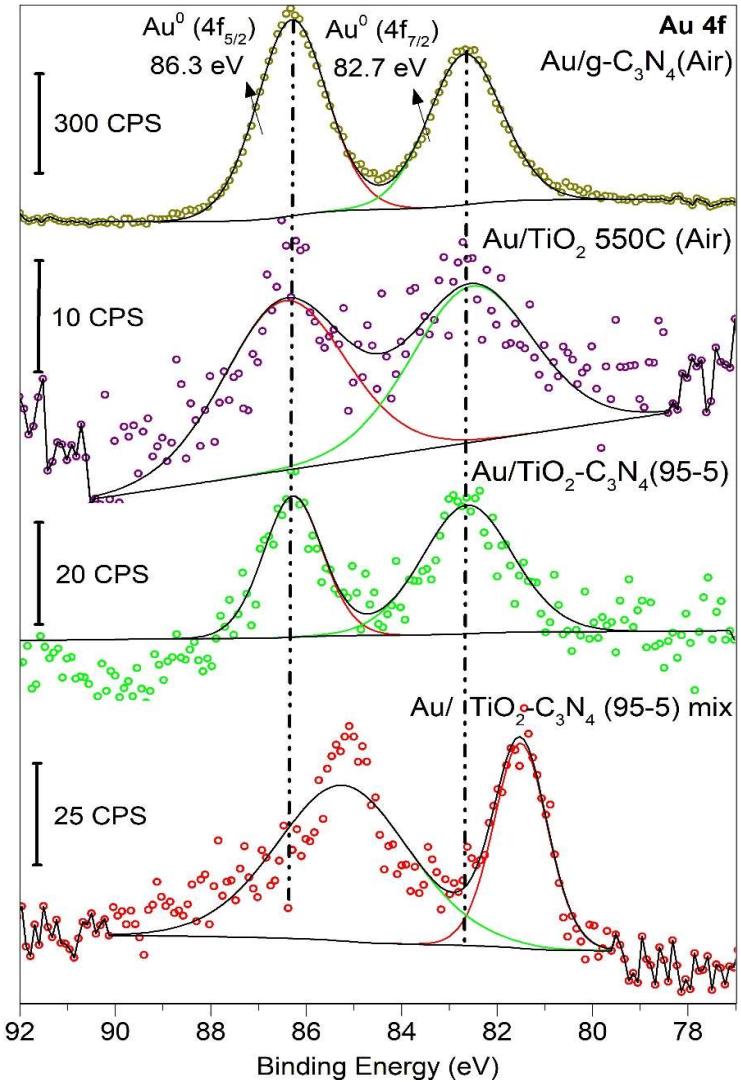

Figure 3.43. XPS Au 4f spectra of the Au/TiO_2-gC_3N_4-(95-5)-Air composite, Au/TiO_2-gC_3N_4-(95-5) physical mixture, Au/TiO_2 550 °C (Air), and Au/g-C_3N_4 (Air) three references.

The O 1s signals in Au/TiO_2 550C (Air) reference (**Fig. 3.44**) displays 3 characteristic contributions of TiO_2 species at 533.2, 531.3, and 529.3 eV ascribed for adsorbed H_2O or O^{2-} species, hydroxyl surface groups (-OH), and Ti-O (major peak), respectively. Au/g-C_3N_4 (Air) only presents the –OH contribution but in a lesser relative amount than on TiO_2-based materials. However the poorly hydroxylated surface of g-C_3N_4 support seems not to be so limiting for Au NPs deposition. For Au/TiO_2-gC_3N_4 (95-5) composite and

physical mixture samples only two contributions are found shifted at lower binding energies in respect to Au/TiO_2 550C (Air). These two contributions are ascribed to hydroxyl surface (-OH) (minor) and Ti-O (major). Globally, the presence of hydroxyl groups in all TiO_2-based samples are of great importance for an efficient Au deposition in the support catalysts. In the case of g-C_3N_4-containing materials, on can assume that Au NPs deposition may mainly be obtained thanks to the surface amino groups of g-C_3N_4.

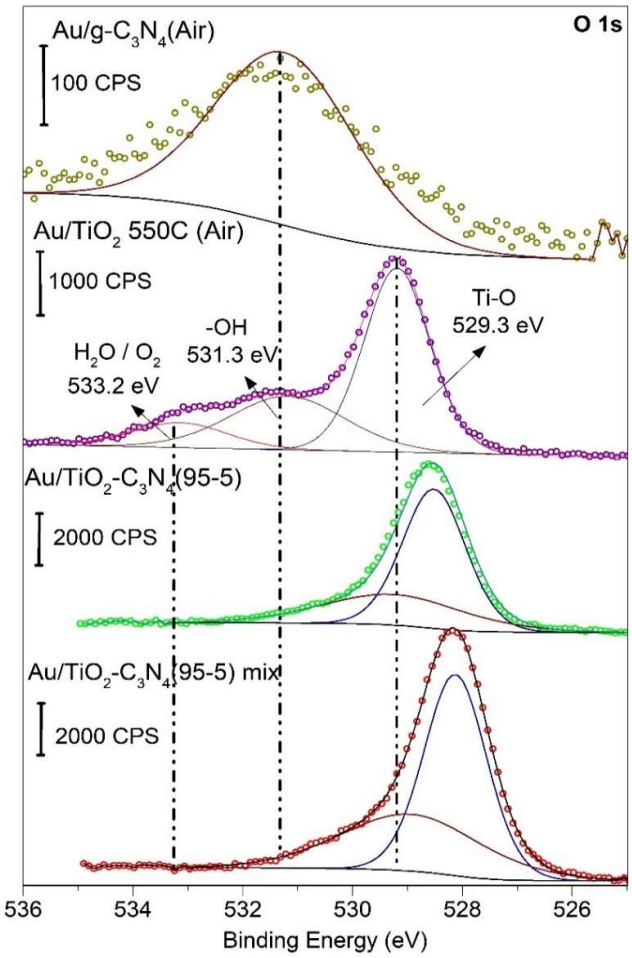

Figure 3.44. XPS O 1s spectra of the Au/TiO_2-gC_3N_4-(95-5)-Air and three references Au/TiO_2-gC_3N_4-(95-5) physical mixture, Au/TiO_2 550 °C, and Au/g-C_3N_4 (Air).

E.2. Band edges position deduction by UV Photoelectron Spectroscopy

From UPS analysis of TiO_2-gC_3N_4 (95-5) composite, g-C_3N_4 (Air) and TiO_2 550C (Air) references (**Fig. 3.45 a**), the valence band maximum (VBM) of each material is obtained. Hence, the TiO_2-gC_3N_4 (95-5) composite exhibit -5.9 eV VBM position which is located in the middle of the two references g-C_3N_4 (Air) (-5.7 eV) and TiO_2 550C (Air) (-6.1 eV) VBM values. This result evidences, that the obtained VBM for the composite exhibits a new hybrid energy state compared to the two separate SCs. That means that its VBM at -5.9

eV shifted toward positive and negative energy in respect to TiO_2 and g-C_3N_4, respectively, presumably resulting from the C 2p and N 2p orbitals (from π-conjugated system of g-C_3N_4) interacting with Ti^{+4} 2p and O^{2-} 1s orbitals from TiO_2 [45]. Also, it has to be underlined that the experimental VBM values obtained for both g-C_3N_4 (Air) and TiO_2 550C (Air) references were slightly similar to the theoretical ones, *ca.* -5.9 and -7.2 eV, respectively, under vacuum conditions [10], which is the case of UPS measurement.

By combining UPS and UV-visible information a speculative schematic band energy diagram was designed (**Fig. 3.45 b**) with the purpose of evidencing the hybrid energy states obtained for TiO_2-gC_3N_4 (95-5) composite.

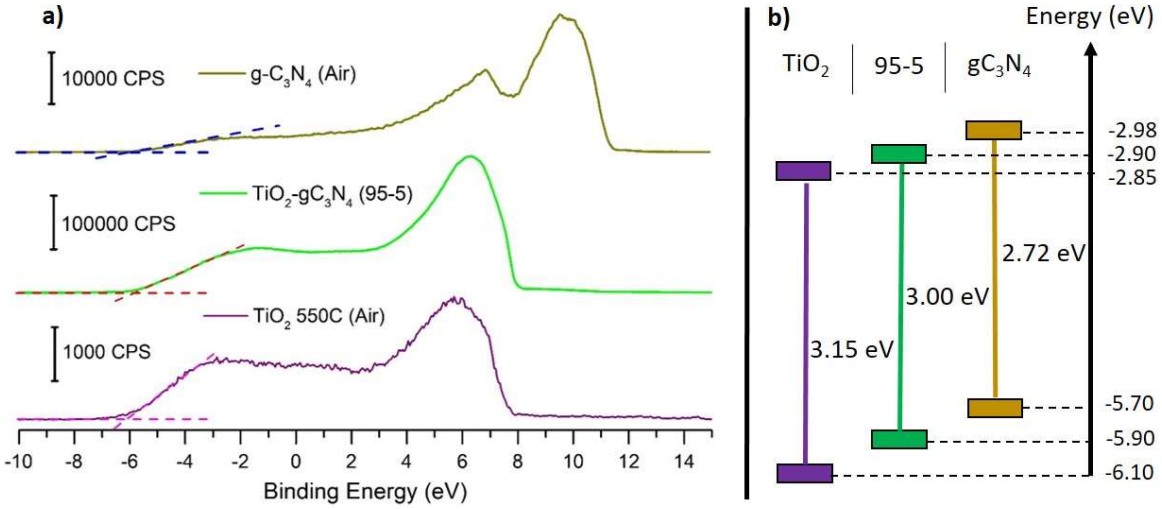

Figure 3.45. a) UPS analysis for the determination of the VBM of TiO_2-gC_3N_4-(95-5)-Air composite and two Au/TiO_2 550 °C and Au/g-C_3N_4 references b) Band energy diagram scheme of materials.

E.3. Electron mobility measurements using TRMC

Time-Resolved Microwave Conductivity (TRMC) measurements were performed at the Laboratoire de Chimie-Physique (Université Paris-Orsay) in collaboration with Professor Colbeau-Justin and were conducted at 360, 450, 500, 550 nm laser pulses (**Fig. 3.46 a, b, c, d**) corresponding to the maximum absorption wavelengths of the three components, *e.g.,* TiO_2, gC_3N_4, and plasmon Au, with the exception of 500 nm, which is an intermediate value between the g-C_3N_4 visible absorption and Au plasmon resonance.

Under UV activation at 360 nm (Fig. 3.46 a), TiO_2-gC_3N_4 (95/5) Air composite presents a significant highest signal among all samples, which is attributed mainly to the presence of both gC_3N_4 and TiO_2 SCs. As is theoretically known, a maximum value of the signal (I_{max}) after the laser pulse excitation reflects the maximum of mobile electrons concentration generation and thus the maximum concentration in dissociated e^-/h^+ pairs created. A higher decay of the signal indicates a higher kinetics of free electron mobility loss either due to an increased probability of charges recombination or to electron trapping, thus lowering their mobility. Hence, TiO_2-gC_3N_4 (95/5)-Air composite exhibits a more intense signal than TiO_2 and g-C_3N_4 references. Analyzing the highest maximum value and the highest signal decay of TiO_2-gC_3N_4 (95/5) Air

composite, one can say that the photoexcitation promotes a higher amount of the photogenerated e^-/h^+ pairs. Then, the excited e^- located on TiO_2 CB can be transferred to the gC_3N_4 CB and be delocalized / trapped in the π-aromatic systems, thus restricting their mobility. A tendency behaviour was observed for all samples with Au NPs, they yielded lower signal intensities in comparison to their counterparts with no presence of Au NPs, and evidencing the effect of electron traps on Au NPs. g-C_3N_4 did not generate any charge carriers in any of the selected wavelengths, presumably for g-C_3N_4 amorphous phase presence.

Under visible light activation at 450 nm (Fig. 3.46 b), only the TiO_2-gC_3N_4 (95/5)-Air photocatalyst were able to generate significant charges. This signal demonstrates the successful photo-sensitization effect of gC_3N_4 to TiO_2 towards higher wavelengths (Visible-light). This effect may comprise the injection of e^- from the CB of the gC_3N_4 to CB of TiO_2, thus allowing an increase spatial separation of charges (heterojunction).

The **signals at 500 nm (Fig. 3.46 c)**, confirm the TiO_2-gC_3N_4 (95/5)-Air photogeneration of charge carriers obtained at 450 nm, meaning that there is an attenuate absorption of photons on behalf of gC_3N_4 but in lower magnitude, since the intensity signal is lower. Hence, one can say that the injection of electrons takes place under the same mechanism previously described. For the **signal at 550 nm (Fig. 3.46 d)**, one can notice that there is no further contribution of any of the components of the material. Essentially, one may assume that no significant Au NPs SPIE was evidenced.

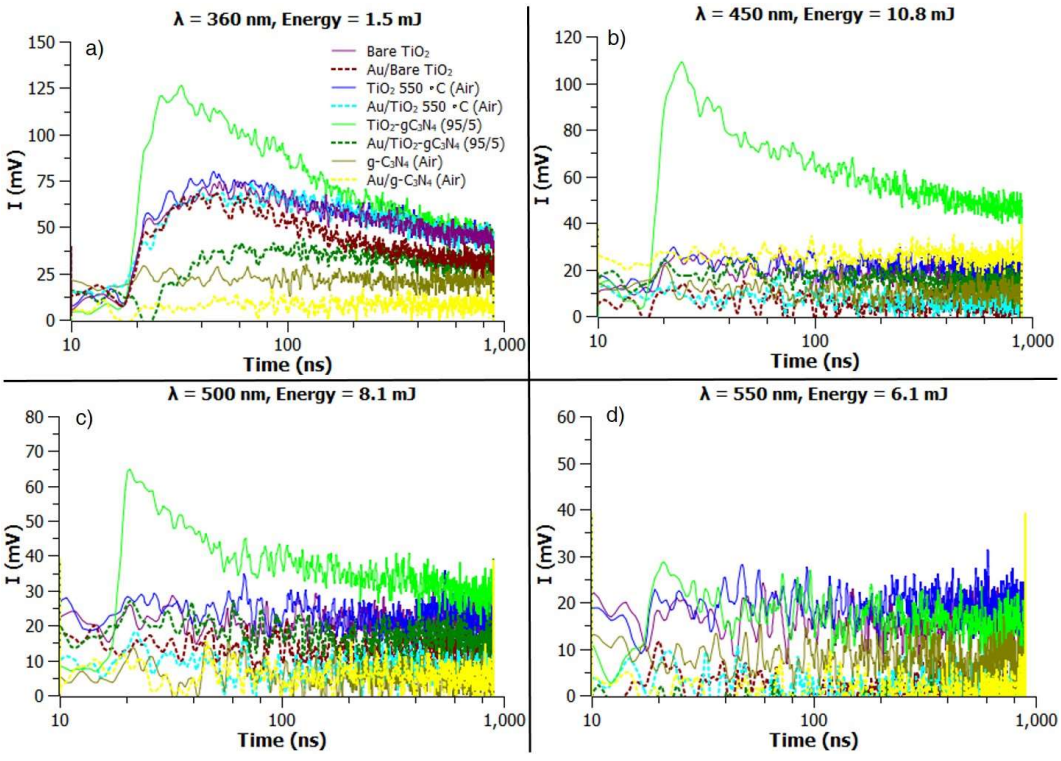

Figure 3.46. TRMC signals of Au/TiO_2-gC_3N_4 (95/5)-Air composite compared to TiO_2-gC_3N_4 (95/5), Bare TiO_2 (P25), Au/Bare TiO_2 (P25), TiO_2 (P25) 550 °C, Au/ TiO_2 (P25) 550 °C, Au/g-C_3N_4 and g-C_3N_4 references at a) 360, b) 450, c) 500, and d) 550 nm.

The main data provided by TRMC are given by I_{max} and the immediate decay (I_{40}/I_{max}) is attributed to the decrease of free electrons. The understanding of the whole decay is not obvious because various processes are taking place simultaneously. Nevertheless, I_{40} ns can be considered as a reference parameter, since its magnitude may be associated to the time of trapped holes relaxation. Therefore, one can underline that TRMC signals at 360, 450, and 500 nm present different intensity and shape (without normalization). Thus, I_{40}/I_{max} ratios were calculated for the mentioned signals, *i.e.,* 360, 450, 500, and 550 nm resulting in 0.92, 0.72, 0.74, 0.49, respectively. One can conclude that the loss of free electrons mobility is higher at the highest I_{40}/I_{max} value, meaning that TiO_2-gC_3N_4 (95/5) Air composite may present a trend from faster to slower recombination on the order of 360, 450, 500, and 550 nm. Those results can also be confirmed by the % decay obtained for the mentioned wavelengths, 8, 28, 26, 51%, which means that the electron recombination is less pronounced for TiO_2, than for gC_3N_4. Nevertheless, TiO_2 coupled with gC_3N_4 exhibited an extended generation of charge carriers in the Visible region, a moderate recombination rate in the 450-500 nm range, and thus a higher lifetime of charge carriers, leading to a beneficial charge carriers spatial separation.

After normalization of the signals (due to different energy density), the comparison at different wavelengths (**Fig. 3.47**) on the TiO_2-gC_3N_4 (95/5) Air photocatalyst evidences the diminishment of the signal when exciting at higher wavelengths, which was expected due to the limitation of light absorption towards deep visible range for the composite.

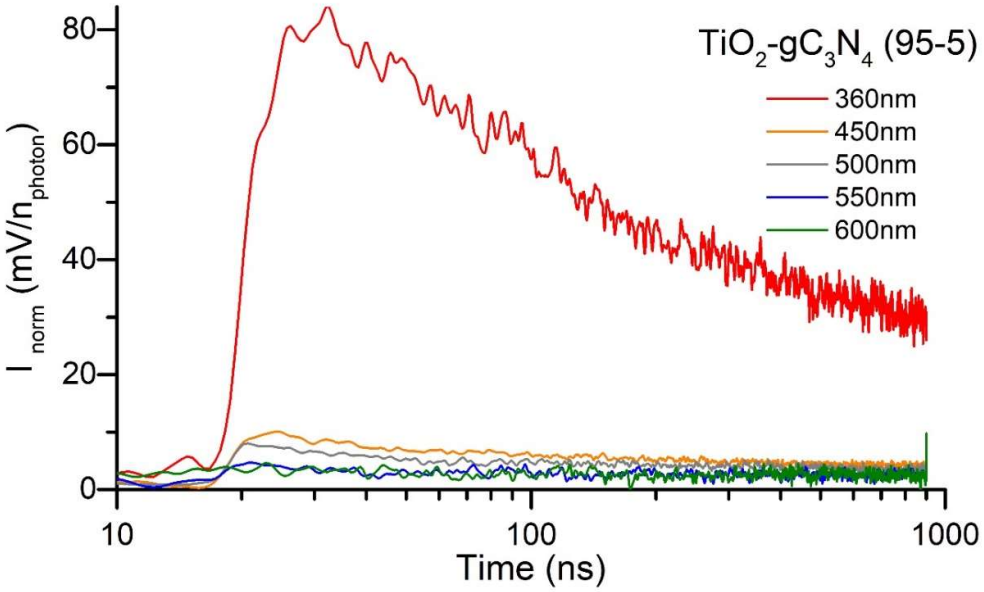

Figure 3.47. Comparison of normalized signals of Au/TiO_2-gC_3N_4 (95/5)-Air composite at 360, 450, 500, 550, and 600 nm.

E.4. Zeta potential measurements

From the auto-titration measurements (**Fig. 3.48**), it can be observed that all samples exhibit a similar linear decay tendency at various pH´s, with the exception of Au/TiO_2 550 °C (Air) reference, which present quite constant zeta potential values in the pH region from 6.5 to 3.2. Following the IEP values in a descending trend from g-C_3N_4 (Air), Au/Bare TiO_2 (P25), Au/TiO_2-gC_3N_4 (95/5)-physical mixture, Au/TiO_2-gC_3N_4 (95-5), Au/g-C_3N_4(Air), and Au/TiO_2 550 °C (Air) the corresponding values are 5.20, 5.12, 4.68, 3.06, 3.03, and 1.83, respectively. The first interesting observation is that the presence of Au NPs onto g-C_3N_4 (Air) support provides a more negatively charged particles at the same pH values. It can thus be assumed that this behaviour applies for all the other samples, by lower in more or least extend the zeta potential and consequently IEP. Additionally, the samples with deposited Au NPs can be divided in three classes. The lowest IEP value is for Au/TiO_2 550 °C (Air), the intermediates are for Au/g-C_3N_4 (Air), Au/TiO_2-gC_3N_4 (95-5), and the highest are for Au/Bare TiO_2 (P25), Au/TiO_2-gC_3N_4 (95/5)-physical mixture, and g-C_3N_4(Air). The IEP´s value of Au/g-C_3N_4 (Air) is in a good agreement with previous works [46], surprisingly the physical mixture is more alike to the surface charge behaviour of Au/g-C_3N_4 rather than for Au/TiO_2. Conclusively, Au/TiO_2-gC_3N_4 (95-5)-Air composite presents a similar behaviour than Au/g-C_3N_4 (Air), which might be associated with the more homogeneous coverage of Au NPs along the support surface.

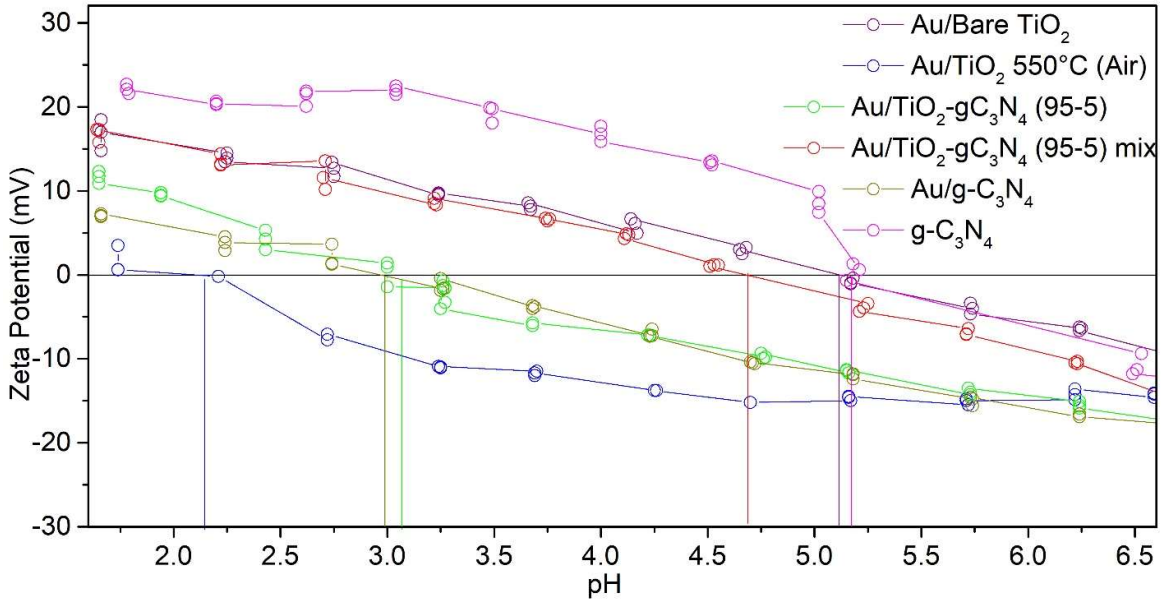

Figure 3.48. Auto-titration of Au/TiO_2-g-C_3N_4 (95-5)-Air zoom composite and references to obtain the IEP.

F) Summary-Discussion

This third chapter was focused on the elaboration, detailed characterizations and photocatalytic evaluation of binary TiO_2(P25)-gC_3N_4-atm and ternary 0.3 w.% Au/ TiO_2(P25)-gC_3N_4-atm (with atm = Air and NH_3) composites.

F.1. Binary TiO_2(P25)-gC_3N_4 composites

F.1.1. Synthesis and composition determination

For this purpose, a two-pot successive method was carried out consisting in (1) a prior wet impregnation of g-C_3N_4 precursors (Mel + DCDA) onto TiO_2 (P25) support, followed by (2) solid-state g-C_3N_4 polycondensation reaction in presence of dried pre-impregnated precursors onto TiO_2 under the selected atmosphere. In addition to atmosphere synthesis, the second parameter to study was the relative massic proportions between TiO_2 and g-C_3N_4. In order to cover the broader range of compositions, two approaches were conducted, first a screening method (g-C_3N_4 proportions ranging from 25 to 75 wt. %) followed by the zoom method aiming at focusing on g-C_3N_4 proportions going from 2.5 to 10%.

At this first stage, it was necessary to establish a mathematical model that allows to predict and thus to control the theoretical TiO_2-gC_3N_4 massic composition of the binary composite. This model (first established for synthesis performed under air) was validated on both the screening composites-Air and –NH_3 after comparing with TGA quantification. However, as the exact determination of g-C_3N_4 content was not possible on the zoom composites-atm, the theoretical composition was considered.

F.1.2. Characterizations

Systematic thermal (TGA), structural (XRD) and surface (FT-IR, BET and porosity) characterizations were performed on the binary-atm composites.

F.1.2.1. Synthesis under Air

Screening TiO_2/g-C_3N_4 composites (range of 70-30/30-70 massic compositions).

From TGA analyses, one has observed that whatever the binary samples, g-C_3N_4 decomposition temperature is shifted toward lower temperature (compared to the reference bulk g-C_3N_4), evidencing contact with TiO_2 NPs helping for thermal oxidation. In addition, for the lowest g-C_3N_4 content (30%), an additional contribution was obtained at much lower temperature, assigned to even higher quality of TiO_2-gC_3N_4 heterojunctions. XRD characterizations evidenced, for all the samples, the presence of g-C_3N_4 by observation of diffraction peaks corresponding to the interlayer stacking of π-conjugated aromatics systems. However, it was not possible to distinguish the features assigned specifically to TSCN and TSTCN phases. BET determination revealed a linear decrease of surface area when decreasing the g-C_3N_4 content. Porosity measurements evidenced the parallel building of different pores channels.

Zoom TiO_2/g-C_3N_4 composites (range of 97.5-2.5/90-10 massic compositions).

TGA analyses did not allow to determine the experimental g-C_3N_4 content, thus only theoretical values were considered for this family of composites. In the same manner, XRD and FT-IR analyses did not allow to identify the presence of g-C_3N_4; due to the important dilution, only the main features related to TiO_2 were noticed. However, from BET and porosity characterizations, it could be observed that pore volume increased when increasing g-C_3N_4 content, whereas the surface area did not change significantly compared to the TiO_2 550 (Air) reference.

F.1.2.2. Synthesis under NH_3

Screening TiO_2/g-C_3N_4 composites (range of 70-30/30-70 massic compositions).

The experimental g-C_3N_4 contents determined from TGA were close to the theoretical one (less than 8% of relative uncertainty), thus validating the mathematical model. As for the screening series under air, the richest-g-C_3N_4 composite (77%) only showed one slightly shifted weight loss contribution that could be assigned to interaction with TiO_2 NPs. In addition, the intermediate-g-C_3N_4 composite (52%) exhibited a second additional contribution, previously referred as higher quality of TiO_2-gC_3N_4 heterojunction domains. But furthermore, for the lowest g-C_3N_4 content (27%), only the contribution at much lower temperature was identified, evidencing the almost exclusive presence of high quality SCs heterojunction domains. From DRX analyses, one can underline that synthesis under NH_3 led to larger mean crystallite sizes for g-C_3N_4, whereas the number of layers was identical compared to the synthesis performed under air. From these observations one can assume that NH_3 synthesis atmosphere may provide optimal conditions for interlayer expansion or exfoliation, also confirmed by larger surface areas in comparison with synthesis carried out under air. In addition, the pore volumes increased when increasing g-C_3N_4 content, those pore volumes being larger than the one determined on the screening series under air. It also confirms the higher porosity of g-C_3N_4 (NH_3) and g-C_3N_4 (Air) references characterized in details in **chapter 2**.

Zoom TiO_2/g-C_3N_4 composites (range of 97.5-2.5/95-5 massic compositions).

As for the zoom series under air, TGA did not permit to determine g-C_3N_4 content. In the same manner, the presence of g-C_3N_4 was not possible by means of XRD analysis. However a significant decrease of anatase crystallite size was noticed for the binary composites, going from 18 nm on the TiO_2 550 (NH_3) reference to 10 nm on the composites. We speculate that one of the reason could be the high abrasive effect of g-C_3N_4 (NH_3) domains in very high quality interface with TiO_2 NPs. As for the zoom series under air, BET values did not notably change. However, introduction of small amounts of g-C_3N_4 yield an important pore volume increase, specific for syntheses performed under NH_3.

F.2. Ternary TiO_2(P25)-gC_3N_4 composites

The same Au NPs deposition method onto the as-synthesis binary composites was used than the one described for g-C_3N_4-atm support (**chapter 2, section C.1**).

F.2.1. Characterizations

F.2.1.1. Synthesis under Air.

From ICP-AES measurements, showing that Au NPs deposition yield on the composites was the same than on TiO_2 references and lower than on g-C_3N_4 (Air), it could be deduced a higher affinity toward g-C_3N_4 surfaces compared to TiO_2 ones. This feature was confirmed by higher density of deposited Au NPs onto rich-gC_3N_4 binary composites. Furthermore, the smallest Au NPs size, but also the narrower monomodal distribution, were observed for the Au/TiO_2-gC_3N_4 (30-70) composite; for that composite, the Au NPs mean size was smaller than on the TiO_2 and g-C_3N_4 references, suggesting the role of beneficial TiO_2-gC_3N_4 interface for Au deposition. UV-Vis absorption measurements of the screening composites exhibited the contribution of g-C_3N_4 component at 450-460 nm, characteristic of π-π^* electronic transitions in π-conjugated systems of TST and ST basic units. For this g-C_3N_4 rich composites, an additional band tail was also identified, assigned to n-π^* electronic transition due to interlayer deformation (as already mentioned in **chapter 2**). This contribution was more or less overlapped with SPIE signal raising from Au NPs. In the case of rich-gC_3N_4 composites, TiO_2 contribution is partially masked. At the opposite, the zoom composite series with much smaller g-C_3N_4 content, exhibited the main general optical properties than Au/TiO_2 550 (Air), except a slight red-shift evidencing the presence of g-C_3N_4.

F.2.1.2. Synthesis under NH_3

ICP-AES ad TEM observations revealed the same main features than the ones observed for the composites synthetized under air: better affinity for Au NPs deposition onto the g-C_3N_4 (NH_3) surfaces. The smallest Au NPs size and narrower distribution were observed for the Au/TiO_2-gC_3N_4 (23-77) composite. However, the most significant difference between the ternary composites synthetized under air and under NH_3 is related to optical properties. Indeed, in addition to the contributions already mentioned for the series synthetized under air, here one can observe an additional contribution, attributed either to N-doping of TiO_2 and/or to the presence of oxygen-deficient TiO_2, leading to band gap narrowing.

F.3. Photocatalytic activity toward H_2 production and complementary characterizations

All the composites and reference samples were evaluated under solar-light irradiation and compared in terms of H_2 massic production rate, expressed in μmol $(H_2).h^{-1}.gcat^{-1}$.

F.3.1. The ternary composites (NH_3)

They revealed the lowest photocatalytic activities, much less performant than the corresponding mechanical mixtures than the TiO_2 550 (NH_3) and g-C_3N_4 (NH_3) references.

F.3.2. The ternary composites (Air)

They can be classified into two categories, the screening series and the zoom series.

The screening series exhibited low H_2 production performance, with lower H_2 production compared to the corresponding Au/TiO_2 550 (Air) and g-C_3N_4 (Air) references. The photocatalytic activity of that family of composites was evaluated under solar and visible-light irradiation. The 0.3 % Au/TiO_2-gC_3N_4 (95-5) exhibited the best activity amongst all the samples also comprising the corresponding references and mechanical mixtures. Consequently, that ternary composite was evaluated in more details. It was observed that it led to the cumulated formation of 21.9 mL and 5.0 mL of H_2 over 2,5 h of reaction respectively under solar and visible light irradiation. This activity was much higher than for the TiO_2 (P25) reference that produced for comparison 16.1 mL and 2.8 mL, respectively, even if the corresponding Internal Quantum Yields were not significantly different. It must also be mentioned that cycling tests showed a slight deactivation after the second evaluation cycle. It was mainly attributed to TEOA degradation and consequent poisoning of the active sites.

F.4. Complementary characterization of the Au/TiO_2-gC_3N_4 (95-5)-Air composite

UPS characterization led to the conclusion of the presence of new hybrid valence band position (at -5.9 eV), intermediate between that of the g-C_3N_4 (Air) (-5,7 eV) and of TiO_2 550 (Air) references, presumably with slightly better properties toward the reduction half-reaction, compared to TiO_2.

TRMC measurements allowed to obtain interesting information at different wavelengths excitations, in terms of generation of dissociated e^-/h^+ pairs (related to signal intensity) and of life-time of mobile electrons (related to the decay of the signal).

At 360 nm, the Au/TiO_2-gC_3N_4 (95-5) (Air) composite showed the highest density of dissociated e^-/h^+ pairs and the more rapid loss of electron mobility, compared to the binary composite and to the corresponding references. The second observation was explained as the trapping/delocalisation of free electrons (after generation) in the π-aromatic systems of g-C_3N_4, thus limiting further their recombination with holes.

At 450 nm, only the composite was able to generate significant charges, pointing out the sensitization of g-C_3N_4 to TiO_2, probably by injection of electrons from the CB of g-C_3N_4 to that of TiO_2.

At 500 nm, the same, but attenuated phenomena was observed.

At 550 nm, no signal was detected, underlining the absence of SPIE effect from Au NPs.

F.5. Structure/Photocatalytic activity correlations

F.5.1. Overall discussion-correlations as a function of g-C_3N_4 content

To compare and discuss the photocatalytic activities of the different binary TiO_2(P25)-gC_3N_4 and ternary Au/TiO_2(P25)-gC_3N_4-atm nanocomposites in correlation with their physico-chemical properties, different contributions and effects have to be considered.

F.5.1.1. On TiO_2 (P25)-gC_3N_4 binary systems

From the surface characterization (**Fig. 3.49**), one can underline that the BET area trend of TiO_2-gC_3N_4 composites for both Air and NH_3 atmospheres in function of gC_3N_4 content is different. However, the overall trend for both cases is a decay, even though the decay for composites-Air is more pronounced in comparison with the composites-NH_3 decay. Generally, this decay might be associated with two phenomena. For composites synthesized in air S_{BET} tend to diminish progressively in function of the evolution of g-C_3N_4 precursors amount forming the polymeric g-C_3N_4 structure, without changing drastically its anatase crystallite size. On the NH_3 synthesized composites, the loss of specific surface area might be due to a wrapping and / or entanglement of different g-C_3N_4 bulk-domains around TiO_2 NPs. At the same time, the formation of polymeric g-C_3N_4 in presence of TiO_2, might catalyze the initial g-C_3N_4 bulk domains with 26 and 20 layers (NH_3 and air, respectively) to transform them in smaller domains or crystallites with a exfoliation-type effect, consequently increasing their available surface area, and eventually increasing the amount of line contact between the two SCs.

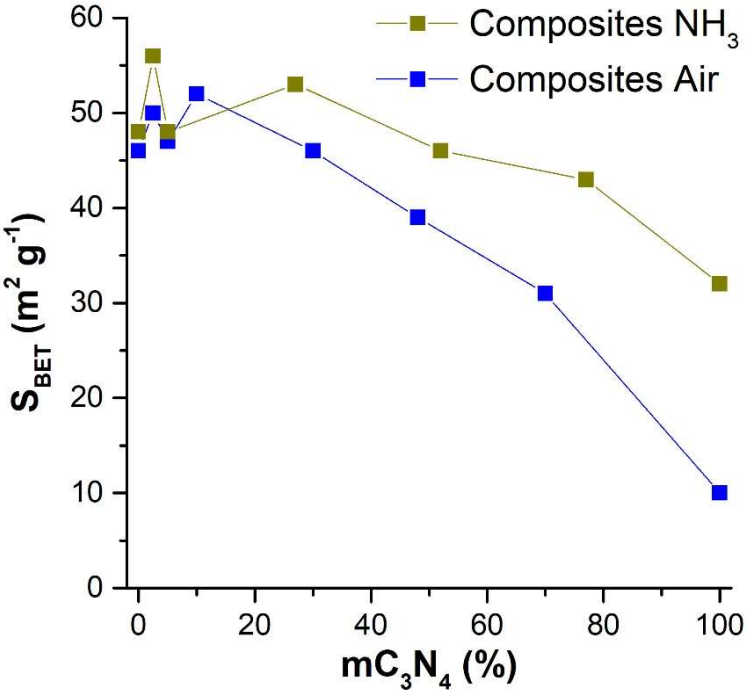

Figure 3.49. Correlation of the specific surface area in function of g-C_3N_4 content of all (screening and zoom) TiO_2 (P25)-gC_3N_4 composites and references synthesized under Air and NH_3 atmospheres.

From the thermal analysis of the screening composites (**Fig. 3.50**), one can notice that the decay of the main weight loss contribution in function of the g-C_3N_4 content in both atmospheres is different. One can say that the decay trend for the composites-Air follows an almost proportional trend, while for the composites-NH_3 it does not follow a specific trend, but a drastic decay for only one composite. Bearing in mind, that the experimental error associated for TGA is approximately 10%, one can say that weight losses on composites-Air present no significant difference. However, there is a significant difference specifically of TiO_2-gC_3N_4 (75-25) NH_3 in respect to the other two composites relative proportions, meaning that the g-C_3N_4 is not equally compared to its counterparts or to its g-C_3N_4 references. One can point out that all the composites (whatever the atmosphere) present a lower decomposition temperature than their g-C_3N_4 references, meaning that g-C_3N_4 domains are in more or less intimate contact with TiO_2. This influences the polymeric g-C_3N_4 structure, despite is strong chemical, thermal, structural stability due to its characteristic π-conjugated system of the two TST and ST unit motifs.

More importantly, this result also suggest, that the formation mechanism of g-C_3N_4 into the composites must be different (for the same g-C_3N_4 content) by just changing the nature of the atmosphere (reductive or oxidant).

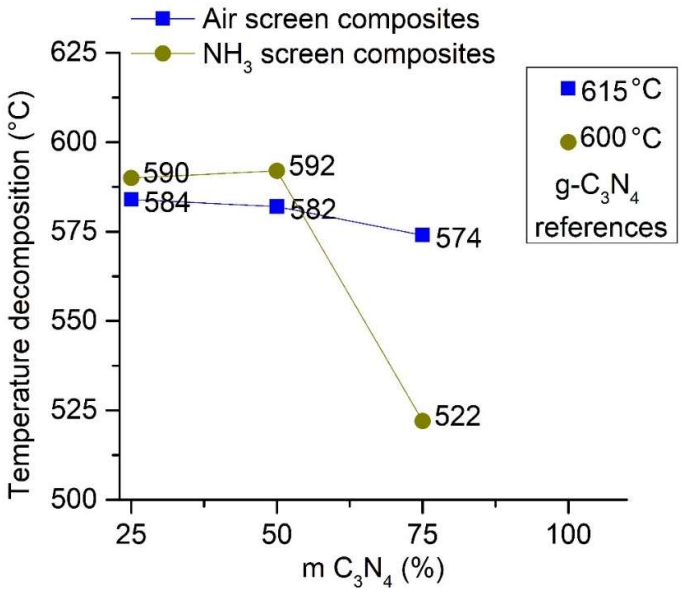

Figure 3.50. Correlation of the temperature decomposition of the second contribution (at higher temperature) determined from TGA analysis in function of g-C_3N_4 content of TiO_2 (P25)-gC_3N_4 screening composites and references synthesized under Air and NH_3 atmospheres.

The colors (**Fig. 3.51**) of all TiO_2-gC_3N_4 composites synthesized in Air and NH_3 atmospheres show different variation of tonalities. One can notice that for the TiO_2-gC_3N_4 air composites, it follows a progressive colorization from white TiO_2 until dark yellow g-C_3N_4. Nevertheless, the behaviour for TiO_2-gC_3N_4 NH_3 composites is different. The two low g-C_3N_4 content (≤ 5 wt. %) composites are yellowish, but the intermediate and rich g-C_3N_4 content (≥ 25-75 wt. %) present a light brownish tone for all three. This

result suggest, that the g-C_3N_4 formed domains in this case might differ from the bulk g-C_3N_4 references.

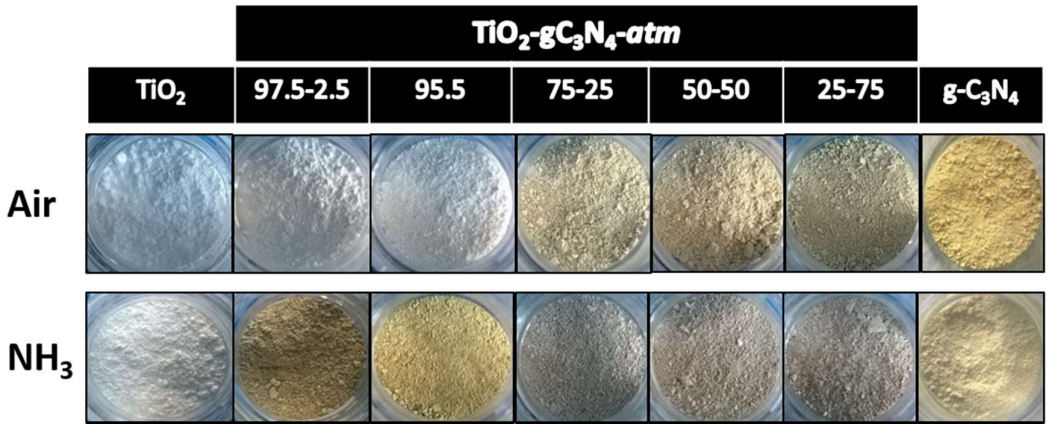

Figure 3.51. Comparison of the color in function of g-C_3N_4 content of all (screening and zoom) TiO_2 (P25)-gC_3N_4 composites and references colors synthesized under Air and NH_3 atmospheres.

F.5.1.2. On Au/TiO_2 (P25)-gC_3N_4 ternary systems

Optical measurements evidenced the three expected absorptions for the three components, *i.e.* TiO_2 (λ ≈ 385 nm), g-C_3N_4 (λ ≈ 460 nm), and Au plasmon resonance (λ ≈ 550 nm). An additional contribution towards the visible range was observed for some TiO_2-gC_3N_4 composites. It is well pronounced for both screening and zoom NH_3 composites, which is ascribed for N-doped TiO_2 or Ti^{4+} reduction to Ti^{3+}, as described elsewhere [34]. In the case of screening Air composite, an additional tail was observed, presumably for g-C_3N_4 deformation layer that induces n→π* electronic transition [11], as already mentioned in chapter 2 for Au/g-C_3N_4 materials.

From TEM, it can be noticed that all samples followed a more or less monodispersion of Au NPs, with different surface coverages, with exception of TiO_2 550 °C (NH_3) reference, which follows more likely a bidispersed distribution. The Au NPs mean particle size present the same value centered *ca.* 2.7 nm for TiO_2-gC_3N_4 (25-75), independently of the atmosphere. However, the TiO_2-gC_3N_4 (95-5)-atm composites exhibit different Au NPs size for Air and NH_3, respectively 3.4±1.1 and 4.1±1.4 nm. This result suggests, that the growth mechanism of Au NPs on these two similar supports is different. In terms of Au NPs coverage, the low g-C_3N_4 content composites exhibit only few round-shaped Au NPs. On the contrary, rich g-C_3N_4 content composites show dense Au NPs regions, independently of the synthesis atmosphere.

From the photocatalytic evaluation tests, Au/TiO_2(P25)-gC_3N_4-(95-5) (Air) composite exhibit the highest activity under both solar and visible-light activation. It can be thus assumed that different phenomena are playing a key role, *e.g.,* TiO_2 photosensitization, electronic trapping site, co-catalytic effect from Au NPs, electronic communication between the band energies position of the SCs, suggestion a staggered heterojunction type II, enabling a more efficient separation of charge carriers. Furthermore, one cannot exclude the possibility of an additional synergy effect from the heterojunction of

anatase/rutile of TiO_2(P25) NPs [16] which may be in contact as well. However, we found no evidence of the SPIE effect resulting from Au NPs deposition.

Fig. 3.52 summarizes a detailed scheme of the possible charge transfer pathways.

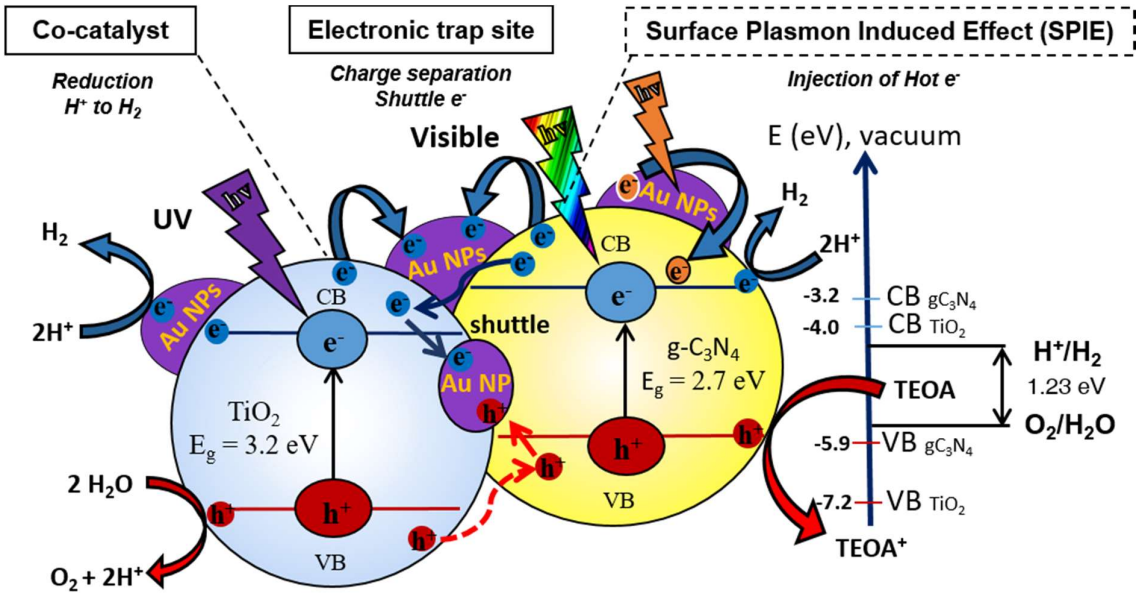

Figure 3.52. Schematic illustration of the proposed H_2 production mechanism for Au/TiO_2(P25)-gC_3N_4 (95-5) Air composite, including the two half reactions of water splitting, the SCs CB/VB positions, and the different possible electron transfers pathways.

G) References

[1] K. Nakata, A. Fujishima, TiO2 photocatalysis: Design and applications, J. Photochem. Photobiol. C Photochem. Rev. 13 (2012) 169–189. doi:10.1016/J.JPHOTOCHEMREV.2012.06.001.

[2] K. Maeda, T. Takata, M. Hara, N. Saito, Y. Inoue, H. Kobayashi, K. Domen, GaN:ZnO Solid Solution as a Photocatalyst for Visible-Light-Driven Overall Water Splitting, J. Am. Chem. Soc. 127 (2005) 8286–8287. doi:10.1021/ja0518777.

[3] I. Tsuji, H. Kato, A. Kudo, Visible-Light-Induced H2 Evolution from an Aqueous Solution Containing Sulfide and Sulfite over a ZnS-CuInS2-AgInS2 Solid-Solution Photocatalyst, Angew. Chemie Int. Ed. 44 (2005) 3565–3568. doi:10.1002/anie.200500314.

[4] A. Kudo, I. Mikami, Photocatalytic activities and photophysical properties of Ga2-xInxO3 solid solution, J. Chem. Soc. Faraday Trans. 94 (1998) 2929–2932. doi:10.1039/a805563g.

[5] X. Wang, K. Maeda, A. Thomas, K. Takanabe, G. Xin, J.M. Carlsson, K. Domen, M. Antonietti, A metal-free polymeric photocatalyst for hydrogen production from water under visible light, Nat. Mater. 8 (2009) 76–80. doi:10.1038/nmat2317.

[6] R. Marschall, Semiconductor Composites: Strategies for Enhancing Charge Carrier Separation to Improve Photocatalytic Activity, Adv. Funct. Mater. 24 (2014) 2421–2440. doi:10.1002/adfm.201303214.

[7] Y.-P. Yuan, L.-W. Ruan, J. Barber, S.C. Joachim Loo, C. Xue, Hetero-nanostructured suspended photocatalysts for solar-to-fuel conversion, Energy Environ. Sci. 7 (2014) 3934–3951. doi:10.1039/C4EE02914C.

[8] B. Hvolbæk, T.V.W. Janssens, B.S. Clausen, H. Falsig, C.H. Christensen, J.K. Nørskov, Catalytic activity of Au nanoparticles, Nano Today. 2 (2007) 14–18. doi:10.1016/S1748-0132(07)70113-5.

[9] C. Marchal, Synthèse et réactivité de nanocomposites Au / g-C3N4 / TiO2 pour la production d'hydrogène par procédé photocatalytique sous illumination solaire et visible, Http://Www.Theses.Fr. (2017). https://www.theses.fr/2017STRAF011 (accessed December 21, 2018).

[10] W.-J. Ong, L.-L. Tan, Y.H. Ng, S.-T. Yong, S.-P. Chai, Graphitic Carbon Nitride (g-C3N4)-Based Photocatalysts for Artificial Photosynthesis and Environmental Remediation: Are We a Step Closer To Achieving Sustainability?, Chem. Rev. (2016). doi:10.1021/acs.chemrev.6b00075.

[11] Y. Chen, B. Wang, S. Lin, Y. Zhang, X. Wang, Activation of n → π* Transitions in Two-Dimensional Conjugated Polymers for Visible Light Photocatalysis, J. Phys. Chem. C. 118 (2014) 29981–29989. doi:10.1021/jp510187c.

[12] Q. Liang, Z. Li, Z.-H. Huang, F. Kang, Q.-H. Yang, Holey Graphitic Carbon Nitride Nanosheets with Carbon Vacancies for Highly Improved Photocatalytic Hydrogen Production, Adv. Funct. Mater. 25 (2015) 6885–6892. doi:10.1002/adfm.201503221.

[13] M.R. Hoffmann, S.T. Martin, W. Choi, D.W. Bahnemann, Environmental Applications of Semiconductor Photocatalysis, Chem. Rev. 95 (1995) 69–96. doi:10.1021/cr00033a004.

[14] H. Park, Y. Park, W. Kim, W. Choi, Surface modification of TiO2 photocatalyst for environmental applications, J. Photochem. Photobiol. C Photochem. Rev. 15 (2013) 1–20. doi:10.1016/J.JPHOTOCHEMREV.2012.10.001.

[15] I. Papailias, T. Giannakopoulou, N. Todorova, D. Demotikali, T. Vaimakis, C. Trapalis, Effect of processing temperature on structure and photocatalytic properties of g-C3N4, Appl. Surf. Sci. 358 (2015) 278–286. doi:10.1016/j.apsusc.2015.08.097.

[16] B. Ohtani, O.O. Prieto-Mahaney, D. Li, R. Abe, What is Degussa (Evonik) P25? Crystalline composition analysis, reconstruction from isolated pure particles and photocatalytic activity test, n.d. https://eprints.lib.hokudai.ac.jp/dspace/bitstream/2115/44837/1/JPPA216-2-3_179-182.pdf (accessed January 22, 2019).

[17] A. Thomas, A. Fischer, F. Goettmann, M. Antonietti, J.-O. Müller, R. Schlögl, J.M. Carlsson, Graphitic carbon nitride materials: variation of structure and morphology and their use as metal-free catalysts, J. Mater. Chem. 18 (2008) 4893. doi:10.1039/b800274f.

[18] M.J. Bojdys, J.-O. Müller, M. Antonietti, A. Thomas, Ionothermal synthesis of crystalline, condensed, graphitic carbon nitride., Chemistry. 14 (2008) 8177–82. doi:10.1002/chem.200800190.

[19] S. Brunauer, P.H. Emmett, E. Teller, Adsorption of Gases in Multimolecular Layers, J. Am. Chem. Soc. 60 (1938) 309–319. doi:10.1021/ja01269a023.

[20] D. Zywitzki, H. Jing, H. Tüysüz, C.K. Chan, High surface area, amorphous titania with reactive Ti $^{3+}$ through a photo-assisted synthesis method for photocatalytic H $_2$ generation, J. Mater. Chem. A. 5 (2017) 10957–10967. doi:10.1039/C7TA01614J.

[21] J. Zhang, X. Chen , K. Takanabe, K. Maeda, K. Domen, J.D. Epping, X. Fu, M. Antonietti,

X. Wang , Synthesis of a Carbon Nitride Structure for Visible-Light Catalysis by Copolymerization, Angew. Chemie Int. Ed. 49 (2010) 441–444. doi:10.1002/anie.200903886.

[22] B. Jürgens, E. Irran, J. Senker, P. Kroll, H. Müller, W. Schnick, Melem (2,5,8-Triamino-tri- s -triazine), an Important Intermediate during Condensation of Melamine Rings to Graphitic Carbon Nitride: Synthesis, Structure Determination by X-ray Powder Diffractometry, Solid-State NMR, and Theoretical Studies, J. Am. Chem. Soc. 125 (2003) 10288–10300. doi:10.1021/ja0357689.

[23] A.Y. Liu, M.L. Cohen, Prediction of new low compressibility solids., Science. 245 (1989) 841–2. doi:10.1126/science.245.4920.841.

[24] F. Vigneron, A. Piquet, W. Baaziz, P. Ronot, A. Boos, I. Janowska, C. Pham-Huu, C. Petit, V. Caps, Hydrophobic gold catalysts: From synthesis on passivated silica to synthesis on few-layer graphene, Catal. Today. 235 (2014) 90–97. doi:10.1016/J.CATTOD.2014.04.016.

[25] D. Gajan, K. Guillois, P. Delichère, J.-M. Basset, J.-P. Candy, V. Caps, C. Coperet, A. Lesage, L. Emsley, Gold Nanoparticles Supported on Passivated Silica: Access to an Efficient Aerobic Epoxidation Catalyst and the Intrinsic Oxidation Activity of Gold, J. Am. Chem. Soc. 131 (2009) 14667–14669. doi:10.1021/ja903730q.

[26] L. Chen, X. Zeng, P. Si, Y. Chen, Y. Chi, D.-H. Kim, G. Chen, Gold Nanoparticle-Graphite-Like C3N4 Nanosheet Nanohybrids Used for Electrochemiluminescent Immunosensor, Anal. Chem. 86 (2014) 4188–4195. doi:10.1021/ac403635f.

[27] P. Suchomel, L. Kvitek, R. Prucek, A. Panacek, A. Halder, S. Vajda, R. Zboril, Simple size-controlled synthesis of Au nanoparticles and their size-dependent catalytic activity, Sci. Rep. 8 (2018) 4589. doi:10.1038/s41598-018-22976-5.

[28] A.B. Jorge, D.J. Martin, M.T.S. Dhanoa, A.S. Rahman, N. Makwana, J. Tang, A. Sella, F. Corà, S. Firth, J.A. Darr, P.F. McMillan, H2 and O2 Evolution from Water Half-Splitting Reactions by Graphitic Carbon Nitride Materials, J. Phys. Chem. C. 117 (2013) 7178–7185. doi:10.1021/jp4009338.

[29] Y. Wang, X. Wang, M. Antonietti, Polymeric graphitic carbon nitride as a heterogeneous organocatalyst: from photochemistry to multipurpose catalysis to sustainable chemistry., Angew. Chem. Int. Ed. Engl. 51 (2012) 68–89. doi:10.1002/anie.201101182.

[30] Valery N. Khabashesku, A. John L. Zimmerman, J.L. Margrave, Powder Synthesis and Characterization of Amorphous Carbon Nitride, Chem. Mater. 12 (2000) 3264–3270. doi:10.1021/CM000328R.

[31] A. Du, S. Sanvito, Z. Li, D. Wang, Y. Jiao, T. Liao, Q. Sun, Y.H. Ng, Z. Zhu, R. Amal, S.C. Smith, Hybrid Graphene and Graphitic Carbon Nitride Nanocomposite: Gap Opening, Electron–Hole Puddle, Interfacial Charge Transfer, and Enhanced Visible Light Response, J. Am. Chem. Soc. 134 (2012) 4393–4397. doi:10.1021/ja211637p.

[32] J. Tauc, Optical properties and electronic structure of amorphous Ge and Si, Mater. Res. Bull. 3 (1968) 37–46. doi:10.1016/0025-5408(68)90023-8.

[33] † Oliver Diwald, † Tracy L. Thompson, † Tykhon Zubkov, ‡ Ed. G. Goralski, ‡ and Scott D. Walck, J.*,. John T. Yates, Photochemical Activity of Nitrogen-Doped Rutile TiO2(110) in Visible Light, (2004). doi:10.1021/JP031267Y.

[34] Ryuhei Nakamura, and Tomoaki Tanaka, Y. Nakato*, Mechanism for Visible Light Responses in Anodic Photocurrents at N-Doped TiO2 Film Electrodes, (2004). doi:10.1021/JP048112Q.

[35] W. Fang, M. Xing, J. Zhang, A new approach to prepare Ti3+ self-doped TiO2 via NaBH4 reduction and hydrochloric acid treatment, Appl. Catal. B Environ. 160–161 (2014) 240–246. doi:10.1016/J.APCATB.2014.05.031.

[36] P. Jiménez, C. Marchal, T. Cottineau, V. Caps, V. KELLER, Influence of gas atmosphere during synthesis of g-C3N4 for enhanced photocatalytic H2 production from water on Aug-C3N4 composites, J. Mater. Chem. A. (2019). doi:10.1039/C9TA01734H.

[37] L. Shen, Z. Xing, J. Zou, Z. Li, X. Wu, Y. Zhang, Q. Zhu, S. Yang, W. Zhou, Black TiO2 nanobelts/g-C3N4 nanosheets Laminated Heterojunctions with Efficient Visible-Light-Driven Photocatalytic Performance, Sci. Rep. 7 (2017) 41978. doi:10.1038/srep41978.

[38] P. V. Zinin, L.-C. Ming, S.K. Sharma, V.N. Khabashesku, X. Liu, S. Hong, S. Endo, T. Acosta, Ultraviolet and near-infrared Raman spectroscopy of graphitic C3N4 phase, Chem. Phys. Lett. 472 (2009) 69–73. doi:10.1016/j.cplett.2009.02.068.

[39] X. Wei, C. Shao, X. Li, N. Lu, K. Wang, Z. Zhang, Y. Liu, Facile in situ synthesis of plasmonic nanoparticles-decorated g-C $_3$ N $_4$ /TiO $_2$ heterojunction nanofibers and comparison study of their photosynergistic effects for efficient photocatalytic H $_2$ evolution, Nanoscale. 8 (2016) 11034–11043. doi:10.1039/C6NR01491G.

[40] Y. Cui, J. Zhang, G. Zhang, J. Huang, P. Liu, M. Antonietti, X. Wang, Synthesis of bulk and nanoporous carbon nitride polymers from ammonium thiocyanate for photocatalytic hydrogen evolution, J. Mater. Chem. 21 (2011) 13032. doi:10.1039/c1jm11961c.

[41] J.S. Kim, J.W. Oh, S.I. Woo, Improvement of the photocatalytic hydrogen production rate of g-C3N4 following the elimination of defects on the surface, Catal. Today. 293–294 (2017) 8–14. doi:10.1016/J.CATTOD.2016.11.018.

[42] A. Vinu, Two-Dimensional Hexagonally-Ordered Mesoporous Carbon Nitrides with Tunable Pore Diameter, Surface Area and Nitrogen Content, Adv. Funct. Mater. 18 (2008) 816–827. doi:10.1002/adfm.200700783.

[43] P. Lignier, M. Comotti, F. Schü, J.-L. Rousset, V. Rie Caps, Effect of the titania morphology on the Au/TiO 2-catalyzed aerobic epoxidation of stilbene, (n.d.). doi:10.1016/j.cattod.2008.04.032.

[44] V. Caps, S. Arrii, F. Morfin, G. Bergeret, J.-L. Rousset, Structures and associated catalytic properties of well-defined nanoparticles produced by laser vaporisation of alloy rods, Faraday Discuss. 138 (2008) 241–256. doi:10.1039/B706131E.

[45] Z. Lu, L. Zeng, W. Song, Z. Qin, D. Zeng, C. Xie, In situ synthesis of C-TiO2/g-C3N4 heterojunction nanocomposite as highly visible light active photocatalyst originated from effective interfacial charge transfer, Appl. Catal. B Environ. 202 (2017) 489–499. doi:10.1016/J.APCATB.2016.09.052.

[46] B. Zhu, P. Xia, W. Ho, J. Yu, Isoelectric point and adsorption activity of porous g-C3N4, Appl. Surf. Sci. 344 (2015) 188–195. doi:10.1016/J.APSUSC.2015.03.086.

Chapter 4

Synthesis, characterization, and (photo) catalytic evaluation of TiO_2(NTs)-gC_3N_4 and Au/TiO_2(NTs)-gC_3N_4 composites

A) Introduction

The evaluation of the (photo) catalytic activity of the studied materials in the present chapter will take place by using two reaction models, catalytic and photocatalytic reactions. The **catalytic oxidation of carbon monoxide** ($CO + O_2$ reaction) has been described as one study case for further fuel cell application. It is also mentioned that CO oxidation rates are enhanced by the presence of hydrogen while using any kind of oxide supports ($CO + O_2 + H_2$), also called as **preferential oxidation reaction (PROX)**. Another reaction model that will be investigated is the **photocatalytic Hydrogen (H_2) production**, which responds to the searching of a high performant material able to store solar energy efficiently. The goal of this second approach is to use hydrogen as the future energy carrier, complementary to petroleum use.

PROX is fundamentally a catalytic surface reaction driven by mainly the nature of the support, but not only. For that reason, the presence of available surface groups either from a catalyst or a metal co-catalyst to interact with the reactional medium plays a key role and influences overall activity of the material. The objective consists in eliminating the CO in the PROX gas mixture before it arrives to the fuel cell. CO is well-known as poisoning the fuel cell catalyst, namely Pt-based materials. Gold (Au) has been studied as a low temperature CO oxidation catalyst for the past three decades [1,2]. Au-catalyzed reaction is assisted by functional groups on the surface of the support. Here, it is the first time that TiO_2-gC_3N_4 support decorated with Au NPs are studied for PROX reaction and correlated with their physico-chemical properties.

Nowadays, **H_2 production** is yield at 96 % on fossil fuels and 4 % on water, this last being considered as a renewable source [3]. From water splitting technologies, "artificial photosynthesis", photocatalysis is considered a potential process for transforming solar energy into chemical "solar" fuels, *e.g.,* H_2 [4]. As Au/g-C_3N_4 (**chapter 2**) and Au/TiO_2(P25)-gC_3N_4 (**chapter 3**) composites were performed for H_2 production, in this last chapter a series of Au/TiO_2(nanotubes)-gC_3N_4 composites will be tested for H_2 production [5,6].

As frequently mentioned, despite of TiO_2 exhibits convenient characteristics for photo catalysis applications, this semiconductor suffers from intrinsic limitations, principally its large band gap (E_g > 3.1-3.2 eV), preventing its absorption at visible region wavelengths. In order to overcome this main limitation, several possible strategies were executed to improve its visible light response. Amongst different strategies we have chosen **heterojunction** systems formation of TiO_2-SC2 (possessing a narrower band-gap) that envisage to extend TiO_2 absorption wavelength towards visible-light region. In addition, the ideal staggered configuration (type II) also hinders recombination of the photogenerated carriers and promotes synergetic effects [7].

Here, the strategy, following the previous chapter related on the study of ternary Au/TiO_2(P25)-gC_3N_4-atm (Air and NH_3) composites, is to evaluate the impact of TiO_2 morphology when changing from TiO_2(P25) to TiO_2 nanotubes (NTs). The main challenge consists in the elaboration of an effective 1D (TiO_2 NTs) / 2D (g-C_3N_4)

interface. As it has been observed in chapter 3 that Au/TiO_2(P25)-gC_3N_4-NH_3 composites led to detrimental effects on photocatalytic activity for H_2 production, for that reason this **chapter 3** only focuses on the elaboration of TiO_2(NTs)-containing composites synthesized under air.

Hence, the elaboration of ternary Au/TiO_2(NTs)-gC_3N_4-Air composites are introduced to evaluate the impact of the surface chemistry, variation of SCs ratio, use of oxidative (Air) atmosphere, and the Au/SC specific activation on the activity of gold catalysts for both photocatalytic H_2 production and catalytic CO oxidation.

In this **chapter 4**, the engineering modulation of TiO_2(NTs) with g-C_3N_4 is achieved by performing the polycondensation of g-C_3N_4 precursors in the presence of TiO_2 NTs already synthesized, strategy which have been already proven efficient in generating a strong TiO_2(P25)/gC_3N_4 interface. Both model reactions, H_2 production and PROX are evaluated by depositing Au NPs with low loading (*ca.* 0.3 wt. %) onto the binary support TiO_2(NTs)-gC_3N_4-Air by comparing to their homologs Au/TiO_2(NTs) and Au/g-C_3N_4 materials.

B) Synthesis and characterization of TiO_2 nanotubes (NTs)

B.1. Synthesis of TiO_2 NTs

TiO_2 NTs were synthesized via hydrothermal synthesis method (**Fig. 4.1**), also called as Kasuga's method, starting from commercial TiO_2 (P25) nanoparticles as precursor. Typically, the synthesis comprises 5 general steps: **(1)** TiO_2 P25 is added into a vessel containing a concentrated NaOH (10 M) solution, then the resulting solution is agitated for 1h at 300 rpm to solubilize and dissolve TiO_2 NPs, **(2)** the solution is transferred in a closed stainless steel batch reactor and a thermal treatment is applied at 130 °C in autogenic pressure conditions in a furnace for 48h to growth layered nanosheets followed by **(3)** a consecutive rinsing step with distilled water and diluted HCl (1 M) inducing the curving and wrapping of the nanosheets into nanotubes, **(4)** the titanates nanotubes are dried at 110 °C for 10 h and finally **(5)** a last calcination step takes place to crystallize the formed TiO_2 NTs at 380 °C for 2h with a ramp of 5 °C/min.

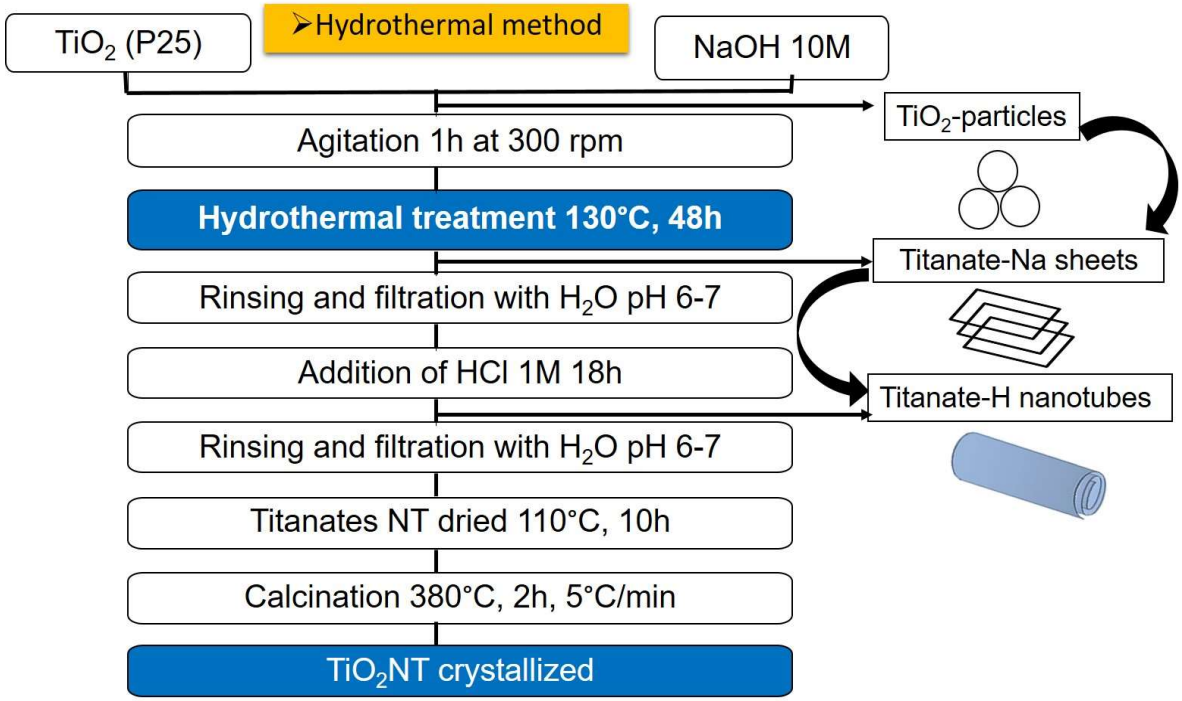

Figure 4.1. Kasuga hydrothermal synthesis method [8].

B.2. Characterization of TiO_2 NTs

The following section is devoted to the characterization of TiO_2 NTs obtained by Kasuga synthesis method (380 °C) and then mimicking the polycondensation condition of g-C_3N_4 synthesis under air (550 °C) in terms of morphological (TEM), structural (XRD), surface (BET) and optical (UV-Vis) properties in comparison with TiO_2 P25 precursor.

B.2.1. TEM observations

TEM images (**Fig. 4.2 a-d**) show the influence of final thermal treatment on TiO_2 NTs. By Kasuga's method, the obtained TiO_2 NTs are not fully crystalline yet, one can describe them as partially amorphous. From TEM image it can be observed that the TiO_2 NTs treated at 380 °C are well formed presenting length, internal and external diameters of *ca.* 130, 5.0, and 10 nm (**Table 4.1**), respectively. However, after thermal treatment at 550 °C one can notice two phenomena (1) TiO_2 NTs broke, and (2) the broken tubes get agglomerated, thus, shortening mainly their length to reach *ca.* 110 nm. Also, it seems that sintering occurred to form TiO_2 nanoparticles. This phenomena might occur by the destabilization due to temperature of the Hydrogen and Van deer Waals bond interactions inside TiO_2 roll-network that previously keep them as entangled nanotubes.

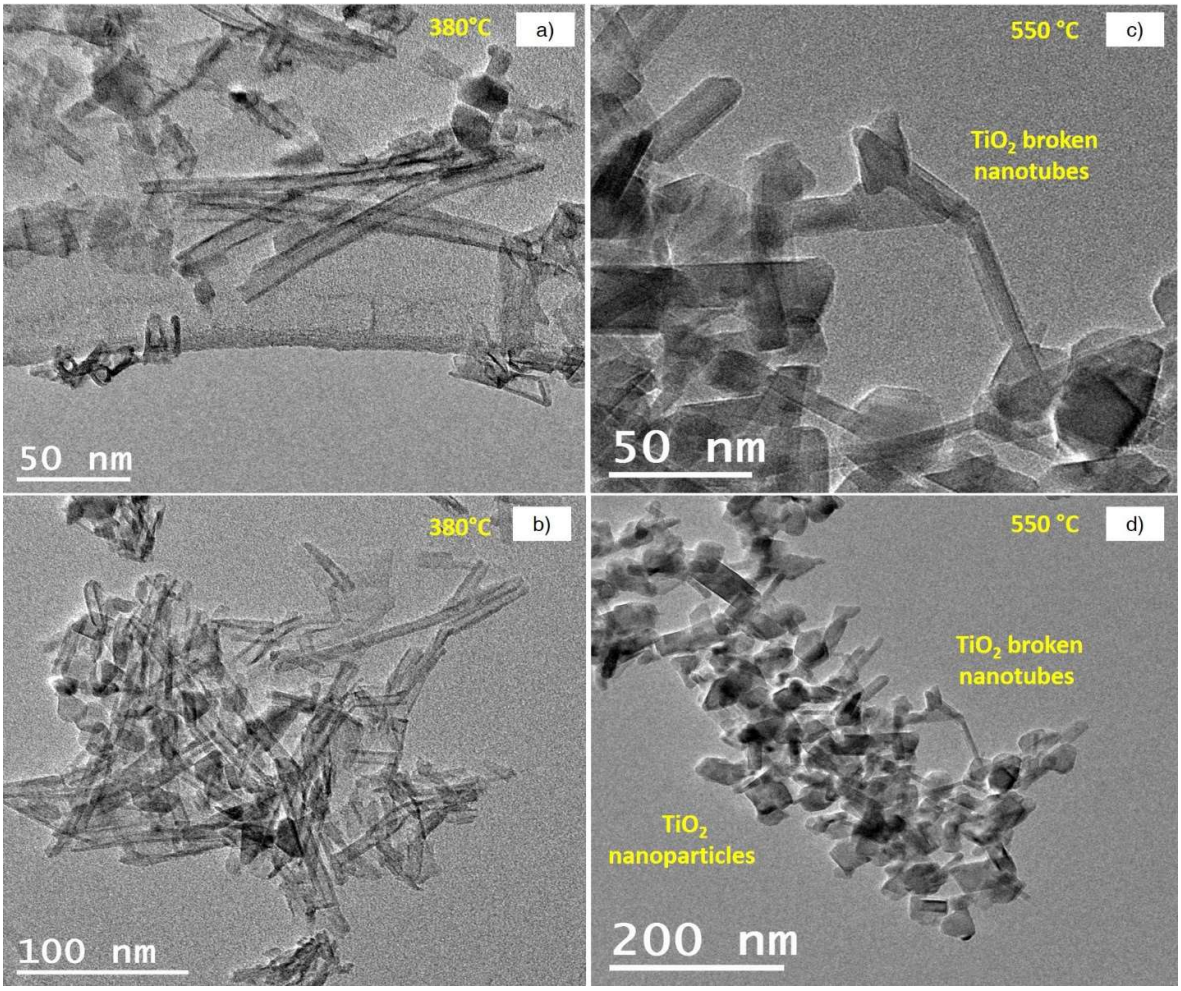

Figure 4.2. TEM images for TiO_2 NTs calcined at a, b) 380 °C (hydrothermal conditions) and c, d) 550 °C (polycondensation conditions).

Table 4.18. TiO_2 NTs dimensions before and after thermal polycondensation condition.

Temperature (°C)	Length (nm)	Internal Diameter (nm)	External diameter (nm)
380	130 ± 25	5.0 ± 1.5	10 ± 2
550	110 ± 15	4.7 ± 0.5	8 ± 1

B.2.2. XRD analysis

The XRD pattern (**Fig. 4.3**) of the starting TiO_2 P25 precursor exhibit two main characteristic diffraction peaks at $2\theta = 25.2°$ and $2\theta = 27.4°$, corresponding to the anatase phase, indexed as (101) diffraction plane in good agreement with JCPDS file 89-4921 [9,10], and to rutile phase, indexed as (110) diffraction plane. The additional characteristic peaks of both phases, anatase and rutile, are pointed out within the XRD pattern. A general observation found was that both TiO_2 NTs (380) and (550 °C) only exhibit the characteristic peaks of anatase phase, with no evidence of rutile phase. For the XRD pattern of TiO_2 NTs one can observe that the XRD peaks are thinner and more

intense for the higher temperature (550 °C) in comparison to the lower temperature (380 °C). This result suggest an increase of crystallinity at higher temperature, as reported elsewhere [11].

By Debye-Scherrer relationship, crystallite sizes were calculated. Thus, for TiO_2 P25 both anatase and rutile phases with crystallites sizes of 24 and 41 nm, respectively, were obtained. It must be mentioned that both TiO_2 NTs (380 °C) and (550 °C) present the same anatase crystallite size of 14 nm, which is lower than the precursor one.

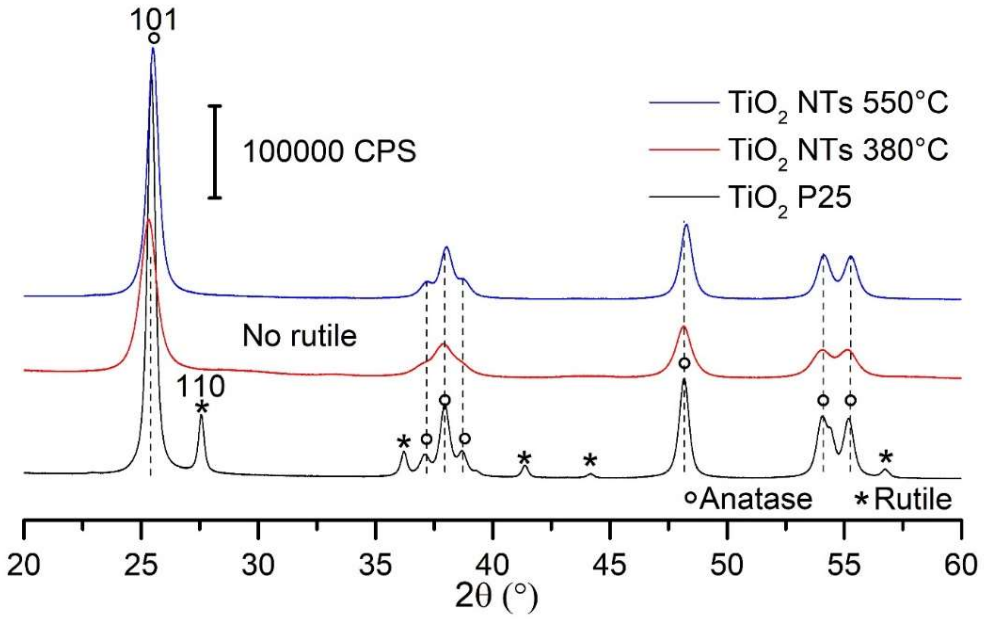

Figure 4.3. General XRD patterns of the TiO_2 P25, and TiO_2 NTs calcined at 380 and 550 °C under Air.

B.2.3. BET determination

From BET measurements (**Table 4.2, Fig. 4.4**), it can be noticed a clear specific surface area difference. S_{BET} for TiO_2 NTs (380 °C and 550 °C) present 144, and 107 $m^2\ g^{-1}$ values, which was approximately 3 and 2 times larger compared to the reference TiO_2 P25 (56 $m^2\ g^{-1}$). This result summarizes one strategy of this chapter to obtain a TiO_2 morphology leading to higher surface area, to achieve a more effective intimate contact with any other SC.

BJH pore-size distributions (**Table 4.2, Fig. 4.4**) exhibit a monomodal type for only TiO_2 P25 with a mean pore size centered between 30 and 40 nm, and a bimodal type for TiO_2 NTs (380 °C and 550 °C) presenting a first contribution of small pore sizes between 7 and 11 nm, and a second contribution for larger size centered at *ca.* 21 nm for both of them.

The first contribution can be assigned to the porosity resulting from internal diameter of the tubes and the second contribution to the porosity resulting from the entangled tubes. It can be observed that increasing the calcination temperature yield to the

diminishment of the first contribution and to a slight increase of the second one. This observation can be correlated to the tubes breaking and agglomeration.

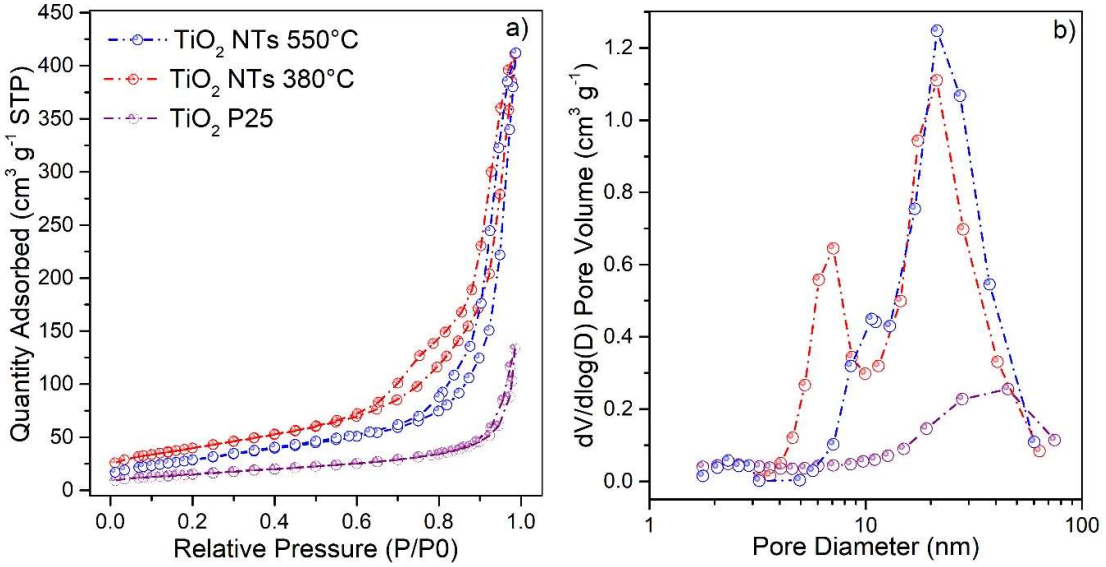

Figure.4.4. Nitrogen adsorption-desorption isotherms of the TiO_2 P25, and TiO_2 NTs calcined at 380 and 550 °C under Air atmosphere.

B.2.4. UV-Vis absorption measurements

From the UV-Vis spectra (**Fig. 4.5 a**), it can be seen the characteristic light absorption of TiO_2 in the UV/A region. However, TiO_2 NTs exhibit a slightly red-shift compared to TiO_2 P25 precursors. From the band-gap determination (**Table 4.2, Fig. 4.5 b**) calculated using Tauc equation [12] band gap values from 3.10 to 3.27 eV were observed.

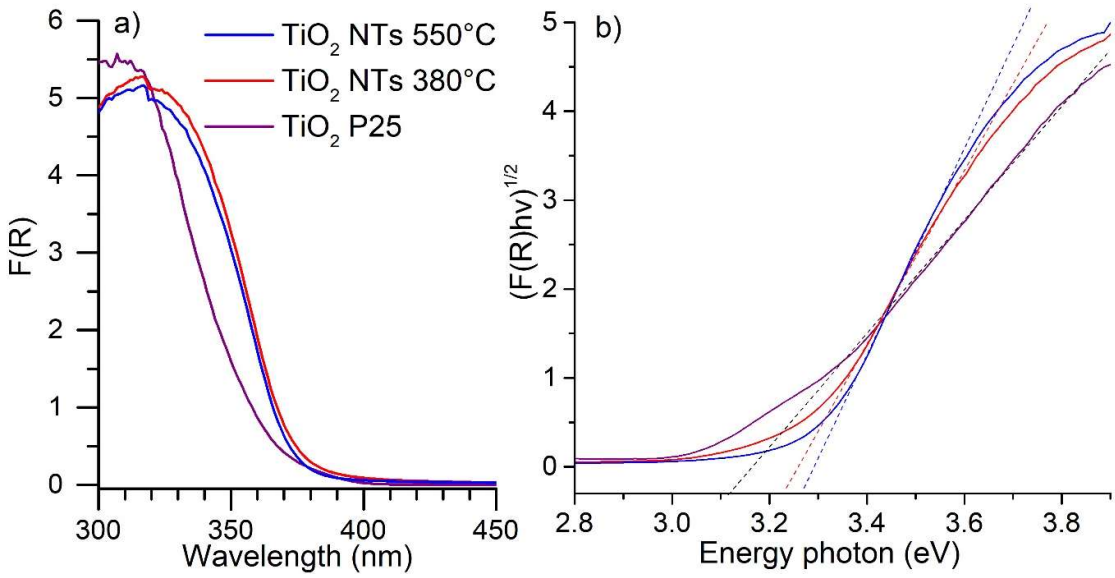

Figure 4.5. a) UV-Vis spectra b) Tauc plot of the TiO_2 P25, and TiO_2 NTs calcined at 380 and 550 °C under Air.

Table 4.19. Crystallite size, specific surface area (S_{BET}), pore size, and band gap of the TiO_2 P25, and TiO_2 NTs calcined at 380 and 550 °C under Air.

Titanium dioxide	Crystallite (nm)	S_{BET} (m^2/g)	Pore size (nm)	Band gap (eV)
TiO_2 P25, Evonik	24 / 41 (Anatase / Rutile)	56±6	46±5	3,10±0.05
TiO_2 NTs 380 °C	14 Anatase	144±14	21±2	3,24±0.05
TiO_2 NTs 550 °C	14 Anatase	107±10	21±2	3,27±0.05

C) Synthesis and characterization of binary TiO_2(NTs)-gC_3N_4 Air photocatalyst

C.1. Synthesis of TiO_2(NTs)-gC_3N_4-Air photocatalysts

The protocol used to synthesize TiO_2-gC_3N_4 composites was already introduced in **chapter 3, section B.1.1**. Here, the same protocol was performed only replacing TiO_2(P25) by TiO_2(NTs) during g-C_3N_4 polycondensation reaction. In the same manner, the model applied for the calculation of g-C_3N_4 content into the TiO_2(NTs)-gC_3N_4 composites is the same than the one already used for TiO_2(P25)-gC_3N_4 composites (of **Chapter 3, section B.2.1.1.a**).

C.2. Characterization of TiO_2(NTs)-gC_3N_4-Air photocatalysts

For the characterization of TiO_2(NTs)-gC_3N_4-Air composites, the same experimental strategy than developed in chapter 3 (**section B.1.2**) of selecting a broad (**screening**) and a narrow (**zoom**) range of relative proportion between the two SCs involved is used. The binary composites were characterized using typically TGA, FT-IR, XRD, and BET techniques to determine thermal, chemical surface, and structural properties. **In the following of this chapter the nomenclature used for TiO_2(NTs)-gC_3N_4-Air composites will be simplified as TiO_2-gC_3N_4.**

C.2.1. Screening method

C.2.1.1. TGA analysis

The resulting normalized weight losses (and thus g-C_3N_4 massic content determination in TiO_2-gC_3N_4 composite) were (26-74) (48-52) and (76-24) corresponding respectively to the theoretical values of (25-75) (50-50) and (75-25). In the following section, the g-C_3N_4

massic content for the screening composites is expressed as the experimental values determined from TGA analysis.

TGA profiles (**Fig. 4.6 a-b**) of the screening TiO_2-gC_3N_4 series (76-24; 48-52; 26-74) composites reveal a main decomposition peak with a maximum located at 552, 567, and 555 °C, respectively. This main weight loss is attributed to the presence of heptazine-base units in all screening composites, in good agreement with previous reports [13,14]. The obtained decomposition temperatures for composites were lower than the one-pot decomposition of g-C_3N_4 reference that occurs at 613 °C. One can suggest that in the composites TiO_2 thermally catalyzes g-C_3N_4 decomposition by oxidation explaining the shift towards lower temperatures. Nevertheless, TiO_2-gC_3N_4 (76-24 and 26-74) composites present a second decomposition peak located at 480 and 493 °C, respectively, corresponding to the lowest and highest content of g-C_3N_4 (24 and 74 wt. %). This secondary decomposition may be ascribed to a second type of g-C_3N_4, (previously mentioned in the TGA analysis of the screening composites of chapter 3) and assigned to g-C_3N_4 and TiO_2 with higher contact quality.

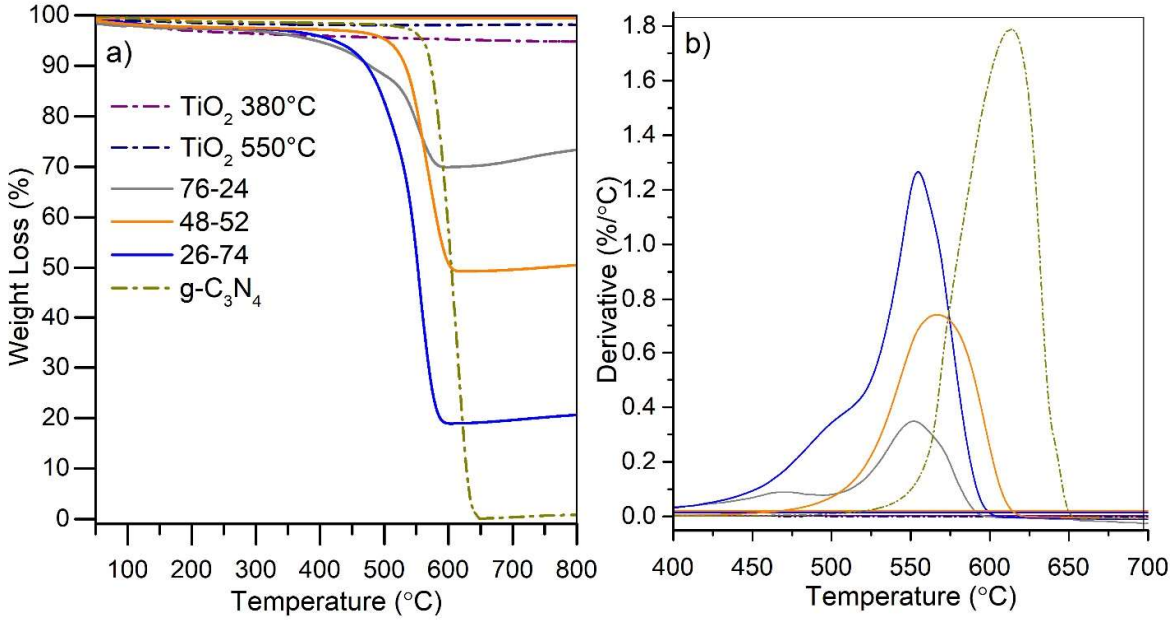

Figure 4.6. a) TGA profiles b) Derivatives of weight loss for TiO_2-gC_3N_4 screening composites and references.

C.2.1.2. FT-IR characterization

FT-IR spectra (**Fig. 4.7**) of the three screening composites present the characteristic absorption signals at 3500-3000 (hydroxyls or amines surface groups), 1640-1240 (tri-s-triazine fingerprints), 890 (N-H deformation) and 800 cm^{-1} (tri-s-triazine ring breathing), evidencing the presence of both SCs on the hybrid binary composite structure. However, one can notice that intensities vary in function of massic g-C_3N_4 content, from more to less pronounced from the highest to lowest content, evidencing one more time the dilution effect of g-C_3N_4.

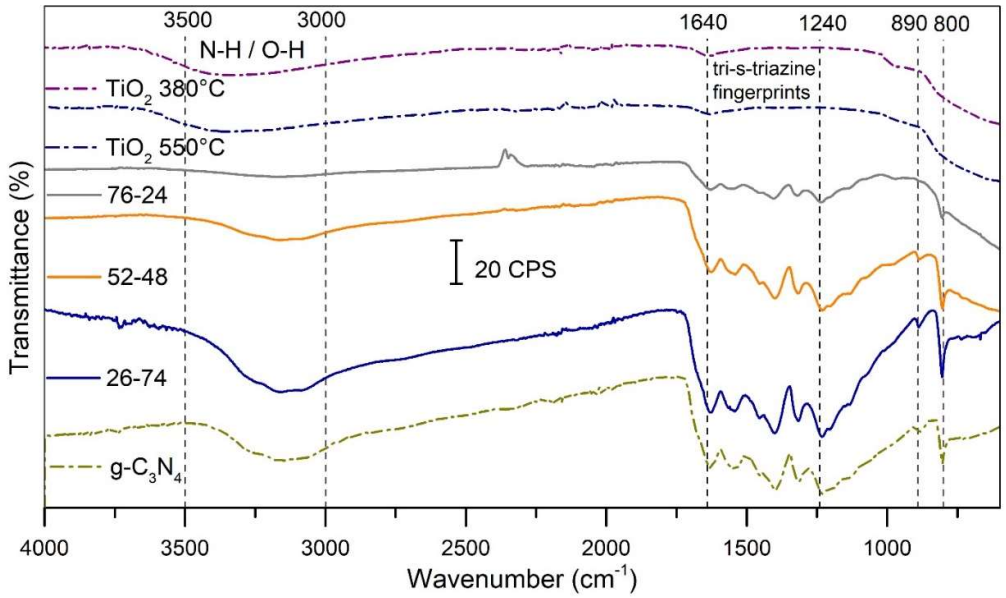

Figure 4.7. FT-IR spectra of TiO_2-gC_3N_4 screening composites and references.

C.2.1.3. XRD analysis

The XRD patterns (**Fig. 4.8 a**) of the screening-Air composites exhibit the main characteristic diffraction peaks at 2θ = 25.2° and 2θ = 27.4°, corresponding to the anatase phase of TiO_2, indexed as (101) diffraction plane in good agreement with JCPDS file 89-4921 [9,10], and to the interlayer stacking of π-conjugated aromatic systems of g-C_3N_4, indexed as (002) diffraction plane, characteristic for graphitic materials [15–17], respectively. By the interlayer stacking diffraction peak intensity of the screening composites, one can notice the variation in function of massic g-C_3N_4 content, from more to less pronounced from the highest to lowest content, evidencing one more time the dilution effect. It has to be underlined that for the case of g-C_3N_4 highest content (TiO_2-gC_3N_4 (26-74) composite), the g-C_3N_4 structure is well defined. By looking more precisely at the diffraction pattern intensity of its graphitic domain, one can say it is in higher proportion compared to the anatase phase. Also, the least intense characteristic diffraction peaks at 13.1 and 17.4 °, ascribed for TSTCN and STCN, respectively, appear on this composite structure, well evidencing the efficient formation of g-C_3N_4 structure on the hybrid binary composite. It must be remind that this feature was not evidenced for the TiO_2(P25)-gC_3N_4-Air screening composites.

After enlargement of the 2θ region ranging from 23.5 to 29.5 ° (**Fig. 4.8 b**), it is noticed that the TiO_2-gC_3N_4 (26-74) composite does not present a significant shift in any of the two diffraction peaks (TiO_2 (anatase) or g-C_3N_4 (interlayer)). Nevertheless, for the case of TiO_2-gC_3N_4 (48-52 and 76-24) composites, both anatase and interlayer stacking diffraction peaks are slightly shifted to lower Bragg angles.

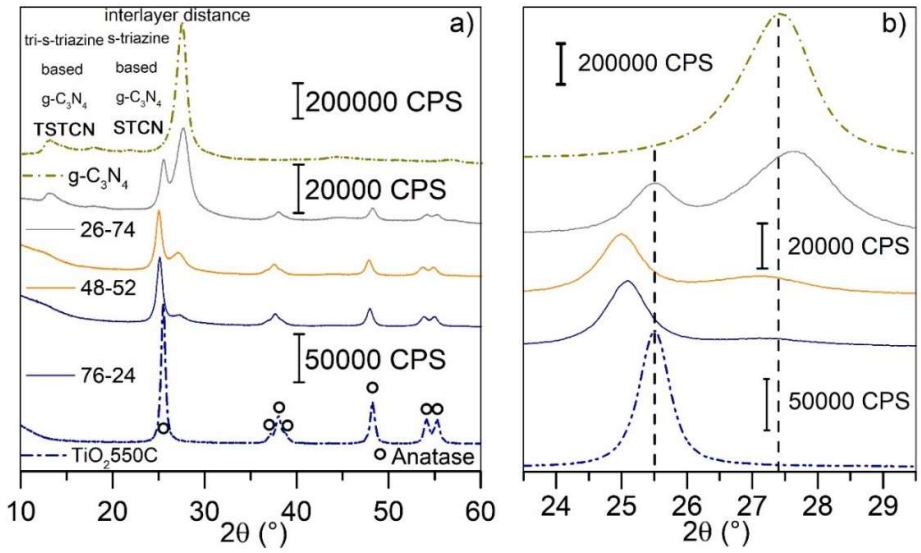

Figure 4.8. a) General XRD patterns b) zoom of the (23.5 – 29.5°) region of the TiO_2-gC_3N_4 screening composites and references.

By using a Debye-Scherrer relationship and fitting the anatase and g-C_3N_4 diffraction peaks, crystallite size were calculated (**Table 4.3**). One can notice that for all the screening composites no significant change on the crystallite size of anatase phase was observed. However, looking at g-C_3N_4 crystallite size, it has to be mentioned that it decreases when diminishing the g-C_3N_4 content. This result suggest a variation on the g-C_3N_4 bulk formation in presence of the TiO_2 during synthesis, presumably for a catalytic thermal effect leading to oxidation of part of g-C_3N_4 in close contact with TiO_2.

Table 4.20. Mean crystallite size of the crystalline phases of the TiO_2-gC_3N_4 screening composite and references.

	Mean crystallite size (nm)		
Sample	Anatase (101)	g-C_3N_4 (002)	N° layers
TiO_2 380 °C	14±1	-	-
TiO_2 550 °C	14±1	-	-
76-24	12±1	5.4±0.4	16±1
48-52	11±1	5.9±0.4	18±1
26-74	12±1	6.0±0.4	19±1
g-C_3N_4	-	6.6±0.4	26±1

C.2.1.4. BET determination

From BET measurements (**Table 4.4, Fig. 4.9 a**), all S_{BET} of the screening composites values present a decay variation from the lowest to highest g-C_3N_4 content, evidencing the dilution effect. In addition, the TiO_2-gC_3N_4 composites (76-24; 48-52; and 26-74)

present S_{BET} 4.6, 3.5, and 3.2 times lower in respect to the TiO_2 550 °C reference, also suggesting a breaking or dimensions diminishment of the TiO_2 NTs. Moreover, screening composites exhibit mainly the contribution of pores ≤ 10 nm however diminishing and shifted to larger pore diameter size when g-C_3N_4 content increases. This pore is ascribed for the internal diameter of the TiO_2 NTs. However, for the second kind of porosity, only present for the TiO_2 references centered at *ca.* 21 nm, it is ascribed for the porosity between the entangled TiO_2 NTs. Concerning the pores volume ($cm^2\ g^{-1}$) of the composites, a significant difference was found between them. It must be mentioned that the lowest pore volume was obtained for TiO_2-gC_3N_4 (48-52) composite with 0.10 $cm^2\ g^{-1}$, whilst the highest was obtained for TiO_2-gC_3N_4 (76-24) with 0.21 $cm^2\ g^{-1}$. This result shows that there is a double difference, which means that on TiO_2-rich composite, larger cavities are obtained. Nevertheless, the cavity of the composites is 6 to 12 times lower than TiO_2 550 °C reference, being the deepest mesopore material of the series.

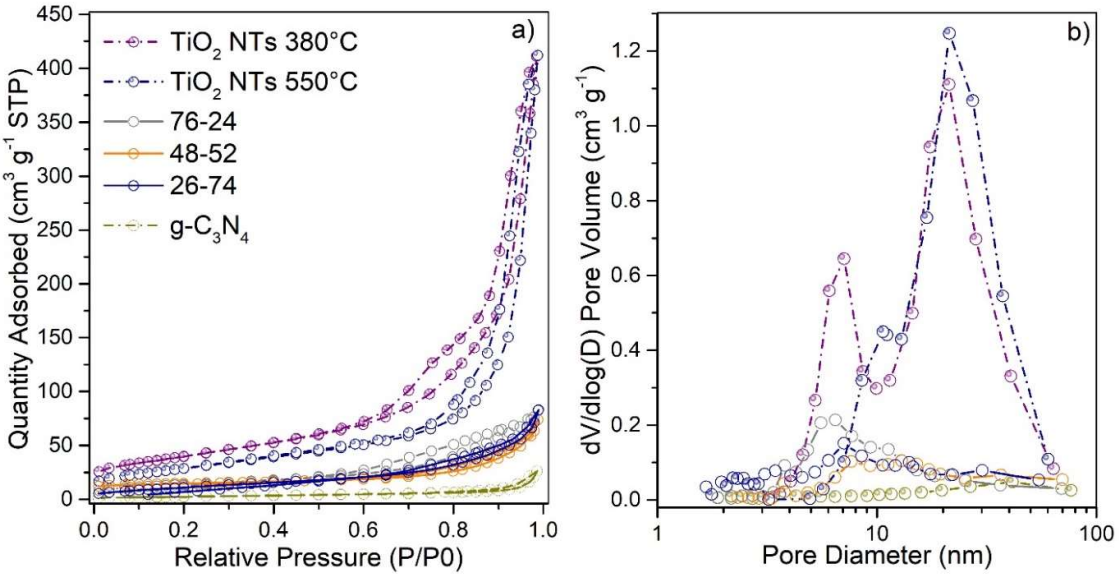

Figure 4.9. a) Nitrogen adsorption-desorption isotherms b) BJH pore-size distribution of the TiO_2-gC_3N_4 screening composite and references.

Table 4.21. Specific surface area (S_{BET}), pore volume (V_{pore}), pore size of the Au/TiO_2-gC_3N_4 screening composites and references.

Sample	S_{BET}* ($m^2\ g^{-1}$)	V_{pore} ($cm^3\ g^{-1}$)	Pore size** (nm)
TiO_2 380 °C	144±14	1.11±0.04	21±2
TiO_2 550 °C	107±10	1.25±0.04	21±2
76-24	50±5	0.21±0.02	7±1
48-52	38±4	0.10±0.02	8±1
26-74	34±3	0.15±0.02	7±1

g-C_3N_4	10±1	0.05±0.02	42±4

* = calculated using BET method; ** = calculated using BJH method

C.2.2. Zoom method- TiO_2(NTs)-gC_3N_4 (97.5-2.5)

For this second series of TiO_2(NTs)-gC_3N_4 composite, dealing with g-C_3N_4 massic loadings lower than 10 wt. %, only one composition was chosen, namely TiO_2(NTs)-gC_3N_4 (97.5-2.5) sample.

C.2.2.1. TGA analysis

From TGA profiles (**Fig. 4.10 a-b**) TiO_2-gC_3N_4 (97.5-2.5) composite no significant and reproducible weight loss was observed. As it was already observed in the case of TiO_2(P25)-gC_3N_4 zoom-Air composites, TGA analysis cannot be used to determined the real amount of g-C_3N_4. Consequently, for this sample, only the theoretical gC_3N_4 massic ratio will be considered.

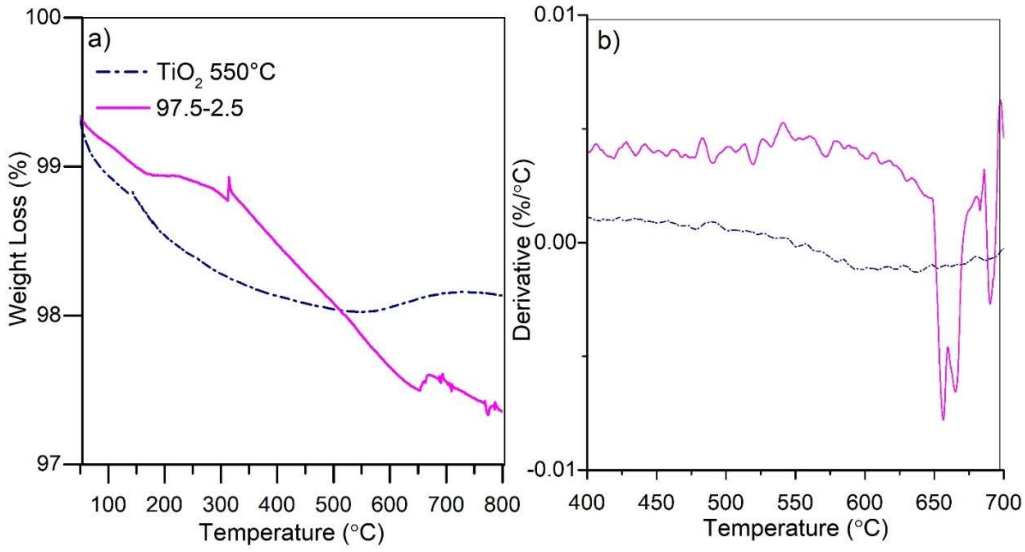

Figure 4.10. a) TGA profiles b) Derivatives of weight loss for TiO_2-gC_3N_4 (97.5-2.5) zoom composite and TiO_2 550 °C reference.

C.2.2.2. FT-IR characterization

FT-IR spectra (**Fig. 4.11**) of the zoom composite present the characteristic vibration bands of TiO_2 reference at 3500 - 3000 cm^{-1} (O-H from the hydroxyl surface groups or N-H from the amines surface groups of g-C_3N_4 skeleton). Despite of the lower proportion of g-C_3N_4 on the TiO_2-gC_3N_4 (97.5-2.5) composite, one can notice that it presents the tri-s-triazine fingerprints characteristic signals at 1640 - 1240 cm^{-1} region, evidencing the formation of g-C_3N_4 within the composite structure (even at low content). Furthermore, no signal was found on 890 or 800 cm^{-1}.

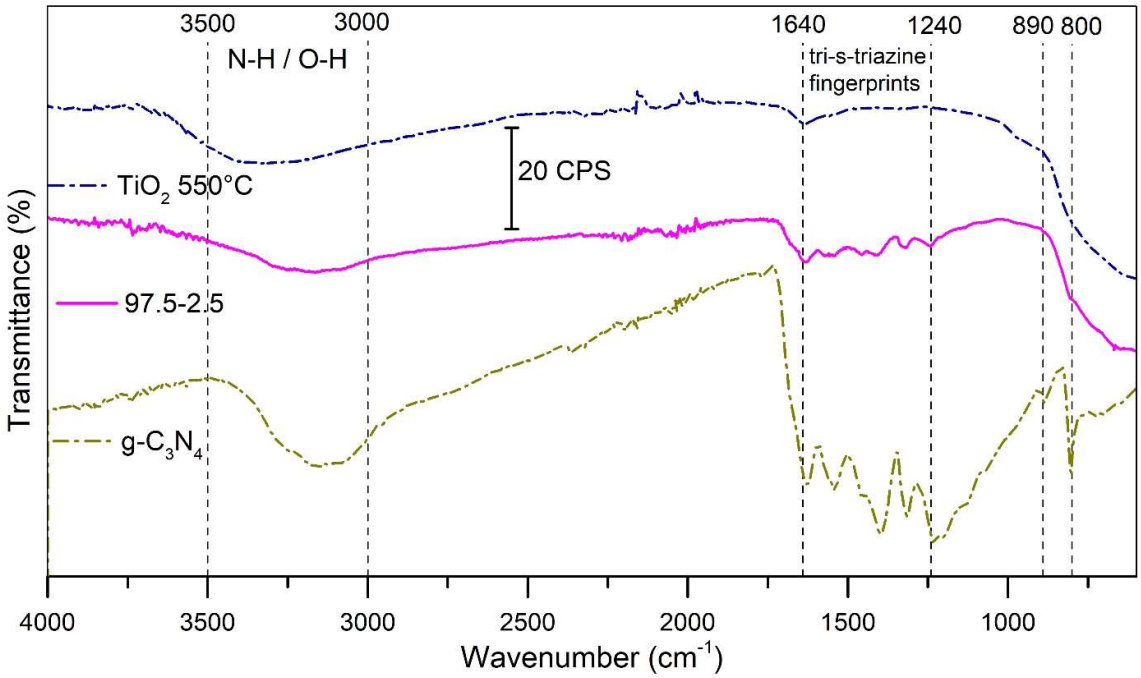

Figure 4.11. FT-IR spectra of TiO_2-gC_3N_4 (97.5-2.5) zoom composite and references.

C.2.2.3. XRD analysis

The XRD patterns (**Fig. 4.12a**) of the zoom air composite exhibit only the main characteristic diffraction peak at 2θ = 25.5° corresponding to the anatase phase of TiO_2, indexed as (101) diffraction plane. Besides, no presence of graphitic (g-C_3N_4) was found, possibly due to the low massic g-C_3N_4 content, which is not enough to be characterized.

After enlargement of the 2θ region ranging from 23.5 to 29.5 ° (**Fig. 4.12b**), it is noticed that the TiO_2-gC_3N_4 (97.5-2.5) composite anatase signal is shifted to lower Bragg angle, meaning that a slight change occurs on its unit cell.

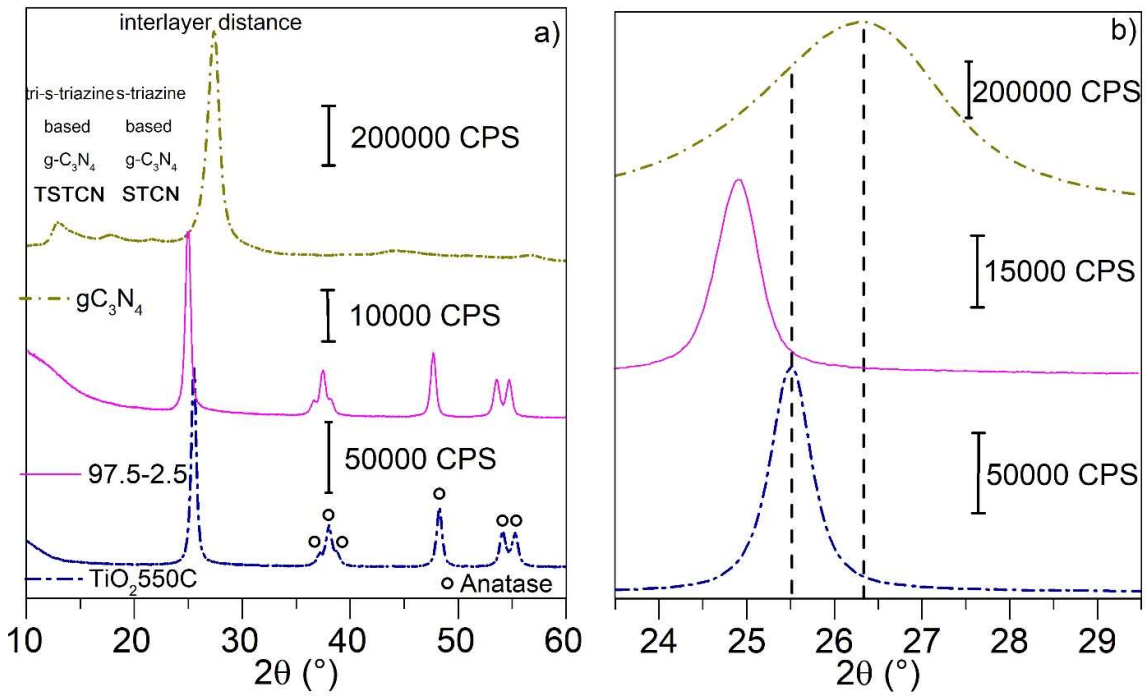

Figure 4.12. a) General XRD patterns b) zoom of the (23.5 – 29.5°) region of the TiO_2-gC_3N_4 (97.5-2.5) zoom composite and references.

By using a Debye-Scherrer relationship and fitting the anatase peak, the crystallite size were calculated. It can be noticed that the presence of small amount of g-C_3N_4 into the TiO_2-gC_3N_4 (97.5-2.5) composite did not induce any significant change on the crystallite size of anatase, *ca.* 14 nm.

C.2.2.4. BET determination

From BET measurements (**Table 4.5, Fig. 4.13 a**), it can be seen that the zoom composite, in addition to references, exhibit mainly a type-IV adsorption-desorption isotherm profile, ascribed for mesoporous materials [18–20]. One can notice that the obtained S_{BET} for the TiO_2-gC_3N_4 (97.5-2.5) composite was almost half of the TiO_2 550 °C reference one, evidencing the same behaviour than obtained in the screening composites, presumably for the same reasons. For the case of the obtained pore size of the TiO_2-gC_3N_4 (97.5-2.5) composite, it was the same value as for the TiO_2 550 °C reference, *ca.* 21 nm. Difference was observed for the pore volume, the TiO_2-gC_3N_4 (97.5-2.5) composite exhibited (0.69 $cm^3\ g^{-1}$) almost the half value compared to the TiO_2 550 °C reference (1.24 $cm^3\ g^{-1}$), meaning that half of the pore volume is covered or blocked by g-C_3N_4 formed.

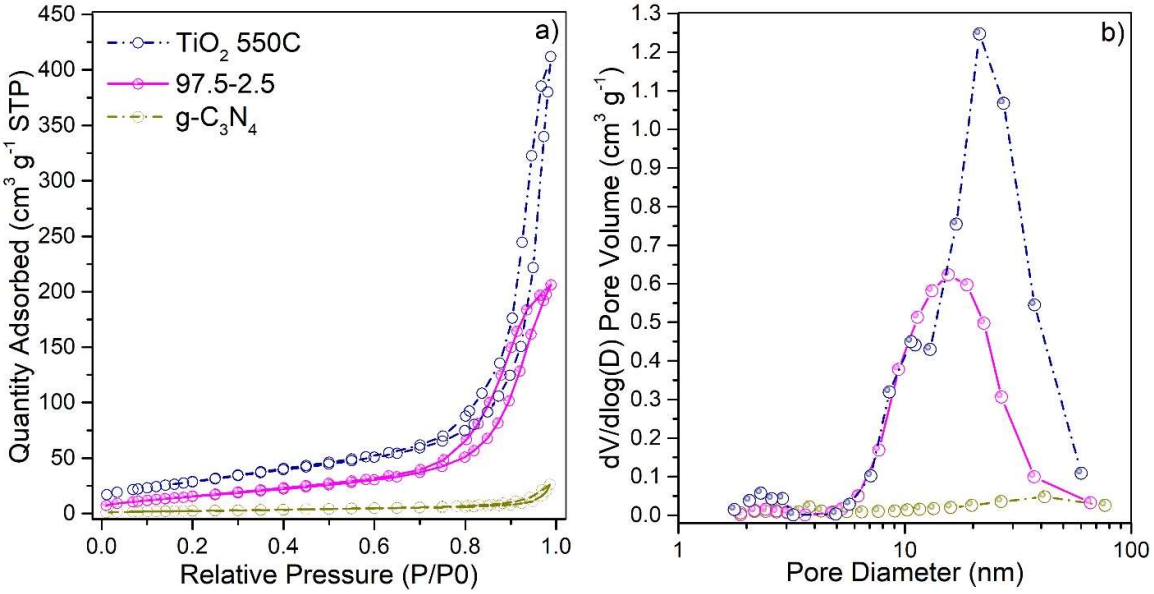

Figure 4.13. a) Nitrogen adsorption-desorption isotherms b) BJH pore-size distribution of the TiO_2-gC_3N_4 (97.5-2.5) zoom composite and references.

Table 4.22. Specific surface area (S_{BET}), pore volume (V_{pore}), pore size of the Au/TiO_2-gC_3N_4 (97.5-2.5) zoom composite and references.

$g\text{-}C_3N_4$	S_{BET}* ($m^2\ g^{-1}$)	V_{pore} ($cm^3\ g^{-1}$)	Pore size** (nm)
TiO_2 550 °C	107±10	1.24±0.02	21±2
97.5-2.5	60±6	0.69±0.03	21±2
$g\text{-}C_3N_4$	10±1	0.05±0.02	42±4

* = calculated using BET method; ** = calculated using BJH method

D) Synthesis and characterization of ternary hybrid Au/TiO_2(NTs)-gC_3N_4-Air composites

D.1. Synthesis of Au/TiO_2(NTs)-gC_3N_4-Air photocatalysts

The method used to deposit Au NPs onto the as-prepared binary composites (TiO_2(NTs)-gC_3N_4) was already described in **chapter 2, section C.1** [21].

D.2. Characterization of Au/TiO_2(NTs)-gC_3N_4 photocatalysts

The ternary composites were characterized with techniques *e.g.,* ICP-AES, TEM, and UV-Vis.

D.2.1. Screening method

D.2.1.1. Elemental analysis

Looking at the Au deposition yields (**Table 4.6**), the results can be interpreted that Au NPs have higher affinity for g-C_3N_4 surfaces than for TiO_2 ones, probably due to higher affinity of the Au precursor for the amines groups rather than for the hydroxyl ones. Indeed, deposition yield increases with g-C_3N_4 content. However, the small variation on Au content ranging from 0.18 to 0.26, might not influence the (photo) catalytic results.

Table 4.23. ICP-AES results of Au/TiO_2-gC_3N_4 screening composites and references.

Sample	Dep. Yield (%)	Au content (wt. %)
TiO_2(NTs)380 °C	70±4	0.21±0.01
TiO_2 (NTs)550 °C	60±3	0.18±0.01
76-26	74±4	0.22±0.01
48-52	86±4	0.26±0.01
26-74	87±4	0.26±0.01
g-C_3N_4	82±4	0.25±0.01

D.2.1.2. TEM observations

TEM images (**Fig. 4.14**) show the example of two samples, Au/TiO_2 550 °C (**a, b**) reference, and Au/TiO_2-gC_3N_4 (76-24) (**c, d**). The composite exhibit a larger Au NP mean particle size than the reference, *ca.* 4.2 and 3.7 nm, respectively. For Au/TiO_2 reference sample, one can notice a low density of Au NPs, presumably due to low amount of hydroxyl groups onto TiO_2 nanotubes surface. The associated standard deviation for the composite is 1.7 nm which is relatively large, probably due to the presence of several Au NPs populations ranging from 2 to 10 nm (large dispersion). For Au/g-C_3N_4 TEM images, please refer **chapter 2 section C 2.2** (Au NPs size of 3.2 nm were observed).

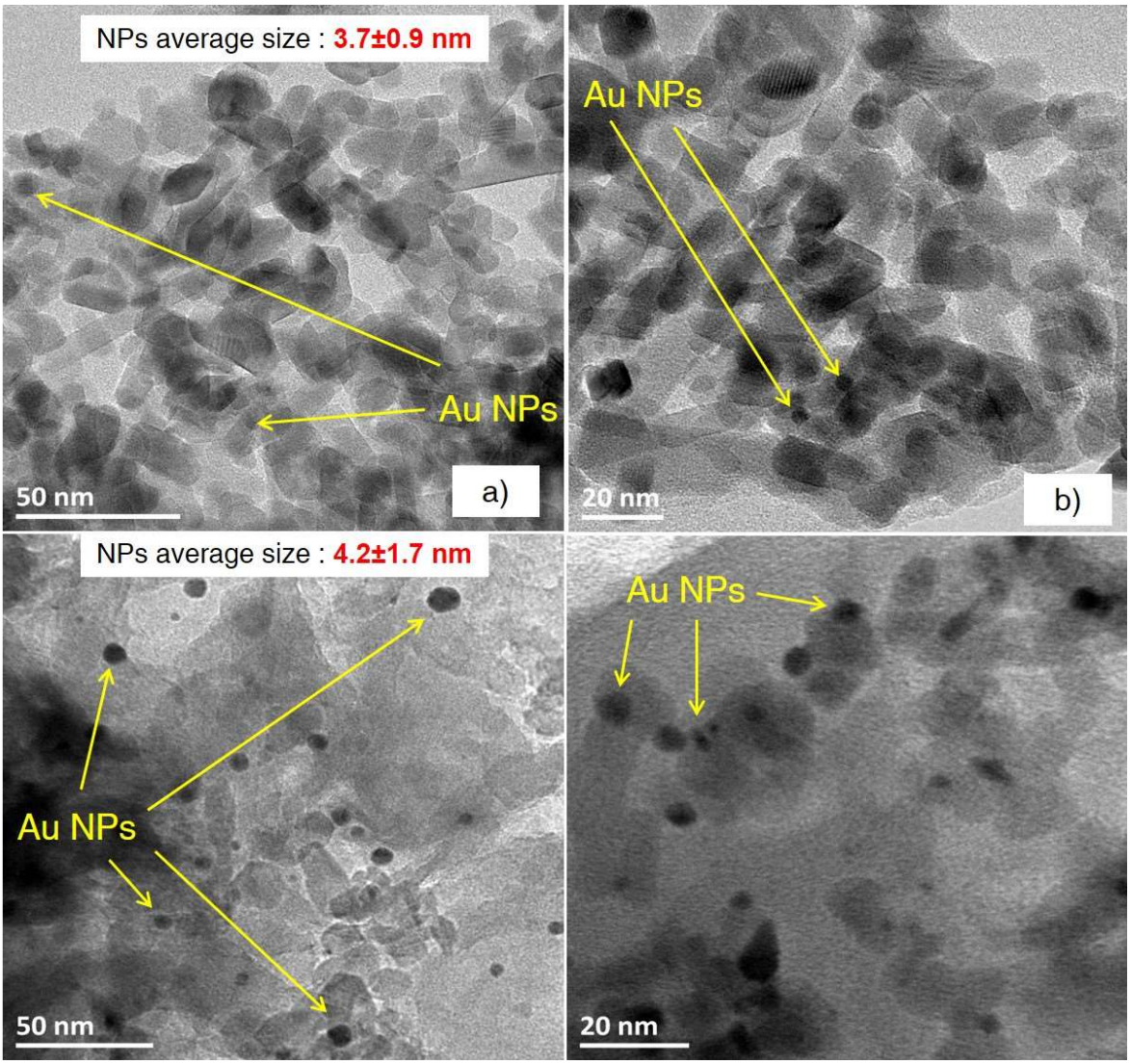

Figure 4.14. TEM images for a, b) 0.3 wt. % Au/TiO_2 550 °C, c, d) 0.3 wt. % Au/ TiO_2-gC_3N_4 (76-24).

D.2.1.3. UV-Vis absorption measurements

Fig. 4.15 (top) presents the color of TiO_2-gC_3N_4 screening composites and references after synthesis at 550 °C. One can notice a similar yellowish tone for all screening composites, the typical yellow powder for g-C_3N_4, and the typical white color for the two TiO_2 nanotubes calcined references.

From the UV-vis spectra (**Fig. 4.15 a**), one can observe that the three screening composites exhibit a maximum absorption in the UV/blue range of the spectra, with an absorption band edge at 450-460 nm (ascribed for g-C_3N_4, $\pi \rightarrow \pi^*$) [14,22–25]. It must be noticed that TiO_2 absorption contribution is more or less overlapped with g-C_3N_4 one. Another much smaller contribution with a maximum located at *ca.* 550 nm is ascribed to the presence of Surface Plasmon Induced Effect (SPIE) of Au NPs. For this purpose, **Fig. 4.15a (inset)** shows that the SPIE absorption is quite weak for Au/g-C_3N_4, more

pronounced for Au/TiO_2(NTs) two references, and is overlapped for all Au/TiO_2-gC_3N_4 screening composites. More or less intense SPIE signal can be attributed to the fact that Au NPs do not resonate in the same manner depending on the interaction with the support. Additional n→π* electronic transition on behalf of a pronounced layer deformation on g-C_3N_4, respectively [14] can be also present.

From the band-gap determination (**Fig. 4.16b**) calculated using Tauc equation [12], one can notice a slight variation between the screening composites (2.54 – 2.68 eV), but very close to the g-C_3N_4 value (2.70 eV).

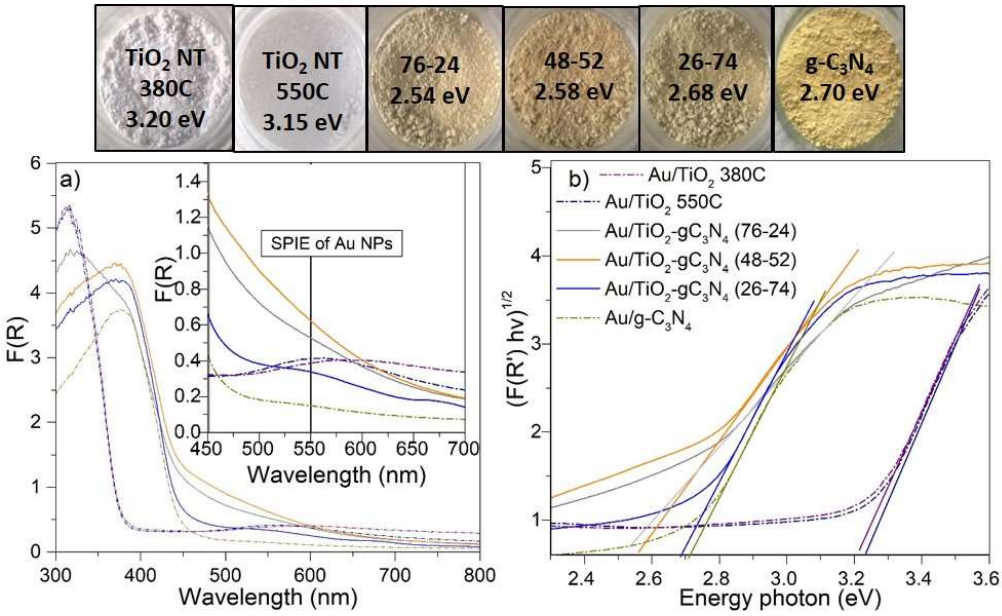

Figure 4.15. a) UV-Vis spectra of Au/TiO_2-gC_3N_4 screening composites and references Inset) zoom of the spectral domain corresponding to SPIE signal of Au NPS at approximately 550 nm. b) Tauc plot to determine the apparent band gap of Au/TiO_2-gC_3N_4 screening composites.

D.2.2. Zoom method Au/TiO_2(NTs)-gC_3N_4(97.5-2.5)

D.2.2.1. Elemental analysis

The deposition yield (**Table 4.7**) obtained for Au/TiO_2(NTs) 550°C reference, Au/TiO_2-gC_3N_4 (97.5-2.5) composite, and Au/g-C_3N_4 reference are 60, 63, and 82 %, respectively, confirming the better affinity toward g-C_3N_4 and meaning that low g-C_3N_4 content do not greatly impact TiO_2(NTs) surface properties. Even though there is an Au deposition yield difference over the samples, one can expect that this variation on Au content (from 0.18 to 0.25) do not greatly impact the photocatalytic H_2 production of the materials.

Table 4.24. ICP-AES results of Au/TiO_2-gC_3N_4 zoom composite and references.

Sample	Dep. Yield (%)	Au content (wt. %)
TiO_2 550 °C	60±3	0.18±0.01
97.5-2.5	63±3	0.19±0.01

g-C_3N_4	82±4	0.25±0.01

D.2.2.2. TEM and PSD characterization

TEM images (**Fig. 4.16**) show two samples, Au/TiO_2 550 °C (**a, b**), and Au/TiO_2-gC_3N_4 (97.5-2.5) (**c, d**). Au/TiO_2-gC_3N_4 (97.5-2.5) composite exhibits the smallest Au NP mean particle size (3.1 nm) associated with the smallest standard deviation (0.6 nm). Whilst, the reference Au/TiO_2 550 °C shows larger mean particle size (3.7 nm), with larger standard deviation (0.9 nm). The lower Au NPs size obtained for the composite sample (comprising only 2.5 wt. % of g-C_3N_4), compared to the one observed on the composite containing 24% of g-C_3N_4 (**Fig. 4.16 c, d**), presumably comes from a good synergy between the two SCs interface or to the fact that the low content of g-C_3N_4 influences the growth of Au NPs of ≤ 5 nm. No agglomerates of Au NPs were observed. For Au/g-C_3N_4 TEM images, please refer to **chapter 2 section C 2.2**, where Au NPs size of 3.2 nm were observed

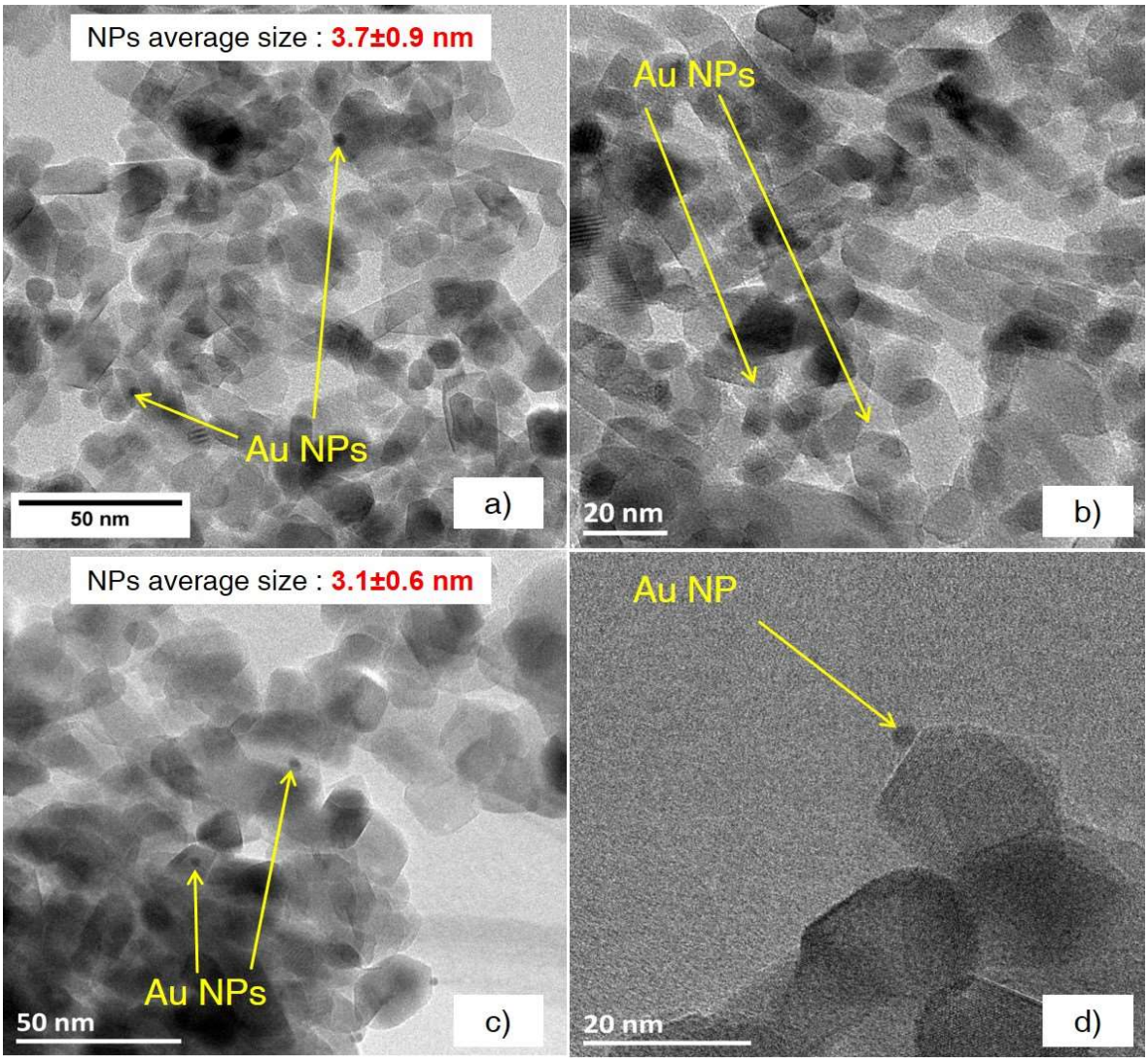

Figure 4.16. TEM images for Au/TiO_2-gC_3N_4 zoom composite and reference, including the mean particle size with their corresponding standard deviation, a, b) 0.3 wt. % Au/TiO_2 550 °C, c, d) 0.3 wt. % Au/ TiO_2-gC_3N_4 (97.5-2.5).

From the particle size distribution (**Fig. 4.17**) (also containing the screening composite with higher g-C_3N_4 content (24 %) for comparison), one can notice that the two composite samples display a monomodal distribution and only for Au/g-C_3N_4 reference case displays a quasi-bimodal profile. Both composites follow a similar Au NPs size distribution than their close reference, for example Au/TiO_2-gC_3N_4 (97.5-2.5) present NPs ranging from 2 to 6 nm, and Au/TiO_2 550°C exhibit sizes from 3 to 7 nm, both with a predominant Au NPs size population centered at 4-5 nm. Regarding the mean Au NPs size of the composites, Au/TiO_2-gC_3N_4 (76-24) and Au/TiO_2-gC_3N_4 (97.5-2.5) display 4.2 ± 1.7 and 3.1 ± 0.6 nm results, showing that a higher g-C_3N_4 content leads to larger deposited Au NPs with higher dispersion degree.

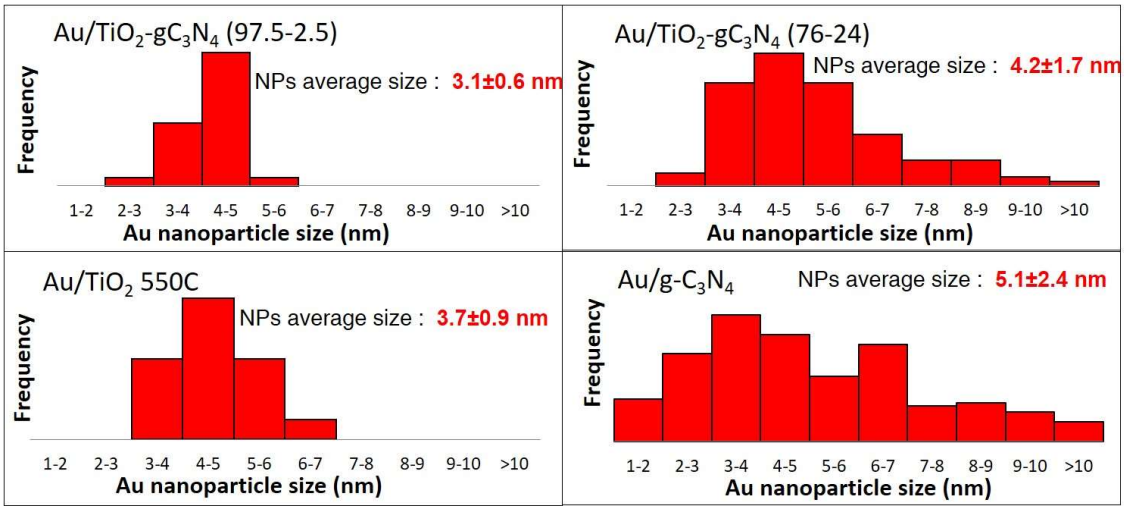

Figure 4.17. Particle size distribution of screening (76-24) and zoom (97.5-2.5) composites and references synthesized under air obtained by TEM.

D.2.2.3. UV-Vis absorption measurements

Fig. 4.18 (top) shows the color of TiO_2-gC_3N_4 zoom composites and references after synthesis (550 °C). It can be observed the characteristic colors for the two references, and the low g-C_3N_4 content composite did not yield a color change, remaining white as TiO_2.

From the UV-vis spectra (**Fig. 4.18 a**), one can observe that the Au/TiO_2-gC_3N_4 (97.5-2.5) composite exhibit a maximum absorption in the UV/blue range of the spectra, with an absorption band edge at 386 nm, ascribed for TiO_2. A second contribution with a maximum located at *ca.* 550 nm is ascribed to the presence of Surface Plasmon Induced Effect (SPIE) of Au NPs. For this purpose, **Fig. 4.18 a (inset)** shows an equal SPIE absorption for Au/TiO_2(NTs) 550°C reference and Au/TiO_2-gC_3N_4 (97.5-2.5) composite, suggesting an easier resonance of their deposited Au NPs allowing a higher absorption at this characteristic plasmon wavelength in comparison with the Au/g-C_3N_4 reference.

From the band-gap determination (**Fig. 4.18 b**) calculated using Tauc equation [12], one can notice a slight variation between the zoom composite and Au/TiO_2(NTs) 550°C reference, meaning that a low g-C_3N_4 content into the composite do not impact significantly its optical properties (as evidenced on the absorption spectra).

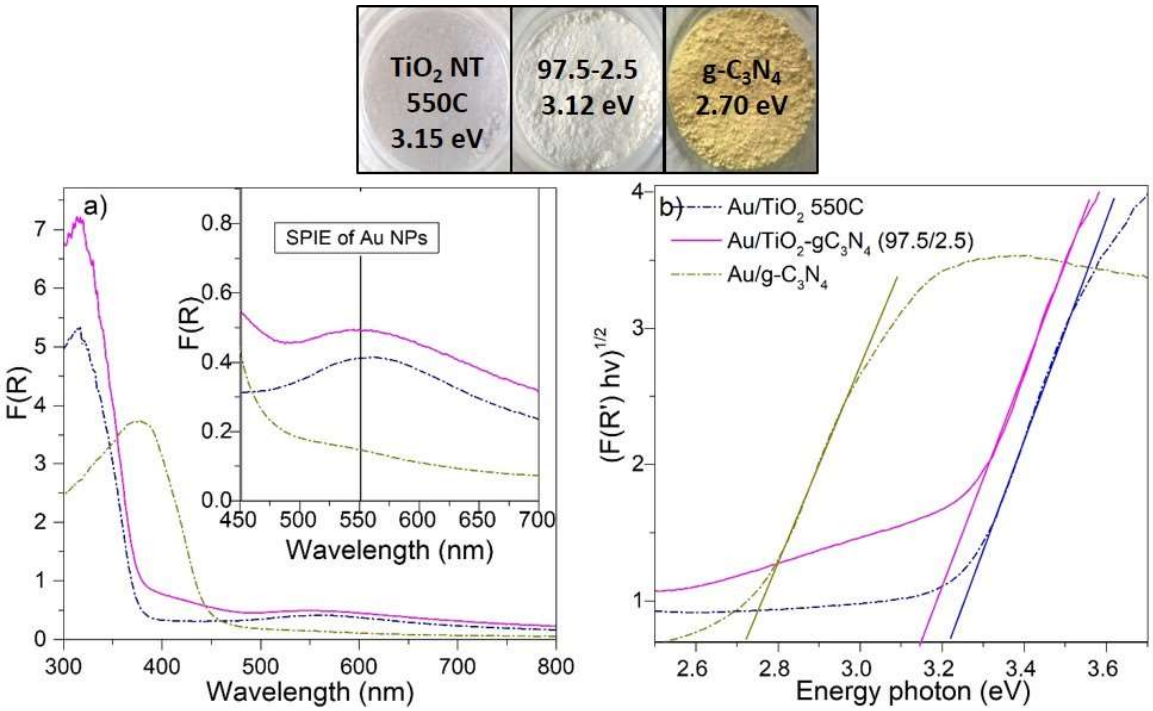

Figure 4.18. a) UV-Vis spectra of Au/TiO_2-gC_3N_4 (97.5-2.5) zoom composites and references Inset) zoom of the spectral domain corresponding to SPIE signal of Au NPS at approximately 550 nm b) Tauc plot to determine the apparent band gap of Au/TiO_2-g-C_3N_4 zoom composites.

D.2.2.4. XPS model analysis

From the survey spectra (**Fig. 4.19 a**), one can observe that major contributions are N 1s and C 1s for Au/g-C_3N_4 and Au/TiO_2-gC_3N_4 (26-74) samples and Ti 2p and O 1s for TiO_2-based samples. Then, the minor contributions are O 1s for Au/g-C_3N_4 reference and C 1s for TiO_2-rich samples. Also, for the five samples, a very low intensity peak was present for Au 4f characteristic signal. The characteristic **Au 4f signals** (**Fig. 4.19 b**) exhibit the two typical contributions at *ca.* 86.3 and 82.7 eV attributed to bulk Au^0 $4f_{7/2}$ and Au^0 $4f_{5/2}$, respectively. Amongst the samples, the intensity varies, for the Au/g-C_3N_4 reference exhibiting the highest, presumably for a better exposure of the Au NPs on the surface.

From **Table 4.8**, one can notice the binding energy position of Au $4f_{7/2}$ in the five samples were shifted toward lower binding energy compared to the theoretical Au^0 bulk, *ca.* 84 eV [26]. This shift was larger than -0.4 eV in all samples, confirming a charge transfer from TiO_2-based support to the Au NPs. This result also suggest different Au NPs/support interactions leading to different Au 4f binding energy shifts. Concerning, the Au/Ti atomic ratio results, they exhibit the lowest values for the two TiO_2 references and the low g-C_3N_4 content composite (zoom), evidencing the lowest amount of Au NPs available on the surface supports. However, for the high g-C_3N_4 content composite (screening) the ratio increases significantly (*ca.* 0.072), confirming higher surface Au NPs density and more accessible at the surface. Moreover for Au/g-C_3N_4, the Au/C

atomic ratio is larger than Au/Ti ratios on Au/TiO_2 references, which confirms that on g-C_3N_4 surface the Au NPs are denser, more exposed, and more accessible on the surface.

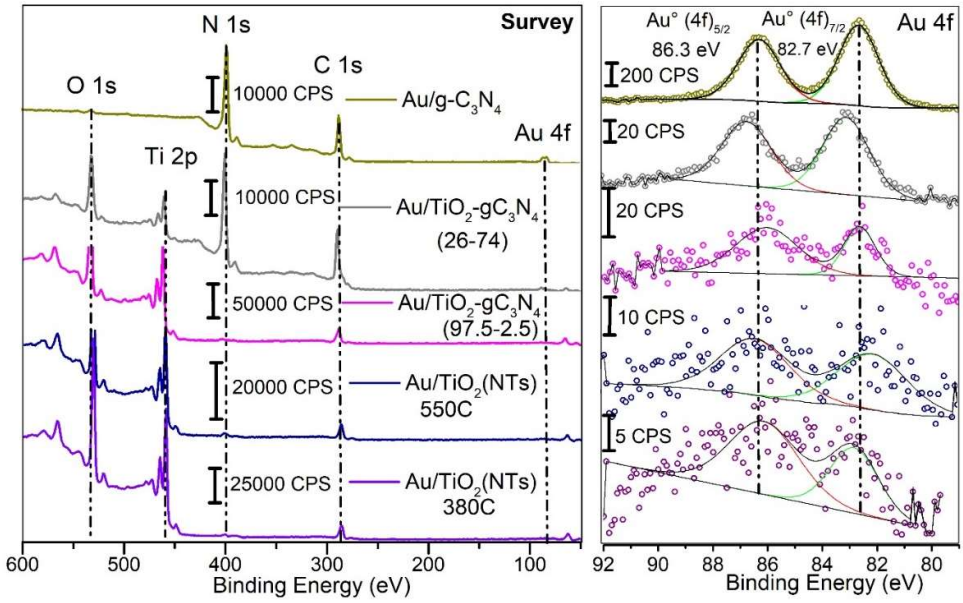

Figure 4.19. XPS a) survey and b) Au 4f spectra of the Au/TiO_2-gC_3N_4 (97.5-2.5; 26-74) composites and the three references Au/g-C_3N_4, Au/TiO_2(NTs) 380 and 550 °C.

Fig. 4.20 shows the O1s spectra of g-C_3N_4 reference material before and after the Au NPs deposition takes place. One can highlight that after the Au NPs are deposited onto g-C_3N_4 surface in addition to binding energy shift, the disappearance of one contribution, out of two, is observed. Consequently, the only remaining peak at 529.7 eV corresponds to a non-reported oxygen specie (to the best of our knowledge), meaning that probably the peak at 532.1 eV (hydroxyl group) was the one which disappeared due to the anchoring functionality that host Au NPs.

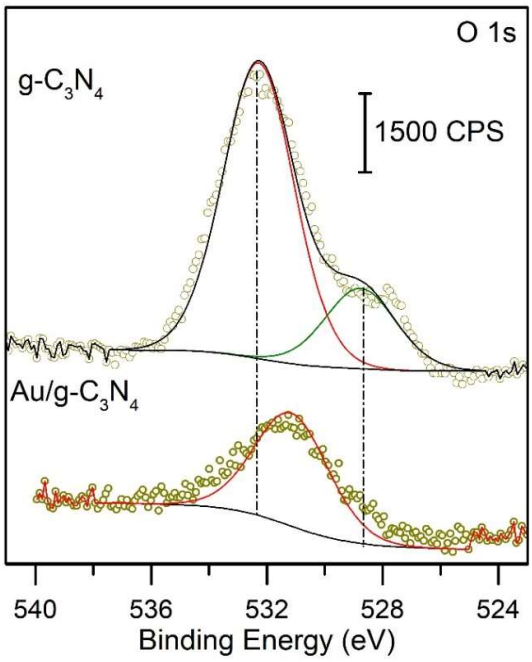

Figure 4.20. XPS O 1s of the Au/g-C_3N_4 and g-C_3N_4 samples.

The **C 1s signal** in the two (screening and zoom) composites Au/TiO_2-gC_3N_4 (97.5-2.5) and (26-74) (**Fig. 4.21 a**) displays 3 contributions. The signal located at 286.1 eV, can be ascribed for C-O bond coming from the O-Ti-O-C-N interactions [28], evidencing the TiO_2-gC_3N_4 interface and confirming the heterojunction. The other two contributions are the two characteristic signals for bare g-C_3N_4 at 287.3 and 284.6 eV, attributed for sp^2-bonded C of N=C-$(N)_2$ from the heterocyclic ring [29] and C-C bond (adventitious carbon), respectively. The main difference on these mentioned signals in both composites is that they are shifted toward higher binding energy (≥ 0.4 eV) compared to the Au/g-C_3N_4 reference, presumably due to chemical environmental change around C atoms due to interaction with e^- attracting species.

For the references case of Au/TiO_2 550C and Au/TiO_2 380C, they display only two contributions, the major contribution (284.6 eV) is attributed to the adventitious carbon and the minor contribution (288.4 eV) is attributed to C=O from carbonyl groups or from O_2 adsorbed species.

The **Ti 2p signal** in the four TiO_2-based samples, Au/TiO_2 550°C, Au/TiO_2 380°C, Au/TiO_2-gC_3N_4 (97.5-2.5) and (26-74) (**Fig. 4.21 b**) displays 2 main contributions at 463.9 and 458.2 eV ascribed to Ti $2p_{1/2}$ and Ti $2p_{3/2}$, respectively, characteristic for Ti^{4+} in TiO_2. Nevertheless, the screening composite (Au/TiO_2-gC_3N_4 (97.5-2.5)) presents a significant shift (*ca.* 0.6 eV) toward higher energy for both Ti^{4+} peaks compared to the reference Au/TiO_2 550°C, suggesting a possible chemical environment change. However when comparing the reference Au/TiO_2 550°C with (Au/TiO_2-gC_3N_4 (97.5-2.5)) zoom composite, no significant shift was found. Hence, one cannot exclude the presence of two minor contribution from satellite peaks at 463.5 and 458.2 eV ascribed for Ti^{3+} $2p_{1/2}$ and

Ti^{3+} $2p_{3/2}$, respectively, on TiO_2-based samples (references, and composites). This hypothesis was already described in **chapter 3 section E.1** for Ti 2p spectra as a result of Ti^{4+} reduction with $NaBH_4$ Au deposition.

The **N 1s signal** in the three g-C_3N_4–based samples, the reference Au/g-C_3N_4, Au/TiO_2-gC_3N_4 (97.5-2.5) and (26-74) samples (**Fig. 4.21 c**) displays 2 characteristic contributions, a major one at 399.9 and a minor one at 397.9 eV assigned to sp^2-hybridized pyridine nitrogen of C=N-C from the heterocyclic ring and to the N-$(C)_3$ tertiary nitrogen, respectively [30–32]. Hence, it has also to be mentioned that both composites signals were significantly shifted (≥ 0.4 eV) toward higher binding energy compared to Au/g-C_3N_4 reference, that observation might suggest a modification of chemical environment of N atoms assigned to an interaction with an e- attractive species. However it must be underlined that for the case of Au/TiO_2-gC_3N_4 (26-74) composite, a third minor contribution was observed at 401.4 eV, ascribed for N-H (terminal amine groups) of polymeric gC_3N_4 structure.

The **O 1s signals** in the four TiO_2-based samples, Au/TiO_2 550°C, Au/TiO_2 380°C, Au/TiO_2-gC_3N_4 (97.5-2.5) and (26-74) (**Fig. 4.21 d**) show 2 characteristic contributions of TiO_2 species at 530.1 and 529.4 eV attributed to hydroxyl surface groups (-OH) (minor contribution) and Ti-O (major contribution), respectively. Hence, high g-C_3N_4 content composite (screening) shows a significantly shifted (≥ 0.4 eV) toward higher binding energy compared to Au/g-C_3N_4 reference, suggesting that for small amounts of g-C_3N_4 (zoom composite, 2.5 wt. %) no influence is observed on the oxygen chemical environment.

Au/g-C_3N_4 sample only presents the –OH contribution but in a lesser relative amount than on TiO_2-based materials. However the poorly hydroxylated surface of g-C_3N_4 support seems not to be so limiting for Au NPs deposition. Globally, the presence of hydroxyl groups in all TiO_2-containing samples are of great importance for an efficient Au deposition. Specifically on g-C_3N_4-containing materials, one can assume that Au NPs deposition efficiency may be driven thanks to the additional surface amino groups of g-C_3N_4.

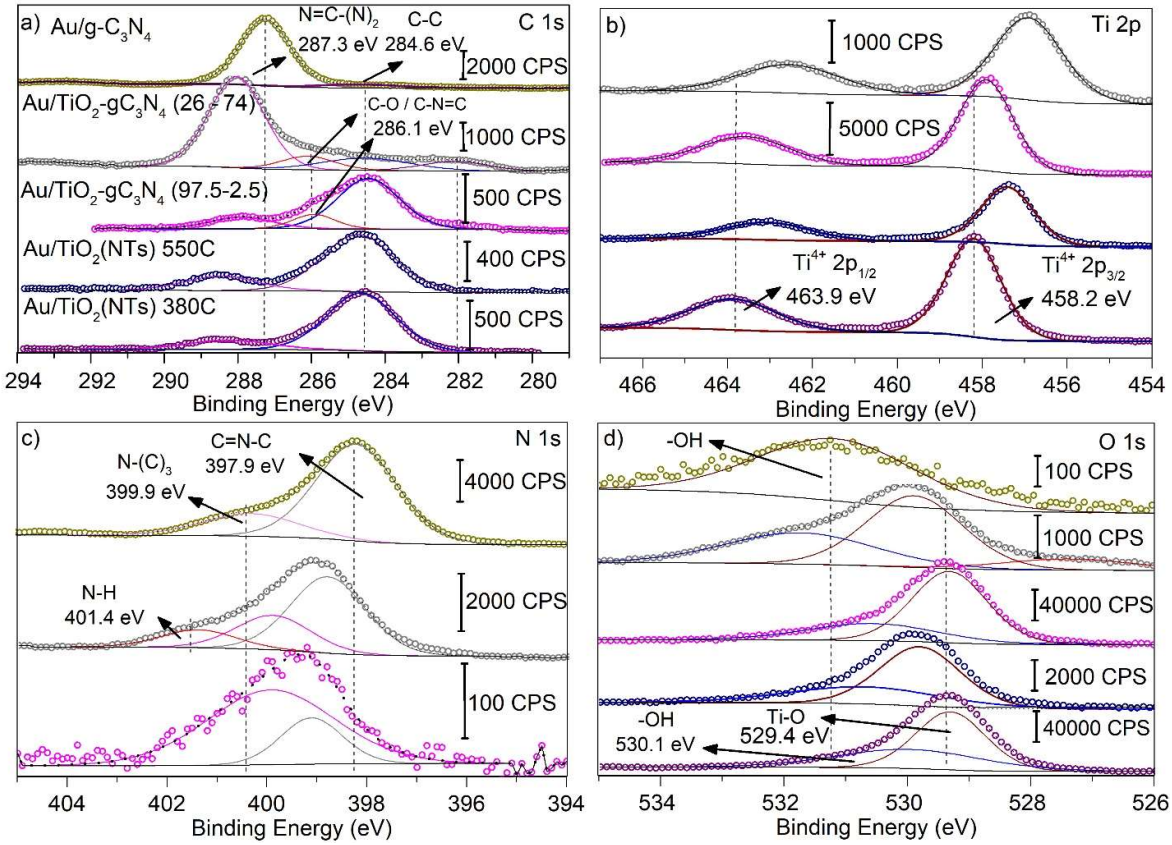

Figure 4.21. XPS a) C 1s b) Ti 2p c) N 1s d) O 1s spectra of the Au/TiO_2-gC_3N_4 (98-2; 25-75) composites and the three Au/g-C_3N_4, Au/TiO_2 references calcined at 380 and 550 °C.

C/N (**Table 4.8**) is directly related to the g-C_3N_4 degree of polycondensation, and the g-C_3N_4 reference exhibits the theoretical value of 0.75, which means a good g-C_3N_4 skeleton was formed. Contrarily, Au/TiO_2-gC_3N_4 (97.5-2.5) (26-74) composites obtained lower values compared to Au/gC_3N_4 reference, suggesting different g-C_3N_4 skeleton than for bare g-C_3N_4.

Table 4.25. XPS data of the Au/TiO_2(NTs)-gC_3N_4 composites and references.

Sample	Au $4f_{7/2}$	Au/Ti	Au/C	C/N
TiO_2 380 °C	82.8 (Au $^{\delta-}$)	0.003	0.029	-
TiO_2 550 °C	82.1 (Au $^{\delta-}$)	0.007	0.060	-
97.5-2.5	82.6 (Au $^{\delta-}$)	0.004	0.039	0.68
26-74	83.1 (Au $^{\delta-}$)	0.072	0.079	0.61
g-C_3N_4	82.6 (Au $^{\delta-}$)	-	0.241	0.75

E) (Photo) catalytic evaluation of Au/TiO_2(NTs)-gC_3N_4 composites

For the evaluation of Au/TiO_2(NTs)-gC_3N_4 composites performances two model reactions were used: photocatalytic hydrogen production from water splitting (massic reaction rate (μmol h^{-1} g_{cat}^{-1})) and preferential catalytic oxidation of carbon monoxide (CO (%) conversion). For the case of H_2 production, the results in this section were divided into screening and zoom methods (**chapter 3 section B.3, Fig. 3.2**). Whilst for the case of PROX reaction one composite of each series with low, *ca.* 2.5 % (zoom) and high, *ca.* 74 % (screening) g-C_3N_4 content were tested.

E.1. Photocatalytic performance of Au/TiO_2(NTs)-gC_3N_4 composites under solar light irradiation

The photocatalytic performances of Au/TiO_2-gC_3N_4 and references are evaluated by using the experimental set-up introduced in **chapter 2 section D.1.1** [21]. The following section will introduce the photocatalytic H_2 production test.

E.1.1. Screening method

The blue columns represent the screening composites and references Au/TiO_2 550 °C and Au/g-C_3N_4 (**Fig. 4.14**). One can observe that the reference Au/TiO_2 550 °C is the most active sample (leading to 638 μmol h^{-1} g_{cat}^{-1} of H_2 production), and the lowest activity is observe with Au/g-C_3N_4 (leading to 41 μmol h^{-1} g_{cat}^{-1}) in comparison to the three screening composites. For the screening proportions composition of 76-24, 48-52, 26-74 yielded 66, 266, and 140 μmol h^{-1} g_{cat}^{-1}, respectively. Despite of low H_2 massic rate yields obtained with the three composites, one can notice that the optimal proportion can be found at Au/TiO_2-gC_3N_4 (50-50), which presents the highest H_2 yield in reference to its counterparts.

Regarding, the Au/TiO_2-gC_3N_4 physical mixtures (mixture between 0.3 wt. % Au/TiO_2(NTs) 550C and 0.3 wt. % Au/g-C_3N_4) (purple columns) with the equivalent screening proportion compositions (76-24, 48-52, 26-74), they exhibit a proportional decay trend for H_2 production yielding 518, 367, 160 μmol h^{-1} g_{cat}^{-1}, respectively, assuming that it is the only result of dilution effect when increasing g-C_3N_4 content. One can observe the activity superiority of the physical mixtures over the composites, meaning that for this case the composites did not present any beneficial effect in photocatalytic terms.

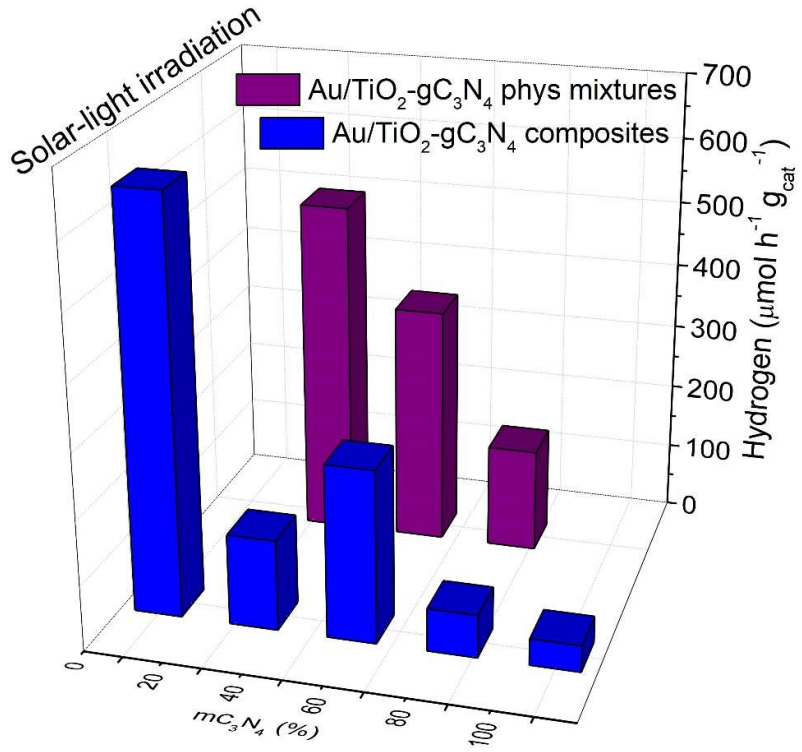

Figure 4.22. Mean hydrogen formation rate per hour and per mass with 1 vol% TEOA of Au/TiO_2-gC_3N_4 screening composites and references. Additionally, physical mixtures equivalent to the screening proportions composition were added for comparison.

E.1.2. Zoom method

For the photocatalytic H_2 production Au/TiO_2-gC_3N_4 (97.5-2.5) composite and Au/TiO_2 550°C reference (**Fig. 4.23**) samples lead to 383 and 638 μmol h^{-1} g_{cat}^{-1} of H_2 production, respectively. This result evidences that the nanocomposite did not bring any activity enhancement in respect to the reference. The physical mixture sample shows a very similar photocatalytic H_2 production, *ca.* 392 μmol h^{-1} g_{cat}^{-1}, than the composite, evidencing that no activity enhancement was obtained.

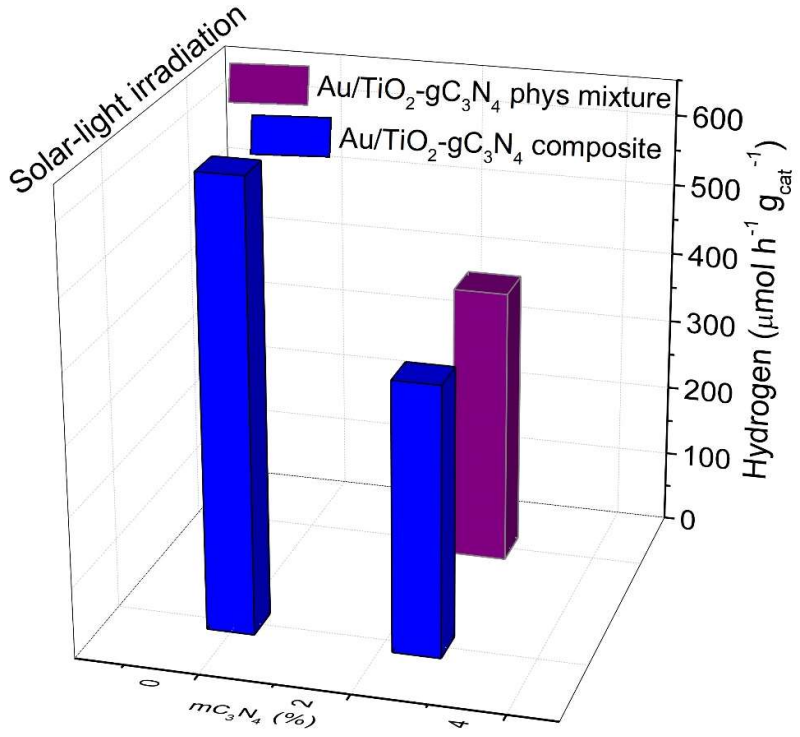

Figure 4.23. Mean hydrogen formation rate per hour and per mass with 1 vol% TEOA of Au/TiO_2-gC_3N_4 (97.5-2.5) zoom composite and one reference. Additionally, the physical mixture equivalent to the zoom proportion composition was added for comparison.

E.2. Catalytic CO Oxidation performance of Au/TiO_2(NTs)-gC_3N_4 composites during thermal activation in absence of hydrogen

The catalytic performance of Au/TiO_2-gC_3N_4 and references are evaluated by using the experimental set-up introduced in the following section. Also, the catalytic oxidation of CO test is used as the model reaction.

E.2.1. Experimental set-up

In details, catalytic tests are performed in a fully automated (CETRIB SARL, Andlau, France) fixed-bed flow reactor (with internal diameter of 10 mm) loaded with 26 mg of catalyst and placed in the isothermal zone of a cylindrical furnace (**Fig. 4.24)**. The gas mixture balanced in He, *i.e.* 1% CO / 1% O_2 for CO oxidation were introduced at a total flow rate of 100 mL min^{-1} (1 atm, GHSV ~ 15,000 h^{-1}). The composite is heated at 1°C min^{-1} from 20 to 300 °C and then cooled down at the same rate. CO conversion is determined on the basis of on-line Compact Gas Chromatograph (Interscience, Belgium) analysis, using external calibration.

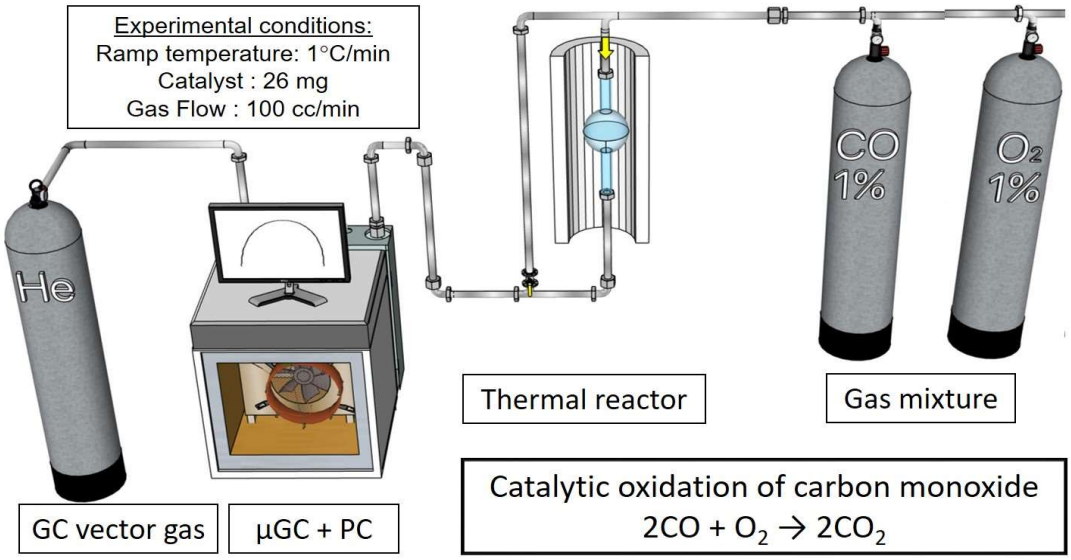

Figure 4.24. Catalytic set-up and its components, showing the CO Oxidation. Designed with Sketchup ©.

E.2.2. Evaluation of catalytic activity toward conversion of CO during thermal activation in absence of hydrogen

From CO conversion values in the pure CO oxidation reaction, one can notice that the Au/g-C_3N_4 reference and the C_3N_4-rich Au/TiO_2-gC_3N_4 (26-74) composite exhibit a very low value. Less than 8 % of CO is indeed converted at 330 °C. This result is in a good agreement with literature, since it has been reported that in the absence of oxygen-based surface groups onto the support (g-C_3N_4 case) the catalyst activity is negligible and Au NPs are essentially inactive [34]. The Au/TiO_2 reference and Au/TiO_2-gC_3N_4 (97.5-2.5) composite show higher activity. They both exhibit a $T_{light\ off}$ < 225 °C with a maximum CO conversion of 39 and 64 %, respectively, at 330 °C. This is consistent with the nature of the catalytic supports, namely TiO_2 and a TiO_2-rich composite. These supports are indeed known to be "active" [35] as they contain oxygen-based surface groups, which remain exposed to the reaction media and may work in synergy with Au NPs to ensure oxygen activation [36]. Besides, the Au/TiO_2-gC_3N_4 (97.5-2.5) composite shows the best activity, 1.5 times higher than the Au/TiO_2 550 °C reference and 20 times higher than Au/g-C_3N_4.

It is well-known that the surface chemistry of the support plays a key role on the growth and effective deposition of metallic NPs. TEM has evidenced small variations of Au NPs average size depending on the nature of the support (Au/TiO_2, Au/g-C_3N_4, Au/TiO_2-gC_3N_4 (97.5-2.5)-zoom NC, Au/TiO_2-gC_3N_4 (76-24)-screening NC with 3.7, 5.1, 3.1, and 4.2 nm, respectively). The TiO_2-rich composite actually exhibits the largest average Au particle size (lowest gold dispersion) and its superior CO oxidation activity can thus not be attributed to a higher number of exposed gold atoms. However, porosity analysis has given evidence of a significant porosity change (for the smallest pores) on the zoom NC, which resulted in a decrease in the overall pore volume by about a half (0.69 $cm^3\ g^{-1}$) as compared to the TiO_2 550 °C reference (1.24 $cm^3\ g^{-1}$). This means that the smaller pore volume, which represents about half of the overall pore volume is covered or blocked by

g-C_3N_4 formed during its synthesis. By contrast, the screening NC exhibits mainly the contribution of the smaller pores, *i.e.* those ≤ 10 nm (internal diameter of the TiO_2 NTs) with a total pore volume of 0.21 cm^2 g^{-1}, six times lower than that of the TiO_2 550 °C reference, accompanied by the second (larger) pore disappearance. Therefore, a scheme design of 1D TiO_2 (NTs) / 2D g-C_3N_4 can be postulated showing heterojunction interfaces for the two NCs type. The interparticle space between the entangled NTs may be covered with g-C_3N_4 for the screening NC case while the internal diameter is filled with linear g-C_3N_4 structure in the zoom NC case. More details about the architecture configuration are presented in summary discussion section.

In our conditions, and due to the particular features (nanotubes easy aggregation, breaking, blocking of TiO_2 porosity during *in-situ* g-C_3N_4 synthesis, …) related to TiO_2 1D morphology compared to TiO_2 3D one, that ideal heterojunction configuration probably not occurred in our case. However, a beneficial effect of the heterojunction configuration obtained in the zoom composite has been observed in the catalytic oxidation of carbon monoxide (1.5 times higher than TiO_2 reference). Due to synergy effect of both the good quality of interfacial contact between the two SCs, and to the presence of Au NPs, allowing the two types of surface groups (hydroxyl and amines) being exposed to either welcome Au NPs or to interact with the reactant.

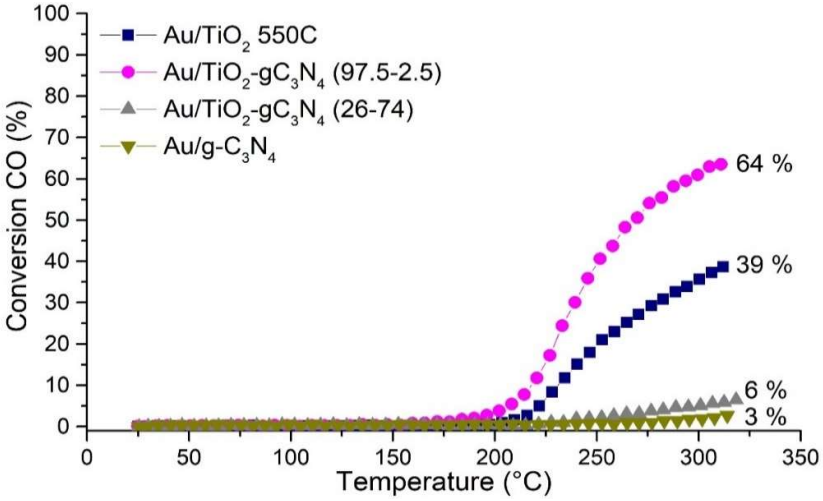

Figure 4.25. Catalytic activity of Au NPs supported on g-C_3N_4, TiO_2, TiO_2-gC_3N_4 (97.5-2.5), and TiO_2-gC_3N_4 (26-74) as a function of temperature.

F) Summary-Discussion

Following increased photocatalytic performances of some Au/TiO_2(P25)-gC_3N_4 composites highlighted in **chapter 3**, this fourth chapter was dedicated to the impact of changing TiO_2 morphology from 3D granular morphology (TiO_2 P25) to 1D morphology (TiO_2 nanotubes) in binary (TiO_2(NTs)-gC_3N_4) and ternary (0.3 wt.% Au/TiO_2(NTs)-gC_3N_4) composites synthesized under air. For that purpose, the same synthesis and experimental strategies than the ones optimized in **chapter 3** were applied. The resulting composites were evaluated toward two reactions, (1) photocatalytic H_2 production (in presence of 1 vol. % TEOA as sacrificial agent) and CO conversion (in the context of PROX reaction).

F.1. Binary TiO_2(NTs)-gC_3N_4 composites

Screening TiO_2/g-C_3N_4 composites (range of (76-24/24-76) massic compositions).

As observed in **chapter 3**, experimental g-C_3N_4 content determined from TGA analyses were very close (less than 4% of relative error) to the theoretical values, confirming once more the mathematical model developed in the previous chapter is accurate. In the same manner, a shift of 100°C in the decomposition temperature related to bulk g-C_3N_4 domains were noticed, evidencing bulk-like domains interacting with TiO_2. In addition, for two composites, a second weight loss contribution was also observed at even lower temperature (at *ca.* 480°C), that might be assigned to higher quality interface or contact between both SCs. FTIR measurements confirmed the presence of both SCs. XRD analyses also revealed the fingerprint of TSTCN and STCN phases, which was not the case for the TiO_2(P25)-gC_3N_4-Air screening systems. Furthermore, no variation of anatase crystallite size was detected when varying g-C_3N_4 content, whereas a diminishment of the numbers of layers with the diminution of g-C_3N_4 concentration has to be mentioned. It must also be underlined that a drastic decrease of porosity occurred compared to TiO_2 NTs references. This pore volume diminution affects preferentially the porosity contribution resulting from TiO_2 NTs entanglement, even if the internal diameter porosity of TiO_2 NTs also diminish.

Zoom TiO_2-gC_3N_4 composite (range: only 97.5-2.5 massic composition was studied).

From XRD analyses, the presence of g-C_3N_4 could not be evidenced, as already observed in **chapter 3** for the zoom-Air composites. However, FTIR measurements allowed to evidence the presence of g-C_3N_4. It must also be underlined that even at low g-C_3N_4 content, a drastic decrease in surface area and pore volume was observed compared to TiO_2 (NTs), assuming an important blocking of nanotubes porosity by adding only 2.5 wt.% of g-C_3N_4.

F.2. Ternary Au/TiO_2(NTs)-gC_3N_4 composites

F.2.1. Screening range.

The same Au NPs deposition method onto the as-synthesis binary composites was used than the one described in chapters 2 and 3 to reach 0.3 wt. % of deposited Au NPs. From ICP-AES measurements, one could confirm the higher deposition yield on g-C_3N_4-rich surfaces, certainly due to higher affinity of Au precursor for surface amine groups compared (of g-C_3N_4) to hydroxyl ones (of TiO_2). The better Au NPs coverage on g-C_3N_4 support than on TiO_2 NTs was also confirmed by XPS (determination of Au/Ti and Au/C surface atomic ratio). Therefore, from XPS analysis, O-Ti-O-C-N interactions seems to be evidenced. This feature was confirmed by TEM observation (on TiO_2/g-C_3N_4 (76-24) composition) showing higher density of deposited Au NPs onto rich-gC_3N_4 binary composites. UV-Vis analyses mainly exhibited the signature of g-C_3N_4 SC, more or less overlapped with SPIE and TiO_2 contributions.

F.2.2. Zoom range: only TiO_2-gC_3N_4 (97.5-2.5) composition was studied

Low g-C_3N_4 content did not significantly impact surface properties of TiO_2 (NTs) in terms of total Au deposition. However, from TEM observation lower Au NPs sizes were determined (3.1 nm) compared to the above mentioned screening composite (4.2 nm) and to the TiO_2 (NTs) 550°C reference (3.7 nm), meaning that higher g-C_3N_4 content led to larger Au NPs with higher dispersion degree. UV-Vis signal mainly exhibited TiO_2 contribution. Additionally, SPIE signal was more or less attenuated. No characteristic g-C_3N_4 contribution was evidenced, only a slight red-shift was detected but with no impact on the band-gap (as it was already the case on Au/TiO_2(P25)-gC_3N_4 zoom composites).

F.3. (Photo) catalytic activity toward H_2 production and CO conversion

F.3.1. Photocatalytic hydrogen production.

The previously characterized screening- and zoom composites were evaluated under solar-light irradiation and compared to their mechanical-mixtures homologues and to Au/TiO_2 (NTs) and Au/g-C_3N_4 references in terms of H_2 massic production rate, expressed in μmol (H_2).h^{-1}.g_{cat}^{-1}. No beneficial effects of associating TiO_2(NTs) and g-C_3N_4 was observed, whether with the composites or with the physical mixtures, contrarily to what was noticed with the association of TiO_2(P25) and g-C_3N_4. It can be supposed that the 1D TiO_2 morphology is not favourable for high quality interaction with the 2D-gC_3N_4 sheets probably due to strong agglomeration properties of TiO_2(NTs), thus hindering the beneficial properties of heterojunction formation between the two SCs. This might also negatively impact Au NPs deposition and dispersion. Furthermore, association with gC_3N_4, even at low content led to a drastic decrease of porosity compared to TiO_2(NTs).

F.3.2. Catalytic CO oxidation.

It has been observed that Au/TiO_2 (NTs)-gC_3N_4 (97.5-2.5) composite exhibited much higher activity towards CO oxidation than the Au/TiO_2 (NTs) and Au/g-C_3N_4 references but also better performance than the g-C_3N_4-rich composite. According to literature, g-C_3N_4 lack of oxygen activation capacity (while in contact with Au NPs), since oxygen content is very poor, is the main reason why CO conversion for both reference and g-C_3N_4-rich composite were very low. Contrarily, for the TiO_2-based samples, richer in oxygen content promoting easier oxygen activation (while anchored Au NPs), resulted in higher CO conversions compared to g-C_3N_4-based samples. Nevertheless, between the two TiO_2-based samples there was a small difference in their composition, namely Au/TiO_2 (NTs)-gC_3N_4 (97.5-2.5) has a small g-C_3N_4 massic content (≤ 2.5) which provides a new type of functional groups coming from the amines of its polymeric structure. Therefore, the combination of hydroxyl (OH-) surface groups from TiO_2, bridge secondary amines (-NH) and/or edge primary amine (–NH_2) surface groups both from g-C_3N_4 may coexist in the hybrid support to enhance oxygen/nitrogen activation with anchored Au NPs which brings a positive synergic effect that enhances CO conversion. One cannot exclude the beneficial Au-catalysed reaction yields due to the architectural configuration resulting from the TiO_2 (NTs)-gC_3N_4 interface.

F.4. Structure/(Photo) catalytic activity correlations

To compare and discuss the (photo) catalytic activities of the different binary TiO_2-gC_3N_4 and ternary Au/TiO_2-gC_3N_4 nanocomposites, different contributions and effects have to be considered.

F.4.1. On TiO_2 (NTs)-gC_3N_4 binary systems

The specific surface area characterization can be correlated in function of gC_3N_4 content (**Fig. 4.27**). Thus, it can be observed that the BET values obtained follow a decay trend of TiO_2(NTs)-gC_3N_4 composites when increasing gC_3N_4 content, equivalent to the one obtained for TiO_2(P25)-gC_3N_4 composites from **chapter 3**, even though the trend follows a much more important decay. One can observe significant differences from the TiO_2 550°C reference (0 % m_{C3N4}) to the low g-C_3N_4 content sample, TiO_2(NTs)-gC_3N_4(97.5-2.5), varying from 107 to 60 m^2 g^{-1}, respectively. This result suggest that the TiO_2 NTs loose approximately half of its specific surface area, due to **(1)** the TiO_2 nanotubes breaking and agglomeration (evidenced and confirmed by TEM, **Fig. 4.2**) but also to **(2)** the porosity blocking due to TiO_2 NTs coverage by g-C_3N_4 linear sheets, after the g-C_3N_4 polycondensation thermal treatment occurred. Lastly, one cannot exclude that the formation of polymeric g-C_3N_4 in presence of TiO_2 (any morphology), might catalyse the initial formed g-C_3N_4 bulks to transform them in even smaller bulks with an exfoliation-type effect.

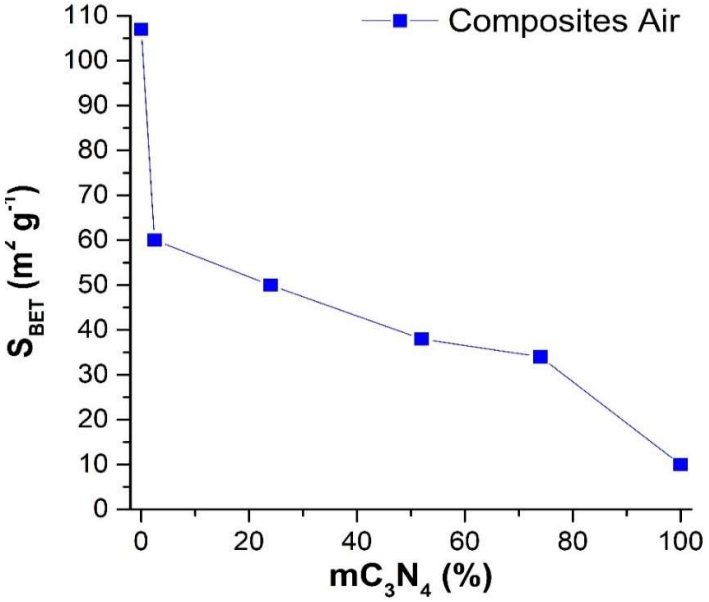

Figure 4.26. Correlation of the specific surface area in function of g-C_3N_4 content of all (screening and zoom) TiO_2 (NTs)-gC_3N_4 composites and corresponding references.

The colors (**Fig. 4.27**) of all TiO_2-gC_3N_4 composites shows different tonalities. The TiO_2-gC_3N_4 screening composites follow a light to dark reddish detonation while increasing g-C_3N_4 content, suggesting that the g-C_3N_4 formed in this case might not be equivalent to the bare one. Nevertheless, the low g-C_3N_4 content (≤ 5 wt. %) zoom composite shows a white color comparable to TiO_2 NTs reference.

Figure 4.27. Comparison of the color in function of g-C_3N_4 content of all (screening and zoom) TiO_2 (NTs)-gC_3N_4 composites and references.

F.4.2. On Au/TiO_2 (NTs)-gC_3N_4 ternary systems

From UV-Vis measurements were observed the three expected absorptions for the three components, *i.e.* TiO_2 ($\lambda \approx 385$ nm), g-C_3N_4 ($\lambda \approx 460$ nm), and Au plasmon resonance ($\lambda \approx$ 550 nm. An additional contribution towards the visible range was observed for some TiO_2-gC_3N_4 screening and zoom composites, possibly due to the Ti^{4+} reduction to Ti^{3+} [34] generating simultaneously oxygen vacancies. One cannot exclude the contribution of g-C_3N_4 deformation layer that induces $n \rightarrow \pi^*$ electronic transition [11] mentioned for Au/g-C_3N_4 composites in **chapter 2**.

From TEM, one can observe that the lowest Au NPs sizes were obtained for low g-C_3N_4 content composite (zoom), *ca.* 3.1±0.6 nm compared to the other samples, especially its closest reference Au/TiO_2 (3.7±0.9 nm). Also, the same behaviour than the one found on the composites-Air from **chapter 3** was observed in this **chapter 4**. Low g-C_3N_4 content composite (zoom) showed only a few Au NPs sizes, contrarily to rich g-C_3N_4 content composite (screening) presenting a wider range of Au NPs sizes, meaning that density of Au NPs is not the most important parameter to correlate with (photo) catalytic activity since Au/TiO_2 (NTs)-gC_3N_4 (97.5-25) composite was the one that performed the better toward CO conversion. One can say that well Au NPs coverage (high density) undergo preferentially onto the rich g-C_3N_4 support surface improving Au NPs coverage and dispersion.

Fig.4.28 summarizes the possible architectural configuration designs when 1D TiO_2 (NTs) and the 2D g-C_3N_4 formed heterojunction interfaces. The scheme also points out the higher affinity of the Au NPs being deposited onto the g-C_3N_4 support surface rather than onto TiO_2 one. However, in our conditions, and due to the particular features (nanotubes easy aggregation, breaking, blocking of TiO_2 porosity during *in-situ* g-C_3N_4 synthesis, …) related to TiO_2 1D morphology compared to TiO_2 3D one, that ideal heterojunction configuration probably not occurred in our case.

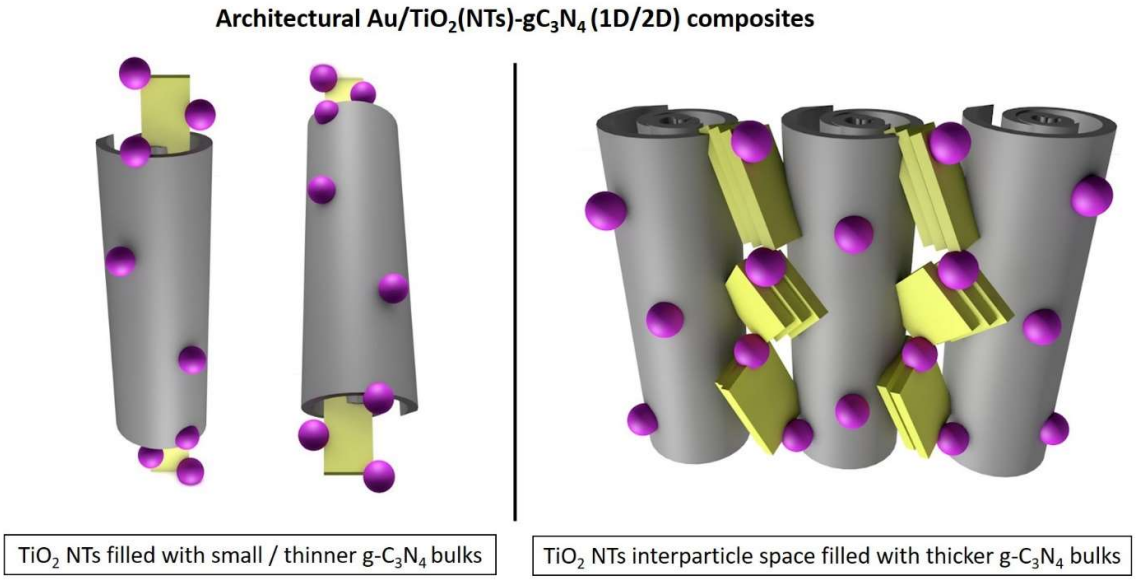

Figure 4.28. Speculative scheme of the Au/TiO_2 (NTs)-gC_3N_4 (1D/2D) architectural possibilities. Designed with Sketchup ®.

G) References

[1] M. Haruta, T. Kobayashi, H. Sano, N. Yamada, Novel Gold Catalysts for the Oxidation of Carbon Monoxide at a Temperature far Below 0 °C, Chem. Lett. 16 (1987) 405–408. doi:10.1246/cl.1987.405.

[2] M. Haruta, N. Yamada, T. Kobayashi, S. Iijima, Gold catalysts prepared by coprecipitation for low-temperature oxidation of hydrogen and of carbon monoxide, J. Catal. 115 (1989) 301–309. doi:10.1016/0021-9517(89)90034-1.

[3] I.E.A. (IEA), Technology Roadmap Hydrogen and Fuel Cells, 2015. www.iea.org/t&c/ (accessed December 16, 2018).

[4] A. Fujishima, K. Honda, Electrochemical photolysis of water at a semiconductor electrode., Nature. 238 (1972) 37–38. doi:10.1038/238037a0.

[5] A.J. Bard, Photoelectrochemistry and heterogeneous photocatalysis at semiconductors, J. Photochem. 10 (1979) 59–75. doi:10.1016/0047-2670(79)80037-4.

[6] A.J. Bard, Photoelectrochemistry, Science (80-.). 207 (1980) 139–144. doi:10.1126/science.207.4427.139.

[7] R. Marschall, Semiconductor Composites: Strategies for Enhancing Charge Carrier Separation to Improve Photocatalytic Activity, Adv. Funct. Mater. 24 (2014) 2421–2440. doi:10.1002/adfm.201303214.

[8] † Tomoko Kasuga, *, † Masayoshi Hiramatsu, † Akihiko Hoson, ‡ and Toru Sekino, K. Niihara‡, Formation of Titanium Oxide Nanotube, Langmuir. (1998) 3160–3163. doi:10.1021/LA9713816.

[9] B. Ohtani, O.O. Prieto-Mahaney, D. Li, R. Abe, What is Degussa (Evonik) P25? Crystalline composition analysis, reconstruction from isolated pure particles and photocatalytic activity test, n.d. https://eprints.lib.hokudai.ac.jp/dspace/bitstream/2115/44837/1/JPPA216-2-3_179-182.pdf

(accessed January 22, 2019).

[10] K. Nakata, A. Fujishima, TiO2 photocatalysis: Design and applications, J. Photochem. Photobiol. C Photochem. Rev. 13 (2012) 169–189. doi:10.1016/J.JPHOTOCHEMREV.2012.06.001.

[11] W. Wang, O.K. Varghese, M. Paulose, C.A. Grimes, Q. Wang, E.C. Dickey, A study on the growth and structure of titania nanotubes, J. Mater. Res. 19 (2004) 417–422. doi:10.1557/jmr.2004.19.2.417.

[12] J. Tauc, Optical properties and electronic structure of amorphous Ge and Si, Mater. Res. Bull. 3 (1968) 37–46. doi:10.1016/0025-5408(68)90023-8.

[13] W.-J. Ong, L.-L. Tan, Y.H. Ng, S.-T. Yong, S.-P. Chai, Graphitic Carbon Nitride (g-C3N4)-Based Photocatalysts for Artificial Photosynthesis and Environmental Remediation: Are We a Step Closer To Achieving Sustainability?, Chem. Rev. (2016). doi:10.1021/acs.chemrev.6b00075.

[14] Y. Chen, B. Wang, S. Lin, Y. Zhang, X. Wang, Activation of n → π* Transitions in Two-Dimensional Conjugated Polymers for Visible Light Photocatalysis, J. Phys. Chem. C. 118 (2014) 29981–29989. doi:10.1021/jp510187c.

[15] X. Wang, K. Maeda, A. Thomas, K. Takanabe, G. Xin, J.M. Carlsson, K. Domen, M. Antonietti, A metal-free polymeric photocatalyst for hydrogen production from water under visible light, Nat. Mater. 8 (2009) 76–80. doi:10.1038/nmat2317.

[16] A. Thomas, A. Fischer, F. Goettmann, M. Antonietti, J.-O. Müller, R. Schlögl, J.M. Carlsson, Graphitic carbon nitride materials: variation of structure and morphology and their use as metal-free catalysts, J. Mater. Chem. 18 (2008) 4893. doi:10.1039/b800274f.

[17] M.J. Bojdys, J.-O. Müller, M. Antonietti, A. Thomas, Ionothermal synthesis of crystalline, condensed, graphitic carbon nitride., Chemistry. 14 (2008) 8177–82. doi:10.1002/chem.200800190.

[18] S. Brunauer, P.H. Emmett, E. Teller, Adsorption of Gases in Multimolecular Layers, J. Am. Chem. Soc. 60 (1938) 309–319. doi:10.1021/ja01269a023.

[19] D. Zywitzki, H. Jing, H. Tüysüz, C.K. Chan, High surface area, amorphous titania with reactive Ti $^{3+}$ through a photo-assisted synthesis method for photocatalytic H $_2$ generation, J. Mater. Chem. A. 5 (2017) 10957–10967. doi:10.1039/C7TA01614J.

[20] J. Zhang, X. Chen , K. Takanabe, K. Maeda, K. Domen, J.D. Epping, X. Fu, M. Antonietti, X. Wang , Synthesis of a Carbon Nitride Structure for Visible-Light Catalysis by Copolymerization, Angew. Chemie Int. Ed. 49 (2010) 441–444. doi:10.1002/anie.200903886.

[21] P. Jiménez, C. Marchal, T. Cottineau, V. Caps, V. KELLER, Influence of gas atmosphere during synthesis of g-C3N4 for enhanced photocatalytic H2 production from water on Aug-C3N4 composites, J. Mater. Chem. A. (2019). doi:10.1039/C9TA01734H.

[22] A.B. Jorge, D.J. Martin, M.T.S. Dhanoa, A.S. Rahman, N. Makwana, J. Tang, A. Sella, F. Corà, S. Firth, J.A. Darr, P.F. McMillan, H2 and O2 Evolution from Water Half-Splitting Reactions by Graphitic Carbon Nitride Materials, J. Phys. Chem. C. 117 (2013) 7178–7185. doi:10.1021/jp4009338.

[23] Y. Wang, X. Wang, M. Antonietti, Polymeric graphitic carbon nitride as a heterogeneous organocatalyst: from photochemistry to multipurpose catalysis to sustainable chemistry., Angew. Chem. Int. Ed. Engl. 51 (2012) 68–89. doi:10.1002/anie.201101182.

[24] Valery N. Khabashesku, A. John L. Zimmerman, J.L. Margrave, Powder Synthesis and Characterization of Amorphous Carbon Nitride, Chem. Mater. 12 (2000) 3264–3270. doi:10.1021/CM000328R.

[25] A. Du, S. Sanvito, Z. Li, D. Wang, Y. Jiao, T. Liao, Q. Sun, Y.H. Ng, Z. Zhu, R. Amal, S.C. Smith, Hybrid Graphene and Graphitic Carbon Nitride Nanocomposite: Gap Opening, Electron–Hole Puddle, Interfacial Charge Transfer, and Enhanced Visible Light Response, J. Am. Chem. Soc. 134 (2012) 4393–4397. doi:10.1021/ja211637p.

[26] P. Lignier, M. Comotti, F. Schü, J.-L. Rousset, V. Rie Caps, Effect of the titania morphology on the Au/TiO 2-catalyzed aerobic epoxidation of stilbene, (n.d.). doi:10.1016/j.cattod.2008.04.032.

[27] B. Zhu, P. Xia, Y. Li, W. Ho, J. Yu, Fabrication and photocatalytic activity enhanced mechanism of direct Z-scheme g-C3N4 /Ag2WO4 photocatalyst, Appl. Surf. Sci. 391 (2017) 175–183. doi:10.1016/j.apsusc.2016.07.104.

[28] X. Wei, C. Shao, X. Li, N. Lu, K. Wang, Z. Zhang, Y. Liu, Facile in situ synthesis of plasmonic nanoparticles-decorated g-C $_3$ N $_4$ /TiO $_2$ heterojunction nanofibers and comparison study of their photosynergistic effects for efficient photocatalytic H $_2$ evolution, Nanoscale. 8 (2016) 11034–11043. doi:10.1039/C6NR01491G.

[29] P. V. Zinin, L.-C. Ming, S.K. Sharma, V.N. Khabashesku, X. Liu, S. Hong, S. Endo, T. Acosta, Ultraviolet and near-infrared Raman spectroscopy of graphitic C3N4 phase, Chem. Phys. Lett. 472 (2009) 69–73. doi:10.1016/j.cplett.2009.02.068.

[30] Y. Cui, J. Zhang, G. Zhang, J. Huang, P. Liu, M. Antonietti, X. Wang, Synthesis of bulk and nanoporous carbon nitride polymers from ammonium thiocyanate for photocatalytic hydrogen evolution, J. Mater. Chem. 21 (2011) 13032. doi:10.1039/c1jm11961c.

[31] J.S. Kim, J.W. Oh, S.I. Woo, Improvement of the photocatalytic hydrogen production rate of g-C3N4 following the elimination of defects on the surface, Catal. Today. 293–294 (2017) 8–14. doi:10.1016/J.CATTOD.2016.11.018.

[32] A. Vinu, Two-Dimensional Hexagonally-Ordered Mesoporous Carbon Nitrides with Tunable Pore Diameter, Surface Area and Nitrogen Content, Adv. Funct. Mater. 18 (2008) 816–827. doi:10.1002/adfm.200700783.

[33] R. Van Hardeveld, F. Hartog, The statistics of surface atoms and surface sites on metal crystals, Surf. Sci. 15 (1969) 189–230. doi:10.1016/0039-6028(69)90148-4.

[34] J.A. Singh, S.H. Overbury, N.J. Dudney, M. Li, G.M. Veith, Gold Nanoparticles Supported on Carbon Nitride: Influence of Surface Hydroxyls on Low Temperature Carbon Monoxide Oxidation, ACS Catal. 2 (2012) 1138–1146. doi:10.1021/cs3001094.

[35] M.M. Schubert, S. Hackenberg, A.C. van Veen, M. Muhler, V. Plzak, R.J. Behm, CO Oxidation over Supported Gold Catalysts—"Inert" and "Active" Support Materials and Their Role for the Oxygen Supply during Reaction, J. Catal. 197 (2001) 113–122. doi:10.1006/JCAT.2000.3069.

[36] G.C. Bond, D.T. Thompson, Gold-catalysed oxidation of carbon monoxide, Gold Bull. 33 (2000) 41–50. doi:10.1007/BF03216579.

General conclusions and outlook

A) General conclusions

From chapter1, the literature review confirmed the importance of transforming solar into chemical energy via **solar fuels**, *e.g.,* **H_2** as an **energy vector** in the current energy crisis. A recent state-of-the-art of hydrogen production technologies currently used in society and the ones under research and development was covered, focusing on renewable processes like **water-splitting**, which is the main reaction model for evaluation of the materials elaborated in the frame of this PhD work. This first chapter also includes an overview of the physico-chemical properties and modifications of the materials used for this thesis, namely **g-C_3N_4, TiO_2,** and **Au NPs**.

From chapter 2, dealing with the influence of g-C_3N_4 synthesis atmosphere, it was pointed out that **Au/g-C_3N_4-NH_3** composite produced the highest amount of H_2 production (*ca.* **324 µmol h^{-1} g_{cat}^{-1}** under **solar-light irradiation** and **26 µmol h^{-1} g_{cat}^{-1}** under **visible-light irradiation**) with assistance of TEOA (1 vol. %) as sacrificial agent. The superiority of this binary composite amongst the others relies on several facts. This composite presented the largest g-C_3N_4 crystallite size, the thickest stack of layers, the presence of tilt angularity on the distorted C_3N_4 sheets, the largest S_{BET}, the largest V_{pore} even though the pore size were very similar, the narrowest monomodal distribution with the best surface coverage and the lowest average Au NPs size (*ca.* 3.2±1.1 nm) yielding more intimate contact and higher quality of interface between Au NPs and g-C_3N_4 support compared to its g-C_3N_4 counterparts. The following general charge transfer mechanism was proposed:

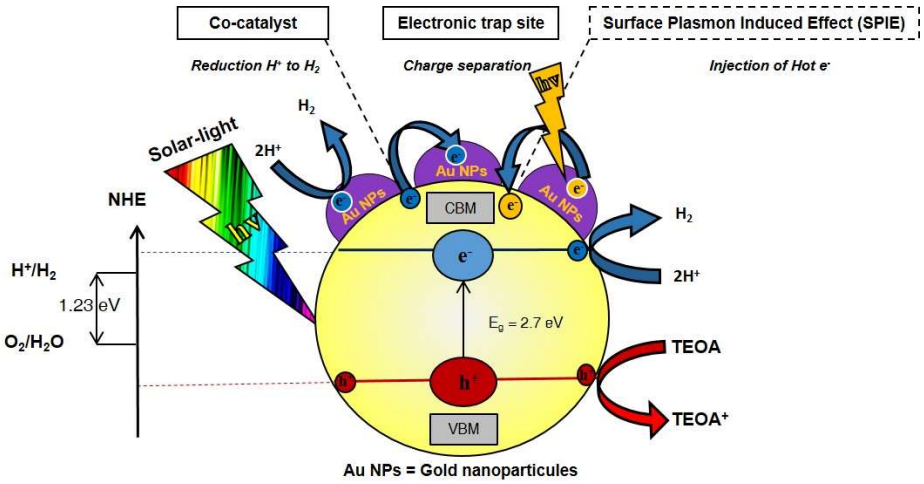

Besides the materials chemistry characterization and structure-activity correlation insights mentioned in **chapter 2**, an additional calculation of the ratio between tri-s-triazine and s-triazine based-C_3N_4 phases were determined and used for the first time to point out the effect of the different continuous gas flow atmospheres during synthesis.

Based on recent reported literature, in more and less comparable experimental conditions, a brief analysis of comparison of the photocatalytic activity of the most performant binary composite (**Au/g-C_3N_4-NH_3**) was carried out. One can notice, that the

photocatalytic activity of the above mentioned composite under solar-light irradiation is only slightly exceeded by the Pt/g-C_3N_4 material (**Table 26**) [3]. Nevertheless, it has to be pointed out that Pt is more expensive metal than Au. Also, the temperature of the measurement is 5 °C higher than in our conditions, which implies a possible contribution of H_2 via thermal catalysis according with Arrhenius relationship. Finally, the metal loading and sacrificial agent is 10 times higher than in our conditions, which means that our composite is performing better than all the compared samples whether under solar or visible-light irradiation. It is difficult to compare with Antonietti's [2] pioneer publication since they do not report irradiance and / or working temperature. Furthermore comparing with Zhang *et al* work [4], they do not use any sacrificial agent, thus the H_2 production under solar-light irradiation is very low in comparison with our results, but is slight higher under visible-light irradiation. However, the visible H_2 production reported as half in comparison to the solar by cutting the UV photons (5% of solar spectra) is questionable, therefore is not recommended to compare with this result.

Table 26. Comparison of activities of the most performant composite Au/g-C_3N_4-NH_3 and literature.

H_2	Irradiance	Temp.	Co-catalyst		Sacrificial agent		Composite	Precursor	Temp.	Time	Ref.
µmol h^{-1} g^{-1}	mW cm^{-2}	°C	Metal	Loading	Molecule	Concentration			°C	h	
324	23.6	20	Au	0.3	TEOA	1 v/v	Au/g-C_3N_4	Mel+DCDA	550	3	1
26	3.6										
50	300W Xe	N.r.	Pt	3.0	TEOA	10 v/v	Pt/g-C_3N_4	Cyanamide	550	4	2
392	4.4	25	Pt	3.0	TEOA	10 v/v	Pt/g-C_3N_4	Melamine	600	3	3
80	Not reported	20	Pt	3.0	No S.A. was used		Pt/g-C_3N_4	Urea	550	2	4
35	2.18										

From <u>chapter 3</u>, focused on Au/TiO_2(P25)-gC_3N_4-*atm* (with atm = Air, NH_3), **Au/TiO_2(P25)-gC_3N_4 (95-5)-Air** ternary composite produced the highest amount of H_2 production (*ca.* **1839 µmol h^{-1} g_{cat}^{-1}** under **solar-light** irradiation and **419 µmol h^{-1} g_{cat}^{-1}** under **visible-light** irradiation) with assistance of TEOA (1 vol. %) as sacrificial agent. This enhanced activity was possibly due to slight red-shift evidencing optically the presence of g-C_3N_4 in addition to Au/TiO_2 (P25) characteristic absorption, and to the formation of new hybrid energy VBM position (shown by UPS analysis) in between the two VBM position of the corresponding references. In addition, photogenerated charge dynamics was studied thanks to TRMC measurements. It was shown that at **360 nm** pulse laser excitation, the highest density of dissociated e^-/h^+ pairs was noticed as well as the trapping/delocalisation of free electrons (after generation) in the π-aromatic systems of g-C_3N_4, thus limiting further their recombination when compared to the corresponding references. At **450 nm,** it was also possible to evidence a sensitization effect of TiO_2 (P25) by g-C_3N_4 while e^- from the CB of g-C_3N_4 may be injected to the CB of TiO_2. It must be mentioned that one could not confirm the presence of SPIE properties.

It must be underlined that very low amount (1 % v/v) of TEAO (sacrificial agent) was used to avoid H_2 production issued from its transformation and thus to consider in majority H_2 issued from water splitting. However, it was associated with a slight deactivation after the 2nd cycle of test (**chapter 2 and 3**), certainly by poisoning some active sites of the support by TEOA dealkylation degradation products.

From all the different and complementary studies, the following speculative charge transfer mechanisms was postulated.

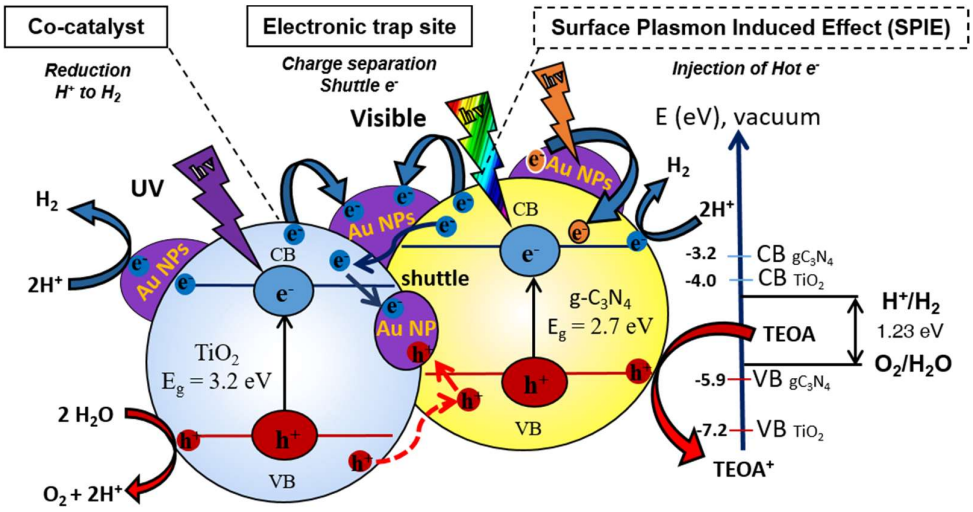

Following the literature comparison analysis, this time for the case of the most performant ternary composite of the present chapter, Au/TiO_2(P25)-gC_3N_4-Air, one can see that it is presenting superior H_2 production yield of the order of 5 and 17 % than the composite reported by Marchal *et al* [5] under solar and visible-light irradiation, respectively. Bearing in mind, that the proportion of the SCs is the same (TiO_2(P25)-gC_3N_4-95-5), except the TiO_2 nature, in our composite case is used commercial P25 TiO_2 and the other study used TiO_2 sol-gel. Another significant difference between both composites is the Au loading, in our case it was targeted 0.3 % with approximately 80% deposition yield, which means that in reality only 0.24% were effectively deposited, and for the other composite they have used 0.5 % Au, which is double amount. Considering that Au NPs essentially function as co-catalyst but also as e^- trap site, this different amount provides another evidence that the present composite is amongst the most performant composite reported in literature (as the best of our knowledge) in comparable experimental conditions. Finally, to compare the Au/TiO_2(P25)-gC_3N_4-Air with the composite reported by Rather *et al* [6], they only reported the value under visible-light irradiation, which is higher for 30 µmol. Yet, they used a different sacrificial agent (MeOH), and in 25 times higher amount. Also, the working temperature condition is 5 °C higher than ours, which has already been mentioned to explain the slight higher H_2 production. Another problem, is that they do not report the irradiance of the light spectrum used, and this is an important parameter, since it defines the up-coming and concentration of photons.

Table 27. Comparison of activities of the most performant composite Au/TiO_2(P25)-gC_3N_4-Air & literature.

H_2	Irradiance	Temp.	Co-catalyst		Sacrificial agent		Composite	Proportion	Reference
µmol h^{-1} g^{-1}	mW cm^{-2}	° C	Metal	Loading	Molecule	Concentration			
1839	23.6	20	Au	0.3	TEOA	1 v/v	Au/TiO_2(P25)-gC_3N_4	95-5	Not published
419	3.6								
1750	12.5	20	Au	0.5	TEOA	1 v/v	Au/TiO_2(sol-gel)-gC_3N_4	95-5	5
350	5.1								
450	330-750 W m^{-1}	25	Au	0.75	MeOH	25 v/v	Au/TiO_2(gC_3N_4)	90-10	6

From chapter 4, related to the impact of TiO_2 morphology, it was shown that **Au/TiO_2(NTs)-gC_3N_4 (97.5-2.5)-Air** composite converted the highest amount of CO (**64%**) (in the frame of PROX reaction), that could be attributed to the co-existence of different surface species taking advantage of TiO_2-gC_3N_4 interface at low g-C_3N_4 content.

From H_2 production tests under solar light irradiation, it must be underlined that none of the Au/TiO_2(NTs)-gC_3N_4 composites led to enhanced activity compared to the TiO_2 (NTs) references. The association of TiO_2 (NTs) with g-C_3N_4 resulted in detrimental effects. It was assumed that this lowered activity was mainly due to two phenomena **(1)** TiO_2 NTs agglomeration and partial breaking during gC_3N_4 synthesis at 550°C and **(2)** coverage and blocking of TiO_2 NTs porosity by g-C_3N_4 sheets inside of the tubes and in-between the entangled tubes. The following schematic architecture can be proposed.

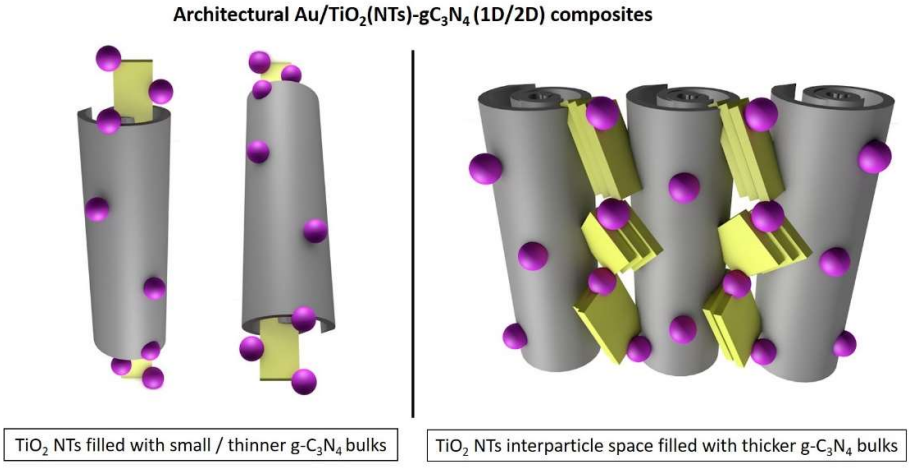

However, TiO_2(NTs)-gC_3N_4 interface resulted in a narrower monomodal distribution with lowest average Au NPs size (*ca.* 3.1±0.6 nm) . From XPS analysis showing Au $4f_{7/2}$ shift, a charge transfer from TiO_2-based support to the Au NPs was evidenced. Au/Ti and Au/C atomic ratios also confirmed highest surface density of Au NPs onto g-C_3N_4 surfaces. This feature was also confirmed by TEM observations.

B) Outlook

From this study, it was evidenced that optimal TiO_2(P25)-gC_3N_4 composition and interface quality can significantly increase photocatalytic activity toward H_2 production under solar and visible light activation from water in the presence of very low amount of sacrificial agent. We thus wanted to further take advantage of TiO_2 surface area by

using high surface area TiO_2 nanotubes. Unfortunately we did not succeed in the elaboration of a high quality TiO_2 (NTs)-gC_3N_4 interface. The challenge here is to obtain this high quality interface between a 1D and a 2D semiconductor. Consequently, alternative synthesis strategies have to be found for that purpose.

TiO_2 nanotubes were obtained via hydrothermal synthesis method, described in **chapter 4**. However, nanotubes agglomeration and entanglement due to high surface energy, in addition to tubes breaking cause a difficulty to form effective heterojunction interfaces with g-C_3N_4 and also for Au NPs deposition. A solution to overcome this important limitation may be to use dispersing agents (polymers, micelles, etc.) to avoid agglomeration and entanglement between the nanotubes thus to provide a more exposed surface area accessible to secondary chemical species in liquid phase. Nevertheless, the chosen dispersing agents should not react with any precursor or atmosphere used.

One could also imagine, in the described two-steps methodology for TiO_2-gC_3N_4 binary composite elaboration, that the liquid phase impregnation of the g-C_3N_4 precursor onto the as-synthetized TiO_2 NTs takes place under sonication, followed by freeze-drying (in order to avoid nanotubes agglomeration) before g-C_3N_4 solid-state synthesis.

Another strategy aiming at obtaining better TiO_2(NTs)-gC_3N_4 interface could be focused on the addition of already synthetized g-C_3N_4 during hydrothermal TiO_2 synthesis to obtain a one-pot synthesis methodology (simpler method) with probably different kinds of heterojunction interfaces between the two SCs.

Following the positive results (on H_2) obtained for Au/g-C_3N_4-NH_3 and Au/TiO_2(P25)-gC_3N_4(95-5)-Air composites, one can deposit **bimetallic systems** by coupling Au with other interesting metals (Au/Pt, Au/Cu, etc.) on the same supports (g-C_3N_4-NH_3 and TiO_2(P25)-gC_3N_4 (95-5)-Air) to further extend their performance. Pt can be a potential suggestion since it's the most active M for (photo) catalytic applications and Cu since presents a maximum wavelength (λ = 485 nm) different than Au but still in the visible range. Several parametric studies can be conducted, *e.g.,* changing metals proportions, controlling the morphology of the monometallic system (triangles, pyramids, rods, etc.) and of the bimetallic system (embedded, core shell. etc.).

From a mechanistic point of view, in order to get deeper insights about charge separation and transfer kinetics mechanisms, complementary experiments can be performed: **(1)** time-resolved spectroscopy (absorption or emission); **(2)** electrochemical analysis such as impedance spectroscopy or photocurrent measurements; **(3)** photo luminescence (transient or steady state) **(4)** Pump-probe spectroscopy.

To obtained more details from **UPS analysis**, an internal reference (for example by addition of trace amounts of gold) with known Fermi level can be added to each sample analysis to be able to calculate the specific Fermi level and consequently to propose a more accurate band structure diagram of the composite photocatalysts.

The design of the photocatalytic reactor should also be greatly improved. The used photocatalytic reactor possesses a central immersed lamp position, making it impossible

to use commercial optical filters and test the photonic contribution at different wavelengths, for calculation of the corresponding quantum yields.

C) References

[1] P. Jiménez, C. Marchal, T. Cottineau, V. Caps, V. Keller, Influence of gas atmosphere during synthesis of g-C_3N_4 for enhanced photocatalytic H_2 production from water on Aug-C_3N_4 composites, J. Mater. Chem. A. (2019). doi:10.1039/C9TA01734H.

[2] X. Wang, K. Maeda, A. Thomas, K. Takanabe, G. Xin, J.M. Carlsson, K. Domen, M. Antonietti, A metal-free polymeric photocatalyst for hydrogen production from water under visible light, Nat. Mater. 8 (2009) 76–80. doi:10.1038/nmat2317.

[3] Z. Huang, F. Li, B. Chen, G, Yuan, Hydrogen from Water over Openly-Structured Graphitic Carbon Nitride Polymer through Photocatalysis, ChemSusChem. 9 (2016) 478-484. doi: 10.1002/cssc.201501520

[4] G. Zhang, Z. Lan, L. Lin, S. Lin, X. W, Overall water splitting by Pt/g-C3N4 photocatalysts without using sacrificial agents, Chem.Sci. 5 (2016) 3062-3066. doi: 10.1039/C5SC04572J

[5] C. Marchal, T. Cottineau, M.G. Méndez-Medrano, C. Colbeau-Justin, V. Caps, V. Keller, Au/TiO_2-gC_3N_4 Nanocomposites for Enhanced Photocatalytic H_2 Production from Water under Visible Light Irradiation with Very Low Quantities of Sacrificial Agents, Adv. Energy Mater. (2018) 1702142. doi:10.1002/aenm.201702142.

[6] R. Rather, S. Singh, B. P, A C_3N_4 surface passivated highly photoactive Au-TiO_2 tubular nanostructure for the efficient H_2 production from water under sunlight irradiation, Appl. Cat. B. Env. (2017) 9-17. doi: 10.1016/j.apcatb.2017.05.002

Appendix

A) Appendix 1. Au loading study

In order to select the Au loading amount, a parametric study was performed depositing different loading amounts (0.3, 0.6, and 0.9 wt. %) onto both g-C_3N_4 and TiO_2 NTs.

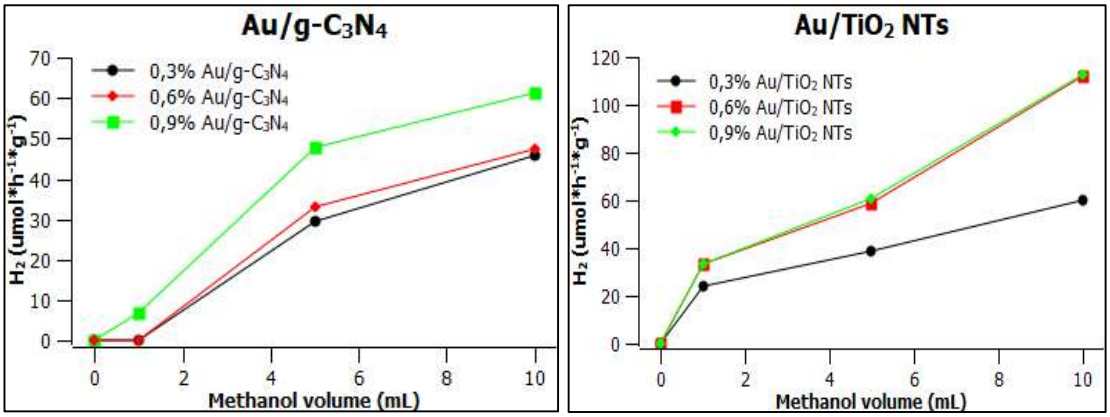

Figure A.1. Left. H_2 production for different Au loadings onto g-C_3N_4. **Right.** H_2 production for different Au loadings onto TiO_2 NTs.

Due to the different nature of both SCs g-C_3N_4 and TiO_2 NTs, the deposition of Au NPs took place separately increasing the Au loading to study the influence of Au loading.

One can see that for the case of Au/g-C_3N_4 materials, between 0.3 and 0.6 wt. % Au loading there was no significant difference on H_2 production. Therefore, is preferable to use less quantity (0.3 %). For the case of Au/TiO_2 NTs materials between 0.6 and 0.9 wt. % Au loading no significant difference on H_2 production was found, and the 0.3 wt. % Au/TiO_2 NTs sample exhibited almost half of H_2 compared to its counterparts. Recalling that the general aim of the thesis of testing different composites in function of their TiO_2/g-C_3N_4 proportion and TiO_2 morphology, we have chosen the minimum Au loading (0.3 wt. %) as minimum to produce sufficient H_2 and be able to conduct and study the desired parameters.

B) Appendix 2. Relative error of massic H_2 production

The sample tested by triplicate was 0.3 % wt. Au/TiO_2(NT) 550C-Air to determine the **relative error, *ca.* 10%.**

1		2		3	
Time (h)	H_2	Time (h)	H_2	Time (h)	H_2
0.00	0.00	0.00	34.85	0.00	17.42
0.04	98.94	0.04	138.65	0.04	118.80
0.07	194.70	0.08	227.41	0.08	211.05
0.11	282.39	0.11	299.90	0.11	291.14
0.15	347.28	0.15	353.21	0.15	350.24
0.19	578.65	0.19	401.68	0.19	490.17
0.23	551.07	0.23	443.46	0.23	497.26
0.26	536.69	0.27	484.23	0.26	510.46
0.30	556.54	0.31	505.86	0.30	531.20
0.34	571.22	0.34	530.73	0.34	550.97
0.38	614.26	0.38	540.77	0.38	577.51
0.41	542.82	0.42	563.43	0.42	553.13
0.45	549.18	0.46	578.94	0.45	564.06
0.49	641.23	0.50	604.33	0.49	622.78
0.52	645.07	0.53	617.16	0.53	631.11
0.56	638.45	0.57	619.51	0.57	628.98
0.60	566.26	0.61	631.66	0.60	598.96
0.64	551.10	0.65	634.77	0.64	592.94
0.67	630.83	0.69	638.15	0.68	634.49
0.71	620.85	0.73	650.28	0.72	635.57
0.75	622.35	0.76	650.12	0.76	636.23
0.79	627.11	0.80	660.68	0.79	643.90
0.82	565.86	0.84	651.97	0.83	608.91
0.86	565.17	0.88	662.80	0.87	613.98
0.90	560.03	0.91	653.21	0.91	606.62
0.94	636.05	0.95	656.84	0.94	646.44
0.97	624.00	0.99	660.39	0.98	642.20
1.01	585.90	1.03	664.08	1.02	624.99
1.05	549.74	1.07	673.57	1.06	611.65
1.09	538.41	1.10	670.95	1.09	604.68
1.12	606.49	1.14	673.36	1.13	639.92
1.16	615.11	1.18	675.10	1.17	645.11
1.20	532.86	1.22	669.88	1.21	601.37
1.24	601.08	1.25	672.10	1.25	636.59
1.27	582.08	1.29	659.49	1.28	620.79
1.31	587.04	1.33	673.59	1.32	630.31
1.35	588.17	1.37	669.56	1.36	628.86
1.39	595.13	1.41	665.50	1.40	630.32
1.43	560.56	1.44	679.77	1.43	620.16

1.46	588.41	1.48	673.54	1.47	630.97
1.50	562.91	1.52	681.15	1.51	622.03
1.54	569.46	1.56	676.94	1.55	623.20
1.58	548.83	1.59	675.94	1.59	612.39
1.61	538.86	1.63	669.34	1.62	604.10
1.65	528.30	1.67	670.09	1.66	599.19
1.69	526.10	1.71	674.66	1.70	600.38
1.73	529.86	1.75	673.74	1.74	601.80
1.77	530.04	1.78	670.26	1.77	600.15
1.80	540.29	1.82	664.17	1.81	602.23
1.84	556.29	1.86	667.42	1.85	611.85
1.88	550.24	1.90	658.11	1.89	604.17
1.92	563.78	1.93	661.04	1.93	612.41
1.95	530.95	1.97	655.99	1.96	593.47
1.99	539.92	2.01	666.23	2.00	603.08
2.03	538.11	2.05	662.48	2.04	600.29
2.07	566.50	2.09	666.93	2.08	616.72
2.11	529.43	2.12	662.93	2.11	596.18
2.14	550.27	2.16	659.50	2.15	604.88
2.18	555.50	2.20	658.27	2.19	606.88
2.22	515.69	2.24	658.17	2.23	586.93
2.26	504.63	2.27	656.79	2.27	580.71
2.29	560.26	2.31	661.34	2.30	610.80
2.33	569.27	2.35	657.20	2.34	613.24
2.37	546.69	2.39	659.91	2.38	603.30
2.41	529.43	2.43	657.50	2.42	593.46
2.45	528.38	2.46	653.87	2.45	591.13
2.48	569.76	2.50	664.31	2.49	617.03
2.52	569.27	2.54	655.20	2.53	612.24
2.56	534.38	2.58	669.33	2.57	601.85
2.60	547.98	2.61	654.40	2.61	601.19
2.63	537.14	2.65	671.55	2.64	604.35

Actual value	592.54	698.81	643.87	
Measured value	586.18	691.20	638.69	
Absolute error	6.36	7.62	5.18	**Average**
Relative error	10.8	11.0	8.1	**10.0**
H_2 (μmol h^{-1} g_{cat}^{-1})	586.18	691.2	638.7	**638.7**

C) Appendix 3. TEM mapping - Quantitative data

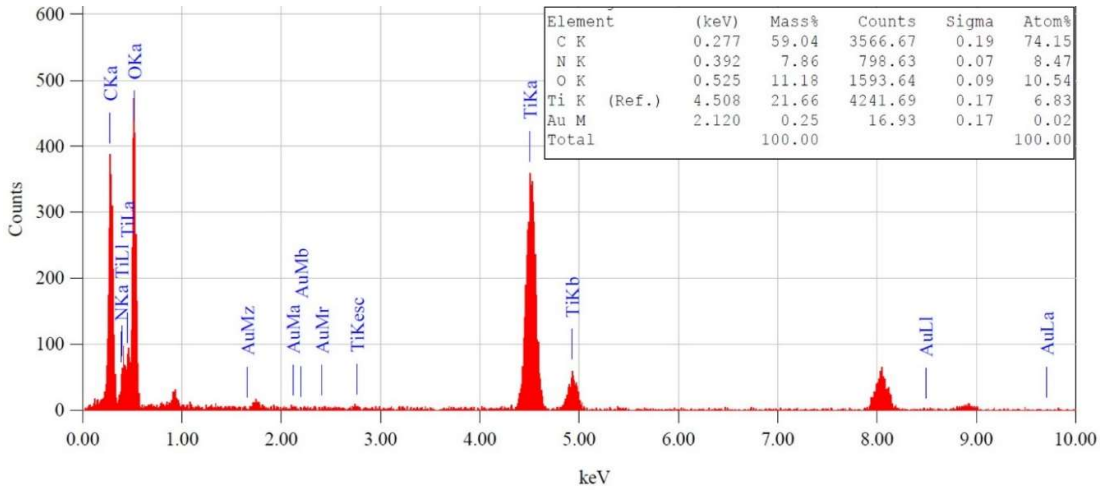

Figure A.2. Elemental quantitative analysis of 0.3 %. wt Au/TiO_2(P25)-gC_3N_4 (95-5) Air composite.

D) Appendix 4. Characterization techniques: Acquisition conditions and general principle

This appendix shows the experimental acquisition conditions and the scientific principle of each characterization technique that was used on this thesis.

D.1. Fourier-Transform Infrared Spectroscopy (FT-IR)

D.1.1. Acquisition conditions

Fourier Transform Infrared (FT-IR) spectra were recorded with a Thermo Fisher Nicolet iS10 spectrometer in the 525-4000 cm^{-1} range. The characteristic doublet of atmospheric CO_2 2340/2360 cm^{-1} signal could not be totally removed from the spectra after background subtraction due to physisorbed CO_2.

D.1.2. Principle

Infrared radiation passes through the sample, then monochromator, and it finally arrives to the detector as shown in **Fig. A.3**. Absorption in the infrared region results in changes in vibrational and rotational status of the molecules.

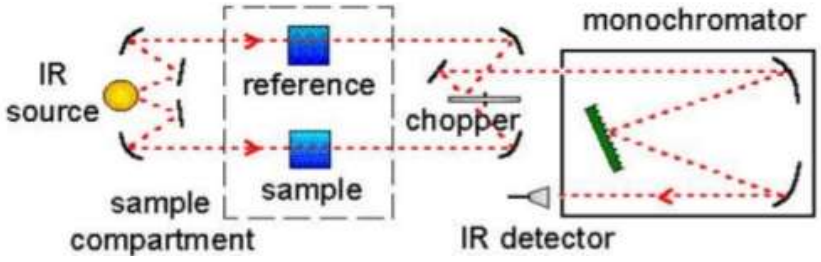

Figure A.3. Optical components on FTIR spectrophotometer.

D.2. Raman characterization

D.2.1. Acquisition conditions

Near Infra-Red (NIR) Raman spectra were collected with a LabRAM ARAMIS instrument equipped with a Synapse CCD Detector, an Olympus BX41 Microscope and a 785 nm laser (Laser Quantum MPC600 PSU) in the selected range of 300-1800 cm^{-1} (after 1800 cm^{-1} no significant peak was detected). The working laser power (84 mV) was carefully chosen to minimize both heating effect and fluorescence. The experimental conditions used were as follow: slits opening of 200 μm, grating with 1200 lines mm^{-1}, aperture hole of 600 μm, objective 10x, no filter, and acquisition time of 5s two times. A duo scan was applied in the x and y axis of the chosen area in order to average the signal over a 300*300 μm^2. Baseline correction was done with LabSpec 5 software, by applying four auto polynom baseline smooth steps (3, 5, 7, and 8 degrees) for each sample.

D.2.2. Principle

Raman spectroscopy studies the vibrational and rotational transitions for a molecule in interaction with the light from an electromagnetic beam based on stokes and anti-stokes scattering features as shown in **Fig. A.4**.

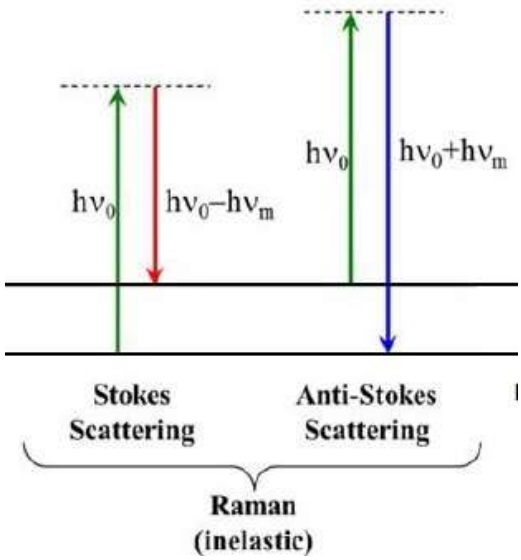

Figure A.4. Raman energy principle.

D.3. Structural characterization (XRD)

D.3.1. Acquisition conditions

X-ray diffraction (XRD) measurements were carried out on a Bruker D8-Advance diffractometer equipped with a Lynx Eye detector and operating at 40 kV and 40 mA, in a θ–θ mode using the Kα radiation of Cu at 1.5418 Å. The datasets were acquired in step scan mode over the 2θ range 5–35° (for **chapter 2** samples) and 5–60° (for **chapters 3 and 4** samples), using a step interval of 0.0329◦ and a counting time of 4 s per step. Samples were deposited on a round-shaped glass plate. Average thickness of graphitic

stacks of g-C_3N_4 sheets was determined using the Debye-Scherrer equation based on the full width at half-maximum (FWHM) and the position of the (0 0 2) reflection at $2\theta = 27.3°$. The interlayer distance of the layers stack and the in-plane distance of the s-triazine and the tri-s-triazine (heptazine) were calculated using the Bragg's law equation $2 * d_{hkl} * \sin(\theta) = n * \lambda$, where d_{hkl} represents the distance between 2 planes of (hkl) Miller index (Å), θ corresponds to Bragg's angle, n is the diffraction order and λ stands for the wavelength of incident beam (Å). A triplicate measurement of g-C_3N_4-NH_3 was used to obtain the uncertainty of the d_{space} distances. The number of layers was calculated with the method described elsewhere [16], using the ratio between thickness of the graphitic stacks and the d spacing of the (0 0 2) planes of the graphitic material. From the peaks at $2\theta = 13.1°$ (in plane diffraction peak of g-C_3N_4 based tri-s-triazine phase; TSTCN) and $2\theta = 17.4°$ (in plane diffraction peak of g-C_3N_4 based s-triazine phase; STCN) it was possible to determine their proportion by fitting the two indicated peak areas by using Casa XPS software 1.1.

D.3.2. Principle

Bragg Law is the main physical definition for understanding XRD principle, since it introduces the simpler crystal case (small and basic unit cell) with atoms of the crystalline linear network as shown in **Fig. A.5**.

$$2d_{hkl} * \sin\theta = n * \lambda$$

$2d_{hkl}$ = distance between 2 planes of the Miller index (Å)

Θ = Bragg´s angle

n = diffraction order

λ = wavelength of incident beam (Å)

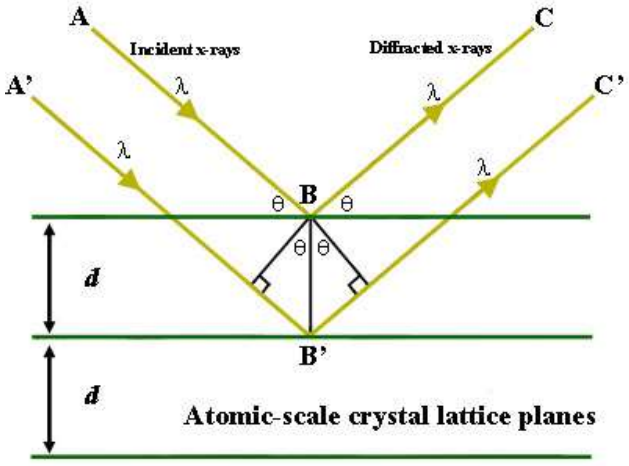

Figure A. 5. X-ray Diffraction principle (mode 2θ).

Debye-Scherrer relationship determines the average crystallite size of each crystalline phase present in the material. Thus, it is only applicable to nano-sized particles with grain sizes ranging from 0 to 1 µm.

$$\tau = \frac{k * \lambda}{\beta * \cos\theta}$$

k = shape factor, crystallite size dependent, normally nearby 1 value

Θ = Bragg´s angle

β = full width at half maximum (FWHM)

λ = wavelength of incident beam (Å)

D.4. Thermal stability (TGA)

D.4.1. Acquisition conditions

Thermo gravimetric analyses (TGA) were performed using a TA Instrument Q5000IR. Each sample was placed in a platinum crucible and heated from room temperature up to 900 °C with a heating rate of 10 °C min^{-1} under an air flow of 25 mL min^{-1}. Standard deviation on the decomposition temperature of the as-prepared samples is ± 10°C.

D.4.2. Principle

Thermogravimetric analysis measures the mass variation of a sample undergoing a regime of temperature increase under controlled atmosphere. This technique also makes it possible to measure the thermal stability of the sample as well as to determine the quantity of products and / or residues accumulated or adsorbed by the sample and sometimes the quantity of certain components of a material.

D.5. X-ray photoelectron spectroscopy (XPS)

D.5.1. Acquisition conditions

X-ray Photoelectron Spectroscopy (XPS) measurements were performed in an ultrahigh vacuum (UHV) Thermo-VG scientific spectrometer equipped with a CLAM4 (MCD) hemispherical electron analyser. The Al Kα line (1486.6 eV) of a dual anode X-ray source was used as incident radiation. Survey and high resolution spectra were recorded in constant pass energy mode (100 and 20 eV, respectively). The energy shift due to electrostatic charging was subtracted using the carbon adventitious signal of g-C_3N_4, *i.e.* the C 1s peak (284.6 eV). Surface atomic ratios were derived from XPS spectra using a Shirley-type background using the appropriate experimental sensitivity factors of the normalized photo ionization cross-section of the atomic subshells following Scofield.

D.5.2. Principle

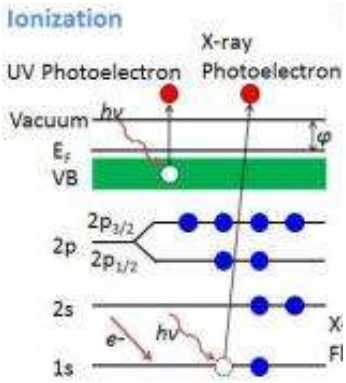

Figure A.6. Incident photons in a SC creating X-ray and UV photoelectrons.

In photoelectron spectroscopy (PES) recorded electrons are emitted when the surface is irradiated with photons (**Fig. A.6**). The technique is based on the photoelectric effect. The atoms in solids are ionized and the electrons with binding energies (E_b) absorb photons with energy $h\nu$ (1486.6 eV for Al K_a) and escape from the solid body with kinetic energy E_k:

$$E_k = h\nu - E_b - \emptyset$$

where the material work function

$$\emptyset = E_{vacuum} - E_F$$

Following ionization with photoelectron emission from core levels or valence band, the atom will release energy by Auger electron emission or X-ray fluorescence. The E_k is measured using an electron energy analyser which generates a spectrum with a series of photoelectron peaks. The E_b of the peaks are characteristic of each element.

- The peak areas can be used (with appropriate sensitivity factors) to determine the composition of the materials surface.
- The peak shape and E_b can be slightly altered by the chemical state of the emitting atom providing chemical bonding information. The XPS is not sensitive to hydrogen or helium, but can detect all other elements.

In function of the incident photon energy (wavelength), the photoelectric effect could generate X-ray photoelectrons with X-rays photons between 100 eV-10 keV (soft X-rays, wavelengths: 10 - 0.1 nm) is applied to probe deep core levels.

D.6. Ultraviolet photoelectron spectroscopy (UPS)

D.6.1. Acquisition conditions

Ultraviolet Photoelectron Spectroscopy (UPS) measurements were performed in an ultrahigh vacuum (UHV) Thermo-VG scientific spectrometer equipped with a CLAM4 (MCD) hemispherical electron analyser. During the UPS measurement (hv = 21.2 eV), a bias of 15.32 V was applied to the sample to avoid interference of the spectrometer threshold in the UP spectra. The values of the VBM were determined by fitting a straight line onto the leading edge and take into account the $E_{cut\text{-}off}$.

D.6.2. Principle

It follows the exactly same principle than XPS, with the only difference on the energy level of the photoelectron ionized. In function of the incident photon energy (wavelength), the photoelectric effect could generate ultraviolet photoelectrons which uses photons in the ultraviolet spectral range of 10-50 eV (wavelengths: 100 to 25 nm). It is applied to study the valence and conduction bands and to measure work function.

The first step is to determine the binding energy of the cut-off by using the UPS spectra. Tracing a line from the top point to the half of the peak, the cut-off can be obtained. Then, the signaled x axis value corresponds to the cut-off binding energy. The binding energy (x axis) can be corrected as follows:

$$\text{B.E. (corrected)} = - \text{B.E. (raw)} + E_{\text{cut-off}} + E_{\text{incident}}$$

The inflexion point on the UPS high resolution spectra gives the valence band maximum (VBM) value, and by using the experimental optical band gap (from UV-Vis measurements), the conduction band minimum (CBM) can be thus calculated.

D.7. BET surface area measurements

D.7.1. Acquisition conditions

Nitrogen adsorption-desorption isotherms were obtained using a Micromeritics Asap 2420 porosimeter using N_2 as an adsorbent at 77K. Materials were outgassed at 250 °C under a primary vacuum for 2h in order to desorb impurities from their surfaces and eliminate any water. Specific surface areas were calculated by the Brunauer, Emmett and Teller (BET) method in the relative pressure (p/p_0) range 0.05-0.3 and using t-plots methods. Pore-size distributions were calculated by the Barret-Joyner-Halenda (BJH) method which is specific for mesoporous solids.

D.7.2. Principle

Adsorption is regarded as the accumulation of atoms or molecules on the surface of a material. This process creates a film of the adsorbate (the molecules or atoms being accumulated) on the adsorbent's surface. Adsorption phenomena is described by **isotherms**, *i.e.,* the amount of adsorbate on the adsorbent as a function of its pressure (if gas) or concentration (if liquid) at constant temperature.

An **adsorption isotherm** is obtained by measuring the amount of gas adsorbed across a wide range of relative pressures at a constant temperature (typically **N_2, 77K**). Conversely **desorption isotherms** are achieved by measuring gas removed as pressure is reduced.

Therefore, an adsorption theory can be introduced for multi-points strategy: **Brunauer-Emmett-Teller (BET)**, which uses the following linear equation arrangement that can be reproduced on different adsorption-desorption isotherms presented in **Fig. A.7**.

$$\frac{P}{V_m(P - P^\circ)} = \frac{1}{V_m C} + \frac{(C-1)}{V_m C}\frac{P}{P^\circ}$$

v = weight of gas adsorbed

Vm = weight of adsorbate as monolayer

P/P0 = relative pressure

C = BET constant

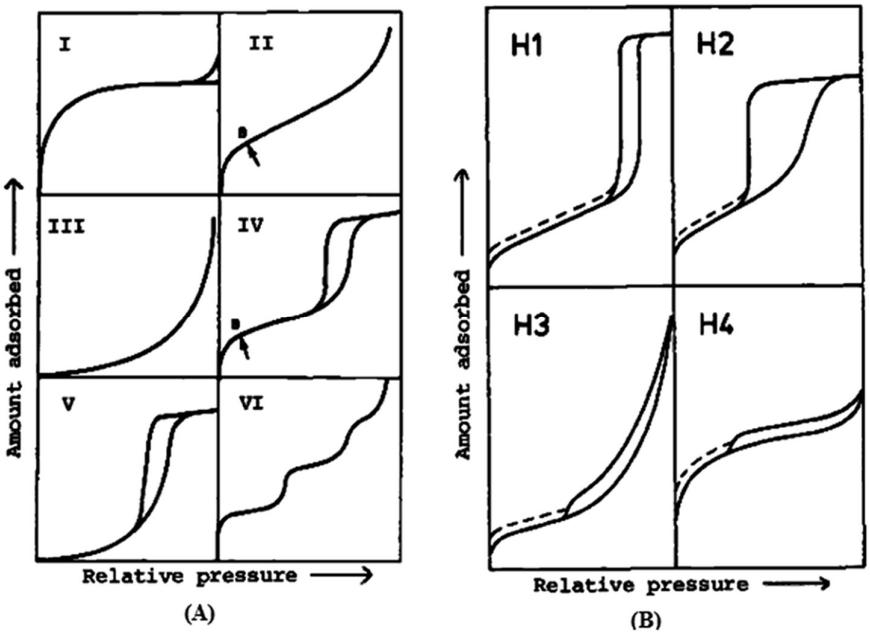

Figure A.7. A) 6 types of isotherms of adsorption-desorption **B)** 4 types of histeres loops.

D.8. Zeta potential measurements

D.8.1. Acquisition conditions

Zeta potential (ζ) measurements were obtained using a Zetasizer Nano ZS (Malvern Instruments Ltd. UK) equipped with an automatic titrator-diluter Malvern MPT-2. The sample container was connected through a capillary system, and with a peristaltic pump with a folded capillary cell (DTS 1060). The zeta potential was obtained from the electrophoretic mobility of the suspension by using the Smoluchowski equation, due to the polar nature of the solvent. Thus, each sample was measured three times at every pH value. The pH titration was programmed from pH 8 to pH 4 using a 0.5 pH interval. To change the pH of the sample, 3 titrants solutions were used sodium hydroxide ca. 0.01 mol L^{-1} and hydrochloric acid ca. 0.01 mol L^{-1} / 0.1 mol L^{-1}. The isoelectric point (IEP) was determined at the pH value where the zeta potential was zero (Hunter 1981).

D.8.2. Principle

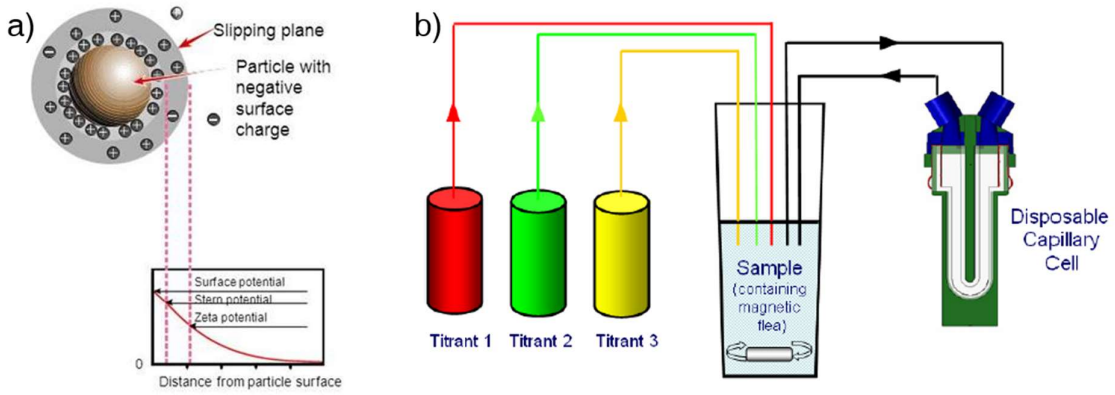

Figure A.8. a) Schematic representation of zeta potential b) Multiple automatic titration schematic system having three titrants for changing the pH of the sample and circulating it into the disposable capillary cell situate in Zetasizer Nano.

Zeta potential or electro-kinetic potential is a physical property of a particle in suspension. On a colloidal dispersion is a measure of the electrostatic repulsion between particles and the surrounded environment. **Figure A.8 a)** shows the definition of zeta potential in a depth explanation. The liquid surrounding the particle exists as two parts; an inner region (Stern layer) where the ions are strongly bound and an outer (diffuse) region where they are less associated. Within the diffuse layer there is a notional boundary inside which the ions and the particle form a stable entity. When a particle moves (e.g. due to gravity), ions within the boundary move it. Those ions beyond the boundary stay with the bulk dispersant. The potential at this boundary (surface of hydrodynamic shear) is the zeta potential. To measure the zeta potential, Henry´s equation related to electrophoretic mobility is used:

$$U_E = \frac{2\,\varepsilon\,z\,f(ka)}{3\,\eta}$$

Where U_E = electrophoretic mobility, z = zeta potential, ε = dielectric constant, η = viscosity, $f(ka)$ = Henry´s function, k (Debye length) = "thickness" of the electrical double layer, a = radius of the particle. The electrophoretic determination of zeta potential is highly influenced by the media polarity. Two postulates were presented for non-polar and polar medias, Hückel and Smoluchowski, respectively (**Fig. A.9**).

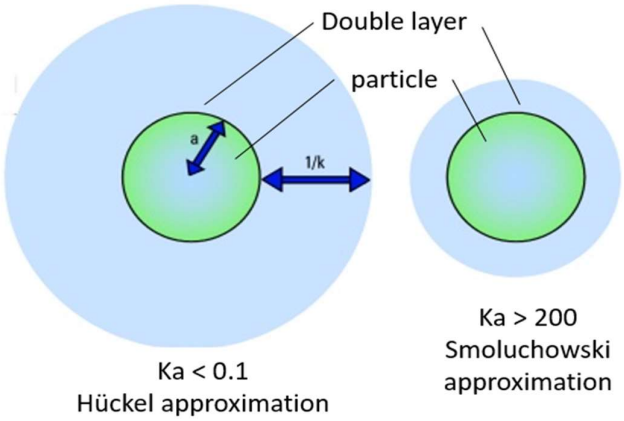

Figure A.9. Schematic illustration of Hückel and Smoluchowski´s approximation used for the conversion of electrophoretic mobility into zeta potential.

The automatic titration works with different titrants. These will be used according with initial pH of interest solution and also interest pH study range.

D.9. Electron mobility measurements using TRMC

D.9.1. Acquisition conditions

The incident microwaves were generated by a Gunn diode of the k_α band at 30 GHz. Pulse light source was an OPO laser (EKSPLA, NT342B) tunable from 225 to 2000 nm. It delivers 8 ns fwmh pulses with a frequency of 10 Hz. The light energy densities received by the sample were 1.2, 10.8, 8.1, 6.1 mJ cm^{-2} at 360, 450, 500, and 550 nm, respectively.

D.9.2. Principle

Time resolved microwave conductivity (TRMC) measurements were acquired as described elsewhere [19]. TRMC allows quantitative and qualitative detection of radiation-induced charge separation by time-resolved measurement of the changes in microwave absorption resulting from the production and decay or charged carriers via transfer phenomena steps, namely, concentration, effective mobility of the carriers formed, and predominant mechanisms during the decay: electron trapping, charge-carrier recombination dynamics, lifetimes, and interfacial reactions [20,21]. For this purpose, a quantification parameter as the % decay can be calculated by knowing two parameters the maximum number (I_{max}) and the number at 40 ns (I_{40}) of charge carriers, following the **equation 16**:

$$\%\ decay = \frac{I_{max} - I_{40}}{I_{max}} * 100$$

TRMC technique consists on the measurement of the change of the microwave power reflected by a sample, $\Delta P(t)$, induced by its laser pulsed illumination. The relative difference $\Delta P(t)/P$ can be correlated, for small perturbations of conductivity, to the difference of the conductivity $\Delta o(t)$ following **equation 17**:

$$\frac{\Delta P(t)}{P} = A\Delta\sigma(t) = Ae\sum_i \Delta n_i(t)\mu_i$$

where $\Delta n_i(t)$ is the number of excess charge-carriers i at time t and μ_i their mobility. The sensitivity factor A is independent of time, but depends on different factors such as the microwave frequency or the dielectric constant. Considering that the trapped species have a small mobility, which can be neglected, Δn_i is reduced to mobile electrons in the conduction band and holes in the valence band. And in the specific case of TiO_2, the TRMC signal can be attributed to electrons because their mobility is much larger than that of the holes.

The TRMC measurements were made at the LCP (Physico-Chemistry Laboratory from University Paris Sud) with Prof. Christophe Justin-Colbeau and Dr. Mohamed Nawfal.

D.10. Elemental analysis by Inductively Coupled Plasma Atomic Emission Spectroscopy (ICP-AES)

D.10.1. Acquisition conditions

Elemental analyses of the composites were performed using Inductively Coupled Plasma Atomic Emission Spectroscopy (ICP-AES). First, the powder samples were digested at about 215°C and 60 bar in a microwave digestion system (Multiwave 3000, Anton Paar, Austria) using an aqua regia mixture prepared with 2 mL HNO_3 (Fluka, Trace SELECT >69%, Germany) and 4 mL HCl (Fluka, Trace-SELECT >37%, Germany). Secondly, analysis of diluted filtrates was carried out, after filtration of residual particles, by Inductively Coupled Plasma Optical Emission Spectroscopy (ICP-OES, Varian 720ES, France) at 197.742 nm (Au). Multi-element standards were prepared by dilution of 1000 mg L^{-1} certified single element standards (CPI International, The Netherlands) in aqua regia media to minimize matrix effect errors. A spike on a digested sample allowed checking that the recovered concentrations were 100% ± **10%.** The limit of detection of the instrument is 0.1 mg L^{-1} for Au. Analysis of the Au component of the Au/SC1 and Au/SC1-SC2 composite allowed us to calculate deposition yields (η_{Dep}) which are defined as the ratio between the actual deposited mass of Au (Au_{Exp}, deduced from ICP-AES analysis) and the mass of Au introduced during deposition step (Au_{Theo}, target loading) as shown in following equation.

$$\%\eta_{Dep} = \frac{\%\, wt.\, Au_{Exp}}{\%\, wt.\, Au_{Theo}} * 100$$

D.11. Transmission electronic microscopy (TEM)

D.11.1. Acquisition conditions

High Resolution Transmission Electron Microscopy (HRTEM) was performed on a JEOL 2100F LaB_6 TEM/STEM microscope operating at 200 kV and with a point-to-point resolution of 0.21 nm and X-Ray microanalysis silicon drift detector (SDD). The sample was sonicated in ethanol before a drop of the suspension was deposited onto a microscopic copper TEM grid covered with carbon film for observation. For statistical determination on gold nanoparticles size and for relative distances (d_{hkl}) determination

by Electronic Diffraction (ED) pattern analysis, ImageJ 1.43 was used. The data analysis was based on the center distance of the image until the respective circle points.

The TEM observations were made at the ICPMS (Institute of Physics and Materials Chemistry of Strasbourg) with Dr. Dris Ihiawakrim.

D.11.2. Principle

TEM is also a high-resolution imaging technique where the incident beam is transmitted through a sample capable of producing images of the surface of a sample using the principle of electron-matter interactions (**Fig. A.10**). It makes it possible to highlight the morphology and the structure of the studied sample.

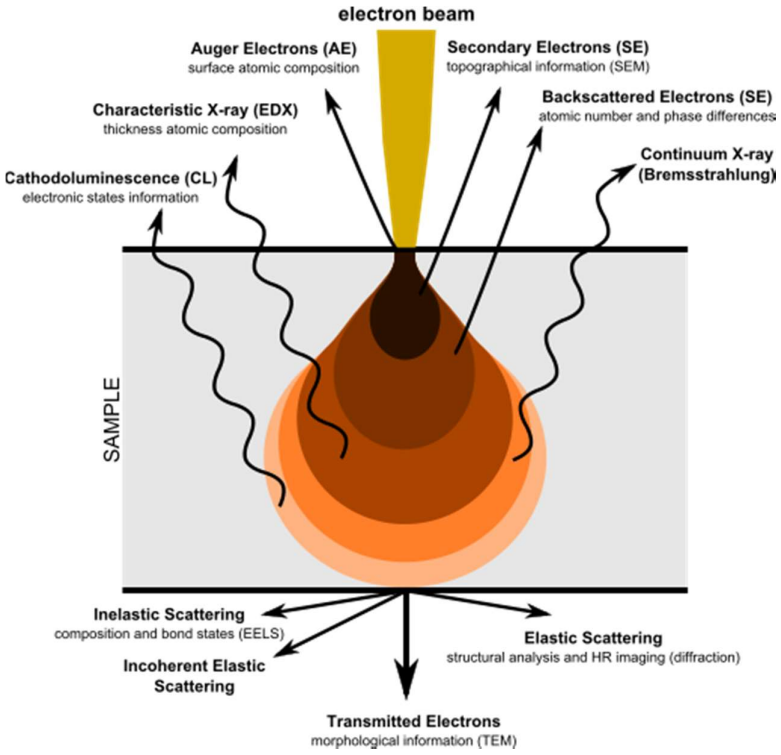

Figure A.10. Interaction of electron and matter.

The principle consists in scanning, by a beam of electrons, the surface of a sample. Some particles are re-emitted and collected by different detectors to form a 3D image.

D.12. UV-Vis spectroscopy

D.12.1. Acquisition conditions

UV–vis absorption spectra were recorded on a Perkin Elmer Lambda 950 Scan spectrophotometer equipped with a 100 mm diffuse reflectance integrating sphere. For clarity of the results, diffuse reflectance R_d spectra were converted in Kubelka-Munk unit according to $F(R) = (1 - R_d)^2/2R_d$, where $R_d = R_{sample}/R_{BaSO4}$ ($BaSO_4$ as standard). For obtaining the apparent band gap (Eg) of the semiconductors, Tauc equation was used $(F(R)*hv)^s = hv\text{-}Eg$, where h is the constant of Plank, v the frequency, s a coefficient depending of the direct (2) or indirect (1/2, g-C_3N_4 and TiO_2) nature of the BG transition.

D.12.2. Principle

UV-Visible spectroscopy gives information on the luminous absorption properties of materials. UV-Vis is based on the analysis of the intensity of a monochromatic ray after reflection (reflection-mode spectroscopy), or through (transmission mode spectroscopy) the sample, with respect to the intensity incidental radiation. The absorbance A of a sample is defined as a function of the transmittance T which corresponds to the ratio of the transmitted beam intensity I on the incident beam intensity I_0.

$$A = - \log (T) = - \log (I/I_0)$$

The range of analysis extends from UV (200 to 400 nm) to near infrared (800 nm). The wavelengths are scanned, when the energy of a photon is sufficient to make an energy transition, the system absorbs it, which gives rise to an absorption line. UV-Visible spectroscopy is an analytical technique particularly suitable for semiconductor analysis. The semiconductors absorb the radiation in the UV-Visible range, which gives rise to characteristic absorption lines which make it possible to determine the gap energy, E_{gap}.

The powder analysis requires the use of an integrating sphere and the acquisition of the spectra is done in reflection mode (diffuse reflectance). To determine the absorption coefficient, it is necessary to determine the Kubelka-Munk function (F (R)) which is equivalent to the absorbance (A). The Kubelka-Munk function is obtained via the reflectance R according to equation

$$F(R) = \frac{(1-R_d)^2}{2R_d}$$

F (R): Kubelka-Munk function
$R_d = R_{sample}/R_{BaSO4}$ ($BaSO_4$ as standard)
s: is ½ in the case of an indirect gap SC and 2 in the case of a direct gap SC

The Tauc curves are obtained by plotting (F (R) hυ) s as a function of the energy hυ (eV) of the incident ray. By performing a linear regression at the point of inflection of the curves, one can determine the gap of the SC at the intersection of the abscissa axis.

hυ: energy (eV)
Eg: Band gap (eV)

Résumé détaillé
Introduction générale

A) Transition énergétique

Le modèle économique actuel a entraîné une vaste consommation de produits de base modernes. Cette tendance a commencé avec la révolution industrielle lorsque la société a adopté une économie basée sur les combustibles fossiles. Ce changement a conduit à des décennies de prospérité industrielle alimentée par le pétrole, ce qui a entraîné une forte dépendance à l'égard de cette ressource limitée. La prospérité dont jouit la société ne s'est pas ralentie malgré les prédictions de M. King Hubbert et ses mises en garde concernant l'épuisement imminent des réserves de pétrole de la Terre [1]. La prévision a gagné en véracité avec la première crise pétrolière de 1973 à 1979 [2,3], et depuis lors, les émissions de CO_2 continuent à augmenter sans atteindre. La combustion de combustibles fossiles, puis le dégagement et l'accumulation de CO_2 qui en ont résulté ont créé le fameux « effet de serre », qui a entraîné une élévation de la température de la Terre avec des conséquences imprévisibles [4]. Au cours des dernières décennies, cela a suscité un débat sur la nécessité de modifier l'approvisionnement en énergie primaire de la société, débat qui a abouti à l'élaboration et à la promotion de nouvelles lois, par exemple. Protocole de Kyoto [5] et accord de Paris [6]. Dans ce contexte, le système de transport adopté et les différents processus industriels qui continuent à utiliser les combustibles fossiles en tant que matière première doivent être remplacés par d'autres moyens, à savoir des sources renouvelables, pour garantir une Terre durable.

B) Combustibles fossiles vs solaires

Les combustibles fossiles sont principalement riches en énergie, un gallon d'essence ayant une énergie équivalente à 121,8 MJ. Cette densité énergétique est un atout majeur pour stocker les combustibles fossiles dans un espace volumétrique approprié de conteneurs et de réservoirs, ce qui facilite par conséquent leur transport. Néanmoins, le principal inconvénient réside dans la durée de vie des réserves, qui dépend de nombreux facteurs, notamment de la gestion des pays industrialisés en fonction de la rapidité avec laquelle ils souhaitent les transformer et du volume de production. Ce scénario démontre clairement la nécessité de substituer une partie des combustibles fossiles par tout autre moyen. Les énergies renouvelables sont considérées comme une voie potentielle pour remplacer les combustibles fossiles [6-8]. Parmi les énergies renouvelables développées et existantes telles que les courants océaniques, le vent, l'hydroélectricité, la biomasse, la géothermie et le solaire, l'énergie solaire est la solution la plus prometteuse en raison de l'utilisation de la source d'énergie la plus puissante connue: le soleil [3,7, 9]. Parmi les technologies d'énergie solaire consistant à convertir la lumière solaire en énergie chimique, on peut mentionner la photocatalyse. La photocatalyse est considérée comme une technologie prometteuse pour les processus de photosynthèse artificielle. Le terme de «photosynthèse artificielle» vient de l'idée de reproduire la photosynthèse naturelle pour générer des molécules de stockage d'énergie à partir de CO_2 et d'eau en utilisant la lumière solaire, ce que l'on appelle les

combustibles solaires. Les systèmes photocatalytiques artificiels pour obtenir des processus de combustibles solaires doivent remplir plusieurs critères pour pouvoir être mis en œuvre. Les caractéristiques souhaitables des matériaux (photo) catalytiques sont la durabilité, un processus de synthèse simple, un coût modéré, un processus facilement évolutif et un rendement et une efficacité quantiques élevés. Cependant, a notre connaissance, il n'existe aucun matériau de ce type répondant à toutes les exigences mentionnées. Pour réaliser ce processus, un photocatalyseur durable basé sur des hétérostructures avancées à composants multiples et actif sous lumière visible est souhaitable.

Objectifs de la thèse

L'objectif général de ce projet de recherche est de concevoir, synthétiser et caractériser de nouveaux nanocomposites 2D à base de nitrure de carbone graphitique (g-C_3N_4) ayant une activité supérieure à celle des matériaux de pointe pour les applications photocatalytiques et catalytiques, en appliquant trois stratégies:

(1) Modification d'atmosphère de synthèse de g-C_3N_4

a) Réducteur (H_2, NH_3), oxydant (Air) et inerte (Ar, N_2)

(2) Couplage de g-C_3N_4 avec TiO_2 pour obtenir des composites à base d'hétérojonction TiO_2-g-C_3N_4

a) Variation de la proportion relative de TiO_2-gC_3N_4 synthétisé sous deux atmosphères (Air et NH_3)

b) Modification de la morphologie du TiO_2, 0D (P25 NP) et 1D (NT)

Les matériaux synthétisés selon les deux stratégies ont été décorés avec des NP Au avec une charge constante (0,3% en masse) pour former une jonction Au / SC afin d'évaluer les différences chimiques des différents supports. L'utilisation de NPs Au sur les supports repose sur deux objectifs principaux **(1)** l'utilisation d'une partie plus large du spectre solaire (surtout visible) par photoactivation de la jonction Au/SC et **(2)** l'évaluation de la performance des matériaux Au/(SC1 -SC2) en utilisant l'évolution de H_2 comme réaction modèle avec ajout d'un agent sacrificiel, pour tirer parti des fonctionnalités des Au NPs:

a) Propriétés co-catalytiques

b) Propriétés de piégeage d'électrons

c) Effet induit par les plasmons de surface (SPIE)

A) Stratégie

Ce projet porte sur la synthèse, la caractérisation et l'évaluation des performances (photocatalytiques) de nouveaux nanocomposites à base de Au/g-C_3N_4 et Au/TiO_2-gC_3N_4. Deux approches ont été réalisées.

(1) La première étude comprend l'optimisation de la synthèse de g-C_3N_4 en étudiant l'influence de l'atmosphère gazeuse au cours de la synthèse dans le but d'améliorer les performances de production photocatalytique de H_2 des composites binaires Au/g-C_3N_4. Les meilleures atmosphères de synthèse ont ensuite été choisies pour la synthèse des hétérostructures ternaires Au/TiO_2-gC_3N_4 suivantes.

(2) La deuxième étude a consisté en la synthèse de systèmes à hétérojonction TiO_2-gC_3N_4 afin d'obtenir un contact de bonne qualité entre les deux semi-conducteurs en fonction de la proportion et de l'atmosphère de synthèse utilisée. En règle générale, la qualité du contact interfacial intime définit l'efficacité de l'hybridation des orbitales, la création de nouvelles lacunes dans la bande interdite pour améliorer l'absorption visible, la durée de vie et le transport des espèces photogénérées, ainsi que la création de nouvelles porosités pour améliorer la diffusion des réactifs et produits et des paires e^-/h^+. À cette fin, deux morphologies différentes de TiO_2 ont été choisies, des nanoparticules (NP) et des nanotubes (NT) de TiO_2. Pour les deux systèmes, TiO_2(NP)-gC_3N_4 et TiO_2(NT)-gC_3N_4, deux atmosphères de synthèse ont été utilisées, Air et NH_3.

Ces différents nanomatériaux photocatalytiques ont été évalués en ce qui concerne la production de H_2 à partir d' H_2O sous irradiation solaire et visible à l'aide d'une faible quantité d'agent sacrificiel (1% vol. Triethanolamine). Pour certains échantillons une partie de la réaction préférentielle d'oxydation (PROX) notamment la conversion de CO, également été étudié. D'un point de vue fondamental, des études approfondies structure-activité ont été réalisées afin de corréler les propriétés structurelles, morphologiques, optiques et électroniques des nanocomposites à leurs activités (photo)catalytiques.

B) Plan de la thèse

Cette thèse décrit des recherches sur la conception et la synthèse de nanomatériaux à base de g-C_3N_4 décorés avec des NPs Au pour des applications principalement photocatalytiques et corrélées avec leurs propriétés physico-chimiques.

Le **chapitre 1** comprend une revue de littérature. Cette étude bibliographique présente une vue d'ensemble et une évaluation des progrès actuels du contexte énergétique, des technologies de production d'hydrogène les plus récentes et de la photocatalyse à base de semi-conducteurs et de métaux, en particulier pour les matériaux g-C_3N_4, TiO_2 et Au NP, ainsi que leurs applications, spécifiquement pour deux réactions modèles principalement la production photocatalytique de H_2 et dans une moindre mesure la catalyse PROX thermique (conversion du CO).

Le **chapitre 2** présente les matériaux g-C_3N_4 et Au/g-C_3N_4 introduits pour mettre en évidence l'effet de l'atmosphère pendant la synthèse de polycondensation. Cette étude porte sur l'influence de l'atmosphère gazeuse (agent réducteur, inerte et oxydant) au cours de la synthèse du g-C_3N_4, ce qui est assez peu étudié dans la communauté des chercheurs (cette étude a récemment été publiée dans le **Journal of Materials Chemistry A**) et sert de référence pour moduler les propriétés électroniques de g-C_3N_4 en fonction de l'application désirée. Une analyse approfondie tentant de corréler les propriétés physico-chimiques a l´activité photocatalytique a également été entreprise.

Le **chapitre 3** présente les composites binaires et ternaires TiO_2(NPs P25) -gC_3N_4 et Au/TiO_2-(NPs P25)-gC_3N_4, qui ont été caractérisés en détail et évaluer selon leur activité en production photocatalytique de H_2 en utilisant le même modèle de réaction que dans le chapitre 2. La stratégie expérimentale de ce chapitre est basée sur l'évaluation de l'influence de la proportion relative des SCs TiO_2 (P25 NP) et g-C_3N_4 dans le composite TiO_2(P25 NPs) -gC_3N_4 lors de la modification de l'atmosphère de synthèse (Air et NH_3).

Le **chapitre 4** montre les composites binaires et ternaires TiO_2(NTs)-gC_3N_4 et Au/TiO_2 (NTs)-gC_3N_4, qui ont été caractérisés en détail et évalués selon deux réactions modèles (1) la production photocatalytique de H_2, utilisés dans les chapitres 2 et 3, et (2) la conversion catalytique du CO. La stratégie expérimentale de ce chapitre a consisté à évaluer la modification de la morphologie du TiO_2, en utilisant des nanotubes de TiO_2(NT) en remplacement de TiO_2 granulaire TiO_2 (P25). Bien que la synthèse de TiO_2(NT) implique une étape supplémentaire, outre l'imprégnation par voie humide de précurseurs de g-C_3N_4 suivie de l'étape de polycondensation thermique pour obtenir du TiO_2(NT)-gC_3N_4, l'idée était d'augmenter la surface spécifique, qui est généralement proportionnelle à l'activité, et aussi de tirer parti de la configuration 1D TiO_2 (NT), plus favorable à un transfert direct des electron photogénérées pour améliorer la séparation spatiale.

Synthèse, discussion des résultats, et performance photocatalytiques

Chapitre 2 : g-C_3N_4 et binaires matériaux Au/g-C_3N_4

A) Synthèse

Les échantillons de g-C_3N_4 sont synthétisés par polycondensation thermique d'un rapport équimolaire de mélamine (Mel; 1,92 g) et de dicyandiamide (DCDA; 1,28 g) comme décrit ailleurs [10] et représentés sur la **Fig. 1**. Les précurseurs Mel et DCDA sont placés dans un creuset en alumine avec un couvercle. La polycondensation thermique est effectuée dans un four tubulaire à 550 ° C pendant 3 h en appliquant une rampe de chauffage de 5 ° C min^{-1} dans un flux continu de 100 ml min^{-1} de l'atmosphère désignée, à savoir Air, H_2, NH_3, N_2. et Ar. Ces échantillons seront comparés au g-C_3N_4 synthétisé sous air statique dans un four à moufle (comme préparé couramment par la communauté scientifique dans ce domaine) et à une référence commerciale (Fairlandtech), g-C_3N_4 commercial, synthétisée sous vide [11]. Les échantillons tels que préparés sont désignés par g-C_3N_4-atm, où atm représente la nature de l'atmosphère utilisée lors de la synthèse, de l'échantillon commercial ou de l'air statique. Pendant cette période de traitement thermique, les précurseurs subissent une transformation en g-C_3N_4 (TSTCN) à base de phase g-C_3N_4 de tri-s-triazine et s-triazine (STCN) et partiellement en phase amorphe. Dans le cas des phases cristallines, TSTCN et STCN, le mécanisme de formation était déjà mentionné dans **le chapitre 1, section D.2**. Cependant, la proportion exacte des différentes phases est difficile à calculer.

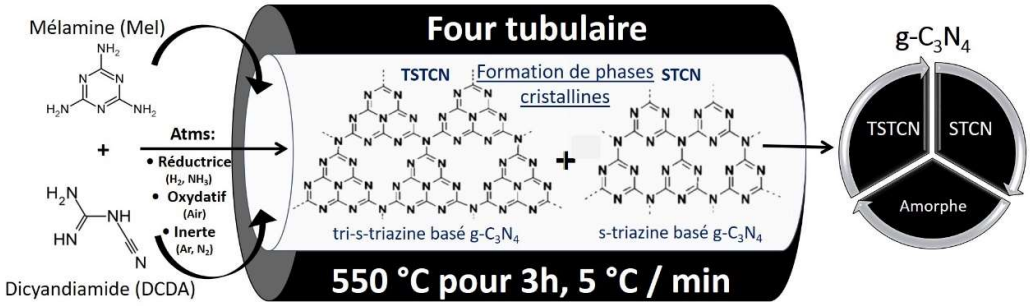

Figure 1. Synthèse de polycondensation thermique continue de g-C_3N_4 sous différentes atmosphères [12].

Des échantillons Au/g-C_3N_4 ont été préparés par réduction chimique de précurseurs de l'acide chloroaurique ($HAuCl_4$) [13] en présence des échantillons de g-C_3N_4 tels que préparés et illustrés schématiquement sous la **figure 2**. Le support (300 mg) est dispersé dans un mélange méthanol/éthanol (91/9 v/v, 55 ml) avec un sonicateur à pointe (700 W, 20 kHz) pendant 30 min (T_0), en utilisant 30% de la puissance de sonication maximale. Le mélange est ensuite transféré dans un ultrasons à bain (280 W, 50/60 Hz) et refroidi à la température ambiante (22 °C) avant que la sonication ne soit activée. Un volume donné d'une solution méthanol / éthanol de $HAuCl_4$ (2,5 (± 0,2) x 10^{-3} mol L^{-1}) est ensuite ajouté afin de cibler une charge en or de 0,3% en masse. %, sélectionnés selon une étude paramétrique réalisée antérieurement (**Fig. A.1, Annexe 1**). La sonication a été effectuée pendant 1 h (T_1) avant d'ajouter 5 ml d'une solution fraîche de solution de $NaBH_4$ dans du méthanol/éthanol (2,5 x 10^{-2} mol L^{-1}). La sonication est ensuite poursuivie pendant 10 min (T_2) pour garantir la réduction complète de Au^{+3} en Au métallique.

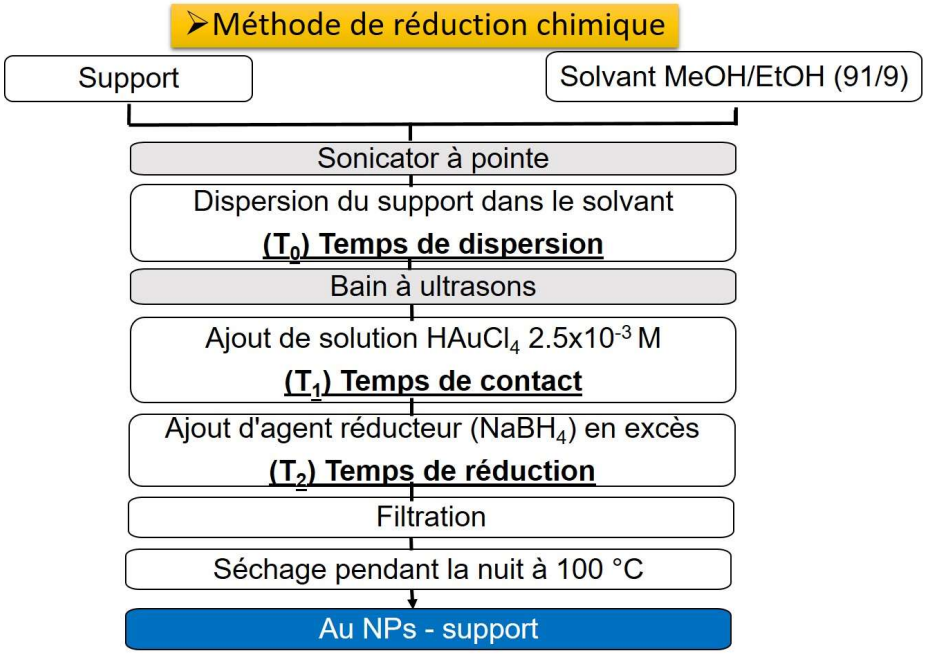

Figure 2. Dépôt de Au NP par méthode de réduction chimique [13].

B) Performances photocatalytiques

Les activités photocatalytiques des échantillons tels que préparés sont évaluées en fonction de plusieurs critères, à savoir la vitesse de production de H_2, l'évolution cumulative de H_2, la stabilité (tests de cyclage) et le rendement quantique interne (IQY). Tous les tests mentionnés sont effectués en utilisant le matériau semi-conducteur en suspension dans l'eau sous irradiation artificielle solaire et en ajoutant une très faible quantité de triéthanolamine (TEOA) en tant qu'agent sacrificiel (1% en volume) dans un montage photocatalytique. Ce système photocatalytique est également appelé **photoréacteur à particules en suspension**, comme illustré sur la **Fig. 2**. Les avantages d'un réacteur à particules en suspension reposent sur la simplicité du système à quatre composants: H_2O (réactif), une lampe lumière artificielle (source de photons pour l'activation) un photocatalyseur en suspension (pour scinder la molécule d'eau) et un agent sacrificiel. De même, la photodissociation de l'eau par conversion directe de l'énergie solaire en énergie chimique, sans utiliser de biais supplémentaire pour améliorer la séparation des porteurs de charge photogénérées, est un processus de production d'H_2 de relativement simple. Un autre avantage est le coût raisonnable de la mise en place ce type de configuration. Ainsi, en raison de tous les avantages mentionnés, c'est une approche attrayante pour évaluer l'activité des matériaux.

Dans les détails, la production de H_2 a été réalisée dans un récipient en quartz contenant 1 L d'eau désionisée Milli-Q et du TEOA (1% en volume) (pH = 11), équipé d'un tube de quartz à gaine centrale interne contenant une lampe halogène à vapeur de mercure (BLV-Licht du céramique-métal 150 W), simulant une lumière solaire artificielle. L'enveloppe de quartz est appropriée pour contenir la lampe car elle a une faible teneur en impuretés permettant aux photons UV et visibles de passer à travers sans presque aucune absorption. De plus, le récipient en quartz est enveloppé d'une feuille d'aluminium pour éviter les pertes de photons. Une irradiation simulée sous lumière visible a été obtenue en ajoutant une solution de Nigrosine de 0,1 g L^{-1} à la solution de refroidissement s'écoulant dans le tube de quartz plongeant afin de couper les photons UV. La chemise est reliée à un bain d'eau de refroidissement pour la refroidir en permanence (à 20 ° C) pendant toute l'expérience afin d'éviter toute augmentation de la température de l'eau due à un éventuel échauffement dû à la source lumineuse. En effet, selon la loi d'Arrhenius, une légère augmentation de la température de l'eau (≥ 2,5 ° C) dans ce type de système entraîne une augmentation de la vitesse de réaction et donc une augmentation de la production de H_2 par le biais d'une source d'activation thermique additionnelle à l'activation par la lumière. Les tests photocatalytiques sont réalisés en mettant en suspension 250 mg de catalyseur dans de l'eau ultra pure sous un flux d'azote continu (100 mL min^{-1}) et sous agitation mécanique à 700 tr / min. Pour la condition d'agitation continue, un barreau d'agitation magnétique en PTFE est utilisé pour produire un écoulement radial. Par conséquent, les particules de photocatalyseur sont induites par rotation dans le liquide sous forme de suspension. Les tests sont effectués à la pression atmosphérique. Le réacteur comprend également un scellement hermétique à l'aide d'un anneau en silicium qui s'ajuste entre le sommet de la cuve en quartz et le couvercle en acier inoxydable. Ce système assure une étanchéité à l'air tout au long de l'acquisition en phase gazeuse continue, garantissant

de ne quantifier que les gaz dégagés à l'intérieur du récipient à quartz. Avant d'allumer la lampe, une purge préalable à l'azote (Alphagaz 2, SMARTOP) à 500 mL min^{-1} pendant 1 h a pour but d'éliminer l'O_2 résiduel. En effet, les quantités restantes d'O_2 peuvent entraîner des résultats biaisés, car l'O_2 résiduel peut réagir avec le H_2 produit et produire H_2O (réaction inverse indésirable). Après la purge à l'azote, la lampe est allumée et les produits de la réaction sont analysés en ligne toutes les 100 s au moyen d'un analyseur de chromatographie en phase gazeuse (µGC). Typiquement, le test photocatalytique quantitatif dure 2,5 h, en considérant une erreur relative de 10% sur la vitesse massique de production H_2.

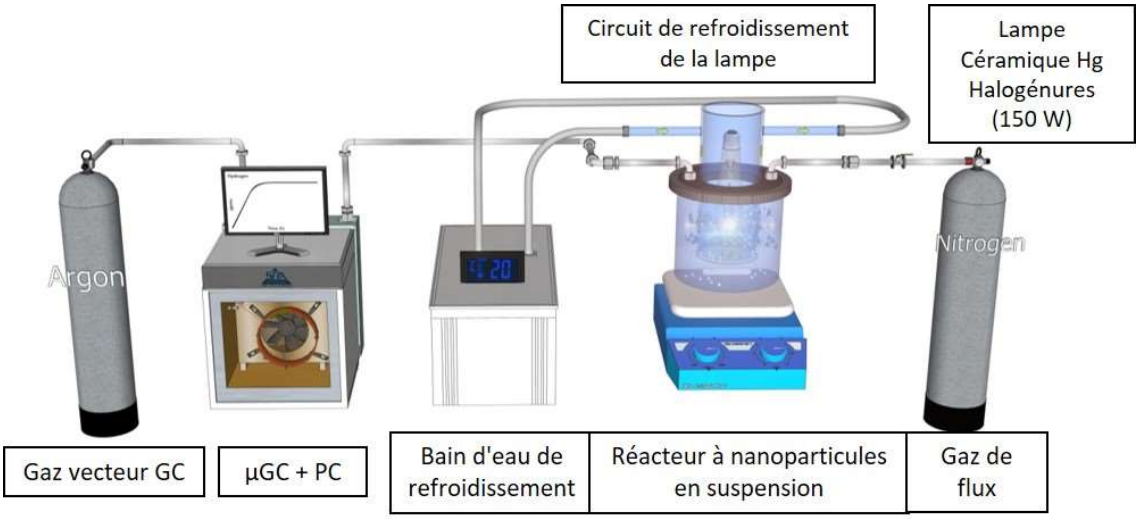

Figure 2. Schéma du montage photocatalytique avec tous ses composants. Conçu avec Sketchup ©.

D'après les résultats de production de H_2 obtenus sous **irradiation artificielle solaire** (**Fig. 3**), les échantillons peuvent être divisés en trois catégories principales en fonction de l'amplitude de leur activité: le plus actif, Au/g-C_3N_4-NH_3 (conduisant à 324 H_2 µmol h^{-1} g_{cat}^{-1}), ceux qui présentent une activité modérée, Au/g-C_3N_4-Comm-N_2-Air statique-Ar (donnant 125, 101, 99 et 75 H_2 µmol h^{-1} g_{cat}^{-1}, respectivement), et les matériaux moins performants, Au/g-C_3N_4-Air-H_2 (produisant respectivement 41 et 36 H_2 µmol h^{-1} g_{cat}^{-1}). On peut remarquer la supériorité de Au/g-C_3N_4-NH_3, présentant une activité entre 3 et 9 fois supérieure au deuxième composite le plus actif (Au/g-C_3N_4-Comm) et au photocatalyseur le moins actif (Au/g-C_3N_4-H_2), respectivement.

Sous **irradiation artificielle visible** (**Fig. 3**), le nanocomposite Au/g-C_3N_4-NH_3 est le seul à présenter une activité mesurable avec 26 µmol h^{-1} g_{cat}^{-1} H_2 produite. Cependant, il convient de souligner que l'utilisation de Nigrosine comme filtre entraîne une diminution de l'émission globale du flux de photons, en plus de la coupure des photons UV.

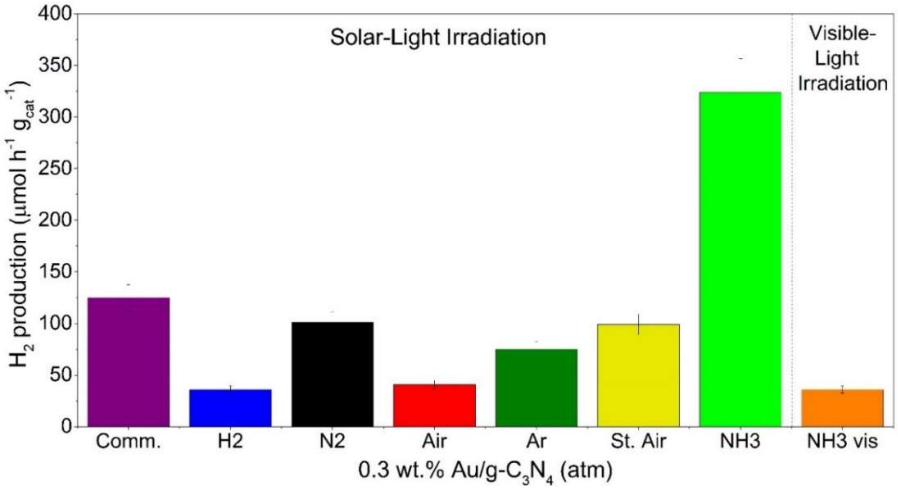

Figure 3. Vitesse moyenne de production d'hydrogène par heure et par masse de photocatalyseur avec 0,3% m Au/g-C_3N_4-atm en utilisant 10 ml de TEOA (1% en volume) comme agent sacrificiel sous irradiations solaire et visible artificielles.

Les valeurs de rendement quantique interne (IQY) ont été déterminées en mesurant l'absorbance de la suspension de photocatalyseur à la même concentration (0,25 g L^{-1}) que dans le test photocatalytique. Ces absorbances ont été mesurées au niveau des orifices d'entrée et de sortie de la sphère d'intégration, afin de mesurer principalement l'absorbance de l'échantillon tout en minimisant la contribution de la diffusion des particules de catalyseur. Pour la détermination du flux de photons, l'irradiance absolue de la lampe a été mesurée à l'aide d'un spectroradiomètre ILT900-R (technologies lumineuses internationales) exactement dans les mêmes conditions expérimentales que lors des mesures photocatalytiques.

Le rendement quantique interne (IQY) a été calculé à l'aide de l'équation suivante :

$$IQY = 2 \times \frac{r_{H_2}}{q_{p\ (Abs)}}$$

Définissant $r_{(H2)}$ en tant que vitesse de formation d'hydrogène (mol h^{-1}) et $q_{p(Abs)}$ en tant que flux de photons absorbés par le matériau photocatalytique, calculé conformément à l'équation suivante:

$$q_{p(Abs)} = \int_{\lambda_{min}}^{\lambda_{max}} \frac{P(\lambda) \times (1 - 10^{A(\lambda)l})}{E(\lambda)}\, d(\lambda)$$

Définissant P (λ), E (λ) et A (λ) respectivement comme la puissance d'irradiation, l'énergie des photons et l'absorbance de la suspension de nanoparticules à une longueur d'onde donnée (λ) de chaque échantillon utilisé dans le réacteur photochimique, considérant un chemin optique l = 5 cm.

La **figure 4** résume les rendements quantiques internes (IQY) déterminés sous irradiations solaire et visible. Activation sous lumière solaire artificielle, Au/g-C_3N_4-NH_3 révèle l'IQY le plus élevé, de 1,85, contre 0,55 pour le matériau commercial Au/g-C_3N_4 et 0,20 pour le moins performant (Au/g-C_3N_4-H_2). Cette valeur est supérieure à celles

calculées pour tous les autres échantillons sous irradiation solaire (incluant également la contribution UVA). Il faut également souligner que le photocatalyseur Au/g-C_3N_4-NH_3 présente un IQY d'environ. 0,60% sous irradiation visible.

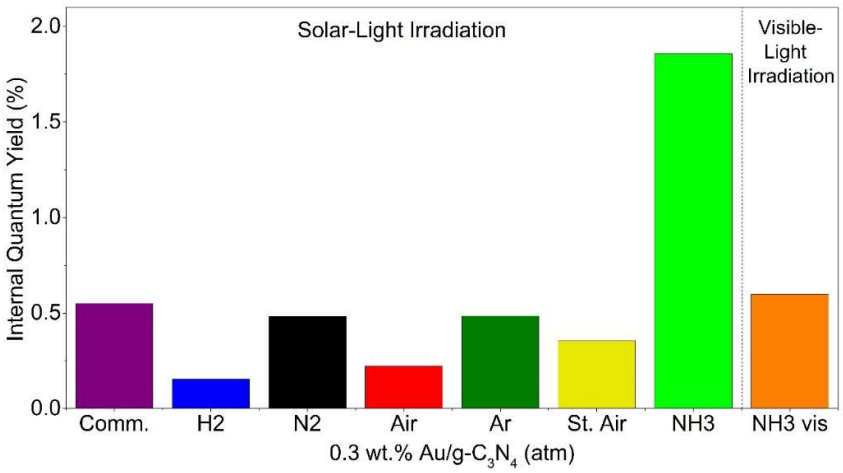

Figure 4. Rendement quantique interne (IQY,%) des composites tels que préparés sous irradiation solaire et visible.

Des tests de stabilité et de recyclage ont été réalisés sous activation solaire en utilisant le même photocatalyseur initial pour les échantillons les plus actifs uniquement, à savoir Au/g-C_3N_4-NH_3. Après chaque test photocatalytique (2,5 h après avoir atteint le plateau de production en H_2), le photocatalyseur a été filtré, lavé et séché. Le photocatalyseur a ensuite été réutilisé comme décrit précédemment dans le réacteur photocatalytique. Il convient de noter qu'après chaque cycle de lavage, une perte de masse de 5% a été prise en compte pour le calcul des vitesses de réaction massiques. Les tests de cyclage réalisés sur le matériau Au/g-C_3N_4-NH_3 le plus performant (**Fig. 5**) permettent d'observer une diminution relative de la production de H_2 de respectivement 20 et 26% après le deuxième et le troisième cycle, par rapport aux premier test. Ce comportement pourrait s'expliquer par la dégradation de la TEOA et la formation de sous-produits susceptibles d'empoisonner le catalyseur [5].

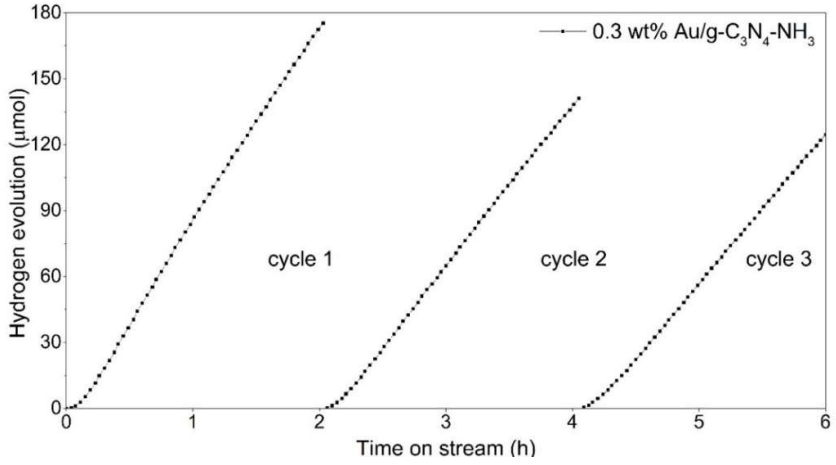

Figure 5. Tests de cyclage sur 0,3% en masse Au/g-C_3N_4-NH_3 avec 1% en volume de TEOA sous irradiation solaire.

Après différentes caractérisations et analyses complémentaires effectuées, il n'a pas été possible de confirmer la présence de SPIE sur les composites Au/g-C_3N_4 synthétisés et étudiés. La **figure 6** résume un schéma détaillé des voies de transfert de charge possibles.

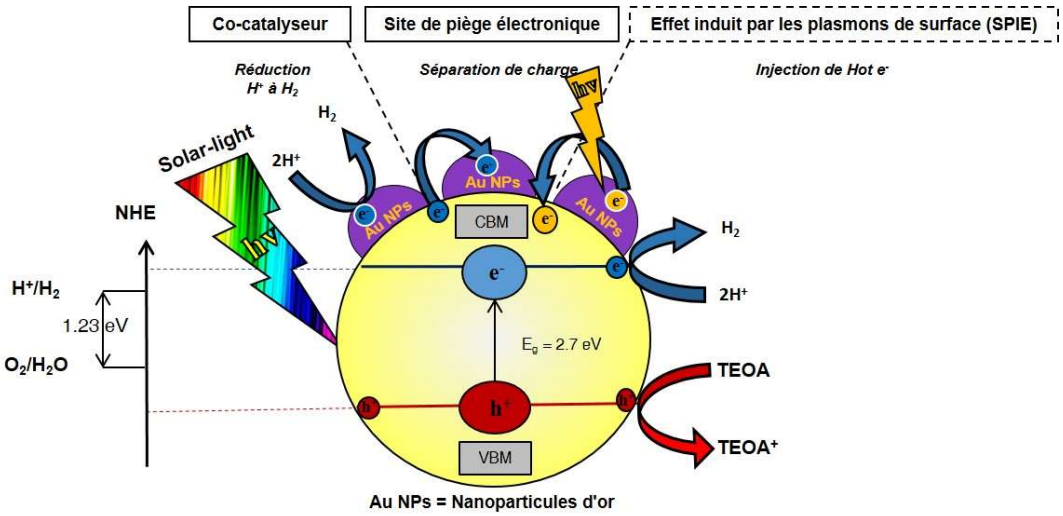

Figure 6. Schéma du mécanisme de production de H_2 proposé pour le composite Au/g-C_3N_4-NH_3, soulignant les deux demi-réactions de la dissociation de l'eau et des différentes voies de transfert d'électrons.

Chapitre 3 : Composites binaires TiO_2(P25)-gC_3N_4 et composites ternaires Au/TiO_2(P25)-gC_3N_4

A) Synthèse

Les méthodes d'imprégnation par voie humide présentent plusieurs avantages par rapport à d'autres méthodes physiques ou chimiques, telles que l'utilisation de conditions douces (pression atmosphérique et température ambiante), l'utilisation d'un solvant universel et respectueux de l'environnement (eau), ainsi que de matériels de laboratoire simples. Par conséquent, la méthode d'imprégnation humide est connue comme un "processus vert".

Dans notre cas, la méthode d'imprégnation humide consiste en deux étapes successives:

(i) Une imprégnation préalable en milieu humide de précurseurs de g-C_3N_4 (Mel + DCDA) sur du TiO_2 (commercial) (P25) suivie d'un séchage pendant une nuit à 100 °C et

(ii) Réaction de polycondensation à l'état solide de g-C_3N_4 en présence de précurseurs préimprégnés sur TiO_2.

Typiquement, la première étape d'imprégnation par voie humide comprend un mélange à l'état solide de précurseurs de g-C_3N_4 (Mel et DCDA dans une proportion équimolaire) avec le TiO_2 P25 disponible dans le commerce (acheté dans Evonik Industry). Ensuite, un petit volume d'eau est ajouté dans le récipient contenant tout le mélange solide, conduisant à la dissolution des précurseurs Mel et DCDA. Le mélange est maintenu sous agitation douce jusqu'à évaporation du solvant. Ainsi, le solide résultant (type gel)

est ensuite placé dans un four à moufle pendant une nuit à 100 °C. Le solide obtenu est gratté du bécher et transféré dans un creuset en alumine pour subir la polycondensation thermique dans un four tubulaire à 550 ° C pendant 3 h avec une rampe de chauffage de 5 ° C min^{-1} sous un flux continu de 100 ml min^{-1} sous atmosphère de synthèse (comme décrit précédemment dans le **chapitre 2** pour la synthèse de g-C_3N_4-atm). Les étapes de synthèse mentionnées sont résumées schématiquement sur la **Fig. 7**.

Les atmosphères choisies ont été sélectionnées sur la base des résultats obtenus après évaluation des performances d'évolution de H_2 sur les échantillons de g-C_3N_4-atm (**chapitre 2**). Il convient de rappeler que les échantillons synthétisés les plus photoactifs étaient 0,3% en masse. % Au/g-C_3N_4-NH_3 et 0,3% en masse % Au/g-C_3N_4-Air. Ainsi, ces deux atmosphères de synthèse (NH_3 et Air) ont été sélectionnées pour l'élaboration de composites binaires TiO_2-gC_3N_4 selon le protocole résumé ci-dessous.

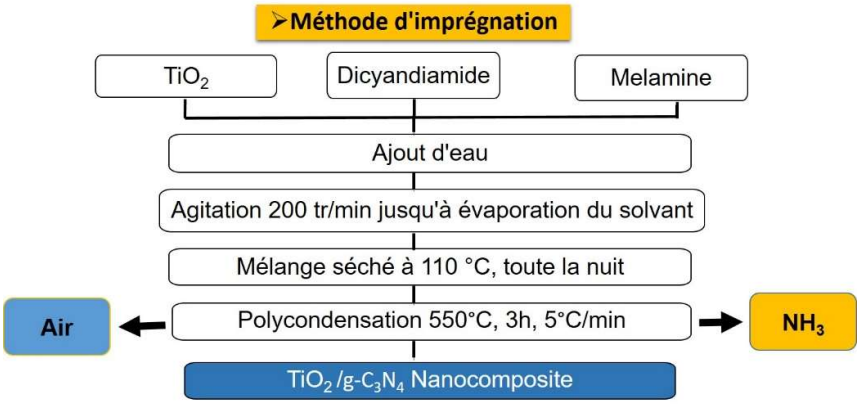

Figure 7. Schéma de la synthèse des systèmes binaires d'hétérojonction TiO_2/gC_3N_4 – atm obtenus par la méthode d'imprégnation.

Les proportions relatives de TiO_2 et de g-C_3N_4 dans les composites à hétérojonctions binaires ont été choisies pour mener l'étude paramétrique des **chapitres 3 et 4**. Ainsi, un ensemble de nanocomposites binaires est synthétisé selon le même principe de polycondensation thermique de g-C_3N_4 en présence du TiO_2, tel que préparé. La principale différence réside dans la morphologie de TiO_2. Dans les **chapitres 3 et 4**, les nanoparticules de TiO_2 P25 (NP) et de TiO_2 (NT) ont été choisies, respectivement, pour être associées à g-C_3N_4.

Afin de couvrir la gamme la plus large de proportions relatives d'hétérojonctions, une première méthodologie de criblage a été appliquée pour sélectionner une première série de proportions massiques relatives de TiO_2-gC_3N_4 de 75-25, 50-50 et 25-75, respectivement. Le but était de sélectionner des proportions opposées et intermédiaires pour visualiser et comparer équitablement les différents composites avec leurs propriétés physico-chimiques associées. Par conséquent, après avoir obtenu les résultats photocatalytiques des composites de criblage, il a été décidé d'étendre l'étude à une gamme plus étroite de proportions relatives d'hétérojonctions vers une teneur plus élevée en TiO_2 (ou une teneur plus faible en g-C_3N_4). Cette approche est définie comme la méthode du zoom, avec les proportions massiques relatives de TiO_2-gC_3N_4 de 97,5-2,5, 95-5 et 90-10, respectivement. Cette méthodologie est résumée dans la **figure 8**.

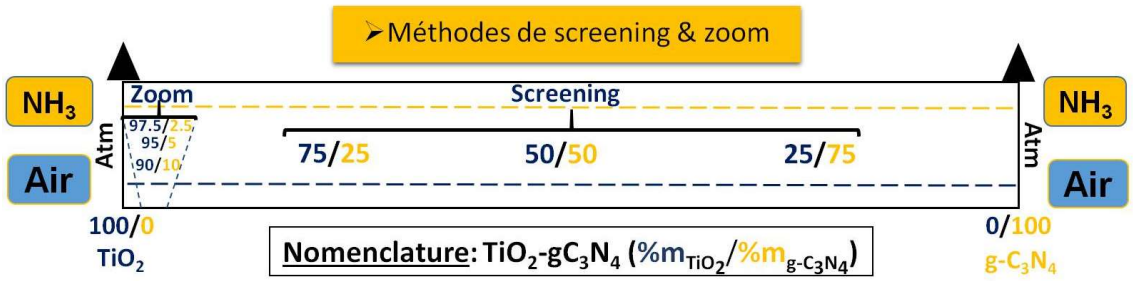

Figure 8. Schéma des méthodes de screening et zoom appliquées pour sélectionner les proportions TiO_2-gC_3N_4.

B) Performances photocatalytiques

D'après la **figure 9 (gauche)**, on peut observer que l'échantillon de référence Au/TiO_2 calciné à 550 ° C (Air) présente l'activité la plus élevée avec une vitesse de production d'H_2 1541 µmol h^{-1} g_{cat}^{-1}. Cette vitesse de réaction tend à diminuer lorsque l'on augmente la teneur en g-C_3N_4, l'échantillon de référence Au/g-C_3N_4 (Air) conduit à l'activité la plus faible (produisant 41 µmol h^{-1} g_{cat}^{-1}).

Parallèlement, des échantillons de mélanges physiques présentant la même teneur en g-C_3N_4 ont été testés dans les mêmes conditions expérimentales à des fins de comparaison. Les taux de production de H_2 des mélanges physiques Au/TiO_2-gC_3N_4, correspondant aux proportions équivalentes de 75/25, 50/50, 25/75, ont montré une tendance non proportionnelle, donnant un rendement de 1077, 818, 468 H_2 µmol h^{-1} g_{cat}^{-1}, respectivement. On peut souligner la supériorité des mélanges physiques par rapport aux composites de criblage, ce qui signifie que l'interaction chimique des deux SC appliquant la réaction en deux étapes n'est pas bénéfique avec les proportions testées.

D'après la production moyenne de H_2 (**Fig. 9 droite**) obtenue pour le composite zoom Au/TiO_2-gC_3N_4-Air irradié sous lumière solaire artificielle, une seule référence a été sélectionnée (Au/TiO_2 550 ° C (Air)), car le taux de formation de H_2 pour la référence Au/g-C_3N_4 (Air) était très faible par rapport aux valeurs obtenues pour la formation de H_2 pour les composites à très faible teneur en g-C_3N_4 (teneur élevée en TiO_2). On peut noter un taux de formation de H_2 nettement supérieur pour la composition Au/TiO_2-gC_3N_4-(95-5) par rapport à ses homologues avec 10 et 2,5% en masse. % g-C_3N_4 et par rapport à la référence Au/TiO_2 550 ° C (Air). Suivant la même idée appliquée pour le procédé de criblage, le composite le plus performant (c'est-à-dire contenant 5% en masse de g-C_3N_4) a été comparé à un mélange mécanique contenant également 5% en masse. % g-C_3N_4. Dans ce cas, on peut souligner que, contrairement aux résultats obtenus avec une teneur plus élevée en g-C_3N_4 (méthode de criblage), le composite synthétisé à 5% en masse. % g-C_3N_4 à un rendement supérieur du mélange physique équivalent. Ainsi, on peut supposer qu'une teneur plus faible en g-C_3N_4 conduit à une interface de meilleure qualité entre les SC g-C_3N_4 et TiO_2.

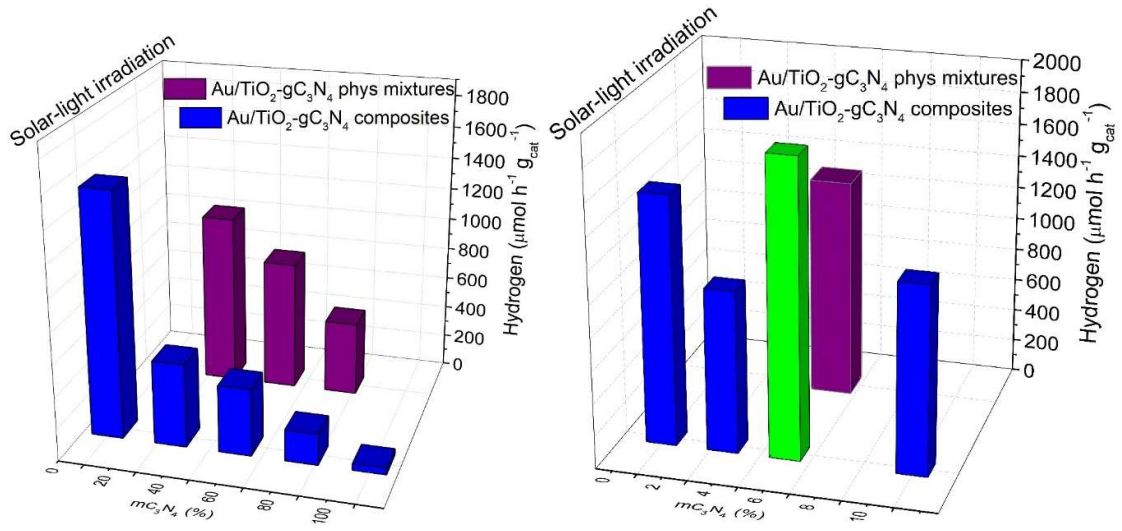

Figure 9. Taux moyen de formation d'hydrogène par heure et par masse avec 1% en volume de TEOA pour les composites Au /TiO_2-gC_3N_4-Air screening (gauche) et zoom (droite) et pour les références sous irradiation solaire. De plus, des mélanges physiques équivalents à la composition des composites ternaires ont été ajoutés à des fins de comparaison.

Suite à la mise en évidence des performances photocatalytiques intéressantes de **Au/TiO_2 (P25)-gC_3N_4- (95-5)-Air**, une analyse plus détaillée de son activité photocatalytique vis-à-vis de la production d'H_2 sous irradiation solaire et visible a été réalisée en terme de vitesse de production d'H_2, de production cumulée d'H_2, de stabilité et de rendements quantiques internes **(section D du chapitre 2)**, en utilisant les échantillons de référence pertinents.

La production moyenne d'H_2 (**Fig. 10**) permet d'observer la supériorité notable du composite Au/TiO_2-gC_3N_4- (95-5) (produisant 1839 µmol h^{-1} g_{cat}^{-1}) par rapport à Au/TiO_2(P25), Au/TiO_2 550 °C (Air), Au/TiO_2-gC_3N_4-(95-5), et Au/g-C_3N_4 avec des différences relatives de 31, 16, 27, 98%, respectivement, sous lumière solaire artificielle . Ce résultat suggère un effet synergique entre les deux SC au niveau de cette composition (95-5), probablement suffisant pour obtenir une photosensibilisation accrue du TiO_2, une meilleure séparation des porteurs de charges.

On retrouve la même tendance lors d'un test de production de H_2 sous irradiation visible artificielle. On peut noter l'augmentation relative de la production de H_2 obtenue sur le composite Au/TiO_2-gC_3N_4-(95-5) (produisant 419 µmol h^{-1} g_{cat}^{-1}) en référence à Au/TiO_2(P25), Au/TiO_2 à 550 °C (Air) et au mélange physique Au/TiO_2-gC_3N_4-(95-5) (45%, 21% et 27%, respectivement).

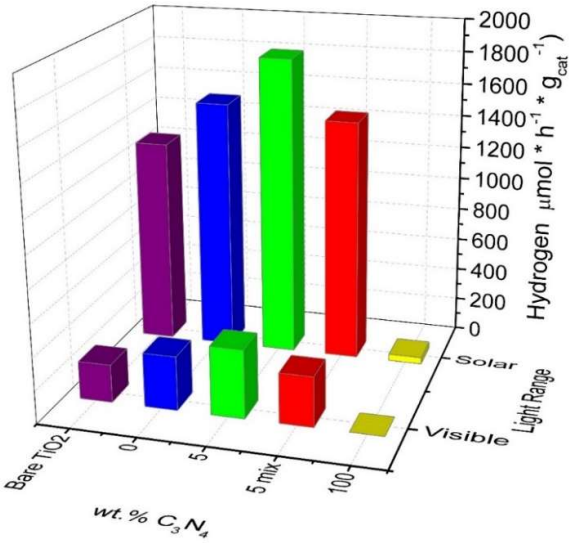

Figure 10. Taux moyen de formation d'hydrogène par heure et par masse avec 1% en volume de TEOA pour le composite Au/TiO_2-gC_3N_4 (95/5)-Air, références, et par un mélange physique avec un rapport massique équivalent sous irradiation solaire et visible.

Le dégagement cumulé d'hydrogène (**Fig. 11 gauche**) obtenu sous irradiation solaire permet d'observer la même tendance que pour le taux de formation massique moyen d'hydrogène. Le composite Au/TiO_2(P25)-gC_3N_4-(95-5) présente la production d'H_2 cumulée la plus élevée avec **978 µmol en 2,5 h**, qui correspond à **21,9 mL** de H_2 formé.

D'après le dégagement d'hydrogène cumulé (**Fig. 11 droite**) obtenu sous irradiation visible, on peut observer la même tendance que pour le taux de formation massique d'hydrogène moyen correspondant. Les échantillons Au/TiO_2-gC_3N_4 (95-5) présentent la quantité d'H_2 cumulée la plus élevée avec **224 µmol** en seulement 2,5 h, ce qui correspond à **5,0 mL** de H_2 formé.

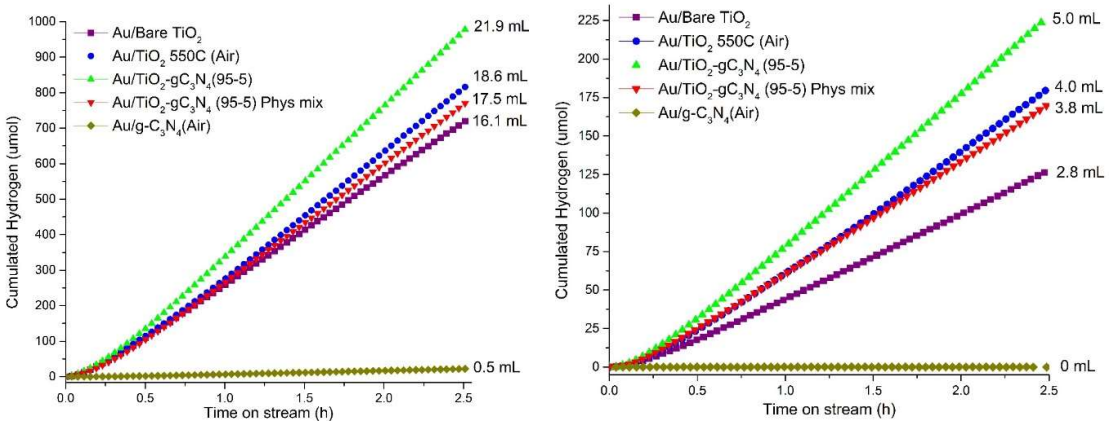

Figure 11. Evolution cumulée de l'hydrogène avec 1% en volume de TEOA sous irradiation solaire (gauche) et visible (droite) pour le composite Au/TiO_2-gC_3N_4 (95/5) - Air, trois références et un mélange physique avec le même rapport massique (95-5).

À partir de la détermination du rendement quantique interne (IQY) (**Fig. 12**), on peut voir la même tendance indépendamment de l'irradiation utilisée (solaire ou visible). Il n'y a qu'une légère différence entre les références de TiO_2 et le composite Au/TiO_2 (P25)-

gC_3N_4 (95-5) (non significatif). On peut donc en conclure que l'absorption de la lumière (densité des photons absorbés) est un paramètre important qui contribue à l'activité du matériau, mais pas le seul. Il convient de souligner que, pour le mélange physique Au/TiO_2(P25)-gC_3N_4 (95-5), l'IQY est 3,3 fois inférieur à celui du composite à teneur identique en g-C_3N_4.

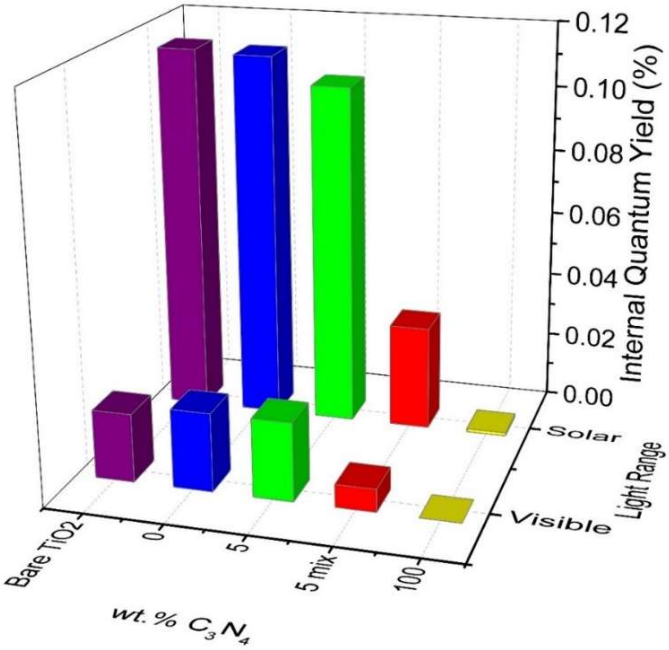

Figure 12. Rendement quantique interne (IQY %) du composite Au/TiO_2-gC_3N_4 (95/5), trois références, et la mélange physique avec le même rapport de masse sous irradiation solaire et visible.

La **figure 13** résume un schéma détaillé des voies de transfert de charge possibles.

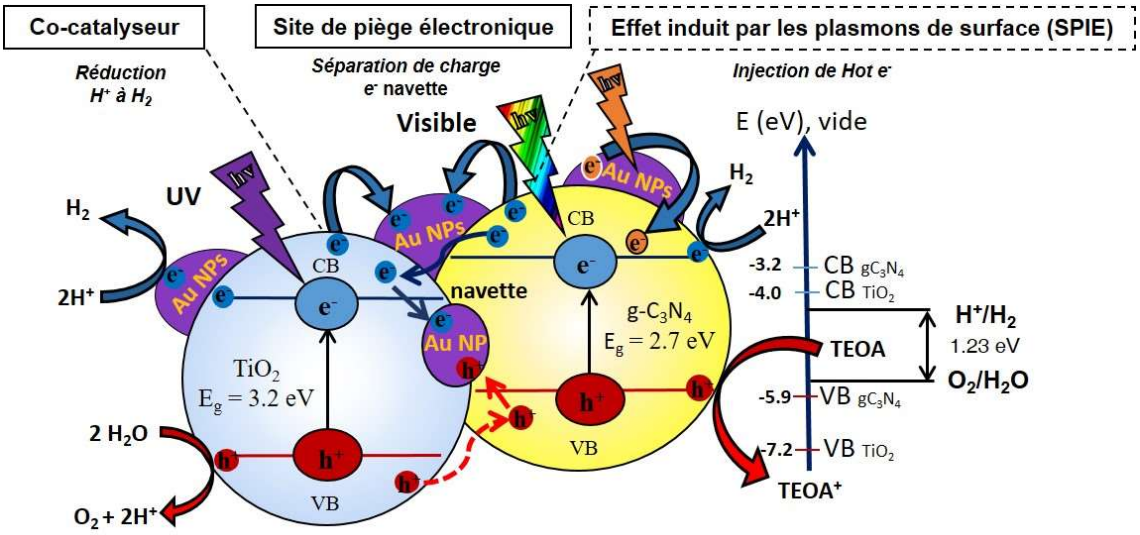

Figure 13. Illustration schématique du mécanisme de production de H_2 proposé pour le composite Au/TiO_2 (P25)-gC_3N_4 (95-5), comprenant les deux demi-réactions de la dissociation de l'eau, les positions CB / VB des SC et les différentes voies de transfert d'électrons possibles.

Chapitre 4 : Composites binaires TiO_2(NT) -gC_3N_4 et composites ternaires Au/TiO_2(NT)-gC_3N_4

A) Synthèse

Les TiO_2 NTs ont été synthétisés via la méthode de synthèse hydrothermale (**Fig. 14**), également appelée méthode de Kasuga, à partir de nanoparticules commerciales de TiO_2 (P25) en tant que précurseur. Typiquement, la synthèse comprend 5 étapes générales: **(1)** On ajoute du TiO_2 P25 dans un récipient contenant une solution concentrée de NaOH (10 M), puis on agite la solution résultante pendant 1 heure à 300 tr m^{-1} pour solubiliser et dissoudre les NP de TiO_2, **(2)** la solution est transférée dans un réacteur discontinu en acier inoxydable fermé et un traitement thermique est appliqué à 130 °C dans des conditions de pression autogéniques dans un four pendant 48h résultant à la croissance de nanofeuillets stratifiées, suivi de **(3)** une étape de rinçage consécutif à l'eau distillée et au HCl dilué (1 M) induisant la courbure et l'enroulement des nanofeuillets en nanotubes, **(4)** les nanotubes de titanates sont séchés à 110 ° C pendant 10 h et enfin **(5)** une dernière étape de calcination a lieu pour cristalliser les TiO_2 NT formés à 380 °C pendant 2h avec une rampe de 5 °C/min.

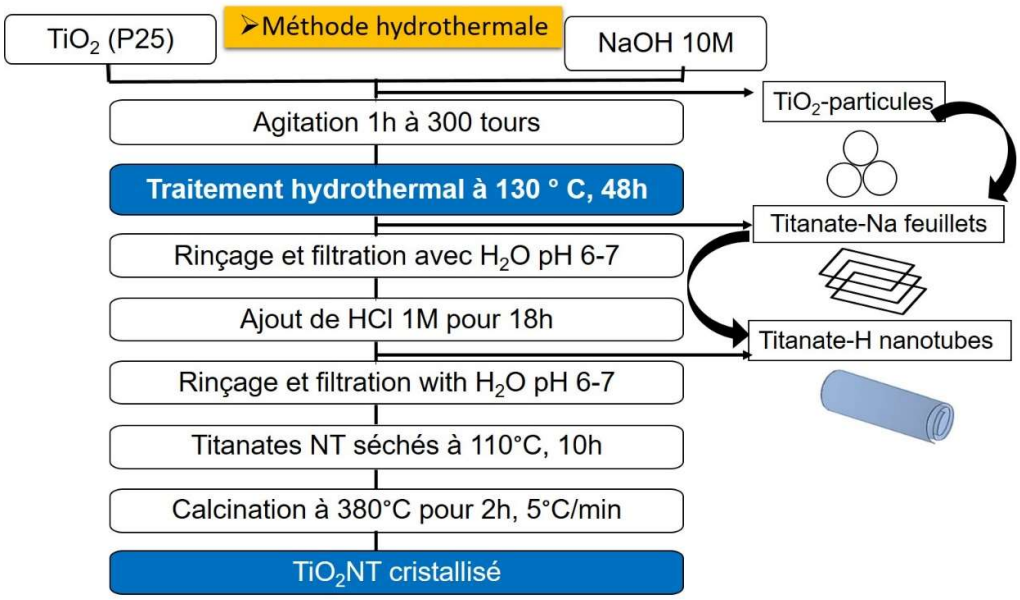

Figure 14. Méthode de synthèse hydrothermale de Kasuga (15).

Le protocole utilisé pour synthétiser les composites TiO_2-gC_3N_4 a déjà été présenté au **chapitre 3**, **section B.1.1**. Ici, le même protocole a été réalisé uniquement en remplaçant TiO_2 (P25) par TiO_2(NT) au cours de la réaction de polycondensation de g-C_3N_4. De la même manière, le modèle appliqué pour le calcul de la teneur en g-C_3N_4 dans les composites TiO_2(NTs)-gC_3N_4 est identique à celui déjà utilisé pour les composites TiO_2 (P25)-gC_3N_4 (du **chapitre 3, section B.2.1.1.a**).

B) Performances photocatalytiques

Les colonnes bleues représentent les composites de criblage et les références Au/TiO_2 550 °C et $Au/g\text{-}C_3N_4$ (**Fig. 15**). On peut observer que la référence Au/TiO_2 550 °C est l'échantillon le plus actif (conduisant à 638 µmol h^{-1} g_{cat}^{-1} de production de H_2), et que l'activité la plus basse est observée avec $Au/g\text{-}C_3N_4$ (conduisant à 41 µmol H_2 h^{-1} g_{cat}^{-1}) par rapport aux trois composites de criblage. Pour les proportions de criblage, une composition de 76-24, 48-52, 26-74 a donné respectivement 66, 266 et 140 µmol H_2 h^{-1} g_{cat}^{-1}. Malgré les faibles vitesses massiques de production en H_2 obtenus avec les trois composites, on peut noter que la proportion optimale trouvée avec $Au/TiO_2\text{-}gC_3N_4$ est (50-50), qui présente le rendement en H_2 le plus élevé par rapport à ses homologues.

En ce qui concerne le mélange physique $Au/TiO_2\text{-}gC_3N_4$ (mélange entre 0,3% en masse Au/TiO_2(NT) 550C et 0,3% en masse $Au/g\text{-}C_3N_4$) (colonnes violettes) avec les compositions à proportions équivalentes (76-24, 48-52, 26-74), ils présentent une tendance de décroissance proportionnelle pour la production de H_2, donnant respectivement 518, 367, 160 µmol h^{-1} g_{cat}^{-1}. On suppose que c'est le résultat de l'effet de dilution lors de l'augmentation de la teneur en $g\text{-}C_3N_4$. On peut observer la supériorité d'activité des mélanges physiques sur les composites, ce qui signifie que dans ce cas, les composites ne présentent aucun effet bénéfique en photocatalyse.

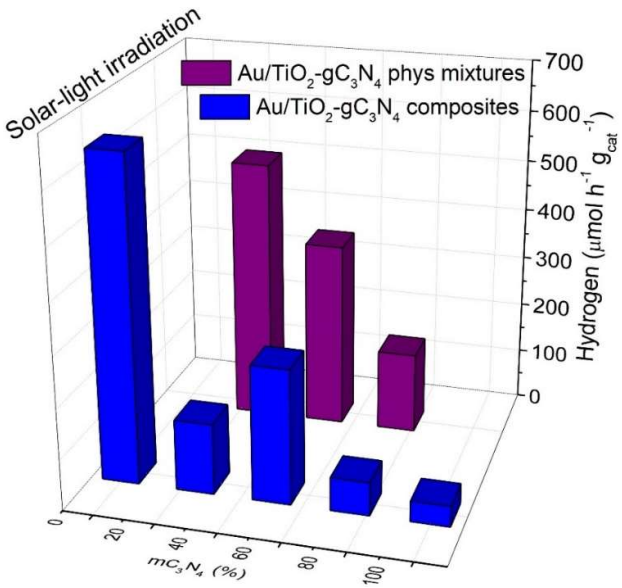

Figure 15. Vitesse moyenne de formation d'hydrogène par heure et par masse avec 1% en volume de TEOA pour les composites de criblage $Au/TiO_2\text{-}gC_3N_4$ et pour les références. De plus, des mélanges physiques équivalents de même composition ont été ajoutés à des fins de comparaison.

Pour la production photocatalytique de H_2, les échantillons composites $Au/TiO_2\text{-}gC_3N_4$ (97,5-2,5) et de référence Au/TiO_2 550 °C (**Fig. 16**) donnent respectivement 383 et 638 µmol h^{-1} g_{cat}^{-1} de H_2. Ce résultat montre que le nanocomposite ternaire n'a apporté aucune amélioration d'activité par rapport à la référence. L'échantillon correspondant au mélange physique montre une production de H_2 photocatalytique très similaire par rapport au composite environ 392 µmol H_2 h^{-1} g_{cat}^{-1}, démontrant qu'aucune augmentation de l'activité n'a été obtenue.

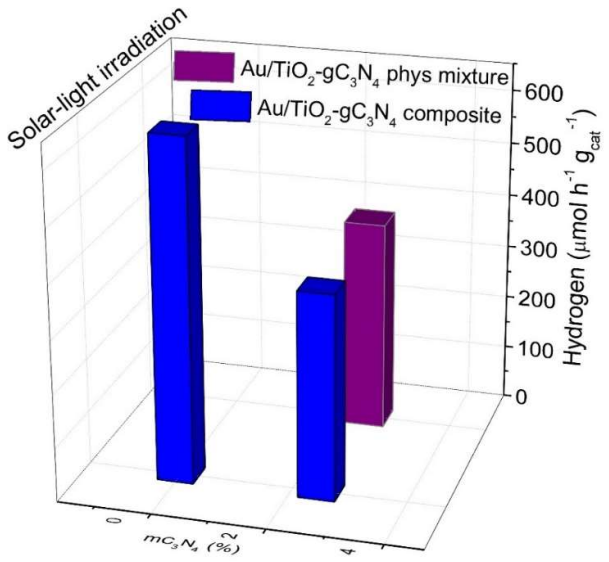

Figure 16. Vitesse moyenne de formation d'hydrogène par heure et par masse 1% en volume de TEOA pour le composite Au/TiO_2-gC_3N_4 (97,5-2,5) et pour une référence. De plus, le mélange physique avec une composition équivalent à été ajouté à des fins de comparaison.

C) Performances catalytiques

Dans le détail, les tests catalytiques sont effectués dans un réacteur à flux fixe (de 10 mm de diamètre interne) entièrement automatisé (CETRIB SARL, Andlau, France) avec 26 mg de catalyseur et placé dans la zone isotherme d'un four cylindrique (**Fig. 17**). Le mélange gazeux équilibré dans l'He, c'est-à-dire 1% CO / 1% O_2 pour l'oxydation du CO, a été introduit à un débit total de 100 mL min^{-1} (1 atm, GHSV ~ 15 000 h^{-1}). Le composite est chauffé à 1 °C min^{-1} de 20 à 300 °C puis refroidi à la même vitesse. La conversion du CO est déterminée sur la base d'une analyse en ligne par chromatographe en phase gazeuse compacte (Interscience, Belgique), à l'aide d'un étalonnage externe.

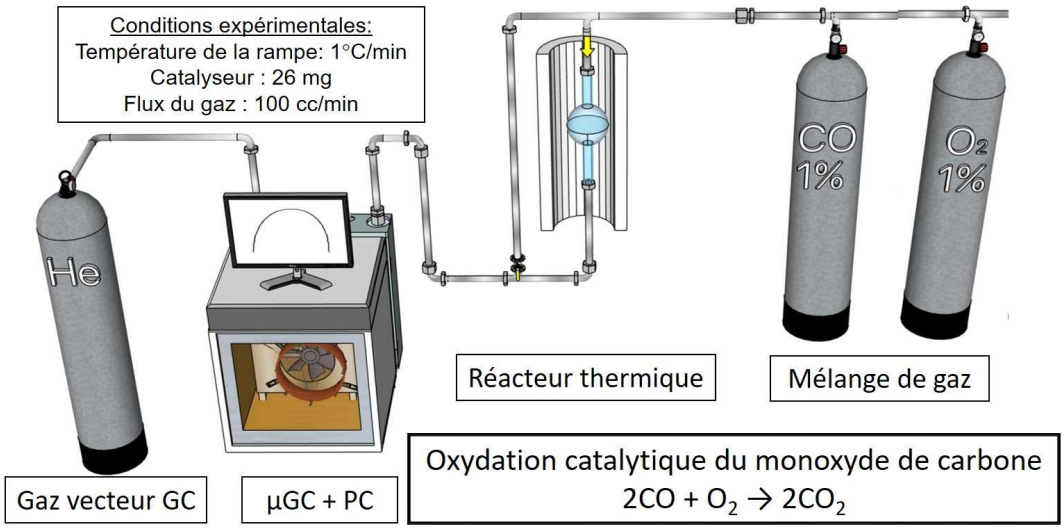

Figure 17. Configuration catalytique et ses composants, montrant l'oxydation du CO. Conçu avec Sketchup ©.

D'après les valeurs de conversion du CO (**Fig. 18**) dans la réaction d'oxydation du CO pur, on peut noter que la référence Au/g-C_3N_4 et le composite Au/TiO_2-gC_3N_4 (26-74) riche en C_3N_4 présentent une valeur très faible. Moins de 8% de CO est converti à 330 °C. Ce type de résultat a déjà été rapporté en l'absence de groupes de surface oxygènes (cas du g-C_3N_4), et l'activité catalytique est donc négligeable. La référence Au/TiO_2 et le composite Au/TiO_2-gC_3N_4 (97,5-2,5) montrent une activité plus élevée. Ils présentent tous deux une température de reaction <225 ° C avec une conversion maximale du CO de 39 et 64%, respectivement, à 330 ° C. Ce dernier composite, le plus actif est riche en TiO_2. Il est bien connu que ces supports sont "actifs" [16] car ils contiennent des groupes de surface oxygènes, qui restent exposés au milieu réactionnel et peuvent fonctionner en synergie avec les NP Au pour assurer l'activation de l'oxygène [17]. En outre, le composite Au/TiO_2-gC_3N_4 (97,5-2,5) montre la meilleure activité, 1,5 fois supérieure à celle de la référence Au/TiO_2 550 ° C et 20 fois supérieure à celle de Au/g-C_3N_4, ce qui témoigne d'un effet synergique.

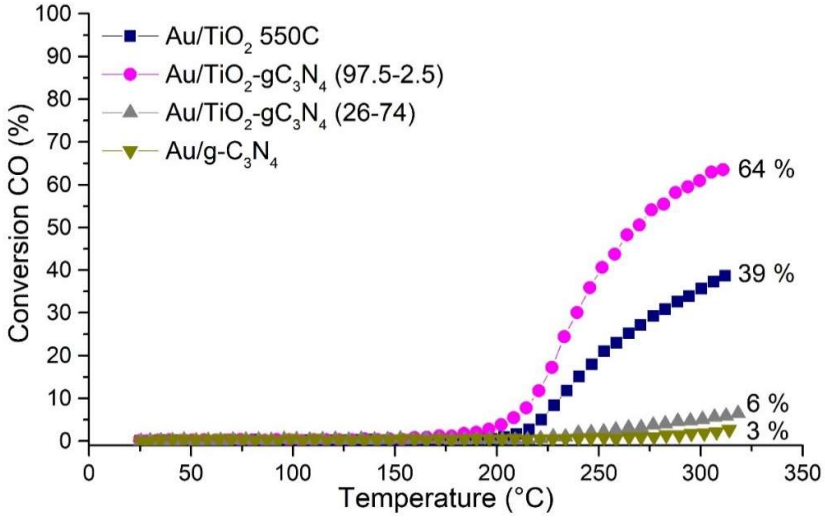

Figure 18. Activité catalytique des NP Au supportées sur g-C_3N_4, TiO_2, TiO_2-gC_3N_4 (97,5-2,5) et TiO_2-gC_3N_4 (26-74) en fonction de la température.

Caractérisations détaillés des matériaux binaires et ternaires

Pour les caractérisations approfondies et les discussions associes, veuillez consulter la partie anglaise de ce manuscrit.

Conclusions générales

Dans le **chapitre 1**, l'analyse de la littérature a confirmé l'importance de la transformation de l'énergie solaire en énergie chimique au moyen de combustibles solaires, par exemple l'H_2 en tant que vecteur énergétique dans le contexte de la crise énergétique actuelle. Un état de l'art récent des technologies de production d'hydrogène actuellement utilisées dans la société et des technologies en cours de recherche et développement a été abordé, en se concentrant sur les processus renouvelables tels que la séparation de l'eau, qui est le principal modèle de réaction pour l'évaluation des

matériaux élaborés dans le cadre de cette thèse. Ce premier chapitre comprend également un aperçu des propriétés physico-chimiques et des modifications des matériaux utilisés pour cette thèse, à savoir les NP de g-C_3N_4, TiO_2 et Au.

Dans le **chapitre 2**, traitant de l'influence de l'atmosphère de synthèse de g-C_3N_4, il a été souligné que le composite binaire **Au/g-C_3N_4-NH_3** produisait la plus grande quantité de H_2 (environ **324 µmol h^{-1} g_{cat}^{-1}** sous irradiation **solaire**) et **26 µmol h^{-1} g_{cat}^{-1}** sous irradiation **visible**) avec l'aide de TEOA (1% en volume) en tant qu'agent sacrificiel. La supériorité de ce composite binaire parmi les autres repose sur plusieurs aspects. Ce composite présentait la plus grande taille de cristallites de g-C_3N_4, l'empilement de couches le plus épais, la présence d'un angle d'inclinaison des feuillets déformés de C_3N_4, le plus grand S_{BET}, la plus grande V_{pore}, même si la taille des pores était très similaire, la distribution monomodale la plus étroite la meilleure couverture de surface et la taille moyenne la plus petite de NPs Au (environ 3,2 ± 1,1 nm), permettant un contact plus intime et une qualité d'interface supérieure entre le NPs Au et le support g-C_3N_4 par rapport à ses homologues g-C_3N_4.

Outre les informations détaillées sur la caractérisation des matériaux et la corrélation structure-activité mentionnées au chapitre 2, un calcul supplémentaire du rapport entre les phases C_3N_4 à base de tri-s-triazine et de s-triazine a été utilisé pour la première fois afin de souligner l'effet des différentes atmosphères de flux gazeux continu pendant la synthèse.

Du **chapitre 3**, axé sur Au/TiO_2(P25)-gC_3N_4-atm (avec atm = Air, NH_3), **Au/TiO_2(P25)-gC_3N_4 (95-5)-Air** il a été montre que e composite ternaire a produit la plus grande quantité de H_2 (environ **1839 µmol h^{-1} g_{cat}^{-1}** sous irradiation solaire et **419 µmol h^{-1} g_{cat}^{-1}** sous irradiation visible) avec l'aide de TEOA (1% en volume) en tant qu'agent sacrificiel. Cette activité accrue est probablement due à un léger décalage de l'absorption vers le rouge mettant en évidence optiquement la présence de g-C_3N_4 en plus de l'absorption caractéristique de Au/TiO_2(P25) et à la formation d'une nouvelle position d'énergie hybride VB max (indiquée par analyse UPS) entre les deux positions VB max des références correspondantes. De plus, la dynamique de charges photogénérées a été étudiée grâce aux mesures TRMC. Il a été montré qu'à une excitation laser pulsée de 360 nm, la densité la plus élevée de paires e^-/h^+ dissociées était observée, ainsi que le piégeage / délocalisation des électrons libres (après la génération) dans les systèmes π-aromatiques de g-C_3N_4, limitant ainsi davantage leur recombinaison par rapport aux références correspondantes. À 450 nm, il était également possible de mettre en évidence un effet de sensibilisation de TiO_2(P25) par le g-C_3N_4 avec injection des électrons de la CB de g-C_3N_4 dans la CB de TiO_2. Il faut également mentionner que l'on ne pouvait pas confirmer la présence de propriétés SPIE induites par les NPs Au.

Il faut souligner qu'une très faible quantité (1% v/v) de TEAO (agent sacrificiel) a été utilisée pour éviter la production de H_2 issue de sa transformation et donc pour prendre en compte en majorité le H_2 issu de la scission de l'eau. Cependant, il a été associé à une légère désactivation après le 2e cycle d'essai (**chapitres 2 et 3**), certainement en empoisonnant certains sites actifs du support par les produits de dégradation résultant de la dealkylation de TEOA.

Dans le **chapitre 4**, concernant l'impact de la morphologie du TiO_2, il a été montré que le composite ternaire Au/TiO_2 (NT)-gC_3N_4 (97,5-2,5)-Air convertissait la plus grande quantité de CO (64%) (dans le cadre de la réaction PROX). Cela pourrait être attribué à la coexistence de différentes espèces de surface oxygènes tirant parti de l'interface TiO_2-gC_3N_4 à une faible teneur en g-C_3N_4.

D'après les tests de production de H_2 sous irradiation solaire, il convient de souligner qu'aucun des composites Au/TiO_2(NT)-gC_3N_4 n'a conduit à une activité accrue par rapport aux références au TiO_2(NT). L'association de TiO_2(NT) avec le g-C_3N_4 a eu des effets néfastes. On a supposé que cette activité réduite était principalement due à deux phénomènes **(1)** agglomération de TiO_2 NT et rupture partielle lors de la synthèse de g-C_3N_4 à 550 ° C et **(2)** couverture et blocage de la porosité de TiO_2 NT par des feuilles de g-C_3N_4 à l'intérieur des tubes et entre les nanotubes enchevêtrés. Une architecture schématique a été proposée dans la **Figure 19**.

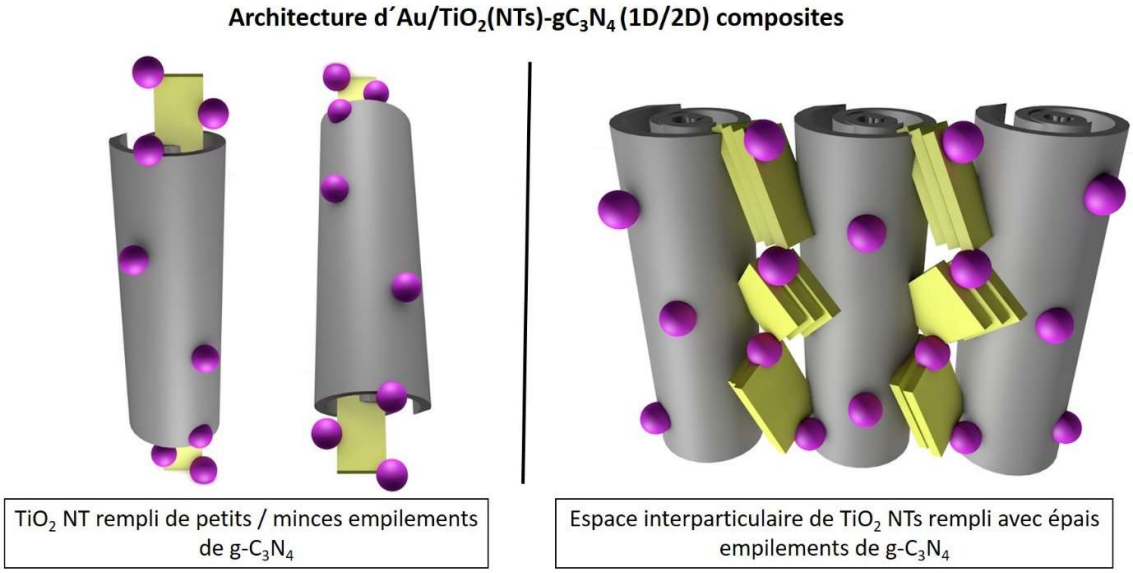

Figure 19. Schéma spéculatif des possibilités architecturales Au/TiO_2(NTs)-gC_3N_4 (1D/2D). Conçu avec Sketchup ®.

Cependant, l'interface TiO_2(NT)-gC_3N_4 a entraîné une distribution monomodale plus étroite avec une taille moyenne de NPs en Au minimale la plus faible (environ 3,1 ± 0,6 nm). Une analyse XPS montrant un décalage de l'énergie de liaison de Au $4f_{7/2}$ montre un transfert de charge du support vers les NP de Au. Les rapports atomiques Au/Ti et Au/C ont également confirmé la densité de surface plus élevée de NP Au sur les surfaces de g-C_3N_4. Cette caractéristique a également été confirmée par l'observation TEM.

Perspectives

Il ressort de cette étude que la composition optimale du TiO_2(P25)-gC_3N_4 (95-5) et la qualité de l'interface peuvent augmenter de manière significative l'activité photocatalytique pour la production de H_2 sous activation solaire et visible à partir de l'eau en présence d'une très faible quantité d'agent sacrificiel. Nous voulions ensuite bénéficier davantage de la surface du TiO_2 en utilisant des nanotubes de TiO_2 à haute surface spécifique. Malheureusement, nous n'avons pas réussi à élaborer une interface TiO_2(NTs)-gC_3N_4 de haute qualité. Le défi consiste ici à obtenir cette interface de haute qualité entre un semi-conducteur 1D et 2D. Par conséquent, des stratégies de synthèse alternatives doivent être trouvées dans ce but.

Les nanotubes de TiO_2 ont été obtenus par la méthode de synthèse hydrothermale, décrite au **chapitre 4**. Cependant, l'agglomération et l'enchevêtrement de nanotubes en raison d'une énergie de surface élevée, ainsi que la rupture des tubes, compliquent la formation d'interfaces d'hétérojonctions efficaces avec le g-C_3N_4 ainsi que le dépôt de qualité de NPs Au. Une solution pour surmonter cette limitation importante pourrait consister à utiliser des agents dispersants (polymères, micelles, etc.) pour éviter l'agglomération et l'enchevêtrement entre les nanotubes afin de fournir une surface plus exposée accessible aux espèces chimiques secondaires en phase liquide. Néanmoins, les agents dispersants choisis ne doivent réagir avec aucun précurseur, ni avec aucune atmosphère utilisée.

On pourrait également imaginer, dans la méthodologie décrite en deux étapes pour l'élaboration des composites binaires TiO_2-gC_3N_4, que l'imprégnation en phase liquide du précurseur de g-C_3N_4 sur les TiO_2 NT sous forme synthétisée ait lieu sous sonication, suivie par une lyophilisation (afin d'éviter l'agglomération de nanotubes pendant l'étape de séchage) avant la synthèse à l'état solide de g-C_3N_4.

Une autre stratégie visant à obtenir une meilleure interface TiO_2(NT)-gC_3N_4 pourrait être axée sur l'addition de g-C_3N_4 déjà synthétisé au cours de la synthèse hydrothermale de TiO_2 afin d'obtenir une méthodologie de synthèse one-pot (méthode plus simple) avec probablement différents types d'interfaces à hétérojonction entre deux SC.

Suite aux résultats très positifs (sur H_2) obtenus pour les composites binaire Au/g-C_3N_4-NH_3 et ternaire Au/TiO_2(P25)-gC_3N_4 (95-5)-Air, on peut **déposer des systèmes bimétalliques** en couplant les nanoparticules Au avec d'autres métaux intéressants (Au/Pt, Au/Cu, etc.) sur les mêmes supports (g-C_3N_4-NH_3 et TiO_2(P25)-gC_3N_4 (95-5)-Air) afin d'accroître leurs performances. Le Pt peut être une suggestion potentielle car il s'agit du métal le plus actif pour les applications (photo) catalytiques et le Cu car il présente une longueur d'onde de résonance plasmonique (λ = 485 nm) différente d'Au mais toujours dans le visible. Plusieurs études paramétriques peuvent être menées, par exemple modifier les proportions des métaux, contrôler la morphologie du système monométallique (triangles, pyramides, barres, etc.) et du système bimétallique (intégré, coquille principale, etc.).

D'un point de vue mécanistique, afin de comprendre mieux **la séparation des charges et les mécanismes de cinétique de transfert**, certaines expériences complémentaires peuvent être réalisées: **(1)** spectroscopie à résolution temporelle (mode d'absorption ou d'émission); **(2)** analyse électrochimique telle que la spectroscopie

d'impédance ou les mesures de photocourant; **(3)** photoluminescence (transitoire ou stable) **(4)** spectroscopie pompe-sonde.

Pour obtenir plus de **détails de l'analyse UPS**, une référence interne (par exemple en ajoutant des traces d'or) avec un niveau de Fermi connu peut être ajoutée à chaque analyse d'échantillon afin de pouvoir calculer le niveau de Fermi spécifique et par conséquent de proposer une structure de bande plus précise pour les photocatalyseurs composites.

La conception du **réacteur photocatalytique** devrait également être grandement améliorée. Le réacteur photocatalytique utilisé possède une position de lampe immergée centrale, rendant impossible l'utilisation de filtres optiques du commerce et le test de la contribution photonique à différentes longueurs d'onde pour le calcul des rendements quantiques correspondants.

Références

[1] M.K. Hubbert, Energy from Fossil Fuels., Science. 109 (1949) 103–9. doi:10.1126/science.109.2823.103.

[2] M. Grätzel, Photoelectrochemical cells, Nature. 414 (2001) 338–344. doi:10.1038/35104607.

[3] The Future of Solar Energy | MIT Energy Initiative, MIT Energy Initiat. (2015). http://energy.mit.edu/publication/future-solar-energy/ (accessed May 10, 2018).

[4] C.A. Grimes, O.K. Varghese, S. Ranjan, Light, Water, Hydrogen. The solar generation of hydrogen by water photoelectrolysis, Springer US, Boston, MA, 2008. doi:10.1007/978-0-387-68238-9.

[5] S. Oberthür, H. Ott, The Kyoto Protocol : international climate policy for the 21st century, Springer, 1999. https://books.google.fr/books/about/The_Kyoto_Protocol.html?id=-qp7Wt9GvccC&redir_esc=y (accessed May 10, 2018).

[6] I.E.A. (IEA), Key World Energy Statistics 2016, Stat. Rep. (2016) 24, 80. https://www.iea.org/publications/freepublications/publication/key-world-energy-statistics.html (accessed December 28, 2016).

[7] R. Perez, M. Perez, A Fundamental Look at Supply Side Energy Reserves for the Planet, Int. Energy Agency Sol. Heat. Cool. Program. Sol. Updat. 50 (2009) 4–5. https://www.iea-shc.org/data/sites/1/publications/2015-11-A-Fundamental-Look-at-Supply-Side-Energy-Reserves-for-the-Planet.pdf (accessed May 11, 2018).

[8] P. Kruger, Electric power required in the world by 2050 with hydrogen fuel production—Revised, Int. J. Hydrogen Energy. 30 (2005) 1515–1522. doi:10.1016/J.IJHYDENE.2005.04.003.

[9] D.G. Nocera, The Artificial Leaf, Acc. Chem. Res. 45 (2012) 767–776. doi:10.1021/ar2003013.

[10] C. Marchal, T. Cottineau, M.G. Méndez-Medrano, C. Colbeau-Justin, V. Caps, V. Keller, Au/TiO_2-gC_3N_4 Nanocomposites for Enhanced Photocatalytic H_2 Production from Water under Visible Light Irradiation with Very Low Quantities of Sacrificial Agents, Adv. Energy Mater. (2018) 1702142. doi:10.1002/aenm.201702142.

[11] Nicanite Graphitic Carbon Nitride - Nanodiamonds - additives for thermal management and wear resistant nanocomposites, coatings and plating, Carbodeon. (n.d.).

http://www.carbodeon.com/index.php/en/carbodeon-news/nicanite-graphitic-carbon-nitride (accessed May 14, 2018).

[12] P. Jiménez, C. Marchal, T. Cottineau, V. Caps, V. Keller, Influence of gas atmosphere during synthesis of g-C_3N_4 for enhanced photocatalytic H_2 production from water on Au/g-C_3N_4 composites, J. Mater. Chem. A. (2019). doi:10.1039/C9TA01734H.

[13] F. Vigneron, A. Piquet, W. Baaziz, P. Ronot, A. Boos, I. Janowska, C. Pham-Huu, C. Petit, V. Caps, Hydrophobic gold catalysts: From synthesis on passivated silica to synthesis on few-layer graphene, Catal. Today. 235 (2014) 90–97. doi:10.1016/J.CATTOD.2014.04.016.

[14] Y. Pellegrin, F. Odobel, Sacrificial electron donor reagents for solar fuel production, Comptes Rendus Chim. (2016). doi:10.1016/j.crci.2015.11.026.

[15] Tomoko Kasuga, Masayoshi Hiramatsu, Akihiko Hoson, and Toru Sekino, K. Niihara, Formation of Titanium Oxide Nanotube, Langmuir. (1998) 3160–3163. doi:10.1021/LA9713816.

[16] M.M. Schubert, S. Hackenberg, A.C. van Veen, M. Muhler, V. Plzak, R.J. Behm, CO Oxidation over Supported Gold Catalysts—"Inert" and "Active" Support Materials and Their Role for the Oxygen Supply during Reaction, J. Catal. 197 (2001) 113–122. doi:10.1006/JCAT.2000.3069.

[17] G.C. Bond, D.T. Thompson, Gold-catalysed oxidation of carbon monoxide, Gold Bull. 33 (2000) 41–50. doi:10.1007/BF03216579

JIMENEZ-CALVO Pablo

Synthèses, caractérisations et performances de matériaux à base de g-C_3N_4 décorés avec des nanoparticules d´Au pour des applications (photo) catalytiques

Résumé

À ce jour, l'humanité est confrontée simultanément à une crise énergétique et environnementale due principalement à deux facteurs: la croissance démographique et la dépendance aux combustibles fossiles. C'est pourquoi l'urgence d'utiliser des sources d'énergie renouvelables, comme l'énergie solaire est une, solution potentielle. A ce titre, la production d'H_2 décarboné par dissociation solaire de l'eau est une voie prometteuse. Néanmoins, pour atteindre l'objectif mentionné, il faut trouver un système photocatalytique (semi-conducteurs, SCs) idéal, qui nécessite quatre caractéristiques majeures: **(1)** une bonne capacité d'absorption de la lumière visible **(2)** des positions adéquates de BV et BC des SCs par rapport aux potentiels d'oxydation de l'eau et de réduction du proton **(3)** une utilisation efficace des photons absorbés et charges générées et **(4) une** bonne stabilité dans le temps. À cette fin, cette thèse contribue à la conception et à l'optimisation de trois matériaux innovants: les composites Au/g-C_3N_4, Au/TiO_2 (P25)-gC_3N_4, et Au/TiO_2 (NTs)-gC_3N_4 dont l'activité photocatalytique a été corrélé avec les propriétés physico-chimiques pour comprendre leurs performances photocatalytiques de production d'H_2 sous irradiation solaire et visible. De manière annexe, certains de ces matériaux se sont également montrés performants pour les conversions du CO. Pour mettre en évidence l'efficacité des composites préparés, des études comparatives ont été testées en utilisant des références commerciales, pertinentes et les mélanges physiques correspondant.

Mots clés : Energie solaire, (photo)catalyse, H_2, CO conversion, Au/g-C_3N_4, Au/TiO_2-gC_3N_4

Abstract

To date, mankind is facing an energy and environmental crisis simultaneously due to mainly two factors: growth population and the dependency on fossil fuels. For this reason, the urgency of using renewables sources, *e.g.,* solar energy, is a potential solution. For example, non-carbon based H_2 production from solar light driven water photodissociation is a promising approach. Nevertheless, to target the mentioned objective, an ideal photocatalytic system (semiconductors, SCs) has to meet four main features: **(1)** capacity of absorption of visible-light **(2)** suitable VB and CB positions of SCs to undergo the two half reactions of water splitting **(3)** efficient use of absorbed photons and generated charges and **(4)** good stability over time. For this purpose, this thesis contributes to the design and optimization of three innovative materials: Au/g-C_3N_4, Au/TiO_2 (P25)-gC_3N_4, and Au/TiO_2 (NTs)-gC_3N_4 composites. Their photocatalytic activities were correlated with their physico-chemical properties. In addition some of these composites also exhibited interesting CO conversion yields. To highlight the efficiency on the as-prepared composites, comparative studies were tested using commercial, pertinent references, and physical mixtures homologs.

Keywords: Solar energy, (photo) catalysis, H_2, CO conversion, Au/g-C_3N_4, Au/TiO_2-gC_3N_4